ICFA

The 60th ICFA Advanced Beam Dynamics Workshop

FLS2018

March 5-9, 2018
Shanghai Institute of Applied Physics

International Organizing Committee:

Yong Ho Chin, KEK (IOC Chair)
Zhentang Zhao, SINAP (Workshop Chair)
Ralph Assmann, DESY
Hans Braun, PSI
John Byrd, ANL
Marie-Emmanuelle Couprie, SOLEIL
Zhirong Huang, SLAC
Chan Joshi, UCLA
Heung-Sik Kang, PAL
Kwang-Je Kim, ANL
Peter Kuske, HZB
Wei Lu, Tsinghua University Beijing
George Neil, Jefferson Lab
Hideaki Ohgaki, Kyoto University
Jean-Luc Revol, ESRF
David Robin, LBNL
Michele Svandrlik, Elettra and FERMI
Hitoshi Tanaka, SPring-8
Nikolay Vinokurov, BINP
Richard Walker, Diamond
Jiuqing Wang, IHEP
Hans Weise, DESY

Topics:

- Linac-Based Light Sources
- Ring-Based Light Sources
- Compact Light Sources
- Key Technologies

SINAP 中国科学院上海应用物理研究所
Shanghai Institute of Applied Physics, Chinese Academy of Sciences

FOREWORD

60th ICFA ADVANCED BEAM DYNAMICS WORKSHOP
FLS2018
Shanghai, People's Republic of China, March 5-9, 2018

The 60th ICFA Advanced Beam Dynamics Workshop on Future Light Sources, FLS2018, was held on 5-9 March, 2018 at the Hotel Equatorial, Shanghai, China. There were 148 participants representing institutions from Asia, Europe and America. After a lapse of 6 years, FLS2018 restarts the Future Light Sources series.

The scientific program of the workshop was decided by the International Organizing Committee, chaired by Yong Ho Chin (KEK), and the conference was chaired by Zhentang Zhao (SINAP). The workshop was hosted by SINAP - the Shanghai Institute of Applied Physics, CAS. Its Local Organizing Committee was chaired by Zhengchi Hou (SINAP). Eighty-six talks were presented during the plenary and parallel working group (WG) sessions, including 8 plenary, 45 invited and 33 contributed talks. They covered a wide spectrum of topics on accelerator and laser based light sources and related key technologies during the past six years since the last FLS workshop gathering at JLab, USA, in 2012. The talks were well researched, highly informative and well received by the audience.

The four working groups were themed as follows: WG1: Linac based light sources, convened by T. Raubenheimer (SLAC), L. Giannessi (Elettra) and W. Decking (DESY); WG2: Ring based light sources, convened by R. Walker (DLS), Y. Li (BNL) and Q. Qin (IHEP); WG3: Compact light sources, convened by Chunguang Jing (Euclidtechlabs), M.E. Couprie (SOLEIL) and H. Zen (Kyoto University), and WG4: Key technologies, convened by John Byrd (ANL), Joachim Pflueger (European XFEL) and Y.B. Leng (SINAP). The four topics generated heated interest in all breakout sessions and the WG conveners showed strong leadership to engage all participants in the discussions.

The poster session was also a huge success with 38 posters presented. The detailed program and talks are available via the workshop website (https://indico.sinap.ac.cn/e/fls2018). The workshop proceedings are published at the JACoW site.

During the IOC meeting at FLS2018 it was decided to organize the next workshop (FLS2021) at PSI, in Switzerland.

Yong Ho Chin
FLS2018 IOC Chair

Zhentang Zhao
FLS2018 Workshop Chair

COMMITTEES

IOC Members

Name	Affiliation
Yong Ho Chin (IOC Chair)	KEK
Zhentang Zhao (Conference Chair)	SINAP
Jiuqing Wang	IHEP
Wei Lu	Tsinghua University Beijing
Hitoshi Tanaka	SPring-8
Hideaki Ohgaki	Kyoto University
Heung-Sik Kang	PAL
Zhirong Huang	SLAC
John Byrd	ANL
Kwang-Je Kim	ANL
George Neil	Jefferson Lab
David Robin	LBNL
Chan Joshi	UCLA
Richard Walker	Diamond
Peter Kuske	HZB
Hans Weise	DESY
Hans Braun	PSI
Marie-Emmanuelle Couprie	SOLEIL
Jean-Luc Revol	ESRF
Michele Svandrlik	Elettra and FERMI
Nikolay Vinokurov	BINP
Ralph Assmann	DESY

Local Organizing Committee (LOC)

Christine Petit-Jean-Genaz, CERN, Special Advisor to LOC,
Zhengchi Hou, SINAP, Chair
Lie Feng, SINAP, Presentation Manager
Chao Feng, SINAP, Poster Manager
Xin Han, SINAP, Registration Manager
Wenpeng Qi, SINAP, Industrial Exhibition Manager
Haojun Cai, SINAP, IT Manager
Ying Fan, SINAP, Lab Tour Manager

Editorial Board

Xin Han, SINAP
Christine Petit-Jean-Genaz, CERN
Maksim V. Kuzin, BINP SB RAS
Lu Li, IMP

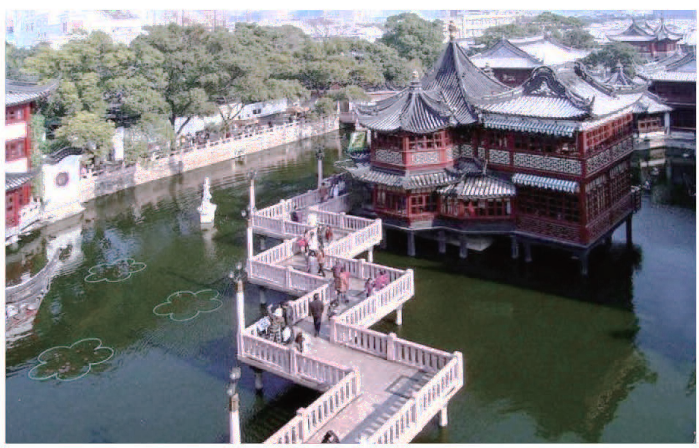

Contents

ISBN: 978-3-95450-206-6 doi:10.18429/JACoW-FLS2018-MOA2PL03

REVIEW OF NEW DEVELOPMENTS IN SUPERCONDUCTING UNDULATOR TECHNOLOGY AT THE APS*

J.D. Fuerst†, Y. Ivanyushenkov, Q. Hasse, M. Kasa, I. Kesgin, Y. Shiroyanagi, E. Gluskin,
Argonne National Laboratory, Argonne, IL, USA

Abstract

Superconducting undulator technology for storage ring light sources has evolved from proof of principle to the working insertion device level. Both planar and helical magnet topologies using NbTi superconductor have been successfully incorporated into functional devices operating in the Advanced Photon Source (APS) storage ring at liquid helium temperatures using cryocooler-based, zero-boil-off refrigeration systems. Development work on higher field magnets using Nb_3Sn superconductor is ongoing at the APS, as are concepts for FEL-specific magnets and cryostats for future light sources.

BACKGROUND – EXISTING DEVICES

The APS currently operates three SCUs in the storage ring. Two are nominally identical vertical gap planar devices with period length 1.8 cm and overall active length 1.1 m. These devices reside in Sectors 1 and 6. The third is a helically wound, circularly polarizing device located in Sector 7 with period length 3.15 cm and overall active length 1.2 m. Device parameters are listed in Table 1.

Table 1: Parameters for SCUs Installed at APS

Parameter	Value	
	Planar	**Helical**
Cryostat length [m]	2.06	1.85
Magnetic length [m]	1.1	1.2
Period [mm]	18	31.5
Magnetic gap [mm]	9.5	29 (diameter)
Beam chamber aperture [mm]	7.2	8(V) x 26(H)
Peak field [T]	0.97	0.42 (B_x=B_y)
K value	1.63	1.2 (K_x=K_y)

Additional details regarding the existing devices as well as a fourth planar device developed for LCLS R&D are provided in [1,2]. For details on magnetic performance see [3]. Table 2 lists the operational statistics for planar device SCU18-1 which has operated in Sector 1 of the APS storage ring since May 2015. Device performance has been highly reliable, with overall availability of 99.99%. Figures 1 and 2 show the devices installed in the APS storage ring.

*Work supported by the U.S. Department of Energy, Office of Science under Contract No. DE-AC02-06CH11357
† fuerst@anl.gov

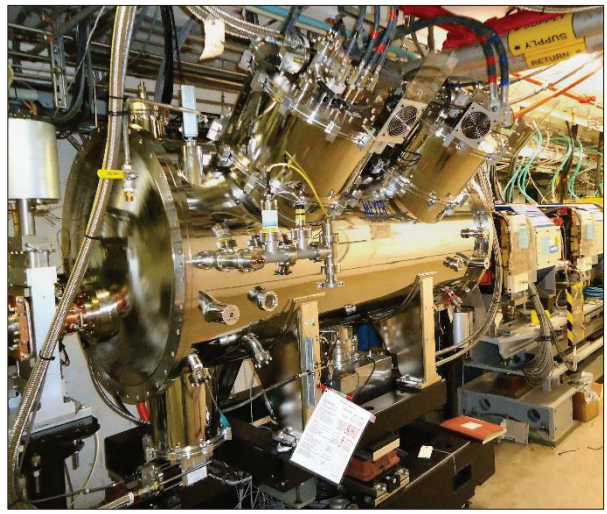

Figure 1: Planar SCU installed in the APS ring, Sector 1.

Figure 2: Helical SCU installed in Sector 7.

Table 2: Operating Statistics for SCU18-1

Year	SCU hours operating	Availability %
2015	3059	99.997
2016	4585	99.990
2017	4818	99.984

ISBN: 978-3-95450-206-6 doi:10.18429/JACoW-FLS2018-MOA2PL03

NEW MAGNET DESIGNS

Planar Polarizing

The APS continues to explore the feasibility of alternative superconductors for SCU magnets such as Nb_3Sn although this activity is in the very early stages. Recent developments in planar magnet mechanical design have focussed on minimizing phase error via tight machining tolerances, gap control, and overall magnet straightness for magnetic lengths beyond 1.5 m. As part of the APS Upgrade a new planar magnet design based on 1.8 m magnetic length is in development. Target phase error will be 2-3 degrees rms with period length 16.5 mm and target field strength approximately 1.1 T. Several features of the existing 1.1-meter magnets will be retained, including: conductor winding technique, liquid helium cooling strategy, gap separation mechanism, control of magnet straightness, and beam vacuum chamber support with thermal isolation from the 4.2 K magnets. Verifying the extension of these techniques to longer magnetic lengths is a crucial element of our development activity. Figure 3 shows a CAD model of a 1.8-meter planar magnet pair.

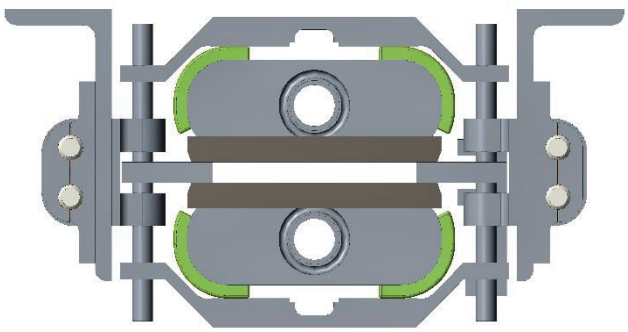

Figure 3: Cross-section of planar magnet pair showing magnet cores with helium cooling passages, pole pieces, gap separator system, and magnet support system. Superconducting wire is not shown.

Circular Polarizing

The helical SCU presently in operation was designed to be compatible with the APS storage ring. Future development of this magnet type will likely focus on free electron laser (FEL) applications where a very small "magnetic gap" is allowed and the subsequent magnetic field is large. These magnets would be installed in a multi-undulator array as opposed to individually as in a storage ring. In that regard their design can be tailored to provide an optimal magnetic length for field tapering. The superconductor in the existing helical SCU is wound continuously into a double-helical "2-lead" rectangular-thread groove machined into the magnet core. Magnet performance is strongly dependent on the machining accuracy of the groove depth and pitch. Future devices may benefit from precision thread grinding, perhaps as a finishing step following the multi-axis CNC milling process. Figure 4 shows a helical magnet core wound with superconducting wire and prepared for epoxy impregnation.

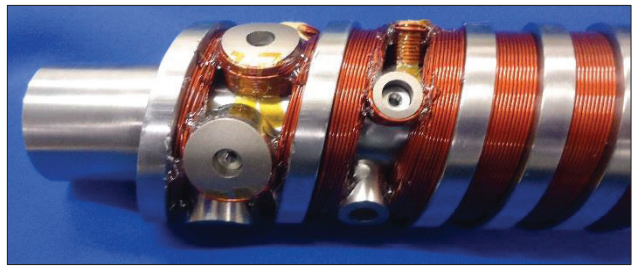

Figure 4: Closeup of the helical SCU wound core showing conductor end turn-around detail.

Universal Polarizing

Development work continues on a universal superconducting undulator capable of arbitrary polarization. At the APS this work takes the acronym SCAPE (Superconducting Arbitrarily Polarizing Emitter) and consists of two orthogonal planar magnet pairs with roughly triangular cross-section, offset longitudinally by ¼-period. The four magnet cores are arranged around an X-shaped beam vacuum chamber. The chamber operates at a higher temperature than the cores and is thermally isolated from them. Two views of the SCAPE geometry are shown in Figs. 5 and 6 while Fig. 7 shows a prototype SCAPE magnet core after winding with NbTi superconductor.

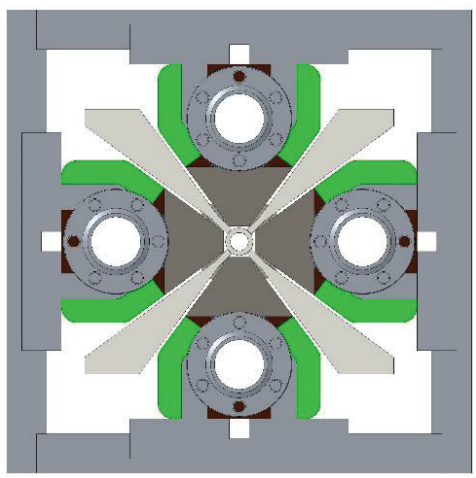

Figure 5: End view of the SCAPE SCU concept.

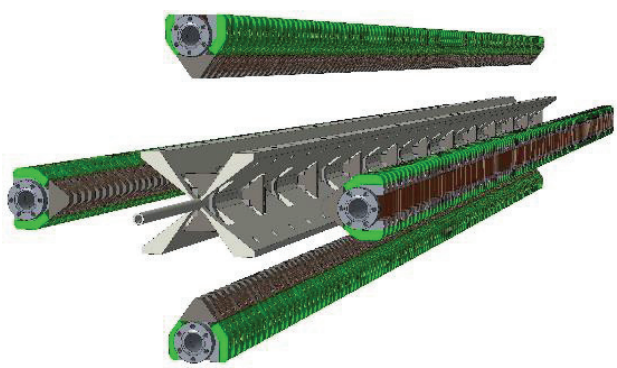

Figure 6: Exploded view of the SCAPE magnet/vacuum chamber concept.

ISBN: 978-3-95450-206-6 doi:10.18429/JACoW-FLS2018-MOA2PL03

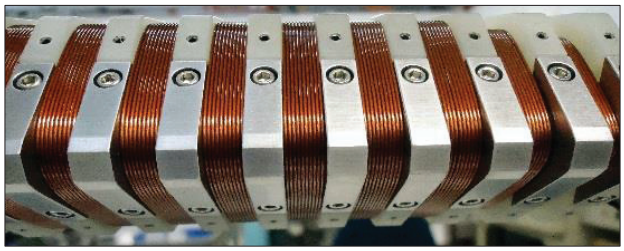

Figure 7: (top) Close-up view of a prototype SCAPE core after winding with superconducting wire.

This magnet technology has application for both storage ring and FEL light sources, providing planar horizontal through circular to planar vertical (as well as intermediate elliptical) polarizations. As in the storage ring-based planar devices, the SCAPE vacuum chamber can operate at elevated temperature relative to the magnets in order to intercept both electron- and photon-based heating and maintain a reasonable 4.2 K heat load to the magnets.

Correctors

Existing SCUs use both internally wound and externally mounted magnets to perform first and second integral correction. Future multi-magnet SCUs will require either dipole chicanes for phase shifting or (for storage ring applications with multiple straight section end stations) canting magnets between the undulator magnets. These devices may be superconducting or cryogenically cooled/normal conducting depending on magnet current requirements and installation complexity. Figure 8 shows a closeup of the helical SCU dipole correctors.

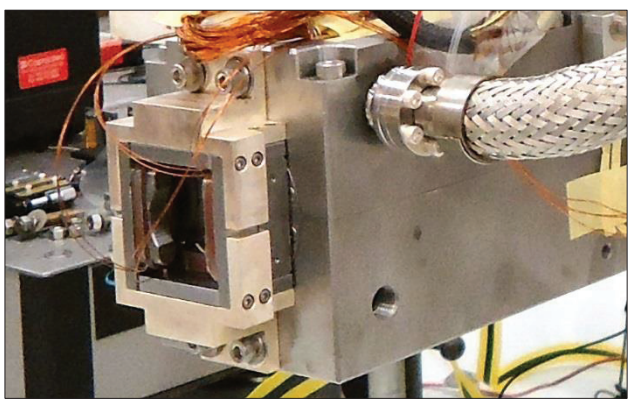

Figure 8: Conduction-cooled helical SCU superconducting horizontal and vertical dipole correction package mounted to the end of the main magnet.

NEW CRYOSTAT DESIGNS

Storage Ring-Specific

Cooling Systems The existing APS SCU cryostat design descends from liquid helium-based, cryocooler-cooled insertion devices developed at the Budker Institute for Nuclear Physics (BINP), Novosibirsk [4]. The relatively sparse and isolated nature of today's storage-ring-based SCU installations argues in favour of individually cooled units (in contrast to a central helium refrigeration plant plus cryogenic distribution system) in terms of capital cost. Careful management of cryogenic heat leak permits use of a reasonable number of 1.5 W, 4.2 K cryocoolers while maintaining zero-boil-off operation. Future plans include pursuit of alternative cryocooler technologies such as a new 2-W class of 4.2 K pulse-tube cryocoolers. Cryogen-free designs present an attractive option by eliminating liquid helium and the associated pressure system and cryogenic leak issues. Regardless of architecture, the cooling system must provide some capacity overhead to allow for recovery from magnet quench within a reasonable interval. During routine operation the excess capacity is dissipated with a regulated heater. The heater power level provides an excellent diagnostic with respect to the overall health of the system.

Alignment Systems Alignment requires precision in both position adjustment and measurement. Development efforts include precise (<10 micron) external adjustment capability for the magnet cold mass with respect to the cryostat when the system is at 4.2 K along with sub-5-micron laser displacement-based position measurement capability [5]. These requirements are particularly important for multi-undulator-magnet cryostats where magnet-to-magnet alignment at the 5-micron level is desirable. Multi-magnet alignment to a common rigid cold mass support is the baseline choice for the APS Upgrade SCU cryostat (see Figure 9) although independent magnet supports with external precision adjustment capability are a potential alternative.

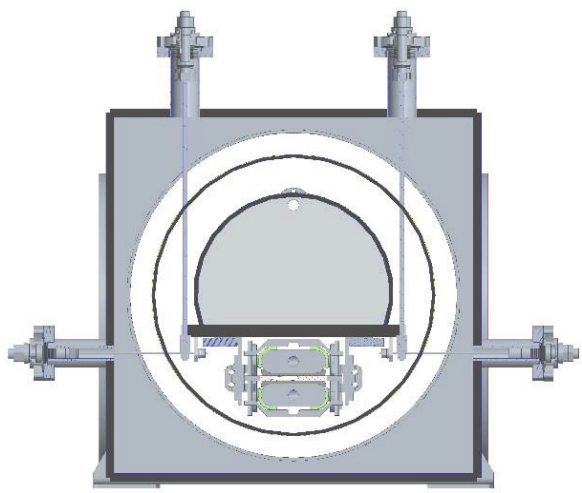

Figure 9: End view of a magnet support and alignment concept for the APS Upgrade SCU cryostat. Externally adjustable low-heat-leak supports provide precise positional control.

Beam Vacuum Chambers SCU magnets must be screened effectively from substantial beam and/or x-ray-induced heating in a storage ring application. An independently cooled beam vacuum chamber provides an adequate screen for planar SCUs. However the helical SCU at the APS is vulnerable to x-ray heating caused by the bending-magnet (BM) beam line immediately upstream. This potentially fatal heat source was mitigated

ISBN: 978-3-95450-206-6 doi:10.18429/JACoW-FLS2018-MOA2PL03

by sophisticated beam orbit correction to steer the BM x-ray fan away from the helical SCU magnet. The vulnerability arises due to the helical magnet core design which completely envelopes the beam vacuum chamber. For the planar geometry, there is no magnet exposure along the horizontal plane of the electron beam orbit (see Figure 3).

FEL-Specific

Cooling Systems An FEL SCU array, perhaps of order 100 m length, lends itself to the use of a centralized cryoplant coupled to a cryogenic distribution system (compared to a very large number of cryocoolers). The 4.2 K heat load per meter is likely around one watt if thermal design discipline similar to the storage-ring-specific cryostat is maintained. However given the available cooling power of even a small liquid helium refrigerator, it is possible to loosen the heat load budget as a means to simplify cryostat design. A small commercial refrigerator is shown in Fig. 10.

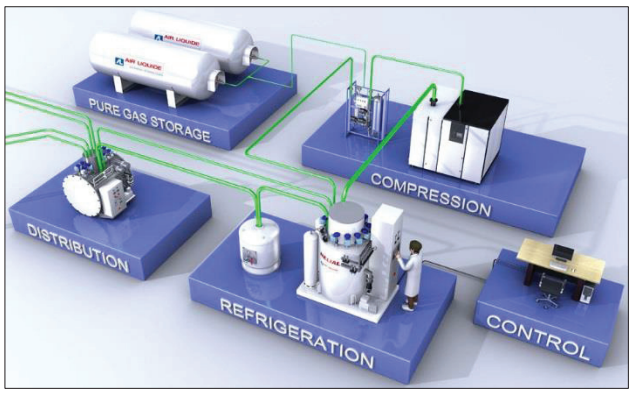

Figure 10: A small helium refrigerator system (from the Air Liquide website).

Alignment Systems FEL requirements push the state of the art and may involve active, beam-based component alignment. Individual control of undulator magnets, focusing quadrupoles and phase shifters may be required. Room-temperature remote adjustment of cold mass supports via cryostat insulating vacuum feed-throughs may be sufficient. Piezo actuators can be located outside of or internal to the insulating vacuum and may find an application for short-distance, fast position adjustment. In the longer term, fiber-optic interferometer-based systems may provide improved precision and multi-channel capability for real-time magnet location measurement as part of an active positioning system

Beam Vacuum Chambers A 4.2 K beam vacuum chamber becomes feasible, in part due to the lower expected beam-induced heating relative to a storage ring but also due to the refrigeration capacity inherent in a centralized helium refrigerator. This could enable smaller magnetic gaps and larger magnetic fields for a given magnet operating current.

Array Segmentation Cryogenic distribution may be external (for example CEBAF at JLab [6]) or internal (LCLS-II [7] and European X-FEL [8]) depending on overall cooling power, capital cost, and maintenance strategy (individually removable cryostats compared to a full-system warm-up for cryostat removal). Figures 11 and 12 illustrate the minimal-segmentation concept where the distribution system resides internal to the cryostat.

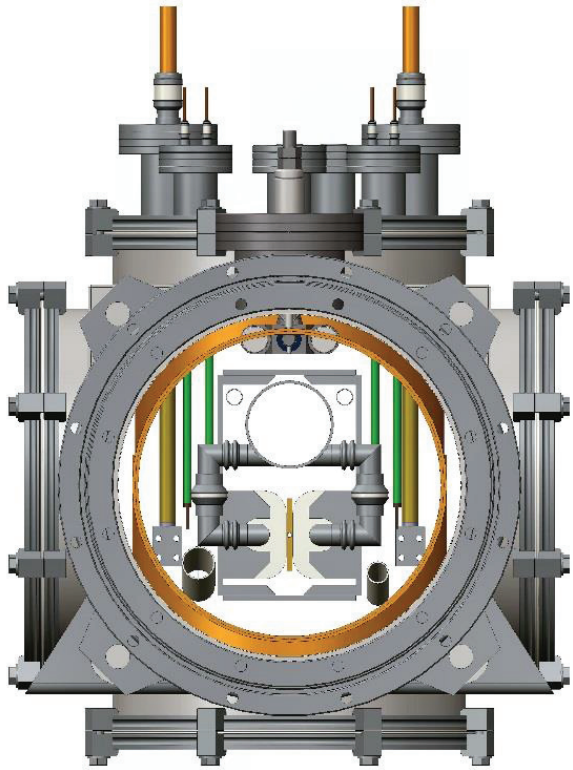

Figure 11: End-section view of a minimally-segmented SCU cryostat showing horizontal-gap planar magnets packaged with internal helium cryogenic distribution.

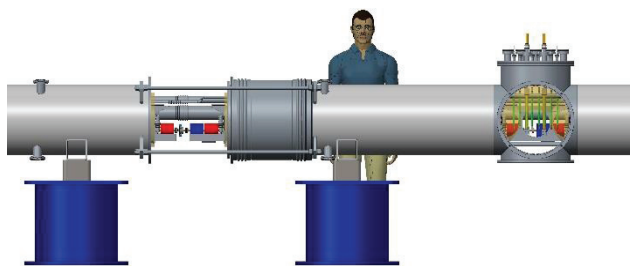

Figure 12: Concept representation of multiple cryostats connected in a minimally-segmented FEL array. The inter-cryostat vacuum vessel spool is shown in the retracted (assembly) position.

Multi-line FEL Cryostats An SCU cryostat represents a space-efficient means of packaging an undulator magnet. As such, it is possible to design a single cryostat capable of housing multiple undulator lines in parallel. Figure 13 shows a cryostat concept containing four parallel helical SCU magnet arrays in parallel, each with an independent beam vacuum chamber. This represents a packing capability which is likely unachievable using permanent magnet undulator technology.

ISBN: 978-3-95450-206-6 doi:10.18429/JACoW-FLS2018-MOA2PL03

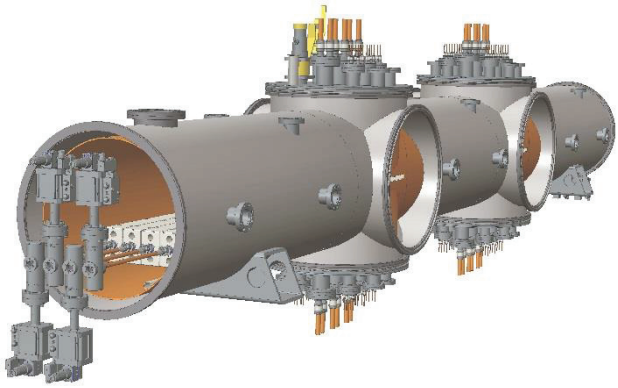

Figure 13: FEL helical SCU concept containing four independently powered SCU arrays in a common cryostat.

CONCLUSION

The APS is working to develop the next generation of superconducting undulator (SCU) technology for future storage ring and FEL light sources. At present there are three SCUs operating in the APS storage ring (two planar, one circular polarizing). Development is underway for a new generation of SCUs for the APS Upgrade. SCU technology is well-suited to FEL applications and development work on FEL-specific devices is ongoing.

ACKNOWLEDGMENT

The submitted manuscript has been created by UChicago Argonne, LLC, Operator of Argonne National Laboratory ("Argonne"). Argonne, a U.S. Department of Energy Office of Science laboratory, is operated under Contract No. DE-AC02 -06CH11357. The U.S. Government retains for itself, and others acting on its behalf, a paid-up nonexclusive, irrevocable worldwide license in said article to reproduce, prepare derivative works, distribute copies to the public, and perform publicly and display publicly, by or on behalf of the Government.The Department of Energy will provide public access to these results of federally sponsored research in accordance with the DOE Public Access Plan.

REFERENCES

[1] Gluskin, E., "Development and performance of superconducting undulators at the Advanced Photon Source," in *Synchrotron Radiation News*, 28:3, 4-8.

[2] Ivanyushenkov, Y. et al., "Status of the development of superconducting undulators at the Advanced Photon Source," in *Proceedings of IPAC2017*, Copenhagen, Denmark, p. 2499-2502.

[3] Kasa. M. et al., "Progress on the magnetic performance of planar superconducting undulators," in *Proceedings of NA-PAC2016*, Chicago, IL, USA, p. 477-479.

[4] Mezentsev, N. and Wallen, E., "Superconducting wigglers," in *Synchrotron Radiation News*, 24:3, 3-9.

[5] Jansma, W.G. et al., "Precision 2D laser scanning: overview and applications,"in *Journal of the CMSC*, Vol. 12, No. 2 (2017) p. 6-13.

[6] Weisend II, J.G. (Ed.), "Cryostat Design," *International Cryogenics Monograph Series*, Springer (2016), p.149.

[7] Peterson, T. et al., "LCLS-II 1.3 GHz cryomodule design – modified TESLA-style cryomodule for CW operation," in *Proceedings of SRF2015*, Whistler, BC, Canada, p. 1417-1421.

[8] Bozhko, Y. et al., "Commissioning and first cooldown of XFEL linac," in *IOP Conf. Ser.: Mater. Sci. Eng* **278** 012100 (2017).

ISBN: 978-3-95450-206-6 doi:10.18429/JACoW-FLS2018-MOP1WA02

THE LCLS-II-HE, A HIGH ENERGY UPGRADE OF THE LCLS-II*

T.O. Raubenheimer†, for LCLS-II/LCLS-II-HE Collaborations
SLAC National Accelerator Laboratory, Menlo Park, USA

Abstract

The LCLS-II is a CW X-ray FEL covering a photon spectral range from 200 to 5,000 eV. It is based on a 4 GeV SRF linac installed in the 1st km of the SLAC linac tunnel. This paper will describe a high energy upgrade, referred to as the LCLS-II-HE, which will increase the beam energy to 8 GeV and the photon spectral range to 12.8 keV; this range may be extended through 20 keV with improvements of the electron injector and beam transport. The LCLS-II-HE received the US DOE CD-0 approval, Mission Need, and has developed a CDR in support of a CD-1 review scheduled for summer 2018.

INTRODUCTION

The development of X-ray free-electron lasers (XFELs) has launched a new era in X-ray science by providing ultrafast coherent X-ray pulses with a peak brightness that is nearly one billion times higher than previous X-ray sources. As the world's first hard X-ray FEL, the LCLS has already demonstrated tremendous scientific impact across broad areas of science, based on fundamental studies of the behavior of matter at the atomic length scale and femtosecond timescale. A comprehensive scientific overview of the first five years of LCLS operation was recently published [1]. Numerous similar facilities are just beginning operation or are under construction around the world [2].

While the LCLS has delivered unprecedented peak brightness, with a repetition rate of 120 Hz, the average brightness is modest, similar to that of a synchrotron source. Furthermore, many experiments require attenuation of the peak intensity in order to avoid perturbation of the sample by the X-ray probe. In these cases, signal accumulation times often become prohibitive, thus rendering many experiments impractical. The LCLS-II will provide ultrafast X-rays in the soft and tender X-ray range (0.2-5 keV) at repetition rates up to 1 MHz with two independent XFELs based on adjustable-gap undulators: a soft X-ray undulator (SXU) covering the range from 0.2 to 1.3 keV, and a hard X-ray undulator (HXU) covering the range from 1 to 5 keV. This development is driven by important new science opportunities that have been identified and advanced over the past decade through scientific workshops, both in the U.S. and around the world [3].

The extension of the LCLS-II to the hard X-ray regime is motivated by the scientific need for precision measurements of structural dynamics on atomic spatial scales and fundamental timescales. Such measurements are essential for addressing many of the transformative opportunities identified in the latest report from the Basic Energy Sciences Advisory Committee (BESAC) [4], and will provide detailed insight into the behavior of complex matter, real-world heterogeneous samples, functioning assemblies, and biological systems on fundamental scales of energy, time, and length. The LCLS-II High Energy Upgrade (LCLS-II-HE) is a natural extension to LCLS-II, extending the high-repetition-rate capabilities into the critically important "hard X-ray" regime (spanning from 5 keV to at least 12.8 keV and potentially up to 20 keV) that has been used in more than 75% of the LCLS experiments to date.

The LCLS-II-HE upgrade will build on the LCLS-II, described in Refs. [5] and [6], and will add significant capability to the facility. The changes in the LCLS-II capability are summarized below and illustrated in Fig. 1.

- The photon spectral range from the hard X-ray undulator at MHz-rate will be extended from 1 – 5 keV to 1 – 12.8 keV using electrons beams with energies between 3.3 and 8 GeV with the possibility of X-ray energies approaching 20 keV given the success of off-project R&D programs;
- The hard X-ray undulator will include the capability for self-seeding the MHz-rate X-ray beam;
- The soft X-ray undulator will be able to produce X-rays between 0.2 and 1.3 keV or access the tender X-ray region between 1 – 5 keV at MHz-rates coincidently with the production of MHz-rate hard X-rays;
- The hard X-ray beamlines and instruments will be upgraded to maximize the science from the MHz-rate high energy FEL beams;
- And, the hard X-ray experimental hall will be modified to incorporate an additional experimental instrument and also better optimize the usage of the existing instruments;
- The performance of LCLS and LCLS-II operational modes and techniques will not be negatively impacted by the LCLS-II-HE including the generation of X-ray pulses with high peak power (100's of GW) at 120 Hz using the copper linac.

The layout of the LCLS-II-HE accelerator is shown schematically in Fig. 2. The facility will use the existing accelerator tunnels at SLAC. The increase in beam energy from LCLS-II to LCLS-II-HE is due to an increase in acceleration gradient and an increase in the SRF linac length. In particular, the SRF linac will be extended to fill the first km of the existing SLAC linac tunnel which has been largely cleared of legacy equipment.

To construct the LCLS-II-HE, SLAC will continue the partnership with other national laboratories having recent technical leadership in the critical SRF technologies. In a

* Work supported by US DOE Contract No. DE-AC02-76SF00515.
† torr@stanford.edu

ISBN: 978-3-95450-206-6 doi:10.18429/JACoW-FLS2018-MOP1WA02

process similar to that pursued by the LCLS-II project, the partner laboratories will be responsible for delivering significant portions of the project scope to SLAC. Cornell University, FNAL, and JLab will be engaged with increasing the accelerating gradient of the accelerator cavities for new cryomodules while the SRF linac and associated systems are expected to be provided by a combination of FNAL and JLab which have the experience of producing the LCLS-II cryomodules.

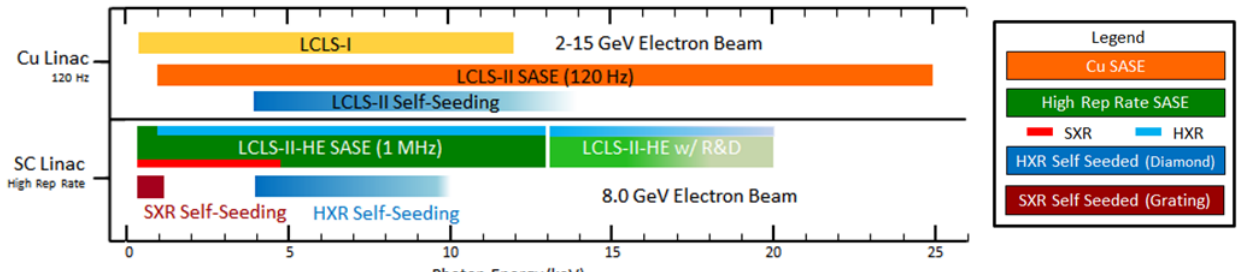

Figure 1: Photon energies from the SRF and CuRF linacs for both SASE and self-seeded operation, assuming 8.0 GeV SRF electrons and 3-to-15 GeV CuRF electron beams. Access to higher photon energies from the CuRF or SRF linacs will be possible given the success of off-project R&D programs.

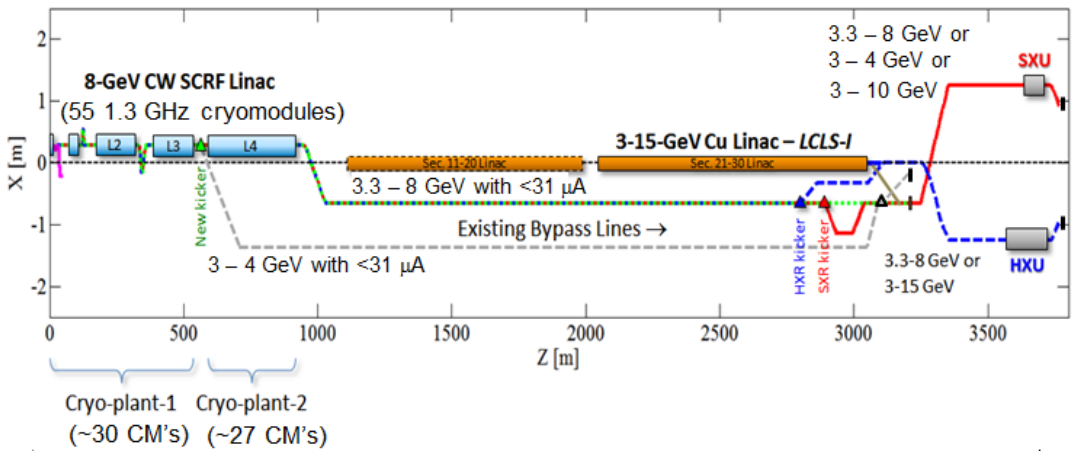

Figure 2: Layout of the LCLS-II-HE facility with 8 GeV at the end of the SRF-Linac and 15-GeV in the normal-conducting linac. An additional 3.8-GeV pulsed extraction line is included to allow a low-energy extraction into the SXU FEL while the HXU FEL runs with high energy (3.3-8 GeV or 3-15 GeV) electrons.

ACCELERATOR PARAMETERS

The primary challenge for the LCLS-II-HE is achieving the high rate performance at 12.8 keV. The LCLS-II is designed to deliver 5 keV photons with a beam energy of 4 GeV and thus, based on the FEL photon energy scaling with γ^2, one would expect that 13 keV could be attained with a beam energy of 6.5 GeV. However, at these short wavelengths, the FEL performance is limited by the beam emittance in the undulator. Given the expected performance of the LCLS-II injector and the LCLS-II HXR undulator, a minimum beam energy of 8 GeV is required to generate 13 keV FEL photons.

The design of the LCLS-II left an opportunity to upgrade the linac energy by installing additional cryomodules and also by increasing the acceleration gradient. The LCLS-II cavities and cryomodules are being qualified at 19 MV/m but the LCLS-II operating specification is ~15.5 MV/m. The SLAC tunnel has 250 meters of empty space following the SRF linac in which 20 additional cryomodules can be added. With cavities operating at an average $Q_0 \approx 2.7\times10^{10}$, the cryoplant will allow operation of the extended linac at an average gradient of ~19.4 MV/m to achieve an 8-GeV electron beam, doubling the energy at the linac end and extending the spectral range of the MHz-rate FEL to 13 keV.

To achieve the desire Q_0, an implementation of the nitrogen-doping [7] process was developed for the LCLS-II. The process adopted by LCLS-II [8,9,10] is producing cavities with average performance better than specified. On average, cavities in vertical test can achieve an average maximum gradient >20 MV/m with an average $Q_0 > 3\times10^{10}$ as illustrated in Fig. 3. After installation in the cryomodules, the maximum gradient appears to

ISBN: 978-3-95450-206-6 doi:10.18429/JACoW-FLS2018-MOP1WA02

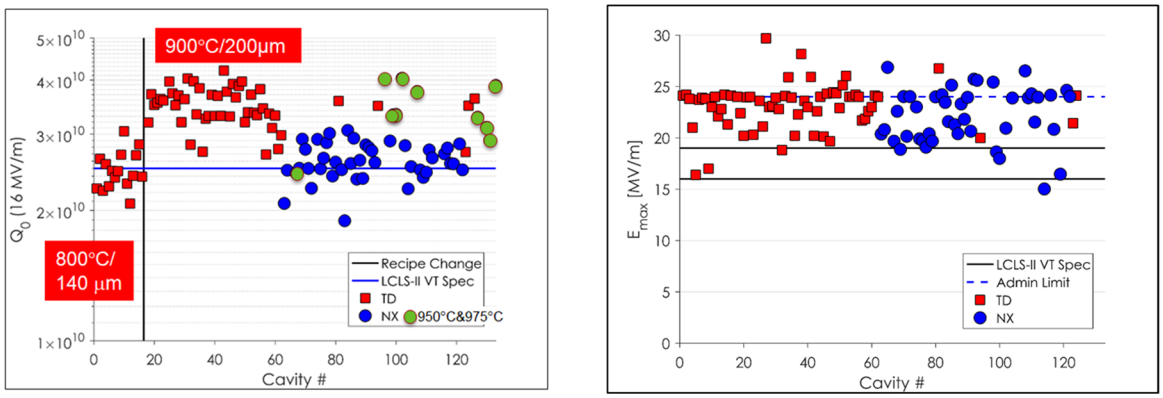

Figure 3: Left: LCLS-II cavity Q0 measured at the nominal 16 MV/m gradient; the vertical line indicates a change in bake temperature and a few cavities have been treated at >950 °C as indicated in the plot legend. Right: Maximum LCLS-II cavity gradient achieved in the vertical testing. Note that a 24 MV/m administrative gradient limit was imposed in many cases.

decrease by 10~15% which is consistent with results observed at the European XFEL (EuXFEL) [11]. It is expected that the LCLS-II cryomodules should be robust at an average gradient of 18 MV/m.

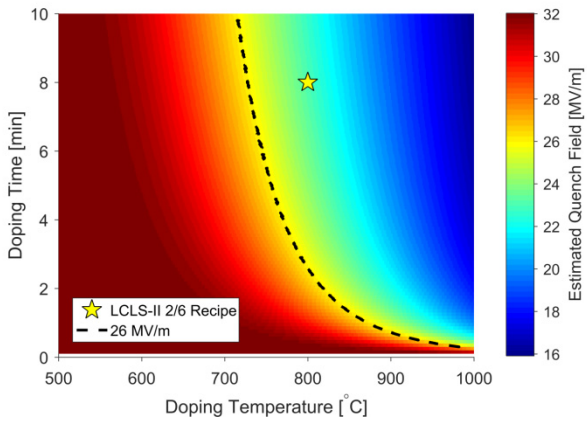

Figure 4: Expected SRF gradient performance as a function of N_2 doping temperature and time based on a simulation from Ref [12].

The LCLS-II N_2-doping choice was chosen to maximize the Q_0 at 16 MV/m. As illustrated in Fig. 4, it is expected that a small variation in the doping procedure would yield still higher gradients at the expense of Q_0. An R&D program will be initiated to establish a gradient of 24.5 MV/m at $Q_0 > 2.7\times10^{10}$.

The LCLS-II-HE cryomodule will be the same as those for the LCLS-II which were designed at Fermilab and are based heavily on the EuXFEL design. The assembly and installation procedures will be adopted from those developed for the EuXFEL.

The main operating parameters for the LCLS-II-HE SRF linac are listed in Table 1, along with those of the LCLS-II SRF linac. The number of 1.3-GHz cryomodules is increased from 35 to 55 and the gradient of most of the LCLS-II cryomodules is increased from ~16 to 18 MV/m while the gradient in the 20 new LCLS-II-HE cryomodules would be further increased to 20.8 MV/m. The maximum average beam power delivered by the linac would be increased to 375 kW, which could consist of 31 µA at 8 GeV and 31 µA at 3.8 GeV in the 2nd bypass line discussed below.

ACCELERATOR LAYOUT

In operation, the LCLS-II-HE upgrade will want to simultaneously support a soft X-ray program with photons between 0.2 and 1.3 keV and a hard X-ray program with X-rays between 1 and 13 keV. Assuming the LCLS-II-HE upgrade reuses the LCLS-II SXR and HXR undulators, this could be facilitated by extracting some of the beam at an energy between 3 and 4 GeV for the soft X-ray program while accelerating the rest to a final energy between 3.3 and 8 GeV for the hard X-ray program. Thus, a mid-point extraction of a 'low energy' beam will be included.

A schematic of LCLS-II-HE is illustrated in Fig. 2, where an additional pulsed extraction line is added after linac segment L3 to transport ~3.8-GeV beam to the SXR undulator (dashed gray line) and a new linac segment, L4, follows to accelerate the undeflected beam to 8 GeV. The energy upgrade will add 20 new cryomodules, each having essentially the same design as those being developed for the LCLS-II, to generate the 8-GeV electron beam. This upgrade reuses the LCLS-II injector, linac, cryoplants, undulators, beam transport systems, and existing tunnels. The implementation will require some modification to the cryogenic distribution system which is shown in Fig. 5, the addition of a new extraction point for the ~3.8-GeV beam, which will be injected into an existing bypass line (gray-dashed line in Fig. 2), and a new beam dump at the end of this transport line.

The new ~3.8 GeV extraction enables the LCLS-II-HE to operate with essentially three independent sources of electrons: those from the end of L3 at ~3.8 GeV, those from the end of L4 where the electron energy can range

ISBN: 978-3-95450-206-6 doi:10.18429/JACoW-FLS2018-MOP1WA02

from 3.3 to 8 GeV, and those from the 120 Hz copper linac (CuRF) with a beam energy between 3 and 15 GeV.

The design is based on the LCLS-II injector [13] and the bunch compression system. No hardware changes will be made upstream of the middle of the LCLS-II L3 and the configuration of the injector, L0, laser heater, L1, and BC1 will be identical to that designed for LCLS-II. There are three reasons for this: (1) extensive optimization of the LCLS-II injector and bunch compression system has been performed [14,15] and the LCLS-II-HE upgrade will reuse much of this effort; (2) radiation shielding for backward traveling dark current is challenging around the LCLS-II gun and laser and it will likely need to be increased with changes to the gradient in L0 and L1; and (3) the beam energy is low in this region so energy stability and reliability is important, which a lower gradient tends to afford.

Table 1: LCLS-II and LCLS-II-HE SRF Linac Parameters

SCRF-Linac Parameters	LCLS-II	LCLS-II-HE	Unit
Final electron energy	3.3 - 4.0	3.3 - 8.0	GeV
Electron energy at L3/L4 extraction point	-	3.3 - 4.0	GeV
Electron Bunch Charge	0.01 – 0.30	0.01 – 0.30	nC
Max. bunch repetition rate	929	929	kHz
Average electron beam power in L2-L4	<0.25	<0.25	MW
Average electron power in BSY	<0.25	<0.375	MW
Max. avg. electron current in L0-L3	62	62	μA
Max. avg. electron current in L4	--	31	μA
Max. avg. electron current in Low Energy Extraction line	--	31	μA
Total Number of 1.3-GHz Cryomodules	35	55	-
Total Number of 3.9-GHz Cryomodules	2	2	-
Installed 1.3 GHz RF Voltage	4.65	8.64	GeV
Active SCRF accelerator length	296	462	m
1.3 GHz Cryomodules in L0, L1, L2, L3	1, 2, 12, 20	1, 2, 12, 13	-
1.3 GHz Cryomodules in L4	--	27	-
RF Overhead (spare cavities)	6.1	4.1	%
Mean RF Gradient in powered cavities: L0-L1	< 16.0	< 16.0	MV/m
Mean RF Gradient in powered cavities: L2-L3	< 16.0	18.0	MV/m
Mean RF Gradient in powered LCLS-II cavities: L4	--	18.0	MV/m
Mean RF Gradient in powered LCLS-II-HE cavities: L4	--	20.8	MV/m
Installed 2K cryo-capability	8.0	8.0	kW
Expected heat load at max energy: L0-L3	3.7	3.5	kW
Expected heat load at max energy: L4	-	3.8	kW

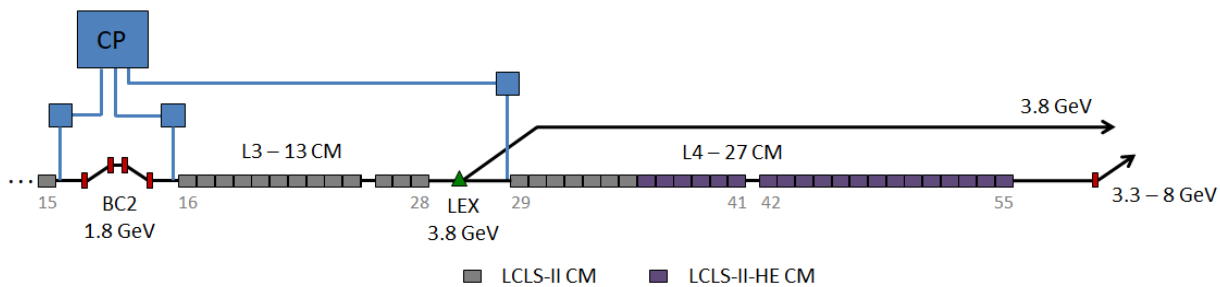

Figure 5: LCLS-II-HE SRF expansion and layout. Each gray block represents one 12-m long 1.3-GHz cryomodule (CM), with 55 total CM's. A fast extraction kicker is added at 3.8-GeV to optionally feed the SXU FEL at 3.8 GeV. The cryo-distribution (CP – blue lines) is also shown. CM's upstream of BC2 are not shown.

EXPERIMENTAL SYSTEMS

The LCLS-II-HE upgrade will also require a revision to the existing X-ray instrument suite. This involves three different types of upgrades/modifications: (i) repetition rate enhancements (X-ray optics, detectors, lasers, data systems) consistent with the high average power beam and pulse rate, (ii) relocations to maximize experiment capacity and operational efficiency, and (iii) new instrumentation to augment present capabilities.

ISBN: 978-3-95450-206-6 doi:10.18429/JACoW-FLS2018-MOP1WA02

The configuration of the Far Experimental Hall for LCLS-II-HE is illustrated in Fig. 6. The revised instrument plan includes:

- Modifying the Far Experimental Hall (FEH) to accommodate an additional X-ray hutch
- Replacing the XCS instrument with a new instrument (Dynamic X-ray Scattering, DXS) designed for both high-resolution inelastic X-ray scattering and X-ray photon correlation spectroscopy
- Bifurcating the present CXI instrument into two beamline branches and hutches (with two micro-focus chambers and a nano-focus chamber) to improve efficiency and optimize high-sensitivity experimental techniques
- Relocating the MFX instrument on a new branch line to improve efficiency
- Relocating the MEC instrument to a new, shielded location to permit higher-power laser-matter interactions
- Adapting the design of the Tender X-ray Imaging (TXI) instrument in hutch NEH1.2 for LCLS-II, extending its energy reach to combine tender and hard X-ray beams.

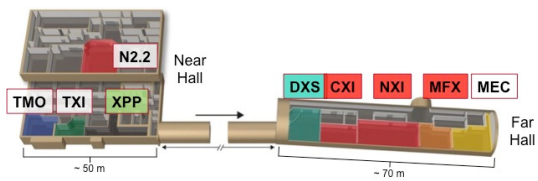

Figure 6: Schematic layout of the LCLS X-ray experimental end stations at the completion of the LCLS-II-HE project, with the Far Experimental Hall reconfigured to include one additonal hutch.

PERFORMANCE SIMULATIONS

Start-2-End (S-2-E) simulations have been performed for the LCLS-II using *IMPACT-T* and *IMPACT-Z* [16,17] and *Genesis* [18]. Included in the tracking are 3D space charge forces, longitudinal wakefields in the linac, CSR in the bends and relevant drift sections, incoherent synchrotron radiation (ISR) in the bends, second-order optics (*e.g.*, chromatic and geometric effects), resistive-wall wakefields in the undulators, and 3D time-dependent FEL simulations [19]. To accurately model the shot-noise in the electron beam in these simulations, the number of macro-particles that are used is equal to the actual number of electrons.

At this time, the hard X-ray simulations are performed using the LCLS-II S-2-E beam distributions at 4 GeV from IMPACT [20,21,19] scaled to the 8 GeV beam energy. This approach is believed to be conservative as most of the deleterious effects such as Longitudinal Space Charge (LSC) force and Coherent Synchrotron Radiation (CSR) which drive the microbunching instability will be moderated by the higher beam energy in the Bypass line.

The FEL performance simulations start from these scaled LCLS-II beams for 100 pC or 20 pC and use *Genesis* to calculate the expected FEL gain and radiation properties. In all these simulations, the post-saturation taper is optimized in *Genesis* using time-dependent simulations which makes the evaluations computationally intensive. An example from the upper end of the tuning range at 12.8 keV with a 20 pC beam are shown in Fig. 7.

The expected average brightness from the LCLS-II-HE is illustrated in Fig. 8 where the purple curves illustrated the expected LCLS-II performance and the red solid curve shows the expected LCLS-II-HE performance at 8 GeV. These calculations are based on the expected performance of the unmodified LCLS-II injector. The dashed red curve shows the performance increased that would arise from a factor of four improvement in the beam emittance at the undulator which might be possible as a result of an injector R&D program.

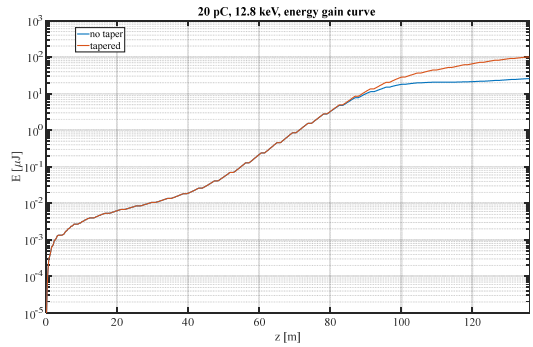

Figure 7: Genesis simulation of X-ray pulse energy at 12.8 keV from a 20 pC LCLS-II bunch scaled to 8 GeV at the HXR undulator.

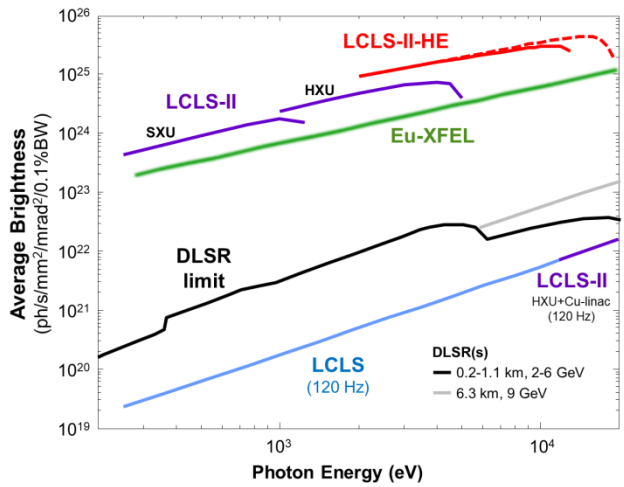

Figure 8: Expected average brightness from LCLS-II and LCLS-II-HE.

ACKNOWLEDGEMENTS

The LCLS-II-HE is being developed by a team of roughly 30 scientists and engineers at SLAC and partner laboratories and the design effort relies heavily on the LCLS-II construction team. This work is supported in part by DOE Contract No. DE-AC02-76SF00515.

ISBN: 978-3-95450-206-6 doi:10.18429/JACoW-FLS2018-MOP1WA02

REFERENCES

[1] C. Bostedt, S. Boutet, D. M. Fritz, et al., Reviews of Modern Physics 88, 015007 (2016).

[2] I. Schlichting, W. E. White, and M. Yabashi, J. Synchrotron Radiat. 22, 471 (2016).

[3] "New Science Opportunities enabled by LCLS-II X-ray Lasers," (https://portal.slac.stanford.edu/sites/lcls_public/Documents/LCLS-IIScienceOpportunities_final.pdf, 2015).

[4] J. C. Hemminger, "Challenges at the Frontiers of Matter and Energy: Transformative Opportunities for Discovery Science - BESAC Report U.S. D.O.E.," (http://science.energy.gov/~/media/bes/besac/pdf/Reports/CFME_rpt_print.pdf, 2015).

[5] J. N. Galayda, Proc. of IPAC'14, Dresden, Germany, p. 935 (2014).

[6] LCLS-II Technical Design Report, T.O. Raubenheimer, ed. (2017).

[7] A. Grassellino, et al., "Nitrogen and argon doping of niobium for superconducting radio frequency cavities: A pathway to highly efficient accelerating structures," Supercond. Sci. Technol. 26, 102001 (2013).

[8] A. Crawford, et al, "The joint high Q0 program for LCLS-II," Proc. of IPAC 14, Dresden, Germany, p. 2627 (2014).

[9] D. Gonnella, et al, "Nitrogen-doped 9-cell cavity performance in a test cryomodule for LCLS-II," J. Appl. Phys. 117, 023908 (2015).

[10] D. Gonella, et al, Nucl. Instr. And Meth. A, 883, 143-150 (2018).

[11] N. Walker, et al., "Performance analysis of the European XFEL SRF cavities, from vertical test to operation in the modules," WE1A04, Proc. Linac 2016, East Lansing, MI (2016).

[12] D. Gonnella. The Fundamental Science of Nitrogen-Doping of Niobium Superconducting Cavities. PhD Thesis. Cornell University (2016).

[13] F. Zhou, et al., "the LCLS-II njector beamline design and RF coupler correction," MOP021, Proc. of FEL'15, Daejeon, Korea (2015).

[14] G. Marcus and J. Qiang, LCLSII-TN-17-04 (2017).

[15] G. Marcus et al., TUP007, FEL'2015, Daejon, Korea (2015).

[16] J. Qiang et al., *J. Comput. Phys*., **163**, 434 (2000).

[17] J. Qiang et al., *Phys. Rev. ST Accel. Beams*, **9**, 044204 (2006); J. Qiang et al., *Phys. Rev. ST Accel. Beams*, **12**, 100702 (2009).

[18] S. Reiche, et. al., Start-To-End Simulation for the LCLS X-ray FEL, *Nuclear Instruments and Methods in Physics Research*, **A483** 70 (2002).

[19] G. Marcus and J. Qiang, LCLSII-TN-17-04 (2017).

[20] G. Marcus et al., TUP007, FEL'2015, Daejon, Korea (2015).

[21] J. Qiang et al., WEP070, FEL'2015, Daejon, Korea (2015); J. Qiang, WEA3IO02, NAPAC'2016, Chicago, USA (2016).

ISBN: 978-3-95450-206-6 doi:10.18429/JACoW-FLS2018-MOP1WB01

LATTICE DESIGN FOR PETRA IV: TOWARDS A DIFFRACTION-LIMITED STORAGE RING

I. Agapov *, R. Brinkmann, Y.-C. Chae, X.N. Gavalda, J. Keil, R. Wanzenberg,
Deutsches Elektronen Synchrotron, Notkestrasse 85, Hamburg, Germany

Abstract

Machine design for the PETRA III storage ring upgrade – PETRA IV – aiming at a 10-30 pm emittance range has been ongoing at DESY. We present the design challenges and approaches for this machine, the baseline lattice and the alternative lattice concepts currently under consideration.

INTRODUCTION

PETRA III has been in operation as a synchrotron radiation user facility since 2009 [1, 2], being at the time of construction the world's record holder for the smallest electron beam emittance (1 nm rad at 6 GeV) among hard x-ray sources. An extension project has been ongoing since 2014 [3], and potential of reducing the emittance with the existing lattice comprising a mixture of DBA and FODO cells has been studied [4], putting the ultimate emittance of such lattice type at around 500 pm for PETRA circumference of 2304 meters. With the advance of the multi-bend achromat (MBA) technology pioneered by MAX IV, many light sources, and among them all large hard x-ray facilities – ESRF, APS, and SPRING 8 – have proposed machine upgrades reducing the emittance by orders of magnitude. With PETRA IV design studies [5] DESY has started the preparation phase for the MBA-based upgrade project which will be essential to maintain the laboratory's role in cutting edge research with synchrotron radiation.

DESIGN OBJECTIVES

The upgrade plan of PETRA III to PETRA IV aims at building a unique light source, with an ultra-low horizontal emittance in the range between 10 pm rad and 30 pm rad at a beam energy of 6 GeV. In addition to the three existing experimental halls in the northeast of the storage ring, it is foreseen to build a new experimental hall in the southwest just opposite to the Max von Laue Hall. The general layout of PETRA IV is shown in Fig. 1. The storage ring will provide 18 straight sections of approximately 5 m length and four longer straight sections in the four experimental halls. With canting four straight sections and splitting another four undulator beams by appropriate optics, thirty parallel undulator stations could be realised. The first beamline in each experimental hall has its undulator located in the long straight sections separating the arcs. For these four beamlines, the undulator length is not limited by length of the straight section but only by the available acceptance and the electron beam parameters (e. g., β-functions) can be optimised for highest possible brightness. Fig. 2 shows the brightness that could be reached with PETRA IV in one of the four long straight sections. Ultra-low emittance and a reduced number of electron bunches for timing experiments are conflicting design goals that can not be met with a single mode of operation of PETRA IV. Therefore, it is planned to provide two operation modes for PETRA IV, the high-brightness, high-coherence continuous mode and a timing mode with fewer bunches with increased bunch charge but with larger emittance and thus slightly reduced brightness.

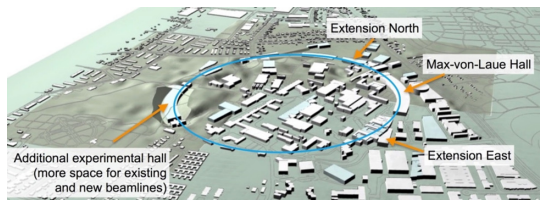

Figure 1: Layout of the PETRA IV facility.

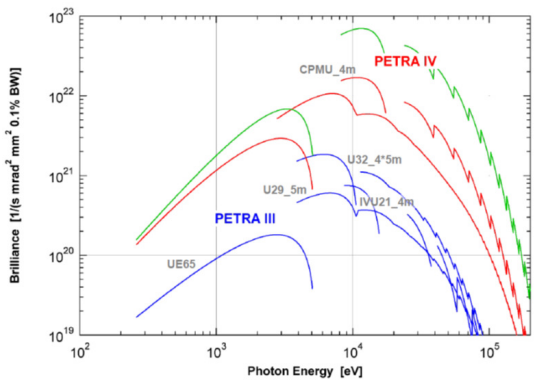

Figure 2: Comparison of brightness between PETRA III and PETRA IV. Red curve: ε_x = 15 pm, κ = 100%, β_x=5 m, β_y=2.5 m. Green curve: ε_x = 10 pm, κ = 50%, β_x=1 m , β_y=1 m.

For lattices in the 10-30 pm range the intra-beam scattering plays an important role and limits the emittance that can be achieved in practice with reasonable bunch charges (see e.g. Figure 3). Although the zero-current emittance scales with beam energy as γ^{-2}, IBS changes this dependency as shown in Figure 4 (calculations for the reference lattice), and the beam energy of approx. 6 GeV appears optimal for emittance minimization.

The insertion devices have significant impact on beam parameters, providing emittance damping or emittance blow-up depending on ID field strength, ID length, number of IDs, and dispersion and beta function at the ID. A typical scenario without canting results in emittance damping and

* ilya.agapov@desy.de

ISBN: 978-3-95450-206-6 doi:10.18429/JACoW-FLS2018-MOP1WB01

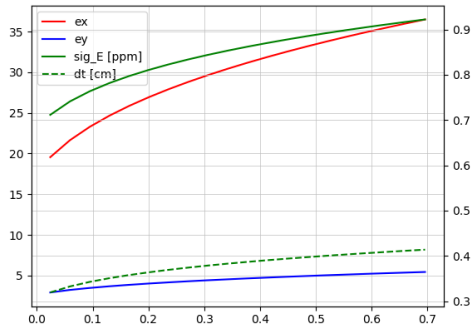

Figure 3: Example of bunch parameters (emittance in pm) vs. bunch charge (in mA) at 6 GeV, 10% coupling.

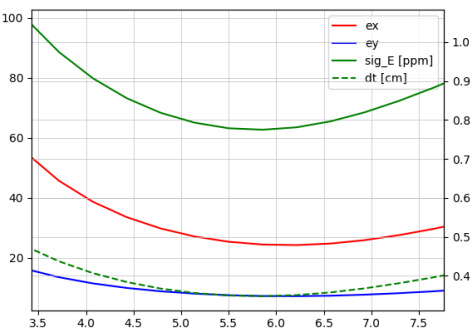

Figure 4: Example of bunch parameters (emittance in pm) vs. beam energy (in GeV) for 0.1 mA bunch charge.

some energy spread growth as shown in Figure 5. A typical peak field if the undulator of 1 T should be assumed.

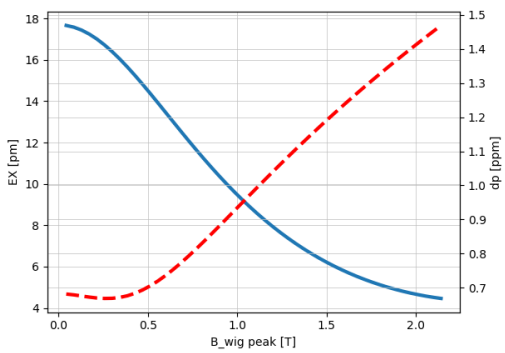

Figure 5: Effect of undulators/damping wigglers with zero dispersion at the ID (no canting), reference lattice, 24 mm period undulators of 5 m length.

Only some beamlines require canting, and the solution that incorporates it without the need to readjust the cell optics is based on a 3-magnet bump as shown in Figure 6.

It can be shown that for a ring where the energy spread is dominated by insertion devices, as will be the case for

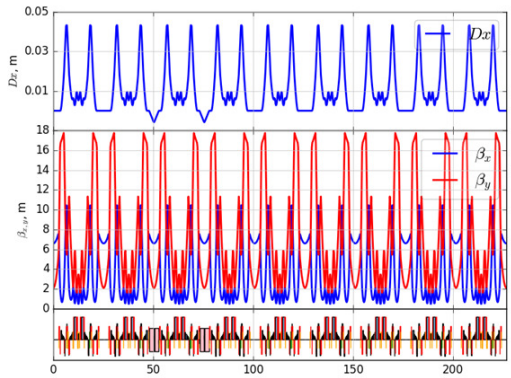

Figure 6: Optics functions of a lattice octant with selective cell canting.

PETRA IV, the maximum canting angle can be estimated as $\theta[mrad] \approx (\frac{2\varepsilon_{RING}[pm]}{\beta[m]\sigma_p[ppm]})^{1/2}$ and is in the order of 4 mrad for β=2 m. For the reference lattice, however, only 2 mrad canting can be integrated without significant degradation of emittance if all IDs are canted, which is mostly due to a larger β_x and non-optimum dispersion. 4 mrad cantining can be integrated if only small number of insertions are canted, as discussed before.

The discussion in this section was based on the example of the reference lattice without (introduced next), with long straight sections removed for simplicity, which results in a small change of equilibrium beam parameters. It however applies with only small modifications to other lattice types in the same emittance range. The projected parameters of PETRA IV are summarized in Table 1. A more detailed discussion of the evolution of the lattice concept is presented in the next section.

Table 1: Parameters of PETRA III / IV without Intrabeam Scattering

Parameter	PETRA III	PETRA IV (without DW)
Energy [GeV]	6	6
Total current [mA]	100	100-200
Nat. emittance ϵ_0 [pm rad]	1280	15 - 30
Energy spread σ_p [10^{-3}]	1.23	0.7 - 1.5
Energy loss/turn U_0 [MeV]	5.1	1 - 5
Momentum compaction factor α_c [10^{-3}]	1.13	0.0146
Dispersion at SF D_x [cm]	750	4.2

STORAGE RING LATTICE

PETRA IV storage ring layout is shown in Figure 7. Place for damping wigglers is foreseen in the west and the north. The RF stations are in the south, and the injection in the south-east. The injection channel will have to be refurbished to inject into the middle of a high-beta straight section. In all lattices a high-beta insertion ($\beta_x \approx$100 m) is foreseen.

ISBN: 978-3-95450-206-6 doi:10.18429/JACoW-FLS2018-MOP1WB01

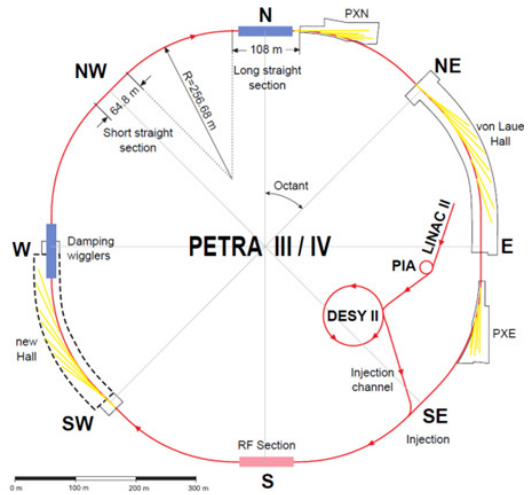

Figure 7: Schematic layout of PETRA IV and its injectors.

7BA Hybrid ESRF-type (H7BA)

For PETRA IV an ESRF-like MBA lattice has been studied with priority. The cell is scaled to 25 m length, and the phase advances are adjusted such that an octant forms a 4^{th} order geometric achromat. In that case the phase advances of the 8 long straight sections are not critically influencing the dynamic aperture, and can be used for tune adjustment. The bare lattice emittance is approx. 15 pm (strong dependency on insertion devices was discussed previously) and the energy spread 0.7 ppm. The optics is shown in Figures 8 and 9. Dynamic aperture is shown in Figure 10. Local momentum acceptance is around 2.5-3%.

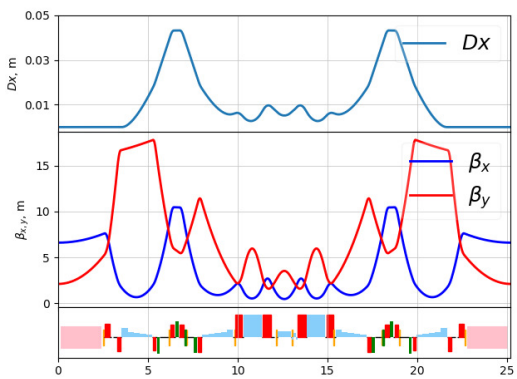

Figure 8: H7BA (reference) lattice.

Phase Space Exchange Based on 6BA (T6BA)

A round beam lattice based on the phase space exchange principle has been investigated in parallel. It is based on 6BA cells with non-interleaved sextupole arrangement. The phase space exchange requires global sum chromaticity correction, which allows for only one pair of horizontally focusing sextupoles per cell. Six octants have no ID straights and form long achromats as shown in Figure 11. Nine 23 m undulator cells form other two octants (Figure 12). Skew qaudrupole sections in two long straight sections are used to flip the

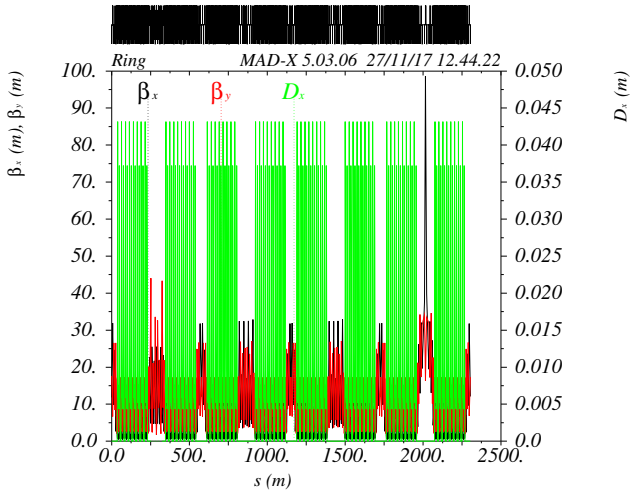

Figure 9: H7BA (reference) lattice.

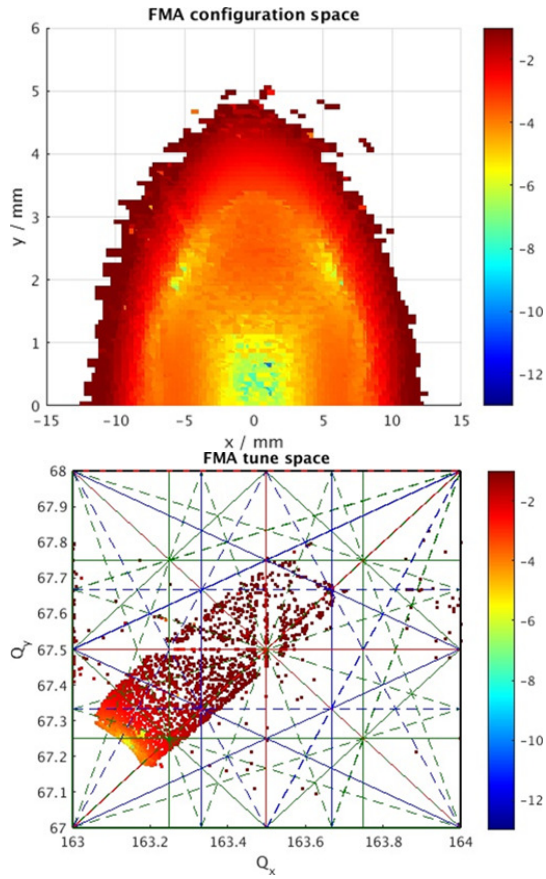

Figure 10: Dynamic aperture and tune diagram of the H7BA (reference) lattice.

betatron oscillation modes. Optics functions are shown in Figure 13. The on-momentum DA is in excess of 2 mm mrad (limitation comes from the path lengthening effect in conjunction with synchrotron oscillations, see Figure 14). The limitation of the optics to round beams only is however a major disadvantage. We consider implementing a flexi-

ISBN: 978-3-95450-206-6 doi:10.18429/JACoW-FLS2018-MOP1WB01

ble phase space exchange with the reference H7BA lattice, such that round beam could be only one operation mode in addition to the flat beam mode.

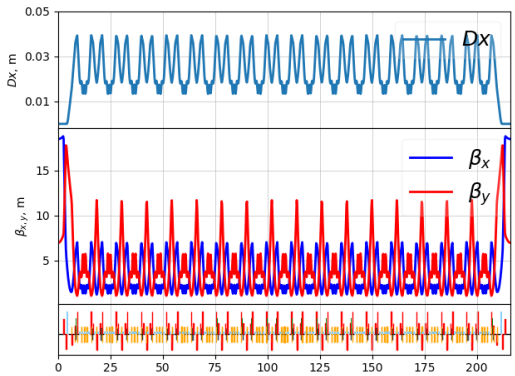

Figure 11: Octants without ID straights.

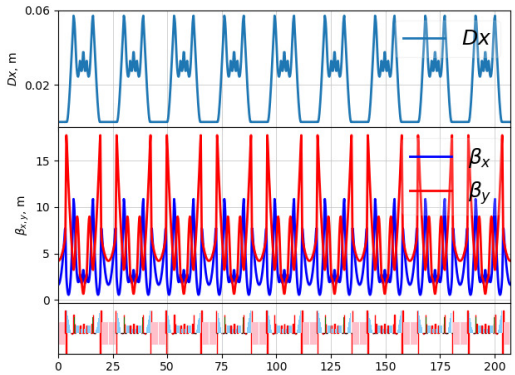

Figure 12: Octants with ID straights.

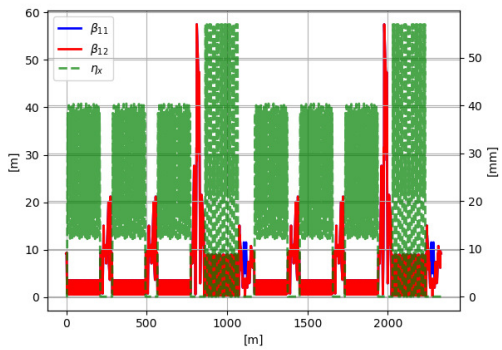

Figure 13: Coupled lattice functions.

Double -I (DMI)

This design is composed of a combination of arcs based on 11 double -I cells (Fig. 15) with a non-interleaved sextupole scheme with a betatron phase advance of 180° in both planes and arcs based on 8 ESRF-H7BA cells with straight sections for insertion devices. As it is well known, such interleaved sextupole scheme allows to reduce the effects of the

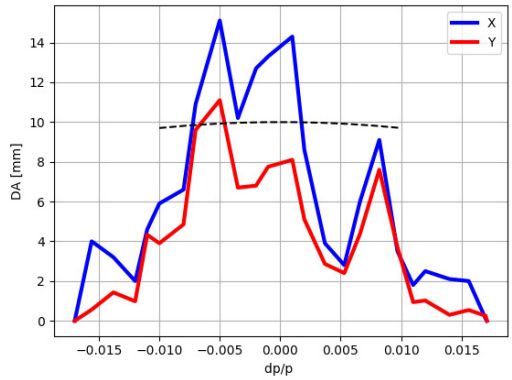

Figure 14: DA and MA of the phase space exchange lattice. Limitation of the DA due to path lengthening effect for a typical RF setup is shown as a dashed line.

geometric aberrations induced by the sextupoles providing a larger dynamic aperture. The bare horizontal emittance of such lattice without damping wigglers is 29.7 pm rad. The dynamic aperture without errors of the double -I lattice is bigger than the dynamic aperture of the PETRA IV reference lattice (4 mm mrad vs. 1.3 mm mrad).

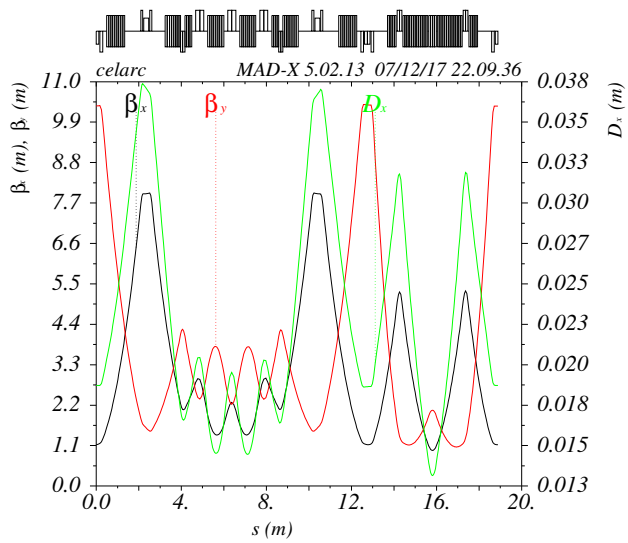

Figure 15: A unit cell of the DMI lattice.

OTHER SUBSYSTEMS

Magnet design is ongoing in collaboration with Efremov Institute St. Petersburg. Magnet designs with up to 150 T/m fields (20 mm air gap) have been proposed. In the lattice design we however been assuming a more conservative 100 T/m limitation for quadrupoles. Design studies for sextupoles are ongoing. For the RF system 100 MHz or 500 MHz single-cell normal conducting cavities and corresponding 3^{rd} harmonic cavities are under consideration, impedance modeling and beam dynamics simulations to determine bunch charge limitations are ongoing. Vacuum

ISBN: 978-3-95450-206-6 doi:10.18429/JACoW-FLS2018-MOP1WB01

system design is ongoing. Experimental NEG self-activation and impedance studies are planned at PETRA III to provide further guidance. R&D into lightweight stable girder design has been ongoing in collaboration with AWI Bremerhacen.

SUMMARY AND OUTLOOK

Design study for the PETRA upgrade is ongoing, and a reference lattice based on H7BA cell is in place A simpler and more robust 6BA solution exploiting the no-undulator arcs (double -I) exists, but has to be worked out in more detail. Decision on the lattice type and CDR are expected in 2019, a whitepaper based on reference lattice is currently in preparation. Projected baseline parameters are: 100 or 200 mA current, 15pm/5pm emittances, 0.1% energy spread, pulse duration 30-100 ps (FWHM). Possibility of timing/hybrid modes (40 or 80 bunches) is open, we need to further investigate bunch dynamics with high charge and higher harmonic cavity (instability thresholds, feedback performance). Tolerance studies and commissioning simulations are ongoing R&D on technical subsystems has been launched, and CDR preparation is in full swing.

REFERENCES

[1] PETRA III TDR, DESY 2004-035, 2004

[2] K. Balewski, Commissioning of PETRA III, in *Proc. IPAC'10*, Kyoto

[3] W. Drube *et al*., https://doi.org/10.1063/1.4952814

[4] V. Balandin *et al*., Emittance reduction possibilities in the PETRA III magnet lattice, in *Proc. IPAC'15* Richmond,USA

[5] l. Agapov *et al*., Research activities towards a conversion of PETRA III into a diffraction limited synchrotron light source, in *Proc. IPAC'17*, Copenhagen

ISBN: 978-3-95450-206-6 doi:10.18429/JACoW-FLS2018-MOP1WB03

CURRENT AND FUTURE OF STORAGE RING BASED LIGHT SOURCES IN KEK

N. Higashi*, K. Harada, T. Honda, Y. Kobayashi, N. Nakamura, KEK, Tsukuba, Japan
K. Hirano, Hiroshima Univ., Higashi-Hiroshima, Japan

Abstract

KEK (High Energy Accelerator Research Organization, Tsukuba, Japan) has two storage-ring light sources. One is Photon Factory (PF). This is the first storage-ring light source in X-ray region in Japan, and the user-run started in 1983. The ring energy is 2.5 GeV, and the emittance has been reduced to 36 nmrad from 460 nmrad through some improvements. Another is Photon Factory Advanced Ring (PF-AR). The ring energy is 6.5 GeV, and the single-bunch operation and hard X-ray are featured. The user-run started in 1987, and the emittance is 293 nmrad. The magnetic lattice is almost the same as the original one. Now we consider the future plans of KEK light sources. One is the fully new facility applying DQBA lattice, named KEK-LS. The circumstance is 571 m, and the emittance is 315 pmrad @ 3 GeV and 500 mA. In parallel with that, two plans of the only replacements of the lattices reusing existing tunnels of PF and PF-AR are considered. For the PF upgrade, only the arc lattice will be replaced with a new lattice employing combined bends, and the emittance will be improved to 8 nmrad from 35 nmrad. For the PF-AR update, fully replacement will be carried out with a new HMBA lattice, and the expected emittance is 520 pmrad @ 3 GeV and 500 mA.

PRESENT STATUS

KEK is one of the biggest laboratory in Japan focusing on Accelerator Science, and has not only the high-energy accelerator for the particle experiments but also light sources for the research such as material science and biology. We have two ring-based light source: Photon Factory (PF) and Photon Factory Advanced Ring (PF-AR).

Photon Factory

PF ring began the user operation in 1982 with the horizontal emittance about 460 nm·rad [1,2]. The emittance reduced to about 128 nm·rad by the low emittance configuration in 1986 [3], and about 36 nm·rad by the high-brilliance reconstruction in 1997 [4]. Before the reconstruction in 1997, the normal cell consists of two bending magnets. After the reconstruction, the normal cell consists of only one bending magnet. The number of the quadrupoles, sextupoles and the normal cells were doubled in order to reduce emittance. By the straight sections upgrade in 2005, the lengths of the existing straight sections were extended and new four straight sections for the in-vacuum insertion device were installed. At present, the insertion devices were installed to the all available straight sections.

* nao.higashi@kek.jp

Photon Factory Advanced Ring

PF-AR is 6.5 GeV light source dedicated to the single bunch operation. The ring originally constructed as an accumulation ring (AR) for TRISTAN project in 1984. Because KEKB, the successor of TRISTAN adopted the full-energy injection from LINAC, AR becomes PF-AR, the full-time synchrotron radiation facility. The circumference of PF-AR is 377 m with four long straight sections. East and west long straight sections are used for RF cavities. North and south straights are originally used for detector development for TRISTAN. Presently, the insertion device is installed in the north straight section and just small accelerator components in south. Because the original injection and extraction systems are installed to the south half of the ring, the experimental hall for SR users are concentrated only in the north half of the ring. The emittance of the present FODO structure lattice is about 300 nmrad for 6.5 GeV that is about two orders of magnitude worse than those of present advanced SR facilities.

FUTURE PLAN

Now we are planning a construction of a fully-new light source called KEK-LS. This is based on the ESRF-type HMBA (Hybrid Multi Bend Achromat) lattice, and promoted to be constructed in KEK Tsukuba campus. Recently, we improved the design reported in the conceptual design report (CDR) in Oct. 2016 to add the two quadrupole magnets to the short straight section. We call this new lattice DQBA (Double Quadruple Bend Achromat) lattice, and it has more flexibility of the lattice design, better emittance and larger dynamic apertures than the CDR design. In parallel with this, the upgrades for the existing facilities of PF and PF-AR are considered. For the PF upgrade, the limited improvement of the arc part to double the bending magnet and introduce the combined bend will be applied. For the PF-AR upgrade, the full-replacement of the lattice will be carried out employing the flexible DQBA KEK-LS lattice. The scales of the budget and the improvements of the emittance are summarized in Table 1. In the following, the each project is explained in detail.

KEK-LS

KEK-LS is a fourth generation 3.0 GeV light source and promoted to be constructed in KEK Tsukuba campus. We start the lattice design from the example lattice of 3 GeV EBS with 20 cells [5, 6]. Then, the short straight section of 1.2 m was added in order to double the number of the insertion device. We reported this design as CDR [7]. The circumference is about 570 m, and the horizontal natural

ISBN: 978-3-95450-206-6 doi:10.18429/JACoW-FLS2018-MOP1WB03

Table 1: Each Budget Scale and Emittance of Ring-Based Future Light Source in KEK

	Rough budget size [million US$]	Current emittance [nm·rad]	Improved emittance [nm·rad]
KEK-LS	300	-	0.315 (CDR ver. with 500 mA)
PF Upgrade	20	35.4	8.073 (with 450 mA)
PF-AR Upgrade	100	295.2	0.520 (with 500 mA)

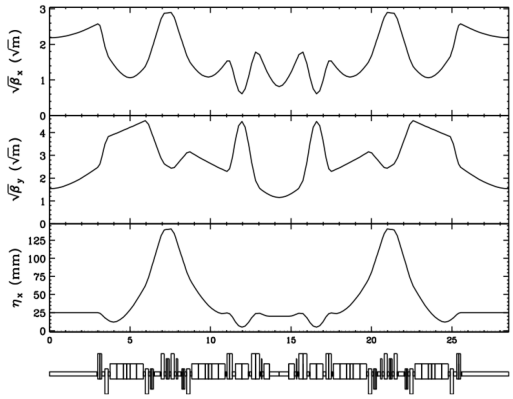

(a) Present CDR version

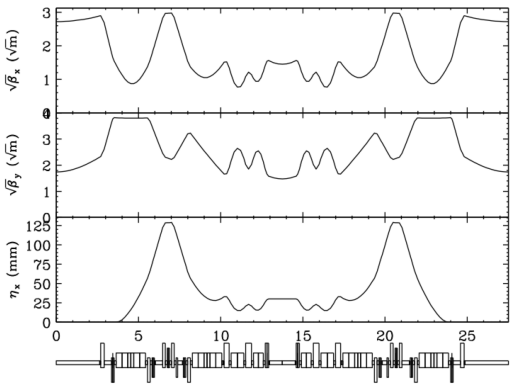

(b) 5m section achromat for DQBA

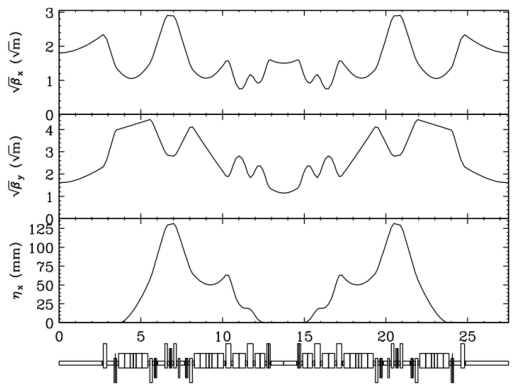

(c) Complete achromat for DQBA

Figure 1: Optics of the normal cell.

emittance about 133 pm·rad. Since the original example lattice has very small amplitude and momentum dependent tune shifts and results in the large dynamic apertures, the small distortions were accumulated during the lattice studies and the dynamic apertures and lattice flexibility become

Table 2: Parameters of the Ring

	Symbol [Unit]	CDR (a)	New DQBA (b)	(c)
Energy	E [GeV]	3.0		
Cell number	N_s	20		
Circumference	C [m]	570.721		
RF freq.	f_{RF} [MHz]	500.0735096		
Harmonic Number	h	952		
RF voltage	V_{RF} [MV]	2.5		
Beam current	I [mA]	500		
Betatron tune	ν_x	48.58	47.10	
	ν_y	17.62	17.15	
Horizontal emittance (w/o IBS)	[pm·rad]	133	121	253
(effective, 5 m sec., w/o IBS)	[pm·rad]	160		
(effective, short st., w/o IBS)	[pm·rad]	225	204	
(500 mA w/ IBS)	[pm·rad]	315	228	366
Residual dispersion (@ long straight)	[mm]	25	0	0
(@ short straight)	[mm]	20	3	0
Bucket height	$\Delta E/E$ [%]	4.5	4.5	4.0
Energy loss	U_0 [MeV/rev.]	0.30	0.26	0.26
Momentum compaction	α [$\times 10^{-4}$]	2.2	2.4	3.1
Damping time	τ_x [ms]	29.3	21.5	23.4
	τ_y [ms]	38.3	43.1	43.1
	τ_z [ms]	22.6	43.4	37.2
y/x coupling	[%]	2.6	3.5	2.2
Vertical emittance	ε_y [pmrad]	8.2	8.0	8.1
Momentum Aperture	[%]	2.8	4.0	4.0
Horizontal Aperture	[σ_x]	150	200	200
Touschek lifetime	[hour]	2.4	17.0	27.0
Energy spread (0 mA)	σ_E/E [$\times 10^{-4}$]	6.4	7.2	6.7
(500 mA)	σ_E/E [$\times 10^{-4}$]	7.9	9.7	8.5
Bunch length (0 mA)	[mm]	2.7	2.8	2.9
(500 mA)	[mm]	3.3	3.8	3.8

deteriorated. In order to recover and improve the performance, the two quadrupoles are added to the short straight sections [8]. For this modification, the flexibility of the lattice design, the emittance and the dynamic apertures are improved. The similar lattice was already examined for the DIAMOND II as DTBA [9]. Following this, we call the improved HMBA lattice as DQBA. In this following, we show the shortage of present CDR version lattice and advantage of the DQBA lattice for the KEK-LS.

The parameters of the CDR version lattice is shown in Table 2 and the optics in Figure 1 (a). Firstly, the momentum aperture is about 3 %. For this lifetime, the estimated beam loss is about three times larger than the present PF ring during the hybrid mode (lowest lifetime mode). Though this may be too permissive, the longer lifetime is better. For the second, the insertion device causes the emittance growth [10] because of the low horizontal beta and the residual dispersion at the straight section. While the achromatic long straight section can be realized by about 15 % effective emittance deterioration, the achromat of the short straight section results in the very large emittance. At the short straight section, the residual dispersion is 25 mm and the horizontal beta function 0.66 m. With these parameters, The

ISBN: 978-3-95450-206-6 doi:10.18429/JACoW-FLS2018-MOP1WB03

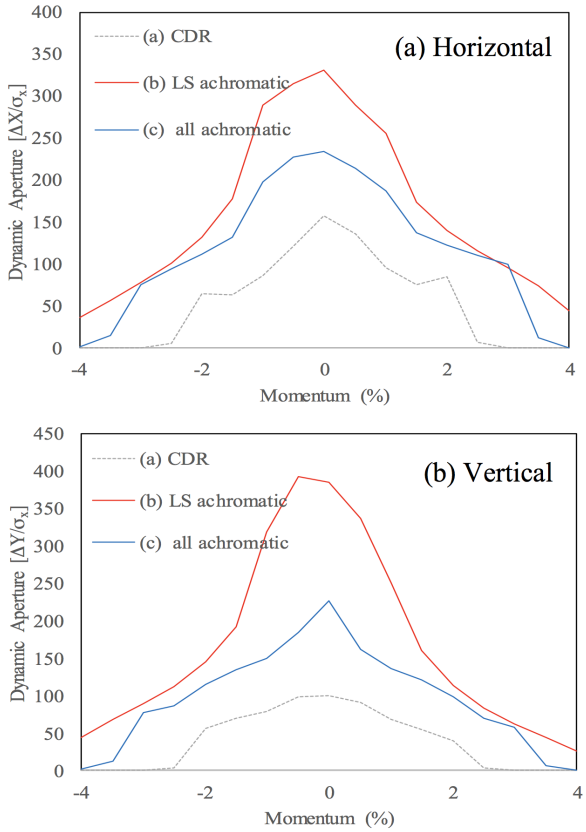

Figure 2: Dynamic aperture for each design of KEK-LS.

short in-vacuum insertion device of 0.6 m length results in the significant emittance growth.

The DQBA option was firstly developed in collaboration with ESRF. It has better emittance and apertures than the CDR version. Figure 1 and Table 2 shows the two cases for DQBA version; the case (b) has the achromatic long straight section with the chromatic short straight section, and for the case (c), both straight sections are completely achromatic. The effective emittance in the Table 2 shows the emittance including the effects of the dispersion function and energy spread. For the case of 500 mA, the effect of intra-beam scattering (IBS) is considered[1]. With larger momentum and horizontal amplitude aperture, the lifetime certainly may be longer for DQBA case than that of CDR case. The dynamic aperture with magnetic errors are shown in Figure 2. The assumed magnetic errors are the Gaussian random magnetic errors of the standard deviation 1 σ for the alignment errors of 50 μm, the magnetic field fluctuation of 0.05 %, and skew rotation of the magnets of 0.1mrad. The results shows the average of 100 random seeds. The systematic magnetic errors like the higher order components of the magnets and the effect of the insertion devices are not included.

[1] Presently, the estimation of Touschek lifetime are very rough, and not calculated by LMA (local momentum acceptance) method. It seems that some important effect is not included and calculated lifetime seems to be too long.

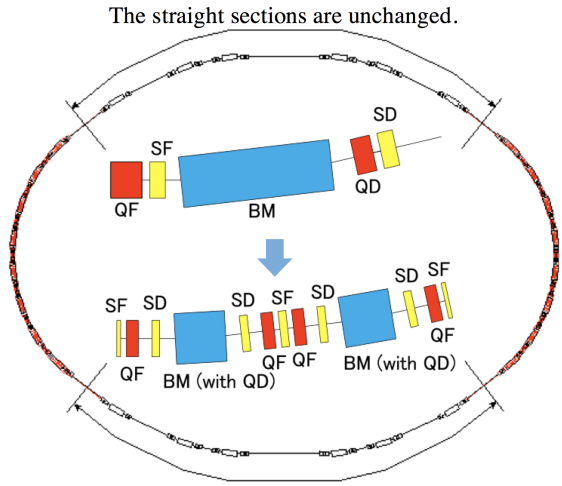

Figure 3: Lattice Modification of PF Upgrade.

For the DQBA cases, the maximum quadrupole magnetic field is about 60 T/m. The minimum magnetic spacing is 12 cm core to core. If we can relax these parameters, it is easier to design the hardware. The precise calculation of lifetime and simulation including more types of errors are required. The quadrupoles are only used to optics change from (b) to (c). The matching of beta function is required to select the optics cell by cell.

PF Upgrade

The present horizontal emittance of the Photon Factory (PF) ring is about 35.4 nm·rad. By the reconstruction of the normal cells at the arc section, the emittance can be reduced to about 8 nm·rad. In this proceedings, the design, optimization and simulation results for the low emittance lattice are shown.

Figure 3 shows the section for the reconstruction. While the straight sections are unchanged, the arcs are reconstructed. Similar to the reconstruction in 1997, the numbers of the normal cells are doubled by replacing the present 1.9 m length bending magnet to the new two short combined function magnets of 0.65 m length. While the horizontal emittance of the present normal cell is about 41 nm·rad, it reduces to 4.6 nm·rad by doubling the cell number. The parameter of the ring is shown in Table 3. Although the chromaticity is not largely increased, the strong chromatic sextupoles by about ten times are required due to the small dispersion function. In order to realize them, the diameter of the magnetic poles of the sextupoles are reduced from 90 mm to about 40 mm.

For the large dynamic aperture, the linear optics of the straight sections are designed to be transparent for the sextupoles. The matching section at the end of the normal cell consists of one bending magnet and no sextupole, and the identical 14 normal cells form the arc section. For the large dynamic aperture, the tune advance of the straight section with the matching sections are adjusted to be integer or the half integer. If the sextupoles are installed to the dispersive

ISBN: 978-3-95450-206-6 doi:10.18429/JACoW-FLS2018-MOP1WB03

Table 3: Parameters of the PF Upgrade

	Symbol [Unit]	PF Upgrade
Energy	E [GeV]	2.5
Circumference	C [m]	187.0
Emittance	ε_0 [nm·rad]	8.073
Emittance of Normal Cell	ε_{NC} [nm·rad]	4.561
Energy spread	σ_E/E	1.64×10^{-3}
Momentum compaction	α	4.39×10^{-3}
Betatron tune	ν_x, ν_y	12.1, 6.2
Chromaticity	ξ_x, ξ_y	-17.573, -25.117
Energy loss	U_0 [MeV/rev.]	0.513
Damping time	τ_x, τ_y, τ_z[ms]	3.040, 6.109, 6.171
Revolution freq.	f_{rev} [MHz]	1.60253
RF freq.	f_{RF} [MHz]	500.100
Harmonic Number	h	312
RF voltage	V_{RF} [MV]	1.70
Synchrotron tune	ν_s	-0.009
Bunch length	σ_z [mm]	10.475
Bucket height	$\Delta E/E$ [%]	1.7

section of the long straight section, the total strength of the sextupoles can be largely reduced. The dynamic aperture, however, also largely reduced. Although the error of the tune advance for the transparency is acceptable to some extent, the sextupole component at the long straight sections are unacceptable for the large aperture.

Figure 4 shows the simulated dynamic aperture after the COD correction with the random magnetic errors of the alignment errors of 50 μm, field fluctuation of 0.05 % and rotation of 0.1 mrad. Even with these errors, the dynamic aperture is as wide as that of the present PF ring. At the injection point, the present dynamic aperture is about 24 mm for the ideal case. For the new lattice, β_x is 10.25 m and the horizontal dynamic aperture is about 23 mm with 80 σ aperture. With the worst case of the simulation, it may be about 17 mm with 60 σ aperture. The optics of the straight sections are almost unchanged. The injection scheme and the minimum gap of the in-vacuum undulators can be kept unchanged. The brilliances of the insertion devices are improved by 7-8 times [11].

PF-AR Upgrade

Photon Factory Advanced Ring (PF-AR) has been operated for users over 30 years from 1987. The lattice and optics are almost not changed from the original one as the TRISTAN booster ring constructed in 1984. The lattice employs FODO structure and the horizontal emittance for the 6.5 GeV user run is about 300 nm·rad. In order to improve the performance of PF-AR dramatically, the full replacement of the accelerator to the ESRF-type HMBA (Hybrid multi bend achromat) lattice is examined. In order to geometrically fit the new lattice to the present PF-AR tunnel, the new ring consists of 12 cells with four long straight sections. The emittance is improved to about 500 pm·rad at 3.0 GeV.

In order to fit the circumference, we determined the cell number 12. We started the design from the ring consisting of the identical 12 normal cells with the circumference of about 330 m and the emittance of about 0.5 nm·rad for 3.0 GeV. We add the short straight section to double the numbers

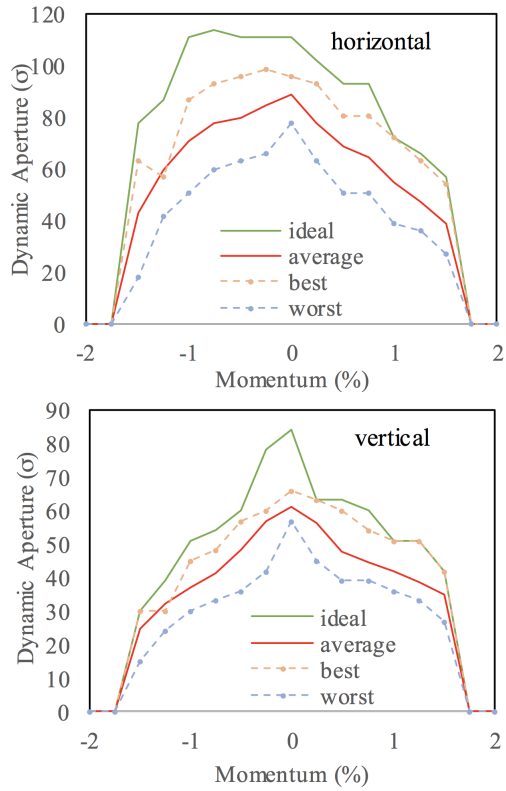

Figure 4: The Dynamic Aperture of PF Upgrade.

of available insertion devices. In order to fit the ring for the existing accelerator tunnel, we adjusted the length of the straight sections of the symmetrical 12 cells. The required geometrical adjustments are shown in Figure 5.

Assuming the magnetic errors similar to present PF ring as the Gaussian random alignment errors of 50 μm, field fluctuation of 0.05 %, and rotation of 0.1 mrad, the simulated dynamic aperture after COD correction is show in Figure 6. With errors, the momentum aperture is about 3.5 % and

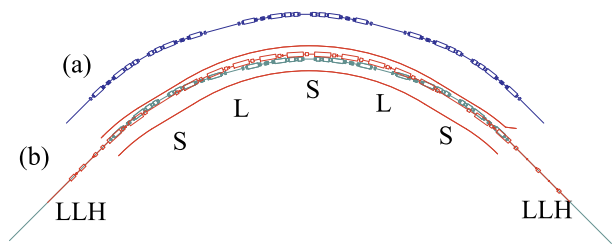

Figure 5: Geometrical adjustment of the long straight section to fit the existing tunnel arc. Figures show the quarter of the ring. The blue figure (a) is the symmetrical ring with twelve identical normal cells for the starting point of the design. The red figure in (b) shows the existing PF-AR lattice of FODO structure and the tunnel wall of the arc section. The green figure shows the new lattice for the replacement. S is the short straight section of 1.68 m, L the arc long straight of 2.7 m. LLH is the very-long straight section that has about 23 m length between two bending magnets at the both sides.

ISBN: 978-3-95450-206-6 doi:10.18429/JACoW-FLS2018-MOP1WB03

the horizontal amplitude 150 σ_x. Here, σ_x is the amplitude normalized with the horizontal beam size. The dynamic aperture is large enough to adopt the conventional injection system and the estimated Touschek lifetime is about 5.6 hours. The parameters of PF-AR upgrade are summarized at Table 4.

Table 4: Parameters of the Ring

	Symbol [Unit]	PF-AR Upgrade	
Energy	E [GeV]	3.0	
Cell number	N_s	12	
Circumference	C [m]	374.28	
RF freq.	f_{RF} [MHz]	500	
Harmonic Number	h	544	
Energy loss	U_0 [MeV/rev]	0.4259744	
Momentum compaction	α	5.6715×10^{-4}	
Damping time	τ_x, τ_y, τ_z[ms]	8.365, 17.58, 19.59	
RF voltage	V_{RF} [MV]	2.5	
Bucket height	$\Delta E/E$ [%]	3.58	
Betatron tune	ν_x, ν_y	28.7, 10.2	
Beam current	I_b [mA]	0	500
Horizontal emittance	ε_x [pm·rad]	481.15	520.23
Vertical emittance	ε_y [pm·rad]	-	7.8
y/x coupling	[%]	-	1.5
Touschek lifetime	[hour]	-	5.6
(3.5 % $\sigma_{\Delta p}$, 150 σ_x)			
Energy spread	-	9.79×10^{-4}	1.01×10^{-3}
Bunch length	[mm]	5.21	5.37

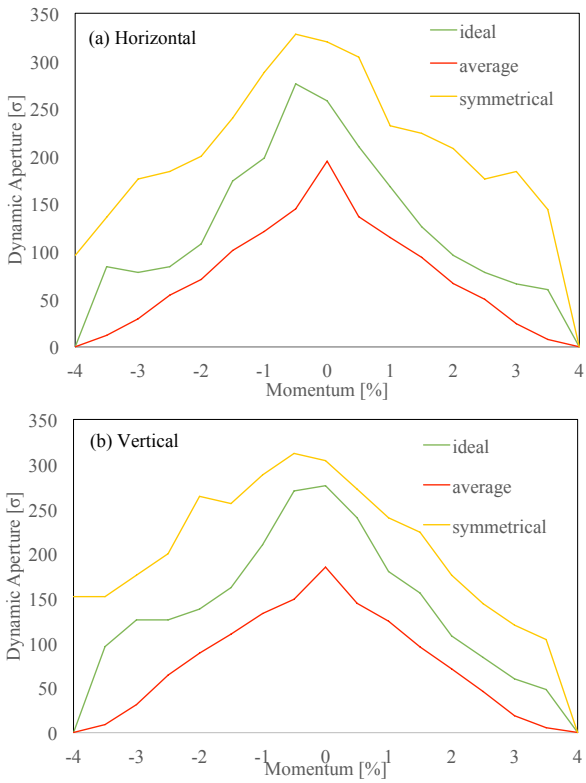

Figure 6: Dynamic aperture with reasonable magnetic errors after COD correction. The line "average" shows the averaged dynamic aperture for 100 random error seeds. The line "ideal" shows the aperture without errors and "symmetrical" for the symmetrical 12 cells case without errors.

SUMMARY

PF and PF-AR have provided user-runs over 30 years. Although some improvements were carried out to reduce the emittance, those international competitive powers are gradually decreasing. HMBA lattice recently appeared is pretty attractive, and we are now promoting a new 4th generation light source of KEK-LS based on the ESRF-type HMBA lattice. This new project is very powerful as an alternative of PF and PF-AR. However, its construction cost are estimated to be 100 million US$ roughly, therefore we are considering other projects with relatively small scale in parallel with KEK-LS project. We will proceed to consider which the best candidate is, comparing the expected qualities and the costs.

REFERENCES

[1] S. Kamada, Y. Kamiya , M. Kihara, "Lattice of Photon Factory Storage Ring", Proc. of PAC 1979, p.3848.

[2] "PF Ring Design Handbook", 1979.

[3] Y. Kamiya, M. Kihara, "Low emittance configuration for Photon Factory storage ring", KEK Internal 85-10, Dec, 1985 (in Japanese).

[4] M. Katoh, Y. hori, "Report of the Design Study on a High Brilliance Configuration of the PF Storage Ring", KEK Report 92-20, Feb., 1993 (in Japanese).

[5] ESRF Orange Book, http://www.esrf.eu/Apache_files/Upgrade/ESRF-orange-book.pdf

[6] Pantaleo Raimondi, private communications.

[7] KEK-LS CDR, http://kekls.kek.jp/ (in Japanese).

[8] Simone Liuzzo, KEK visit for 6/25-7/10, 2016.

[9] R. Bartolini, et.al., "Concepts for a low emittance-high capacity storage ring for the DIAMOND light source", Proceedings of IPAC2016, Busan, pp.2943-2946.

[10] M. Katoh and Y. Kamiya, "Effect of Insertion Devices on Beam Parameters", Proc. of PAC 1987, pp. 437-439.

[11] K. Tsuchiya, private communications.

ISBN: 978-3-95450-206-6 doi:10.18429/JACoW-FLS2018-MOP2WB01

ACCELERATOR PHYSICS STUDIES FOR THE HIGH ENERGY PHOTON SOURCE IN BEIJING*

Y. Jiao†, X.H. Cui, Z. Duan, Y.Y. Guo, D.H. Ji, J.Y. Li, X.Y. Li, Y.M. Peng, Q. Qin, S.K. Tian, J.Q. Wang, N. Wang, Y.Y. Wei, G. Xu, H.S. Xu, F. Yan, C.H. Yu, Y.L. Zhao, Key Laboratory of Particle Acceleration Physics and Technology, IHEP, CAS, Beijing 100049, China

Abstract

The High Energy Photon Source (HEPS) is the next ring-based light source to be built in China, with an emittance of tens of picometers, and a circumference of about 1.3 km. After 10 years' evolution, the design for the HEPS is recently basically determined. In this report we will briefly introduce the latest HEPS lattice design and the progress in related physics studies.

INTRODUCTION

The High Energy Photon Source (HEPS) is a 6-GeV, 1.3 km, ultralow-emittance storage ring light source to be built in the Huairou District, northeast suburb of Beijing. After iterative discussions, the goal emittance of the HEPS storage ring lattice design is to obtain a natural emittance of below 100 pm.rad.

As the R&D project for HEPS, the HEPS test facility (HEPS-TF) has started in 2016, and is to be completed by the end of Oct., 2018. The goals of the HEPS-TF project are to develop key hardware techniques that are essentially required for constructing a diffraction-limited storage ring light source, and meanwhile, to complete the design for the HEPS project. The main goal of accelerator physics studies is to obtain an 'optimal' lattice design for the HEPS, study the related physics issues and ensure there is no show-stopper from beam dynamics point of view, and give as detailed parameter list and tolerance budget table as possible for various hardware systems.

For the sake of the R&D of key hardware techniques and studies of the related physics issues of the HEPS-TF project, a baseline lattice with 48 identical hybrid-7BAs, a natural emittance of about 60 pm and a large ring acceptance that promises different injection schemes was proposed [1].

For the HEPS project, in 2017, we finished the conceptual design report and the feasibility study report. Now we are preparing the preliminary design report, hoping that we could start the construction before 2019.

Recently, a new lattice with a lower natural emittance, i.e., 34 pm, was proposed for the HEPS project, which still consists of 48 hybrid-7BAs but in 24 periods, and contains superbends and anti-bends.

Based on this lattice, we are carrying out related physics studies, including collective effect study, error effect and lattice calibration simulation, injection system design, injector design, etc. In the following, we will briefly overview the evolution of the lattice design and introduce the status of the related physics studies.

* Work supported by NSFC (11475202, 11405187, 11205171)
† jiaoyi@ihep.ac.cn

LATTICE DESIGN & PHYSICS STUIDES

Early in 2008, a kilometre-scale storage ring light source with beam energy of 5 to 6 GeV was proposed to be built in Beijing [2] (called Beijing Advance Photon Source that time). Extensive efforts have been made on the lattice design and related physics studies. As shown in Fig. 1, over the past ten years, the lattice structure has been continuously evolved, from DBA, standard 7BA, TBA, standard 7BA with high-gradient quadrupoles, hybrid 7BA with high-gradient quadrupoles [3-15], to the latest structure, hybrid 7BA with super-bends and anti-bends. The beam energy was fixed to 6 GeV around 2014. The circumference was fixed to 1360.4 m in 2017.

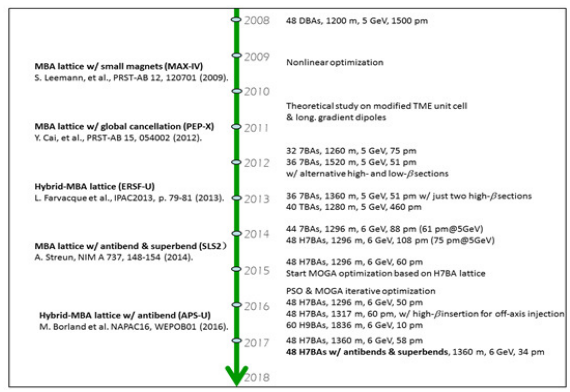

Figure 1: Evolution of the HEPS lattice over the past ten years. The figure also shows several project designs in the world on the left side of the time axis.

Optimization studies [1] based on the HEPS lattice with 48 identical hybrid-7BAs show that there is a trade-off between the emittance (brightness) and the ring acceptance. If satisfying only the dynamic aperture (DA) requirement of on-axis swap-out injection, the HEPS ring emittance can be pushed down to ~45 pm.rad; if pursuing large ring acceptance that allows for accumulation injections, the DA can be optimized to be close to (if not larger than) 10 mm in the injection plane, while keeping the emittance to be around 60 pm.rad. The main reason for this trade-off is that the beta function requirements for the DA and brightness optimization are different and even in conflict.

After discussing with beamline experts, we noticed that there are not so many users preferring high brightness as expected. Some users require high flux while not necessarily high brightness. And some users like wide covering range of the synchrotron radiation wavelength, and do not care much about high flux or high brightness. So we decided to look for an alternative high-low beta design. In

ISBN: 978-3-95450-206-6 doi:10.18429/JACoW-FLS2018-MOP2WB01

this way, we can further push the beta function of one straight section down to close the optimal values for the highest possible brightness, and match the beta function of another straight section to moderate values for a large enough dynamic aperture.

Furthermore, we systematically compared different ultralow-emittance unit cells (details will be shown elsewhere), and found that the unit cell with a longitudinal gradient dipole in the middle and horizontal focusing quadrupoles with small anti-bending angles on two sides (as proposed in [16]) has the largest potential to minimize the emittance.

These considerations, together, bring about the latest HEPS lattice with a natural emittance of 34 pm. The optical functions along one period (two 7BAs) are shown in Fig. 2.

One important property of this design is that it provides a flexible source for dipole beam lines. The dipole within the central unit cell is a longitudinal gradient dipole with highest magnetic field in its central slice. Study shows that once the total bending angle and the dipole length of this dipole are kept the same, one can vary the field of the central slice from 0.5 to 3 T to provide X-rays with different critical photon energy, while causing little perturbation to the ring optics and nonlinear performance.

As shown in Fig. 3, the DA of the bare lattice is about 6 mm and 4 mm in x and y planes. The 'effective' momentum acceptance (considering the limitation of integer and half integer resonances [17]) is about 3%. When considering errors, after appropriate correction, the DA can be recovered to ~80% of that of the bare lattie.

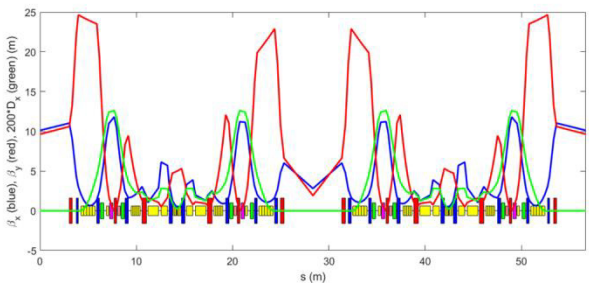

Figure 2: Optical functions along one period of the latest HEPS design.

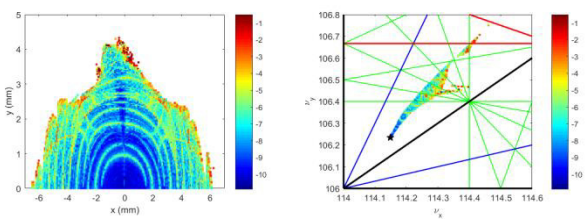

Figure 3: Dynamic aperture and corresponding frequency map of the latest HEPS design (bare lattice).

Injection to the Ring

We consider mainly the on-axis swap-out injection, while reserving possibilities for other injection schemes, especially the on-axis longitudinal injection (e.g., [18]). Two operational modes with different filling patterns are considered, i.e., low-charge mode (200 mA with 680 bunches) and high-charge mode (200 mA with 63 bunches).

To inject a high-charge bunch to the ring, while avoiding the strong collective effects at the lower energy of the booster ramping loop, we chose the 'high-energy accumulation' scheme. In this scheme, the booster at 6 GeV is used as a accumulator ring, and an extra transport line from the storage ring to the booster [19] is designed.

Especially for the high-charge mode, when the charge of the stored bunch of the ring reduces by a certain factor (e.g., from 14 nC to 12 nC), this bunch will be extracted and injected to the booster after passing through the transport line from the ring to the booster. The bunch will merge with an existing bunch in the booster (e.g., 2 nC) which has been injected from the linac and accelerated to 6 GeV. And then the merged bunch (in this example, now the charge is recovered to 14 nC) is extracted from the booster and re-injected to the ring.

This scheme needs high transfer efficiency, e.g., at least above 90%, to avoid too much beam loss during this process. We are carrying out simulation studies with the aim to clarify the error tolerance for the elements of the injection, extraction systems and the transport lines.

Error Study and Lattice Calibration

In presence of typical alignment, magnetic field, and BPM errors, simulations indicate that it is very difficult to accumulate the beam in the storage ring. To deal with this problem, we developed an automatic correction procedure that can gradually reduce the amplitude of the particle oscillation and finally realize storage of the beam [20].

We have simulated the lattice calibration process [21] with the AT program. For the HEPS lattice, by looking inside the error sources, we found the nonzero offset in sextupole is main contributors of DA reduction. Thus we included the sextupole alignment in the lattice calibration simulation, which helps recover the nonlinear performance. Later we will include the insertion devices in the lattice model, and simulate the correction process.

Collective Effects

The fundamental frequency of the HEPS RF system is chosen to 166.6 MHz. To relieve the strong intrabeam scattering (IBS) and Touscheck effects related to the increasing beam density with the decreasing emittance, we adopt third-order harmonic RF cavities with frequency of 499.6 MHz. The bunch length can be lengthened by about 3 times.

For the latest lattice, assuming the coupling factor is 10%, the Touschek lifetime was evaluated, about 5 and 0.7 hours for the low-charge mode and high-charge mode, respectively. Regarding such a poor lifetime, top-up injection is necessary and is under study for the HEPS.

The impedance budget of the HEPS storage ring was estimated [22]. It was found that the main contributions to the longitudinal impedance are resistive wall impedance and elements with large quantity, and the transverse broadband impedance is dominated by the resistive wall impedance due to the small-aperture vacuum chamber.

ISBN: 978-3-95450-206-6 doi:10.18429/JACoW-FLS2018-MOP2WB01

Based on the impedance model, the collective effects were evaluated with both analytical analysis and numerical simulations, especially for the high-charge mode for the HEPS lattice.

Among the single bunch instabilities, the transverse mode coupling instability is the strongest one. It leads to a threshold current of ~ 0.1 mA at zero chromaticity. This problem, however, can be solved with a positive chromaticity. Actually, in HEPS design, we set the corrected chromaticities to (+5, +5).

For the coupled bunch instabilities, the main contributors are the high-order modes (HOMs) of RF cavities and the resistive wall impedance (the full aperture of the vacuum chamber is on the level of 25 mm). In the storage ring, HOM damper has been carefully designed and optimized to damp the HOMs of the superconducting cavities. With the damped HOMs, we did not observe HOM induced coupled-bunch instabilities at 200 mA in macro-particle simulations. Nevertheless, to cure the instabilities and ensure stable operation, feedback system with damping time of shorter than 0.5 ms is required.

Injector Design

The HEPS injector consists of a linac and a booster. The booster will be located in a separate tunnel from the ring, in order to reduce the effect of the ramping cycle of the booster to the particle motions of the ring.

Inspite of the 'high-energy accumulation' scheme, it is still needed to store a bunch in the booster with a high enough charge, e.g., not less than 2 nC. To relieve the limitation due to collective effects, the linac energy was increased from 300 MeV to 500 MeV, and the booster lattice is changed from a 15BA to a FODO structure. The FODO lattice allows larger momentum compaction factor and a smaller average beta function, which is helpful to increase the bunch charge threshold at lower energy of the booster. As a price, the natural emittance of the booster at 6 GeV is increased from 4 nm to 40 nm.

CONCLUSION

After approximately ten years' evolution, a storage ring lattice with a natural emittance of 34 pm was basically reached for the HEPS project. Based on this lattice, studies on related physics issues are underway. So far we did not find great risks. Nevertheless, there are many issues still need to be looked inside to finally reach a complete design for the HEPS project.

REFERENCES

[1] Y. Jiao, et al., "Status of HEPS Lattice Design and Physics Studies", SAP2017, Jishou, Hunan, China, 2017.8.

[2] X. Jiang et al., "BAPS Preliminary Design Report", internal report, 2012.

[3] G. Xu, and Y. Jiao, "Towards the ultimate storage ring: the lattice design for Beijing Advanced Photon Source", Chin. Phys. C, 37(5), 057003 (2013).

[4] Y. Jiao, G. Xu, and D.H. Ji, "Latest design and optimization of the PEPX-type lattice for HEPS", SAP2014, Lanzhou, 2014.8.

[5] Y. Jiao, G. Xu, S.Y. Chen, Q. Qin, and J.Q. Wang, "Advances in physical design of diffraction-limited storage ring", High Power Laser and Particle Beams, 2015, 27(04): 045108.

[6] G. Xu and Y.M. Peng, Chin. Phys. C, vol. 39, p. 067001, 2015.

[7] Y. Jiao and G. Xu, "PEPX-type lattice design and optimization for the High Energy Photon Source", Chin. Phys. C, 39(6), 067004 (2015).

[8] G. Xu, Y. Jiao, and Y. Peng, "ESRF-type lattice design and optimization for the High Energy Photon Source", Chin. Phys. C, vol. 40, p. 027001, 2016.

[9] Y. Jiao, "Improving nonlinear performance of the HEPS baseline design with a genetic algorithm", Chin. Phys. C, vol. 40, p. 077002, 2016.

[10] G. Xu, et al., "Recent Physical Studies for the HEPS Project", IPAC2016, WEPOW026, Busan, Korea, 2016.5.

[11] Y. Jiao, et al., "Progress in the design and related studies on the High Energy Photon Source", Physics Procedia 84, p. 40-46, 2016.

[12] Y. Jiao and G. Xu, "Optimizing the lattice design of a diffraction-limited storage ring with a rational combination of particle swarm and genetic algorithms", Chin. Phys. C, 41(2): 027001 (2017).

[13] G. Xu, et al., "Progress of the Lattice Design and Physics Studies on the High Energy Photon Source", IPAC2017, WEPAB052, Copenhagen, Denmark, 2017.5.

[14] Y. Jiao, S.Y. Chen, G. Xu, "Candidate HEPS Lattice Design With Emittances Approaching the Diffraction Limit of Hard X-Rays", IPAC2017, WEPAB054, Copenhagen, Denmark, 2017.5.

[15] Y.M. Peng, et al., "The Off-Axis Injection Lattice Design of HEPS Storage Ring", IPAC2017, MOPIK079, Copenhagen, Denmark, 2017.5.

[16] A. Streun, A. Wrulich, Nucl. Instr. Meth., A, Vol. 770, p.98-112, 2015.

[17] Y. Jiao, Z. Duan, and G. Xu, "Characterizing the nonlinear performance of a DLSR with the effective acceptance of the bare lattice", IPAC2017, WEPAB055, Copenhagen, Denmark, 2017.5.

[18] G. Xu *et al.*, "On-axis beam accumulation enabled by phase adjustment of a double-frequency RF system for diffraction-limited storage rings", IPAC16, WEOAA02, Busan, Korea, 2016.

[19] Y.Y. Guo et al., "High energy transport line design for the HEPS project", IPAC17, MOPIK082, Copenhagen, Denmark, 2017.05.

[20] Y.L. Zhao et al., "First turns around strategy for HEPS", IPAC17, MOPIK082, Copenhagen, Denmark, 2017.05.

[21] D.H. Ji et al., "Study of HEPS performance with error model and simulated correction", IPAC17, MOPIK081, Copenhagen, Denmark, 2017.05.

[22] N. Wang et al., "Development of the impedance model in HEPS", IPAC17, WEPIK078, Copenhagen, Denmark, 2017.05.

ISBN: 978-3-95450-206-6 doi:10.18429/JACoW-FLS2018-MOP2WB04

STUDY OF MULTI-BEND ACHROMAT LATTICES FOR THE HALS DIFFRACTION-LIMITED STORAGE RING

Zhenghe Bai†, Lin Wang
National Synchrotron Radiation Laboratory, USTC, Hefei 230029, China

Abstract

In this paper, two multi-bend achromat (MBA) lattice concepts, the locally symmetric MBA and MBA with interleaved dispersion bumps, are described, which have been used to design the Hefei Advanced Light Source (HALS), a soft X-ray diffraction-limited storage ring proposed at NSRL. In these two MBA concepts, most of the nonlinear effects caused by sextupoles can be cancelled out within one lattice cell as in the hybrid MBA proposed by ESRF EBS, but the available family number of sextupoles in one cell can be more than that in the hybrid MBA so that, for example, the tune shift with momentum can be better controlled to increase the dynamic momentum aperture (MA). Using the two MBA concepts, three kinds of lattices, 8BA, 6BA and 7BA, have been studied for the HALS, showing large on- and off-momentum dynamic apertures and large enough dynamic MA.

INTRODUCTION

Hefei Light Source (HLS) was a second-generation synchrotron light source at NSRL, which was operated in 1991. After about 20 years' operation, HLS started a major upgrade to improve its performance, which was successfully finished in 2014. After the upgrade, the beam emittance was reduced from 160 nm·rad to 40 nm·rad, and the number of the straight sections for insertion devices was increased to 6. Also after the upgrade, a proposal was put forward at NSRL to build a new soft X-ray diffraction-limited storage ring, which was named Hefei Advanced Light Source (HALS). At present, the beam energy of the HALS storage ring is chosen to be 2.4 GeV, and the beam emittance is aimed at less than 50 pm·rad.

The HALS storage ring lattice was initially designed [1] following the main feature of the hybrid multi-bend achromat (MBA) concept proposed by ESRF EBS [2]. But due to the limited families of sextupoles that can be used in one cell, it is hard to increase the dynamic MA. So we considered to develop other MBA concepts, in which not only the nonlinear cancellation can be done within one cell as in the hybrid MBA, but also the family number of sextupoles that can be used in one cell can be more than 3.

LOCALLY SYMMETRIC MBA LATTICES FOR HALS

In the locally symmetric MBA lattice concept [3], the beta functions of each cell are made locally symmetric about two mirror planes, between which the phase advances satisfy:

$$\mu_x=(2m+1)\pi,\ \mu_y=n\pi, \qquad (1)$$

as shown in Fig. 1. The sextupoles are also placed locally symmetric about the two mirror planes so that most of the nonlinear effects can be cancelled out within one cell, and there can be placed many families of sextupoles in this lattice. According to the position of the midplane in Fig. 1, the locally symmetric MBA can be classified into two kinds. If the midplane is at the middle of the arc section, it is called the first kind; while if the midplane is at the middle of the long straight section, it is called the second kind.

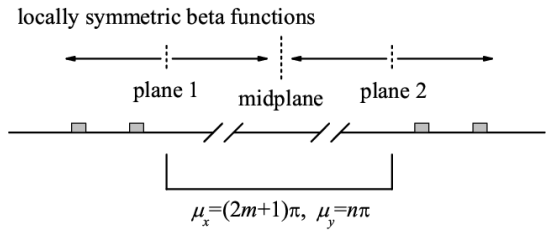

Figure 1: Schematic of locally symmetric MBA lattice.

The locally symmetric MBA of the first kind was used to design an 8BA lattice for the HALS storage ring, and the second kind was used to design a 6BA, which are shown in Fig. 2 and Fig. 3, respectively. Table 1 lists their main parameters. In the 8BA lattice, seven families of sextupoles and one family of octupole were employed for nonlinear dynamics optimization, and the 6BA lattice had five families of sextupoles and two families of octupoles. The nonlinear optimization results of the 8BA lattice with chromaticities corrected to (1, 1) are shown in Fig. 4, Fig. 5 and Fig. 6. The optimized DA is about 150 sigma; the dynamic MA at long straight sections is larger than 7%; and the off-momentum DAs are also large. In addition, from Fig. 5 we can see that if the chromaticities are corrected to slightly higher values, the dynamic MA can be further increased. The nonlinear optimization results of the 6BA lattice are also rather good, see Ref. [3].

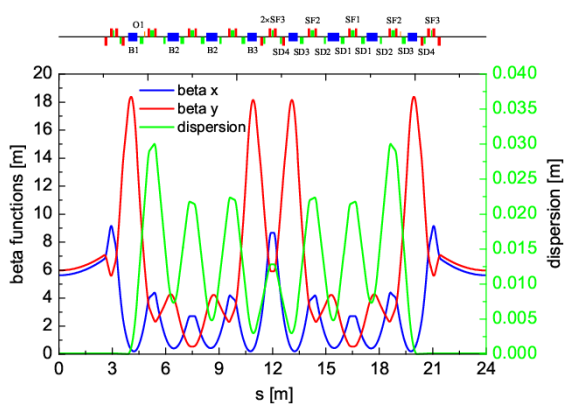

Figure 2: The HALS 8BA lattice.

† baizhe@ustc.edu.cn

ISBN: 978-3-95450-206-6 doi:10.18429/JACoW-FLS2018-MOP2WB04

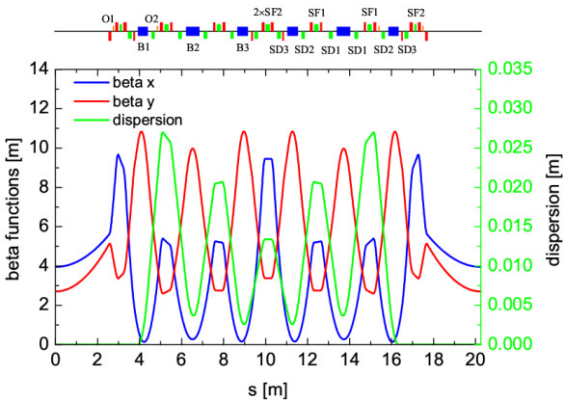

Figure 3: The HALS 6BA lattice.

Table 1: Main Parameters of the HALS 8BA and 6BA Lattice Rings

Parameter	8BA	6BA
Energy	2.4 GeV	2.4 GeV
Circumference	576 m	648 m
Number of cells	24	32
Natural emittance	35.8 pm·rad	26.5 pm·rad
Transverse tunes	76.205, 27.258	88.374, 23.284
Natural chromaticities	-136, -116	-204, -100
Momentum compaction factor	5.96×10^{-5}	3.42×10^{-5}
Beta functions at long straights	5.632, 5.977 m	3.904, 2.761 m

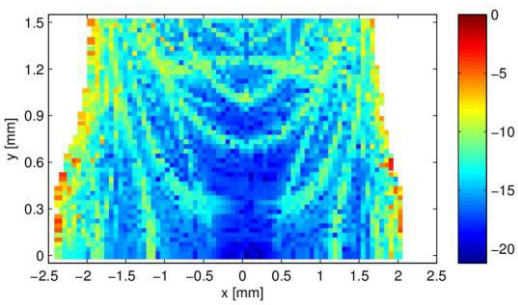

Figure 4: The optimized DA of the HALS 8BA lattice.

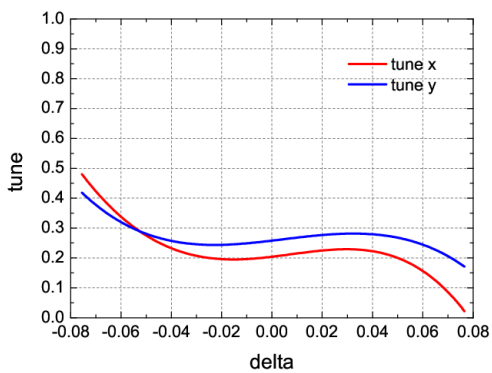

Figure 5: Tunes vs. momentum offset of the HALS 8BA lattice.

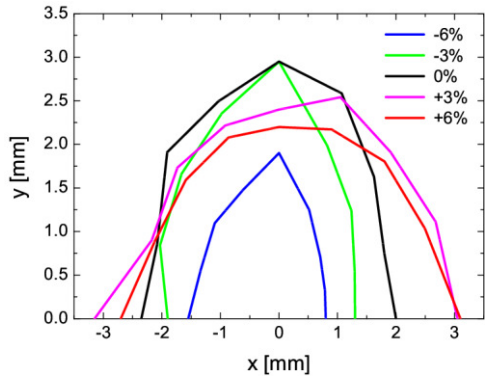

Figure 6: Off-momentum DAs of the HALS 8BA lattice.

7BA LATTICE WITH INTERLEAVED DISPERSION BUMPS FOR HALS

Inspired by the hybrid 7BA and the locally symmetric 6BA, we proposed a second MBA concept, the MBA with interleaved dispersion bumps [4]. In this concept, two pairs of dispersion bumps are created in each cell, which are interleaved from the nonlinear cancellation point of view, as shown in Fig. 7. Following this concept, a 7BA lattice was designed for the HALS storage ring, which is shown in Fig. 8, and the main parameters of the 7BA lattice ring are listed in Table 2. Six families of sextupoles, three in each pair of bumps, were employed for nonlinear optimization, and the chromaticities were corrected to (3, 3). The optimized DA is about 200 sigma, and the dynamic MA at long straight sections is about 8%, see Fig. 9 and Fig. 10, respectively. From Fig. 11 we can see that the off-momentum horizontal DAs are also large.

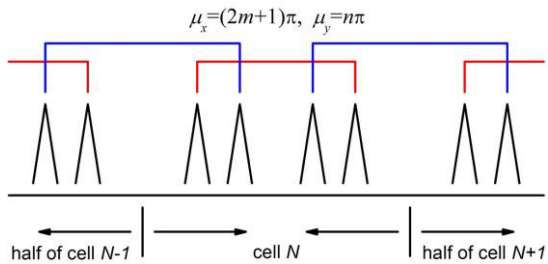

Figure 7: Schematic of MBA lattice with interleaved dispersion bumps.

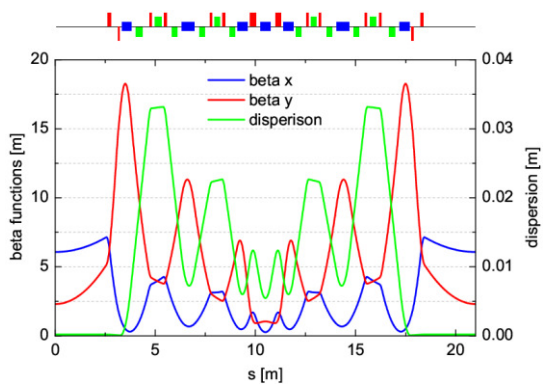

Figure 8: The HALS 7BA lattice.

ISBN: 978-3-95450-206-6 doi:10.18429/JACoW-FLS2018-MOP2WB04

Table 2: Main Parameters of the HALS 7BA Lattice Ring

Parameter	Value
Energy	2.4 GeV
Circumference	672 m
Number of cells	32
Natural emittance	32.1 pm·rad
Transverse tunes	78.273, 29.345
Natural chromaticities	-103, -117
Momentum compaction factor	5.75×10^{-5}
Beta functions at long straights	6.068, 2.299 m

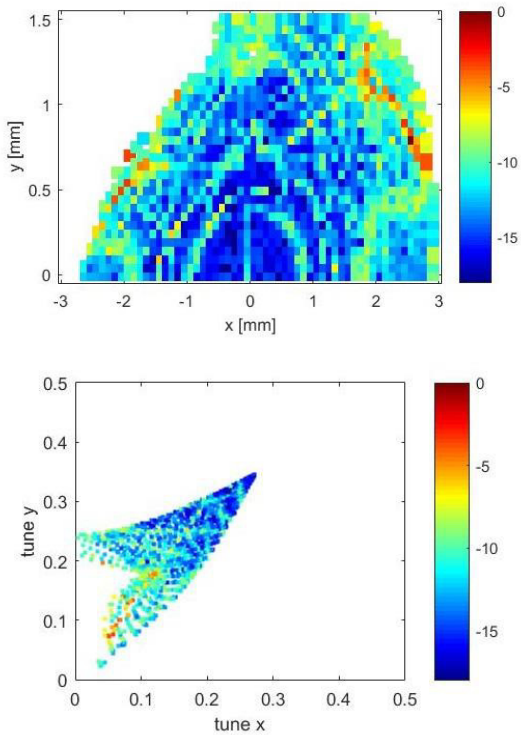

Figure 9: Frequency map analysis for the optimized DA of the HALS 7BA lattice.

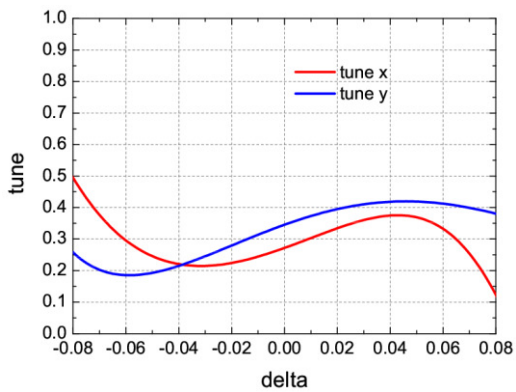

Figure 10: Tunes vs. momentum offset of the HALS 7BA lattice.

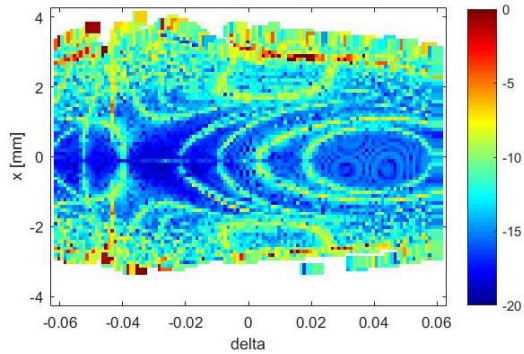

Figure 11: Horizontal DAs vs. momentum offset of the HALS 7BA lattice.

CONCLUSION AND OUTLOOK

Two MBA lattice concept, the locally symmetric MBA and MBA with interleaved dispersion bumps, have been described, which follow the same philosophy, i.e. doing nonlinear cancellation within one cell and also having many knobs to be used in one cell. Three lattices, an 8BA, a 6BA and a 7BA, have been designed with natural emittances of about 30 pm·rad for the HALS storage ring using these two MBA concepts. The optimized nonlinear dynamics results for these three lattices were rather good, showing large on- and off- momentum DAs and large enough dynamic MA (larger than 7%), which could not only guarantee a very long beam lifetime, but also promise the implementation of longitudinal injection [5] for the HALS. Besides, at present a lower-emittance 7BA lattice with longitudinal and reverse bending magnets is being studied using the MBA with interleaved dispersion bumps.

ACKNOWLEDGEMENTS

This work was supported by the National Natural Science Foundation of China (11605203, 11475167), the National Key Research and Development Program of China (2016YFA0402000), and the Chinese Universities Scientific Fund (WK2310000058).

REFERENCES

[1] Zhenghe Bai, et al., "Initial Lattice Design for Hefei Advanced Light Source: A VUV and Soft X-ray Diffraction-limited Storage Ring", Proceedings of IPAC2016, Busan, Korea, 2016.

[2] L. Farvacque, et al., "A Low-Emittance Lattice for the ESRF", Proceedings of IPAC2013, Shanghai, China, 2013.

[3] Zhenghe Bai, et al., "Design Study for the First Version of the HALS Lattice", Proceedings of IPAC2017, Copenhagen, Denmark, 2017.

[4] Zhenghe Bai, et al., "Multi-bend Achromat Lattice with Interleaved Dispersion Bumps for a Diffraction-limited Storage Ring", SAP2017, Jishou, China, 2017.

[5] M. Aiba, et al., "Longitudinal injection scheme using short pulse kicker for small aperture electron storage rings", Phys. Rev. ST Accel. Beams 18, 020701, 2015.

ISBN: 978-3-95450-206-6 doi:10.18429/JACoW-FLS2018-TUA2WB02

MULTI-BEND LATTICE ANALYSIS TOWARDS A DIFFRACTION LIMITED RING BASED LIGHT SOURCE

E. Karantzoulis, Elettra – Sincrotrone Trieste, Italy

Abstract

An analysis of lattice configurations up to 10 bend achromat is presented aiming towards diffraction limited ring based light source. The described analysis can apply to any type of a ring based light source however for practical reasons we consider Elettra that has been operating for users for 25 years; to stay competitive for world-class photon science in the future, a massive upgrade of the storage ring is needed. The optimum solution is based on certain design criteria, constraints regarding certain accelerator components and their implications on beam dynamics and user requirements. The space available for insertion devices as well as the impact of anti-bends on the design is also addressed. Two proposed realistic lattices are further discussed taking into account different criteria and user requirements. Those lattices reduce the emittance of the present machine by more than one order of magnitude but at the same time respect many other criteria such as realistic magnet gradients, magnets with magnetic length equal to the physical length, drift space enough for radiation extraction, large available space for insertion devices, minimal shift of the beam lines etc.

INTRODUCTION

Located on the outskirts of Trieste, Elettra operates for users since 1994 being the first third generation light source for soft X-rays in Europe. During those 25 years many improvements have been made to keep the machine competitive with the more modern light sources. At present the Elettra storage ring operates at 2.0 GeV (75% of the user time) and 2.4 GeV (25% of the user time) with beam currents of 310 mA and 160 mA, respectively. The total operating time is about 6400 hours/year of which 5000 are dedicated to the users on a 24/7 basis [1]. The storage ring lattice is a double-bend achromat (DBA) with an emittance of 7 nm-rad at 2 GeV and 10 nm-rad at 2.4 GeV. The ring has a twelve-fold symmetry with 12 long straight sections 11 of which host insertion devices (IDs) most occupying the 4.5 m per achromat pure space available for IDs.

The insertion devices (IDs) include 3 wigglers (one superconducting, one permanent magnet and one electromagnetic elliptical) and 8 undulators (3 sections host Apple-II type undulators). Another short undulator is installed in an additional 1.5 m short straight section in the arcs. Ten beam lines use the radiation from six bending magnets to yield the current total of 28 independently operating beam lines. Since 2010, Elettra has been operating in top-up mode, injecting 1 mA of current every 6 / 20 min at 2 GeV / 2.4 GeV, respectively

After 25 years of serving the user community with excellent results, a major upgrade towards what it is called the "ultimate" light source is planned to maintain its leadership for its energy range of synchrotron research and to enable new science and new technology developments to the general benefit.

Following the general trend of the rings for synchrotron light the new generation is generally characterized by a further increase of the brilliance and coherence of the photon source as compared to today's X-ray beams.

The brilliance of the source in general is given by:

$$B = \frac{flux}{4\pi^2 \Sigma_x \Sigma_{x'} \Sigma_y \Sigma_{y'}} \tag{1}$$

and the coherence fraction by:

$$\zeta = \frac{(\lambda / 4\pi)^2}{\Sigma_x \Sigma_{x'} \Sigma_y \Sigma_{y'}} \tag{2}$$

while the brilliance of the n^{th} harmonic of a well matched undulator for the corresponding λ_n photon wavelength is given by:

$$B_n = \frac{F_n}{4\pi^2 (\varepsilon_x + \lambda_n / 2\pi)(\varepsilon_y + \lambda_n / 2\pi)} \tag{3}$$

clearly those quantities become large by further reduction of the emittance of the stored electron beam at levels capable of providing a diffraction limited X-ray source also in the horizontal plane while such a limit has already been achieved at Elettra for the vertical plane. Elettra 2.0 thus, aims to provide intense beams in the range of VUV to X-rays for the analytical study of matter with very high spatial resolution.

Already in the 90's people were speculating on diffraction limited light sources [2] although the times were not yet ripe. Development in accelerator technologies during the last twenty years led to many important results featuring new magnet design, innovative vacuum and material technologies as well as important improvements in beam monitoring and feedback systems. Those new capabilities and technologies, which were not available or were at their infancy when the present Elettra storage ring was conceived, provide today a solid basis for the realization of the new machine.

Studies being carried out at Electra resulted in a new storage ring lattice design based on the multi-bend

emanuel.karantzoulis@elettra.eu (2018)

ISBN: 978-3-95450-206-6 doi:10.18429/JACoW-FLS2018-TUA2WB02

achromat concept and producing plausible versions of the new lattice [3-6].

OBTAINING A LOW EMITTANCE

The techniques in obtaining low emittances are well known and documented in the literature; a short description is presented here for the sake of completeness.

The emittance of a storage ring is given by:

$$\varepsilon_{x0}[mrad] = F_x(q_x, lattice)\frac{E^2(GeV)}{N_d{}^3} \qquad (4)$$

where N_d is the number of dipole magnets, E the ring energy and F_x a form factor depending on the H-function ($H=\gamma_x\eta_x^2+2\alpha_x\eta_x\eta'_x+\beta_x\eta'^2_x$) which is determined by the shape of the horizontal betatron and dispersion function in the dipoles and the horizontal damping partition number j_x (usually having values between 1 and 2). Low emittance can therefore be reached if betatron and dispersion functions have a minimum at the dipole locations. Such minimizing configuration can be achieved using unit cells consisting of one dipole and some quadrupoles. For space optimization unit cells of one dipole with a deflection angle ϕ and superimposed vertically focusing quadrupole component situated between two horizontally focusing quadrupoles are considered. From the above eq. 4 one sees that the more such unit cells the ring has, the smaller the emittance becomes since the dependence is one over the third power of the dipole number N_d. At the same time the more such unit cells are included in the lattice the less free space for insertion devices is available. It is important also to consider that the H-function minimisation of the unit cells leads to larger chromaticities which require stronger sextupoles, leading to problems with non linear dynamics and reduction of the dynamic aperture i.e. reduction of lifetime and difficulty with off-axis injection. It is then clear that a compromise should be found between the requested emittance, the free space needed for insertion devices and the accepted level of dynamic aperture and non linear effects. Furthermore in general it is preferable to have dispersion zero in the long straights where insertion devices are situated. This requires a matching of the Twiss functions to wished values in the straight section. Matching with minimised emittance is achieved when the outer dipoles of the arc have a magnetic length and deflection angle less than ϕ [2]. Those magnetic lattices are called multi-bend achromats (MBA).

ANALYSIS OF MBA LATTICES FOR THE NEW ELETTRA

The lattice of the actual Elettra is a double bend achromat. Its circumference is 259.2 m, twelve straight sections and 7 nm-rad emittance at 2 GeV. To see how the emitance is reduced assuming multi-bend achromats at 2 GeV keeping the same circumference and the same 12-fold symmetry, all optics up to 10-bend achromats were created, analyzed and plotted versus the number of dipoles per achromat (Fig. 1).

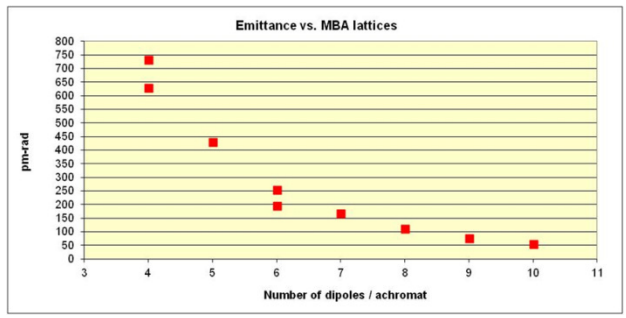

Figure 1: Emittance versus number of dipoles per achromat for an Elettra like ring at 2 GeV.

As can be seen from the above graph, one order of magnitude reduction of the actual emittance of Elettra occurs already for a 4-bend achromat or higher. For 4 and 6 BAs two solutions are shown. The solutins that show a reduction are achieved by using longitudinal gradient dipoles and anti-bends. Another beam parameter is the beam size achieved. In the table 1 below the emittances and the corresponding beam sizes in the long straight sections (LS) are shown.

Table 1: Emittance and beam size for various MBA lattices at 2 GeV for an Elettra size ring. The last column shows the brilliance increase factor compared to that of the actual machine for a certain undulator.

Number of dipoles / achromat	Emittance (nm-rad) @ 2 GeV	σ_x (μm) @ LS	σ_y (μm) @1% coupling @ LS	Brilliance increase factor at 1keV
2	7	240	14	
4	0.74 (0.63)	80	4.5	13 (15)
5	0.43	70	3	22
6	0.25 (0.19)	55	2.2	35 (43)
7	0.17	40	1.9	46
8	0.11	26	1.7	60
9	0.075	22	1.5	73
10	0.054	20	1.3	84

However many our users and partners are also interested in including super-bends, increasing the number of undulators, performing time resolved experiments and even consider the possibility to be able to go at a higher energy (2.4 GeV) as in the actual machine. This means that the available free space for insertion devices or other equipments is important.

In the next Figure 2 the free space per achromat is shown for up to 9-bend structure. The read colour indicates the pure free space for insertion devices in the long straights (dispersion free) whereas the green colour indicates free space for IDs or other equipment such as an Rf cavity in the arcs. From the graph below it is observed that only the 4 to 6 bend achromats give more or equal free space to that of the actual Elettra. This is due to the smaller magnet size, but then from 7 to 9 bend there is a reduction due to the increasing number of unit cells per achromat.

ISBN: 978-3-95450-206-6 doi:10.18429/JACoW-FLS2018-TUA2WB02

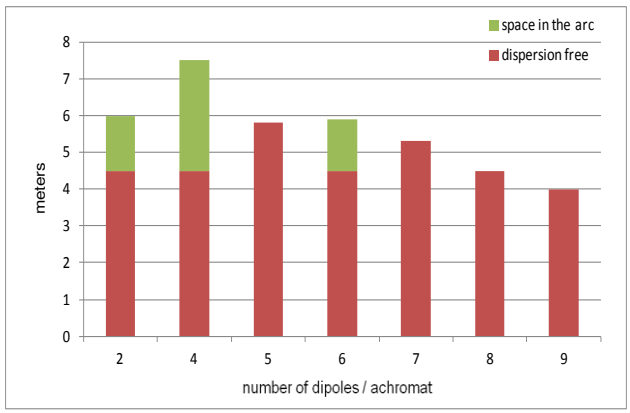

Figure 2: Free space per achromat for IDs or other equipment for various MBAs.

REQUIREMENTS FOR ELETTRA 2.0

The requirements for the new machine were defined in collaboration with some key users during a workshop back in 2014 as follows:

- Energy 2 GeV
- Emittance reduction by more than 1 order of magnitude
- Electron horizontal beam size less than 60 um
- Intensity 400 mA, maintain the filling patterns as before (hybrid, single bunch etc.)
- Use the same building and almost the same ring circumference (~260 m)
- Free space available for insertion devices (ID) not less than that of the actual Elettra
- Maintain the existing ID beam lines at the same position
- Maintain the existing bending magnet beam lines
- Use the existing injectors

From the above requirements and the analysis presented previously, the best candidate for Electra 2.0 is a 6BA lattice however also the 4BA lattice is quite attractive although its emittance reduction is not as high as in the case of 6BA (see table 1) and the horizontal beam size is larger than 60 microns (80 micron). However there is ample available free space and the lattice uses fewer and more relaxed magnets, it can thus work easily also at 2.4 GeV. Such a lattice may be a good candidate for a multivalent machine that needs to incorporate also the possibility of a variable bunch length. Since as mentioned before after the PHANGS workshop in December 2017 at ICTP Trieste, partners and users expressed interest in other aspects of the new machine, a trade between brilliance and the other aspects may be found. In the next we present a highly specialized version the so called S6BA lattice and a multivalent version the so called S4BA lattice. Note that the S6BA is the current official version that is also presented in the conceptual design report (CDR) already publicly available since 2017 [7].

THE S6BA LATTICE

The symmetric six bend achromat (S6BA) lattice consists of 6 quad-dipole-quad cells per achromat creating an invariant optic under relative position shifts between them. Thus relative long straight section can be created in the arcs without appreciable change of the optics functions increasing thus the space available for insertion devices.

The S6BA optics (basic version), shown in Figure 3 has an emittance of 0.25 nm-rad with working point (33.3, 9.2) and natural chromaticities (-75,-51).

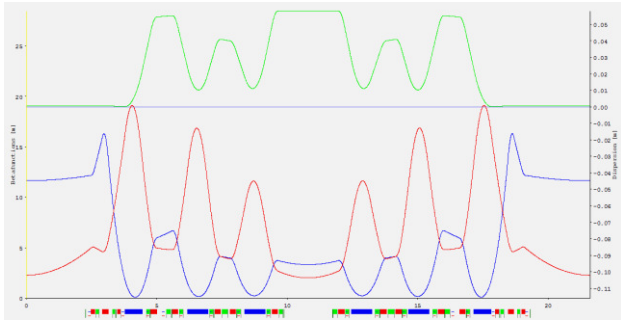

Figure 3: The S6BA lattice.

The corresponding horizontal beam size at the straight sections is 40 μm in the horizontal and 3 μm in the vertical at 1% coupling (however higher coupling i.e. towards round beams to avoid resistive wall effects is preferable) and the divergence is 6 μrad. The dipoles will be combined having a dipole field of 0.8 T (compared with 1.2 T at 2 GeV of the actual Elettra) and their maximum gradient is ≤15 T/m (compared with 2.8 T/m in Elettra). The quadrupoles have a maximum gradient of ≤50 T/m (compared with 15 T/m in Elettra).

The dispersion in the arcs is low (58 mm compared with 400 mm in the actual Elettra) meaning that also the short straight sections (1.8 m long) situated in the middle of the arc can be used for insertion devices or even, due to the very small and similar beam dimensions in both long and short straight sections, in-vacuum insertion devices with a 4.5 mm gap can be easily installed without additional optic elements.

Since the dipole fields of the lattice are now lower cannot be used for the dipole based beam lines but for the infrared beam line.

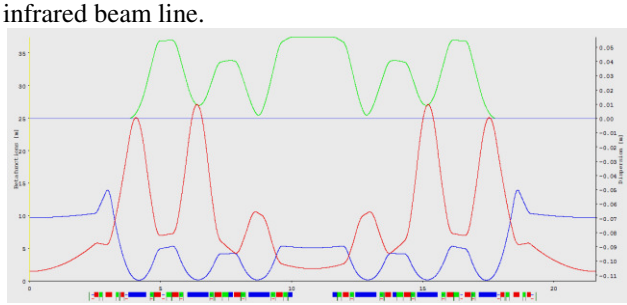

Figure 4: The S6BA lattice with anti-bends and two longitudinally focusing dipoles.

Two possible solutions were considered: either to install a short wiggler in the short straight section or to

ISBN: 978-3-95450-206-6 doi:10.18429/JACoW-FLS2018-TUA2WB02

install a super-bend. Both solutions may contribute to an emittance increase of the bare lattice depending upon their field and number. Another solution however exists by using some longitudinal gradient dipoles and anti-bends. In that case (Fig. 4) the dipoles that will serve a beam line can have a peak field of 2.2 T and the emittance is reduced to 0.19 nm-rad but the available free space in the arc is reduced to 1.55 m, still acceptable. In this version of S6BA four anti-bends are used to reduce the dispersion on the 3rd and 4th bending magnet that now has the following profile (Fig. 5)

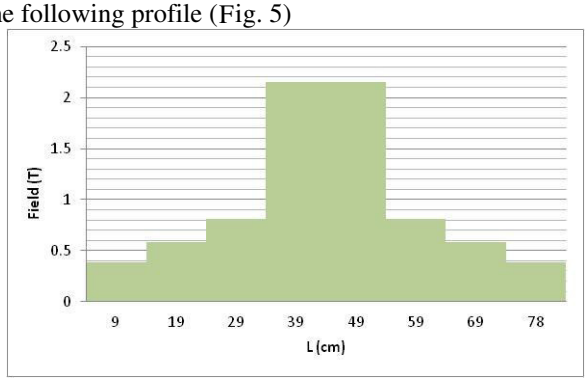

Figure 5: High field magnet profile.

The S6BA lattice basic version could also work at 2.4 GeV with a further reduction of the free space in the arc.

THE S4BA LATTICE

The symmetric four bend achromat (S4BA) lattice consists of 4 quad-dipole-quad cells per achromat (Fig. 6) creating an invariant optic under relative position shifts between them similar to those of the S6BA

The S4BA optics (basic version), shown in Fig. 6 has an emittance of 0.73 nm-rad with working point (24.3, 15.2) and natural chromaticities (-46,-58).

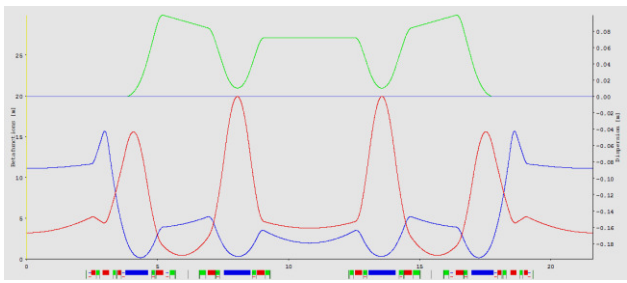

Figure 6: The S4BA lattice.

The corresponding horizontal beam size at the straight sections is 80 μm in the horizontal and 4.5 μm in the vertical at 1% coupling (however higher coupling i.e. towards round beams to avoid resistive wall effects is preferable) and the divergence is 11 μrad. The dipoles will be combined having a dipole field of 0.8 T (compared with 1.2 T at 2 GeV of the actual Elettra) and their maximum gradient is ≤12 T/m (compared with 2.8 T/m in Elettra). The quadrupoles have a maximum gradient of ≤36 T/m (compared with 15 T/m in Elettra).

The dispersion in the arcs is still low (76 mm compared with 400 mm in the actual Elettra) meaning that also the short straight sections (3.4 m long) situated in the middle of the arc can be used for insertion devices or even, due to the very small and similar beam dimensions in both long and short straight sections, in-vacuum insertion devices with a 4.5 mm gap can be easily installed without additional optic elements.

Similarly to the S6BA the longitudinal gradient version of the S4BA (Fig. 7) reduces further the emitance to 0.63 nm rad with the 2 and 3rd dipole having a field profile similar to the one in Fig. 5. As before, due to the anti-bends the free space in the arc is reduced to 2.8 m.

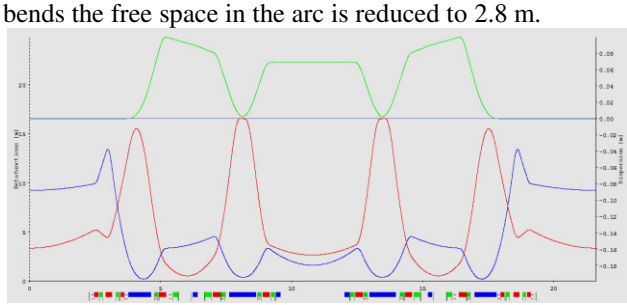

Figure 7: The S4BA lattice with anti-bends and two longitudinally focusing dipoles.

This lattice can without any change work also at 2.4 GeV although in that case the emittance increases to 0.9 nm-rad.

THE CURRENT ELETTRA 2.0 LATTICE

The S6BA at 2 GeV is considered the best possible lattice for Electra 2.0. It reduces the emittance by a factor 28 in a rather small circumference of about 260 m (12 achromats) while the requirement of the available free space to be at least as in the actual machine, results in having quite strong gradients in all magnets with an impact on the dynamic aperture. To investigate the DA, 6-dimensional (6-D) particle tracking was performed (2000 turns), including both betatron and synchrotron oscillations in the presence of classical synchrotron radiation emission and radiofrequency (RF) acceleration using Elegant [8,9] including alignment and field errors.

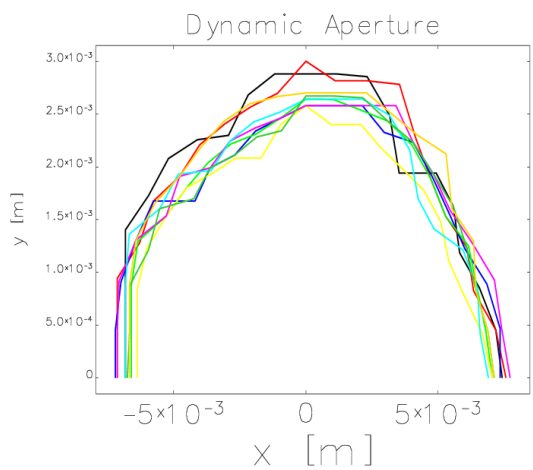

Figure 8: DA of the lattice with errors and all current insertion devices.

ISBN: 978-3-95450-206-6 doi:10.18429/JACoW-FLS2018-TUA2WB02

In Figure 8 the dynamic aperture (that can be further optimised) is shown including all errors and also all current insertion devices. As position errors were taken, 20 μm between magnets in a girder, 100 μm between girders and 100 μrad in angle. Field errors were taken as 0.01%. Values refer to the standard deviation of a Gaussian distribution with 3-sigma cutoff. As can be seen from Figure 8 the dynamic aperture is ±7 mm horizontally and ±2.5 mm vertically. This aperture allows off-axis injection and the use of the injectors as in the present machine.

In Figure 9 the injection efficiency versus the horizontal bump is shown for the current injection scheme configuration. With an injection bump of about 7 mm the predicted efficiency is above 95%.

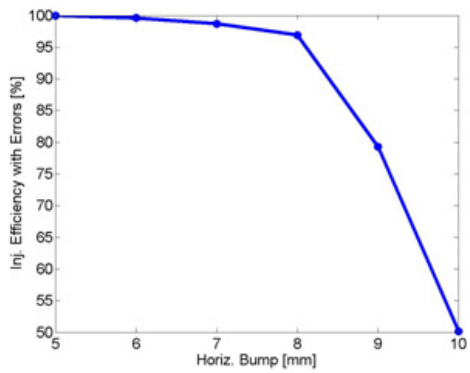

Figure 9: Injection efficiency versus the horizontal beam bump amplitude.

MAGNETS

Due to the demand for large free space available for IDs or other the magnets have to be longitudinally short and the distance between them is between 50-70 mm. Due to that the magnets are designed to have their magnetic length almost equal to their physical length [10].

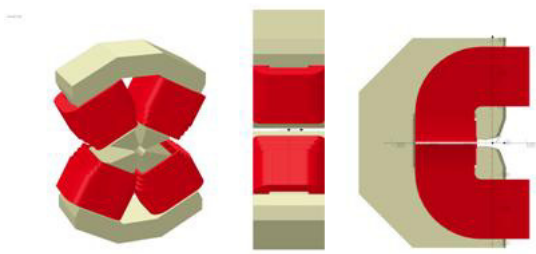

Figure 10: Quadrupole and dipole profiles.

The maximum length of the dipoles is 0.84 m and of the quadrupoles 0.22 m with bore radius at 28 mm. All magnets will be air-cooled. There will be 72 dipoles, 192 quadrupoles, 240 sextupoles of which 120 will be combined for providing dipole (correctors) and skew quadrupole field. Additionally 72 pure correctors are foreseen.

In Figure 10 a quadrupole and its profile are shown. One can readily check that coils do not hang out the yoke. All magnets including correctors are designed and a quadrupole prototype is under construction.

LIFETIME ISSUES

In general we opt for a cylindrical vacuum chamber of 23 mm internal diameter (except for light exits and the low gap chambers) with some parts made out of stainless steel or copper and other parts of aluminium with NEG. Such configuration can give vacuum similar to the existing machine i.e. 4 nTorr of N_2 dynamic pressure. Assuming 1% coupling, 400 mA stored intensity and 2.4 MV effective RF voltage, the Touschek lifetime is 19 hours and including elastic (1021 h) and inelastic scattering (27 h) the total linear lifetime becomes 11 hours taken the "zero" current bunch length of 1.73 mm. However when performing 4-D tracking using OPA [11] whereby particles start on axis but with momentum deviation $\Delta p/p$, the total lifetime is reduced to 6.5 hours indicating also a momentum acceptance of 7%. The above investigation suggests that the new machine will be also Touschek dominated and using the third harmonic cavity (3HC) one expects a threefold increase in lifetime.

Due to small emittance intra-beam scattering becomes important. For the "zero" current bunch length (3HC off) a 92 % emittance increase at 400 mA is estimated whereas in the case of bunch lengthening (3HC on) the emittance increase is 46% as seen in figure 6. Hence, the already existing third harmonic cavity (3HC) should also be used for Elettra 2.0.

CONCLUSIONS

Electra 2.0 will operate at 2 GeV replacing the actual machine in the same tunnel. The lattice will be the symmetric 6-bend achromat (S6BA) with an emittance of 250 pm-rad and very small spot size and divergence (< 60 μm horizontal, 3 μm vertical, < 6 μrad). The photon source points from the insertion devices will remain unchanged. For the dipole beam lines various options are offered: either to be served from a LG dipole of 2.2 T or by a short 2 T wigglers or by installing super-bends. In all those cases the dipole beam lines have to be shifted accordingly. Functioning at 2.4 GeV is possible by reducing the free space in the arcs or the diameter of the vacuum chamber. Short pulses are possible if a dedicated straight section will be available.

The new machine will be diffraction limited in the horizontal plane for $\lambda \geq 15$Å while in the vertical at 1% coupling for $\lambda \geq 0.15$Å whereas its coherent fraction at 1keV will be 38%.

REFERENCES

[1] E. Karantzoulis, A. Carniel, M. Cautero, B. Diviacco, S. Krecic, R. Visintini, "Elettra status, present upgrades and plans", in *Proc. 8th Int. Particle Accelerator Conf. (IPAC'17)*, Copenhagen, Denmark, May 2017, pp. 2657-2659 (2017);

ISBN: 978-3-95450-206-6 doi:10.18429/JACoW-FLS2018-TUA2WB02

[2] D. Einfeld, M. Plesko, "A modified QBA optics for low emittance storage rings", *Nucl. Inst. Meth. in Phys. Res. A* 336 (1993) p. 402.
[3] E. Karantzoulis, "Evolution of Elettra towards an ultimate light source", in *Proc. 5th Int. Particle Accelerator Conf. (IPAC'14)*, Dresden, Germany, June 2014, paper MOPRO075, pp. 258-260.
[4] E. Karantzoulis, "Electra 2.0 - The next machine ", in *Proc. 6th Int. Particle Accelerator Conf. (IPAC'15),* Richmond, VA, USA, May 2015, paper TUPWA052, pp. 1532-1534.
[5] E. Karantzoulis, "The diffraction limited light source Electra 2.0", in ***Proc. 8th Int. Particle Accelerator Conf. (IPAC'17),*** Copenhagen, Denmark, May 2017, pp 2660-2662, (2017)
[6] E. Karantzoulis, "Elettra 2.0 - The diffraction limited successor of Elettra", *Nuclear Inst. and Methods in Physics Research,* A 880 (2018) 158–165
[7] E. Karantzoulis, S. Bassanese, D. Baron, A. Bianco, F. Bille, R. Borges, P. Borsi, A. Buonnano, E. Busetto, A. Carniel, D. Castronovo, K. Casarin, M. Cautero, V. Chenda, S. Cleva, I. Cudin, S. Di Mitri, R. De Monte, B. Diviacco, A. Fabris, R. Fabris, P. Furlan, G. Gaio, F. Giacuzzo, G. Kourousias, S. Krecic, G. Loda, M. Lonza, A. Martinolli, E. Mazzucco, M. Miculin, D. Morelli, L. Novinec, C. Pasotti, R. Passuello, L. Pivetta, R. Pugliese, L. Rebuffi, L. Rumiz, L. Sturari, C. Scafuri, G. Stopar, P. Tosolini, G. Tromba, R. Visintini, A. Vascotto, M. Zaccaria, D. Zangrando "Elettra 2.0 Technical Conceptual Design Report", ST/M-17/01, Elettra–Sincrotrone Trieste, internal document (2017)
[8] M. Borland, "Elegant", version 31.0.0, APS, (2016).
[9] S. Di Mitri, contribution to ST/M-17/01, Elettra - Sincrotrone Trieste, internal document (2017)
[10] D. Castronovo, contribution to ST/M-17/01, Elettra - Sincrotrone Trieste, internal document (2017)
[11] A. Streun, "OPA version 3.39", PSI, (2014).

ISBN: 978-3-95450-206-6 doi:10.18429/JACoW-FLS2018-TUA2WB04

ION INSTABILITY IN THE HEPS STORAGE RING *

S.K. Tian †, N. Wang
Key Laboratory of Particle Acceleration Physics and Technology, Institute of High Energy Physics, Chinese Academy of Sciences, 100049 Beijing, China

Abstract

Ionisation of residual gases in the vacuum chamber of an accelerator will create positively charged ions. For the diffraction limit storage ring，the ion effect has been recognized as one of the very high priorities of the R&D for the High Energy Photon Source (HEPS), due to the ultra-low beam emittance and very high intensity beam. In this paper, we have performed a simulation based on the weak-strong model and analytical estimate to investigate characteristic phenomena of the fast-ion instability.

INTRODUCTION

The ionization of the residual gas in the vacuum pipe by the circulating electron beam will create positive ions. These ions could be trapped in the potential well of the stored beam under certain conditions [1].The accumulation depends on several factors，e.g. the filling pattern (the number of bunches, bunch spacing, beam current), transverse beam sizes (beam emittances，the storage ring optics) and the property of the ions (the mass, the charge).

Generally speaking, ion effects can be divided into two categories. One is called conventional ion trapping instability and the other is called fast beam-ion instability (FBII) [2, 3]. The former occurs mainly in the storage rings when bunches are uniformly filled. If some conditions are satisfied, the ions are accumulated over many turns and trapped by the beam potential all the time. These ions mutually couple to the motion of beam particles and lead to a beam instability in the ring. This instability can be partially suppressed by intentionally leaving a gap after the bunch train. These gaps will make the ions over focused and eventually lost to the vacuum chamber wall [4]. However, the diffraction limit storage ring light source feature an extremely small beam emittance (nanometer scale) and many bunches (a few hundreds) operation. The bunch spacing is therefore not very long enough, single passage ion instability, which is called fast beam-ion instability, is dominant. In this case, ions created by the head of the train via ionization of the residual gas perturb the tail during the passage of a single electron bunch train.

The High Energy Photon Source (HEPS), a kilometre scale quasi-diffraction limited storage ring light source with the beam energy of 6 GeV, is to be built in Beijing area and now is under extensive design. Extensive efforts have been made on the lattice design and relevant studies of this project. A hybrid 7BA design for the HEPS has been made. The design beam current is 200 mA, and basically two filling patterns are under consideration. One is the high brightness mode with 680 bunches (1.3nC, 0.3mA), followed by a 10% gap; the other one is the timing mode, with 63 bunches (14.4nC, 3.2mA) of equal bunch charges uniformly distributed around the ring. The main parameters were listed in Table 1.

Table 1: HEPS Lattice Design Parameters

Parameters	Values
Energy E_0	6 GeV
Beam current I_0	200 mA
Circumference	1360.4 m
Natural emittance ε_{x0}	58.4 pm.rad
Working point υ_x/υ_y	107.37/82.43
Natural chromaticity (H/V)	-214/-133
No. of super-periods	48
ID section length L_{ID}	6.15m
RMS energy spread	8.20×10^{-4}
Momentum compaction	3.43×10^{-5}
Energy loss per turn	1.959 MeV

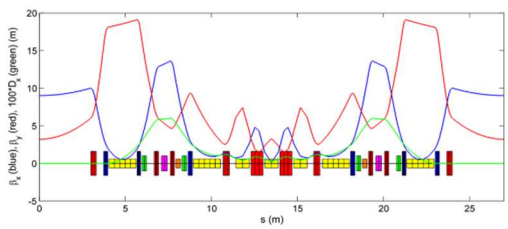

Figure 1: Optical functions and lattice structure for one cell of the HEPS storage ring.

ION TRAPPING

The ions generated by beam-gas ionization will experience a force from the passing electron bunch, which can be regarded as a thin lens focusing element followed by a drift space before the next bunch passes. Based on the linear theory of ion trapping [5], the ions with a relative molecular mass greater than $A_{x,y}$ will be trapped horizontally (vertically) in the potential well of the beam. The $A_{x,y}$ in units of amu is given by:

$$A_{x,y}(s)=\frac{N_e r_p L_{sep}}{2\left(\sigma_x(s)+\sigma_y(s)\right)\sigma_{x,y}}, \quad (1)$$

Where N_e is the number of particles per bunch, r_p (~1.535×10^{-18}m) is the classical proton radius, L_{ess} is the bunch separation in meters, $\sigma_x(s)$, is the local horizontal rms beam size, and $\sigma_y(s)$ is the local vertical rms beam size.

The ions should be trapped both in x and y directions simultaneously, so the critical mass in units of amu is given by:

$$A_{crit}(s)=\frac{N_e r_p L_{sep}}{2\min\left(\sigma_x(s),\sigma_y(s)\right)\left(\sigma_x(s)+\sigma_y(s)\right)}. \quad (2)$$

* Work supported by NSFC (11475202, 11405187, 11205171)
† tiansk@ihep.ac.cn

ISBN: 978-3-95450-206-6 doi:10.18429/JACoW-FLS2018-TUA2WB04

Any singly-ionized species with atomic mass greater than A_{crit} will be trapped. Using the beam parameters of Table 1 with the emittance coupling factor κ=10% and the optical functions shown in Figure 1, the critical mass for the high brightness mode with 680 bunches was shown in Figure 2.

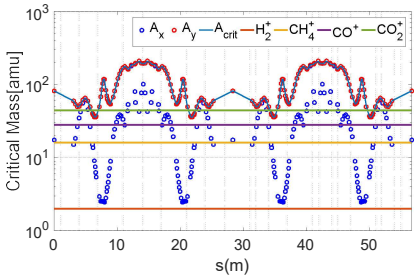

Figure 2: Calculated critical mass along the ring.

The critical mass will vary along the ring. A given ion may be trapped in some parts of the lattice, but not in others. The minimum value of critical mass is about 35.7(amu), so that only CO2+ can be trapped, the trapped fraction is about 5.8%.

FAST BEAM-ION INSTABILITY

Models of the Beam-Ion Interaction

There are several models to investigate the beam-ion interaction. The residual gas ionized ions could be represented by a single macro particle or a continuous distribution along the longitudinal direction in analytic theory. While they are represented by many macro particles in the simulation. The models, which are depicted in Figure 3, are summarized as follows [6]:

1) Electrons and ions are expressed as one macro particle each. The interaction force between the beam and the ion is linear, which is applicable for small amplitudes ($y<<\sigma_y$) [2].
2) Electrons and ions are expressed as one macro particle each. The interaction force between the beam and the ion is linear, the ion decoherence and the variation of the ion frequency along the beam line are included [3].

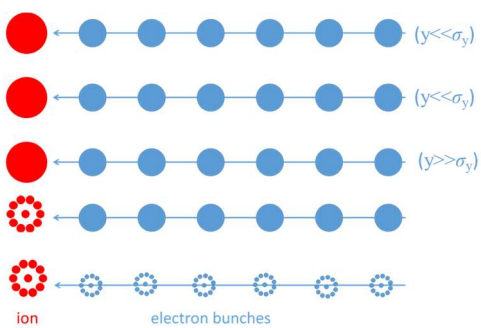

Figure 3: Various models for the beam-ion interaction.

3) Electrons and ions are expressed as one macro particle each. For very large oscillation amplitudes ($y>>\sigma_y$), the beam-ion force becomes very nonlinear [7].
4) A bunch is represented by a macro particle, while the ions are represented using many macro particles. It is called a weak–strong model [8].
5) Both the bunch and the ion cloud are represented by many macro particles. It is called a strong–strong model.

Analytic Theory of the Rise-Time

Analytical expressions for the growth rate at the end of the bunch train have been derived using three different models (Model 1~3 that shown in Figure 3) [9].

Simple linear treatment for small amplitude ($y<<\sigma_y$), the initial vertical perturbation of magnitude increase quasi-exponentially as [2]:

$$y = \hat{y}\frac{1}{2\sqrt{2\pi}(t/\tau_c)^{1/4}}\exp(\sqrt{t/\tau_c}), \tag{3}$$

With a characteristic time:

$$\frac{1}{\tau_c} = \frac{4d_{gas}\sigma_{ion}\beta N_e^{3/2} n_b^2 r_e r_p^{1/2} L_{sep}^{1/2} c}{3\sqrt{3}\gamma\sigma_y^{3/2}(\sigma_y+\sigma_x)^{3/2}A^{1/2}}, \tag{4}$$

Where $d_{gas} = p/(kT)$ is the residual gas density (where p is the gas pressure, k Boltzmann constant, and T the absolute temperature), β the average vertical beta function, n_b the number of bunches in the train, γ the beam energy in units of the rest energy, A the ion mass in units of amu, r_e(~2.8×10^{-15}m) the classical electron radius, c the speed of light, and σ_{ion} the ionization cross section.

Take into account the decoherence of ion oscillations due to the ion frequency spread, Eq. (3) is replaced by a purely exponential growth [3]:

$$y \propto \exp(t/\tau_e) \tag{5}$$

With an e-folding time of:

$$\frac{1}{\tau_e} \approx \frac{1}{\tau_c}\frac{c}{4\sqrt{2}\pi L_{sep} n_b a_{bt} f_i} \tag{6}$$

Where

$$f_i = \frac{c}{\pi}\sqrt{\frac{QN_e r_p}{3AL_{sep}\sigma_y(\sigma_x+\sigma_y)}} \tag{7}$$

denotes the coherent ion oscillation frequency, and $2a_{bt}$ the peak-to-peak ion-frequency variation (a_{bt}~0.1-1,for HEPS lattice optics, we set a_{bt}=1). Eq.(5) is also only valid for amplitudes small compared with the beam size.

For very large oscillation amplitudes($y>>\sigma_y$), a linear growth is expected [7]:

$$y \sim \sigma_y \frac{t}{\tau_H} \tag{8}$$

with a time constant:

$$\frac{1}{\tau_H} \approx \frac{1}{\tau_c}\frac{c}{2\pi f_i L_{sep} n_b^{3/2}} \tag{9}$$

The fast beam–ion instability arises when the ions are trapped between bunches. In other words, if the transverse velocity of ions is so small that they stay within the bunch size before the next bunch arrives which pulls them back in, the trapping condition is then fulfilled. The trapping condition can approximately be written as:

$$4L_{sep} f_i / c \le 1 \tag{10}$$

ISBN: 978-3-95450-206-6 doi:10.18429/JACoW-FLS2018-TUA2WB04

For a single bunch train consisting of n_b bunches followed by a long gap, the ion line density at the tail of the bunch train is given by:

$$\lambda_i = \sigma_{ion} \frac{P}{kT} N_e n_b \tag{11}$$

The effective ion density is defined as [10]:

$$\rho_{i.eff} = \frac{\lambda_i}{k_y \sigma_y (\sigma_x + \sigma_y)} \tag{12}$$

k_y represents the ion's distribution, for a flat electron beam, k_y=3/2.

Table 2: Parameters and Predicted Oscillation Growth Rates for HEPS

HEPS	mode1	mode2	mode3	mode4
E [GeV]	6	6	6	6
C [m]	1360.4	1360.4	1360.4	1360.4
β_x/β_y [m]	4.4/5.9	4.4/5.9	4.4/5.9	4.4/5.9
L_{sep} [m]	1.8	21.6	1.8	21.6
n_B	680	63	680	63
N_b[10^{10}]	0.83	9.0	0.83	9.0
σ_x [μm]	15.1	15.1	282.4	334.9
σ_y [μm]	5.9	5.9	100.4	119.1
P [nTorr]	1	1	1	1
$\rho_{i,eff}$[10^{13}m^{-3}]	21.5	21.6	0.063	0.045
f_i [MHz]	82.6	78.5	4.2	3.6
$4L_{sep}f_i/c$	1.98	22.6	0.1	1.0
τ_c [μs]	0.005	0.005	31	51.3
τ_e [ms]	0.031	0.031	10.6	14.8
τ_H [ms]	0.285	0.086	97.5	41.6

In Table 2 we list parameters and predicted instability rise times for the two filling patterns of HEPS. We use the average value of the beta function and the emittance coupling factor κ=10% to get the rms beam size. The projected rise times are are unprecedentedly small: the characteristic time τ_c is of the order of nanoseconds, the e-folding time τ_e and τ_H is a few hundred microseconds or less. From the Table 2, we note that, using Eq.(10), in HEPS the ions are not stably trapped between bunches, it will lead to a reduction of the instability growth rate.

The ion density exhibits exponential decay during the bunch gap with an exponential time constant of the order of the ion's oscillation period. This feature makes the multi bunch train filling pattern a very effective way to reduce the ion density for an electron ring with high beam current and low emittance. In Figure 4, we show the ion density w/ and w/o exponential decay along the ring for brightness mode.The mode 3 and mode 4 in Table 2 show the average ion density with density reduction between bunches for brightness mode and timing mode. We keep the ion line density and the ratio of the transverse beam size to recalculate the transverse beam size with Eq.(12). In such situations, there is a obviously decrease the instability growth rate

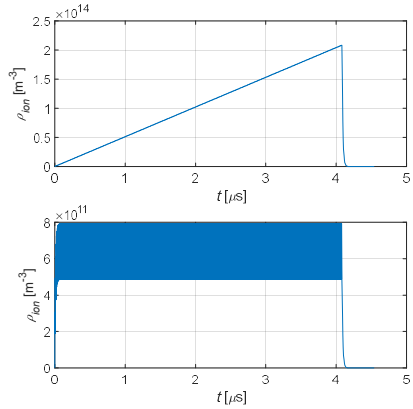

Figure 4: Ion density along the ring. up: without density reduction between bunches; down: consider density reduction between bunches.

Simulation Model and Assumptions

We employ a weak-strong code to simulate the interactions between the electrons and ions [9]. We assumed the bunch length was much larger than bunch transverse size and the bunch spacing was much larger than the bunch length, so only the transverse distribution was taken into consideration in the ionization process. Neither electron bunch length nor synchrotron oscillation was taken into consideration. The electron bunch was treated as the strong one, i.e. a rigid Gaussian bunch. Only its barycentre motion is taken into account. The ions are treated as macro particles which are ionized by the previous electron bunch, its distribution is the same as the electron bunch. The motion of ions is non-relativistic without longitudinal drift and they are assumed to move freely in the bunch interval. The number of ions is increased with respect to the bunch index in the bunch train, the ion line density per bunch is given by $\lambda_{ion} = N_b \sigma_{ion} d_{gas}$. We assume that the first bunch in the train only produces the ions and it does not interact with the ions, while the trailing bunches in the train will produce the ions and interact with the ions created by the preceding bunches. After one turn interaction, we assume that the ions are cleared away from the beam vicinity. The new ions will be produced by the beam in the second revolution turn. The adjacent beam ion interaction points are connected through the linear transfer matrix.

The major species of the residual gas in the vacuum chamber are Carbon Monoxide (CO) and Hydrogen (H_2). Since the cross section of collision ionization for CO is about 6 times higher than that for H_2 in this beam energy regime. Therefore in the simulation, CO^+ ions are regarded as the dominant instability source and its pressure sets to be 1.0 nTorr.

Beam-Ion Force

The interaction between ions and electron beam is based on the Bassetti–Erskine formula, for an ion with electric charge +e in the in the field of the Gaussian bunch, the Coulomb force exerted on it can be calculated [11]:

$$F(x,y) = -2N_e r_e m_e c^2 f(x,y) \tag{13}$$

ISBN: 978-3-95450-206-6 doi:10.18429/JACoW-FLS2018-TUA2WB04

Where (x, y) are the horizontal and vertical position with respect to the bunch center, m_e the electron mass. $f(x, y)$ is well known Bassetti–Erskine formula as:

$$f(x,y) = -\sqrt{\frac{\pi}{2(\sigma_x^2-\sigma_y^2)}}\left[w\left(\frac{x+iy}{\sqrt{2(\sigma_x^2-\sigma_y^2)}}\right) - \exp\left(-\frac{x^2}{2\sigma_x^2}-\frac{y^2}{2\sigma_y^2}\right) w\left(\frac{x\frac{\sigma_y}{\sigma_x}+iy\frac{\sigma_x}{\sigma_y}}{\sqrt{2(\sigma_x^2-\sigma_y^2)}}\right)\right], \quad (14)$$

here

$$w(z) = \exp\left(-z^2\right)\left[1-erf\left(-iz\right)\right], \quad (15)$$

$$erf\left(x\right) = \frac{2}{\sqrt{\pi}}\int_0^x \exp\left(-x^2\right)dx \quad (16)$$

So we can write the kick to the rigid electron bunch by an ion with distance of (x_{ie}, y_{ie}) and sum together for all of the ions as:

$$\Delta y_e' + i\Delta x_e' = \frac{2N_e r_e}{\gamma}\sum_i f(x_{ie}, y_{ie}) \quad (17)$$

Similarly, due to the reaction force, the kick to an ion with mass M_i is given by:

$$\Delta y_i' + i\Delta x_i' = -2N_e r_e c\frac{m_e}{M_i} f(x_{ie}, y_{ie}) \quad (18)$$

Where $(\Delta x_e', \Delta y_e')$ and $(\Delta x_i', \Delta y_i')$ are the transverse angle kick to the centre-of-mass of electron bunch and ion respectively.

Simulation Results

In the simulations, the time evolution of the growth of beam dipole amplitude is computed and recorded in every turn. The transverse oscillation amplitude of the bunch centroid is half of the Courant-Synder invariant and given by:

$$J_z = \frac{1}{2}\left[\gamma_z z^2 + 2\alpha_z zz' + \beta_z z'^2\right], z \in (x, y) \quad (19)$$

Where α_z, β_z, γ_z are the Twiss parameters of the ring lattice. We compare the square root of J_z with the beam size which is represented by the square root of transverse emittance ε_z. Both of these quantities are in units of $m^{1/2}$.

We perform simulations on the fast beam ion instability for four different beta function in Table 3.

Table 3: Different β Function Selected for Simulation

Case	β_x[m]	β_y[m]	τ_e[ms]
Case1	4.4	5.9	4.5
Case2	10	15.5	0.77
Case3	3	15.5	1.3
Case4	9	4	6.8

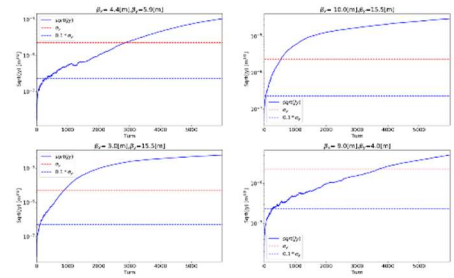

Figure 5: Maximum vertical amplitude of bunches with respect to number of turns.

The growth time of FBII in different β function cases could be estimated from the time duration of maximum amplitude growth of beam from 0.1σ to 1.0σ, shown in Figure 5, by exponential fitting [12]. The estimated growth time is also shown in Table 3.

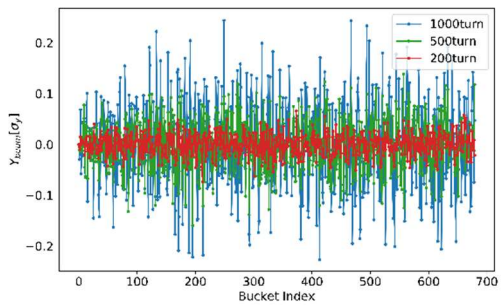

Figure 6: Beam oscillation pattern in different turns.

The amplitude of the beam oscillations due to the interaction with the ions versus the bucket index is shown in Figure 6. It indicates that the beam oscillation grows with respect to the time (number of turns).

CONCLUSION

We have investigated the analytic and simulation studies to investigate the fast-ion instabilities for the HEPS storage ring that showed a rapid growth time. The growth times for various b function cases in the ring were obtained by using a weak-strong simulation method. The simulation results also showed that the bunch by bunch feedback of about 100 turns is required to cure the fast-ion instabilities.

REFERENCES

[1] Bozoki, Eva S., and Henry Halama. "Ion related problems for the XLS ring." *Nuclear Instruments and Methods in Physics Research Section A: Accelerators, Spectrometers, Detectors and Associated Equipment* 307.2-3 (1991): 156-166.

[2] T.O.Raubenheimer, and F. Zimmermann. "Fast beam-ion instability. I. Linear theory and simulations.", *Physical Review E* Vol. 52.5 , pp. 5487–5498 ,1995.

[3] G.V. Stupakov, T.O. Raubenheimer, and F. Zimmermann," Fast beam-Ion Instability II: Effect of Ion Decoherence", *Physical Review E*, Vol. 52.5, pp. 5499–5504, 1995.

[4] Wang, Lanfa, *et* al. "Ion effects in the Electron Damping Ring of the International Linear Collider", No. SLAC-PUB-11932. Stanford Linear Accelerator Centre (SLAC), 2006.

[5] Y.Baconnier, *et al.*, "The stability of ions in bunched beam machines", CERN/SPS/802 (1980)

ISBN: 978-3-95450-206-6 doi:10.18429/JACoW-FLS2018-TUA2WB04

[6] Kim, Eun-San, and Kazuhito Ohmi. "Simulations on the Fast-Ion Instability in the International Linear Collider Damping Rings." *Japanese Journal of Applied Physics* 48.8R (2009): 086501.

[7] S.A. Heifets, "Saturation of the ion induced transverse blow up instability", in *Proc.* the International Workshop on Collective Effects and Impedance for B-Factories (CEIBA95), KEK Proceedings 96- 6, Aug. 1996, p. 270

[8] Wang, L., *et al.*,. "Suppression of beam-ion instability in electron rings with multibunch train beam fillings." *Phys. Rev. ST Accel. Beams*, vol. 14, p. 084401, 2011.

[9] Ohmi, Kazuhito. "Numerical study for the two-beam instability due to ions in electron storage rings." *Physical Review E* 55.6 (1997): 7550.

[10] F. Zimmermann., *et* al. "Experiments on the fast beam ion instability at the ALS." No. SLAC-PUB-7617. 1997.

[11] Bassetti, M., and George A. Erskine. "Closed expression for the electrical field of a two-dimensional Gaussian charge". No. CERN-ISR-TH/80-06. 1980.

[12] Xia, Guoxing, and Eckhard Elsen. "Simulation Study of Fast Ion Instability in the ILC Damping Ring." *EUROTeV-Report-2008-004* (2008).

ISBN: 978-3-95450-206-6 doi:10.18429/JACoW-FLS2018-TUP1WD02

A STUDY ON THE IMPROVED CAVITY BUNCH LENGTH MONITOR FOR FEL*

Q. Wang, Q. Luo†, B. G. Sun‡, Y. L. Yang, Z. R. Zhou, P. Lu, F. F. Wu, L. L. Tang, T. Y. Zhou, X. Y. Liu, J. H. Wei,
NSRL, University of Science and Technology of China,
230029 Hefei, P. R. China

Abstract

Bunch length monitors based on cavities have great potential especially for future high quality beam sources because of many advantages such as simple structure, wide application rage, and high signal-to-noise ratio (SNR). The traditional way to measure bunch length needs two cavities at least. One is reference cavity, whose function is to get the beam intensity. The other one is defined as main cavity, which is used to calculate the bunch length. There are some drawbacks. To improve performance, the mode and the cavity shape are changed. At the same time, the position and orientation of coaxial probe are designed to avoid interference modes which come from the cavity and beam tube according to the analytic formula of the electromagnetic field distribution. A series simulation based on CST is performed to verify the feasibility, and the simulation results reveal that the improved monitor shows good performance in bunch length measurement.

INTRODUCTION

Bunch length is one of the main characteristics of charged particle beam in accelerator. There is growing interest in the generation, measurement and application of short electron bunches, so precise bunch length measurement methods are necessary for developing the future light sources. To measure the bunch length, many methods have been developed in the past decades. Bunch length monitor based on cavities has great potential especially for high quality beam sources because of many advantages such as simple structure, wide application rage, and high signal noise ratio. What's more, the cavities with different modes show the ability of combined measurement of bunch length, beam intensity, position and quadrupole moment so that the whole diagnostic system is simplified and compact. In this paper, a series of studies about improved cavity bunch length monitors for the National Synchrotron Radiation Laboratory Infrared Free Electron Laser (FELiChEM) are presented. The beam parameters, used in the analytical calculation and simulation of this paper, are listed in Table 1.

* Supported by The National Key Research and Development Program of China (Grant No. 2016YFA0401900, 2016YFA0401903), the National Science Foundation of China (Grant No. 11375178, 11575181) and the Fundamental Research Funds for the Central Universities (WK2310000046).

† luoqing@ustc.edu.cn
‡ bgsun@ustc.edu.cn

Table 1: Electron Beam Parameters of IR-FEL

Parameter	Value
Beam energy	30~50 MeV
Bunch charge	1 nC
Bunch length, rms	2~5 ps
Bunch repetition rate	476 MHz
Beam pipe radius	17.5 mm
Macro pulse length	13 μs
Macro pulse repetition rate	10 Hz

THEORETICAL BASIS

Cavity bunch length monitor is usually composed of two cavities with different working frequencies. When a Gaussian bunch passed through the axis of the vacuum chamber, the symmetric TM0n0 modes could be excited in the cavities. The power of one mode can be written as [1].

$$\begin{cases} P_1 = [I_0 \exp(-\frac{\omega_1^2 \sigma_\tau^2}{2})]^2 R_1 \\ P_2 = [I_0 \exp(-\frac{\omega_2^2 \sigma_\tau^2}{2})]^2 R_2 \end{cases} \quad (1)$$

Where the subscripts stand for the cavities' serial number, σ_τ is the bunch length, I_0 is pulse current, ω is resonance frequency of the mode, and R is cavity shunt impedance. The σ_τ and I_0 are quantified by solving this two simultaneous power equations.

DESIGN IMPROVEMENTS

Design of the System

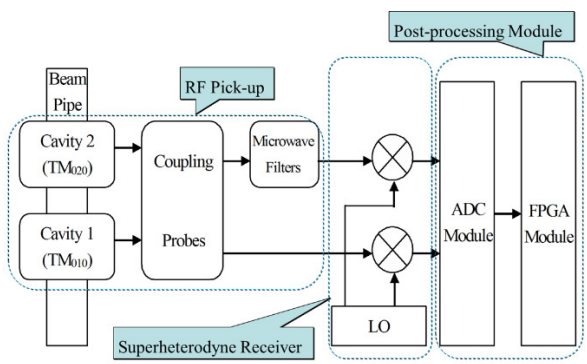

Figure 1: The schematic diagram of a single cavity.

The framework of the whole diagnostic system is shown in Fig. 1. The RF pick-up is composed of two cav-

ISBN: 978-3-95450-206-6 doi:10.18429/JACoW-FLS2018-TUP1WD02

ities on the beam pipe and the coupling probes. The microwave filters are needed sometimes. In a general way, the frequencies of the output signals from the RF pick-up are very high. For this reason, the superheterodyne receiver that consists of is introduced in our design to achieve the down-conversion. High speed data acquisition system consists of high speed ADC, high density FPGA and high performance DSP chips is used as signal processing system and the sampling rate can be 1 Gsps.

Cavity Monitors with High Order Modes

Based on Eq. (1), further derivation leads to the expression of the cavity bunch length monitor theoretical resolution

$$\Delta\sigma_\tau = \frac{(10^{-SNR/10})}{4\pi^2(f_2^2 - f_1^2)\sigma_\tau} \tag{2}$$

Where SNR stands for signal to noise ratio. From the Eq. (2), it can be seen that the resolution depends on the system SNR and the difference of the square of working frequencies. In traditional cavity bunch length monitor, both the two cavities resonate at TM010 mode [2]. Therefore, working frequency and resolution are restricted by the radius of the cavity and beam pipe. For this reason, the bunch length monitor based on high order mode cavity is proposed. The improved method is able to reach higher frequency with larger cavity radius, for higher order eigenmode TM020 is utilized [3]. It means that this design overcome the difficulty of working frequency restriction caused by beam pipe radius and get higher resolution [4].

The physical design of the improved device has been completed and the simulation measurement has provided a fairly high resolution. The two cavities are modeled in CST Microwave Studio, and the simulation results are presented in Table 2.

Table 2: Simulation Results

Bunch Length (ps)	Simulation Results (ps)	Resolution (when SNR = 70 dB) (ps)
5	5.068	0.0429
4.5	4.570	0.0476
4	4.074	0.0536
3.5	3.582	0.0612
3	3.088	0.0714
2.5	2.596	0.0857
2	2.102	0.1071

It can be seen that high order eigenmode TM020 can also be used to measure bunch length. The improved cavity monitor with high order modes achieves higher resolution than the traditional devices [1]. At the same time, the system is able to show a good performance when the SNR is greater than or equal to 70 dB.

Single Cavity Bunch Length Monitor

Traditional cavity bunch length monitor using two cavities would not only make the configuration complex but also take up too much space. In this section, the design and simulation of a bunch length monitor utilizing only one cavity are presented. Compare with the traditional way, the new method does not need reference cavity. Two eigenmodes of a rectangular cavity, TM310 mode and TM130 mode, are utilized to measure beam current and bunch length，so that the promoted monitor is simplified and compact. To control the working frequencies of the eigenmodes, the tuning screws are introduced in the cavity. Only when the modes' working frequencies are equal to the bunch harmonic frequencies, can the modes resonate at optimum performance. For this reason, we have the TM310 mode resonate at 2.856 GHz and the TM130 mode work at 7.616 GHz in practice. The two probes penetrated to the cavity are used to couple out the two modes' signals, respectively. The positions of the two probes are adjusted to avoid coupling of the other mode. The schematic of the device is shown in Fig. 2.

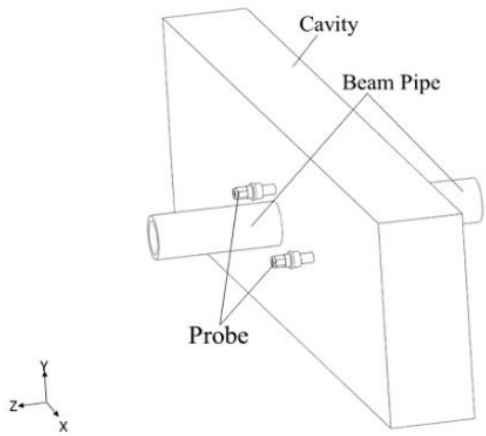

Figure 2: The schematic of the single cavity bunch length cavity.

The physical design of the single cavity bunch length monitor has been completed now [5]. The monitor is modeled in CST Microwave Studio, and the simulation results are presented in Table 3.

Table 3: Simulation Results

Bunch Length (ps)	Simulation Results of Single Cavity (ps)	Relative Error of Single Cavity (%)	Simulation Results of Traditional Double Cavity (ps)	Relative Error of Traditional Double Cavity (%)
5	5.707	1.403	5.068	1.360
4.5	4.572	1.603	4.570	1.556
4	4.075	1.871	4.074	1.841
3.5	3.579	2.245	3.582	2.354
3	3.084	2.806	3.088	2.931
2.5	2.594	3.741	2.596	3.821
2	2.098	4.882	2.102	5.112

ISBN: 978-3-95450-206-6 doi:10.18429/JACoW-FLS2018-TUP1WD02

From the diagram it can be seen that the simulation measurement provides a fairly high accuracy. The single cavity monitor is even slightly better than the traditional double cavities monitor when the bunch length is short.

The Influence of Beam Position

As far as actual cavity is concerned, without regard to the electronics noise, the decisive factor affecting the resolution is beam position. When passing through the cavity with a position offset, the bunch will excite dipole modes such as TM110. These modes may make an impact on the output signals and reduce SNR. The output signals in time domain and in frequency domain are shown in Fig. 3 and Fig. 4, respectively. The amplitude deviation owing to the position offset is regarded as noise. Simulations based on the above description were required to evaluate the influence of beam offsets at different working frequencies and different working modes. The results are shown in Fig. 5 to Fig. 10.

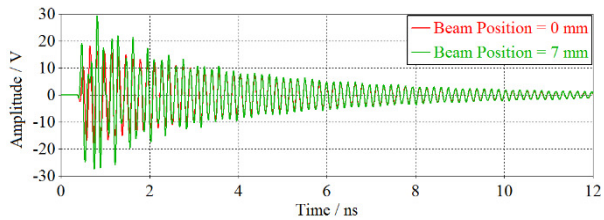

Figure 3: The output signal in time domain.

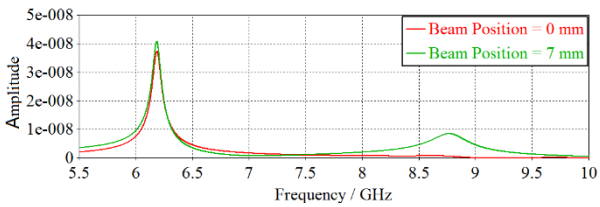

Figure 4: The output signal in frequency domain.

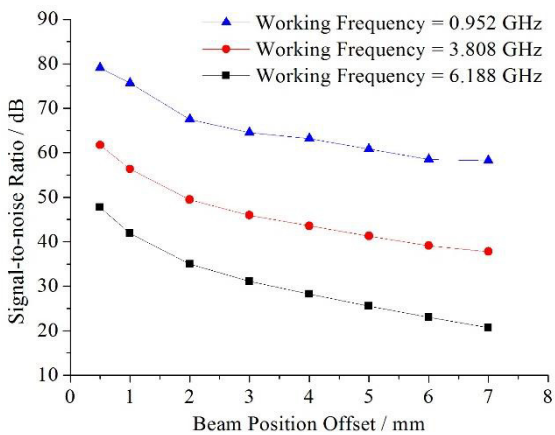

Figure 5: SNRs vary with beam position offsets.

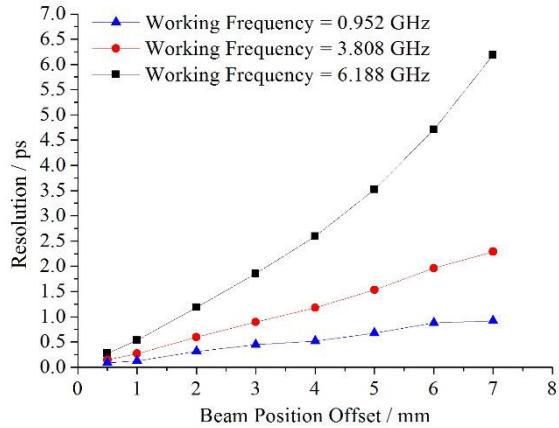

Figure 6: Resolutions vary with beam position offsets.

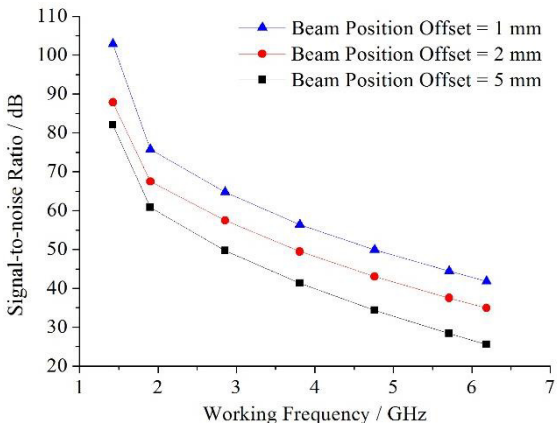

Figure 7: SNRs vary with working frequencies.

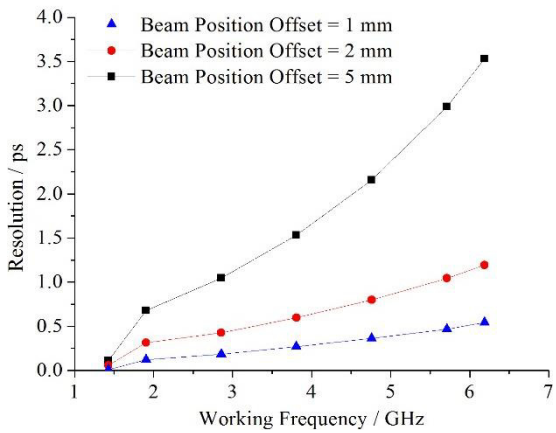

Figure 8: Resolutions vary with working frequencies.

ISBN: 978-3-95450-206-6 doi:10.18429/JACoW-FLS2018-TUP1WD02

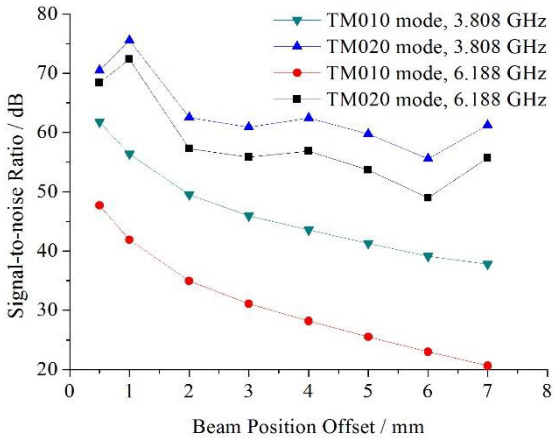

Figure 9: SNRs vary with beam position offsets.

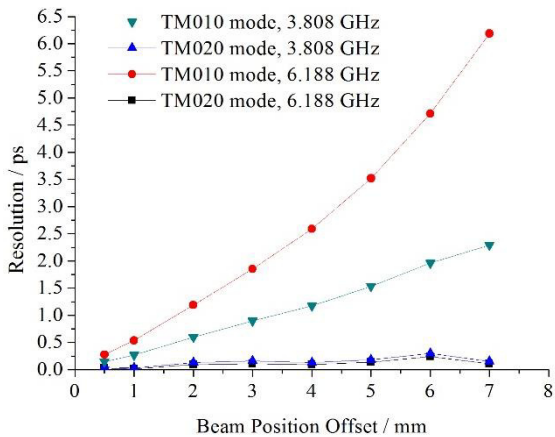

Figure 10: Resolutions vary with beam position offsets.

According to the graphs, it can be seen that the father away the beam sets from the axis of the cavity, the greater the deviation is. At the same time, beam offset will introduce greater noise when working frequency is higher. What's more, using TM020 mode is able to obtain high SNR and high resolution compared with the traditional cavity with TM010 mode.

CONCLUSION

In this paper, a series of studies about improved cavity bunch length monitors for the National Synchrotron Radiation Laboratory Infrared Free Electron Laser (FELiChEM) are presented. Firstly, according to the characteristics of FELiChEM, the framework of the whole diagnostic system is designed. After that, the relationship between resolution and SNR is deduced and the factors which make effect on the system SNR is analyzed. To remove the limitation that working frequency and resolution are restricted by the radius of beam pipe, the bunch length monitor based on high order mode cavity is proposed. And then, a kind of new method to measure bunch length of FEL with single cavity is presented. Finally, the laws of resolution change caused by some decisive factors such as beam position, working frequency and electromagnetic mode are analysed, which offers the theoretical support for the design and application of bunch length monitor in the future light sources.

REFERENCES

[1] Y. Y. Cui *et al.*, "Bunch length measurement in BEPCII linac by harmonic method", *High Power Laser and Particle Beams*, vol. 17, no. 12, pp. 1901-1904, Dec. 2015.

[2] H. H. Braun and C. Martinez, in *Proc. EPAC'1998*, pp. 1559-1561.

[3] J. Guo, Z. R. Zhou, Q. Luo, and B. G. Sun, "Design and simulation of TM020 cavity bunch length monitor", *High Power Laser and Particle Beams*, vol. 28, no. 9, p. 095104, Sep. 2016.

[4] Q. Wang *et al.*, in *Proc. IPAC'17*, pp. 309-311.

[5] Q. Wang, Q. Luo, and B. G. Sun, "Design and simulation of a bunch length monitor for linac based on single cavity", *High Power Laser and Particle Beams*, vol. 29, no. 11, p. 115101, Nov. 2017.

ISBN: 978-3-95450-206-6 doi:10.18429/JACoW-FLS2018-TUP1WD03

THE DEVELOPMENT AND APPLICATIONS OF THE DIGITAL BPM SIGNAL PROCESSOR AT SINAP*

L.W. Lai†, Y.B. Leng, Y.B. Yan, W.M. Zhou, F.Z. Chen, J. Chen, S.S. Cao,
SSRF, SINAP, Shanghai, China

Abstract

A Digital BPM signal processor has being designed in SINAP since 2009. It is a general platform that can be used for the signal processing of a variety of BPM, like stripline BPM, cavity BPM and button BPM. After years of optimization, the DBPM has been used massively on DCLS and SXFEL. And the turn-by-turn resolution of the storage ring DBPM on SSRF is 0.34μm. This topic will introduce the development and applications of the DBPM at SINAP, also the future DBPM development for next generation light source will be discussed here.

INTRODUCTION

BPM is an important diagnostic instrument in accelerator. It provides the beam position in tunnel, which can be used for accurate beam control and other beam parameters measurements. There have a variety of BPM sensors for different occasions on accelerator, such as stripline BPM, button BPM, cavity BPM, shoebox BPM, et.al. Except for the sensor, the BPM signal processing electronic is a key component of the BPM system. The signal processing system can mainly including RF signal conditioning, ADCs digitizing analogue signal into digital signal, FPGA processing digital signal and calculate the beam position, data acquisition in CPU sending out the results and communicating with control center through LAN. Figure 1 is the block diagram of BPM signal processing system.

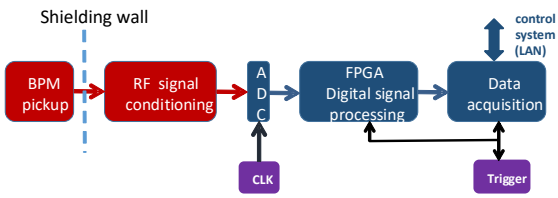

Figure 1: BPM signal processing system.

BPM sensors are installed at the concerned place of the accelerator, larger accelerator always containing more BPMs. For example SSRF is a 432m electron storage ring and contains about 200 BPMs, and future Shanghai Hard X-ray FEL will have more than 200 BPMs along the 3km facility. Since 2009, SSRF started the development of DBPM processor, the objective is to develop a stand-alone general hardware platform that can be used for diverse signal processing applications on accelerator. The first version DBPM completed at about 2011, and lab-tests and on-line beam tests have been carried out. The results shown that the turn-by-turn data resolution can be better than 1μm, and the 10Hz SA data can be read correctly [1]. After five years' optimization, a second version DBPM has been designed and firstly made mass field application on DCLS and SXFEL, and small amount DBPMs is under test on SSRF.

The DBPM specification is listed in Table 1.

Table 1: DBPM Specifications

Parameter	Value
Channels	4
Central Frequency	500MHz
Bandwidth	~20MHz
Dynamic range	31dB
ADC bits	16
ADC bandwidth	650MHz
Max ADC rate	125MSPS
FPGA	Xilinx xc5vsx50t
Clock	Ext./Int.
Trigger	Ext./Self/Period
Software	Arm-Linux/EPICS

Figure 2 is the architecture of the processor. RF conditioning and ADCs are located on RF board, others on digital carrier board. Figure 3 is the hardware of RF board and digital board.

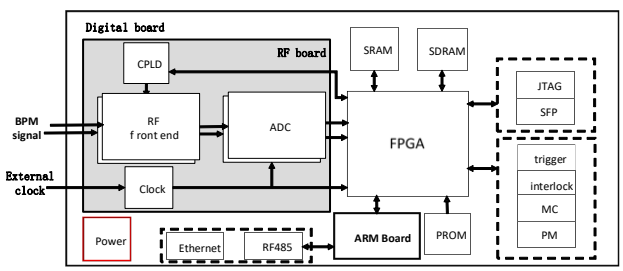

Figure 2: Processor architecture.

*Supported by The National Science Foundation of China (Grant No.11305253, 11375255, 11575282); The National Key Research and Development Program of China (Grant No. 2016YFA0401990, 2016YFA0401903).
† lailongwei@sinap.ac.cn

ISBN: 978-3-95450-206-6 doi:10.18429/JACoW-FLS2018-TUP1WD03

Figure 3: DBPM hardware.

APPLICATIONS ON FEL

The DBPM is made mass field application (about 80 sets) firstly on two FEL facilities in China, DCLS and SXFEL[2], both accelerators are constructed by SINAP. The FEL contains two types of BPM, stripline BPM and cavity BPM. The stripline BPM signal is processed directly with DBPM, while the cavity BPM signal (about 4.7GHz) is down-converted to 500MHz firstly before into the DBPM. Figure 4 is the field picture of DBPM cabinet and the control panel in center room.

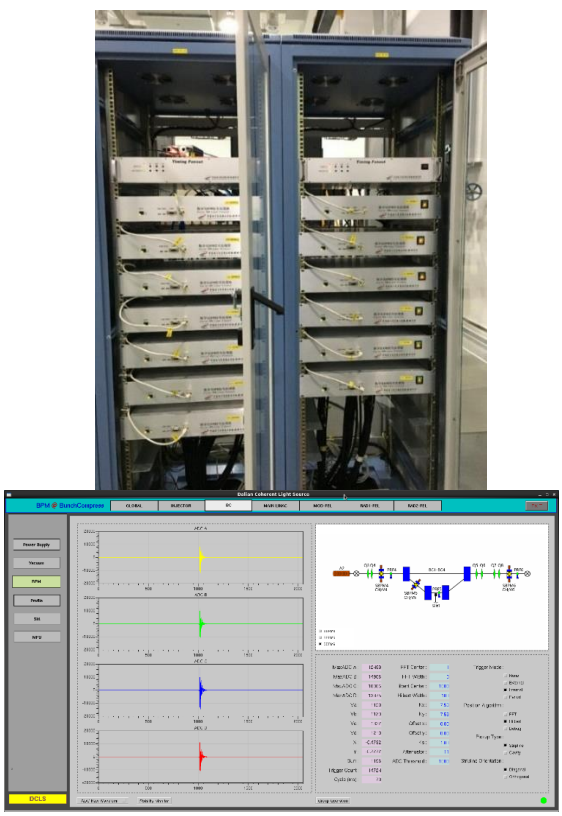

Figure 4: DBPM cabinet and control panel.

On first version, both stripline and cavity BPM signal processing algorithms are implemented in EPICS IOC on ARM, including Hilbert and FFT. The complicated software consumes too much ARM computing power, can only meets the operation under 10Hz bunch rate. However, DCLS and FEL plan to run at 50 bunch rate in future. At the bottom of 2017, the signal processing algorithms are implemented in FPGA, and whole firmware and software are upgraded. The signal processing power is greater than 100Hz bunch rate now.

The performance evaluation is carried out on DCLS by feeding two DBPMs with divided BPM (or IF) signal. Figure 5 is the RMS resolutions of stripline DBPM and Cavity DBPM at different bunch charge. The RMS of stripline DBPM and cavity DBPM at 500Pc is about 2.27μm and 0.54μm respectively.

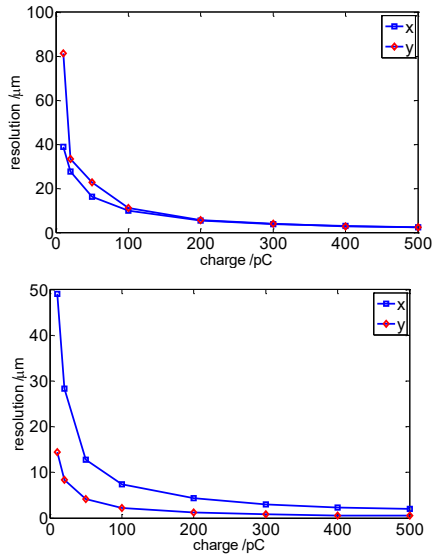

Figure 5: RMS of Stripline DBPM (up) and cavity DBPM (down).

The cavity BPM k factor is measured by moving the BPM. Figure 6 is the result of horizontal k factor of CBPM7 at DCLS. The k is about 0.37 after linear fitting.

The beam direction of cavity BPM is judged by measuring the phase difference between position cavity and reference cavity. There may have 2π phase jump in one direction that needs correction. Figure 7 shows the phase correction and the phase jump between two directions.

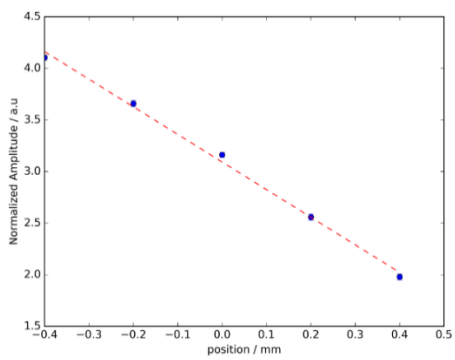

Figure 6: Cavity BPM k measurement.

ISBN: 978-3-95450-206-6 doi:10.18429/JACoW-FLS2018-TUP1WD03

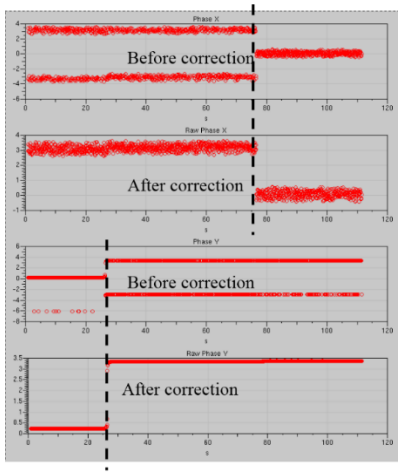

Figure 7: Cavity BPM phase.

APPLICATIONS ON SSRF

The new DBPM for SSRF storage ring has been tested at the Jan. of 2018. The tests including resolution evaluation and accuracy check with Libera Brilliance. There have a spare BPM at 11 unit. A pickup signal is divided into 4 and put into a DBPM to measure the RMS resolution, the data RMS of turn-by-turn (16384 samples), FA50kHz (1171 samples) and FA10kHz (235 samples) is 0.34μm, 0.15μm, 0.09μm respectively. Figure 8 shows the TBT resolution.

Signals from BPM four pickups are divided and put into DBPM and Libera Brilliance to check the accuracy (assuming the measurements of Libera Brilliance are accurate). Figure 9(up) is the spectrum of TBT data, two lines fit quit well. Figure 9(down) is long time SA data of Libera Brilliance and DBPM. There have obvious difference between them before correction. The difference is introduced by current dependency of DBPM, which comes from the difference between four channels. Curve fitting algorithm is applied on the four channels to eliminate the effection. It shows that two lines fits quit well after correction.

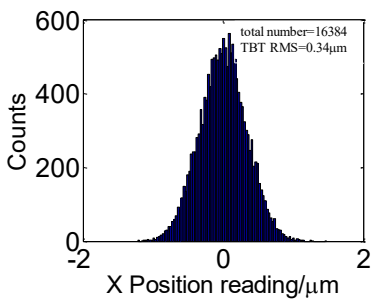

Figure 8: Turn-by-turn data RMS.

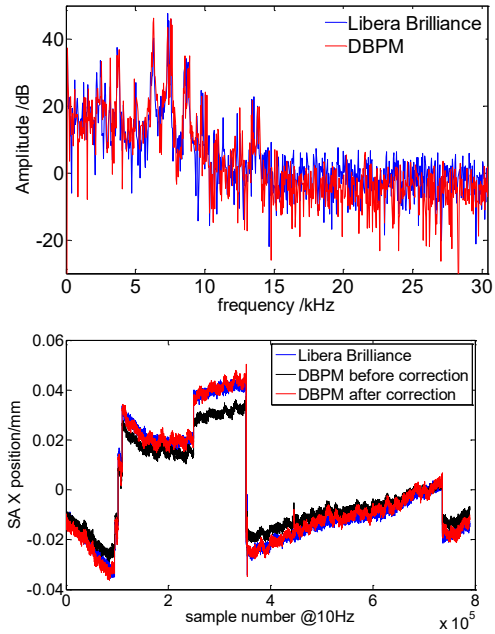

Figure 9: Comparison between DBPM and Libera Brilliance, TBT(up) and SA(down).

OTHER PROCESSORS

Except for the developed DBPMs mentioned above, the SINAP is developing other higher performance processors. One is bunch-by-bunch DBPM, some good results have achieved [3]. Another is RF-sampling processor, which can digitize the RF signal of cavity BPM directly [4]. The signal processing system on FEL will be improved greatly by applying the RF-sampling processor.

CONCLUSION

A general DBPM has been developed at SINAP by developing different firmware and software on same hardware for different applications. The DBPM have made mass on-line application on DCLS and SXFEL, and already made long time evaluations on SSRF, the TBT RMS is 0.34μm and SA results fits well with Libera Brilliance, it can be used for future replacement.

REFERENCES

[1] Lai Longwei, Leng Yongbin, Yi Xing, et.al. “Optimization of signal processing algorithm for digital beam position monitor (in Chinese)”, High power laser and particle beams, Vol. 25, No. 1, Jan. 2013 pp.109-113.

[2] L.W. Lai, Y.B. Leng, Y.B. Yan, et,al. “Design and Performance of Digital BPM Processor for DCLS and SXFEL”, proceedings of IPAC2017.

[3] Yongbin Leng , Zhichu Chen, Longwei Lai, et.al. “Bunch by bunch DBPM processor development and preliminary experiment in SSRF”, Proceedings of IPAC2015, Richmond, VA, USA, p. 984-986.

[4] L.W. Lai, Y.B. Leng, J. Chen, et,al. “The Application of direct RF sampling system on cavity BPM signal processing”, Proceedings of IBIC2017, Grand Rapids, Michigan, USA.

ISBN: 978-3-95450-206-6 doi:10.18429/JACoW-FLS2018-TUP2WD03

TURN-BY-TURN MEASUREMENTS FOR SYSTEMATIC INVESTIGATIONS OF THE MICRO-BUNCHING INSTABILITY*

J. L. Steinmann†, M. Brosi, E. Bründermann, M. Caselle, S. Funkner, B. Kehrer, M. J. Nasse, G. Niehues, L. Rota, P. Schönfeldt, M. Schuh, M. Siegel, M. Weber and A.-S. Müller
Karlsruhe Institute of Technology, Karlsruhe, Germany

Abstract

While recent diffraction-limited storage rings provide bunches with transverse dimensions smaller than the wavelength of the observed synchrotron radiation, the bunch compression in the longitudinal plane is still challenging. The benefit would be single cycle pulses of coherent radiation with many orders of magnitude higher intensity. However, the self-interaction of a short electron bunch with its emitted coherent radiation can lead to micro-bunching instabilities. This effect limits the bunch compression in storage rings currently to the picosecond range. In that range, the bunches emit coherent THz radiation corresponding to their bunch length. In this paper, new measurement setups developed at the Karlsruhe Institute of Technology are described for systematic turn-by-turn investigations of the micro-bunching instability. They lead to a better understanding thereof and enable appropriate observation methods in future efforts of controlling and mastering the instability. Furthermore, the described setups might also be used as high repetition rate bunch compression monitors for bunches of picosecond length and below.

MICRO-BUNCHING INSTABILITY

The micro-bunching instability (MBI) is a longitudinal instability that arises due to the self-interaction of a bunch with its emitted electro-magnetic field[1]. This interaction can be modelled by a synchrotron-radiation impedance whose real part corresponds to the emitted radiation. The impedance has a low frequency cutoff due to the shielding of the vacuum chamber [2] and a high frequency cutoff due to the particle energy. The shielded wavelengths can be approximated with the shielding cutoff $\lambda = 2h\sqrt{h/R}$ with h being the beam pipe height and R the particles radius of curvature, while the high frequency cutoff can be approximated by the critical frequency of the synchrotron radiation $f_c = 3\gamma^3 c/(4\pi R)$. Therefore, the impedance has significant strength if $\gamma^3\sqrt{h^3R^{-3}} \gtrapprox 2$. While this applies to almost all light sources, only a few heavy particle machines reach high enough energies. However, also future colliders will be confronted with high amount of synchrotron radiation.

In order to generate a significant wake potential, the bunch spectrum and the impedance need to overlap. As a rule of thumb, storage rings with a few meters bending radius and some tens of centimeters beam-pipe height typically have a cutoff around hundred gigahertz, leading to a critical bunch length around ten picoseconds. At first, the additional wake potential leads to potential well distortion and a change of bunch shape. Then, above a critical bunch charge, a self-amplified system is formed since the distorted bunch shape increases the wake potential further. This leads to the formation of sub-structures on the bunch profile and a blow-up of the bunch in phase space. The blow-up is much faster and stronger than the damping time and no equilibrium is reached. The bunch is blown up, until the wake potential becomes negligible. Then, the radiation damping shortens the bunch, until the threshold is hit again. Consequently, a sawtooth behaviour is observed.

Due to the characteristic bunch size of a few picoseconds and even smaller substructures, signatures of the instability can be seen in the terahertz frequency range where outbursts of coherent radiation are observed. Obviously, the behaviour is beam current dependent, too.

The relevant time scales when observing the MBI reach from a few turns during the start of a burst, over some milliseconds between consecutive bursts, to minutes and hours when analyzing current dependent changes. Consequently, the diagnostics need to be single shot, turn-by-turn and be able to record for long time scales. In this paper, we will present recent diagnostic systems developed and evaluated at the Karlsruhe Institute of Technology (KIT).

KARLSRUHE RESEARCH ACCELERATOR

The Karlsruhe Research Accelerator (KARA) is the 2.5 GeV storage ring of the KIT. It can be varied for a broad range of parameters (see Table 1). A special short-bunch mode is established at 1.3 GeV.

Table 1: KARA Parameters

L	110.4	m
f_{RF}	499.7	MHz
h	32	mm
Energy	0.5 to 2.5	GeV
V_{RF}	150 to 1500	kV
α_c	1.6×10^{-4} to 1×10^{-2}	
$\sigma_{z,0}$	1.9 to 45	ps

* Funded by the German Federal Ministry of Education and Research (Grant No. 05K16VKA) & Initiative and Networking Fund of the Helmholtz Association (contract number: VH-NG-320). M. Brosi, P. Schönfeldt and J. Steinmann acknowledge the support of the Helmholtz International Research School for Teratronics (HIRST).
† johannes.steinmann@kit.edu
[1] For a good summary of the topic see Ref. [1].

ISBN: 978-3-95450-206-6 doi:10.18429/JACoW-FLS2018-TUP2WD03

THz DIAGNOSTICS USING KAPTURE

KAPTURE (KArlsruhe Pulse Taking and Ultrafast Readout Electronics)[3–5] is an in-house built DAQ system for ultra-fast detector pulses with a bunch-to-bunch repetition rate. It uses the memory efficient approach to only sample and store the detector pulse, neglecting the noise in-between. In contrast to state-of-the-art oscilloscopes, the 4 GBytes/s of raw data can be streamed out continuously to the readout computer via PCI-Express.

KAPTURE consists of four 12-bit ADCs whose sampling trigger points can be adjusted in 3 ps steps each. Several operation modes can be configured.

The standard mode allows the reconstruction of the detector pulse amplitude and the arrival time. For this, the detector is connected to a 1-to-4 splitter, distributing the detector signal to the four sampling channels. By setting the individual delays of the channels, the pulse can be sampled with up to 330 GSa/s local sampling rate.

Another operation mode is the use of four individual detectors instead of the output of the power splitter. In this way the pulse amplitudes of the detector responses of all detectors are intrinsically sampled synchronously. This allows the operation as single-shot spectrometer, when detectors sensitive in different frequency ranges are used. However, only a single sampling point per detector and pulse is taken.

Snapshot Measurements

By using KAPTURE and a fast THz detector, the outbursts of radiation due to the MBI can be studied turn-by-turn and even bunch-by-bunch. Figure 1 shows raw data of a broadband THz detector recorded with KAPTURE. The intensity fluctuations are clearly visible for each bunch. Depending on their bunch current, the bunches display different bursting behaviors, i.e., the temporal evolution of a burst and the repetition rate.

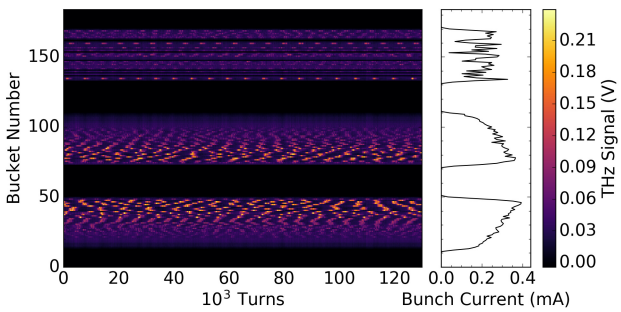

Figure 1: The fluctuating THz signal (color-coded) of each of the 184 RF buckets is shown for 130 thousand consecutive turns. The bursting behavior differs for bunches with different currents. The right hand side shows the filling pattern, consisting of three trains [6].

Usually, the dynamics of the MBI are shown in a spectrogram, where the fluctuations at a given bunch current are measured. The conventional procedure, involving a single bunch, takes hours of measurement time, where the bunch charge is changed between measurements. With KAPTURE providing a bunch-by-bunch sampling, the measurement time can be shortened drastically [6] by using the information from multiple bunches at once. To cover the current range of interest, a tailored filling pattern (see right panel of Fig. 1) is created with a bunch-by-bunch feedback system [7]. By sorting the bunch signals by their charge, the current dependent effects can be studied by a single acquisition.

This method was used to quickly map the instability thresholds as well as the bounds of the short bunch-length bursting (SBB) (a weak instability, further information in [8, 9]) for different settings of the RF voltage and the momentum compaction factor α_c [9]. The resulting thresholds are displayed in Fig. 2 together with the prediction from a simulation by Bane, Cai, and Stupakov [8] using the dimensionless parameters CSR strength $S_{\mathrm{CSR}} = I_{\mathrm{n}} R^{1/3} \sigma_{\mathrm{z},0}^{-4/3}$ and shielding factor $\Pi = \sigma_{\mathrm{z},0} R^{1/2} h^{-3/2}$ (following the definition in [8, 9]).

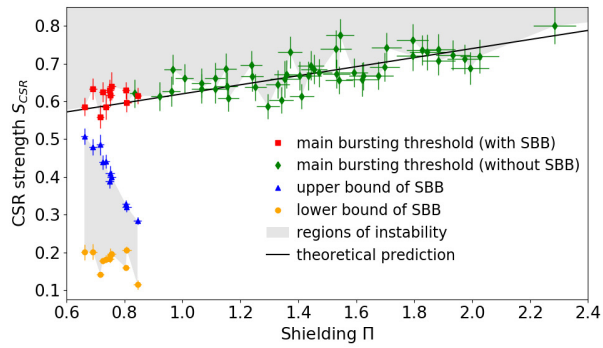

Figure 2: The MBI threshold displayed in CSR strength as a function of the shielding parameter for measurements at different machine parameters. The prediction by [8] is shown as black line. The error bars display the standard deviation error of the measurements [9].

4-Channel Spectrometer

Another operation mode of KAPTURE is the use of different detectors in parallel. With its four sampling channels, up to four detectors can be read out synchronously by KAPTURE. The setup presented here consists of four waveguide coupled Schottky detectors, each sensitive in a different frequency range. The synchrotron radiation is coupled out at the diagnostic port of the IR2 beamline and split with wire grids into four equal parts, each focused to an individual detector. Such a setup is depicted in Fig. 3.

An example measurement of a radiation outburst, detected with four diodes simultaneously, is shown in Fig. 4. A different phase of the periodic signals is observed, indicating changing spectral components.

For more information see Refs. [10, 11].

ISBN: 978-3-95450-206-6 doi:10.18429/JACoW-FLS2018-TUP2WD03

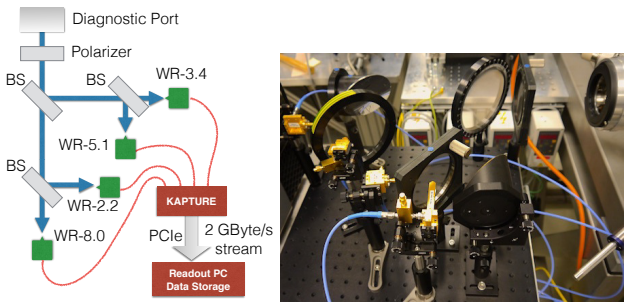

Figure 3: The synchrotron radiation emitted at the diagnostic port is first polarized and then divided into four beams by three wire-grid beam splitters (BS). The split beams are focused onto four detectors, each one sensitive in a different frequency band. The single-shot measurements are sampled and read out by the KAPTURE system.

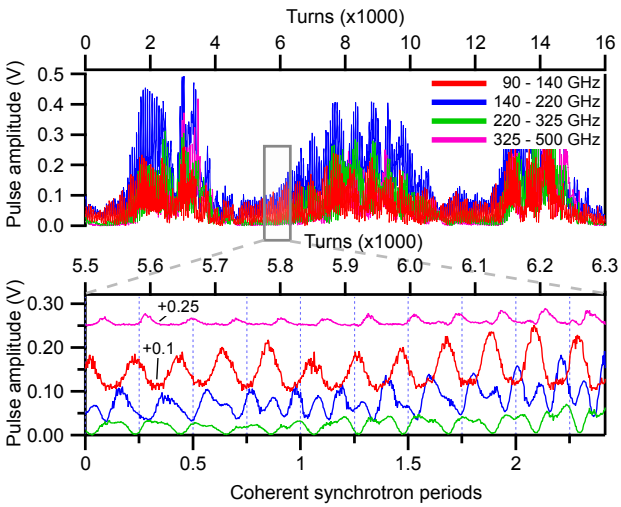

Figure 4: KAPTURE allows the continuous readout of four detectors in parallel. Each detector is sensitive in a different frequency range, leading to a four-channel single-shot spectrometer. A phase shift between the different frequencies can be observed in the zoom-in.

ELECTRO-OPTICAL BUNCH PROFILE MEASUREMENTS

To measure the longitudinal bunch profile we use our permanently installed electro-optical (EO) near-field setup. The fundamental detection scheme was first demonstrated in [12]. In 2013, we installed the first, and up to now only, EO near-field setup in a storage ring [13]. The layout (EOS v1) was identical to the design originally developed for the SwissFEL injector test facility [14] at PSI.

The electro-optical spectral decoding (EOSD) setup combined with the ultra-fast line camera KALYPSO (described below) as spectrometer allows turn-by-turn single-shot measurements. The working principle of this method is depicted in Fig. 5: A vertically polarized laser pulse (1) is first sent through a polarization-maintaining dispersive fiber (2). Thereby, the fs laser pulses are stretched to picoseconds resulting in a frequency chirp. Inside an EO crystal (3), brought in close vicinity to the electron beam, the polarization of the laser pulse is changed depending on the electrical field present. Due to the chirp the temporal profile of the electron bunch is encoded in the frequency profile of the laser pulse. Using a polarizing beam splitter (4), the polarization modulation is turned into an intensity modulation that can be probed using a spectrometer (5). To be precise, the refractive index of the crystal is $n_0 > 1$, so what is actually measured is not the Coulomb field of the electrons, but a wakefield created at the crystal surface facing the arriving electrons. Additional electric fields can influence the measurement. The most prominent one in bunch-profile measurements is the part of the Coulomb field penetrating the crystal from the bottom [16]. At later times reflections can occur from various surfaces [17]. When the bunch spacing is too small, these fields can influence the measurement of the next bunch.

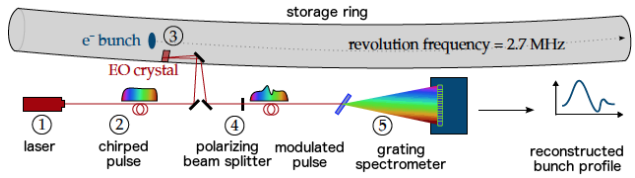

Figure 5: Working principle of the EO setup. See text for details. [15]

In 2016, we optimized the in-vacuum geometry (EOS v2) to account for the needs of a circular accelerator. To achieve a higher signal at low bunch charges, we increased the crystal thickness and reduced the distance between the electron beam and the laser path. This comes at the cost of increased influence of the electric fields coming from the bottom side of the crystal. The new layout was also designed [18] to minimize the effect of remaining wakefields at the position of a consecutive bunch to allow a closer bunch spacing (see Fig. 6).

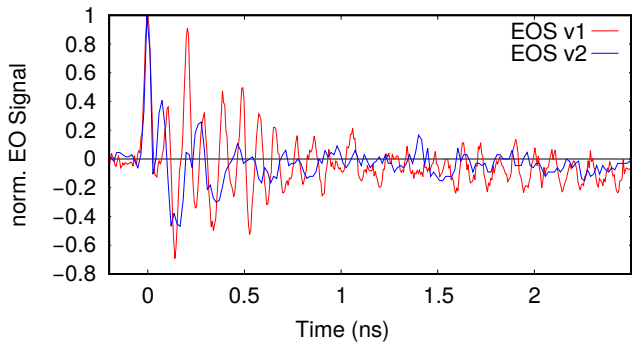

Figure 6: EO measurements performed with the EOS v1 and improved EOS v2 in-vacuum geometry. This comparison clearly shows the reduced trailing wakefields especially at 2 ns, the location of a subsequent bunch during multi-bunch operation. [18]

ISBN: 978-3-95450-206-6 doi:10.18429/JACoW-FLS2018-TUP2WD03

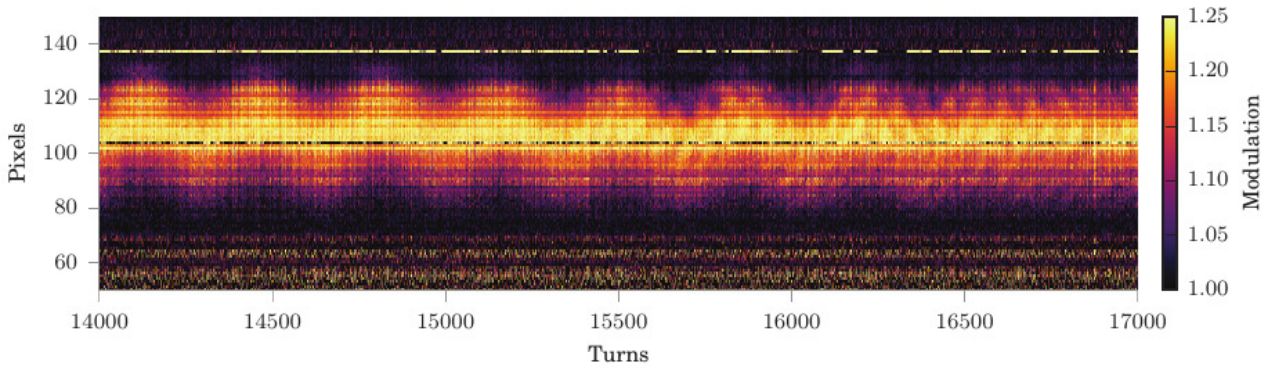

Figure 7: Raw EO measurement data recorded using KALYPSO over multiple turns. The acquisition rate was set to 2.7 Mfps, so that each vertical line corresponds to a single-shot and turn-by-turn measurement of the longitudinal bunch profile. The synchrotron oscillation of the electron bunch is clearly visible. Starting from turn 15500, the formation of substructures due to the MBI can be observed. The full dataset consists of 5×10^5 turns, one turn corresponding to 368 ns. [19]

Using the MHz line-array KALYPSO (KArlsruhe Linear arraY detector for MHz rePetition rate SpectrOscopy) [19] that was developed in collaboration between DESY, PSI, the University of Łódź, and KIT for exactly that purpose, it is now possible to track the longitudinal profile of an individual electron bunch on a turn-by-turn basis for theoretically infinite times without gaps. KALYPSO includes of a photon sensitive line array. Each of the 256 pixels is individually connected to the front-end electronics, allowing a readout rate of 2.7 Mfps. The line array can be based either on Si or InGaAs depending on the desired range of wavelengths. When using silicon, back illumination provides higher quantum efficiency.

The continuous streaming capability with turn-by-turn resolution of this setup is illustrated in Fig. 7. It shows synchrotron oscillation, as well as the formation of substructures due to the MBI in the second half of the panel.

TIME-RESOLVED ENERGY SPREAD STUDIES

As the energy spread cannot be measured directly, it is accessed via the horizontal bunch size in a dispersive region. For the equilibrium state, they are related according to Eq. 1.

$$\sigma_x = \sqrt{\beta_x \cdot \epsilon_x + (D_x \cdot \sigma_\delta)^2} \qquad (1)$$

Therefore, the horizontal beta function and dispersion at the imaging source point as well as the emittance are required. They can be determined using the Accelerator Toolbox for MATLAB [20] and LOCO for fitting the quadrupole strengths [21]. For the equilibrium case below the bursting threshold, where no deformation of the energy profile of the bunch is expected, this leads to reasonable good agreement between the measured horizontal bunch size and the calculated one according to Eq. 1.

To allow for time-resolved studies of the horizontal bunch size we are using a setup based on a fast-gated intensified camera (FGC) [22] located at the visible light diagnostics port [23]. The combination of the gating function of the camera and a fast, rotating mirror allows single-turn images of one bunch, see Fig. 8 for the principle scheme of this process.

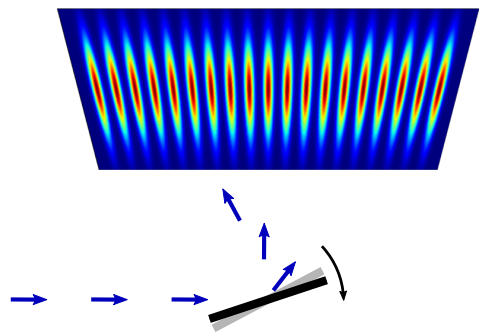

Figure 8: Functional principle of the rotating mirror. It sweeps the incoming light over the sensor of the camera. Due to the gating of the camera, a single bunch can be tracked in a multi-bunch environment.

On the current camera sensor, up to 60 individual spots can be analyzed. A minimum separation of 6 turns is achieved between two spots, due to the revolution frequency of 2.7 MHz and the rotation speed of the mirror.

The final image on the FGC sensor is the convolution of the charge distribution and the filament beam spread function (FBSF). The FBSF is the extension of the point spread function for a moving source. It is determined from simulations of the imaging process using the software OpTalix [24]. To overcome the problems coupled to a deconvolution (e.g. a correct estimation of the signal-to-noise ratio) we fit a convolution of a Gaussian curve with the FBSF to the spot profiles to get a measure for the horizontal bunch size.

For a single spot and its profile, such a fit is illustrated in Fig. 9.

The setup is embedded into the hardware synchronization scheme [25] and thus enables simultaneous studies of the energy spread and the CSR emission. One example for such a synchronized measurement is illustrated in Fig. 10.

ISBN: 978-3-95450-206-6 doi:10.18429/JACoW-FLS2018-TUP2WD03

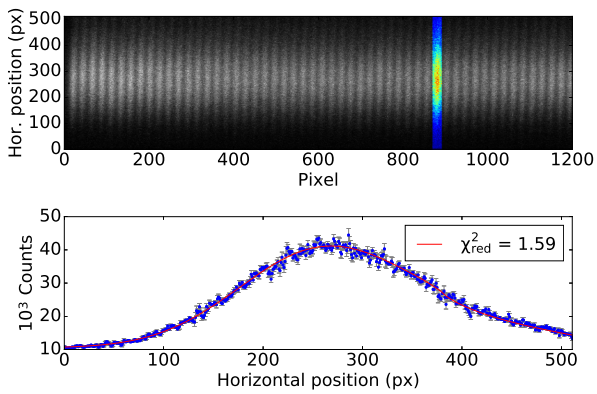

Figure 9: Top: Raw image of the FGC showing 53 single-turn images (spots) of the same bunch, each separated by 500 turns. For one spot, highlighted in color, the corresponding horizontal profile as well as the fit are shown on the bottom.

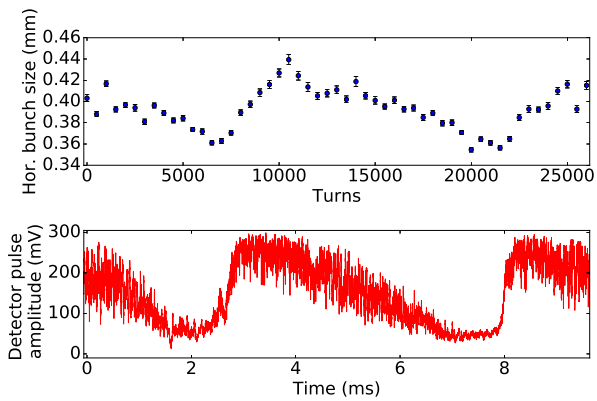

Figure 10: Horizontal bunch size as a measure for the energy spread (top) and the simultaneously recorded CSR intensity using a broadband Schottky diode (bottom). [26]

It shows that the energy spread as well as the CSR intensity perform a modulation with the same period length. At the onset of CSR burst, the energy spread reaches a minimum and is blown up in the following until a certain limit is reached, where damping effects start to dominate leading to a shrinking of the energy spread. This shrinking holds until a certain lower level is reached, where the energy spread hits a lower threshold coupled to the onset of the next burst (see [26]).

SUMMARY AND OUTLOOK

The micro-bunching instability (MBI) limits the reduction of the bunch length in a storage ring. To analyze this instability, we have set up and developed several single-shot high repetition-rate diagnostics stations. We have presented an overview of our various diagnostic methods to analyze the emitted CSR, the energy spread, and the longitudinal bunch profile. These diagnostic stations allow the synchronous analysis of the longitudinal phase space, and enable new insights into the dynamics of the MBI. Our findings also influence the development of our open-source Vlasov-Fokker-Planck solver Inovesa [27], which reproduces most features of the MBI remarkably well.

The development of the in-house readout electronics is still ongoing, both for KAPTURE and KALYPSO. A version 2 of KAPTURE is already being commissioned [28]. It not only doubles the number of sampling channels to eight, but also the sampling rate of each ADC to 1 GSa/s. This will improve both discussed readout modes, because more detectors can be readout synchronously or a better reconstruction of the detector pulse can be achieved. Furthermore, the sampling of the baseline in-between the pulses is enabled to improve accuracy by removing baseline fluctuations and lower frequency noise.

The four-channel spectrometer setup with individual detectors can hardly be expanded to more detectors as it is limited by space, intensity, and frequency bandwidth. To overcome this issue, at KIT an integrated planar array of super-conducting Y-Ba-Cu-O detectors, to be used with KAPTURE, is developed [29, 30].

Upcoming versions of KALYPSO include a 10 Mfps readout with less than 300 electrons equivalent-noise-charge and new line arrays with 512, 1024 or 2048 pixels as well as with a pitch of 25 µm or 45 µm. The anti-reflection coatings can be optimized for near-infrared (1050 nm), visible (400 nm to 850 nm) and near-ultraviolet (350 nm).

This makes it possible to use KALYPSO for a very wide range of different applications, not only in the field of accelerator physics. In the near future, we will use it for horizontal bunch size measurements in the visible frequency range as well. This overcomes the intrinsic limits of the FGC setup (no turn-by-turn capability, limited number of spots per image) and will allow continuous turn-by-turn studies of the energy spread. First tests were already successful.

KAPTURE and KALYPSO share the same readout architecture. A newly developed high-throughput architecture based on PCI-Express Gen3 and DirectGMA technology will be used to stream data directly to a GPU. This approach has about five times less data latency than other DMA architectures and permits realtime calculations on the GPU and enables their use for beam feedback [31]. Pre-processing before data storage is also a viable option for data reduction of the potentially large amount of data from various sensors and detector systems.

REFERENCES

[1] W. C. C. Biscari, in *ICFA Beam Dynamic Newsletter*, vol. 35, 2004,
URL: http://icfa-usa.jlab.org/archive/newsletter/icfa_bd_nl_35.pdf

[2] T. Agoh, "Steady fields of coherent synchrotron radiation in a rectangular pipe," *Phys. Rev. ST Accel. Beams*, vol. 12, p. 094 402, 9 Sep. 2009,
DOI: 10.1103/PhysRevSTAB.12.094402.

[3] M. Caselle *et al.*, "Commissioning of an Ultra-fast Data Acquisition System for Coherent Synchrotron Radiation De-

ISBN: 978-3-95450-206-6 doi:10.18429/JACoW-FLS2018-TUP2WD03

tection," in *Proceedings of 2014 International Particle Accelerator Conference*, 2014.

[4] M. Caselle *et al.*, "An ultra-fast data acquisition system for coherent synchrotron radiation with terahertz detectors," *Journal of Instrumentation*, vol. 9, no. 01, p. C01024, 2014, DOI: 10.1088/1748-0221/9/01/C01024.

[5] M. Caselle *et al.*, "An ultra-fast digitizer with picosecond sampling time for Coherent Synchrotron Radiation," in *19th IEEE-NPSS Real Time Conference*, May 2014, pp. 1–3, DOI: 10.1109/RTC.2014.7097535.

[6] M. Brosi *et al.*, "Fast mapping of terahertz bursting thresholds and characteristics at synchrotron light sources," *Phys. Rev. Accel. Beams*, vol. 19, p. 110 701, 11 Nov. 2016, DOI: 10.1103/PhysRevAccelBeams.19.110701.

[7] E. Hertle, E. Huttel, A.-S. Müller, N. Smale, D. Teytelman, and M. Höner, "First Results of the new bunch-by-bunch feedback system at ANKA," in *Proceedings of 2014 International Particle Accelerator Conference*, 2014, p. 1739.

[8] K. L. F. Bane, Y. Cai, and G. Stupakov, "Threshold studies of the microwave instability in electron storage rings," *Phys. Rev. ST Accel. Beams*, vol. 13, p. 104 402, 10 Oct. 2010, DOI: 10.1103/PhysRevSTAB.13.104402.

[9] M. Brosi *et al.*, "Systematic Studies of Short Bunch-Length Bursting at ANKA," in *Proceedings, 7th International Particle Accelerator Conference (IPAC 2016)*, Jun. 2016, pp. 1662–1665, DOI: doi:10.18429/JACoW-IPAC2016-TUPOR006.

[10] J. L. Steinmann *et al.*, "Time Resolved Spectral Analysis of Coherent Synchrotron Radiation using a sub-THz 4-Channel Single Shot Spectrometer with 500 MHz Repetition Rate and Continuous Readout," arXiv:1710.09568, 2017, URL: https://arxiv.org/abs/1710.09568

[11] J. Steinmann *et al.*, "4-Channel Single Shot and Turn-by-Turn Spectral Measurements of Bursting CSR," in *Proceedings, 8th International Particle Accelerator Conference (IPAC 2017)*, May 2017, pp. 231–234, DOI: 10.18429/JACoW-IPAC2017-MOPAB056.

[12] I. Wilke, A. M. MacLeod, W. A. Gillespie, G. Berden, G. M. H. Knippels, and A. F. G. van der Meer, "Single-Shot Electron-Beam Bunch Length Measurements," *Phys. Rev. Lett.*, vol. 88, p. 124 801, 12 Mar. 2002, DOI: 10.1103/PhysRevLett.88.124801.

[13] N. Hiller *et al.*, "electro-optical bunch-length measurements at the anka storage ring."

[14] B. Steffen, V. Schlott, and F. Müller, "A compact single shot electro-optical bunch length monitor for the SwissFEL," in *Proceedings of DIPAC09*, (Basel, Switzerland), 2009, URL: https://diagnostics.web.psi.ch/publications/DIPAC09_TUPB42.pdf

[15] L. Rota, "KALYPSO, a novel detector system for high-repetition rate and real-time beam diagnostics," PhD thesis, Karlsruhe Institute of Technology, 2017.

[16] S. Jamison *et al.*, "Electro-optic techniques for temporal profile characterisation of relativistic Coulomb fields and coherent synchrotron radiation," *Nuclear Instruments and Methods in Physics Research Section A: Accelerators, Spectrometers, Detectors and Associated Equipment*, vol. 557, no. 1, pp. 305–308, 2006, DOI: 10.1016/j.nima.2005.10.090.

[17] Q. Wu and X. Zhang, "Free-space electro-optic sampling of terahertz beams," *Applied Physics Letters*, vol. 67, no. 24, pp. 3523–3525, 1995, DOI: 10.1063/1.114909.

[18] P. Schönfeldt *et al.*, "Towards Near-Field Electro-Optical Bunch Profile Monitoring in a Multi-Bunch Environment," in *Proceedings of the International Particle Accelerator Conference*, May 2017, pp. 227–230, DOI: 10.18429/JACoW-IPAC2017-MOPAB055.

[19] L. Rota *et al.*, "KALYPSO: A Mfps Linear Array Detector for Visible to NIR Radiation," in *Proc. of International Beam Instrumentation Conference (IBIC'16), Barcelona, Spain, Sept. 13-18, 2016*, Sep. 2017, pp. 741–744, DOI: 10.18429/JACoW-IBIC2016-WEPG46.

[20] B. Nash *et al.*, "New functionality for beam dynamics in Accelerator Toolbox (AT)," in *Proceedings of IPAC'15*, 2015, pp. 113–116.

[21] J. Safranek *et al.*, "Theme section - LOCO," *ICFA Beam Dynamics Newsletter*, vol. 44, no. SLAC-REPRINT-2009-545, pp. 43–80, 2009.

[22] P. Schütze, *Transversale Strahldynamik bei der Erzeugung kohärenter Synchrotronstrahlung*. Springer, 2017, ISBN: 978-3-658-20385-6.

[23] B. Kehrer *et al.*, "Visible Light Diagnostics at the ANKA Storage Ring," in *Proceedings of IPAC'15, Richmond, USA*, 2015, pp. 866–868.

[24] Optical Engineering Software, *OpTalix Pro*, http://www.optenso.com, 2013.

[25] B. Kehrer *et al.*, "Simultaneous Detection of Longitudinal and Transverse Bunch Signals at ANKA," in *Proceedings, 7th International Particle Accelerator Conference (IPAC 2016)*, Jun. 2016, pp. 109–111, DOI: doi:10.18429/JACoW-IPAC2016-MOPMB014.

[26] B. Kehrer *et al.*, "Time-Resolved Energy Spread Studies at the ANKA Storage Ring," in *Proceedings, 8th International Particle Accelerator Conference (IPAC 2017)*, May 2017, pp. 53–56, DOI: https://doi.org/10.18429/JACoW-IPAC2017-MOOCB1.

[27] P. Schönfeldt, M. Brosi, M. Schwarz, J. L. Steinmann, and A.-S. Müller, "Parallelized Vlasov-Fokker-Planck solver for desktop personal computers," *Phys. Rev. Accel. Beams*, vol. 20, p. 030 704, 3 Mar. 2017, DOI: 10.1103/PhysRevAccelBeams.20.030704.

[28] M. Caselle *et al.*, "KAPTURE-2. A picosecond sampling system for individual THz pulses with high repetition rate," *Journal of Instrumentation*, vol. 12, no. 01, p. C01040, 2017, URL: http://stacks.iop.org/1748-0221/12/i=01/a=C01040

[29] A. Schmid *et al.*, "Single-Shot Spectral Analysis of Synchrotron Radiation in THz Regime at ANKA," in *Proceedings, 7th International Particle Accelerator Conference (IPAC 2016)*, 2016, DOI: 10.18429/JACoW-IPAC2016-MOPMB016.

[30] A. Schmid *et al.*, "An Integrated Planar Array of Ultra-fast Y-Ba-Cu-O Detectors for Spectroscopic Measurements," *IEEE Transactions on Applied Superconductivity*, vol. 27, no. 4, pp. 1–5, Jun. 2017, DOI: 10.1109/TASC.2016.2625763.

[31] L. Rota *et al.*, "A high-throughput readout architecture based on PCI-Express Gen3 and DirectGMA technology," *Journal of Instrumentation*, vol. 11, no. 02, 2016, URL: http://stacks.iop.org/1748-0221/11/i=02/a=P02007

ISBN: 978-3-95450-206-6 doi:10.18429/JACoW-FLS2018-TUP2WD04

PRELIMIARY DESIGN OF HEPS STORAGE RING VACUUM CHAMBERS AND COMPONENTS

P. He, B.L. Deng, D.Z. Guo, Y.S. Ma, B.Q. Liu, Q. Li, Y.C. Yang, L. Zhang, X.J. Wang,
Institute of High Energy Physics, CAS, Beijing, P.R. China

Abstract

The 4th generation ring-based light sources, HEPS (High Energy Photon Source) 7BA lattice has been developed at IHEP. This is 6Gev, 200mA machine which has horizontal emittance ε_h around 60pm.rad to gain the high brilliance photon beam. This compact lattice bring the magnet aperture to 25mm diameter, this will place a demanding set of constraints on the storage ring vacuum system design. Hybrid design has been adopted this lattice which combines conventional chambers incorporating "antechambers" with a variety of simpler tubular chambers made variously of copper-plated stainless steel, and NEG-coated copper tube in the FODO section.

INTRODUCTION

The main issues of low emittance ring vacuum system are providing the effective pumping and handling the higher SR power. The general requirements for vacuum chamber have to be considered for the cost, performance, and required maintenance, these factors will led to a design by which the details of the chamber construction varies according to local spatial constraints and SR loading. The next-generation light source storage ring vacuum system has to be designed in such way which is compatible with a multi-bend achromat(MBA) compact lattice [1]. Three different approaches have been developed: Conventional chamber with antechamber [2], all NEG-coated copper tubes [3], and hybrid design which combines conventional chambers and tubular NEG-coated copper tube [4]. For the HEPS storage ring vacuum system, we choose the hybrid design. This option takes both advantage of type I and type II design, it has good vacuum performance and reduce the vacuum chamber impedance, and also can shorter the required installation time, and easy maintainability. Also the system cost is at the moderate level.

SYSTEM DESIGN

As presently envisioned, a 7BA lattice storage ring will store 200 mA of electron current at an energy of 6 GeV for HEPS. One cell layout of the storage ring is shown in Fig. 1. According to the difference of the magnet function, the sector is divided into four types of sections: quadrupole doublet, longitudinal gradient dipole, multipole straight, FODO (alternately of focusing and defocusing). Vacuum chamber cross-section and material selection will depend on the synchrotron radiation power distribution there and also need integrate with other components(magnet, BPM, et al.). The issues such as space between magnet pole tips, coil gaps for vacuum and photon extraction chambers, all of these need to be considered when we design the vacuum chamber. The different vacuum chamber design will be presented as below.

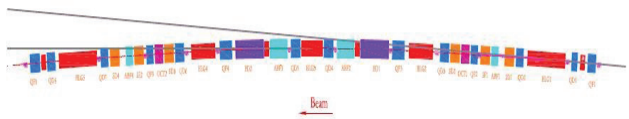

Figure 1: One sector of HEPS lattice layout.

Quadrupole Doublet Chamber

In this section, the fast corrector magnet is located between two quadrupoles, the Inconel segment will be used on this area to limit the impact of eddy current shielding by increasing electrical resistivity (7.4x10^(-7) Ωm→ 1.28x10^(-6) Ωm , 40% higher compare with 316LN stainless steel).

The interior surface, however, will be plated with copper to minimize beam impedance effects. The chamber layout is shown at Fig. 2.

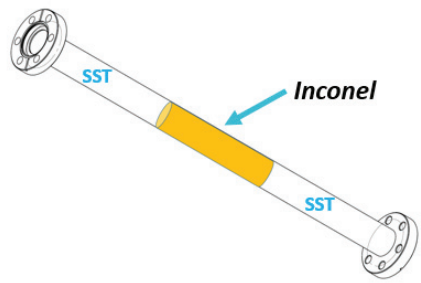

Figure 2: Quadrupole doublet chamber with Inconel segment.

LGD Chamber (Longitudinal Gradient Dipole)

Chambers here will have a 22 mm aperture for the particle beam and antechambers to allow discrete absorbers to intercept bending magnet radiation away from the stored beam (Fig. 3). In order to provide the good vacuum performance, two NEG pump will be add to the antechamber side. Finite element analysis (FEA) was used to calculate the mechanical stresses in vacuum chamber. The primary results show the max. deformation is 0.055mm and max. stress is 17.8MPa, the further optimization of the design still underway.

Straight Multiplet Chamber and X-ray Extraction Chamber

The ray trace simulation indicate that the very less bending magnet radiation shooting on the chamber wall in the straight multiplet section even without antechamber and just very simple tubular chamber. The key-hole chamber is applied here for the x-ray extraction which

ISBN: 978-3-95450-206-6 doi:10.18429/JACoW-FLS2018-TUP2WD04

coming from the insertion device (undulator). The chambers cross section is shown in Fig. 4.

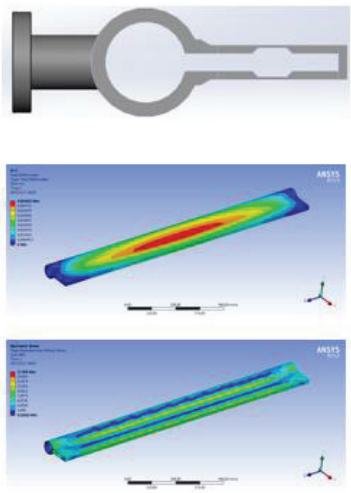

Figure 3: LDG chamber cross section.

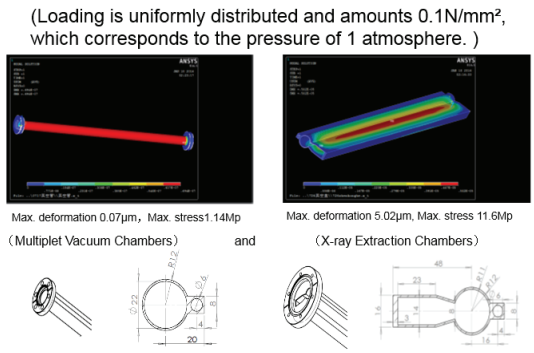

Figure 4: Multiplet chamber and X-ray extraction chamber.

FODO NEG-Coated Copper Chamber

Due to the higher synchrotron radiation power will shining on the vacuum chamber wall in this central FODO area, we design the chamber by using the oxygen-free copper material to maximize the thermal conductivity. And also a cooling water tube will adjoin the outboard wall to remove synchrotron radiation heat. The "in-line absorber" concept design will use GlidCop stub in the end of the chamber to absorb the radiation power and protect the following BPM components (see Fig. 5).

Figure 5: Copper tube in FODO section.

The mechanical stress analysis is shown in Fig. 6. The NEG coating will applied on the inner surface of the chamber to provide the distributed pumping. Getter films deposited on the inner surface of the chamber would transform the vacuum chamber from an outgassing source into a pump.

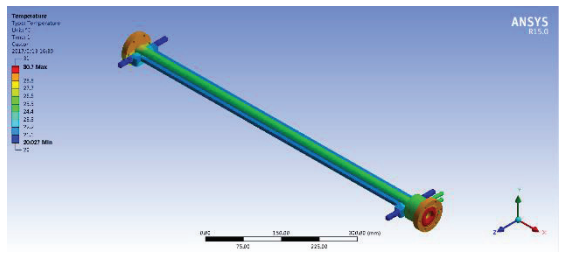

Figure 6: Mechanical analysis of copper tube.

COMPONENT DESIGNS

Zero Impedance Flange

This kind of flange means with no slit and no step between the two flanges which was developed at Sirius [3], on the basis of the model developed at KEK [5]. It is smooth inner surface, and additional effort is made so that electron beam only sees copper in traversing a flange (Fig. 7). The leak check and vacuum test shows no leaking even after 10 times assemble/disassemble and bake out up to 200° C (Fig. 8).

Figure 7: Zero impedance flange prototype.

Figure 8: Flange under leak check.

RF Shielded Bellow

The bellows will be used between vacuum chambers, they have following functions:

a) Make up for transverse offsets in beamline hardware, and minor misalignments

b) Provide installation personnel with sufficient flexibility to install hardware.

c) Reduce stresses on adjacent vacuum joints.

ISBN: 978-3-95450-206-6 doi:10.18429/JACoW-FLS2018-TUP2WD04

d) Provide adequate expansion and/or contraction ability during thermal cycles.

e) Provide required movements for functioning instruments, such as beam profile viewers.

In storage rings, bellows MUST be shielded from the beam. Otherwise, wake-field will be excited in the cavities to cause damage to the bellows. Most modern designs of RF-shielded bellows should have much smoother transitions, to reduce RF-impedance. The two different RF shielding liners have been designed here: conventional "outside finger" configuration and omega stripe RF shield. The 3D-model are shown in Fig. 9. The K loss factor and impedance will be measured after the two prototypes are delivered to IHEP.

Photon Absorbers

In addition to the "inline absorbers" built into the downstream end of many of the chambers, demountable photon absorbers are also needed at both crotch locations and at the downstream end of each bend chamber.

Preliminary designs have been established for these and analysis is underway to determine required materials, detailed geometry, and cooling water flow.

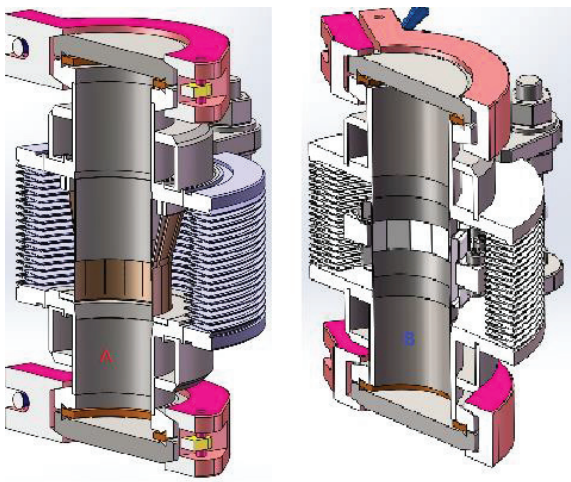

Figure 9: Two configurations of RF shielded bellows (A-outside finger; B-omega stripe).

First prototype of photon absorber was designed by using GlidCop material which has which has high thermal conductivity comparable to that of OFHC copper and can withstand higher stress(Fig. 10). This design need brazing the absorber body into stainless steel flange which show some technical difficulty even use Au-Cu 50-50 filler. While the use of GlidCop for this application is not ideal as the material is expensive, available form limited, and hard to weld. 2nd design has been developed and absorber material is changed to the CrZrCu, this design is whole block 100% machine even for the knife-edge, no braze and no weld at all (Fig. 11). CrZrCu widely available in all sizes from many suppliers and is considerably less expensive. Options to eliminate the need for GlidCop are being investigated by testing the both two types of photon absorber prototypes.

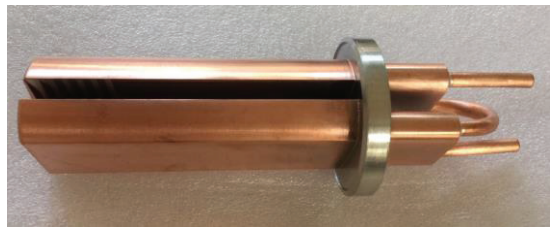

Figure 10: Brazing GlidCop_AL_15 to stainless steel (SST).

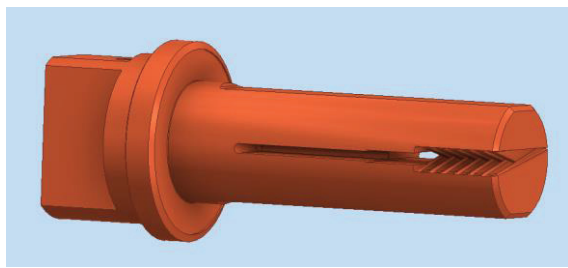

Figure 11: CrZrCu whole block machined absorber.

Synchrotron Ray Trace Analysis

A ray trace analysis (Fig. 12) by using SynRad code illustrates how synchrotron radiation distribution along the sector.

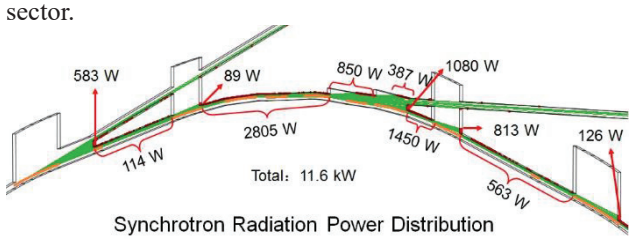

Figure 12: Distribution of bending magnet radiation.

According to SynRad simulation, we know the total bending magnet power approximately 11.6 kW. The higher power radiation generated primarily in central section and at outer ends (near ID straight section). FODO chambers receive more than half of the total power. Straight multiplet chambers receive very little power. These information will provide much help for the vacuum chamber and photon absorber design.

CONCLUSION

A conceptual design has been developed for a storage ring vacuum system of HEPS project. Chamber designs and pumping schemes are still need optimized for the four types of magnet arrangements according to the spatial allowances and synchrotron radiation power distribution there.

ACKNOWLEDGEMENT

The authors recognize and appreciate the help that our colleagues at IHEP and elsewhere around the world have given us in the course of developing these designs.

ISBN: 978-3-95450-206-6 doi:10.18429/JACoW-FLS2018-TUP2WD04

REFERENCES

[1] R. Hettel, *J. Synchrotron Rad.* vol. 21, pp. 843-855, 2014.

[2] M. Hahn *et al.,* "Layout of the Vacuum System for a new ESRF Storage Ring", WEPME026, IPAC'14, Dresden, Germany (2014).

[3] R.M. Seraphim *et al.*, "Vacuum system design for the SIRIUS storage ring", in *Proc. IPAC'15,* Richmond, USA, May 2015, paper WEPMA003, pp. 2744-2746.

[4] B.Stillwell *et al.*, "Conceptual design of a storage ring vacuum system compatible with implementation of a seven ben achromat lattice at the APS", in *Proc. IPAC'14*, Dresden, Germany, Jun. 2014, paper WEPME059, pp. 2409-2411.

[5] Matsumoto, H. *et al*.. Proceedings of EPAC 2006, Edinburgh, Scotland, p. 753. (2006).

ISBN: 978-3-95450-206-6 doi:10.18429/JACoW-FLS2018-TUA2WC01

TRANSPORTATION AND MANIPULATION OF A LASER PLASMA ACCELERATION BEAM*

A. Ghaith†, T. André, A. Loulergue, M. Labat, D. Oumbarek, C. Kitegi, I. Andriyash, F. Briquez, M. Valléau, F. Marteau, O. Marcouillé, F. Blache, F. Bouvet, Y. Dietrich, J. P. Duval, M. El-Ajjouri, C. Herbeaux, N. Hubert, N. Leclercq, A. Lestrade, P. Rommeluere, M. Sebdaoui, K. Tavakoli, M. E. Couprie, Synchrotron SOLEIL, GIF-sur-YVETTE , France
C. Thaury, G. Lambert, S. Corde, J. Gautier, B. Mahieu, K. Ta Phuoc, V. Malka, Laboratoire d'Optique Appliquée, Orsay, France
E. Roussel, Bielawski, C. Evain, C. Szwaj, Laboratoire PhLAM, Lille, France

Abstract

The ERC Advanced Grant COXINEL aims at demonstrating free electron laser amplification, at a resonant wavelength of 200 nm, based on a laser plasma acceleration source. To achieve the amplification, a 8 m long dedicated transport line was designed to manipulate the beam qualities. It starts with a triplet of permanent magnet with tunable gradient quadrupoles (QUAPEVA) that handles the highly divergent electron beam, a demixing chicane with a slit to reduce the energy spread per slice, and a set of electromagnetic quadrupoles to provide a chromatic focusing in a 2 m long cryogenic undulator. Electrons of energy 176 MeV were successfully transported throughout the line, where the beam positioning and dispersion were controlled efficiently thanks to a specific beam based alignment method, as well as the energy range by varying the slit width. Observations of undulator radiation for different undulator gaps are reported.

INTRODUCTION

Laser Plasma Acceleration (LPA) [1–3] has proven to be an efficient way to produce high energy electrons within a short accelerating distance. It can produce a GeV electron beam within a distance of few cms [4], high peak current up to 10 kA and short bunch length (few fs). However, the divergence is quite high of the order of few mrads and so is the energy spread (few %) [5]. A powerful laser focused on a gas chamber ionizes the gas molecules and pushes the electrons out of its path leaving the ions un-affected. This induces a plasma wave with an intense electric field following the direction of the laser. The electron beam caught in between the laser pulse and the plasma wave is accelerated until it surpasses the wave and thus attains maximum energy possible.

Undulator radiation has been successively observed [6–10] using LPA source, while Free Electron Laser (FEL) based applications remain very challenging due to the beam quality that does not fit the FEL requirements:

$$\begin{cases} \epsilon_N < \frac{\gamma\lambda}{4\pi} \\ \sigma_\gamma < \rho \end{cases} \quad (1)$$

where ϵ_N is the normalized emittance, γ the Lorentz factor, λ the radiation wavelength to be amplified, σ_γ the energy spread (FWHM) and ρ the pierce parameter:

$$\rho = \left[\frac{1}{16}\frac{I_{peak}}{I_A}\frac{\lambda_u^2 K^2 [JJ]^2}{4\pi^2\gamma^2\sigma_x\sigma_z}\right]^{1/3} \quad (2)$$

where I_{peak} is the peak current, I_A the Alfven current (17 kA), λ_u the undulator magnetic period, K the deflection parameter proportional to the undulator peak field and period, $[JJ] = J_0(\kappa) - J_1(\kappa)$ ($\kappa = \frac{K^2}{4+2K^2}$), σ_x and σ_z are the horizontal and vertical beam size (rms) respectively.

COXINEL [11–19], among other LPA based projects [20, 21], aims at demonstrating FEL amplification by the help of a dedicated transport line to handle and manipulate the beam properties [22].

BEAM MANIPULATION LINE

The line starts by focusing an intense Sa:Ti laser (800 nm) with 30 TW power, 1.5 mJ energy and 30 fs pulse duration on a gas jet composed of 99% He and 1% N_2. The baseline reference case of the slice beam parameters produced are shown in Table 1 (source). High gradient quadrupoles (~200 T/m) are used to decrease the beam divergence, and a chicane accompanied with a slit to select the desired energy. Table 1 (undulator) presents the electron beam parameters after beam manipulation. The divergence is reduced by a factor of 10 with a beam size of 50 μm corresponding to a normalized emittance of 1.7 mm.mrad that satisfy the first FEL condition. The slice energy spread is reduced by a factor of 10 on the expense of the peak current where the beam is decompressed (longer bunch length). Thus FEL amplification is feasible after such manipulation.

* Work supported by SOLEIL
† amin.ghaith@synchrotron-soleil.fr

ISBN: 978-3-95450-206-6 doi:10.18429/JACoW-FLS2018-TUA2WC01

Table 1: COXINEL Baseline Reference Case at the Source and at the Undulator after Beam Manipulation

Slice Parameters	Source	Undulator
Divergence	1 mrad	0.1 mrad
Beam size	1 μm	50 μm
Bunch length (rms)	3.3 fs	33 fs
Charge	34 pC	34 pC
Peak Current	4.4 kA	440 A
σ_γ	1% rms	0.1% rms
ϵ_N	1 mm.mrad	1.7 mm.mrad

MAGNETIC ELEMENTS

The first magnetic element placed 5 cm after the gas jet is a triplet of permanent magnet based quadrupoles with high tunable gradient (QUAPEVAs) [23]; followed by a chicane composed of four electro-magnet dipoles; a set of four electro-magnet quadrupoles to ensure good focusing inside the undulator; a cryo-ready undulator and finally a dipole dump (see Fig. 1).

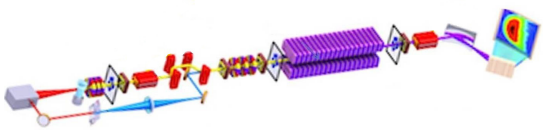

Figure 1: Schematic view of COXINEL transport line. Left to right: Laser, gas jet, permanent magnet quadrupoles [23], four electro-magnet dipoles (chicane), four electro-magnet quadrupoles, undulator and dipole dump.

QUAPEVAs

The QUAPEVA [23] is composed of two superimposed quadrupoles, one placed at the center following a Halbach configuration, surrounded by another that consists of four rotating cylindrical magnets to provide the gradient variability (see Fig.2). Table 2 shows the QUAPEVA parameters alongside the characteristics of the magnets and poles.

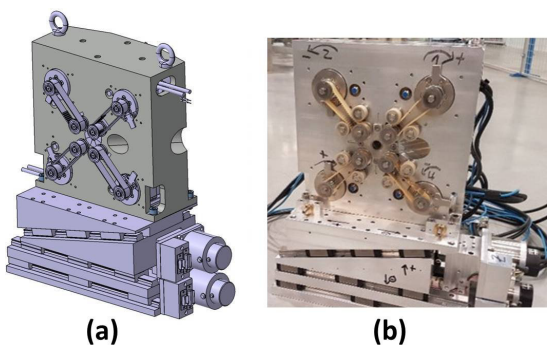

Figure 2: (a) mechanical design, (b) actual device.

Table 2: QUAPEVA Parameters

Parameters	Value	Unit
Gradient (G)	110 - 200	T/m
Remanent Field (B_r)	1.26	T
Coercivity (H_{cj})	1830	kA/m
Pole saturation	2.35	T

Chicane

The chicane consists of four electro-magnet dipoles with a maximum field of 0.55 T. Figure 3 shows the dipoles installed on the transport line. In the center, an adjustable slit with varying width is placed [24, 25]. Once the beam passes through the first two dipoles it is dispersed longitudinally and horizontally as shown in Fig. 4, and by closing the slit one is able to select a smaller energy range.

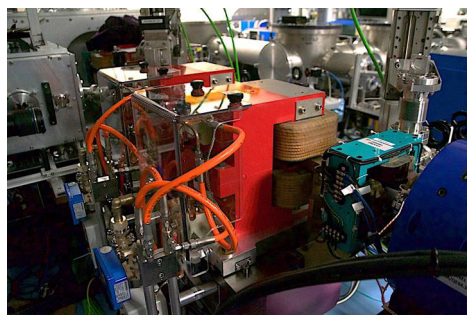

Figure 3: Second section of the chicane.

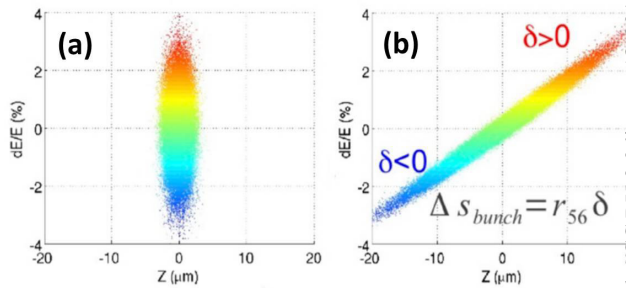

Figure 4: (a) Electron beam before the chicane, (b) after the first two dipoles of the chicane.

Quadrupoles

A set of four electro-magnet quadrupoles is installed after the chicane as shown in Fig. 5 to enable good focusing inside the undulator. The magnetic length of the quadrupole is 200 mm with a maximum gradient attained at 20 T/m.

ISBN: 978-3-95450-206-6 doi:10.18429/JACoW-FLS2018-TUA2WC01

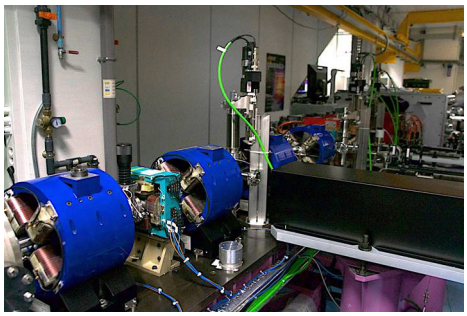

Figure 5: Set of four electro-magnet quadrupoles (blue) and a steerer (cyan) in between the last two.

ELECTRON BEAM DIAGNOSTICS

Electron beam diagnostics are installed all along the line [26]. Five scintillator screens (YAG and LANEX) placed: after the first set of quadrupoles, inside the chicane, before undulator, after undulator and after dipole dump. Two Integrated Current Transformers (ICTs) to measure the beam charge: one after the first set of quadrupoles and one after the undulator.

Beam Transport

The energy of the beam produced ranges from 50 MeV to 200 MeV. Figure 6 shows an electron beam measurement using a dipole and an electron spectrometer placed after the gas jet. The vertical divergence per slice (±5 MeV) is around 1.5 mrad rms.

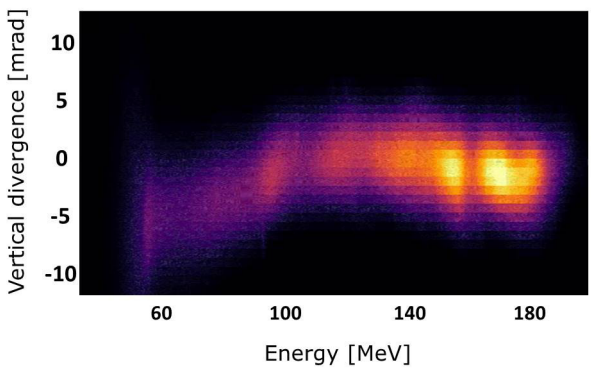

Figure 6: Electron beam measured using a dipole and an electron spectrometer.

Figure 7 shows an electron beam measurement at screen 1 (after the QUAPEVAs) without (a) and with the triplet (b). The large divergent beam is well focused, where the horizontal size is reduced by a factor of 3 and the vertical size by a factor of 2. The cross shape is due to the large energy spread that leads to chromatic effects. Figure 8 shows the electron beam measured at different locations of the transport line (Top) compared to the simulation (Bottom), and they show a very good agreement. The electron beam measured is tilted compared to the simulations due to the skew quadrupolar term of the QUAPEVAs, it has been later corrected using mechanical shims.

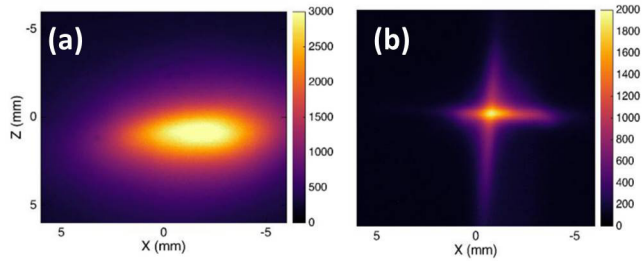

Figure 7: Measured electron beam on a Lanex screen placed 64 cm away from the first set of quadrupoles. (a) without QUAPEVAs, (b) with QUAPEVAs.

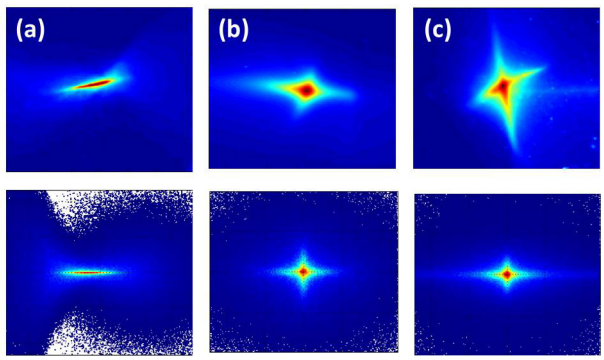

Figure 8: Electron beam measured (Top) and computed (Bottom) along the line. (a): Imager 2 (middle of chicane), (b): Imager 4 (before the undulator), (c) Imager 5 (after the undulator.

PHOTON SOURCE

The source of radiation is a cryo-ready undulator (parameters shown in Table 3), meaning it can function at both room and cryogenic temperatures [27–30]. It is currently operating at room temperature due to infrastructure reasons. Figure 9 shows the undulator installed at COXINEL, it consists of a carriage with a metallic base where the girders are separated by a gap and can be varied by two steps motors.

Table 3: Undulator Parameters

Parameters	Value
Technology	Hybrid cryogenic
Magnet material	CR53-Hitachi ($Pr_2Fe_{14}B$)
Remanence field	1.32 T
Coercivity	1.63 T
Pole material	Vanadium Permendur
Period	18 mm
No of periods	107

ISBN: 978-3-95450-206-6 doi:10.18429/JACoW-FLS2018-TUA2WC01

The resonant wavelength emitted (λ) is expressed as follows:

$$\lambda = \frac{\lambda_u}{2\gamma^2}\left[1 + \frac{K^2}{2} + \gamma^2\theta^2\right] \quad (3)$$

where λ_u is the undulator period, γ the Lorentz factor, $K = 93.4B[\mathrm{T}]\lambda_u[\mathrm{m}]$ the deflection parameter, B the peak field and θ the angle of the emitted radiation with respect to the observer.

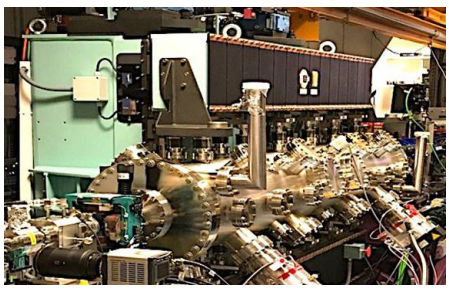

Figure 9: Undulator picture installed on COXINEL transport line.

The undulator can be closed to a minimum gap value of 4.55 mm and vary up to 30 mm. The magnetic field computed by RADIA [31] and measured with a Hall probe versus gap are shown in Fig. 10-a. For an energy of 176 MeV, the radiation spans between 180 nm - 280 nm (see Fig. 10-b).

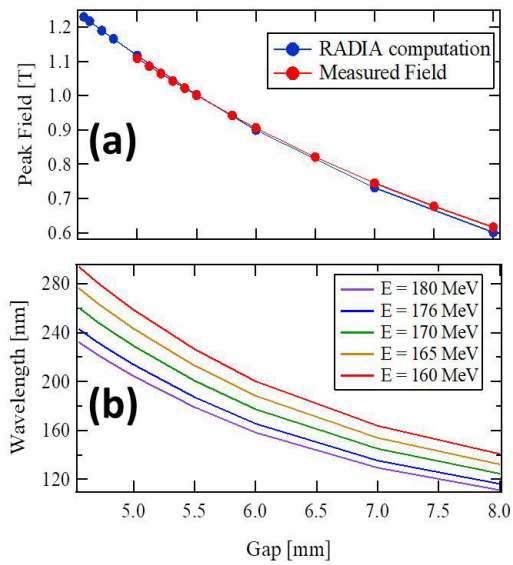

Figure 10: (a) peak field computed (blue) and measured (red) versus undulator gap. (b) theoretical wavelength calculated using Eq. 3.

PHOTON BEAM DIAGNOSTICS

Angular Flux

A Charge Couple Device (CCD) camera is installed 3 m from the exit of the undulator as shown in Fig. 11. Three optical filters were tested: centered around 200 nm with 10 nm bandwidth, centered at 254 nm with 38 nm bandwith; centered at 300 nm with 45 nm bandwidth.

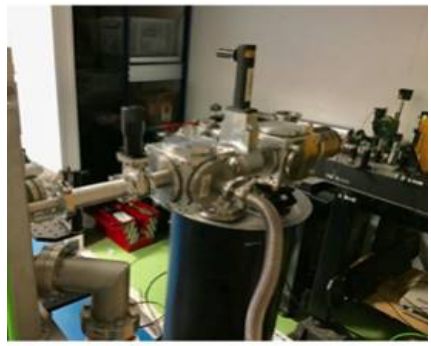

Figure 11: CCD camera installed 3 m from the exit of the undulator.

Figure12a presents a computation of the transverse photon beam shape using SRWE [32] with electron beam parameters computed by beta code. Fig 12-b shows the integrated instensity measurements with the CCD camera compared to simulations for four different optical filter cases (No filter, 300 nm, 254 nm and 200 nm filter). In the case where no optical filter is applied (black), the window captures all the radiation emitted which scales as an exponential decay versus gap ($P \propto B^2$) and the intensity drops when the optical filters are applied. For small gaps (5 mm - 6 mm) there is a bump for the 200 nm filter case, and that is caused by the fact that the on-axis radiation (resonance) have a spectral flux ~ half of the off-axis ones.

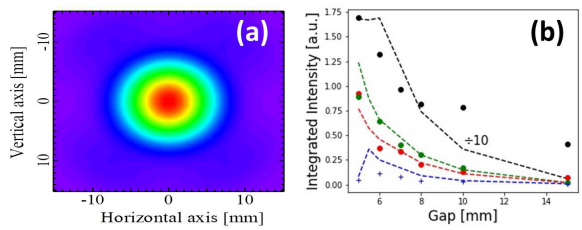

Figure 12: (a) Transverse beam shape computed. (b) Integrated intensity measured by the CCD camera (points) and computed using SRWE (dashed). Different optical filters applied: (red) centered at 300 nm with a 45 nm bandwidth, (green) centered at 254 nm optical filter with a 38 nm bandwidth, (blue) centerd at 200 nm with 10 nm bandwidth, (black) no filter is applied.

Spectral Flux

An iris is placed 2.28 m from the last magnet of the undulator, immediately followed by a spherical lens of focal length 240 mm to focus the radiation at the spectrometer slit placed at a distance equal to the focal length (see Fig. 13).

The flux has been measured with the spectrometer for different undulator gaps. Figure14 shows one of these measurements for a 4.55 mm gap.

ISBN: 978-3-95450-206-6 doi:10.18429/JACoW-FLS2018-TUA2WC01

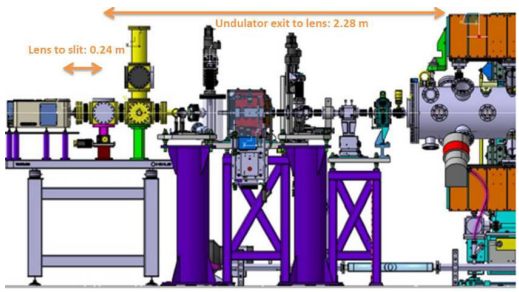

Figure 13: schematic view of photon beam diagnostic line. left to right: undulator, steerer, dipole dump, lens, spectrometer.

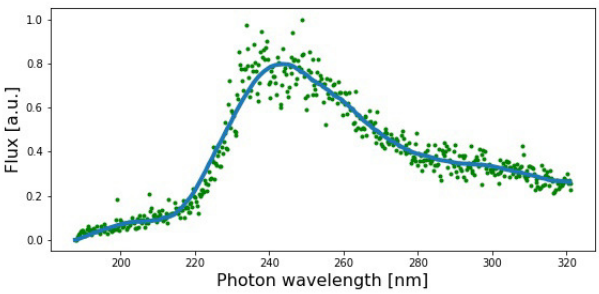

Figure 14: Spectral flux measured with the spectrometer.

CONCLUSION

The COXINEL line enables to control, manipulate and transport of a highly divergent beam produced by laser plasma acceleration source. High gradient permanent magnet quadrupoles enable beam pointing alignment compensation (position control and dispersion compensation) thanks to the transverse adjustable tables. The chicane accompanied with a slit provides a reduction in the energy spread. Undulator radiation has been measured using a CCD camera (Transverse beam shape) and a spectrometer (spectral flux) for different undulator gaps, and gave insight on the electron beam parameters. By further improving the beam quality, attaining free electron laser amplification is not that far fetched.

ACKNOWLEDGEMENT

The authors are very grateful for the support of the European Research Council (ERC) for COXINEL (340015) and the "Triangle de la Physique" for the QUAPEVAs contract.

REFERENCES

[1] T. Tajima, and J. M. Dawson. "Laser electron accelerator." *Physical Review Letters* 43.4 (1979): 267.

[2] E. Esarey, C. Schroeder, and W. Leemans, Physics of laser-driven plasma-based electron accelerators, *Reviews of Modern Physics*, vol. 81, no. 3, pp. 1229, 2009.

[3] V. Malka, J. Faure, C. Rechatin, A. Ben-Ismail, J. Lim, X. Davoine, and E. Lefebvre, Laser-driven accelerators by colliding pulses injection: A review of simulation and experimental results, *Physics of Plasmas(1994-present)*, vol. 16, no. 5, pp. 056703, 2009.

[4] W P. Leemans, *et al.* "Multi-GeV electron beams from capillary-discharge-guided subpetaWatt laser pulses in the self-trapping regime," *Physical Review Letters*, vol. 113, p. 245002, Dec 2014.

[5] C. Rechatin,J. Faure, A. Ben-Ismail, J. Lim, R. Fitour, A. Specka, H. Videau, A. Tafzi, F. Burgy, V. Malka, "Controlling the Phase-Space Volume of Injected Electrons in a Laser-Plasma Accelerator", *Physical Review Letters*, vol. 102, no. 16, pp. 164801, 2009.

[6] H.-P. Schlenvoigt, K. Haupt, A. Debus, F. Budde, O. Jäckel, S. Pfotenhauer, H. Schwoerer, E. Rohwer, J. Gallacher, E. Brunetti, R. Shanks, S. Wiggins, and D. Jaroszynski, "A compact synchrotron radiation source driven by a laser-plasma wakefield accelerator," *Nature Physics*, vol. 4, no. 2, pp. 130–133, 2008.

[7] M. Fuchs, R. Weingartner, A. Popp, Z. Major, S. Becker, J. Osterhoff, I. Cortrie, B. Zeitler, R. Hörlein, G. D. Tsakiris, U. Schramm, T. Rowlands-Rees, S. Hooker, D. Habs, F. Krausz, S. Karsch, and F. Grüner, "Laser-driven soft-X-ray undulator source," *Nature physics*, vol. 5, no. 11, pp. 826–829, 2009.

[8] M. P. Anania *et al.*, "The ALPHA-X beam line: toward a compact FEL," in *Proc. IPAC* 2010 , vol. 5, paper TUPE052, pp. 2263–2265.

[9] G. Lambert, S. Corde, K. T. Phuoc, V. Malka, A. B. Ismail, E. Benveniste, A. Specka, M. Labat, A. Loulergue, R. Bachelard, and M.-E. Couprie, "Progress on the generation of undulator radiation in the UV from a plasma-based electron beam," in *Proc. FEL conf., Nara, Japan* , paper THPD47, pp. 2, 2012.

[10] Plasma accelerator produces first X-rays, `http://www.desy.de/news/news_search/index_eng.html?openDirectAnchor=1261&two_columns=0`

[11] M.-E. Couprie *et al.*,"The LUNEX5 project in France",*Journal of Physics: Conference Series*, vol. 425, n0. 7,pp. 072001, 2013.

[12] M.-E. Couprie *et al.*, "Progress of the LUNEX5 project," in *35th International Free-Electron Laser Conference (FEL 2013)*, New York, NY, USA, Nov. 2013, paper WEPSO05, pp. 502–506.

[13] M.-E. Couprie *et al.*, "Strategies towards a compact XUV free electron laser adopted for the LUNEX5 project," *Journal of Modern Optics*, pp. 1–13, 2015.

[14] M.-E. Couprie *et al.*, "Experiment preparation towards a demonstration of laser plasma based free electron laser amplification", *Proc. FEL'14 (Basel, Switzerland*, paper TUP086, pp. 596.

[15] A. Loulergue, M. Labat, C. Evain, C. Benabderrahmane, V. Malka, and M. Couprie, "Beam manipulation for compact laser wakefield accelerator based free-electron lasers," *New Journal of Physics*, vol. 17, no. 2, pp. 023028, 2015.

[16] M.-E. Couprie *et al.*, "An application of laser–plasma acceleration: towards a free-electron laser amplification," *Plasma Physics and Controlled Fusion*, vol. 58, no. 3, pp. 034020, 2016.

[17] André Thomas *et al*., First electron beam measurements on COXINEL." 7th International Particle Accelerator Conference (IPAC'16), Busan, Korea. 2016.

ISBN: 978-3-95450-206-6 doi:10.18429/JACoW-FLS2018-TUA2WC01

[18] André, Thomas *et al.*, "Electron Transport on COXINEL Beam Line." 8th Int. Particle Accelerator Conf.(IPAC'17), Copenhagen, Denmark, 14â 19 May, 2017. JACOW, Geneva, Switzerland, 2017.

[19] M.-E. Couprie *et al.*, "Towards free electron laser amplification to qualify laser plasma acceleration", *The review of laser engineering*, 45(2):94–98, 2017.

[20] C. B. Schroeder *et al.*, "Application of Laser Plasma Accelerator beams to Free-Electron Laser," 2012 Proc. FEL, Nara, Japan, paper THPD57, pp. 658–61.

[21] M.P. Anania *et al.*, "An ultrashort pulse ultra-violet radiation undulator source driven by a laser plasma wakefield accelerator," *Applied Physics Letters*, vol. 104, no. 26, pp. 264102, 2014.

[22] Loulergue A *et al*., Beam manipulation for compact laser wakefield accelerator based free-electron lasers. New J. Phys. 17, 023028 (2015).

[23] F. Marteau, A. Ghaith, P. N'Gotta, C. Benabderrahmane, M. Valléau, C. Kitegi et al... Variable high gradient permanent magnet quadrupole (QUAPEVA). Applied Physics Letters, 111(25), 253503.

[24] A. Maier, A. Meseck, S. Reiche, C. Schroeder, T. Seggebrock, and F. Gruener, "Demonstration scheme for a laser-plasma-driven free-electron laser," *Physical Review X*, vol. 2, no. 3, pp. 031019, 2012.

[25] M.-E. Couprie, A. Loulergue, M. Labat, R. Lehe, and V. Malka, "Towards a free electron laser based on laser plasma accelerators," *Journal of Physics B: Atomic, Molecular and Optical Physics*, vol. 47, no. 23, pp. 234001, 2014.

[26] Labat, M., Hubert, N., El Ajjouri, M., Cassinari, L., Bourrassin-Bouchet, C., Loulergue, A., Couprie, M. E. (2014). Electron beam diagnostics for COXINEL. THP087, these proceedings, FEL, 14.

[27] Benabderrahmane, C., Valléau, M., Berteaud, P., Tavakoli, K., Marlats, J.L., Nagaoka, R., Béchu, N., Zerbib, D., Brunelle, P., Chapuis, L. and Dallé, D., 2013. Development of a 2 m Pr2Fe14B cryogenic permanent magnet undulator at SOLEIL. *In Journal of Physics: Conference Series* Vol. 425, No. 3, p. 032019 .

[28] Couprie, M.E., Briquez, F., Sharma, G., Benabderrahmane, C., Marteau, F., Marcouillé, O., Berteaud, P., El Ajjouri, T., Vétéran, J., Chapuis, L. and Valléau, M., 2015, May. Cryogenic undulators. "In Advances in X-ray Free-Electron Lasers Instrumentation III" *International Society for OpticsandPhotonics.* Vol. 9512, p. 951204

[29] Valléau, M., Benabderrahmane, C., Briquez, F., Berteaud, P., Tavakoli, K., Zerbib, D., Chapuis, L., Marteau, F., Marcouillé, O., El Ajjouri, T. and Vétéran, J., 2016, July. Development of cryogenic undulators with PrFeB magnets at SOLEIL. In AIP Conference Proceedings (Vol. 1741, No. 1, p. 020024). AIP Publishing.

[30] Benabderrahmane, C., Valléau, M., Ghaith, A., Berteaud, P., Chapuis, L., Marteau, F., ... Mary, A. (2017). Development and operation of a $Pr_2Fe_{14}B$ based cryogenic permanent magnet undulator for a high spatial resolution x-ray beam line. *Physical Review Accelerators and Beams*, 20(3), 033201 .

[31] Chubar, Oleg, Pascal Elleaume, and Joel Chavanne. "A three-dimensional magnetostatics computer code for insertion devices." Journal of synchrotron radiation 5.3 (1998): 481-484.

[32] Chubar, Oleg, and P. Elleaume. "Accurate and efficient computation of synchrotron radiation in the near field region." proc. of the EPAC98 Conference. 1998.

ISBN: 978-3-95450-206-6 doi:10.18429/JACoW-FLS2018-TUA2WC02

'LWFA-DRIVEN' FREE ELECTRON LASER FOR ELI-BEAMLINES

A.Y. Molodozhentsev*, G. Korn, L. Pribyl, ELI-BL, Institute of Physics of CAS, Prague, Czech Republic
A.R. Maier, University of Hamburg and CFEL, Hamburg, Germany

Abstract

Free-electron lasers (FEL) are unique light source for different applications on the femto-second scale, including for instance studying of the most basic reaction mechanisms in chemistry, structural biology and condense physics. Laser wake field acceleration (LWFA) mechanism allows to produce extremely short electron bunches of a few-fs length with the energy up to a few GeV providing peak current of many kA in extremely compact geometries. This novel acceleration method therefore opens a new way to develop compact "laser-based" FEL. ELI-beamlines (ELI-BL) is an international user facility for fundamental and applied research using ultra-intense lasers and ultra-short high-energy electron beams. In frame of this report we present conceptual solutions for an electron beam transport of a compact "LFWA" based soft X-ray FEL, which can deliver a photon peak brightness up to 10^{31} photons/sec/mm^2/mrad^2/0.1%BW. A combination of this achievement with novel laser technologies will open a new perspective for the development of extremely compact FELs with few or even sub-femtosecond photon bunches for a very wide user community.

INTRODUCTION

A few years ago, a new type of large-scale laser infrastructure specifically designed to provide high peak power and focused intensity ultrashort pulses was heralded by the European Community: the Extreme Light Infrastructure (ELI) [1]. ELI will be the world's first international laser research infrastructure. ELI is implemented as a distributed research infrastructure based on 3 specialized and complementary facilities located in the Czech Republic, Hungary and Romania. ELI-beamlines (near Prague, the Czech Republic) will be the high-energy beam facility responsible for development and use of ultra-short pulses of high-energy particles and radiation stemming from the ultra-relativistic interaction. Using laser systems in ELI-BL it will be possible to accelerate electrons up to a few GeV.

The principle of the 'laser-wake-field-acceleration' (LWFA) [2] is based on an ultra-high longitudinal electric gradient, created by the high-intensity laser pulse focused in dense plasma (in a gas-jet, gas-cell or capillary discharge targets). The ponderomotive force pushes the plasma electrons out of the laser beam path, separating them from the ions. A travelling longitudinal electric field can reach several hundreds of GV/m, which is much larger than the accelerating field achievable in conventional accelerators, making LWFA extremely attractive as a compact accelerator to provide high-energy beams for different applications. During last decades, a remarkable progress has been made in the field of electron acceleration based on the LWFA concept. Electron beams with peak energies of multi-GeV have been obtained experimentally [3]. However, a controllable high-quality electron beam with desirable properties such as energy spread, low emittance, small transverse divergence and large beam charge are not demonstrated using a single-stage LWFA setup up to now. Remarkable experimental achievement has been reached recently using a cascaded acceleration [4] of electrons by decoupling the injection and acceleration. Through manipulating electron injection, quasi-phase-stable acceleration, electron seeding in different periods of the wake-field, as well as controlling the energy chirp, the high-quality electron beams have been obtained. The electron beams with energies in the range of 200÷600MeV, with the RMS energy spread of 0.4÷1.2%, the RMS transverse beam divergence of 0.2mrad with the bunch charge of 10÷80pC have been demonstrated experimentally for this new cascaded acceleration scheme [5].

Using recent experimental achievements one can define the parameters of the LWFA electron beam at the exit of the plasma channel as following: the electron beam energy in the range from 300MeV to 1000MeV; the RMS transverse beam size in the horizontal and vertical plane is 1μm or less; the RMS transverse beam divergence in the horizontal and vertical planes is 0.5mrad or less; the RMS bunch length is about 1μm; the RMS relative (total) energy spread is less than 1%; the normalized RMS transverse beam emittance in the horizontal and vertical planes is 0.2π mm.mrad; the bunch charge is about 20÷50pC. In frame of this report we discuss a conceptual solution for a dedicated electron beamline to transport high-energy electrons from a plasma target up to an undulator for a 'demonstration' FEL experiment with a possible expansion of such beamline to use it for a 'laser-driven' FEL, which is under discussion now in the ELI-BL Center.

Uniqueness of the 'laser-driven' FEL is based on the laser properties. The laser pulse of a few tens of fs allows to produce extremely short electron bunch with the bunch duration of a few fs. Such short electron bunch passing through an undulator magnetic field can produce a 'single-spike' coherent photon radiation, if FEL resonance conditions are satisfied. In principle, the 'laser-driven' FEL can operate with high repetition rate (up to 100Hz), which is limited by the current 'state-of-art' of the laser technology.

* Correspond. author: Alexander.Molodozhentsev@eli-beams.eu

ISBN: 978-3-95450-206-6 doi:10.18429/JACoW-FLS2018-TUA2WC02

FEL: UNDULATOR AND RADIATION PARAMETERS

In order to provide effective coupling between electrons and photons the 'peak' undulator deflection parameter (K) should be in the range of (1÷3). The K-value depends on the 'on-axis' magnetic field of the undulator (B_0) and the undulator period (λ_u): $K=eB_0/(m_e c k_u)$, $k_u=2\pi/\lambda_u$. The gain length of the radiation power scales as $L_{g,1D}\sim(\lambda_u K^{-2})^{1/3}$. Bigger value of the deflection parameter leads to smaller power gain-length for the same undulator period. Nevertheless, the peak angular deflection (θ) of the electrons in the undulator magnetic field is proportional to the K-value ($\theta_e=(K/\gamma)$), where γ is the relative electron energy. If K>>1 the electron trajectories will not overlap leading to an incoherent radiation. 'Cryogenic' permanent magnet undulators (CPMU) allow to increase the magnetic field and the K-value without significant reduction of the undulator gap. In comparison with a 'room-temperature' PMU the 'cryogenic' undulator has better magnetic and vacuum performance. In addition, CPMU has also better radiation damage resistance, which allows considering CPMU as a promising candidate for a compact FEL. In frame of this report to estimate the photon properties we use the 'cryogenic' planar undulator designed on praseodymium-based magnets and vanadium permendur poles. The undulator has been developed by the Helmholtz-Zentrum Berlin [6] in the collaboration with University of Hamburg. High remanent magnetic field of the undulator with a period length of λ_u=15mm allows to obtain the on-axis deflection parameter (K) in the range of 1.3÷2.4 in the case of changeable gap size of 6÷3mm, respectively. The total length of the undulator is 2m. Goal of the 'demo' FEL experiment is to demonstrate the FEL regime for low-energies photons and reach the power saturation at the end of an undulator.

In Table 1(A) main parameters of photon beam are summarized for the 'demonstration' FEL setup. The energy of the electron beam is 350MeV. The estimations have been performed taking into account possible degradation of the high-gain FEL performance, caused by effects of energy spread of the electron beam, finite emittance and betatron oscillations of the electron beam, as well as diffraction and optical guiding of the FEL field [7]. The estimated 3D-saturation length is 2.1m. The radiation wave-length is 41nm, the photon energy is 30eV and the radiation bandwidth is 0.72%. The total photon flux is 1.23×10^{13} photons/pulse and the photon peak brilliance is 4.4×10^{29} photons/sec/mm^2/mrad^2/0.1%BW. Successful realization of the 'demo' FEL experiment will open a way to the 'full-scale' 'laser-driven' FEL.

The main parameters of the 'water-window' photon beam for the case of 1000MeV electron beam are summarized in Table 1(B). The 3D-saturation length is estimated as 8.5m, which make the whole setup quite compact. The radiation wave-length is 5nm, the photon energy is 241eV and the radiation bandwidth is 0.2%. The total photon flux is 1.5×10^{12} photons/pulse and the photon peak brilliance is 7.05×10^{30} photons/sec/mm^2/mrad^2/0.1%BW.

In order to demonstrate experimentally the amplification and the saturation of the photon radiation in the compact 'laser-driven' FEL, it is necessary to satisfy the FEL conditions [8] at the entrance of the undulator: (1) the RMS energy spread of the electron beam should be less than a half of the 'Pierce' parameter; (2) the normalized RMS emittance of the electron beam should be less than the coherent normalized emittance. From the list of the 'LWFA-driven' electron beam parameters, discussed above, it is clear that significant energy spread of the 'laser-driven' electrons does not meet the FEL conditions. Moreover, it is necessary to avoid significant growth of the normalized RMS emittance of the electron beam in the dedicated beamline from the 'laser-driven' source up to the undulator to be able to use is for the FEL experiment.

Table 1: Main Parameters of (A) 'Demo' FEL and (B) 'Water -Window' FEL

		A	B
Electron beam in Undulator			
Beam energy	MeV	350	1000
Bunch charge	pC	20	20
RMS bunch duration	fs	2	2
Peak current	kA	4	4
Matched beam size	μm	~ 30	~ 30
Normalized emittance	π mm.mrad	0.3	0.3
'Slice' energy spread	%	0.2	0.2
Photon coherent radiation in Undulator at saturation			
Photon energy, E_{ph1}	eV	30.1	246
Radiation wavelength	nm	41	5
Pierce parameter, ρ	$\times10^{-2}$	0.85	0.29
Coherent normalized RMS emittance, $\varepsilon_{n,coh}$	π mm.mrad	2.24	0.785
Cooperation length (3D), L_{coop}	μm	0.30	0.15
Gain length (3D), $L_{g,3D}$	m	0.107	0.45
Saturation length (3D)	m	~ 2.1	~ 8.5
Total photon flux	$\times10^{13}$ #	1.23	0.5
Radiation bandwidth	%	0.72	0.2
Photon flux per 0.1%bw	$\times10^{12}$ #	1.6	0.74
Photon brilliance	$\times10^{30}$ #	0.44	7.05
Photon pulse power	GW	10.8	5.2
Photon pulse energy	μJ	60	30

 # corresponding units are shown in the text

FEL Saturation Length

The FEL parameters, presented in Table 1 (A,B), depend strongly on the set of the electron beam parameters. Changing the 3D saturation length for different normalized RMS emittance and RMS energy spread has been analysed for the case of the 350MeV electron beam (Fig. 1). Main parameters of such electron beam are mentioned in Table 1(A). From the obtained result one can conclude that to keep the saturation length of 2m it is necessary to have the RMS normalized emittance of 0.2π mm.mrad and the RMS relative energy spread less than 0.4%. Such challenging electron beam parameters can be obtained only in a sense of the 'slice' parameters, which

ISBN: 978-3-95450-206-6 doi:10.18429/JACoW-FLS2018-TUA2WC02

is a fraction of the bunch in the longitudinal directions with the length less than the cooperation length [7,8,16].

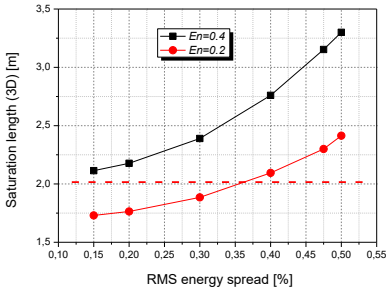

Figure 1: Estimation of the saturation length [7] for the 350MeV electron beam as a function of the RMS energy spread for different transverse normalized RMS emittance.

CONCEPTUAL SOLUTIONS FOR 'LFWA-BASED' FEL BEAMLINE

A dedicated electron beamline for both 'demo' FEL and 'water-window' FEL experiments has to provide: (1) capture of the electrons from the 'LWFA-source'; (2) effective transport of the electron beam with reasonable flexibility and (3) matching of the electron beam to the undulator. The beamline has been designed using the following 'basic' initial parameters of the electron beam: the normalized RMS emittance is equal to 0.2 π mm.marad; the transverse RMS beam size is 1μm; the transverse RMS beam divergence is 0.5mrad; the RMS relative energy spread is 1%. As it is shown below, the initial energy spread has to be reduced down to 0.5% in order to use the 'decompression' scheme without significant increasing the bunch charge, which allows to control the 'slice' parameters of the electron beam at the entrance of the undulator.

The 'capture' block of the electron beamline has to designed to minimize the intrinsic growth of the normalized emittance and to create a 'collimated' or 'focused' electron beam. Such beam should be able to propagate through a long drift space (about 3m) required to separate the laser beam and the electron beam using out-coupling optics. In addition, a set of steering magnets and beam-position monitors should be placed in this drift space to control the electron beam propagation at the beginning of the beamline. The 'capture' block of the beamline should be based on the triplet of the quadrupole magnets and placed at the minimum distance from the 'LWFA-source'. The triplet solution allows to provide a focusing of the electron beam in both transverse plane planes at the same time.

The Halbach-type [9] permanent quadrupole magnets (PQM) based on $Nd_2Fe_{14}B$ material with high gradient of the magnetic field (up to 450T/m, [10]) are chosen for the first focusing block of the beamline. The design of the 'target' vacuum chamber should allow to place the first quadrupole magnet at the distance of 4÷6cm from the source. The aperture of the permanent quadrupole magnets has to be big enough to guarantee the laser beam propagation without hitting the magnet material. For the developed setup of the 'capture' triplet the last quadrupole magnet is the normal electro-magnet with a moderate field gradient, because the required inner radius would be inconveniently large for a permanent quadrupole magnet. In order to adapt the 'capture' block for different electron energy, it is necessary to control the position of the permanent quadrupole magnets along the beamline.

The focusing properties of the quadrupole magnets depend on the energy and the energy spread of the electron beam passing through the magnets, leading to the chromatic aberrations and the emittance growth. There are a few approaches to minimize the chromatic effects without any elements with high-order ('sextupole') nonlinearity of the magnetic field, which can be used in principal for the 'LWFA-based' electron beamline: an 'apochromatic' beamline [11,12] and 'chromatic' matching [13]. In the case of the 'apochromatic' focusing the chromatic changing of the Twiss parameters can be corrected without the use of sextupole magnets. Recently a general method for designing drift-quadrupole beamlines with 'apochromatic' correction has been developed [12]. By using dedicated families of the quadrupole magnets it is possible to eliminate the energy dependence of the focusing to arbitrary order. Usage of such correction approach for the 'LWFA-based' electron beam-line requires additional quadrupole magnets making the electron beam-line quite long. Another disadvantage of this approach: it will not work in the case of a few undulators, because the 'apochromatic' condition can be met at a particular place of the beamline only.

There is another scheme to minimaize the effect of the chromatic aberrations [13], based on a second-order transverse beam manipulation turning large inherent transverse chromatic emittances of the LWFA beams into direct FEL gain advantage. To realize such approach it is necessary to control the high-order matrix elements of the chromatic perturbation. For practical usage it is necessary to consider more robust techniques, which are well-established in conventional accelerators.

For the energy selection one can use a traditional solution, based on the dispersive properties of dipole magnets. Or instead, apply the chromatic energy selection, which combines the advantages of focusing with energy selection in a single device, making the 'chromatic' filter with compact setup [14,15]. Both schemes should use a collimator to stop electrons with large deviation from the nominal beam energy.

In the case of the LWFA acceleration, the electron beam has a remarkably short bunch length (σ_z ~1μm) and significantly large relative energy spread ($\sigma_{\Delta p/p}$ ~1%). During the electron beam propagation through the beamline the bunch length increases (velocity de-bunching), but not enough to change the 'slice' parameters of the beam to be able to satisfy the FEL conditions.

By using a dispersive section ('decompressor') in the beamline the electron bunch can be stretched longitudinally and effectively sorted by energy [16], resulting in a

ISBN: 978-3-95450-206-6 doi:10.18429/JACoW-FLS2018-TUA2WC02

reduction of the local energy spread at the cost of a reduced peak current and an energy chirp. By changing the strength of the 'decompressor' bending magnets it is possible to control the 'slice' parameters of the 'laser-driven' electron beam.

Our conceptual electron beamline contains both schemes: (1) the 'chromatic' filter, based on the energy dependent focusing strength of the quadrupole magnets and (2) the 'decompressor', based on the 'C-shape' chicane with four dipole magnets. This solution of the dedicated electron beam line to transport the electron beam to the undulator for the 'demo-FEL' experiment is presented in Fig. 2. The 'basic' initial parameters of the 350MeV electron beam are the following: the RMS normalized emittance is 0.2 π mm.mrad; the RMS transverse beam size is 1.1μm; the RMS transverse beam divergence is 0.55mrad; the RMS relative energy spread is 1.1% and the RMS bunch length is 0.8μm.

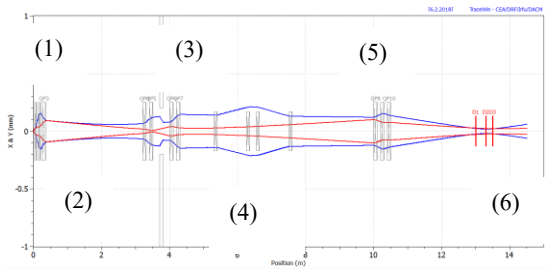

Figure 2: The horizontal and vertical beam envelope ($\sigma_{x,y}$) of the 'laser-driven' 350MeV electron beam for the 'demo' FEL experiment: (1) the 'capture' triplet block, based on PQMs; (2) the 'out-coupling' drift space; (3) the ' chromatic' filter with collimator; (4) the 'decompression' C-type chicane; (5) the 'matching' quadrupole triplet; (6) the undulator unit.

The proposed electron beamline has enough space for beam diagnostics after each 'key' element of the beamline to be able to: (1) measure and correct the beam-centre offset, caused by the quadrupole misalignments; (2) measure the transverse and longitudinal properties of the electron beam; (3) measure the bunch intensity and the propagation efficiency along the beamline. The collimator, placed in the 'chromatic' filter, allows to reduce growth of the normalized transverse emittance, caused by the 'chromatic' aberrations in the quadrupole magnets. For the initial RMS relative energy spread of 1% the propagation efficiency is 89% without any imperfections, if the collimator gap is 400μm. The normalized 'projected' RMS emittance in the horizontal and vertical phase-planes are 0.64 and 0.33 π mm.mrad, respectively. In the middle of the undulator (at the 'beam-waist' position) the RMS beam size in the horizontal and vertical planes are about 20μm. If the collimator in the 'chromatic' filter is opened, the corresponding RMS emittances are 1.30 and 0.35 π mm.mrad, respectively. The RMS beam sizes in the horizontal and vertical planes at the 'beam-waist' position are 31 μm and 22 μm, respectively.

If the 'capture' block of the quadrupole magnets is based on the electro-magnets with the maximum field gradient of 140T/m, the RMS normalized emittance in the 'out-coupling' drift space increases by about 50% and 170% in the horizontal and vertical planes, respectively.

The 350MeV electron beam properties have been analysed for different strength of the decompressor. The effective length of the dipole magnet of the chicane is 9cm. In this case, in order to provide the bending angle of 1degree the dipole magnetic field should be 0.255T. The corresponding R_{56} value is 5.6e-4 m.

The optimization of the electron beam line has been performed using TRACE3D [17] and TraceWin [18] codes.

'Slice' Parameters of the Electron Bunch

The main purpose of the decompression chicane in the electron beamline for the 'laser-driven' 'demo' FEL experiment is control the 'slice' parameters of the electron bunch to get the saturation of the photon radiation in the single undulator module with the length of 2m. By changing the bending angle of the chicane dipole magnets, the 'slice' energy spread and the 'slice' transverse emittance can be controlled. At the same time, the bunch length will be changed leading to variation of the peak current. The reduction of the peak current would lead to increasing the FEL saturation length. The parameters of the decompressor should be determined in a such a way to keep a reasonable (achievable) bunch charge and provide the 'slice' beam parameters, which meet the requirements: the 'slice' relative energy spread should be less than a half of the Pierce parameters ($\sigma_{\Delta p/p,S} < 0.4\%$); the 'slice' transverse normalized emittance should be less than 0.3 π mm.mrad. The bunch change should not be bigger than 50pC, providing the peak current of 4kA (Table 1).

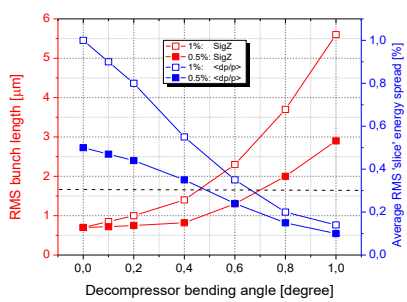

Figure 3: The RMS bunch length (red) and the average RMS 'slice' energy spread (blue) for different bending angle of the 'decompressor' dipole magnets for the case of the 350MeV electron beam, propagating through the electron beamline with different initial energy spread $\sigma_{\Delta p/p}$ of 1% (the 'open' mark) and 0.5% (the 'solid' mark).

The RMS bunch length (red) and the average RMS 'slice' energy spread (blue) for different bending angle of the decompressor dipole magnets are presented in Fig. 3 for the case of 350MeV electron beam, propagating through the electron beamline with different initial energy spread $\sigma_{\Delta p/p}$ of 1% ('open' mark) and 0.5% ('solid' mark).The

ISBN: 978-3-95450-206-6 doi:10.18429/JACoW-FLS2018-TUA2WC02

'slice' energy spread should be less than 0.3% in order to reach the FEL saturation at the end of the 2m undulator for the 'demo' FEL setup (Table 1(A)). To reach such value of the 'slice' energy spread in the case of the initial RMS energy spread of 1%, the bending angle of the 'chicane' dipole magnets should be more than 0.7degree. As a result, the RMS bunch length after the decompressor becomes more than 3μm (Fig. 3). If the initial RMS energy spread of the 'laser-driven' electrons is 0.5%, the required 'slice' energy spread of 0.3% can be obtained for the bending angle of the dipole magnets of 0.6degree. In this case the RMS bunch length after the decompressor is about 1μm, which allows to reduce the bunch charge from 100pC to 40pC keeping the same 'peak' current of the bunch of 4kA (Fig. 4).

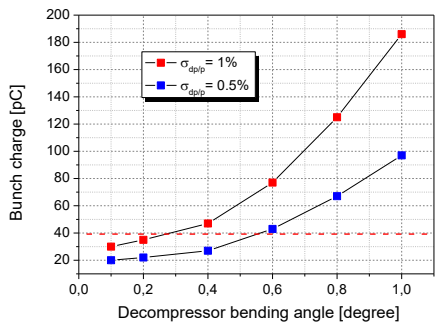

Figure 4: Require bunch charge to provide the peak current of 4kA for different bending angle of the decompressor dipole magnets in the case of different initial RMS energy spread $\sigma_{\Delta p/p}$=1% or 0.5%.

The 'slice' transverse emittance of the electron bunch after the decompressor is presented in Fig. 5 for the initial RMS energy spread of 0.5%. In the case of the bending angle of the decompressor dipole magnets of 0.6degree, the average 'slice' RMS emittances in the horizontal and vertical phase planes are 0.32 and 0.2 π mm.mrad, respectively.

The initial electron beam parameters for the 'demo' FEL experiment have to meet the following requirements in order to reach the radiation saturation at the end of the 2m 'cryogenic' undulator: the transverse RMS beam size is 1μm in both horizontal and vertical planes; the transverse RMS divergence of the electron beam is at least 0.5mrad and the RMS energy spread is not more than 0.5%. The bunch charge is less than 50pC.

The decompression of the electron bunch leads to the energy chirp, so that each 'slice' of the electron bunch will have the own 'central' energy. As the result, the radiation wavelength will be different from slice-to-slice. Nevertheless, for the 'demo' FEL the RMS variation of the radiation wavelength, caused by the energy chirp, will be less than the radiation bandwidth. For the high energy electrons, propagating through a long undulator, the effect of the coherent synchrotron radiation will also contribute into the energy chirp. Detailed study of such effects in combination with other collective effects is required.

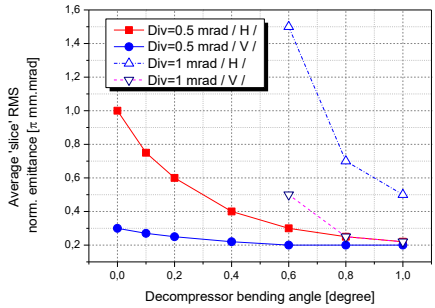

Figure 5: Average 'slice' RMS emittance in the horizontal and vertical phase plans as a function of the 'decompressor' bending angle for the initial RMS energy spread of the electron beam of 0.5% and for different initial divergence of the 'LWFA' electrons (0.5 mrad and 1 mrad).

FEL ANALYSIS

Using the obtained information about the electron beam properties after the decompressor chicane, it is possible to simulate the 'demo' FEL performance. Depending on the bending angle of the chicane dipole magnets three cases have been simulated using the SIMPLEX code [19] for the single module (total length of 2m) of the 'cryogenic' planar undulator, discussed above: (1) the bending angle of 0.2 degree; (2) 0.4 degree; (3) 0.6 degree. The 'slice' RMS energy spread after the decompressor is: (1) 0.44%; (2) 0.35%; (3) 0.24%, respectively. To keep the peak current of 4kA for each set of the chicane magnets the bunch charge for each case is: (1) 23pC; (2) 27pC; (3) 43pC, respectively. The simulated photon pulse energy along the undulator module is presented in Fig. 6 for each set of the parameters. The photon pulse energy at the exit of the undulator depends strongly on the electron beam parameters. The saturation of the photon energy has been reached for the case (3) only with the initial RMS energy spread of 0.5%. The obtained results show that a proper choice of the initial 'LWFA-driven' electron beam parameters and tuning of the decompressor allow to get the FEL amplification and the saturation in the case of 'short' undulator.

The FEL regime has been simulated in the case of the 'water-window' radiation (Table 1(B)). The 'laser-driven' electron beam should have the energy of 1000MeV. The conceptual solutions for the electron beamline from the source up to the undulator entrance remain the same. The permanent quadrupole magnets in the capture focusing block have to be changed and the position of these quadrupole magnets should be optimized to provide focusing at the location of the out-coupling optics. The strength of the electro-quadrupole magnets can be scaled for the high-energy operation. The estimated 3D saturation length for this case is about 9m, so that it is necessary to consider a few segments of the undulator separated by a drift space.

ISBN: 978-3-95450-206-6 doi:10.18429/JACoW-FLS2018-TUA2WC02

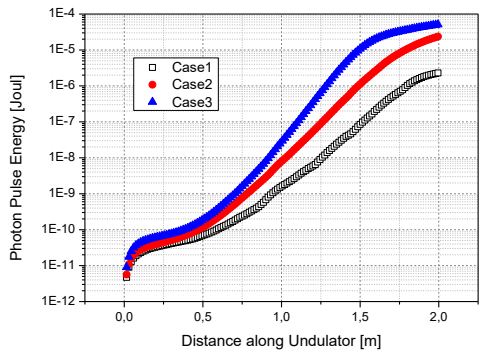

Figure 6: Photon pulse energy along the 'cryogenic' planar HPM undulator, discussed above, for different parameters of the electron bunch after the decompressor (see in the text).

This drift space should be long enough to accommodate additional focusing elements, electron beam diagnostics and 'phase-shift' magnetic structure. For the 'water-window' 'laser-driven' FEL we consider the 'cryogenic' HPM undulator with the segment length of 2.5m, separated by the drift space of 0.75m. The number of the undulator segments is 4. The electron beam parameters, used for the FEL simulations, are summarized in Table 1(B). The photon pulse energy along the undulator segments is presented in Fig. 7. After the 3rd segment of the undulator the saturation of the photon energy has been reached. The total length of the whole setup of the 'laser-driven' FEL including the dedicated electron beamline and 4 'cryogenic' undulator segments is about 25m, which can be integrated in to the existing ELI-BL experimental Hall.

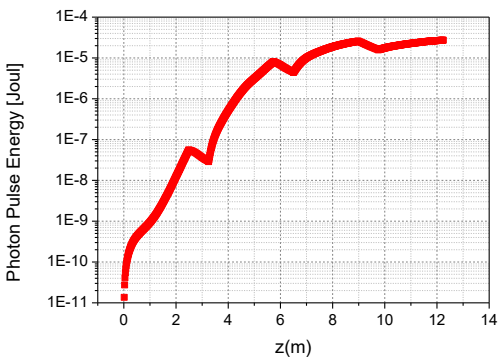

Figure 7: Photon pulse energy evolution along the segments of the 'cryogenic' undulator for the case of the 'laser-driven' electron beam with the energy of 1000MeV (Table 1(B)).

CONCLUSION

The conceptual solutions of the dedicated electron beamline from the 'LWFA-source' up to the undulator have been discussed. These solutions allow to: capture electron beam right after the laser-acceleration and transport the electron beam keeping the normalized RMS emittance under the control. The magnetic chicane, integrated into the electron beamline, provides the required 'slice' parameters of the electron beam for the undulator. The effects of different initial parameters of the 'laser-driven' electron beam have been discussed. The FEL performance has been analyzed for different decompressor strengths. The FEL performance for both 'demo' and 'water-window' FEL has been presented. It was shown that the saturation length can be reduced up to 2m and 9m, respectively. This study should be extended to include collective effects, which would lead to additional degradation of the electron beam properties.

ACKNOWLEDGEMENT

This work has been supported by the project Advanced research using high intensity laser produced photons and particles (CZ.02.1.01/0.0/0.0/16_019/0000789) from European Regional Development Fund.

REFERENCES

[1] ELI beamlines 'White ' book: *https://www.eli-beams.eu/en/projects/eli-white -book/*

[2] T.Tajima and J.Dawson, *Phys.Rev.Lett* 43,267 (1979)

[3] W.Leemans *et al., Phys.Rev.Lett.*113,245002 (2014)

[4] J.S. Liu *et al*, *Phys Rev.Lett 107,* 035001 (2011)

[5] W.T.Wang *et al.*, *Phys.Rev.Lett* 117, 124801 (2016)

[6] J.Bahrdt, Pushing the limits of short period permanent magnet undulators, in *Proc. FEL Conf,* p.435, 2011

[7] M.Xie, LBNL-44381, CBP Note-323, 1999

[8] Z.Huang and K.Kim, *Phys.Rev.AB* 10, 034801 (2007)

[9] K. Halbach, NIM 169(1980), p.1-10

[10] P.Winkler *et al*,in *Proc. IPAC17*, p.4145, 2017

[11] B.W.Montague and F.Ruggiero, CLIC Report Note 37, 1987

[12] C.A.Lindstrom and E.Adli, *Phys.Rev.AB* 19, 071002 (2016)

[13] A. Loulergue *et al., New J.Phys.* 17, 023028 (2015)

[14] I.Hofmann, *Phys. Rev. STAB*, 16, 0413302 (2013)

[15] A.Molodozhentsev *et al,* in *Proc. IPAC16* Conf, p.4005, 2016

[16] A.Maier *et al., Phys.Rev. X* 2, 031019 (2012)

[17] K.R.Crandall and D.P.Rusthoi, TRACE3D Documentation, LA-UR-97-886, 1997

[18] D.Uriot, R.Duperrier and N.Pichoff, TraceWin, CEA Saclay, 2015

[19] T.Takana, *J. Synchrotron Rad.* 22 (2015)

ISBN: 978-3-95450-206-6 doi:10.18429/JACoW-FLS2018-TUP2WA03

HARMONIC LASING IN X-RAY FELS: THEORY AND EXPERIMENT

E. A. Schneidmiller*, B. Faatz, M. Kuhlmann, J. Rönsch-Schulenburg,
S. Schreiber, M. Tischer, M .V. Yurkov
Deutsches Elektronen-Synchrotron (DESY), Notkestrasse 85, D-22607 Hamburg, Germany

Abstract

Harmonic lasing is a perspective mode of operation of X-ray FEL user facilities that allows to provide brilliant beams of higher energy photons for user experiments. Another useful application of harmonic lasing is so called Harmonic Lasing Self-Seeded Free Electron Laser (HLSS FEL) that allows to improve spectral brightness of these facilities. In the past, harmonic lasing has been demonstrated in the FEL oscillators in infrared and visible wavelength ranges, but not in high-gain FELs and not at short wavelengths. In this paper we report on the first evidence of the harmonic lasing and the first operation of the HLSS FEL at the soft X-ray FEL user facility FLASH in the wavelength range between 4.5 nm and 15 nm.

INTRODUCTION

Successful operation of X-ray free electron lasers (FELs) [1–3], based on self-amplified spontaneous emission (SASE) principle [4], down to an Ångström regime opens up new horizons for photon science. Even shorter wavelengths are requested by the scientific community.

One of the most promising ways to extend the photon energy range of high-gain X-ray FELs is to use harmonic lasing which is the FEL instability at an odd harmonic of the planar undulator [5–9] developing independently from the lasing at the fundamental. Contrary to the nonlinear harmonic generation [1, 6, 7, 10–13] (which is driven by the fundamental in the vicinity of saturation), harmonic lasing can provide much more intense, stable, and narrow-band radiation if the fundamental is suppressed. The most attractive feature of saturated harmonic lasing is that the spectral brightness of a harmonic is comparable to that of the fundamental [9].

Another interesting option, proposed in [9], is the possibility to improve spectral brightness of an X-ray FEL by the combined lasing on a harmonic in the first part of the undulator (with an increased undulator parameter K) and on the fundamental in the second part of the undulator. Later this concept was named Harmonic Lasing Self-Seeded FEL (HLSS FEL) [14]. Even though this scheme is not expected to provide an ultimate monochromatization of the FEL radiation as do self-seeding schemes using optical elements [15–17], it has other advantages that we briefly discuss below in the paper.

Harmonic lasing was initially proposed for FEL oscillators [18] and was tested experimentally in infrared and visible wavelength ranges [19–22]. It was, however, never demonstrated in high-gain FELs and at a short wavelength. In this paper we present the first successful demonstration of this effect at the second branch of the soft X-ray FEL user facility FLASH [23] where we managed to run HLSS FEL in the wavelength range between 4.5 nm and 15 nm.

* evgeny.schneidmiller@desy.de

HARMONIC LASING

Harmonic lasing in single-pass high-gain FELs [5–9] is the amplification process of higher odd harmonics developing independently of each other (and of the fundamental harmonic) in the exponential gain regime. In the case of a SASE FEL the fluctuations of the beam current with frequency components in the vicinity of a wavelength

$$\lambda_h = \frac{\lambda_w(1+K^2)}{2h\gamma^2} \qquad h = 1,3,5... \tag{1}$$

serve as an input signal for amplification process. Here λ_w is the undulator period, γ is relativistic factor, h is harmonic number, and K is the rms undulator parameter:

$$K = 0.934\ \lambda_w[\mathrm{cm}]\ B_{\mathrm{rms}}[\mathrm{T}]\ ,$$

B_{rms} being the rms undulator field (peak field divided by $\sqrt{2}$ for a planar undulator with the sinusoidal field).

An advantage of harmonic lasing over lasing on the fundamental at the same wavelength can be demonstrated for the case of a gap-tunable undulator. In this case one uses a higher K-value for harmonic lasing, i.e. for the lasing on the fundamental one has to reduce K to the value K_{re}:

$$K_{re}^2 = \frac{1+K^2}{h} - 1\ . \tag{2}$$

Obviously, K must be larger than $\sqrt{h-1}$.

Then one can derive a ratio of the gain length of the fundamental, $L_g^{(1)}$, to the gain length of a harmonic $L_g^{(h)}$ [9]:

$$\frac{L_g^{(1)}}{L_g^{(h)}} = \frac{h^{1/2} K A_{JJh}(K)}{K_{re} A_{JJ1}(K_{re})}\ . \tag{3}$$

Here $A_{JJh}(K) = J_{(h-1)/2}\left(\frac{hK^2}{2(1+K^2)}\right) - J_{(h+1)/2}\left(\frac{hK^2}{2(1+K^2)}\right)$ is the coupling factor for harmonics with J_n being Bessel functions.

The formula (3) is obtained in the frame of the three-dimensional theory including diffraction of the radiation, emittance, betatron motion (and for an optimized beta-function) but assuming a negligible energy spread. The plot of the ratio of gain lengths (3) is presented in Fig. 1. It is clearly seen that harmonic lasing has always a shorter gain length under above mentioned conditions (and the ratio is larger than that obtained in one-dimensional model [8]). The ratio shown in Fig. 2 starts to diverge rapidly for the

ISBN: 978-3-95450-206-6 doi:10.18429/JACoW-FLS2018-TUP2WA03

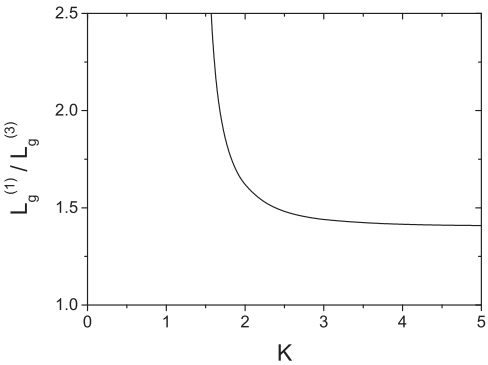

Figure 1: Ratio of the gain length of the retuned fundamental to the gain length of the third harmonic (3) for lasing at the same wavelength versus rms undulator parameter K. The ratio is derived in the frame of the three-dimensional theory for an optimized beta-function and negligible energy spread [9].

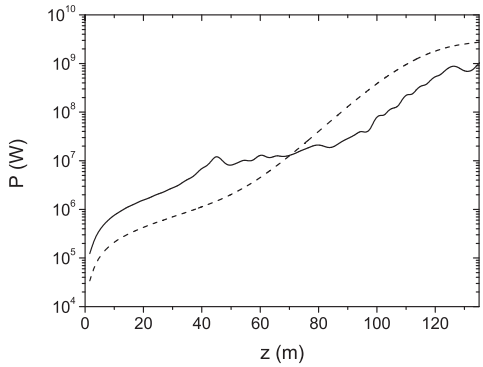

Figure 2: An example for the European XFEL. Averaged peak power for the fundamental harmonic (solid) and the third harmonic (dash) versus magnetic length of SASE1 undulator. The wavelength of the third harmonic is 0.2 Å (photon energy 62 keV). The fundamental is disrupted with the help of phase shifters [11].

values of K approaching $\sqrt{2}$, and lasing at the fundamental becomes impossible below this point. However, there still remains a reserve in the value of parameter K allowing effective lasing at the third harmonic.

Amplification process of harmonics degrades with the increase of the energy spread in the electron beam more rapidly than that of the fundamental. However, in practical situations there is always the range of parameters for which the harmonic lasing still has an advantage [9].

The most attractive feature of the saturated harmonic lasing is that the spectral brightness (or brilliance) of harmonics is comparable to that of the fundamental [9]. Indeed, a good estimate for the saturation efficiency is $\lambda_w/(hL_{sat,h})$, where $L_{sat,h}$ is the saturation length of a harmonic ($h = 1$ for the fundamental). At the same time, the relative rms bandwidth has the same scaling. In other words, reduction of power is compensated by the bandwidth reduction, and the spectral power remains the same. If we consider the lasing at the same wavelength on the fundamental and on a harmonic (with the retuned undulator parameter K), transverse coherence properties are about the same since they are mainly defined by the emittance-to-wavelength ratio. Thus, also the spectral brightness is about the same in both cases.

For a successful harmonic lasing to saturation, the fundamental must be suppressed. There have been different approaches proposed:

- phase shifters disrupting the fundamental but transparent for a harmonic [8, 11];
- spectral filtering when a filter is put into a chicane [11];
- switching between the 3rd and 5th harmonics [24, 25].

Although known theoretically for a long time [5–8], harmonic lasing in high-gain FELs was never demonstrated experimentally. Moreover, it was never considered for practical applications in X-ray FELs. The situation was changed after publication of ref. [9] where it was concluded that the harmonic lasing in X-ray FELs is much more robust than usually thought, and can be effectively used in the existing and future X-ray FELs. In particular, the European XFEL [26] can greatly outperform the specifications in terms of the highest possible photon energy: it can reach 60-100 keV range for the third harmonic lasing, see Fig. 2. It was also shown [24] that one can keep sub-Ångström range of operation of the European XFEL after CW upgrade of the accelerator with a reduction of electron energy from 17.5 GeV to 7 GeV. Another application of harmonic lasing is a possible upgrade of FLASH [27] with the aim to increase the photon energy up to 1 keV with the present energy 1.25 GeV of the accelerator. To achieve this goal, one should install a specially designed undulator optimized for the third harmonic lasing as suggested in Ref. [28].

HARMONIC LASING SELF-SEEDED FEL

A poor longitudinal coherence of SASE FELs [29–31] stimulated efforts for its improvement. Since an external seeding seems to be difficult to realize in X-ray regime, a so called self-seeding has been proposed [15–17]. There are alternative approaches for reducing bandwidth and increasing spectral brightness of X-ray FELs without using optical elements. One of them [33, 34] suggests to use chicanes inside the undulator system to increase slippage of the radiation and to establish long-range correlations in the radiation pulse. Another method was proposed in [9] and is based on the combined lasing on a harmonic in the first part of the undulator (with increased undulator parameter K, see formula (2)) and on the fundamental in the second part. In this way the second part of the undulator is seeded by a narrow-band signal generated via a harmonic lasing in the first part. This concept was named HLSS FEL (Harmonic Lasing Self-Seeded FEL) [14]. Note that a very similar concept was proposed in [35] and was called a purified SASE FEL, or pSASE.

Typically, gap-tunable undulators are planned to be used in X-ray FEL facilities. If maximal undulator parameter K is sufficiently large, the concept of harmonic lasing self-

ISBN: 978-3-95450-206-6 doi:10.18429/JACoW-FLS2018-TUP2WA03

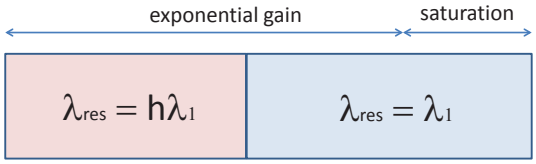

Figure 3: Conceptual scheme of a harmonic lasing self-seeded FEL.

seeded FEL can be applied in such undulators (see Fig. 3). An undulator is divided into two parts by setting two different undulator parameters such that the first part is tuned to a h-th sub-harmonic of the second part which is tuned to a wavelength of interest λ_1. Harmonic lasing occurs in the exponential gain regime in the first part of the undulator, also the fundamental in the first part stays well below saturation. In the second part of the undulator the fundamental is resonant to the wavelength, previously amplified as the harmonic. The amplification process proceeds in the fundamental up to saturation. In this case the bandwidth is defined by the harmonic lasing (i.e. it is reduced by a significant factor depending on harmonic number) but the saturation power is still as high as in the reference case of lasing at the fundamental in the whole undulator, i.e. the spectral brightness increases.

The enhancement factor of the coherence length (or, bandwidth reduction factor), that one obtains in HLSS FEL in comparison with a reference case of lasing in SASE FEL mode in the whole undulator, reads [14]:

$$R \simeq h \frac{\sqrt{L_{\rm w}^{(1)} L_{{\rm sat},h}}}{L_{{\rm sat},1}} \qquad (4)$$

Here h is harmonic number, $L_{{\rm sat},1}$ is the saturation length in the reference case of the fundamental lasing with the lower K-value, $L_{\rm w}^{(1)}$ is the length of the first part of the undulator, and $L_{{\rm sat},h}$ is the saturation length of harmonic lasing. We notice that it is beneficial to increase the length of the first part of the undulator. Since it must be shorter than the saturation length of the fundamental harmonic in the first section, one can consider delaying the saturation of the fundamental with the help of phase shifters [8, 9] in order to increase $L_{\rm w}^{(1)}$. However, for the sake of simplicity, we did not use this option in our experiments.

Despite the bandwidth reduction factor (4) is significantly smaller than that of self-seeding schemes using optical elements [15–17], the HLSS FEL scheme is very simple and robust, and it does not require any additional installations, i.e. it can always be used in existing or planned gap-tunable undulators with a sufficiently large K-value.

One more advantage of the HLSS FEL scheme over the SASE FEL (and in many cases over a self-seeded FEL) is the possibility of a more efficient use of a post-saturation taper [36–38] for an improved conversion of the electron beam power to the FEL radiation power [14,39]. Numerical simulations of the HLSS FEL were presented in [14] for the European XFEL [26] and in [39] for FLASH [27]. In this paper we report on the operation of the harmonic lasing self-seeded FEL.

OPERATION OF HLSS FEL AT FLASH

The first soft X-ray FEL user facility FLASH [1, 27] was upgraded to split the electron pulse trains between the two undulator lines so that the accelerator with maximum energy of 1.25 GeV now drives both lines. In a new separate tunnel, a second undulator line, called FLASH2, with a variable-gap undulator was installed, while a new experimental hall has space for up to six experimental stations [23]. The gap-tunable undulator of FLASH2 consists of twelve 2.5 m long sections with the undulator period of 3.14 cm and the maximum rms K-value about 1.9. This makes it possible (see formula (2)) to study the HLSS FEL scheme with the 3rd harmonic seeding.

First Lasing at 7 nm

On May 1, 2016 we were able to successfully perform the first test of HLSS FEL at FLASH2. Electron energy was 948 MeV, charge 0.4 nC. Initially we tuned 10 undulator sections to a standard SASE, operating in the exponential gain regime at the wavelength of 7 nm (rms K parameter was 0.73); the pulse energy was 12 μJ. Then we detuned the first section, tuned it to the third subharmonic (rms K was 1.9) and scanned it around 21 nm. We repeated the measurements with the first two sections, and then with the first three sections. Note that the fundamental at 21 nm was also in the exponential gain regime, pulse energy after three undulator sections was 40 nJ, i.e. it was far away from saturation (which was achieved at the 200 μJ level). This means, in particular, that the nonlinear harmonic generation in the first part of the undulator is excluded.

One can see from Fig. 4 that the effect is essentially resonant. For example, in the case when three undulator sections were scanned, the ratio of pulse energies at the optimal tune, 21.1 nm, and at the tune of 20 nm is 51 μJ/0.3 μJ = 170. We claim that there can be only one explanation of the effect that we observe in Fig. 4: FEL gain at 7 nm is strongly reduced as soon as the first part of the undulator is detuned, and then the gain is recovered (and becomes even larger) due to the 3rd harmonic lasing in the first part as soon as the resonant wavelength is 21 nm.

We should stress that the pulse energy with three retuned undulator sections (51 μJ) is significantly larger than that in the homogeneous undulator tuned to 7 nm (it was 12 μJ). This is because the gain length of harmonic lasing is shorter than that of the fundamental tuned to the same wavelength (see formula (3), Fig. 2 and refs. [8, 9, 14]). A rough estimate gives us the ratio of gain lengths about 1.4 which is somewhat smaller thah the ratio in Fig. 1. The difference can be explained by a contribution of the energy spread (not included in Fig. 1) and by the fact that the undulator beta-function was larger than an optimum value.

ISBN: 978-3-95450-206-6 doi:10.18429/JACoW-FLS2018-TUP2WA03

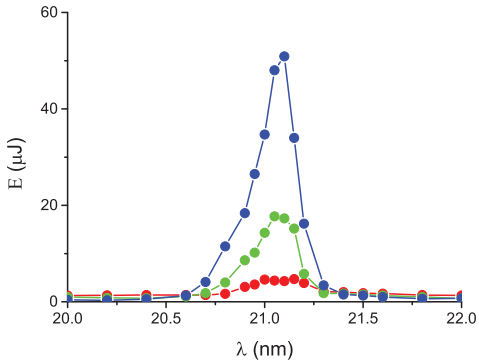

Figure 4: Scan of the resonance wavelength of the first part of the undulator consisting of one undulator section (red), two sections (green), and three sections (blue). Pulse energy is measured after the second part of the undulator tuned to 7 nm.

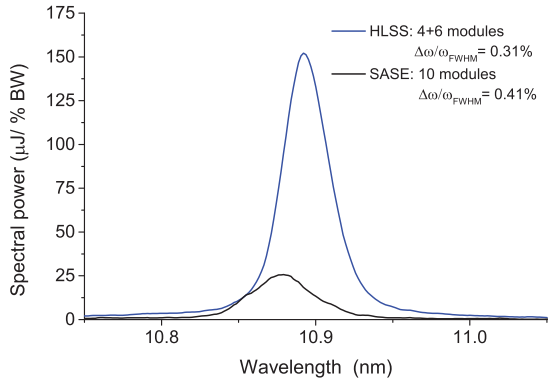

Figure 5: Spectral density of the radiation energy for HLSS FEL configuration (blue) and for SASE FEL (black).

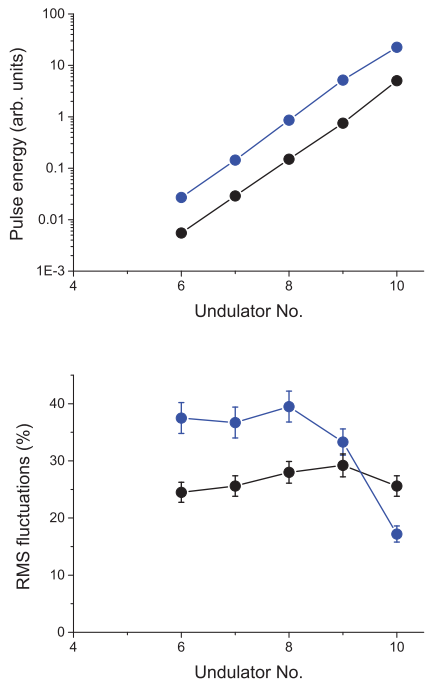

Figure 6: Radiation pulse energy (left plot) and pulse energy fluctuations (right plot) in the second part of the undulator for HLSS (blue) and for SASE (black). Small aperture in front of the MCP detector is used in this measurement.

Improvement of the Longitudinal Coherence at 11 nm

We continued the studies of the HLSS FEL at FLASH2 in June 2016. Since the electron energy was different (757 MeV), we lased at another wavelength, 11 nm. We also used a different charge, 0.25 nC, in this experiment. The undulator settings were similar to the previous case: we used ten undulator modules, rms K-parameter was 0.73 in SASE mode and 1.9 in the first part of the undulator in HLSS mode. The difference with the previous measurements was that we detuned four undulator modules in HLSS regime.

In the same way as in the previous experiment, we performed the scan of the K parameter in the first part of the undulator and saw a resonance behavior again. In combination with the fact that the fundamental at 33 nm was by three orders of magnitude below saturation this proves that we had harmonic lasing in the first part of the undulator. The pulse energies were 11 μJ (53 μJ) in SASE (HLSS) mode.

In Fig. 5 we present the averaged spectra for two study cases: SASE FEL with ten undulator modules and HLSS FEL with four modules tuned to 33 nm and six modules tuned to 11 nm. Let us note that a per cent level discrepancy between the measured wavelength (about 10.9 nm) and the wavelength expected by the undulator server (11 nm) comes from the fact that the server uses electron energy calculated from the RF vector sum and not from a direct measurement of the electron beam energy. However, the red shift of the radiation for the HLSS configuration with respect to the SASE case is real and can be explained by the fact that a seeded FEL radiates more efficiently in the case of a small red shift [31].

The spectra in Fig. 5 are the results of averaging over 50 single-shot spectra in each case. One can see that HLSS FEL indeed has a smaller bandwidth, 0.31%, as compared to 0.41% in the case of SASE FEL. The bandwidth reduction factor is 1.3 from this measurement. The spectral power, however, differs by a factor of six due to an additional increase of pulse energy in HLSS regime. This happens because 3rd harmonic lasing at 11 nm has a shorter gain length than lasing at the same wavelength on the fundamental.

An expected bandwidth reduction factor (or coherence enhancement factor) R from formula (4) can be estimated at 1.7. The discrepancy can in a general case be explained by the energy jitter and/or energy chirp in the electron beam. The energy jitter effect is supposed to give a small contribution to the spectrum broadening since the FLASH accelerator was quite stable during the measurement, the energy stability can be estimated at the level of a few 10^{-4}. A contribution of the energy chirp, however, being converted to a frequency chirp within an FEL pulse, can be significant.

ISBN: 978-3-95450-206-6 doi:10.18429/JACoW-FLS2018-TUP2WA03

Another method of determination of an improvement of the longitudinal coherence (independent of the presence of the frequency chirp in FEL pulses) is based on statistical measurements of the FEL pulse energy along the undulator length. It is well known [30, 31] that in high-gain linear regime the radiation from a SASE FEL has a statistics of a completely chaotic polarized light [32]. Shot-to-shot rms fluctuations of the FEL pulse energy σ are connected with the number of modes by a simple relation: $M = 1/\sigma^2$. Number of modes can be represented as a product of the numbers of longitudinal, M_L, and transverse, M_T, modes. The latter is usually close to one, $M_T \simeq 1.1 - 1.2$ when a SASE FEL is well designed and optimized [40, 41]. If one uses a small aperture to select only the central part of the FEL beam, the pulse energy fluctuations are a measure of the number of the longitudinal modes [42] : $M_L = 1/\sigma^2$. For a given FEL pulse length, the coherence length L_{coh} is inversely proportional to the number of the longitudinal modes, M_L. Making a reasonable assumption that the FEL pulse length is the same in both cases, HLSS and SASE, we end up with a simple ratio of coherence lengths for these two cases:

$$R = \frac{L_{coh}^{HLSS}}{L_{coh}^{SASE}} \simeq \frac{M_L^{SASE}}{M_L^{HLSS}} = \frac{\sigma_{HLSS}^2}{\sigma_{SASE}^2} \qquad (5)$$

In Fig. 6 we present the measurements of the FEL pulse energy and its fluctuations versus undulator length for a small aperture (significantly smaller than the FEL beam size) in front of the MCP detector. In both cases, HLSS and SASE, the maximum of pulse energy fluctuations is achieved within the part of the undulator where the measurements were performed. However, in HLSS case the fluctuations drop down more significantly because the FEL enters nonlinear stage of amplification in this case. As one can see, in the linear regime of the FEL operation (sections 6 to 8) the fluctuations for HLSS case are visibly larger than in the SASE case. The validity of an assumption that pulse length in both cases is the same is justified by the fact that both FEL configurations were driven by the same electron beam under the same conditions. We did the measurements twice for each configuration to make sure that the results are not affected by any drifts in the accelerator. Thus, we can conclude that in the HLSS case we had a smaller number of modes, or a larger coherence length. Using formula (5) with the fluctuations measured behind the 8th undulator section for HLSS and the 9th section for SASE (at these positions with the largest fluctuations we have a similar gain in both modes), we obtain an estimate for the coherence enhancement factor in the end of the exponential gain regime: $R \simeq 1.8 \pm 0.3$. This is in a good agreement with already presented theoretical estimate $R \simeq 1.7$ obtained from (4).

A More Efficient Post-Saturation Taper at 15 nm

In November 2016 we set up HLSS FEL as a configuration with four first undulators tuned to 45 nm and the last eight undulators tuned to 15 nm. The electron energy was 645 MeV, the charge was 100 pC, the rms value of K was 1.9 in the first part of the undulator and 0.73 in the second part. We reached FEL saturation in SASE and HLSS modes, and applied post-saturation taper to improve FEL efficiency [36–38].

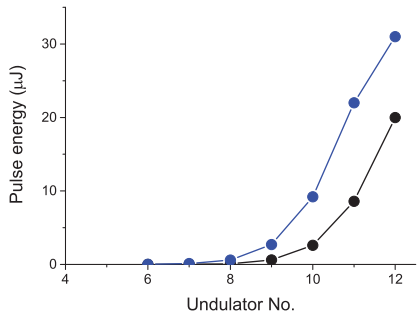

Figure 7: Radiation pulse energy versus position in the undulator for HLSS (blue) and for SASE (black). Post-saturation taper was optimized for both cases.

Post-saturation taper in FLASH2 undulator is implemented as a step-taper (i.e. the undulator K changes from section to section but is constant within a section) with linear or quadratic law. We used quadratic taper and for each mode (HLSS and SASE) optimized two parameters: beginning of tapering and the taper depth. We ended up with the following optimized parameters: beginning of tapering was in the 9th (10th) undulator and the taper depth was 0.9% (0.7%) for HLSS (SASE). Pulse energy was enhanced for HLSS configuration from 18 μJ in non-tapered undulator to 31 μJ when post-saturation taper was applied. In case of SASE FEL the respective enhancement was from 15 μJ to 20 μJ. The pulse energy versus undulator length for both operation modes is presented in Fig. 7. As it was discussed above, the improvement of post-saturation taper regime is achieved in HLSS case for two reasons: an earlier saturation and a better longitudinal coherence than in SASE case.

Lasing at 4.5 nm

In September 2016 we were able to drive HLSS FEL by the electron beam with a higher energy, 1080 MeV, and thus obtain lasing at 4.5 nm in HLSS configuration. Initially, we tuned SASE regime with 12 active undulator sections (rms K value was 0.53), and could establish an onset of saturation with pulse energy at the level of 20 μJ. Then we tuned first three sections to 13.5 nm (increasing rms K value to 1.69), thus providing the third harmonic signal at 4.5 nm for seeding the last nine undulators. The resonant behavior of the output signal together with the fact that the fundamental at 13.5 nm was more than three orders of magnitude below saturation proves that we had the third harmonic lasing at 4.5 nm in the first part of the undulator.

ISBN: 978-3-95450-206-6 doi:10.18429/JACoW-FLS2018-TUP2WA03

REFERENCES

[1] W. Ackermann *et al*., *Nature Photonics* **1**(2007)336.

[2] P. Emma *et al., Nature Photonics* **4** (2010) 641.

[3] T. Ishikawa *et al., Nature Photonics* 6 (2012) 540.

[4] A.M. Kondratenko and E.L. Saldin, *Part. Accelerators* **10** (1980)207.

[5] J.B. Murphy, C. Pellegrini and R. Bonifacio, *Opt. Commun.* **53** (1985)197.

[6] R. Bonifacio, L. De Salvo, and P. Pierini, *Nucl. Instr. Meth.* A293(1990)627.

[7] Z. Huang and K. Kim, *Phys. Rev. E*, 62(2000)7295.

[8] B.W.J. McNeil et al., *Phy. Rev. Lett.* 96, 084801 (2006).

[9] E.A. Schneidmiller and M.V. Yurkov, *Phys. Rev. ST-AB* **15**(2012)080702.

[10] H. Freund, S. Biedron and S. Milton, *Nucl. Instr. Meth. A* 445(2000)53.

[11] E.L. Saldin, E.A. Schneidmiller and M.V. Yurkov, *Phys. Rev. ST-AB* 9(2006)030702.

[12] A. Tremaine *et al., Phy. Rev. Lett.* 88, 204801 (2002).

[13] D. Ratner *et al., Phys. Rev. ST-AB* 14(2011)060701.

[14] E.A. Schneidmiller and M.V. Yurkov, "Harmonic Lasing Self-Seeded FEL", in *Proc. FEL2013*, New York, p.700.

[15] J. Feldhaus et al., Optics. Comm. 140, 341 (1997).

[16] E.L. Saldin, Y.V. Shvyd'ko, E.A. Schneidmiller and M.V. Yurkov, *Nucl. Instrum. and Methods* **A 475**(2001)357.

[17] G. Geloni, V. Kocharyan and E.L. Saldin, *Journal of Modern Optics* **58**(2011)1391.

[18] W.B. Colson, *IEEE J. Quantum Electron.* 17(1981)1417.

[19] S.V. Benson and J.M.J. Madey, *Phys. Rev. A* 39(1989)1579.

[20] R.W. Warren et al., *Nucl. Instr. Meth. A* 296(1990)84.

[21] R. Hajima et al., *Nucl. Instr. Meth. A* 475(2001)43.

[22] N. Sei, H. Ogawa and K. Yamada, *Journal of the Physical Society of Japan* 79(2010)093501.

[23] B. Faatz *et al., New Journal of Physics,* 18(2016)062002.

[24] R. Brinkmann, E.A. Schneidmiller, J. Sekutowicz and M.V. Yurkov, *Nucl. Instrum. and Methods* **A 768**(2014)20.

[25] G. Penn, *Phys. Rev. ST Accel. Beams* 18, 060703 (2015).

[26] M. Altarelli *et al*. (Eds.), XFEL: The European X-Ray Free-Electron Laser. Technical Design Report, Preprint DESY 2006-097, DESY, Hamburg, 2006 (see also http://xfel.desy.de).

[27] S. Schreiber and B. Faatz, "The free-electron laser FLASH", *High Power Laser Science and Engineering*, 3, e20 doi:10.1017/hpl.2015.16.

[28] E.A. Schneidmiller and M.V. Yurkov, *Nucl. Instrum. and Methods* **A 717**(2013)37.

[29] R. Bonifacio, C. Pellegrini and L.M. Narducci, *Opt. Commun.* **50**(1984)373.

[30] E.L. Saldin, E.A. Schneidmiller and M.V. Yurkov, *Opt. Commun.* **148**(1998)383.

[31] E.L. Saldin, E.A. Schneidmiller and M.V. Yurkov, "The Physics of Free Electron Lasers", *Springer*, Berlin, 1999.

[32] J. Goodman, Statistical Optics, (John Wiley and Sons, New York, 1985).

[33] J. Wu, J., A. Marinelli and C. Pellegrini, in *Proc. 32th International Free Electron Laser Conference*, Nara, Japan, 2012, p. 23, http://www.jacow.org

[34] B.W.J. McNeil, N.R. Thompson and D.J. Dunning, *Phys. Rev. Lett.* 110(2013)134802.

[35] D. Xiang *et al., Phys. Rev. ST-AB* **16**(2013)010703.

[36] N.M. Kroll, P.L. Morton, and M.N. Rosenbluth, *IEEE J. Quantum Electron.* 17, 1436 (1981).

[37] W.M. Fawley, Nucl. Instrum. *Methods Phys. Res., Sect. A* 375, 550 (1996).

[38] E.A. Schneidmiller and M.V. Yurkov, *Phys. Rev. ST-AB* **18**(2015)030705.

[39] E.A. Schneidmiller and M.V. Yurkov, in *Proc. IPAC16,* Busan, Korea, p. 725.

[40] E.L. Saldin, E.A. Schneidmiller, and M.V. Yurkov, *Opt. Commun.* 281(2008)1179.

[41] E.L. Saldin, E.A. Schneidmiller, and M.V. Yurkov, *New J. Phys.* 12 (2010) 035010.

[42] E.A. Schneidmiller and M.V. Yurkov, in *Proc. IPAC16,* Busan, Korea, p. 738.

ISBN: 978-3-95450-206-6 doi:10.18429/JACoW-FLS2018-WEA1PL02

DIELECTRIC AND OTHER NON-PLASMA ACCELERATOR BASED COMPACT LIGHT SOURCES*

R. J. England†, Z. Huang
SLAC National Accelerator Laboratory, Menlo Park, CA 94025, USA

Abstract

We review recent experimental progress in developing nanofabricated dielectric laser-driven accelerators and discuss the possibility of utilizing the unique sub-femtosecond electron pulse format these accelerators would provide to create ultra-compact EUV and X-ray radiation sources.

INTRODUCTION

Particle acceleration in dielectric structures driven by ultrafast infrared lasers, a technique we refer to as "dielectric laser acceleration" (DLA), is a new and rapidly progressing area of advanced accelerator research that sets the stage for future generations of high-gradient accelerators of reduced cost and unprecedented compactness. In recent years, there have been several critical experiments: the first demonstration of high-field (300 MV/m) speed-of-light electron acceleration in a fused silica structure [1], acceleration at sub-relativistic energies with an open grating [2], demonstration of a compatible optical-scale beam position monitor [3], high-gradient sub-relativistic acceleration at 220 MV/m [4] and at 370 MV/m [5] in silicon microstructures, and high-gradient (700 MV/m) acceleration of relativistic electrons using femtosecond laser pulses [6]. This approach has been colloquially referred to in the press as an "accelerator on a chip." The high-gradient and wafer size of these accelerators make them very attractive for a future generation of high brilliance extreme ultraviolet (EUV) and X-ray sources. The DLA approach has the distinct features to produce attosecond electron bunches and can operate at 10s of MHz repetition rate. However, there are many accelerator science questions and technical challenges to address since the beam parameters for an accelerator based on this concept would be drastically different from both conventional accelerators and other advanced schemes.

The most powerful XUV and x-ray sources today are enabled by relativistic electron beams driven by state-of-the-art microwave linear accelerator facilities such as the Linac Coherent Light Source (LCLS) at SLAC. Recent research into novel dielectric laser accelerators (DLA) has given rise to the potential for new coherent radiative processes with attosecond pulses using dielectric structures with wavelength-scale periodic features excited by lasers at near-infrared wavelengths [1, 7], and with orders of magnitude higher accelerating fields than is possible with conventional microwave technology [6]. This approach has the potential to produce extremely bright electron beams in an ultra-compact footprint that are suitable for driving superradiant EUV light in a similarly optical-scale laser-induced undulator field. Radiation from each undulator/compressor module would add in amplitude but not in pulse length, maintaining the wide bandwidth and attosecond pulse structure. Preliminary calculations presented below suggest that a compact DLA driven by a 2 μm infrared laser may generate a 10-fC, 200-as electron bunch train at 40 MeV particle energy. After passing 100 undulator/compressor modules, EUV radiation could be generated in a train of 660 as pulses separated by 6.6 fs laser period, with a pulse energy of more than 100 nJ. This attosecond pulse train would form an intense EUV frequency comb that would be extremely valuable for precision spectroscopy.

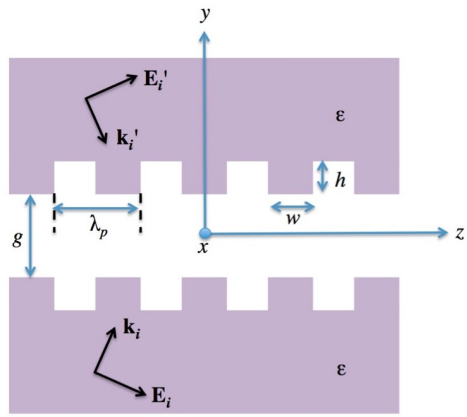

Figure 1: Planar symmetric geometry with periodic variation in z. Two exciting plane waves are shown incident from top and bottom.

LASER-DRIVEN DEFLECTION IN PLANAR STRUCTURE

All DLA structures experimentally tested to date have been of the planar symmetric variety (spatially invariant in one coordinate) and with a longitudinal periodicity along the particle beam axis. We here derive a generic form for the transverse forces in such a geometry which provide some helpful insights regarding development of a compatible laser-driven undulator. The wave equation for a linear material with spatially varying dielectric function $\epsilon(\mathbf{r})$ may be written

$$\nabla^2\mathbf{E} - \nabla(\nabla\cdot\mathbf{E}) = -(\omega/c)^2\mathbf{D} \qquad (1)$$

where $\mathbf{D}$ is the electric displacement field, related to the electric field $\mathbf{E}$ and polarization $\mathbf{P}$ by $\mathbf{D} = \mathbf{E} + 4\pi\mathbf{P}$. We assume a dielectric, non-magnetic material ($\mu = 1$), hence $\mathbf{H} = \mathbf{B}$. Solutions to Eq. 1 for given dielectric function

* Work supported by U.S. Dept. of Energy, National Science Foundation, and Moore Foundation.
† england@slac.stanford.edu

ISBN: 978-3-95450-206-6 doi:10.18429/JACoW-FLS2018-WEA1PL02

$\epsilon(\mathbf{r})$ immediately yield the magnetic field via Faraday's law, $\nabla \times \mathbf{E} = i(\omega/c)\mathbf{B}$. By the Floquet theorem, the solutions to Maxwell's equations subject to periodic boundary conditions along z with periodicity $\mathbf{u} = \lambda_p \hat{\mathbf{z}}$ satisfy $\mathbf{E}(\mathbf{r}+\mathbf{u}) = \mathbf{E}(\mathbf{r})e^{i\psi}$, where ψ is the cell-to-cell phase shift. If the fields are excited by an incident plane wave with wavenumber $\mathbf{k}_i = (\omega/c)\sqrt{\epsilon_i}\,\hat{\mathbf{n}}$, then ψ is given by the projection of the incident plane wave onto the fundamental periodicity. If we define θ to be the usual polar angle between $\hat{\mathbf{n}}$ and $\hat{\mathbf{z}}$ then this gives rise to the projection of the incident wave in the first Brillouin zone: $k_0 \equiv |\mathbf{k}_i \cdot \mathbf{u}| = (\omega/c)\sqrt{\epsilon_i}\cos\theta$, and a corresponding set of Floquet space harmonics with wave numbers $k_n = k_0 + nk_p$ where $k_p \equiv 2\pi/\lambda_p$. The phase velocity of the n'th space harmonic, normalized to speed of light c is thus $\beta_n = \omega/(ck_n)$.

For the considered case, illustrated in Fig. 1 by the example of parallel gratings with rectangular teeth, with a planar-symmetric system invariant in x, and a vacuum region occupying the space $|y| < g/2$, two orthogonal polarizations may be defined relative to the plane of y and z wherein there is variation of the fields. We call these S and P polarization, which respectively give rise to transverse electric (TE) and transverse magnetic (TM) modes, relative to excited surface waves propagating in z within the vacuum gap. For a single laser excitation ($\mathbf{E}_i$ in Fig. 1), the solution to Eq. 1 in the vacuum region yields the following non-vanishing components for S- polarization (TE):

$$\begin{aligned} E_x &= E_0 \sum_n [a_n e^{\Gamma_n y} + b_n e^{-\Gamma_n y}] e^{ik_n z} \\ B_y &= \frac{c}{\omega} E_0 \sum_n k_n [a_n e^{\Gamma_n y} + b_n e^{-\Gamma_n y}] e^{ik_n z} \\ B_z &= i\frac{c}{\omega} E_0 \sum_n \Gamma_n [a_n e^{\Gamma_n y} - b_n e^{-\Gamma_n y}] e^{ik_n z} \end{aligned} \tag{2}$$

and for P-polarization (TM):

$$\begin{aligned} E_y &= -iE_0 \sum_n \frac{k_n}{\Gamma_n} [a_n e^{\Gamma_n y} - b_n e^{-\Gamma_n y}] e^{ik_n z} \\ E_z &= \frac{c}{\omega} E_0 \sum_n k_n [a_n e^{\Gamma_n y} + b_n e^{-\Gamma_n y}] e^{ik_n z} \\ B_x &= iE_0 \sum_n \frac{\omega}{c} \frac{1}{\Gamma_n} [a_n e^{\Gamma_n y} - b_n e^{-\Gamma_n y}] e^{ik_n z} \end{aligned} \tag{3}$$

where $\Gamma_n \equiv \sqrt{k_n^2 - (\omega/c)^2}$ is the transverse decay constant of the n'th space harmonic. The complex coefficients a_n, b_n are determined by boundary condition matching at the dielectric interface and therefore depend upon the specific geometry of the periodic structure. Explicit forms have been derived for a square-tooth grating as depicted in Fig. 1 by, e.g. [8,9]. By virtue of the assumed symmetry, if an otherwise identical plane wave $\mathbf{E}_i'$ propagates from the opposite direction with the same incidence angle, then the resultant mode is of the same form as Eqs. 2 - 3 but with the substitution $a_n \leftrightarrow b_n$. The superposition of the fields excited by both plane waves has the form of Eqs. 2 - 3 but with the replacements

$$[a_n e^{\Gamma_n y} \pm b_n e^{-\Gamma_n y}] \rightarrow 2(a_n + b_n) \begin{cases} \cosh(\Gamma_n y) \\ \sinh(\Gamma_n y) \end{cases} \tag{4}$$

If the two plane-waves are out of phase by π then the roles of cosh and sinh in Eq. 4 are exchanged and $(a_n + b_n) \rightarrow (a_n - b_n)$. The desired acceleration mode is the in-phase TM mode with $n = 1$, wherein $E_z \propto \cosh(\Gamma y)e^{ik_p z}$. The hyperbolic cosine dependence can be seen to approach a transversely uniform field in the limit where $g \ll \Gamma_n^{-1}$ or the case $\Gamma_n \rightarrow 0$ which implies that $k_n = \omega/c$ and hence that the phase velocity of the mode is equal to c. To instead obtain a uniform deflecting force, we consider modes where the transverse force $\mathbf{F}_\perp$ has a cosh-like dependence on y. From the above considerations we see that two solutions satisfy this condition: the double-sided excitation of TM mode with π out-of-phase plane waves and the TE mode with in-phase plane waves. These yield

$$\mathbf{F}_\perp = qE_0 \begin{Bmatrix} (1 - \beta/\beta_n) \\ -i\frac{k_n}{\Gamma_n}(1 - \beta_n\beta) \end{Bmatrix} \begin{Bmatrix} \hat{\mathbf{x}} \\ \hat{\mathbf{y}} \end{Bmatrix} e^{i(k_n z - \omega t)} \tag{5}$$

where the top line corresponds to the TE mode and the bottom line is the TM mode. In both cases $F_z = 0$. We have here taken a single mode n from the summation which is assumed to have a phase velocity β_n that is matched to the electron beam, and have assumed the limit $\Gamma_n g \ll 1$ or $\cosh(\Gamma_n y) \approx 1$. Further the constant $a_n \pm b_n$ has been absorbed into the field amplitude E_0. We see from these expressions that the TE mode vanishes for a synchronous particle ($\beta = \beta_n$) while the TM mode instead scales as $1/\gamma_n^2$. Plettner solves this speed-of-light synchronicity problem by rotating the particle axis by an angle α. In the rotated frame of the beam, the resonant velocity of the mode is in the direction of $\mathbf{k}_n$ which is no longer co-linear with z but now has the form $\mathbf{k}_n = k_n(\cos\alpha\,\hat{\mathbf{z}} - \sin\alpha\,\hat{\mathbf{x}})$. Phase synchronicity is therefore accomplished if $\mathbf{k}_n \cdot \hat{\mathbf{z}} = \omega/\beta c$. For normal laser incidence ($\theta = \pi/2$) this leads to the synchronicity condition $\lambda_p = \beta n \lambda \cos\alpha$. Hence, as compared with the unrotated case, the period λ_p of the grating must be decreased by a factor $\cos\alpha$ to remain synchronous with a speed of light particle. This is geometrically obvious since in the rotated frame the apparent spacing between grating teeth is increased along z. Laser-driven dielectric undulators based upon this and similar concepts have been proposed and could attain very short (mm to sub-mm) periods with multi-Tesla field strengths and fabricated using similar photolithographic methods [10–12].

ATTOSECOND RADIATION GENERATION

Combining the high gradient and high brightness of advanced accelerators with novel undulator designs would enable laboratory-scale demonstrations of key concepts needed for future EUV and X-ray lasers that can transform the landscape of ultrasmall and ultrafast sciences. Attosecond electron current modulation would be automatically created by

ISBN: 978-3-95450-206-6 doi:10.18429/JACoW-FLS2018-WEA1PL02

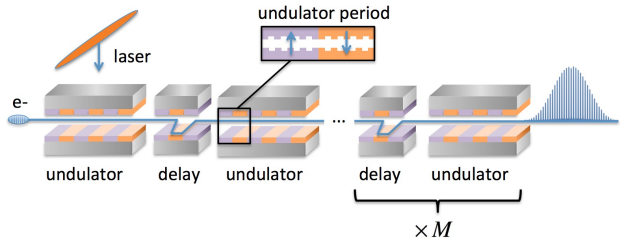

Figure 2: Chain of M laser-driven undulator and delay modules to mode-lock DLA attosecond pulse train.

the DLA structure and phase-locked to the drive laser. The radiative process could then be modelocked via a chain of such laser-driven undulators and compressors as suggested in [13]. This mode-locked radiation would possess the attosecond pulse structure with a well-defined phase within the train. The undulator and delay chain can be made of dielectric structures as well (see, e.g., Ref. [10, 14]), as illustrated in Fig. 2.

In an operating DLA, the optimal bunch charge would be of order a few fC, so we will ingore the FEL gain in the undulator/delay chain. Following Ref. [13] Sec. 3 we rewrite the equations without ρ scaling, yielding the radiation field

$$A(\bar{\nu}) = b_0(\bar{\nu}) N_u \mathrm{sinc}\,(\pi\bar{\nu}N_u)\,\frac{1-e^{-iM\bar{\nu}\bar{s}}}{1-e^{-i\bar{\nu}\bar{s}}}\,e^{-i\bar{\nu}(\bar{s}-\pi N_u)} \quad (6)$$

The corresponding power spectrum is then $P(\bar{\nu}) \propto |A(\bar{\nu})|^2$. Here $\bar{\nu} = (\omega-\omega_0)/\omega_0$ is the undulator fundamental radiation frequency, N_u is the number of undulator periods per section, M is the number of sections of undulator/delay modules, and $\bar{s} = k_0 R_{56}/2 + 2\pi N_u$ is the total slippage per module in units of $\lambda_0/(2\pi)$. The quantity $b_0(\nu)$ is the initial bunching spectrum and is assumed to be constant in the undulator in absence of FEL interaction.

The sinc function shows the typical undulator radiation behavior, with the FWHM spectral width given by $1/N_u$. The last factor in Eq. (6) introduces spectral modes. In Fig. 3, we show an example when $N_u = 5$, $\bar{s} = 2\pi \times 100$, and $M = 10$. About 20 modes are contained in the full spectral bandwidth, and the intensity of the central mode is enhance by $M^2 = 100$.

As discussed in Ref. [13], the mode will not be locked if the electron bunch is randomly distributed, and can be locked if the bunch is energy or density modulated with a modulation wavelength that matches $\bar{s}/k_0$. In a DLA, the attosecond bunch train is generated by some sort of an optical buncher so the mode locking happens naturally. The mode-locking means the XUV radiation will posess the attosecond pulse train with a well-defined phase within the train. The peak power of the core part of the train (not head or tail which may be subject to transient effects) can be calculated as follows.

We will work in the 1D limit (assuming a large transverse beam size and can consider 3D later), the transverse electric field is (see Eq. (3) of Ref. [15])

$$E_x(z,t) = \eta \sum_{j=1}^{N} \frac{e^{ik_r[z-c(t-t_j)]}}{1-\beta_\parallel} H(z, t-t_j) + \text{c. c.}, \quad (7)$$

where $\eta \equiv ecZ_0K_{JJ}/8\pi\sigma_x^2\gamma$, K_{JJ} is the undulator parameter with the usual Bessel function correction, t_j is the electron arrival time at the undulator entrance $z = 0$, $Z_0 = 377\ \Omega$ is the vacuum impedance, $\beta_\parallel$ is the average longitudinal velocity in the undulator, $\lambda_r = (1-\beta_\parallel)\lambda_u$, and H is 1 when $\beta_\parallel c(t-t_j) < z < c(t-t_j)$ and 0 otherwise to take care of the slippage. Although this expression is derived in 1D, the electric field transverse distribution should follow that of the electron beam as

$$E_x(z,t,r) = \eta \sum_{j=1}^{N} \frac{e^{ik_r[z-c(t-t_j)]}}{1-\beta_\parallel} H(z, t-t_j) \times \exp(-\frac{r^2}{2\sigma_x^2}) + \text{c. c.} \quad (8)$$

In the DLA example we consider here, we assume the DLA bunches the electron to attosecond durations. This is supported by recent VORPAL simulations that show 10 as bunches formed in a 1-mm DLA structure. As far as XUV radiation (tens of nm wavelength) is concerned, the electron bunch radiates coherently right away in the undulator as a macro point charge. This can be seen from the above equation that the sum of phases yields N, the number of electrons in the attosecond bunch. We have

$$E_x(z,t,r) = \eta \frac{N}{1-\beta_\parallel} e^{ik_r(z-ct)} \exp(-\frac{r^2}{2\sigma_x^2}) + \text{c. c.} \quad (9)$$

Note that the electric field amplitude is independent of N_u (undulator period), only the length of the wavepacket is determined by $N_u\lambda_u$. This agrees with the intuitive picture. The radiated power per module is given by

$$P_0 = \frac{1}{2Z_0}\int |E_x(z,t,r)|^2 d\mathbf{r} = \frac{Z_0 K_{JJ}^2 Q^2 c^2 \gamma^2}{8\pi\sigma_x^2(1+K^2/2)^2}, \quad (10)$$

where $Q = Ne$ is the total charge in the bunch. After M modules, the radiated power becomes

$$P = M^2 P_0\,. \quad (11)$$

For example, consider a compact DLA driven by a 1 μm infrared laser. We assume the charge per bunch is 10 fC, and the fwhm bunch length is 20 as (6 nm) and is shorter than the radiation wavelength (10 nm). Suppose the electrons are accelerated to 50 MeV, and focused to $\sigma_x = 0.2$ μm and then passed through a Byer-Plettner type of dielectric undulator with $\lambda_u = 200$ μm, and $K = 0.15$ is the deflecting parameter. The undulator fundamental wavelength is $\lambda_0 =$ 10 nm. Since the electron bunch length is comparable to the radiation wavelength, coherent radiation will be emitted at λ_0 from the beginning. After $N_u = 5$ undulator period, the radiation wavepacket is 50 nm or 166 as. If we simply make the undulator longer, it will only elongate the wavepacket

ISBN: 978-3-95450-206-6 doi:10.18429/JACoW-FLS2018-WEA1PL02

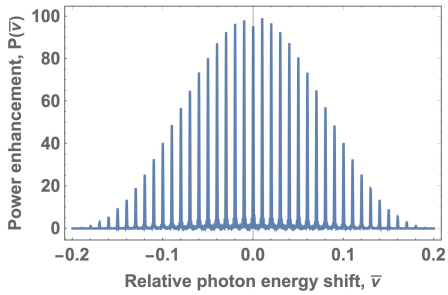

Figure 3: Mode-locked coherent undulator radiation spectrum (see text for details).

and eventually merge the attosecond pulse train. Mode-locking with undulator/chicane module will maintain the wide bandwidth nature and attosecond pulse train. Let us take undulator/chicane module $R_{56}/2 + N_u\lambda_0 = 1$ μm to match the drive laser wavelength and hence the periodicity of the bunch train, then the radiation from adjacent modules will add in amplitude but not in pulse duration. After $M = 10$ such modules, the radiation will maintain 166 as with the peak power given by Eqs. (10) and (11). In this example, $P = 80$ MW, and the single pulse energy is 13 nJ. If the optical laser pulse length is 1 ps, there can be approximately 300 such pulses in each optical pulse (with some transient effects in head/tail of the optical pulse).

Eventually the beam quality (energy spread) limits how many modules can be used in this scheme. Each chicane/undulator module will have $R_{56} \sim 2\,\mu$, so energy spread requirement is

$$\sigma_\delta M R_{56} < 6\text{nm} \quad \text{or} \quad \sigma_\delta < 3\times 10^{-4}\,. \tag{12}$$

There should be focusing after each module in order to keep the constant beam size in the undulators. Since the undulator radiation is transversely coherent, the emittance of the bunch should be

$$\epsilon_{x,y} \leq \frac{\lambda_0}{4\pi} \sim 1\text{nm}\,. \tag{13}$$

This corresponds to the normalized emittance $\gamma\epsilon_{x,y} = 0.1$ μm.

APPLICATIONS

The DLA approach can produce orders of magnitude higher accelerating fields than is possible with conventional microwave technology. The extreme accelerating environment has the potential to produce extremely bright electron beams that are suitable for driving superradiant EUV light in a similarly optical-scale laser-induced undulator field. Furthermore, because of the few-femtosecond optical cycle of near infrared (NIR) mode-locked lasers, laser-driven X-ray free electron lasers could allow attosecond x-ray laser pulses to probe matter on even shorter time-scales than possible today. Combining the high gradient and high brightness of advanced accelerators with novel undulator designs could enable laboratory-scale demonstrations of key concepts needed for future XUV and X-ray lasers that can transform the landscape of ultrasmall and ultrafast sciences. To realize these laboratory-scale, lower-cost, higher performance radiation sources, critical components of laser-driven free electron lasers need to be developed and demonstrated.

Coherent attosecond radiation could potentially be produced using the same operating principles that produce particle acceleration via the “accelerator on a chip" mechanism. These structures operate optimally with optical-scale pulse formats, making high repetition rate (10s of MHz) attosecond-scale pulses a natural combination. The beam is by necessity very close to the exposed micro-structures and there are fundamental questions regarding the impact of the beam impedance upon itself and the remnant fields back on the device itself. This regime has never been studied before and questions arise as to how well the beam will behave in such structures and how well it will ultimately perform. The theoretical and numerical tools to model these processes need to be developed in order to guide experimental studies of attosecond electron and photon generation.

The FEL process has been studied extensively over a broad range of parameters and is quite well understood; however, this is not true in this new regime of ultrashort, attosecond bunches generating X-rays at relatively low electron beam energies. This presents some interesting new opportunities. As the electron energy becomes lower, the impact of the X-ray photon’s momentum on the electron’s momentum becomes significant and quantum effects start to come into play in a way not before seen or measured in “classical" FELs [16]. This has consequences with respect to, among other things, the fundamental physics of coherence between particles, the causal relationships between these particles, and the momentum exchange difference that occurs between incoherent emission and coherent emission. The FEL operated in such a regime might help answer some of these fundamental questions.

CONCLUSION

A DLA-based light source could generate EUV radiation in the 50 eV photon energy range with even lower beam energies (about 40 MeV using a laser driven undulator with a period of 250 μm). However, at these relatively long wavelengths, radiation will slip outof the very short electron bunch after of order 10 undulator periods, and hence make the device inefficient for generation of high-power, attosecond (as) pulses. In a DLA, attosecond electron current modulation is automatically created by the structure and is phase-locked to the drive laser which can be further stabilized using optical techniques. One possible route to mode-lock the radiative process via a chain of laser-driven undulators and compressors is suggested in Ref. [13]. If successfully mode-locked, the EUV radiation would possess the attosecond pulse structure with a well-defined phase within the train. Radiation from each undulator/compressor module would add in amplitude but not in pulse length, maintaining the wide bandwidth nature and attosecond pulse train.

ISBN: 978-3-95450-206-6 doi:10.18429/JACoW-FLS2018-WEA1PL02

This attosecond pulse train would form an intense EUV frequency comb (see Fig. 3) that could be extremely valuable for precision spectroscopy.

ACKNOWLEDGMENT

This work is supported by the U.S. Department of Energy (DE-AC02-76SF00515), U.S. National Science Foundation (ECS-9731293), and the Moore Foundation (GBMF4744). We also thank R. L. Byer, K. P. Wootton, Y-C. Huang, and L. Schachter for helpful comments and discussions.

REFERENCES

[1] E. A. Peralta, K. Soong, et al. “Demonstration of electron acceleration in a laser-driven dielectric microstructure," *Nature* 503, 91-94 (2013).

[2] J. Breuer and P. Hommelhoff, "Laser-based acceleration of nonrelativistic electrons at a dielectric structure," *Phys. Rev. Lett.* 111, 134803 (2013).

[3] K. Soong, E. Peralta, et al. “Electron beam position monitor for a dielectric microaccelerator," *Optics Letters* 39 (16), 4747-4750 (2014).

[4] K. J. Leedle, R. F. Pease, R. L. Byer, and J. S. Harris, “Laser acceleration and deflection of 96.3 keV electrons with a silicon dielectric structure," *Optica* 2, 158-161 (2015).

[5] K. J. Leedle, A. Ceballos, et al. “Dielectric laser acceleration of sub-100 keV electrons with silicon dual-pillar grating structures," *Optics Letters* 40 (18), 4344 (2015).

[6] K. Wootton, et al. “Demonstration of acceleration of electrons at a dielectric microstructure using femtosecond laser pulses," *Optics Letters* 41 (12), 2672 (2016).

[7] R. J. England, et al. "Dielectric Laser Accelerators" *Rev. Mod. Phys.* 86, 1337 (2014).

[8] L. Pilozzi, A. D’Andrea, and R. Del Sole, "Electromagnetic properties of a dielectrid grating I. Propagating, evanescent, and guided waves," *Phys. Rev. B*, 54 (15), 10751 (1996).

[9] A. Hanuka, W. D. Kimura, I. Pogorelski, and L. Schachter, "Quasi-analytic design of a dielectric acceleration structure," *AIP Conference Proceedings* 1812, 060012 (2017).

[10] T. Plettner and R. L. Byer, "Proposed dielectric-based microstructure laser-driven undulator," *Phys. Rev. ST Accel. Beams* 11, 030704 (2008).

[11] F. Toufexis, T. Tang, and S. G. Tantawi, "A 200 μm-period laser-driven undulator," *Proceedings of FEL 2014, Basel, Switzerland* MOP047 (2014).

[12] K. P. Wootton, et al. "Design and optimisation of dielectric laser deflecting structures," *Proceedings of 2015 International Particle Accelerator Conference* (IPAC‘15), WEPJ012 (2015).

[13] E. Kur *et. al.*, "A wide bandwidth free-electron laser with mode locking using current modulation," *New Journal of Physics* 13, 063012 (2011).

[14] T. Plettner *et. al.*, "Photonic-based laser driven electron beam deflection and focusing structures," *Phys. Rev. ST Accel. Beams* 12, 101302 (2009).

[15] Z. Huang, K.-J. Kim, "Coherent spontaneous emission in high gain free-electron lasers," *Proceedings of 1999 Particle Accelerator Conference* (PAC 1999), 2495 (1999).

[16] R. Bonifacio, N. Piovella, G. R. M. Robb, and A. Schiavi, "Quantum regime of free electron lasers starting from noise," *Phys. Rev. ST - Accel. Beams* 9, 090701 (2006).

ISBN: 978-3-95450-206-6 doi:10.18429/JACoW-FLS2018-WEA1PL03

ATTOSECOND TIMING

F. X. Kärtner, M. Xin, and K. Safak
Center for Free-Electron Laser Science, Deutsches Elektronen-Synchrotron and
Physics Department and The Hamburg Center for Ultrafast Imaging, Universität Hamburg,
Hamburg, Germany

Abstract

Photon-science facilities such as X-ray free-electron lasers (XFELs) and intense-laser facilities are emerging worldwide with some of them producing sub-fs X-ray pulses. These facilities are in need of a high-precision timing distribution system, which can synchronize various microwave and optical sub-sources across multi-km distances with attosecond precision. Here, we report on a synchronous laser-microwave network that permits attosecond precision across km-scale distances. This was achieved by developing new ultrafast timing metrology devices and carefully balancing the fiber nonlinearities and fundamental noise contributions in the system. New polarization-noise-suppressed balanced optical crosscorrelators and free-space-coupled balanced optical-microwave phase detectors for improved noise performance have been implemented. Residual second- and third-order dispersion in the fiber links are carefully compensated with additional dispersion-compensating fiber to suppress link-induced Gordon-Haus jitter and to minimize output pulse duration; the link power is stabilized to minimize the nonlinearity-induced jitter as well as to maximize the signal to noise ratio for locking..

INTRODUCTION

Recently, several X-ray FELs (XFELs), such as the European XFEL [1] in Hamburg, FERMI [2] in Italy, SwissFEL in Switzerland and Linac Coherent Light Source (LCLS) [3] and LCLS II [4] in Stanford and Dalian Coherent Light Source (DCLS) and SXFEL in China have been built and are in operation. The length of these facilities ranges from few hundred meters to several kilometers. Many of these facilities aim to generate attosecond X-ray pulses [5] with unprecedented brightness to film physical and chemical reactions with sub-atomic-level spatio-temporal resolution [6, 7]. Significant progress in attosecond science, including the time-domain observation of intramolecular charge transfer [8] and the discovery of ultrafast Auger processes altering the chemistry of matter on an attosecond time scale [9, 10], has been made in the past few years. Thus current XFELs technology will move over the next decade into the attosecond regime. As illustrated in Fig. 1, it is advantages to generate attosecond X-ray pulses and perform attosecond- precision pump-probe experiments. This is supported in an optimum way, if all optical/microwave sources in the XFEL, including the electron gun, injector laser, microwave references of the linear accelerator and bunch compressor, most importantly, the seed laser and pump lasers at the end station are synchronized simultaneously with attosecond relative timing jitter. Therefore, a multi-km attosecond-precision synchronization technique is imperative to unleash the full potential of these billion-dollar photon-science facilities.

The timing system consists of a reference providing extremely stable timing signals, a target signal that needs to be synchronized, a detector that can measure the timing difference between the target signal and the reference, and a control box to lock the timing of the target to that of the reference. If the target device is far away from the reference, a timing link is also necessary to deliver the timing signal from the reference to the target. Without exception, the attosecond-precision synchronization technique also requires these key elements.

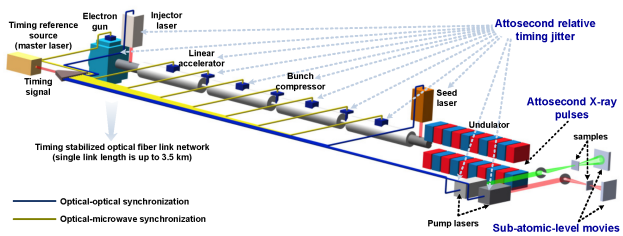

Figure 1: Timing and synchronization system for an attosecond XFEL [11].

The timing reference source in attosecond synchronization can be an atomic clock [12, 13], a continuous-wave (CW) laser [14, 15] or a mode-locked laser [16, 17]. The state-of-the-art technique in each solution can provide an attosecond-jitter-equivalent instability for 1s observation time. In contrast to the other two solutions, a mode-locked laser can simultaneously provide ultralow-noise optical and microwave signals, and the ultrashort optical pulses in time domain can be directly used as time markers for precise timing measurements. So it is an ideal timing source for synchronization applications such as telescope arrays and XFELs, where the target devices are mode-locked lasers and microwave sources.

Another advantage of using mode-locked lasers is that it can provide very high sensitivity during timing detection, thanks to its high pulse peak power. For example, we have developed balanced optical cross-correlators (BOCs) [17, 18] and balanced optical-microwave phase detectors (BOMPDs) [19–21] for optical-optical and optical-microwave timing detection, respectively. Both of them can achieve attosecond precision and >1-ps dynamic range at the same time.

For remote synchronization, the timing link can be implemented as optical fiber link [22]. Optical-fiber-based timing

ISBN: 978-3-95450-206-6 doi:10.18429/JACoW-FLS2018-WEA1PL03

links are very flexible for installation and can be easily fitted into XFELs and other facilities.

Here, we focus on the XFEL application, since it possesses currently the most urgent timing challenge. But the techniques we present here can also easily be adapted to other applications in the future. Based on the discussions above, the best synchronization solution for XFELs, as depicted in Fig. 1, should use a mode-locked laser (master laser) as the timing reference, and optical fiber links to distribute the timing signals to different remote laser/microwave sources. We have been working on this approach over the past decade [22, 23] and already passed the 10-fs precision level [24–26], which is more than an order-of-magnitude better than the best results achieved with traditional microwave signal distribution schemes. In order to meet the strict timing requirements of XFELs, a novel sub-fs-precision timing synchronization system is developed based upon our previous work, and presented here.

JITTER OF THE OPTICAL MASTER OSCILLATOR

Since the optical master oscillator (OMO) in Fig. 1 serves as timing reference for all optical/microwave sub-sources, it must exhibit attosecond-level timing jitter, which needs to be accurately characterized. Here, we use a balanced optical cross-correlator (BOC) [18, 23], which is intrinsically immune to AM-PM noise conversion by directly converting the timing difference of two optical pulses into a voltage signal. The BOC characterization has achieved extremely low noise floors down to 10^{-12} fs^2/Hz for offset frequencies up to the Nyquist frequency of mode-locked lasers [26, 27].

The OMO jitter characterization setup is shown in Fig. 2. The output of two identical lasers (master and slave, with 216.667 MHz repetition rate, 50 mW average power, 170 fs pulse width and 1553 nm center wavelength) were combined by a polarization beam splitter (PBS) and launched into a BOC, which consists of a single 4-mm-long periodically-poled $KTiOPO_4$ (PPKTP) crystal operating in a double-pass configuration with appropriate dichroic beam splitter and mirror (DBS, DM) and a low-noise balanced photodetector (BPD). The BOC output was fed back to the piezoelectric transducer (PZT) of the slave laser (with a sensitivity of 17.4 Hz/V) through a proportional-integral (PI) controller so that the two lasers' repetition rates were locked to each other. Finally, the BOC output was sent to an SSA for jitter characterization.

It can be seen that as feedback gain increases, the low frequency jitter is suppressed below 50 kHz. So in terms of measurement, we can decrease the feedback gain as much as possible (e.g., to -20 dB), then we can obtain the accurate master-laser jitter between 1 kHz and 20 kHz and an upper limit estimate above this frequency range.

The master laser characterization results are displayed in Fig. 3. The top panel shows the jitter spectral density at different feedback gains. As predicted by the simulations, the jitter spectrum is limited by the detector noise floor (grey

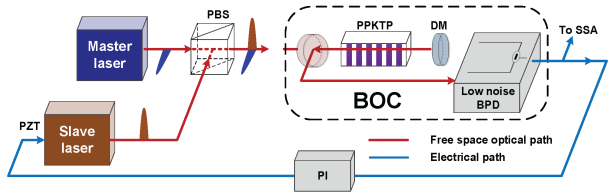

Figure 2: Master-laser (OMO) jitter characterization setup (PBS, polarization beam splitter; DBS, dichroic beam splitter; DM, dichroic mirror; PPKTP, periodically-poled $KTiOPO_4$; PI, proportional-integral controller; BPD, balanced photodetector; PZT, piezoelectric transducer; SSA, signal source analyzer).

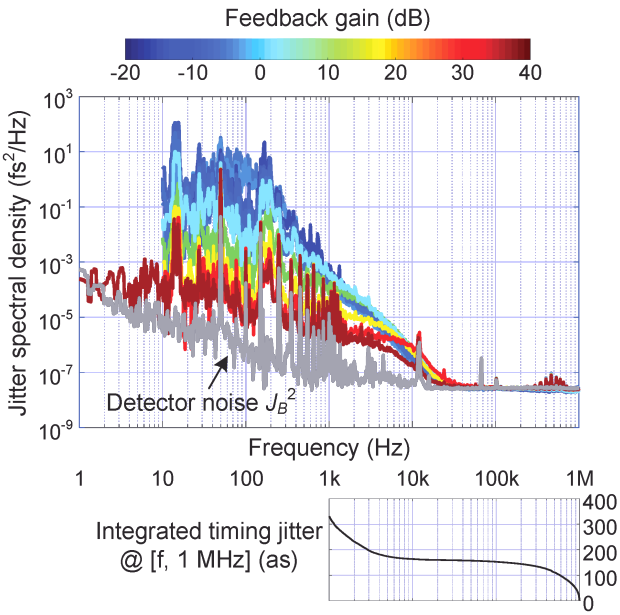

Figure 3: Measured master-laser jitter spectrum and corresponding integrated timing jitter [25].

curve) above 30 kHz. Between 1 kHz and 30 kHz, as the gain decreases, the spectrum approaches the real laser jitter. We choose the lowest gain value (about -15 dB) at which the locking is still stable enough to perform a measurement, and obtain 330 as integrated timing jitter from 1 kHz to 1 MHz, as shown in the bottom panel of Fig. 3. This value gives a very good upper limit estimate of the master laser's jitter. So this laser is definitely capable of providing the reference in an attosecondprecision timing synchronization system.

1550 nm LASER SYNCHRONZATION

To test the local optical-optical synchronization an experimental setup shown in Fig. 4 is constructed. Similar to that in laser characterization, the repetition rates of the slave and master lasers were first locked together with an in-loop BOC, then another out-of-loop BOC was used to evaluate the jitter performance after synchronization. Both of the two BOCs have the same structure as that shown in Fig. 2. In the feedback loop, the output of the in-loop BOC was first filtered

ISBN: 978-3-95450-206-6 doi:10.18429/JACoW-FLS2018-WEA1PL03

by a PI controller. Then the PI output was separated into two paths: the first path was directly sent to the slave laser's PZT without amplification to compensate fast jitter above 10 Hz; the second path was sampled by a data acquisition (DAQ) card, analyzed by a Labview program to generate a DC voltage to compensate slow jitter below 10 Hz, and a voltage amplifier was used to extend the compensation range. This feedback design can effectively optimize the locking bandwidth and compensation range simultaneously.

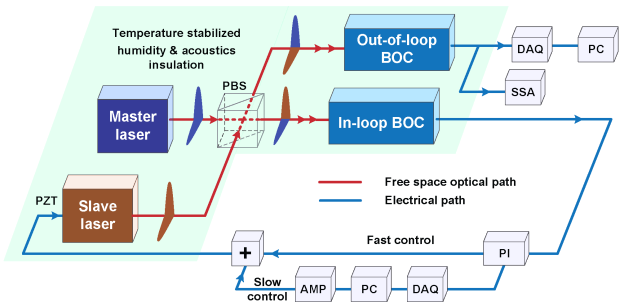

Figure 4: Local optical-optical synchronization (DAQ, data acquisition card; PC, computer, AMP, voltage amplifier; +, voltage summer).

To minimize the thermally-induced timing fluctuations, the two lasers, two BOCs and other free-space optics were mounted on a temperature-stabilized breadboard with a Super-Invar surface sheet. With temperature fluctuations controlled below ±0.05 K, the effective timing instability of free-space beam paths due to thermal expansion is only ±1 as/cm.

Figure 5(a) shows the out-of-loop jitter spectrum from 1 Hz to 1 MHz. The total integrated jitter over this frequency range is only 450 as. A long-term drift measurement was taken and the peak-to-peak drift in 10 hours is 400 as, which gives a root-mean-square (RMS) drift of 71 as (Fig. 6(b)). The Fourier transform of the drift data is also calculated in Fig. 6(c). The integrated drift from 200 μHz to 1 Hz is only 50 as. These results indicate that optical synchronization using BOC can easily achieve attosecond precision. Furthermore, they also provide a precision limit that we can approach in the remote timing synchronization.

SYNCHRONIZATION OF Ti:SAPPHIRE LASERS

In order to investigate the jitter noise limitations in the timing synchronization system, we built a Ti:Sapphire laser synchronization setup on a 4.7-km timing link network [28], as shown in Fig. 5. The same master laser as before was used, and its repetition rate was locked to an RF reference to reduce its drift below ~200 Hz. The slave laser, is a home-built Ti:Sapphire Kerr-lens mode-locked laser operating at 800-nm center wavelength and 1.0833 GHz repetition rate. Then the output of the master laser was split into two separate timing links. Timing link 1 consisted of a 3.5-km polarization-maintaining (PM) dispersion-compensated fiber spool, a PM fiber stretcher, and a fiber-coupled motorized delay line with 560-ps range. Similarly, the components of timing link 2 included a 1.2-km PM fiber spool, a PM fiber stretcher, and a free-space motorized stage with 100-ps range. At the end of each link, there was a fiber-coupled mirror reflecting 10% of the optical power back to the link input. Here, a bidirectional erbium-doped fiber amplifier (EDFA) was also used to provide sufficient power for the backpropagating signal and the link output required for link stabilization and remote synchronization, respectively. At the link inputs, the round-trip pulses were combined with newly emitted ones in one-color (OC)-BOCs. OC-BOCs operate at 1554 nm wavelength and realize the crosscorrelation

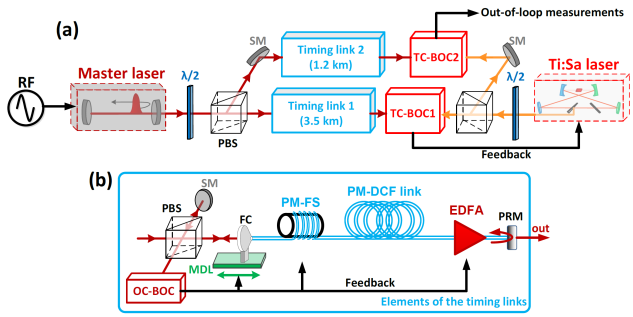

Figure 5: (a) Experimental setup for the synchronization of the Ti:Sa laser on a timing link network with a total length of 4.7 km. (b) Individual elements of the timing stabilized fiber links. Abbreviations: RF: RF reference; FC: fiber collimator; MDL: motorized delay line; PMFS: polarization-maintaining fiber stretcher; PM-DCF: PM dispersion-compensated fiber; EDFA: bidirectional erbium-doped fiber amplifier; PRM: partially reflecting fiber mirror [28].

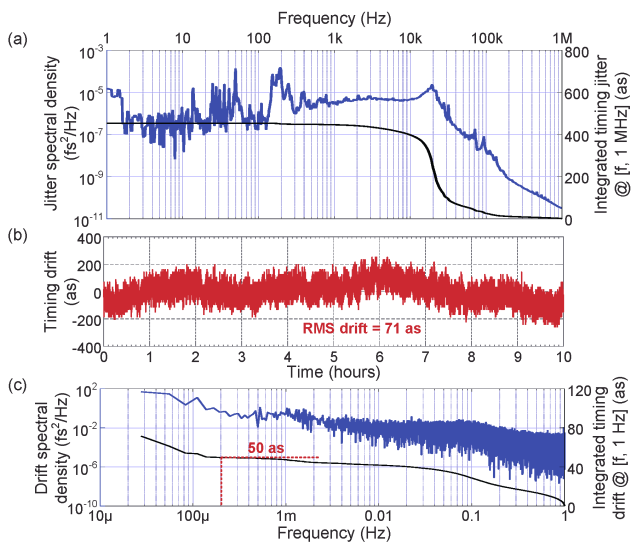

Figure 6: Local optical-optical synchronization measurement results. (a) Out-of-loop jitter spectrum; (b) longterm timing drift (sampling rate: 2 Hz); (c) timing drift spectrum.

ISBN: 978-3-95450-206-6 doi:10.18429/JACoW-FLS2018-WEA1PL03

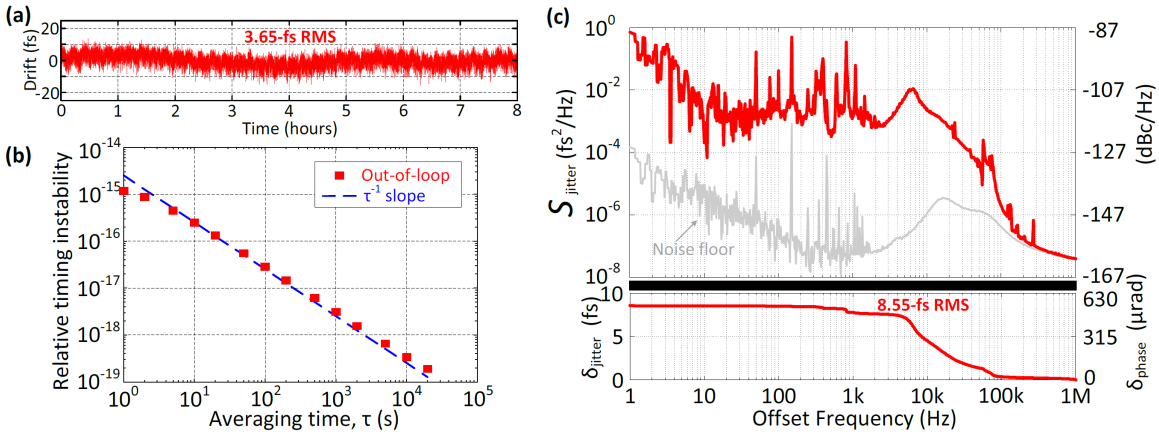

Figure 7: Out-of-loop measurements between the remotely synchronized Ti:Sa laser and timing link 2 output. (a) Timing drift below 1 Hz. (b) Calculated relative timing instability from the drift data. (c) Jitter spectral density S_{jitter} and its integrated jitter δ_{jitter}; right axes: equivalent SSB phase noise $\mathcal{L}(f)$ and its integrated phase δ_{phase} scaled to a 10 GHz carrier frequency. The grey curve shows the noise floor of the free-running TC-BOC2 [28].

with the birefringence between two orthogonally polarized input pulses. OC-BOCs measured the propagation delay fluctuations in the links and generated error voltages, which controlled the fiber stretchers and the motorized delays to compensate for fast jitter and long-term drifts, respectively. The Ti:Sapphire laser was placed at the output location of the timing links. As the OMO and Ti:Sapphire laser operate at different central wavelengths, two two-color BOCs (TC-BOCs) [28] were built between each link output and the Ti:Sapphire laser output. Both of the TC-BOCs were realized with type-I sum-frequency generation between 800-nm and 1550-nm central wavelengths in a beta-barium borate (BBO) crystal. TC-BOC1 synchronized the Ti:Sa laser with link 1 output by tuning the repetition rate via its intracavity PZT mirror. Finally, the free-running TC-BOC2 evaluates the timing precision between the synchronized Ti:Sapphire laser and timing link 2 output.

Figure 7(a) shows the out-of-loop timing drift between the remotely synchronized Ti:Sa laser and timing link 2 output. We were able to keep the complete system synchronized for 8 hours continuously, which is limited by the PZT range of the Ti:Sa laser. The observed drift is only 25-fs peak-to-peak and 3.65 fs RMS for the complete duration without any excess locking volatility. We also calculated the relative timing instability (i.e., timing error in terms of overlapping Allan deviation) from the drift data to investigate the system behavior for different averaging times. As Fig. 7(b) illustrates, the relative timing instability is only 1.2×10^{-15} in 1-s averaging time (τ) and falls to 3.36×10^{-19} at 10,000 s following a deterministic slope very close to τ^{-1}.

The timing jitter spectral density for offset frequencies larger than 1 Hz was measured with a baseband analyzer, which Fourier transformed the TC-BOC2 output. The red curve in Fig. 7(c) shows the out-of-loop jitter between the remotely synchronized Ti:Sa laser and timing link 2 output. The integrated jitter for 1 Hz – 1 MHz is 8.55 fs RMS corresponding to a phase error of 0.5 mrad for a 10 GHz carrier.

SUB-FEMTOSECOND PERFORMANCE

Demonstration of sub-femtosecond timing distribution was achieved with the laser-microwave network shown in Fig. 8a. The timing signal from the master laser is distributed through a network that contains two independent fiber links of 1.2-km and 3.5-km length operated in parallel. The link outputs are used to synchronize a remote

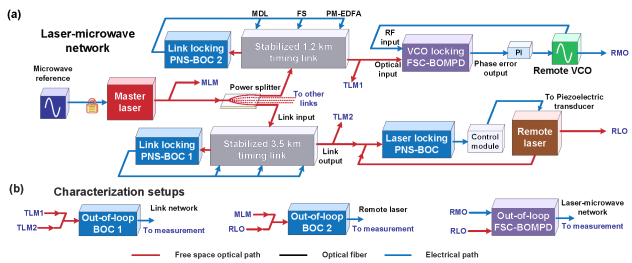

Figure 8: (a) Laser-microwave network (VCO, voltagecontrolled oscillator); (b) Out-of-loop characterization setups [11].

laser (e.g., serving as a pump-probe laser at the FEL end station) and a voltagecontrolled oscillator (VCO) (e.g., serving as a microwave reference of the FEL linear accelerator) simultaneously. New *polarization-noise-suppressed* BOCs (PNS-BOC) and *free-space-coupled balanced optical-microwave phase detectors* (FSC-BOMPD) for improved noise performance have been and implemented. Residual second and third-order dispersion links are carefully compensated with additional dispersion-compensating fiber to suppress link-induced Gordon-Haus jitter and to minimize output pulse duration; the link power is stabilized to minimize the nonlinearity-induced jitter as well as to maximize the SNR for BOC locking. Characterization setups are shown

ISBN: 978-3-95450-206-6 doi:10.18429/JACoW-FLS2018-WEA1PL03

in Fig. 8b, to evaluate the performance of the link network, as shown in Fig. 9.

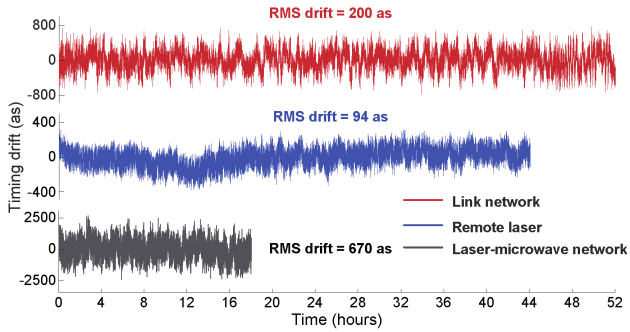

Figure 9: Measured long-term timing drift (sampling rate = 2 Hz).

The residual timing drift between links below 1 Hz is only 200 as RMS (red), and the total integrated timing jitter from 6 µHz to 1 MHz is 580 as (red). Remote laser synchronization over 44 hours without interruption is within 100 as RMS (blue). Overall, an unprecedented long-term precision of 670 as RMS out-of-loop drift over 18 hours (black) [11].

CONCLUSIONS

A sub-femtosecond laser-microwave network has been demonstrated with novel timing devices.

ACKNOWLEDGEMENT

This work was supported by the European Research Council under the European Union's Seventh Framework Program (FP/2007-2013) / ERC Grant Agreement No. 609920 and the Cluster of Excellence "The Hamburg Centre for Ultrafast Imaging–Structure, Dynamics and Control of Matter at the Atomic Scale" of the Deutsche Forschungsgemeinschaft.

REFERENCES

[1] M. Altarelli, R. Brinkmann, M. Chergui, W. Decking, B. Dobson, S. Düsterer, G. Grübel, W. Graeff, H. Graafsma, and J. Hajdu, "XFEL: The European X-Ray Free-Electron Laser", DESY, Technical Design Report, 2006.

[2] E. Allaria *et al.*, "Highly coherent and stable pulses from the FERMI seeded free-electron laser in the extreme ultraviolet", *Nature Photon*, 6 (2012) 699.

[3] P. Emma *et al.*, "First lasing and operation of an ångstrom-wavelength free-electron laser", *Nature Photon*, 4 (2010) 641.

[4] J. Stohr, "Linac Coherent Light Source II (LCLS-II) Conceptual Design Report", SLAC, Design Report, No. SLAC-R-978, 2011.

[5] E. Prat and S. Reiche, "Simple Method to Generate Terawatt-Attosecond X-Ray Free-Electron-Laser Pulses", *Phys. Rev. Lett*. 114 (2015) 244801.

[6] C. Kupitz *et al.*, "Serial time-resolved crystallography of photosystem II using a femtosecond X-ray laser", *Nature* 513 (2014) 261.

[7] H. Öström *et al.*, "Probing the transition state region in catalytic CO oxidation on Ru", *Science* 347 (2015) 978.

[8] F. Calegari, D. Ayuso, A. Trabattoni, L. Belshaw, S. De Camillis, S. Anumula, F. Frassetto, L. Poletto, A. Palacios, P. Decleva, J. B. Greenwood, F. Martín, and M. Nisoli, "Ultrafast electron dynamics in phenylalanine initiated by attosecond pulses", *Science* 346 (2014) 336.

[9] S. K. Son, L. Young, and R. Santra, "Impact of hollow-atom formation on coherent x-ray scattering at high intensity", *Phys. Rev.* A. 83 (2011) 033402.

[10] S. P. Hau-Riege, "Photoelectron dynamics in X-ray free-electronlaser diffractive imaging of biological samples", *Phys. Rev. Lett.* 108 (2012) 238101.

[11] M. Xin, K. Şafak, M. Y. Peng, A. Kalaydzhyan, W. Wang, O. D. Mücke, and F. X. Kärtner, "Attosecond precision multi-km lasermicrowave network", *Light: Science & Applications* 6 (2017) e16187.

[12] C. W. Chou, D. B. Hume, T. Rosenband, and D. J. Wineland, "Optical clocks and relativity", *Science* 329 (2010) 1630.

[13] T. L. Nicholson, S. L. Campbell, R. B. Hutson, G. E. Marti, B. J. Bloom, R. L. McNally, W. Zhang, M. D. Barrett, M. S. Safronova, G. F. Strouse, W. L. Tew, and J. Ye, "Systematic evaluation of an atomic clock at 2×10^{-18} total uncertainty", *Nature Commun.* 6 (2015) 6896.

[14] D. Meiser, J. Ye, D. R. Carlson, and M. J. Holland, "Prospects for a millihertz-linewidth laser", *Phys. Rev. Lett.* 102 (2009) 163601.

[15] C. Hagemann, C. Grebing, C. Lisdat, S. Falke, T. Legero, U. Sterr, F. Riehle, M. J. Martin, and J. Ye, "Ultrastable laser with average fractional frequency drift rate below 5×10^{-19}/s", *Opt. Lett.* 39 (2014) 5102.

[16] T. K. Kim, Y. Song, K. Jung, C. Kim, H. Kim, C. H. Nam, and J. Kim, "Sub-100-as timing jitter optical pulse trains from mode-locked Er-fiber lasers", *Opt. Lett.* 36 (2011) 4443.

[17] A. J. Benedick, J. G. Fujimoto, and F. X. Kärtner, "Optical flywheels with attosecond jitter", *Nature Photon*. 6 (2012) 97.

[18] T. R. Schibli, J. Kim, O. Kuzucu, J. T. Gopinath, S. N. Tandon, G. S. Petrich, L. A. Kolodziejski, J. G. Fujimoto, E. P. Ippen, and F. X. Kärtner, "Attosecond active synchronization of passively mode-locked lasers by balanced cross correlation", *Opt. Lett.* 28 (2003) 947.

[19] J. Kim, J. Chen, Z. Zhang, F. N. C. Wong, F. X. Kärtner, F. Loehl, and H. Schlarb, "Long-term femtosecond timing link stabilization using a single-crystal balanced cross correlator", *Opt. Lett.* 32 (2007) 1044.

[20] J. Kim, F. X. Kärtner, and F. Ludwig, "Balanced optical–microwave phase detectors for optoelectronic phase-locked loops", *Opt. Lett.* 31 (2006) 3659.

[21] M. Y. Peng, A. Kalaydzhyan, and F. X. Kärtner, "Balanced optical-microwave phase detector for sub-femtosecond optical-RF synchronization", *Opt. Express* 22 (2014) 27102.

[22] J. Kim, J. A. Cox, J. Chen, and F. X. Kärtner, "Drift-free femtosecond timing synchronization of remote optical and microwave sources", *Nature Photon.* 2 (2008) 733.

ISBN: 978-3-95450-206-6 doi:10.18429/JACoW-FLS2018-WEA1PL03

[23] M. Y. Peng, P. T. Callahan, A. H. Nejadmalayeri, S. Valente, M. Xin, L. Grüner-Nielsen, E. M. Monberg, M. Yan, J. M. Fini, and F. X. Kärtner, "Long-term stable, sub-femtosecond timing distribution via a 1.2-km polarization-maintaining fiber link: approaching 10^{-21} link stability", *Opt. Express* 21 (2013) 19982.

[24] M. Xin K. Şafak, M. Y. Peng, P. T. Callahan, and F. X. Kärtner, "One-femtosecond, long-term stable remote laser synchronization over a 3.5-km fiber link", *Opt. Express* 22 (2014) 14904.

[25] K. Şafak, M. Xin, P. T. Callahan, M. Y. Peng, and F. X. Kärtner, "All fiber-coupled, long-term stable timing distribution for free electron lasers with few-femtosecond jitter", *Structural Dynamics* 2 (2015) 041715.

[26] J. Kim, J. Chen, J. Cox, and F. X. Kärtner, "Attosecond-resolution timing jitter characterization of free-running mode-locked lasers", *Opt. Lett.* 32 (2007) 3519.

[27] J. A. Cox, A. H. Nejadmalayeri, J. Kim, and F. X. Kärtner, "Complete characterization of quantum-limited timing jitter in passively mode-locked fiber lasers", *Opt. Lett.* 35 (2010) 3522.

[28] K. Şafak, M. Xin, Q. Zhang, S. Chia, O. D. Mücke, and F. X. Kärtner, "Jitter analysis of timing-distribution and remote-laser synchronization systems", *Opt. Express* 24 (2016) 21752.

ISBN: 978-3-95450-206-6 doi:10.18429/JACoW-FLS2018-WEP1WC02

COMPACTLIGHT DESIGN STUDY*

A. Latina†, D. Schulte, W. Wuensch, S. Stapnes, CERN, 1211 Geneva 23, Switzerland
G. D'Auria, R. Rochow, Elettra Sincrotrone Trieste, 34149 Basovizza, Italy
J. Clarke, STFC Daresbury Laboratory, Warrington, WA4 4AD, UK
W. Fang, hanghai Institute of Applied Physics, Shanghai 201800, P. R. China
E. Gazis, Institute of Accelerating Systems and Applications, IASA, Athens, Greece
M. Jacewicz, Uppsala Universitet, UU, Uppsala, Sweden
R. Dowd, ANSTO, Lucas Heights, NSW 2234, Australia
A. Aksoy, Ankara University Institute of Accelerator Technologies, UA-IAT, Ankara, Turkey
H. Prien, VDL Enabling Technology Group, VDL ETG, Eindhoven, Netherlands
M. Ferrario, Istituto Nazionale di Fisica Nucleare, LNF-INFN, Frascati, Italy
R. Geometrante, Kyma S.r.l., Trieste, Italy
A. Mostacci, University of Rome "La Sapienza", Rome, Italy
F. Nguyen, ENEA, Roma, Italiy
F. Perez, ALBA Synchrotron, 08290 Cerdanyola de Vallès, Barcelona, Spain
A. Faus-Golfe, Centre National de la Recherche Scientifique, CNRS, Paris, France
A. Bernhard, Karlsruher Institut für Technologie, KIT, Karlsruhe, Germany
T. Schmidt, Paul Scherrer Institut, 5232 Villigen PSI, Switzerland
D. Esperante, Agencia Estatal Consejo Superior de Investigaciones Científicias, CSIC, Madrid, Spain
M. Aicheler, University of Helsinki, UH/HIP, Helsinki, Finland
A. Cross, University of Strathclyde, USTR, UK

Abstract

H2020 CompactLight Project aims at designing the next generation of compact hard X-Rays Free-Electron Lasers, relying on very high accelerating gradients and on novel undulator concepts. CompactLight intends to design a compact Hard X-ray FEL facility based on very high-gradient acceleration in the X band of frequencies, on a very bright photo injector, and on short-period/superconductive undulators to enable smaller electron beam energy. If compared to existing facilities, the proposed facility will benefit from a lower electron beam energy, due to the enhanced undulators performance, be significantly more compact, as a consequence both of the lower energy and of the high-gradient X-band structures, have lower electrical power demand and a smaller footprint. CompactLight is a consortium of 24 institutes (21 European + 3 extra Europeans), gathering the world-leading experts both in the domains of X-band acceleration and undulator design.

MOTIVATION AND OBJECTIVES

Our aim is to facilitate the widespread development of X-ray FEL facilities across Europe and beyond, by making them more affordable to construct and operate through an optimum combination of emerging and innovative accelerator technologies. We will design a Hard X-ray FEL facility using the very latest concepts for bright electron photo injectors, very high-gradient accelerating structures and novel short period undulators. The resulting facility will benefit from a lower electron beam energy than current facilities, due to the enhanced undulator performance, will be significantly more compact as a consequence of this lower energy as well as due to the application of very high-gradient structures, and also have a much lower electrical power consumption than current facilities through the use of an X-band RF system at 12 GHz. These ambitious but realistic aims will result in much lower construction and running costs making X-ray FELs affordable, even by national institutions or academia. We therefore anticipate that our Design Study will enable FEL facilities to proliferate across all of Europe and beyond much more rapidly than third generation light sources have managed over the past decades.

CompactLight gathers the world-leading experts in these domains, united to achieve two objectives: disseminate X-band technology as a new standard for accelerator-based facilities and advance undulators to the next generation of compact photon sources, with the aim of facilitating the widespread development of X-ray FEL facilities across and beyond Europe by making them more affordable to build and to operate.

A COMPACT HARD X-RAY FEL

A standard layout of an FEL is shown in Fig. 1. It consists of a high-brightness electron source, a pre-acceleration section up to about 300 MeV, a laser heater, to optimize the micro-bunching instability, three linear accelerating sections (L1, L2, and L3 in the figure), and two magnetic chicanes,

* This project receives funding from the European Union's Horizon 2020 research and innovation programme topic Design Studies.
† andrea.latina@cern.ch

ISBN: 978-3-95450-206-6 doi:10.18429/JACoW-FLS2018-WEP1WC02

to achieve acceleration and longitudinal bunch compression before delivering the beam to the undulator lines where the photons are created. CompactLight aims at significantly reduce the footprint of the entire facility, using compact sources, a compact and power efficient rf module, and a compact undulators of the next generation. Table 1 shows the range of parameters that CompactLight sets as target for its design of the next generation hard X-ray facilities.

Table 1: Preliminary Parameters of the Proposed CompactLight Hard X-ray Facility

Parameter	Units	Value
Linac frequency	GHz	12
Linac gradient	MV/m	70
Beam energy	GeV	< 4.6
Bunch Charge	pC	< 250
Normalized emittance	mm mrad	< 0.5
Bunch length	μm	< 8
Pulse duration	fs	< 1 to 50
Pulse repetition rate	Hz	100-1000
Number of bunches per pulse	#	1-3
FEL Parameters		
K value	#	1.13
Minimum wavelength	Å	1
Number of photons per pulse	#	$> 10^{12}$
Pulse bandwidth	%	$\ll 0.1$

Compact Injector Gun

Investigation into high-performance sources able to deliver high brightness, high repetition rate electron beams for the generation of high-flux, highly coherent radiation and integration with CompactLight are the main objectives of CompactLight. Currently, electron sources used in XFELs are based on three RF technologies: 1.3 GHz, 24 MV/m, superconducting L-Band; 2.86 GHz, 17 MV/m, room-temperature S-Band; and 5.7 GHz, 35 MV/m, room temperature C-Band at SACLA and SwissFEL [1]. Recent developments in high-gradient acceleration in S- and in C- bands, where accelerating voltages as high as 55 MV/m in S band have been achieved, are showing the way to a new generation of high-gradient S- band and C- band injector guns. Injectors based on high-gradient X-band, possibly equipped with a K-band linearizer running at 36 GHz, would certainly represent a leap forward toward very compact high-brilliance injectors.

Enabling a new generation of compact high-brightness electron sources will impact the whole electron accelerator-based science community, in particular photon sciences, where electron beams drive a variety of tools such as FELs, electron scattering experiments, imaging and radiation therapy.

A full X-band gun will be presented in [2]. This design is based on the a photo cathode rf gun in [1], operating at 12 GHz with a peak voltage of 200 MV. The cathode is followed by CLIC-like X-band structures with gradient 70 MV/m, able to accelerate the beam up to 300 MeV. A preliminary phase space distribution at the rf gun exit is shown in Fig. 2. As it can be seen on Fig. 2 the beam is accelerated up to 60 MeV by 5.6 cell rf gun and single X-band structure. The projected emittance at the end of first structure is simulated as $\varepsilon = 0.4$ mm.mrad and the bunch length is $\sigma_z \approx 680$ fs. To minimize the uncorrelated energy spread we introduce a chirp by adjusting the phase of X-band structure.

Compact Linac Module

The linacs are composed by a sequence of modules. A module is a physical unit that includes an X-band RF distribution network and X-band accelerating structures, as well as beam diagnostic devices and focusing magnets for beam transport. The aim of the CompactLight Design Study is to determine the key parameters of an FEL facility based on X-band acceleration, including transverse focusing, mechanical stability, alignment tolerances and diagnostics, and then design, assemble and test experimentally all the RF components of such an X-band module. Preliminary studies have outlined the basic parameters of such a module; they are sketched in Fig. 3.

As the feasibility of high-gradient X-band accelerator technology has been proven, the manufacturing of X-band structures is ready to move from individual prototypes to high volume production. Industrialization of X-band components is becoming crucial for facilities and market to grow together. Efficient RF power sources also need to be developed, integrated and industrialized from this perspective. One of the main objectives of CompactLight is the definition of a standard unit for X-band based accelerators, a standardized module inclusive of RF source with optimized pulse compressor, RF distribution network, accelerating structures equipped with magnetic elements and diagnostics. This standard unit will provide a template for industrial involvement.

Compact Undulator

In parallel to X-band developments, undulators have also made significant improvements in capability in recent years, with the promise of more to come. Two new undulator technologies have now been proven on light source facilities, cryogenic permanent magnet undulators and superconducting undula- tors, and both continue to improve in performance as a greater confidence and understanding in each type develops. Neither of these two new technologies has been applied to an XFEL design until now.

Reducing the required electron beam energy through the use of more advanced undulators results in additional savings roughly proportional to the energy reduction. The application of both higher frequency acceleration and advanced undulators could facilitate also the upgrade of existing facilities to higher energy, with the possibility of minimal or no increase in civil construction. Parallel to the development of compact X-band accelerator technologies, CompactLight will push the generation of coherent light beyond the current state-of-the-art, and develop innovative new technologies for

ISBN: 978-3-95450-206-6 doi:10.18429/JACoW-FLS2018-WEP1WC02

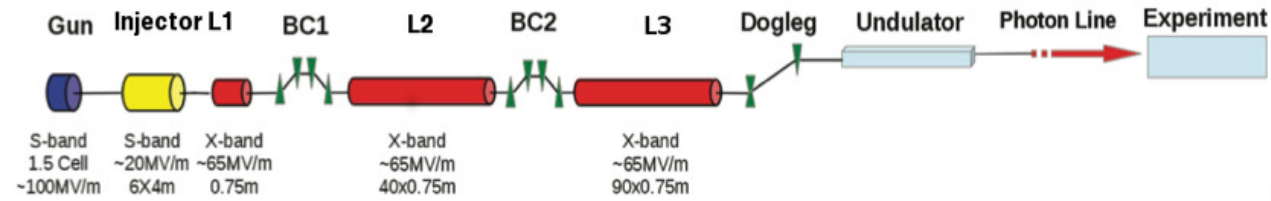

Figure 1: Layout of an FEL facility.

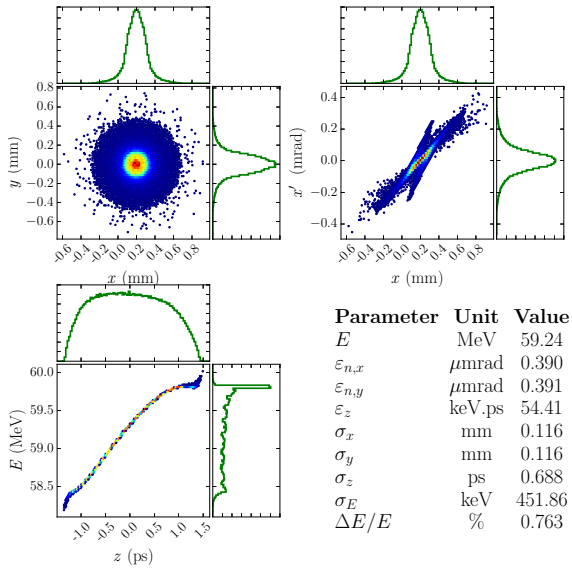

Parameter	Unit	Value
E	MeV	59.24
$\varepsilon_{n,x}$	μmrad	0.390
$\varepsilon_{n,y}$	μmrad	0.391
ε_z	keV.ps	54.41
σ_x	mm	0.116
σ_y	mm	0.116
σ_z	ps	0.688
σ_E	keV	451.86
$\Delta E/E$	%	0.763

Figure 2: Transverse beam distribution (top left), and horizontal (top right) and longitudinal (bottom left) phase spaces with associated histograms representing the projection along the respective axis and beam parameters of the bunch at the exit of first X-band cavity of injector.

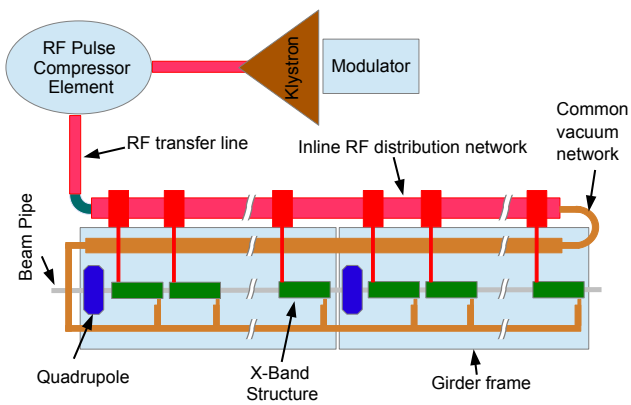

Figure 3: Schematic illustration of an X-band module.

efficient light generation that will lead to the next-generation of compact coherent light facilities, including permanent magnet, or super-conducting undulators. The potential for improving the photon generation process and the FEL operation is a rapidly developing field of research: achieving shorter saturation lengths, shaping the pulses in time and in spectrum domain, two-colour generation, seeding and harmonic lasing are some of the directions being explored.

A review of the state-of-the-art for existing technologies will be performed, together with a study of the emerging technologies, that is technologies whose examples have already proven on storate rings or FELs their potential, but are of recent conception, among these for example cryogenic permanent magnet undulators (CPMU) and superconductive undulators (SCU). Both CPMY and SCU technologies show the potential to reach for short periods while keeping high B values (40%-50% larger than standard PMU's), with the CPMU's notably less subjected to wakefield effects.

With a target beam energy of 4.6 GeV and a K parameter of 1.13, the target wavelength of $\lambda_{\mathrm{FEL}} \simeq$ can be achieved only with undulator periods of $\lambda_U \approx 1.2$ cm. This sets the undulator design. The target undulator performance also determines the specifications on the incoming beam, through the Pierce parameter [3]. Considering electron peak currents within reach, of the order of 2 kA, one needs to have a transverse normalized emittance less than 0.5 mm mrad, and a relative energy spread better than 0.05% in order to achieve a saturation length $L_S \approx 50$ m.

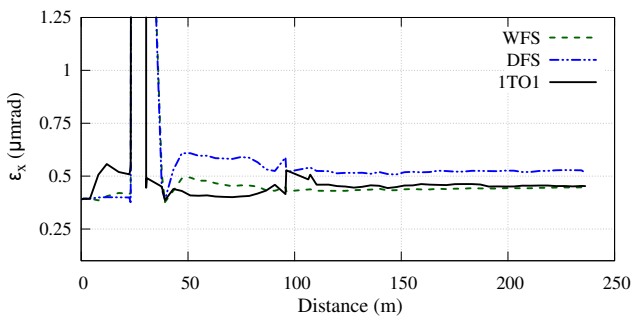

Figure 4: Emittance growth along a preliminary design of a full X-band injector and linac.

Preliminary beam dynamics simulations of the linac and bunch compressors have been performed, the result is shown in Fig. 4. The tests confirmed that sophisticated beam-based alignment techniques developed for CLIC can successfully be applied at CompactLight, allowing one to reach the required performances in terms on beam transport.

CONCLUSIONS

A recently submitted H2020 proposal for a design study of a compact light source called CompactLight has been approved, with start date January 1st 2018. The goals of CompactLight are the design of a full-fledges free-electron laser based on the most advanced technologies for a compact

ISBN: 978-3-95450-206-6 doi:10.18429/JACoW-FLS2018-WEP1WC02

electron injector gun, an X-band based linac, and a short-period/superconductive undulator to enable smaller electron beam energy. The CompactLight consortium consists of 24 institutes (21 European + 3 extra Europeans), gathering the world-leading experts both in the domains of X-band acceleration and undulator design. World-leading experts united to achieve two objectives: disseminate X-band technology as a new standard for new accelerator-based facilities, and advance undulators to the next generation of compact photon sources, with the aim of facilitating the widespread development of X-ray FEL facilities across and beyond Europe by making them more affordable to build and to operate.

REFERENCES

[1] C. Limborg-Deprey, "Achieved Performance of an All X-band Photo-Injector", IPAC2016, Busan, Korea.

[2] A. Aksoy et al. , "Conceptual Design for an hard X-Ray Free Electron Laser based on CLIC X-band Structure", *in publication.*

[3] H. Zhirong and K. Kwang-Je. "Review of X-Ray Free-Electron-Laser Theory", Phys. Rev. ST Accel. Beams. 10, 2007

ISBN: 978-3-95450-206-6 doi:10.18429/JACoW-FLS2018-WEA2WD01

QUAPEVA: VARIABLE HIGH GRADIENT PERMANENT MAGNET QUADRUPOLE

C. Kitegi, T. André, F. Blache, M.E. Couprie, A. Ghaith, J. Idam, A. Loulergue, F. Marteau, D. Oumbarek, M. Sebdaoui, M. Valléau, J. Vétéran, SOLEIL, Gif-sur-Yvette, France
C. Benabderrahmane, J. Chavanne, G. Le Bec, ESRF, Grenoble, France
O. Cosson, F. Forest, P. Jivkov, J. L. Lancelot, Sigmaphi, Vannes, France
C. Vallerand, LAL, Orsay, France
P. N'gotta, MAX IV, Lund, Sweden

Abstract

The magnetic and the mechanical design of a high and variable gradient Permanent Magnet Quadrupole (PMQ) is presented. Seven of them with various lengths, ranging from 26 mm up to 100 mm, for different integrated quadrupole strengths were manufactured. The measured magnetic performance of these devices is also reported. These devices were successfully commissioned to transport laser plasma accelerated electron beam.

INTRODUCTION

Current accelerator projects require strong quadrupole magnets to focus particle beams to ever smaller size. They rely on the very mature resistive magnet technology for gradient below typically 100 T/m. For larger gradient, Permanent Magnet (PM) technology seems to be attractive alternative as the highest gradient value ever reported with a PMQ is 575 T/m for a 2.75 mm bore radius [1]. However, since the first proposal of PM multipole design in the early eighties [2], their use in accelerators stayed marginal. Their relative poor field quality and the small field tuning has limited them to specific applications such as final focus system in colliders [3-5] or in projects where PM technology offers a clear and substantial saving over resistive technology [6].

A fixed gradient quadrupole targeting standard field quality of light source accelerator magnet, which smears the difference between the magnetic performance obtained with resistive and PM accelerator magnets, was recently developed at the ESRF [7].

We present hereafter the design of the QUAPEVA, a variable high gradient PMQ, i.e. with a gradient larger than 100 T/m and 50 % tunability [8-11]. As far as the amplitude of the gradient adjustment is concerned, this design also brings PM accelerator magnet closer to resistive magnet. One prototype and two triplets were manufactured for an experiment dedicated to the demonstration of a COherent X-ray source INferred from Electrons accelerated by Laser (COXINEL) [12]. We first introduce the concept and the parameters for QUAPEVA COXINEL, we then present the magnetic performance of the seven built items.

QUAPEVA CONCEPT

General Description

The magnetic design of QUAPEVA is shown in Fig. 1. The magnet structure is made of two concentric quadrupoles. The inner quadrupole follows the Halbach hybrid arrangement of PM and soft iron poles to drive the PM magnetic flux into the gap. The soft iron poles also smooth the PM magnetic imperfections and thus help improving the field quality. The outer quadrupole is dedicated to the field gradient tuning and is composed with a set of four cylindrical PM magnetized in radial direction. Each magnet is located at the top of one of the inner quadrupole soft iron pole. The soft iron shield placed behind each rotatable magnet limits the field leakage from the outer quadruple.

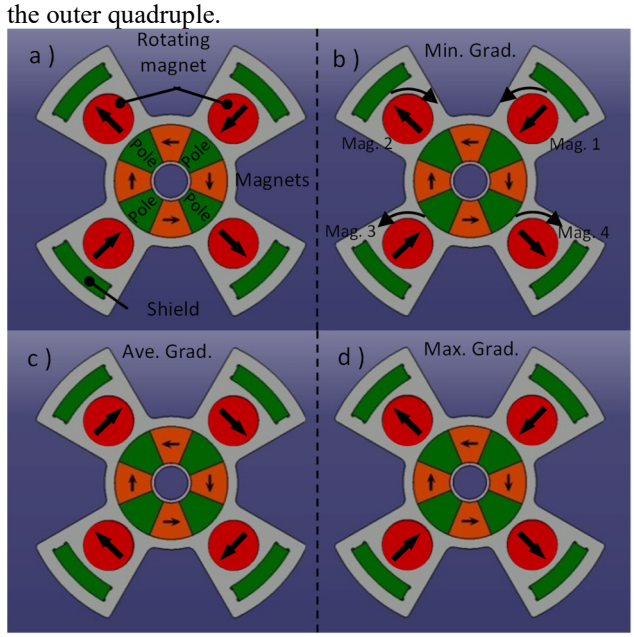

Figure 1: Schematic of the QUAPEVA magnetic design (a). Orientation of the four rotating magnets at minimum gradient (b), average gradient (c) and maximum gradient (d).

ISBN: 978-3-95450-206-6 doi:10.18429/JACoW-FLS2018-WEA2WD01

Table 1: Main Characteristics of the COXINEL QUAPEVA

COXINEL QUAPEVA	Bore Radius	Good Field radius	Material	Length [mm]	Max Grad [T/m]	Tuning Range [T/m]	Max. Int. Grad [T]	Tuning Range [T]	B6 [unit]	B_{10} [unit]
Prototype	6 mm	4 mm	Magnet: $N_2dFe_{14}B$ Remanence: 1.26 T Pole: Fe-Co Alloy Saturation: 2.35 T	100	201	92	21.3	9.7	300	100
1st Triplet				20.6	164	78	5.3	2.5		
				40.7	180	85	8.4	3.9		
				44.7	183	86	9.3	4.3		
				47.1	184	86	9.8	4.5		
2nd Triplet				66	190	88	13.9	6.4		
				81.1	195	89	17.2	7.8		

Gradient Tuning

Changing the orientation of the four magnets magnetization by rotating them around their centre allows for the tuning of the QUAPEVA gradient. There is only one configuration to reach the extremum of the QUAPEVA gradient, while rotating four magnets to set the QUAPEVA gradient to any arbitrary value in between minimum and maximum gradient, offers an infinite combination. However the QUAPEVA being a quadrupole, it is preferable to use the rotation rule defined in Fig. 1 which preserves the symmetry of the quadrupole field, as the soft iron poles of the inner quadrupole can enhance any undesired multipole component generated from the outer structure At minimum gradient the four rotating magnets are oriented so that their magnetization opposes to the one in the soft iron poles. To vary the gradient magnets two magnets are rotated in one direction, the two others in the opposite direction. At intermediate gradient, the magnetic field of the outer quadrupole loops around the inner quadrupole. At maximum gradient, the four rotating magnets are oriented so that their magnetization adds up to the one in the soft iron poles.

COXINEL QUAPEVA

Main Magnetic Characteristics

The main characteristics of the prototype item and the two triplets for COXINEL are listed in Table 1. The first (resp. second) triplet aims at super-matching a 180 (resp. 400) MeV LPA electron beam with a typical 1% energy dispersion into an undulator located several meters downstream the triplet [13]. Except for their magnetic lengths, all these magnets have identical characteristics as indicated in Table1.

The PM design associated with the small bore radius leads to a compact structure of only 90x90 mm² magnetic section while a gradient as high as 201 T/m with a tuning range of 92 T/m is achieved. However the required field quality is less stringent than typical 10^{-3} field quality necessary for light source magnets. Thus, with a normalized dodecapole B_6 and icosapole B_{10} harmonics which the magnitude are respectively 300 and 100 units, the tolerances on systematic multipole errors are relaxed.

Mechanical Layout

A picture of a built QUAPEVA is shown in Fig. 2. The magnetic system is encapsulated in an Aluminium support frame to maintain the poles and the magnets in their positions. The Aluminium support rests on a translation table which allows 10 mm vertical and horizontal displacement. Translation tables are naturally convenient during the installation and the alignment of QUAPEVAs in the COXINEL transport line. They were found to be important equipment for COXINEL, as they enable the implementation of a key feature of the transport line, the so-called Beam Pointing Alignment Compensation (BPAC) [14].

Each magnet of the outer quadrupole is connected to a 3 Nm brushless motor from the manufacturer HARMONIC DRIVE, with in between a 1 to 100 gear ratio reducer. An incremental rotary encoder is fixed to the back of each motor. This solution is compact as the motor and the incremental encoder fits within an envelope of 50x50x50mm³. The rotary encoder coupled with the gear reducer provides a resolution better than 30 μrad.

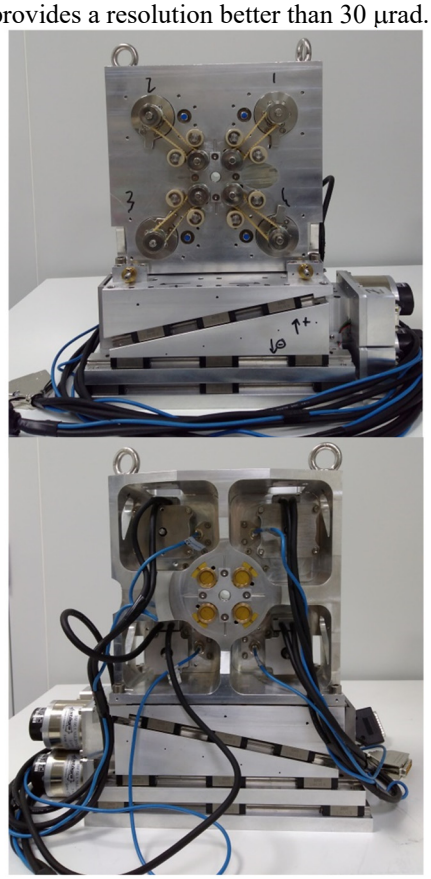

Figure 2: Front (top) and back (bottom) view of an assembled QUAPEVA.

ISBN: 978-3-95450-206-6 doi:10.18429/JACoW-FLS2018-WEA2WD01

MAGNETIC MEASUREMENTS

Most generally, the magnetic measurement goal of a conventional accelerator magnet is to ensure that the manufactured magnet performs as designed and to locate the magnetic axis of the device. For a QUAPEVA, magnetic measurements are also required to align properly the magnetization of the four rotating magnets, prior to validate its magnetic performance. Indeed one disorientated magnet prevents the QUAPEVA from reaching its theoretical extremum gradient. It also causes the QUAPEVA to exhibit a large magnetic center excursion.

Measured gradient tuning

The measured variation of the integrated gradient with respect to the rotation angle of the four magnets is shown in Fig. 3. As expected the variation with the respect to the rotation angle is closed to a sine-like function and the gradient reaches it extremum at $\pm\pi/2$.

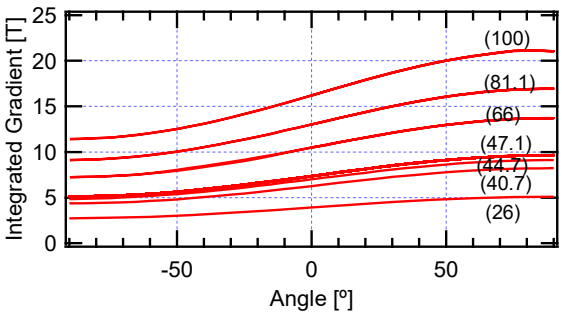

Figure 3: Measured integrated gradient of the seven QUAPEVA. The QUAPEVA length is given in mm in parenthesis.

Figure 4 compares the measured maximum value of the integrated gradient to the design value. Only the gradient of prototype QUAPEVA exceeds its design value, by a small margin, i.e. less than 0.5%. The two triplets exhibit a smaller maximum gradient than designed for. The difference increases as the length decreases and top at almost 4% for the thinner device. A slight discrepancy between the fringe field of a manufactured QUAPEVA and the numerical model would explain this difference as its contribution to the total field decreases with the quadrupole length.

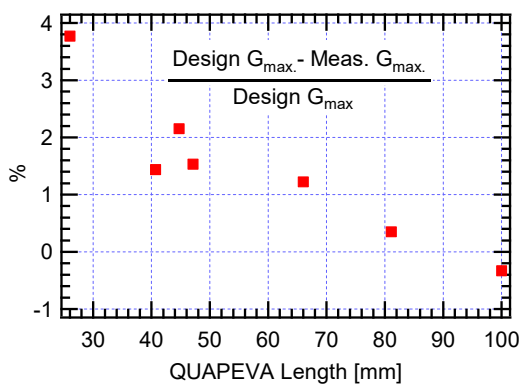

Figure 4: Normalized difference between the maximum measured integrated gradient and the design maximum gradient.

We observe that the variation of the systematic harmonics with respect to the rotation angle of the four magnets is also closed to a sine-like function. The systematic harmonics are at maximum value when the amplitude of the integrated gradient is also at maximum. The first systematics harmonics, measured at maximum gradient along the circle with a 4 mm radius are given in Table 2. The dodecapole harmonic is well within specification while the icosapole component slightly exceeds the 1% target.

Table 2: First Systematic Harmonics Measured at Maximum Gradient and at 4 mm Radius

QUAPEVA Length [mm]	26	40.7	44.7	47.1	66	81.1	100
B_6	195	211	223	209	232	227	221
B_{10}	115	112	119	119	116	120	123

CONCLUSION

The design and the measurement of seven PM quadrupole have been presented in this paper. The built QUAPEVA perform almost as designed and successfully offer a high gradient and a wide gradient tuning. The first triplet was successfully installed and used on COXINEL beam transport line.

ACKNOWLEDGEMENT

The authors are very grateful to the European Research Council for the advanced grant COXINEL (340015) and also to the Fondation de la Coopération Scientifique for the Triangle de la Physique / valorisation contract QUAPEVA (2012-058T). The authors are very thankful for the COXINEL team.

REFERENCES

[1] T. Eichner *et al.*, "Miniature magnetic devices for laser-based, table-top free-electron lasers", *Phys. Rev. ST Accel. Beams*, vol. 10, p. 082401, 2007
[2] K. Halbach, "Design of permanent multipole magnets with oriented rare earth cobalt material", *Nuclear Instr. Meth A,* vol. 187, pp. 109-117, (1981).
[3] J. K. Lim *et al.*, "Adjustable, short focal length permanent-magnet quadrupole based electron beam final focus system" *Phys. Rev. ST Accel. Beams*, vol. 8, p. 072401, 2005
[4] Y. Iwashita, T. Mihara, M. Kumada and M. Spencer, in *Proc. EPAC2006*, pp. 2550
[5] M. Modena *et al.*, in *Proc. IPAC2012*, pp. 3515
[6] B.J.A. Shepherd, J. A. Clark and N. A. Collomb, in *Proc. IPAC2012*, pp. 3530
[7] P. N'gotta, G. Le Bec, and J. Chavanne, *Phys. Rev. ST Accel. Beams,* vol. 19, p. 122401, 2016
[8] F. Marteau *et al.*, Variable high gradient permanent magnet quadrupole (QUAPEVA), Appl. Phys. Lett., vol 111, p 253503, 2017
[9] A. Gaith *et al.*, in Proc. FEL2017, to be published
[10] C. Benabderrahmane, M. E. Couprie, SOLEIL, F. Forest, O. Cosson Sigmaphi, "Multi-pôle magnétique réglable", patent application WO2016034490 (10 March 2016).
[11] C. Benabderrahmane, M. E. Couprie, SOLEIL, F. Forest, O. Cosson Sigmaphi, "Adjustable magnetic multipole," Europe patent application WOBL14SSOQUA/CA (27 August 2015)

ISBN: 978-3-95450-206-6 doi:10.18429/JACoW-FLS2018-WEA2WD01

[12] M. E Couprie *et al.*, "An application of laser–plasma acceleration: towards a free-electron laser amplification," *Plasma. Phys. Contol. Fussion*, vol. 58, no. 3, p. 034020, 2016

[13] A. Loulergue *et al.*, "Beam manipulation for compact laser wakefield accelerator based free-electron lasers", *New J. Phys.*, vol. 17, no. 2, p. 023028, 2015

[14] T. André *et al.*, "Control of laser plasma accelerated electrons for light sources", Nature Comm., to be published

ISBN: 978-3-95450-206-6 doi:10.18429/JACoW-FLS2018-WEA2WD03

ANALYSIS OF ELECTRON TRAJECTORIES IN HARMONIC UNDULATOR WITH SCI-LAB'S MODEL BASED DESIGN CODES

H. Jeevakhan, S. Kumar, National Institute of Technical Teachers' Training and Research, Bhopal,India

G. Mishra, Physics Department, Devi Ahilya University, Indore, India

Abstract

Scilab's X-cos model-based simulation blocks have been used to simulate the trajectories of an electron traversing through a Harmonic undulator. The **trajectory** of electron along X direction has been simulated from Numerical and analytical methods. Analysis given in the present paper is compared with the other codes. Parallel simulation of Harmonic undulator magnetic field along with trajectories of electron is given in the present analysis.

INTRODUCTION

Fourth generation X-Ray Free electron laser (XFEL) light source is the state of art technology and have number of applications in cutting edge multidisciplinary research areas [1]. Spectral properties of out coming radiation in FEL depend upon numbers of parameters such as beam quality, magnetic structure, seed laser, trajectory of electron traversing in undulator and many more. Simulation software such as Radia and Poison are often used to design Undulator and calculate the magnetic field at on and Off axis. The raw data of magnetic field profile obtained from the simulation or measurements by Hall Probe method can be analysed to determine electron trajectories, intensity of spontaneous radiation, FEL gain in stimulated emission.

Model-based development (MBD) is a paradigm shift in software development. It's mainly focuses on executable models of the systems of equations. These models allow a wide range of analysis. Compare to traditional design flow, model-based design condensed development time. The main factors that contributed to the substantial reduction in development time is achieved by using model-based design: clocking, defect discovery, and component interfaces [2].

Scilab/Xcos an open source technology [3] had been used for number of applications such as remote control lab, real time experiments, and CDMA modelling [4-6]. Scilab/Xcos based simulation models for analytical solutions of electron trajectory equations have been presented with some limitations by H Jeevakhan etal [7]. In present analysis X-cos based on model based design has been employed to find the trajectory of the electron moving in the Harmonic undulator, variation of magnetic field along the axis of undulator. We have also presented a model to analyze trajectory in the magnetic field profile given by real undulator measurements and simulated by RADIA software.

PRESENT SIMULATION-UNDULATOR FIELD

Planar undulator magnetic field with additional small harmonic field is considered for simulation and is given by [8-9]

$$B = [0, a_0 B_0 (sin k_u z + \Delta sin k_h z), 0] \quad (1)$$

Where, $k_u = \frac{2\pi}{\lambda_u}$ and $k_h = \frac{2\pi}{\lambda_h}$ where k_u and k_h are undulator and harmonic undulator wave number respectively , λ_u is undulator wave length and $\lambda_h = h\lambda_u$, h is harmonic integer, B_0 is peak magnetic field, $\Delta = \frac{a_1}{a_0}$, a_0 and a_1 controls the amplitude of main undulator field and additional harmonic field respectively

The velocity and trajectory of electron in 'x' direction are deduced by using Lorentz force equation reads as

$$\beta_x = -\frac{K}{\gamma}\left[\cos(\Omega_u)t + \Delta\frac{\cos(h\Omega_u)t}{h}\right] \quad (2)$$

$$\frac{x}{c} = -\frac{K}{\gamma}\left[\frac{\sin(\Omega_u)t}{\Omega_u} + \Delta\frac{\sin(h\Omega_u)t}{h\Omega_u}\right] \quad (3)$$

Where γ is relativistic parameter, $K = \frac{a_0 e B_0}{\Omega_u m_0 c}$ is the undulator parameter, m_0 is rest mass of electron, and $\Omega_u = k_u c$

SIMULATION PARAMETERS

Analytical solution of trajectory along 'x' direction is simulated with the magnetic field given in Eq.(3) and Eq.(1) respectively. Table 1 gives the parameters of simulation used in the analysis. SCILAB's Model based simulation model using Xcos tool boxes has been designed for Eq.(3) and Eq.(1) . Each parameter in Table 1 is identified by a block in the simulation model. The parameter values can be changed by selecting the relevant block and alteration can be done.

Table 1: Parameters used for Simulation

Parameter	Symbol	Values
Undulator parameter	K	1
Number of Undulator periods	N	10
Undulator wavelength	λ	5cm
Relativistic parameter	γ	20
Harmonic integer	h	3
Contribution of harmonic field	Δ	0, 0.1, 0.2, 0.4

ISBN: 978-3-95450-206-6 doi:10.18429/JACoW-FLS2018-WEA2WD03

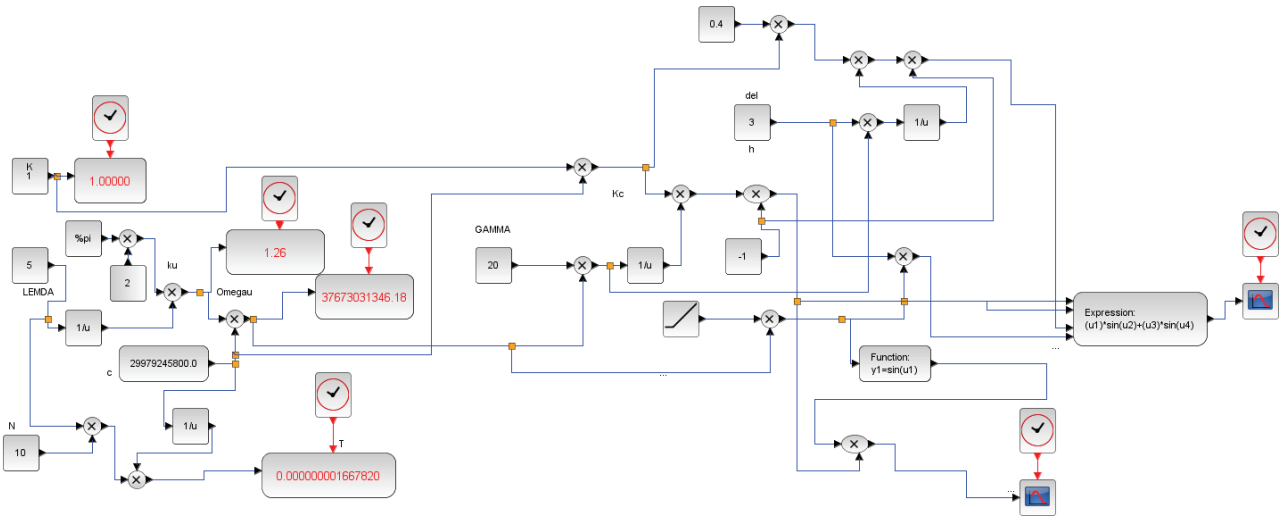

Figure 1: Simulation model of electron trajectory in planar and harmonic undulator.

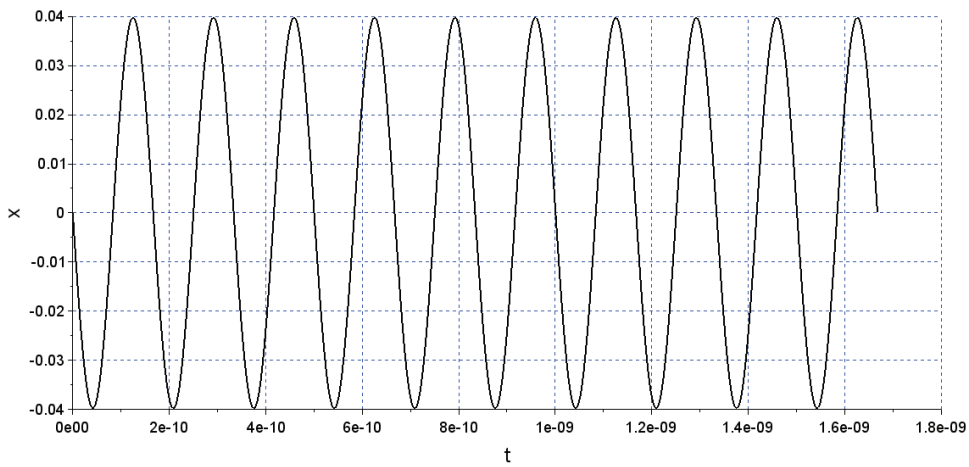

(a)

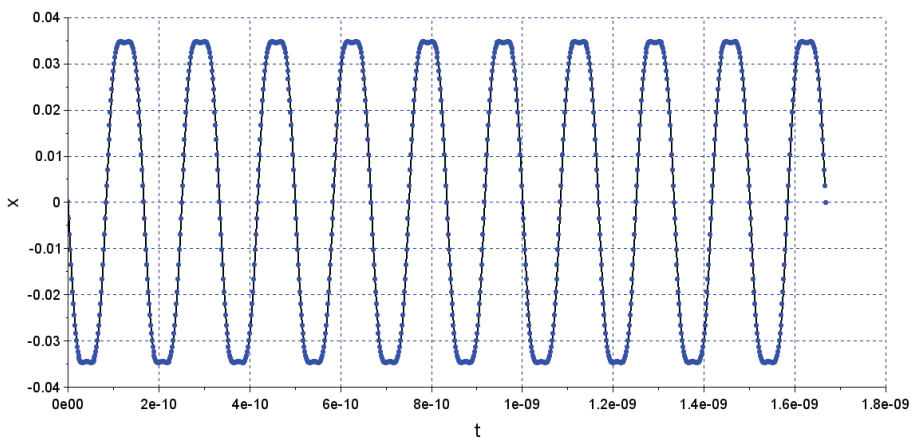

(b)

Figure 2: Trajectory of electron along 'x' in cm v/s time in seconds in planar and harmonic undulator.

ISBN: 978-3-95450-206-6 doi:10.18429/JACoW-FLS2018-WEA2WD03

Figure 1 represents the simulation model for equation (5) by using Scilab X-cos tools box and gives electron trajectory along 'x' direction. The total simulation time is 'T' for which the simulation has to be run is set according to the time of electron travel in insertion device. In present case it comes as 1.667 x 10^{-8} sec. In the preceding work the time interval from '0' to 'T has been set. The final value of trajectories has been stored in workspace and plot has been done in the command window of Scilab. In present model the time variation has been modelled as ramp block and figures have been plot along with the execution of the program. Figure 2a. and Figure 2 b display the parellel simultion for trajectory of electron in 'x' dire in plannar undulator without harmonic content and with harmonic content (Δ=0.4) respectively. Figure (2) b also displays the same simulation done by Fortram code by '.', the overlapping of two simualtion data asserts the correctness of the model desinged.

The advantages of using such simulation blocks instead of designing codes is that we dont have to remmeber the codes and same simulation block can be used for number of simulation parameters. In case to simulate Eq. (1).There is addition or deletion some blocks in the model given in Fig. 1 for simulation of Eq. 1. Figure 3 dspalys the simulation model for plannar and harmonic field. In Fig. 4 the planar undulator field simulataneously simulated with and without harmonic field (Δ=0.2).

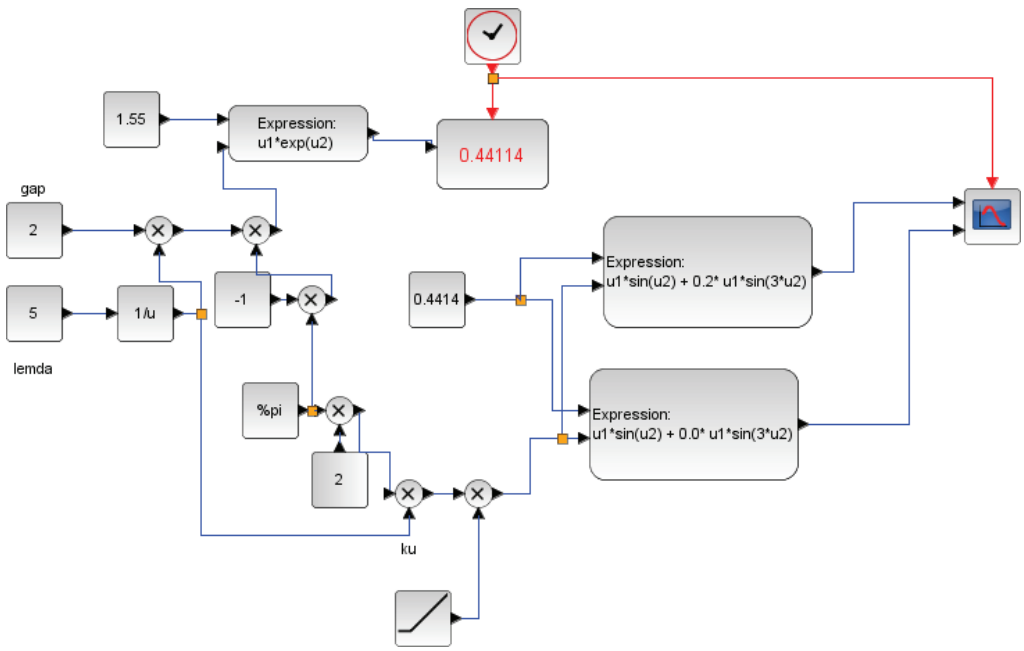

Figure 3: Simulation model for planar and harmonic undulator field in Xcos.

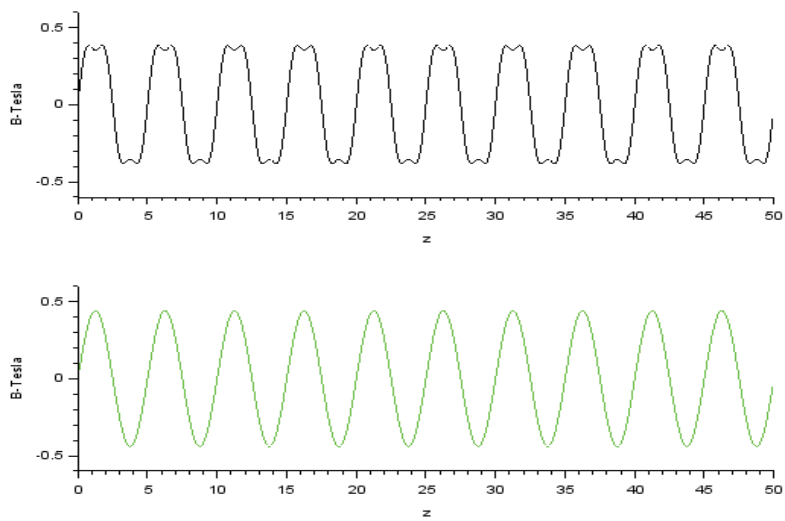

Figure 4:. On axis planar undulator magnetic field with and without harmonic content.

ISBN: 978-3-95450-206-6 doi:10.18429/JACoW-FLS2018-WEA2WD03

We have extended the present work to determine the the trajectory of electron in real undulator devices. Figure 5 displays the model degined for the analysis of trajectory along the undulator with real data of magnetic fields. The trajectory has been determined by product of $e/m_0\,\gamma c$ with double integration of magnetic field data. We have taken the data for magnetic field of proposed superconducting undulator by DAVV Lab, Indore [10] by radia codes. Figure 6 (a) displays the data for double integration with present model and in the same figure, the data for double integration from Mathematica code has also been displayed. Figure 6 (b) gives the trajectory along 'x' direction, simulated in the same model.

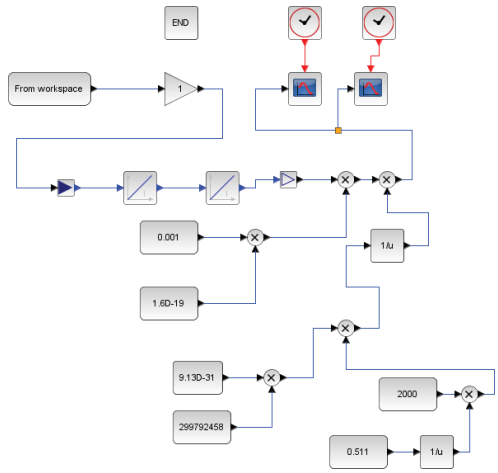

Figure 5: Simulation model for trajectory of electron using magnetic field data (measured by experiments/by simulation from codes).

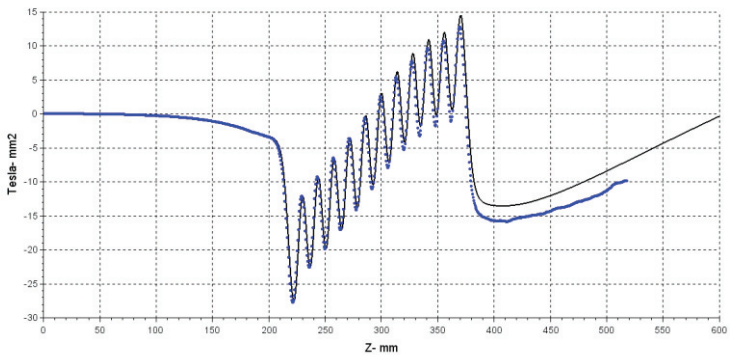

(a)

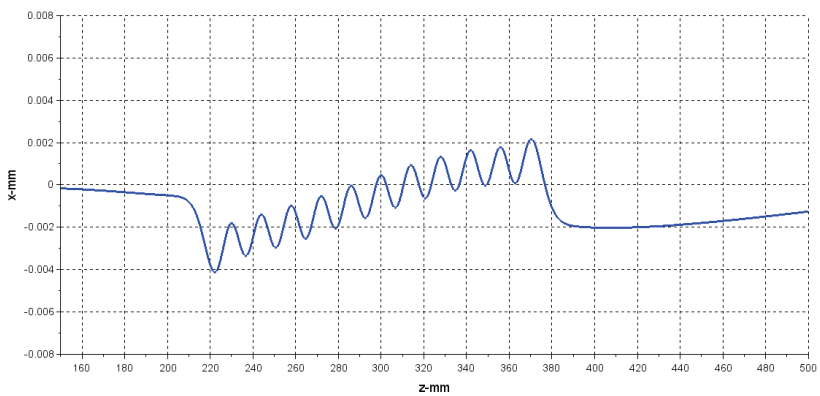

(b)

Figure 6: (a) Displays the double integration of magnetic field and (b) Displays the trajectory of electron using model given in Fig. 5.

ISBN: 978-3-95450-206-6 doi:10.18429/JACoW-FLS2018-WEA2WD03

CONCLUSION

In the present paper Scilab Xcos based model has been used for electron trajectories and magnetic field. Electron trajectory along 'x' direction and variation of magnetic field along 'z' direction has been modelled and simulated for Planar and Harmonic undulator. Expression block and ramp block has been used for variation of data. In present simulation plot of output data has been done parallel to simulation and is part of execution of program. These models do not require a separate plotter tool. In our analysis we have also presented the model for determination of trajectory in real system or in simulation model given by other codes considering the factors of possible errors in planar undulator magnetic field. The above work can be extended as a model for trajector in 'x' and 'y' direction, along with the intensity of spontaneous radiation. The GUI interface for present model is also a future scope of the work.

REFERENCES

[1] W.A. Barletta et al. Nuclear Instruments and Methods in Physics Research A 618 (2010) 69–96.

[2] https://www.umsec.umn.edu.

[3] SCILAB, https://www.scilab.org/

[4] Zoltán Magyar et al, Proceedings of the 9th IFAC Symposium Advances in Control Education

[5] Zoltán Janík, IJOE – Volume 9, Issue 1, February 2013.

[6] Mouhamed Fadel Diagana et al, nt. J. Communications, Network and System Sciences, 2015, 8, 274-281.

[7] H Jeevakhan et al , Indian PAC 2018 proceedings, Jan 2018, ID 267

[8] G. Dattoli, et al, Lectures on FEL Theory and Related Topics, World Scientific, Singapore.

[9] G. Mishra, Mona Gehlot, Jeevakhan Hussain, Journal of Modern Optics, vol. 56, p- 667,2009.

[10] G Mishra et al, J Synchrotron Radiat. 2017 Mar 1;24(Pt 2):422-428. doi: 10.1107/S16005-77517001540. Epub 2017 Feb 16

ISBN: 978-3-95450-206-6 doi:10.18429/JACoW-FLS2018-WEA2WD04

HARMONIC UNDULATOR RADIATION WITH DUAL NON PERIODIC MAGNETIC COMPONENTS

H. Jeevakhan, National Institute of Technical Teachers' Training and Research, Bhopal, India
G. Mishra, Physics Department, Devi Ahilya University, Indore, India

Abstract

Undulator radiation at third harmonics generated by harmonic undulator in the presence dual non periodic constant magnetic field has been analyzed. Electron trajectories along the 'x' and 'y' direction has been determined analytical and numerical methods. Generalized Bessel function is used to determine the intensity of radiation and Simpson's numerical method of integration is used to find the effect of constant magnetic fields. Comparison with previous analysis has also been presented.

INTRODUCTION

Free electron Lasers (FEL) generation is a state of art technology and has large numbers of applications in cutting edge technologies [1]. Tunability and brilliance at lasing wave length in FEL are the key parameters for number of research applications. Lasing wavelength of FEL depends upon the values of undulator parameter, undulator wavelength and relativistic parameter of electron beam. Recent works in FEL theory has emphasised the effect on non periodic magnetic field i.e. constant magnetic field component along or perpendicular or in both directions of the periodic magnetic field of planar undulator on the out coming undulator radiation(UR)[2-3]. Partial compensation on the divergence of UR has been demonstrated by imposing weak constant magnetic component in the analytical form and all the major sources of homogeneous and inhomogeneous broadening have been accounted for the characteristics of the electrons beam by K. Zhukovsky [4]. The constant non-periodic magnetic constituents are studied to compensate the divergence of the electronic beam [5]. Dattoli *et al* has initially reported the effect on UR from planar undulator with constant magnetic field component [6]. The later studies focuses on higher harmonics generation by addition of additional harmonic field [2-5].

Higher harmonic generation has been studied by using Harmonic undulator (HU) consists additional harmonic field along with sinusoidal planar magnetic field[7-13]. HU uses modest electron beam energy and lasing at third harmonic is reported by N.Sei *etal* [14]. The harmonic field can be generated by the addition of shims in the planar undulator structure[15-17]. Constant magnetic field may present due to errors in Undulator design and horizontal component of earth's magnetic field and modify the UR Magnetic field. H Jeevakhan *et al* have presented semi analytical results for the effect of perpendicular constant magnetic field on the gain of HU at higher harmonics [3,18]. In the present paper we have analysed HU with dual non periodic magnetic field. In the previous reported works the independent effect of constant magnetic field, parallel and perpendicular to planar undulator field had been analysed. The combined effect on intensity reduction due dual magnetic field has been presented. The additional harmonic field compensates the intensity loss in UR in presented model.

UNDULATOR FIELD

Planar undulator sinusoidal magnetic field encompasses with a perpendicular constant magnetic field in present analysis and is given by

$$B = \left[B_0\kappa_x, a_0B_0(sink_uz + \Delta sink_hz) + B_0\kappa_y, 0\right] \quad (1)$$

Where, $k_u = \frac{2\pi}{\lambda_u}$ and $k_h = \frac{2\pi}{\lambda_h}$ where k_u and k_h are undulator and HU wave number respectively , λ_u is undulator wave length and $\lambda_h = h\lambda_u$, h is harmonic integer, B_0 is peak magnetic field, $\Delta = \frac{a_1}{a_0}$, a_0 and a_1 controls the amplitude of main undulator field and additional harmonic field, $\kappa_y$and κ_x are the magnitudes of constant non periodic magnetic field parallel and perpendicular to main undulator field.

The velocity of electron passing through undulator is derived by using Lorentz force equation:

$$\frac{dv}{dt} = -\frac{e}{\gamma mc}\left(\bar{v} \times \bar{B}\right) \quad (2)$$

This gives

$$\beta_x = -\frac{K}{\gamma}\left[\cos(\Omega_u)t + \Delta\frac{\cos(h\Omega_u)t}{h} - \kappa_y\Omega_ut\right]$$

$$\beta_y = -\frac{K}{\gamma}\kappa_x\Omega_ut \quad (3)$$

$$\beta_z = \beta^* - \frac{K^2}{2\gamma^2}\left[\left\{\frac{1}{2}\cos(2\Omega_u)t + \frac{1}{2}\left(\frac{\Delta}{h}\right)^2\cos(2h\Omega_p)t + \left(\frac{\Delta}{h}\right)\cos(1\pm h)\Omega_ut - 2\kappa_y\Omega_utcos\,(\Omega_ut) - 2\kappa_y\Omega_utcos(h\Omega_ut)\right\} + (\kappa_x^2 + \kappa_y^2)\Omega_u^2t^2\right] \quad (4)$$

Where $m\ and\ m_0$ are relativistic and rest mass of electron respectively and value of m is governed by the relativistic parameter γ , $K = \frac{a_0eB_0}{\Omega_um_0c}$ is the undulator parameter and $\beta^* = 1 - \frac{1}{2\gamma^2}\left[1 + \frac{K^2+K_1^2}{2}\right]$ with $K_1 = \frac{\Delta K}{h}$ and $\Omega_u = k_uc$.

The solution of Eq. 4 gives the electron trajectory along z direction,

ISBN: 978-3-95450-206-6 doi:10.18429/JACoW-FLS2018-WEA2WD04

$$\frac{z}{c} = \beta^* t - \frac{K^2}{8\gamma^2\Omega_u}\sin(2\Omega_u t) - \frac{K_1^2}{8\gamma^2 h\Omega_u}\sin(2h\Omega_u t) - \frac{KK_1}{2\gamma^2(1\pm h)\Omega_u}\sin(1\pm h)\,\Omega_u t + \frac{K^2\kappa_y t\sin(\Omega_u t)}{\gamma^2} + \frac{K^2\kappa_y\cos(\Omega_u t)}{\gamma^2\Omega_u} + \frac{KK_1\kappa_y t\sin(h\Omega_u t)}{h\gamma^2} + \frac{KK_1\kappa_y\cos(h\Omega_u t)}{h^2\gamma^2\Omega_u} - \frac{K^2(\kappa_x^2+\kappa_y^2)\ \Omega_u{}^2 t^3}{6\gamma^2} \quad (5)$$

The spectral properties of radiation can be evaluated from Lienard - Wiechart integral [19-20],

$$\frac{d^2I}{d\omega d\Omega} = \frac{e^2\omega^2}{4\pi^2 c}\left|\int_{-\infty}^{\infty}\{\hat{n}\times(\hat{n}\times\hat{\beta}\}exp\left[i\omega(t-\frac{z}{c})\right]dt\right| \quad (6)$$

when integrated over undulator length, $T = \frac{2N\pi}{\Omega_u}$ and $'\omega'$ is the emission frequency with variables as

$$\xi_1 = -\frac{\omega K^2}{8\gamma^2\Omega_u},\ \xi_2 = -\frac{\omega K_1^2}{8\gamma^2 h\Omega_u},$$
$$\xi_{3,4} = -\frac{\omega K K_1}{2\gamma^2(1\pm h)\Omega_u}$$
$$\xi_5 = -\frac{\omega K^2\kappa_y}{\gamma^2\Omega_u}, \text{ and } \xi_6 = -\frac{\omega K K_1\kappa_y}{h^2\gamma^2\Omega_u}$$

The brightness expression read as

$$\frac{d^2I}{d\omega d\Omega} = \frac{e^2\omega^2}{4\pi^2 c}\left(\frac{K}{\gamma}\right)^2\left[\left|\hat{\imath}\int_{-\infty}^{\infty}dt\left\{cos(\Omega_u t)+\frac{\Delta}{h}cos(h\Omega_u t)-\kappa_y\Omega_u t\right\}expi(\vartheta t + \varphi t^3)J_m(0,\xi_1)J_n(0,\xi_2)J_p(\xi_3)J_q(\xi_4)J_r(\xi_5)J_s(\xi_5)J_u(\xi_6)J_v(\xi_6)\right|^2 + \left|\hat{\jmath}\int_0^T dt\{\kappa_x\Omega_u t\}\,expi(\vartheta t + \varphi t^3)J_m(0,\xi_1)J_n(0,\xi_2)J_p(\xi_3)J_q(\xi_4)J_r(\xi_5)J_s(\xi_5)J_u(\xi_6)J_v(\xi_6)\right|^2\right] \quad (7)$$

$$\vartheta = \frac{\omega}{\omega_1} - \{m+nh+p(1+h)+q(1-h)+r+s+uh+vh\}\Omega_u$$

$$\varphi = \frac{\omega K^2(\kappa_x^2+\kappa_y^2)\Omega_u{}^2}{6\gamma^2}$$

And Eq. (7) can be further reduced to

$$\frac{d^2I}{d\omega d\Omega} = \frac{e^2\omega^2T^2}{4\pi^2 c}\left\{|I_{x1}+I_{x2}+I_{x3}|^2 + |I_y|^2\right\} \quad (8)$$

With

$$I_{x1} = \frac{K}{2\gamma}\left[J_{m+1}(0,\xi_1)+J_{m-1}(0,\xi_1)\right\}J_n(0,\xi_2)J_p(\xi_3)J_q(\xi_4)J_r(\xi_5)J_s(\xi_5)J_u(\xi_6)J_v(\xi_6)\Big]S(\vartheta,\varphi)$$

$$I_{x2} = \frac{K}{2\gamma}\left[\frac{\Delta}{h}\{J_{n+1}(0,\xi_2) + J_{n-1}(0,\xi_2)\}J_m(0,\xi_1)J_p(\xi_3)J_q(\xi_4)J_r(\xi_5)J_s(\xi_5)J_u(\xi_6)J_v(\xi_6) + \right]S(\vartheta,\varphi)$$

$$I_{x3} = \frac{2i\pi K\kappa_y N}{\gamma}S'(\vartheta,\varphi)\ I_y = \frac{2i\pi K\kappa_x N}{\gamma}S'(\vartheta,\varphi)$$

$$S(\vartheta,\varphi) = \left|\int_0^1 e^{(\vartheta'\tau+\varphi'\tau^3)}d\tau\right| \quad (9)$$

$$S'(\vartheta,\varphi) = \frac{\partial S(\vartheta,\varphi)}{\partial\vartheta} = \left|\int_0^1 \tau e^{(\vartheta'\tau+\varphi'\tau^3)}d\tau\right| \quad (10)$$

$\vartheta' = \vartheta T, \varphi' = \varphi T^3$ and $\tau = {}^t/_T$ is unit interaction time.

For $\kappa_x = 0$, Eq. (8) changes to

$$\frac{d^2I}{d\omega d\Omega} = \frac{e^2\omega^2T^2}{4\pi^2 c}\{|I_{x1}+I_{x2}+I_{x3}|^2\} \quad (11)$$

With altered value of φ as

$$\varphi = \frac{\omega K^2(\kappa_y^2)\Omega_u{}^2}{6\gamma^2}$$

For $\kappa_y = 0$,Eq. (8) changes to

$$\frac{d^2I}{d\omega d\Omega} = \frac{e^2\omega^2T^2}{4\pi^2 c}\left\{|I_{x1}+I_{x2}|^2 + |I_y|^2\right\} \quad (12)$$

With altered value of I_{x1}, I_{x2} φ as

$$I_{x1} = \frac{K}{2\gamma}[J_{m+1}(0,\xi_1) + J_{m-1}(0,\xi_1)\}J_n(0,\xi_2)J_p(\xi_3)J_q(\xi_4)]S(\vartheta,\varphi)$$

$$I_{x2} = \frac{K}{2\gamma}\left[\frac{\Delta}{h}\{J_{n+1}(0,\xi_2) + J_{n-1}(0,\xi_2)\}J_m(0,\xi_1)J_p(\xi_3)J_q(\xi_4) + \right]S(\vartheta,\varphi)$$

$$\varphi = \frac{\omega K^2(\kappa_x^2)\Omega_u{}^2}{6\gamma^2}$$

RESULT AND DISCUSSION

Equation (8) reads the intensity of spontaneous UR extracting from HU with dual non periodic magnetic field. The line shape functions $S(\vartheta,\varphi)$ and $S'(\vartheta,\varphi)$ in Eq.(8) are given by Eq.(9) and Eq.(10) respectively. In earlier reported work [3,6,18] the term in Eq.(8) consisting $S'(\vartheta,\varphi)$ has been neglected due to diminishing value of κ. In our analysis we have included this term in numerical integration and its effect on the line shape function. The parameters used for simulation are listed in Table 1.

Table 1: Parameters Used for Simulation

Parameter	Symbol
Undulator parameter	K=1
Electron bean relativistic parameter	$\gamma = 100$
Undulator wavelength	$\lambda_u = 5cm$
Addition periodic harmonic field number	$h = 3$
Harmonic field parameter	K_1=0 - 0.11
Number of period	N=100

ISBN: 978-3-95450-206-6 doi:10.18429/JACoW-FLS2018-WEA2WD04

Figure 1 illustrates the intensity distribution of radiations given by Eq. (11) and (12) with symmetric electron beam at third harmonic in arbitrary units with selection of parameters given in table 1 and different values of $\kappa_y$and κ_x. There is a shift in resonance and reduction in intensity with effect of non periodic constant field contribution. The lines and the scattered points in the Fig. 1 are for Eq. (11) and Eq. (12) respectively, overlapping of scattered points over lines indicates that both equation results same output. For same values of κ_y or κ_x , the intensity distribution is same irrespective of change in values for arguments of Bessel function as given in Eq. (11) and (12). Values of κ_y at κ_x dominates the intensity distributions irrespective to the change of arguments of Bessel function. The shift in resonance at third harmonic is more or less same to previous reported works [3,18]. For a particular value of κ =0.00008 the resonance shift is around 0.0045 and the intensity reduction is nearly 12 % at third harmonic.

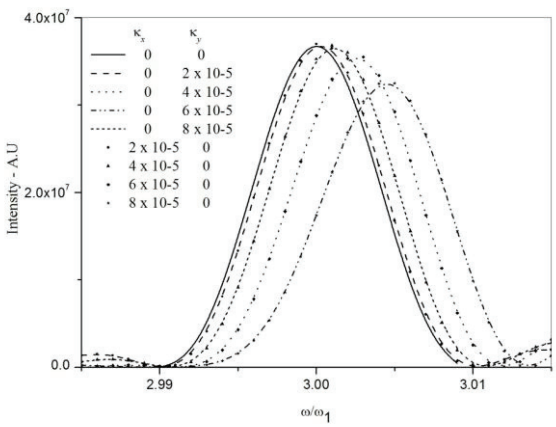

Figure 1: Frequency Spectrum at third harmonic with parameter given in table 1 varying constant magnetic field parameter κ_y and κ_x.

In Fig. 2 we have presented numerical solution for Eq. (8) and it demonstrate the combining effect of both non periodic component on intensity distribution at third harmonic. The line shape function distort from Gaussian for values κ_y and κ_x more than 0.00006. All the parameter are kept same as used in Fig. 1. The intensity degradation for the values of κ_y and κ_x at 0.00004, resembles with the value of either of κ_y and κ_x as 0.00006 as square of later nearly equals to the addition of square of former vales of κ_y and κ_x.

The intensity degradation mainly occurs due to energy spread in the electron beam, and in present case is due to additional non periodic magnetic field. It can be accommodated by additional harmonic field. The harmonic field enhances intensity and compensate the loss due to constant magnetic field. The intensity at third harmonics with constant magnetic field as $\kappa_y = \kappa_x = 0.00006$ and variation harmonic field parameter as K1 = 0.0 to 0.11 is shown in Fig. 3 and keeping all the remaining parameter as given in Table 1. As a particular case intensity reduction by κ = 0.00006 can be compensated by additional harmonic field K1 = 0.11 as manifested in Fig. 3.

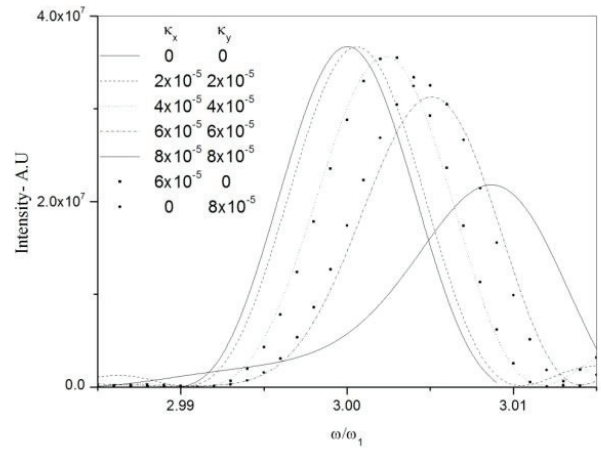

Figure 2: Frequency Spectrum at third harmonics with parameters same given in table 1, varying $\kappa_y = \kappa_x$.

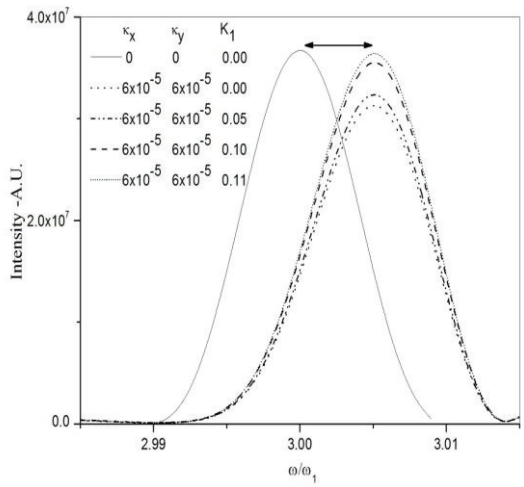

Figure 3: Frequency Spectrum at third harmonics with varying harmonic Field amplitude as K_1=0 and 0.11, $\kappa_y = \kappa_x$ =0.00006, and rest parameters same as in Fig. 1.

ISBN: 978-3-95450-206-6 doi:10.18429/JACoW-FLS2018-WEA2WD04

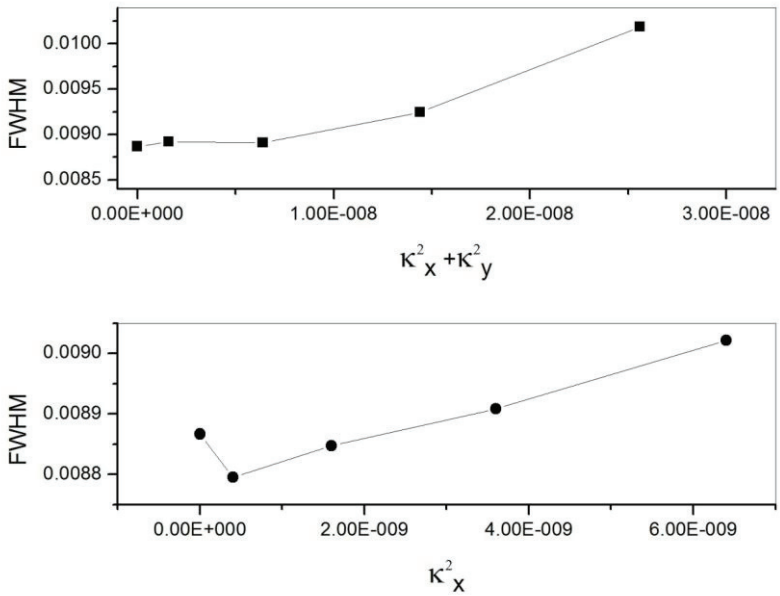

Figure 4: Variation of FWHM at third harmonics with varying κ_y and κ_x and rest parameters same as in Fig. 1.

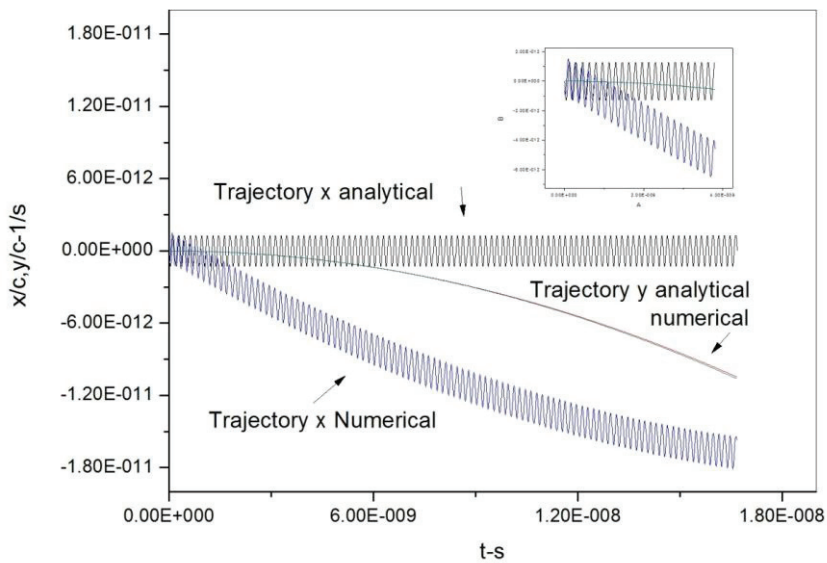

Figure 5: Trajectory of electron along x and y directions at $\kappa_y = \kappa_x = 0.00004$ by analytical and numerical method.

Figure 4 displays the variation of FWHM with κ_x^2 and $\kappa_x^2 + \kappa_y^2$. As from the figure it is clear that along with intensity reduction the FWHM also increases with increase in value of non periodic constant magnetic field. The effect will be more in the presence of dual constant magnetic components. The constant

ISBN: 978-3-95450-206-6 doi:10.18429/JACoW-FLS2018-WEA2WD04

components of magnetic field are also possible reasons for broadening of line shape function along with energy spread in FEL systems.

Equations 3 and 4 are integrated to get trajectory along 'x' , 'y' directions and 'z ' directions. Equation 5 gives the analytical solution of Eq.4. Figure 5 gives graphical representation of the analytical and numerical solutions by Runga-Kutta method of Eq. 3 and 4.The trajectory along 'y' directions by analytical and numerical method nearly coincides, whereas there is a deviation in the values of trajectory along 'x' direction simulated by analytical and numerical method.

In conclusions, we have presented the expression for on axis spontaneous radiation by UR with harmonic and dual constant magnetic field component. There is as an intensity reduction and line shape broadening due to presence of constant magnetic field, along the main field due to error in design and perpendicular to main field due to horizontal component earth's Magnetic field. Enhancement in intensity at third harmonics can be done by additional harmonic field where as shift in resonance remains unaltered. Analytical and Numerical approach has been used to find the trajectory of electron in Multiple magnetic field. The deviation of trajectory from the axis affects out coming on axis intensity. Effect of Electron beam emittance and beam divergence in presence of constant field, properties of out coming radiation at different angle and solution to resonance shift are the future scope of studies for present work.

REFERENCES

[1] W.A. Barletta *et al*. *Nuclear Instruments and Methods in Physics Research A* 618 (2010) 69–96.

[2] K. Zhukovsky *et al, Laser and Particle Beams,* 0263-0346/17 (2017).

[3] Hussain Jeevakhan, G Mishra, Optics Communications335 (2015) 126-128.

[4] K. Zhukovysk , Optics Communications 353(2015) 35–41.

[5] K. Zhukovsky, *Laser and Particle Beams* (2016), 34, 447–456.

[6] G. Dattoli *et al Journal of applied physics* 104, (2008)124507 .

[7] N.Nakao *et al. Nuclear Instruments and Methods in Physics A*, 407, p-474, 1998.

[8] Vikesh Gupta, G. Mishra, Nuclear Instr. and Meth. in Physics Research A,574,p-150,2007.

[9] Y. Yang, Wu Ding, Nuclear Instr. and Meth in Physics Research ,A, 407,p-60,1998.

[10] G. Mishra, Mona Gehlot, Jeeva Khan Hussain, Journal of Modern Optics, vol. 56, p- 667,2009.

[11] G. Mishra, Mona Gehlot, Jeeva Khan Hussain, Nuclear Instruments and Methods in Phy. Res. A, vol.603,p-495,2009.

[12] V.I.R. Niculescu, Minola R. Leonnovici, V. Babin, *Anca Scarisoreanu, Rom. Journ. Phys.,* Vol.53, Nos. 5-6, P-775,2008.

[13] Jeeva Khan Hussain, Vikesh Gupta, G.Mishra, IL *Nuovo Cimento B*, Vol 124 B,2009.

[14] N. Sei, M. Asakawa and K. Yamada, *J. Phys Soc Jpn 9*, 093501 (2010).

[15] M. Asakawa *et al.,Nucl. Instrum. Methods Phys.* Res. A 375, 416 (1996).

[16] M. Gehlot, G. Sharma, G. Mishra, H. Jeevakhan and S. Tripathi, *Chin. Phys. Lett. 3*0,084101 (2013).

[17] G Sharma *et al ,Advances in Synchrotron Radiation* Vol. 3, No. 1 (2014) 1450001.

[18] H Jeevakhan *et al,*Proceedings FEL 2015 MOP004.

[19] J. D. Jackson, "Classical Electrodynamics", Wiley, New York, 1975.

[20] G. Dattoli *et al,* Lectures on FEL Theory and Related Topics, World Scientific, Singapore.

ISBN: 978-3-95450-206-6 doi:10.18429/JACoW-FLS2018-WEP2PT003

UNDULATOR PHASE MATCHING FOR THE THE EUROPEAN XFEL

Y. Li, J. Pflueger, European XFEL GmbH, Hamburg, Germany

Abstract

The undulator system in the European XFEL is mainly comprised 5-m long undulator segments and 1.1 m long intersections in between. In intersections the electron velocity is faster than it inside an undulator and the optical phase is detuned. The detune effect is also from the undulator fringe field where electron longitudinal speed also deviates from the oscillation condition. The total detune effect is compensated by a magnetic device called phase shifter, which is correspondingly set for a specific undulator gap. In this paper we introduce the method to set the phase shifter gap for each K parameter according to the measured magnetic field.

INTRODUCTION

High gain free electron lasers (FELs) using the principle of Self-Amplified Spontaneous Emission (SASE) are so far the only way to generate FEL radiation in the hard X-ray range [1-5]. For VUV radiation alternatives such as harmonic generation exist generate radiation which lead to increased stability [6]. However, aside from such differences both require long undulator systems with lengths from tens of meters up to about 200 meters depending on the radiation wavelength, electron beam and undulator parameters. Such a long undulator system cannot be built as a continuous device. For practical reasons of manufacturing it must be segmented into lengths around typically 5m maximum.

For the FEL process the interruption of the undulator implies a problem: The longitudinal speed of the electrons in the intersection is different to that inside the undulator and therefore the optical phase matching between laser field and electron motion is perturbed. In a fixed gap undulator system such as FLASH [1,2]or LCLS I [3] phase matching can be obtained by choosing the intersection length and tuning the end fields of the undulator segments properly. The phase matching in a gap tunable system is more complicated since the phase mismatch in the intersection changes with undulator gap. With a phase shifter, a small magnetic chicane, an additional delay is induced in the electron orbit. By properly selecting the phase shifter strength and hence the delay the optical phase can be matched at any gap [7].

The European X-ray free electron laser (EXFEL) facility [5] is a large project driven by a 1.8 kilometer long superconducting linac. The SASE FEL is used throughout the European XFEL. An electrons beam is accelerated up to maximum of 17.5 GeV. Then it is guided through the undulator system to generate high quality soft and hard X-rays. The radiation wavelength can be changed by variation of the undulator gap and in addition the beam energy: The hard X-ray range from 0.1 to 0.4 nm is covered by two undulator lines called SASE1 and SASE2. The soft X-Ray wavelength range from 0.4 to 1.6 nm is covered by one undulator line called SASE3.

For all SASE beam lines the undulators and phase shifters are well characterized before installation: Undulators were accurately tuned for small trajectory and phase errors in the operational gap range [8,9]. After tuning the characterization for each segment includes high resolution field maps as a function of gap in 0.5mm steps. They are the basis for the calculation of device properties such as K-Parameter, optical phase errors, trajectory wander etc. All phase shifters were well tuned and characterized as well [10-13].

An undulator system comprised of many segments is best controlled by the K-Parameter, which directly relates to the radiation wavelength, and not by the individual gaps, which differ slightly from segment to segment due to manufacturing and material tolerances. The K-parameter plays a key role and needs to be provided with an accuracy of $\Delta K/K \leq 2 \times 10^{-4}$.

PHASE MATCHING STRATEGY

Practical Situation

One feature of the undulator system for SASE FEL is that all segments must work cooperatively: In order not to deteriorate the FEL process the individual K-parameters need to be provided with an accuracy determined by $\Delta K/K \leq \rho$ where ρ is the Pierce parameter, which for EXFEL is about 2×10^{-4}. Therefore in an undulator system the gaps of individual undulator segments need to be adjusted so all match the same K.

On the other side field measurement on undulators is made by controlling the gap, which can be directly controlled mechanically with micrometer precision. Therefore, the K-parameters for each segment needs to be evaluated by interpolation from measurements made at different gaps.

Phase Matching Criteria

Figure 1 illustrates two undulator cells. Each cell is subdivided into four regions: On going from left to right the beginning of a cell is chosen in the field free region in the very left before the undulator. The region from at the beginning of the cell to the beginning of undulator bulk poles, including the drift space and the undulator fringe field, is called entrance fringe. The phase advance in this part is φ_{Entr}. The periodic field region inside the undulator is called bulk field. The phase advance over this region is φ_{Bulk}. Ideally at the first harmonic the phase advance in this region is 2π per period. Similar to the entrance fringe the region from the end of bulk field to the beginning of phase shifter is called exit fringe with the phase advance φ_{Exit}. In the field free region after the exit fringe the phase shifter is placed. The phase advance over the phase shifter is φ_{PS}. Since the phase shifter has very low fringe fields [7], it does not interfere with the undula-

ISBN: 978-3-95450-206-6 doi:10.18429/JACoW-FLS2018-WEP2PT003

tor and the spatial extension is very close to its physical length of 230mm only. The region after the phase shifter is again field free. Accordingly the phase advance over the first undulator cell can be written as $\varphi_{\mathrm{Und},1} = \varphi_{\mathrm{Entr},1} + \varphi_{\mathrm{Bulk},1} + \varphi_{\mathrm{Exit},1} + \varphi_{\mathrm{PS},1}$.

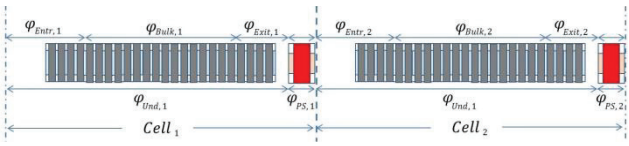

Figure 1: Definition of the different field regions in two sample undulator cells.

Only planar undulators are used at the European XFEL, so only the vertical field B_y plays a role. The horizontal field component B_x resulting from field errors is less than $\approx 10^{-3}$ times smaller than the main field component and can be neglected. The energy radiated per unit solid angle per unit frequency interval $dI(\omega)/d\Omega$ is $dI(\omega)/d\Omega = 2|A(\omega)|^2$ [14, 15]. The on-axis radiation of a planar undulator $A(\omega)$ is written as:

$$A(\omega) = i\left(\frac{e^2}{8\pi^2 c}\right)^{1/2}\frac{k}{\gamma}\int_0^z I_{1y}(z_1)e^{ik[\int_0^{z_1}\frac{1}{2\gamma^2}(1+I_{1y}^2(z_2)dz_2)]}dz_1, \quad (1)$$

where $k = \frac{2\pi}{\lambda_{Rad}}$ is the wave number, λ_{Rad} the radiation wavelength, c is the speed of light, e the electron charge and γ the kinetic energy in units of the electron rest mass. I_{1y} is the 1st field integral of B_y. The argument of the exponential function in Eq. (1) is the optical phase function [15]:

$$\varphi(z_1) = \int_0^{z_1}\frac{k}{2\gamma^2}(1 + I_{1y}^2(z_2)dz_2). \quad (2)$$

For convenience a normalized form of A, A_n, is used. In terms of the optical phase $\varphi(z_1)$ and the 1st field integral Eq. (1) is rewritten:

$$A_n = \int_0^z I_{1y}(z_1)e^{i\varphi(z_1)}dz_1. \quad (3)$$

A_n is complex. A_n for two undulator segments is the vector sum of two complex numbers. Using the normalized form is written as:

$$A_{n,sum} = A_{n,1} + e^{i(\varphi_{Und,1}+\varphi_{PS})}A_{n,2}, \quad (4)$$

where $A_{n,1}$ and $A_{n,2}$ denote A_n of the first and the second undulator, respectively. Both undulators and the corresponding radiation are similar but not identical. Each can be expressed in complex polar coordinates as:

$$A_n = |A_n|e^{i\psi}. \quad (5)$$

ψ is the phase of the radiation complex, A_n and must not be confused with the optical phase φ.

The total A_n of two undulators is the complex sum of two. Eq (4) is then rewritten as:

$$A_{n,sum} = |A_{n,1}|e^{i\psi_1} + |A_{n,2}|e^{i\psi_2}\cdot e^{i(\varphi_{Und,1}+\varphi_{PS})} \quad (6)$$

The maximum for $|A_{n,sum}|$ is obtained if the condition:

$$\psi_1 = \varphi_{und,1} + \varphi_{PS} + \psi_2 + 2n\pi \quad (7)$$

is fulfilled where n is an integer. Eq.(7) is the criterion for calculating the phase matching. Figure 2 gives an illustrative description. A_n of the two undulators are plotted in the complex plane. If Eq. (7) is fulfilled the resulting A_n is longest if $A_{n,1}$ and $A_{n,2}$ are collinear.

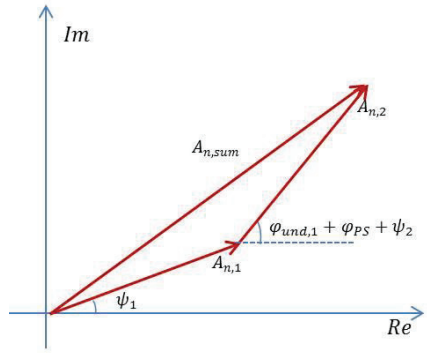

Figure 2: Sum of the $A_n$of two undulators. The length of A_n is maximum if the condition $\psi_1 = \varphi_{und,1} + \varphi_{PS} + \psi_2 + 2n\pi$ is satisfied.

In order to explain the relation between the phase of the complex A_n, ψ, and the optical phase φ, we analyse an undulator field comprised by an ideal bulk field and two ending field. Eq.(3) is expressed by the integral over different parts of an undulator as sketched in Figure 1:

$$A_n = \delta_{entr} + e^{i\varphi_{Entr}}\int_{L_{entr}}^{L_{entr}+L_{bulk}} I_{1y}(z_1)e^{i\varphi(z_1)}dz_1 + \delta_{exit}. \quad (8)$$

Where $\delta_{entr} = \int_0^{L_{entr}} I_{1y}(z_1)e^{i\varphi(z_1)}dz_1$, $\delta_{exit} = e^{i(\varphi_{Entr}+\varphi_{bulk})}\int_{L_{entr}+L_{bulk}}^{L_{entr}+L_{bulk}+L_{exit}} I_{1y}(z_1)e^{i\varphi(z_1)}dz_1$ are the contributions to A_n from the undulator end fields at the entrance and exit. In the end field sections the poles have different strength from the bulk and the optical field is out of resonance. δ_{entr} and δ_{exit} only contribute to the optical phase advance φ_{Entr} and φ_{Exit} but at resonance their contributions to the modulus of A_n are negligibly small. Therefore Eq. (8) is simplified:

$$A_n \approx e^{i\varphi_{Entr}}\int_{L_{entr}}^{L_{entr}+L_{bulk}} I_{1y}(z_1)e^{i\varphi(z_1)}dz_1. \quad (9)$$

The bulk field is expressed by sinus function and expressed in terms of Bessel functions [16]:

$$A_n \approx -e^{i\varphi_{Entr}}K\cdot N\frac{\lambda_u}{2}[J_0(\frac{K^2}{1+0.5K^2}) - J_1(\frac{K^2}{1+0.5K^2})]. \quad (10)$$

Where N is the number of periods. J_0 and $J_1$are the Bessel functions of integer order 0 and 1.

Eq. (10) shows that the contribution from the bulk field to the vector potential is real, since the phase advance per period is 2π. Therefore $\varphi_{bulk} = 0$ and has no effect on the phase of A_s. So ψ, is determined by the entrance field of an undulator:

$$\psi = \varphi_{entr}. \quad (11)$$

Because in an ideal undulator $\varphi_{bulk} = 0$ and $\varphi_{und} = \varphi_{entr} + \varphi_{bulk} + \varphi_{exit}$, the criteria of Eq. (7) for phase matching can be written in the format of optical phase:

$$\varphi_{exit,1} + \varphi_{PS} + \varphi_{entr,2} = 2n\pi. \quad (12)$$

Eq. (12) gives a criterion for the phase matching of two undulators: The optical phase from the last bulk pole of the upstream undulator should change integral times of 2π to the first bulk pole of the next undulator. However, Eq. (12) assumes an ideal bulk field of the undulator with results in a phase advance of 2π per period over the whole undulator. In practice phase errors are unavoidable and the accuracy of Eq. (12) is affected by field errors.

ISBN: 978-3-95450-206-6 doi:10.18429/JACoW-FLS2018-WEP2PT003

MATCHING RESULTS

Comparison of K for Two Undulators

A SASE undulator system such as SASE1 or SASE2 of the European XFEL comprises 35 undulator segments and 34 phase shifters, which have to be matched together by applying the methods derived in the last section. For all these components accurate magnetic measurement data are available: For all undulators there are accurate high resolution field maps.

For demonstration of the method two undulator segments, the U40-X005 and the U40-X006 and one phase shifter, the PS073, are used. The K-parameter of the two undulators is set from 1.5 up to 3.9 with a step size of 0.2. The gap for each segment was fitted to match the desired K-parameter. Fig. 3 illustrates the required gap of the two segments as a function of K. The blue curve shows the difference. It is seen that there is an almost constant difference of about 0.15 mm with a very slight variation with gap. It is due to differences in the mechanics, encoder initialization and magnet structure and shows the need of individual gap adjustment. This is a quite representative for other undulator segments as well.

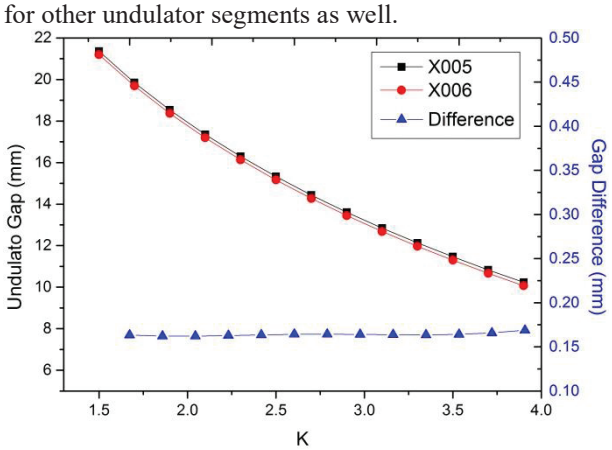

Figure 3: Gap vs. K-parameter for the U40-X005, black squares, and U40-X006, red circles. The difference is shown by the blue triangles.

Phase Matching using the A_n

The condition for proper phase matching is defined by Eq. (7). The real and imaginary part of the normalized A_n using Eq (3) and the phase ψ, can be calculated. Figure 4 demonstrates the phase matching using the hodograph representation.

The abscissa represents the real and the y-axis the imaginary part in arbitrary units. Two cases representing the maximum and minimum K values, 3.9 and 1.7, are chosen for demonstration. Going along a perfect undulator the complex evolves along a straight line starting at 0. For each K value, two conditions called 'matched' and 'anti-matched' are shown. 'Matched' fulfils the phase matching condition, Eq. (7) i.e. 2nπ. For the 'Anti-matched' condition the phase delay between the undulators is (2n+1) π. Results are shown by the left and right plots, respectively. The start angle is different to various K value and it depends on the entrance ending field. It is seen that in the matched condition the A_n of two the undulators, U40-X005 and U40-X006, have the same in length and point in exactly the same direction and the total length of the radiation from two undulators is twice the length of a single one and reaches the maximum intensity as illustrated in Figure 2. In contrast as seen by the right plot in the anti-matched condition A_n of the two undulators have again the same length but reverse direction. Therefore the total length is zero. It should be emphasized that this applies to the forward direction only. The effect of residual field errors is seen by some small wiggles on the lines and resulting small deviations from perfect straightness.

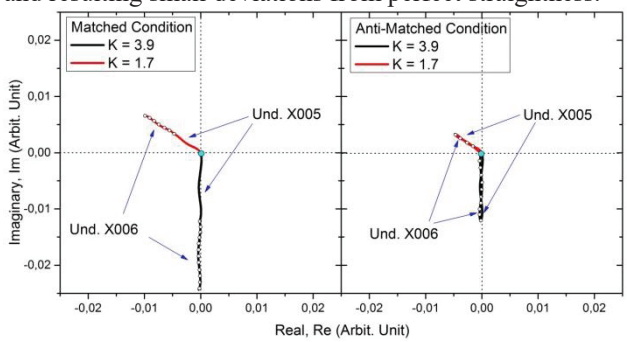

Figure 4: Hodograph of the real and imaginary part of the radiation A_n for two K values. The left plot corresponds matched phasing with 2nπ phase difference. The right plot corresponds anti-matched phasing with (2n+1)π phase difference leading to zero amplitude in forward direction.

Small differences in the ending fields as well as small individual differences in the phase shifter require strict matching of undulators and phase shifters. Figure 5 shows the required phase shifter gap as a function of the undulator K-parameter. The phase shifter can be operated on different phase numbers, ν, [7]. In order to have a sufficiently large tuning range over the whole operational K harmonic number $\nu = 14$ or larger needs to be used. Fig. 5 shows the results. Each curve corresponds to a specific harmonic number. It is seen that the larger the harmonic number the larger the K range. However at large K the space between the curves gets smaller and the phase gets more sensitive to the phase shifter gap.

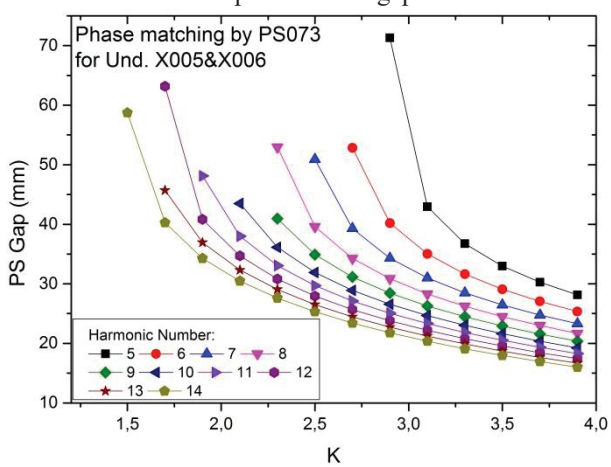

Figure 5: The required gap of phase shifter PS073 placed between U40-X005 and U40-X006 as a function of the K-

ISBN: 978-3-95450-206-6 doi:10.18429/JACoW-FLS2018-WEP2PT003

parameter. The individual curves correspond to different phase numbers. Continuous tuning over the whole K-range requires harmonic numbers ≥14.

Phase Matching by Pole

Phase matching described so far is the most general treatment which based on the complex A_n of the two undulators calculated from their measured fields. Under the assumption that the bulk structure has zero phase error there is a simple alternative using Eq. (12). Only the end field contributes. In reality the problem arises how to select the boundary between bulk and end fields. The applicability of this simplification was again tested using the undulators U40-X005 and U40-X006 and the phase shifter PS073.

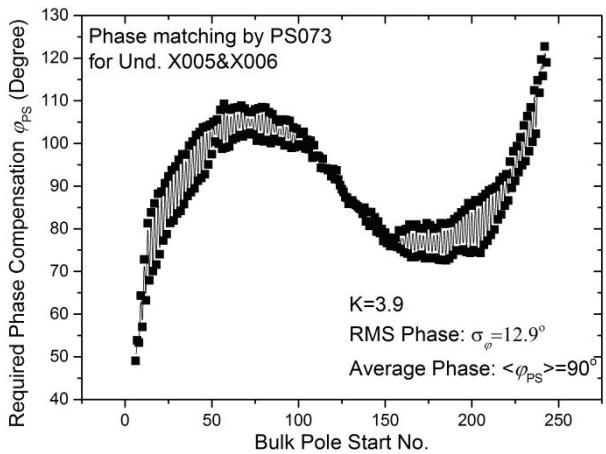

Figure 6: Phase compensation as function of the pole number where the bulk field starts.

Figure 6 shows the required phase compensation of the phase shifter as function of the pole number where the bulk structure starts. It is seen that depending on the start the phase varies significantly from about 50 to 120 degrees with an RMS value of 12.9 degrees. There is no hard criterion to select a specific pole as the start pole for the bulk field. In the bulk structure there is a systematic deviation from a 2π phase advance per period. The explanation is that on all European XFEL undulators small parabolic girder deformations have been observed, which result from changing magnetic forces but they are well within the specifications. Therefore different extensions of the bulk field leads to different phase matching requirements [10]. Since the curve in Figure 6 has some symmetry averaging can be used. The average of the requested phase in Figure 6 is 90° and is used to calculate the phase shifter gap. Now, using Eq. (12) phase shifter gap settings in full analogy to Fig. 5 can be calculated.

Both methods provide comparable results. Instead of reproducing curves such as in Figure 5 a quantitative analysis is given in Figure 7. The black curve shows the difference of the phase shifter gap setting a function of the undulator K-parameter. It does not exceed -7μm. As shown by the blue curve the difference of the phase shifter correction is less than one degree. These differences are negligible and both methods give the same phase matching and can be used for the work.

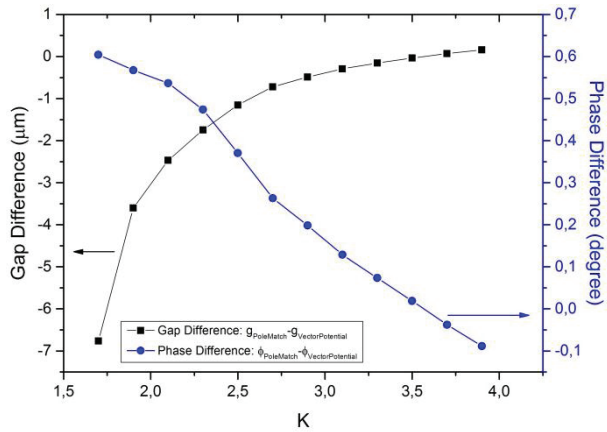

Figure 7: Comparison between the results of two matching criteria. The black curve shows the difference of the required phase shifter gap, the blue curve the phase difference of phase shifter.

CONCLUSION

In this paper the theoretical basis for the proper matching the optical phase of different tuneable undulator segments with the help of phase shifters are worked out. It is used in large distributed undulator systems for SASE FELs. Two matching methods, based on the undulator on-axis radiation and the optical phase, are derived and compared. We prove to the undulator with identical bulk field these two methods are equivalent.

The matching results for two undulator segements in SASE1 are shown as the example. The Gap-K curves for 2nπ phase matching are illustrated and compared.

REFERENCES

[1] "A VUV Free Electron Laser at the TESLA Test Facility" Conceptual Design Report, TESLA-FEL 95-03 (1995)

[2] B. Faatz *et. al.* Nucl. Instr. and Meth. A635(2011) 52

[3] Linac Coherent Light Source, (LCLS I), Conceptual Design Report SLAC-R-593 UC-414, 2002 available under: http://www.slac.stanford.edu/cgi-wrap/getdoc/slac-r-593.pdf

[4] Linac Coherent Light Source II (LCLS-II) Conceptual Design Report, SLAC-R-978; I-060-003-000-00, 2011 available under: http://www.slac.stanford.edu/pubs/slacreports/reports19/slac-r-978.pdf

[5] M. Altarelli *et al*., "The European X-ray Free-electron Laser", Technical Design Report, ISBN 3-935702-17-5, 2006; http://www.xfel.eu/dokumente/technical_documents

[6] The FERMI Project at Elletra, Conceptual Design Report, **ST/F-TN-07/12 (2007).** Available under: https://www.elettra.trieste.it/lightsources/fermi/fermi-machine/fermicdr.html

ISBN: 978-3-95450-206-6 doi:10.18429/JACoW-FLS2018-WEP2PT003

[7] H. Lu, Y. Li, J. Pflueger, "The permanent magnet phase shifter for the European X-ray Free Electron Laser", *Nucl. Instr. and Meth. A* 605 (2009) 399

[8] J. Pflueger, et. al. Proceedings of the FEL2013, August 25-30, New York City, USA, Paper TUPSO60

[9] Y. Li, S. Abeghyan, K. Berndgen, M. Bagha-Shanjani, G. Deron, U. Englisch, S. Karabekyab, B. Ketenoglu, M. Knoll, F. Wolff-Fabris, M. Viehweger, M. Yakopov, J. Pflueger, "Magnetic Measurement Techniques for the Large-Scale Production of Undulator Segments for the European XFEL" Synchrotron Radiation News, Vol. 28, Nr. 3, 2015

[10] Y. Li, B. Ketenoglu, J. Pflueger, "Girder deformation related phase errors on the undulators for the European X-Ray Free Electron Laser", *Phys. Rev. ST-AB* 18, 060704 (2015)

[11] Y. Yang, Y. Li, H. Lu, F. Wolff-Fabris, J. Pflueger, "Shimming Strategy for the Phase Shifters used in the European XFEL", Contribution TUPSO42, FEL2013, Aug 25-30, 2013, New York, USA

[12] Y. Li, J. Pflueger, "High Accuracy shimming technique for the Phase Shifters of the European XFEL", MOPS007, *FEL2014,* August 25-29, Basel , Switzerland

[13] Y. Li, J. Pflueger, "Tuning method for phase shifters with very low first field integral errors for the European X-ray Free Electron Laser" , *Phys. Rev. ST-AB* 8, 030703 (2015)

[14] J. D. Jackson, "Classical Electrodynamics", Chapter 14, John Wiley & Sons Inc, New York, 1962

[15] R.P. Walker, "Interference effects in undulator and wiggler radiation sources", *Nucl. Instr. and Meth.* A335 (1993) 328

[16] S. Krinsky, M.L. Perlman, R.E. Watson in: Handbook of Synchrotron Radiation, Vol 1 Eds. E.E Koch, D.E. Eastmans, Y. Farge *et al*. Chapter 2, North Holland Publishing Company, Amsterdam, 1983

ISBN: 978-3-95450-206-6 doi:10.18429/JACoW-FLS2018-WEP2PT008

MICROBUNCHING INSTABILITY STUDY IN THE LINAC-DRIVEN FERMI FEL SPREADER BEAM LINE*

S. Di Mitri †, S. Spampinati, Elettra – Sincrotrone Trieste S. C. p. A., Basovizza, Trieste, Italy

Abstract

Suppression of microbunching instability (MBI) along high brightness electron beam delivery systems is a priority for Free Electron lasers (FELs) aiming at very narrow bandwidth. The impact of MBI on FEL spectral brilliance is aggravated by the growing demand for multi-user FEL facilities, which adopt multi-bend switchyard lines traversed by high charge density electron beams. This study provides practical guidelines to switchyards design largely immune to MBI, by focusing on the FERMI FEL Spreader line. First, two MBI analytical models [Z. Huang and K.-J- Kim, Phys. Rev. Special Topics - Accel. Beams 5, 074401 (2002); R.A. Bosch, K.J. Kleman and J. Wu, Phys. Rev. Special Topics - Accel. Beams 11, 090702 (2008)] are successfully benchmarked along the accelerator. Being the second model flexible enough to describe an arbitrary multi-bend line, and found it in agreement with particle tracking and experimental results, it was used to demonstrate that a newly proposed Spreader optics provides unitary MBI gain while preserving the electron beam brightness.

INTRODUCTION

In FEL facilities with multiple undulator lines, the strength of the microbunching instability (MBI) is reinforced in multi-bend switchyard lines that connect the accelerator to the individual undulator lines [1–5]. Due to the presence of several dipole magnets traversed by a high charge density beam, those switchyards can dramatically amplify residual density and energy modulations present on the electron beam at the exit of the linac. This study examines MBI growth in the accelerator and switchyard, and provides practical guidelines for switchyard optics designs that are largely immune to MBI, i.e., with unity gain of the instability. We provide a specific solution for the FERMI FEL [6,7] spreader beam line that can be easily implemented within the current space and with existing magnets [8].

MBI in the FERMI linac has been continuously studied since the early stages of machine design [9–11]. MBI concerns led to the choice of operating FERMI both with a so-called laser heater (LH) [12,13], a tool that suppresses MBI via energy Landau damping, and in general using only one active magnetic bunch length compressor [9]. The FERMI laser heater usually improves the FEL spectral brilliance by up to factors 3 or more [13,14]. Nonetheless, there is experimental evidence [11,15] of both enlargement and shot-to-shot variability of the spectral bandwidth for wavelengths 10 nm or shorter. Provisionally, this degradation is assigned to effects originating with residual MBI from the linac and to its further amplification in the spreader.

This paper aims to elucidate the role of the FERMI spreader on the MBI development.

MODELS

The reader is sent to [16] the MBI model developed by Z. Huang and K.-J. Kim (henceforth labeled the "HK-model"), and based on integral equations for the bunching factor, i.e., the Fourier transform of the bunch current density function. The reader is sent to [17] for the MBI model developed by R. Bosch et al. (henceforth labeled the "B-model"), and based on matrix formalism. All collective effects are described by frequency-dependent effective impedances separately calculated for linac straight sections and chicane dipole bend sections.

The HK- and the B-models have been compared by adopting a shot-noise driven initial density modulation that has no corresponding energy modulation. The initial bunching factor is taken to be:

$$b_{sn}(\lambda_0) = \sqrt{\frac{2ec}{I_0\lambda_0}} \tag{1}$$

An additional indicator of the MBI strength, used for the comparison of the two models, is given by the amount of energy spread accumulated by the end of the beam line. Assuming that the final energy modulations are entirely converted into uncorrelated energy spread, the equivalent uncorrelated energy spread (RMS value) from the MBI growth is calculated as the integral of the final energy modulation over all (or user-specified) frequency components [18]:

$$\sigma_{E,MBI} = \frac{1}{2\pi\sqrt{2}}\sqrt{\int d\lambda \frac{\Delta E^2_{MBI}(\lambda)}{\lambda}} \tag{2}$$

The HK- and the B-model both include originally Coherent Synchrotron Radiation (CSR) and Longitudinal Space Charge (LSC) impedance, energy- and transverse emittance-induced Landau damping. They were further revised for the purpose of comparison as follows:

i) the LSC impedance is averaged over the transverse beam dimensions, which vary along the linac, according to the prescriptions in [19,20];
ii) the MBI gain is evaluated by keeping the initial bunching factor, i.e., the low gain regime is retained together with the high gain contribution [13];
iii) the effect of the LH on the electron beam initial energy distribution was calculated as in [21], assuming a laser pulse whose transverse waist size is matched at the midpoint of the LH undulator to that of the electron beam;
iv) for a fair comparison of the two models, the B-model was applied to the FERMI linac by excluding the im-

ISBN: 978-3-95450-206-6 doi:10.18429/JACoW-FLS2018-WEP2PT008

pedance contributions of Coherent Edge Radiation (CER), LSC in the BC1 drift sections, and the geometric longitudinal impedance of RF structures.

CODES BENCHMARKING

The FERMI linac-plus-spreader beam line is sketched in Fig.1. The linac is composed of multiple accelerating structures interleaved by two magnetic bunch compressors (BC1, BC2). BC1 only is active during standard FEL operation. Each branch of the spreader is a dog-leg made of two modified double bend achromatic cells (MDBAs), separated by quadrupole magnets [22]. Since the impact of MBI on the FEL spectrum is stronger at shorter FEL wavelengths, only that part of the spreader that feeds the FEL-2 branch line is considered in the following calculations and discussion.

Figures 2 and 3 compare the two models' prediction, with and without LH. Table 1 compares the final uncorrelated energy spread as computed by the quadratic sum of the initial one and that one induced by MBI (see Eq.2), for the two LH scenarios illustrated in Figs. 2 and 3.

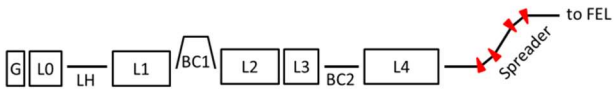

Figure 1: Sketch, not to scale, of the FERMI linac-plus-spreader FEL-2 beam line. This study applies from the exit of L0 to the spreader end. Only the first magnetic bunch compressor, BC1, is active and for these calculations is presumed to give perfect linear compression. Copyright of APS (2018).

Table 1: Total uncorrelated energy spread (RMS value) at the end of the FERMI linac (see Figs.2,3). The energy modulation induced by MBI over the initial wavelength range 0.5–200 μm is assumed to convert entirely into uncorrelated energy spread (see Eq.2).

Laser Heater	HK-model	B-model	Unit
Off	331	338	keV
10 keV	102	110	keV

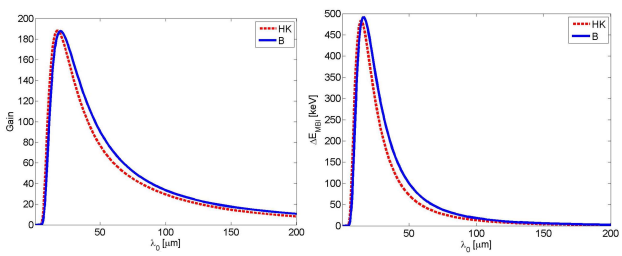

Figure 2: Comparison of MBI gain (top) and energy modulation amplitude (bottom) at the end of the FERMI linac vs. the *initial* density modulation wavelength. The two curves correspond to the separate predictions by the HK-model [16] (dashed line) and the B-model [17] (solid line). The laser heater is off. Copyright of APS (2018).

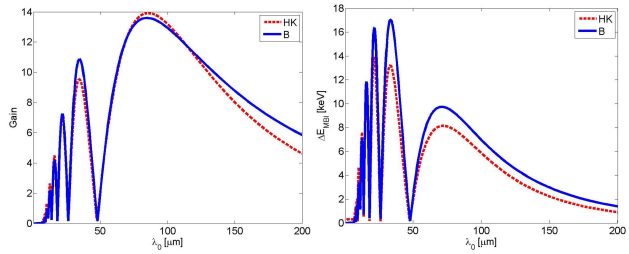

Figure 3: Comparison of MBI gain (top) and energy modulation amplitude (bottom) at the end of the FERMI linac vs. the *initial* density modulation wavelength. The two curves correspond to the separate predictions by the HK-model [16] (dashed line) and the B-model [17] (solid line). The laser heater is off. Copyright of APS (2018).

MBI IN THE FERMI LINAC + SPREADER

The development of MBI along the *whole* FERMI beam delivery system, now including RF impedances and CER, is illustrated in Fig.4. The LH intensity is set to the nominal 10 keV RMS energy spread level. By the end of the FERMI spreader, the total MBI gain increases by a factor up to 10 relative to that seen at the end of the linac, and the energy modulation amplitudes have more than doubled at shorter wavelengths. The up to 40 keV energy modulation amplitudes accumulated at the spreader exit approach the level of the natural beam energy spread in the absence of instability. Moreover, the MBI modulations lie in the *final* wavelength range 0.5–5 μm. These wavelengths are shorter than the FERMI external seed laser pulse length (approximately 30 μm long), and generally longer than the FEL-2 cooperation length (this is 0.3–0.8 μm for FEL output wavelengths in the range 4–10 nm). Thus, one could expect a serious impact of such modulations on the FEL spectrum in terms of shot-to-shot spectral variability and generalized bandwidth enlargement, due to excitation of sidebands on the main seeded line [11,23,24]. These considerations fully justify serious efforts to reducing the contribution of the spreader to the global MBI dynamics, as is done in the next Section.

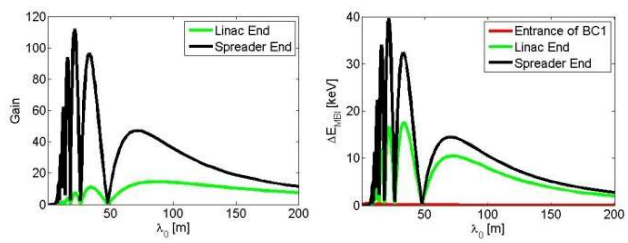

Figure 4: Gain (left) and energy modulation amplitude at the end of the FERMI linac (green) and of the linac-plus-spreader beam line (black). The laser heater is set at 10 keV RMS energy spread before compression. Copyright of APS (2018).

NEW SPREADER OPTICS

The study reported in [25,26] suggests that a quasi-isochronous and achromatic spreader line would see a much reduced MBI gain. More recently, the simultaneous requirement of small MBI gain and preservation of the

ISBN: 978-3-95450-206-6 doi:10.18429/JACoW-FLS2018-WEP2PT008

transverse beam emittance in the presence of CSR head-tail instability [27] led to the prescription of a locally-isochronous beam line whose properties include small variations of R_{56}, π-betatron phase advance between consecutive dipole magnets, low betatron function and relatively large alpha-function at the dipoles [28] (all terms correspond to the bending plane).

These prescriptions were incorporated into a new FERMI FEL-2 spreader design, where the physical length, position and bending angles of the actual beam line were retained. The total R_{56} of the beam line is reduced from its present value of 680 μm down to 1 μm by virtue of the reversed sign of the dispersion function inside the two inner dipoles of the spreader branch.

A comparison of the present (or standard) and new linear optics functions, as well as of the R_{56} term along the line, is given in Fig.5. Figure 6 replicates Fig.4 for the new optics. The new spreader design is substantially transparent to any incoming modulation induced by MBI in the linac, since the curves at the linac end (green) and at the spreader end (black) tend to superimpose, as a consequence of a unity gain through the beam line. It is worth pointing out that the new design requires only a re-adjustment of the strengths of the quadrupole magnets internal to the MDBAs that lies within a range fully compatible with the FERMI operation up to 1.5 GeV beam energy. The present spreader optics preserves the beam horizontal normalized emittance from the CSR head-tail instability at 0.1 μm level [22].

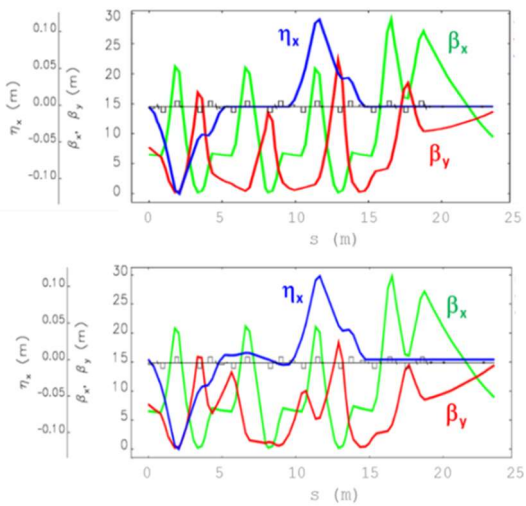

Figure 5: Linear optics functions along the FERMI spreader for the *present* (top) and new optics design. Copyright of APS (2018).

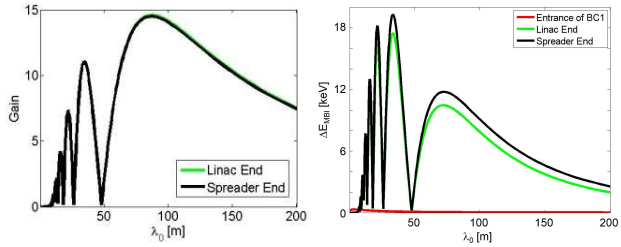

Figure 6: Gain (left) and energy modulation amplitude at the end of the FERMI linac (green) and linac-plus-spreader beam line (black), for the new spreader optics. The laser heater is set at 10 keV RMS energy spread before compression. Copyright of APS (2018).

EXPERIMENTAL RESULTS

The intensity of optical transition radiation (OTR) emitted by the electron beam passing through a 100 μm thick-Al foil (OTR screen) at the end of the FERMI spreader was used as an indicator of the MBI gain at optical wavelengths (the CCD of the OTR screen system is sensitive to radiation wavelengths < 3 μm), as coherent density modulations should strongly increase the OTR emission. The inset of Figure 7 shows the reduction of the bunching factor predicted by the B-model when the new spreader optics is adopted (solid line), in comparison to the standard optics (dashed line). The main plot shows the measured OTR signal integrated over the physical region occupied by the beam spot at the screen, and averaged over many shots. The OTR signal is shown as a function of the LH pulse energy, for the standard (dashed line) and the new spreader optics (solid line). Control of beam sizes was accomplished by means of the last 4 quadrupoles of the spreader line, installed upstream the screen and in a dispersion-free region. In accordance with the model, higher pulse energies suppress the instability at longer wavelengths [13].

The OTR intensity in the presence of the standard spreader optics shows a large sensitivity to the LH setting. A coherent OTR emission shows up as large signal intensity for low heating level, and it disappears for LH energies higher than 1 μJ. On the contrary, the OTR intensity collected in the presence of the new Spreader optics is largely insensitive to the LH setting. The OTR signal value stays at the level of that one collected with the standard optics and large LH energy, ~4 μJ.

In order to verify the simultaneous suppression of MBI and preservation of the beam transverse emittance, the emittances were measured with the quadrupole scan technique [29] at the end of the spreader. The new spreader optics, as well as the standard one, preserves the horizontal emittance from CSR head-tail instability.

ISBN: 978-3-95450-206-6 doi:10.18429/JACoW-FLS2018-WEP2PT008

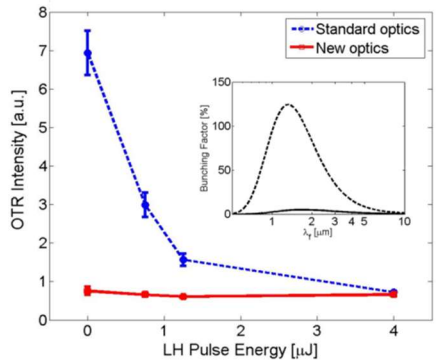

Figure 7: OTR intensity measured at the end of the FERMI spreader vs. LH pulse energy, for the standard (blue dashed) and the new optics configuration (red solid). Error bars are the RMS fluctuation of the OTR signal over 500 consecutive shots. In the inset: bunching factor calculated at the end of the linac-plus-spreader beam line with LH off vs. final (compressed) wavelength of modulation, for the spreader standard (dashed) and new optics (solid). Copyright of APS (2018).

CONCLUSION

A systematic comparison of two analytical models [16,17] for MBI growth in the FERMI linac has been done, including transversally-averaged LSC impedance and realistic LH effect. The two codes are found in good quantitative agreement. Given the flexibility of the B-model introduced in [17] for describing the MBI in an arbitrary transfer line, we applied it to the actual FERMI spreader beam line to FEL-2, where the code was additionally benchmarked with particle tracking runs. This study revealed a significant contribution of the spreader to the amplification of residual MBI exiting the linac, even in the situation where the FERMI laser heater is run at its nominal intensity. As a result, coherent energy modulations at the level of tens of keV in the final wavelength range 0.5–5 μm are expected at the undulator entrance. Due to sideband formation, these modulations are expected to degrade the FEL spectral brilliance at output radiation wavelengths shorter than ~10 nm.

A new spreader optics was designed to simultaneously minimize the spreader MBI gain and preserve the horizontal beam emittance from growth associated with the CSR head-tail instability. Importantly, the new solution does not require any physical change in the existing layout and could be readily implemented. Experimental tests of the new spreader optics confirmed both the negligible MBI gain as measured by the OTR signal, and the preserved beam emittance.

ACKNOWLEDGEMENT

The authors acknowledge R.A. Bosch for providing his script for the B-model; C.-Y. Tsai for providing scripts for the analysis of MBI with Elegant; E. Allaria and E. Roussel for discussions on the MBI modeling and its impact on the FEL spectrum; W. M. Fawley and M. Cornacchia for helpful comments.

REFERENCES

[1] W. Decking and F. Obier, in *Proc. the 11th Europ. Part. Accel. Conf.*, Layout of the Beam Switchyard at the European XFEL, WEPC073, Genoa, Italy (2008).

[2] N. Milas and C. Gough, in *Proc. the 32nd Intern. Free Electron Laser Conf.*, Design of the SwissFEL Switchyard, WEPB16, Malmö, Sweden (2010).

[3] M. Placidi, J.-Y. Jung, A. Ratti, C. Sun, "Compact spreader schemes", *Nucl. Instr. Meth. Phys. Research A*, vol. 768, pp. 14–19, 2014.

[4] B. Faatz *et al.*, "Simultaneous operation of two soft x-ray free-electron lasers driven by one linear accelerator", *New J. Phys.*, vol. 18, p. 062002, 2016.

[5] T. Hara *et al.*, "Pulse-by-pulse multi-beam-line operation for x-ray free-electron lasers", *Phys. Rev. Accel. Beams*, vol. 19, p. 020703, 2016.

[6] E. Allaria *et al.*, "Highly coherent and stable pulses from the FERMI seeded free-electron laser in the extreme ultraviolet", *Nat. Photonics*, vol. 6, pp. 699–704, 2012.

[7] E. Allaria *et al.*, "Two-stage seeded soft-X-ray free-electron laser", *Nat. Photonics*, vol. 7, pp. 913–918, 2013.

[8] S. Di Mitri and S. Spampinati, *Phys. Rev. Accel. Beams*, vol. 20, p. 120701, 2017.

[9] S. Di Mitri, "Machine design and electron beam controlof a single-pass linac for free electron laser: the FERMI@Elettra case study", Ph.D Thesis, ISBN 978-90-367-5176-6,2011.

[10] S. Di Mitri *et al.*, "Design and simulation challenges for FERMI@elettra", *Nucl. Instrum. Methods Phys. Res. A,* vol. 608, pp. 19–27, 2009.

[11] E. Roussel *et al.*, "Multicolor High-Gain Free-Electron Laser Driven by Seeded Microbunching Instability", *Phys. Rev. Lett.*, vol. 115, p. 214801, 2015.

[12] E.L. Saldin, E.A. Schneidmiller, M. Yurkov, "Longitudinal space charge-driven microbunching instability in the TESLA Test Facility linac", *Nucl. Instrum. Methods Phys. Res. A*, vol. 528, p. 355.

[13] S. Spampinati *et al.*, "Laser heater commissioning at an externally seeded free-electron laser", *Phys. Rev. Special Topics – Accel. Beams*, vol. 17, p. 120705, 2014.

[14] S. Spaminati *et al.*, Commissioning of the FERMI@Elettra Laser Heater, in *Proc. the 34th Intern. Fre Electron Laser Conf.*, MOPD58, Nara Japan (2012).

[15] E. Allaria *et al.*, The FERMI free-electron lasers, J. Synchrotron Rad. 22 (2015) 485–491.

[16] Z. Huang and K.-J- Kim, "Formulas for coherent synchrotron radiation microbunching in a bunch compressor chicane", *Phys. Rev. Special Topics – Accel. Beams*, vol. 5, p. 074401 (2002).

[17] R.A. Bosch, K.J. Kleman and J. Wu, "Modeling two-stage bunch compression with wakefields: macroscopic properties and microbunching instability", *Phys. Rev. Special Topics – Accel. Beams*, vol. 11, p. 090702 (2008).

[18] D. Ratner, C. Behrens, Y. Ding, Z. Huang, A. Marinelli, T. Maxwell, and F. Zhou, "Time-resolved imaging of the microbunching instability and energy spread at the Linac Coherent Light Source", *Phys. Rev. Special Topics – Accel. Beams*, vol. 18, p. 030704 (2015).

[19] J. Qiang, R. D. Ryne, M. Venturini, A. A. Zholents, and I. V. Pogorelov, "High resolution simulation of beam dynamics in electron linacs for x-ray free electron lasers", *Phys.*

ISBN: 978-3-95450-206-6 doi:10.18429/JACoW-FLS2018-WEP2PT008

Rev. Special Topics – Accel. Beams, vol. 12, 100702 (2009).

[20] M. Venturini, "Models of longitudinal space-charge impedance for microbunching instability", *Phys. Rev. Special Topics – Accel. Beams*, vol. 11, p. 034401 (2008).

[21] Z. Huang *et al*., "Measurements of the linac coherent light source laser heater and its impact on the x-ray free-electron laser performance", *Phys. Rev. Special Topics – Accel. Beams*, vol. 13, p. 020703 (2010).

[22] S. Di Mitri, M. Cornacchia, S. Spampinati, "Cancellation of Coherent Synchrotron Radiation Kicks with Optics Balance", *Phys. Rev. Lett.*, vol. 110, p. 014801,2013.

[23] D. Ratner *et al*., "Experimental Demonstration of a Soft X-Ray Self-Seeded Free-Electron Laser", *Phys. Rev. Lett.* vol. 114, p. 054801 (2015).

[24] Z. Zhang, R. Lindberg, W. M. Fawley, Z. Huang, J. Krzywinski, A. Lutman, G. Marcus, and A. Marinelli, *Phys. Rev. Accel. Beams*, vol. 19, p. 050701 (2016).

[25] M. Venturini and A. Zholents, Modeling microbunching from shot noise using Vlasov solvers, *Nucl. Instr. Meth. Phys. Research A*, vol. 593, pp. 53–56, 2008.

[26] R. Bosch, K.J. Kleman and J. Wu, in *Proc. 23rd Part. Accel. Conf.*, WE5RFP057, Vancouver, BC, Canada (2009).

[27] Ya.S. Derbenev, J. Rossbach, E.L. Saldin and V.D. Shiltsev, Microbunch radiative head-tail interaction, in *Proc. TESLA-FEL'95*, DESY, Hamburg, Germany (1995).

[28] C.-Y. Tsai, S. Di Mitri, D. Douglas, R. Li, and C. Tennant, "Conditions for coherent-synchrotron-radiation-induced microbunching suppression in multibend beam transport or recirculation arcs", *Phys. Rev. Accel. Beams*, vol. 20, 024401 (2017).

[29] M. G. Minty and F. Zimmermann, Beam Techniques – Beam Control and Manipulation, SLAC-R-621 (2003) and in *Proc. Lectures given at the US Particle Accelerator School*, University of Chicago and Argonne National Laboratory (1999).

ISBN: 978-3-95450-206-6 doi:10.18429/JACoW-FLS2018-WEP2PT014

STRONG FOCUSING LATTICE DESIGN FOR SSMB

Tenghui Rui†, Xiujie Deng, Alex Chao[1], Wenhui Huang, Chuanxiang Tang,
Tsinghua University, Beijing, China
[1] also at SLAC, Menlo Park, USA

Abstract

A storage ring applicable for SSMB operation is a critical part of a high average power SSMB EUV light source. A lattice for SSMB based on longitudinal strong focusing is under design in Tsinghua University. To generate and maintain micro-bunching in a storage ring in this scenario, the momentum compaction has to be small. A lattice with low momentum compaction factor is presented in this work. The lattice of the current design consists of two MBA cells with isochronous unit cells to minimize local and global momentum compaction, and two straight sections for insertion devices. The design energy of the ring is 400MeV and the circumference is 94 meters. Nonlinear effects such as higher order momentum compactions will continue to be optimized.

INTRODUCTION

To develop microchips with etched circuit lines smaller than 0.1um, new technology is needed. Extreme ultraviolet lithography is a next generation of lithography technology and the wavelength is expected to be 13.5nm, while DUV's wavelength is 193nm or 248nm. A microprocessor made with the EUVL technology would be a hundred times more powerful than today's. SSMB (Steady State Micro-Bunching) is a promising scheme for high average power EUV light sources.

When electrons are grouped into micro bunches spaced at the wavelength of desired radiated light, the radiation process is coherent and the brightness of the resulting light is orders of magnitude higher than that of an equivalent incoherent light source. In a linac based light source such as conventional FELs, the electron bunch passes through the radiator once, leading to low duty cycles, and thus the average radiation power is limited. In the contrast, storage rings offer a much higher repetition rate and potentially produce much higher average radiation power. In this work, our attempts at designing a storage ring applicable for SSMB operation are presented.

LOW MOMENTUM COMPACTION LATTICE

Based on conventional formulas, the bunch length in a storage ring is related to momentum compaction factor and RF parameters.

$$\sigma_z = \frac{\eta\sigma_\delta C}{2\pi\nu_s} = \frac{(\alpha_c - 1/\gamma^2)\sigma_\delta C}{2\pi\nu_s}, \quad (1)$$

where α_c is the momentum compaction factor, γ is the Lorentz factor, and ν_s is the synchrotron tune. Synchrotron tune depends on RF parameters and momentum compaction factor [4]:

$$\nu_s = \sqrt{\frac{heV|\eta \cos \phi_s|}{2\pi\beta^2 E}}, \quad (2)$$

where h is the harmonic number, V is the RF voltage and ϕ_s is the synchronous phase. According to these formulas, equilibrium bunch length is proportional to the square root of slip factor, and by reducing momentum compaction, the bunch length can be shortened to realize sustained micro bunching.

Momentum compaction factor is directly defined as the integral of the dispersion function.

$$\alpha_c = \frac{1}{C}\int \frac{\eta_x}{\rho} ds. \quad (3)$$

To achieve low momentum compaction, the most straightforward way to do is to make the dispersion in bending magnets cancel out. Figure 1 shows a conventional double bend achromat. The strengths of the quadrupole magnets between the two dipole magnets are chosen such that the dispersion function is symmetric about the central quadrupole. To achieve low momentum compaction, the strength of the central quadrupole can be tuned to introduce asymmetry into the dispersion function. As is shown in Fig.2, the dispersion function in the two bending magnets is opposite in sign. As a result, the compaction factor can be small.

Figure 3 shows the layout of the first version of the SSMB lattice. The calculation of the beta function is done with Elegant.[1] The lattice consists of four cells. Each cell consists of two dipole magnets with cancelling dispersion function. Each pair of the cells has symmetrical optical functions so two cells form a four bend achromat with the straight sections on both ends free of dispersion. The dispersion free sections can accommodate equipment like RF cavity or undulator.

† email address: rth13@mails.tsinghua.edu.cn

ISBN: 978-3-95450-206-6 doi:10.18429/JACoW-FLS2018-WEP2PT014

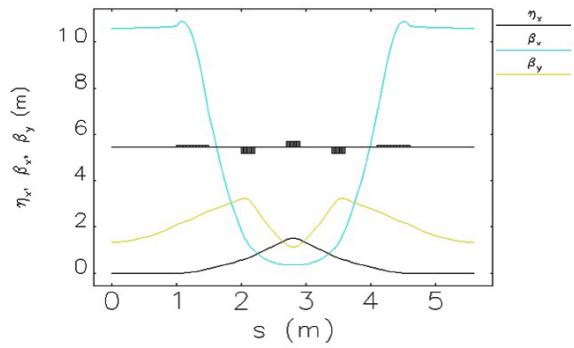

Figure 1: A conventional DBA structure.

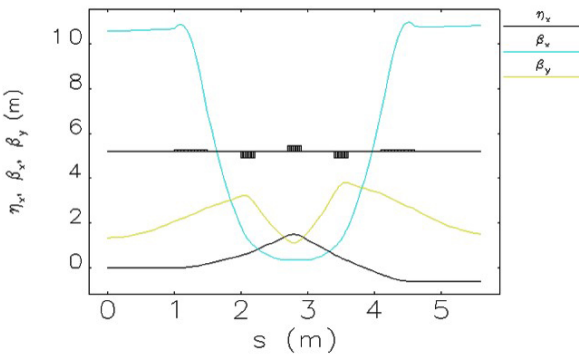

Figure 2: A DBA with the central quadrupole tuned to introduce asymmetricity to reduce momentum compaction.

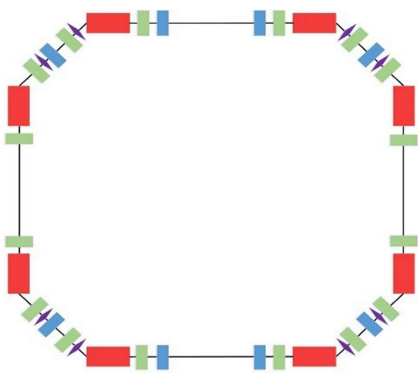

Figure 3: Layout of the lattice.

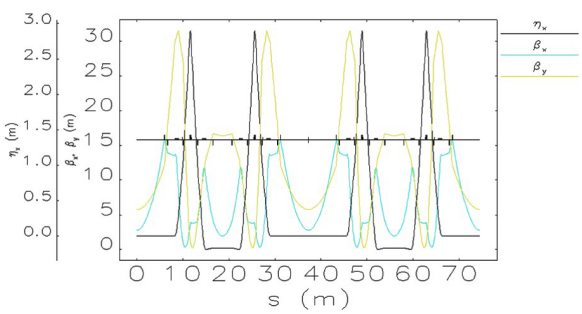

Figure 4: Optical function of the lattice.

The momentum compaction factor of the lattice is optimized to be 1e-6 and the natural energy spread is 3.5e-4, so the bunch length should be less than 1um assuming the synchrotron tune to be about 0.1. It's possible to modulate a longer bunch to several smaller bunch in this ring with a 1um modulator. However, further simulation indicates that this is not the case. In deriving the bunch length formula above, it's neglected that the path length of each electron in a bunch is fluctuating by photon emission. The magnitude of this fluctuation depends on local parameters of the ring. Consider an electron that moves along the design orbit, after it emits a photon and then travels to another location in the ring. Assuming the derivatives of dispersion functions and beta functions to be zero at both locations, to simplify the algebra, the orbit change due to photon emission is ([2]):

$$\Delta z = -\frac{\varepsilon}{E}\left(\Delta R_{56} + \frac{\eta_1\eta_2}{\sqrt{\beta_1\beta_2}}\sin\psi\right). \quad (4)$$

The bunch length after taking this effect into account is ([2]):

$$\sigma_z^2 = \sigma_{z,sands}^2 + \delta_\delta^2\left(\Delta R_{56}^2 + \frac{\eta_1^2\eta_2^2}{2\beta_1\beta_2}\right). \quad (5)$$

As a result, when the momentum compaction is reduced, the second term dominates. Figure 5 and figure 6 shows the comparison between 1um bunch modulations with and without photon emission. With photon emission, the structure of the bunch is smeared and micro bunching is unsustainable.

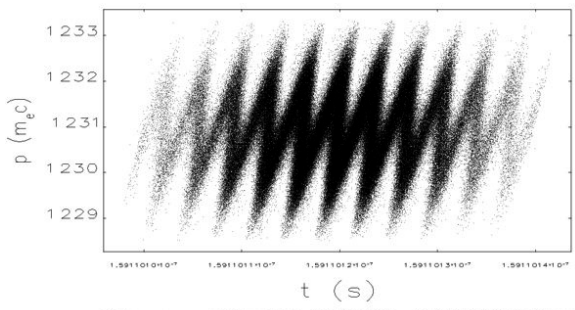

Figure 5: Bunch modulation without photon emission [3].

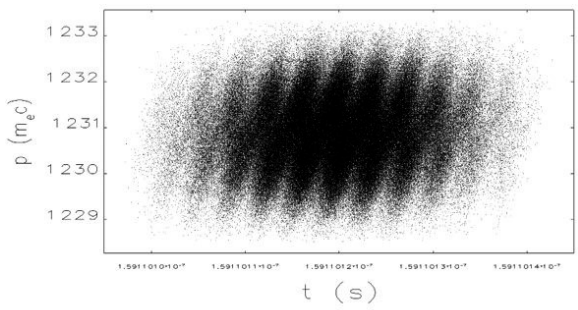

Figure 6: Bunch modulation with photon emission [3].

The possible solution to this problem is to reduce the bending angle of the dipole magnets. By reducing the bending angle, synchrotron radiation is weaker and both the R56 and the dispersion function are smaller. As a result, the second term in equation 3 is so small that the first term dominates again.

ISBN: 978-3-95450-206-6 doi:10.18429/JACoW-FLS2018-WEP2PT014

ISOCHRONOUS CELL

To study the effect of quantum excitation and find a suitable lattice for SSMB, a new test cell is designed. The layout and optical functions of the test cell are shown in figure 7.

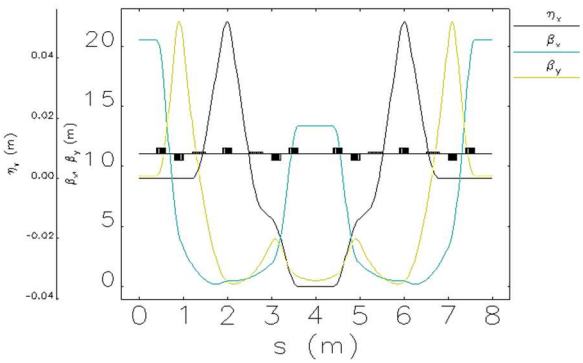

Figure 7: Layout and optical functions of the new cell.

The length of the bending magnet is set to be 0.3m, while the bending angle can be changed to create cells with different dispersion function. The profile of dispersion remains the same when changing the bending angle, so R56 of the cell remains small. The cell is an achromatic structure so both ends of the cell is free of dispersion, which can accommodate an RF cavity for modulation. With 1nm modulation, the bending angle of the dipoles is varied from 0.5° to 9°. The bunch lengthening effect is plotted in Fig. 8. With increasing bending angle, the bunch length increases quartically. For our final EUV cell, we expect the micro bunches to be a few nm long, so the bunch lengthening effect should be kept within 1nm. As a result, the total bending angle of an isochronous cell should not exceed 30°.

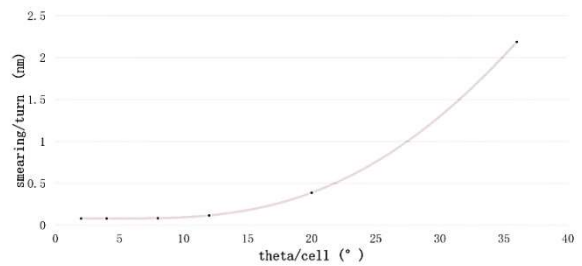

Figure 8: Bunch lengthening effect and the bending angle of the cell [3].

The current lattice layout is shown in Fig. 9-11. Each arc consists of 12 isochronous cells. The bending angle of the dipole magnets is 13°. Unlike the test cell, the current cell is not achromatic, so the R56 of each dipole can be optimized to be zero and each of the dipoles is isochronous. A dispersion suppression cell is designed to provide a 10m dispersion free section for future upgrade such as a strong longitudinal focusing scheme. The dispersion suppression cell consists of a half isochronous cell and a small corrector magnet whose bending angle is -1 °. The momentum compaction factor is 1e-6 and the second order momentum compaction factor is 0.025. Nonlinear momentum compaction becomes the dominant limitation for bunch length shortening when further reducing the linear compaction factor, so more optimization is needed by using sextupoles.

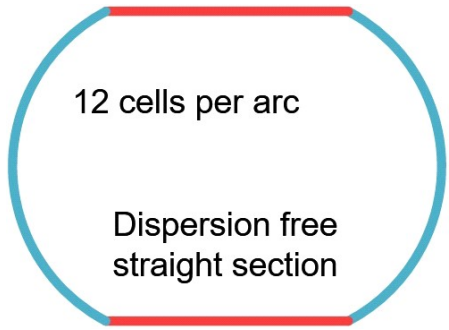

Figure 9: The layout of the current lattice.

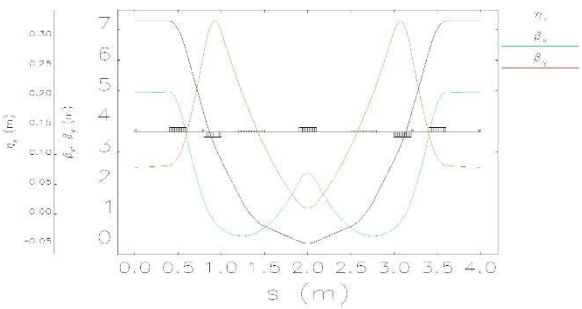

Figure 10: Layout and optical functions of the current isochronous cell.

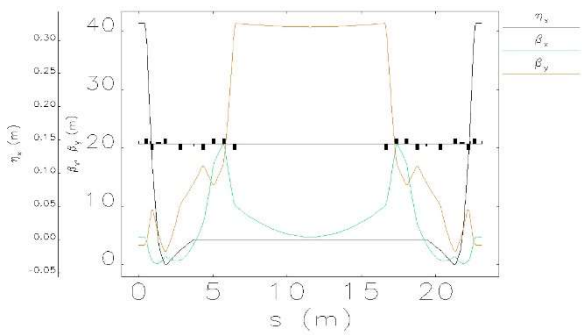

Figure 11: Layout and optical functions of the matching cell.

CONCLUSION

To store micro bunches in a storage ring, not only does the global momentum compaction have to be small, but also the local momentum compaction. When electrons emit photons while travelling through bending magnets, the path length of each electron fluctuates because of the local momentum compaction. As a result, the bunch length is much larger compared to the results of conventional formulas. To suppress this bunch lengthening effect, a lattice consists of isochronous cell is designed. The momentum compaction factor is optimized to be 1e-6 before nonlinear momentum compaction becomes dominant. To further shorten the bunch length, more

ISBN: 978-3-95450-206-6 doi:10.18429/JACoW-FLS2018-WEP2PT014

optimization is needed. A longitudinal strong focusing insertion cell will be the next phase of this work.

REFERENCE

[1] Borland, Michael. Elegant: *A flexible SDDS-compliant code for accelerator simulation.* No. LS-287. Argonne National Lab., IL (US), 2000.

[2] Alex Chao, private communication.

[3] Xiujie Deng, private communication.

[4] Lee, Shyh-Yuan. *Accelerator physics*. World Scientific Publishing Company, 2011.

ISBN: 978-3-95450-206-6 doi:10.18429/JACoW-FLS2018-WEP2PT021

THE DESIGN AND TEST OF A STRIPLINE KICKER FOR HEPS

H. Shi, J. H. Chen, L. Wang, N. Wang, L. H. Huo, P. Liu, G. W. Wang, X. L. Shi,
Key Laboratory of Particle Acceleration Physics and Technology, Institute of High Energy Physics,
Chinese Academy of Sciences, Beijing 100049, China

Abstract

A fast stripline kicker is adopted for High Energy Photon Source (HEPS) on-axis injection. The optimization of a prototype 750 mm long kicker has been finished. The 3D simulation results show the final design of wide vane with end cover lowers the beam loss about 31% than the original design does. We develop a feedthrough model with machinable glass ceramic and achieve a VSWR under 1.3 in 0~2 GHz. The assembly of kicker and commercial feedthroughs has been tested with Keysight E5071C. The testing results of S parameters and TDR value show a good agreement with simulation ones.

INTRODUCTION

High Energy Photon Source (HEPS) is a storage ring light source with the beam energy of 6 GeV. The effective dynamic aperture (DA) is about 2.5 mm (horizontal) and 3.5 mm (vertical), which is not large enough for off-axis injection [1]. On-axis swap-out injection or on-axis longitudinal accumulating injection schemes are proposed, and a very fast kicker is required for both on-axis injection systems [2].

In the HEPS test facility (HEPS-TF) project, a stripline kicker of 750 mm long has been designed and tested as one of key hardware techniques. Figure 1 gives the section view of the stripline kicker and high voltage feedthroughs. The design has been optimized to satisfy the specifications of the kicker, such as the matching odd-mode impedance, field uniformity in good field region, and minimizing the local electric field in operation voltage, which are shown in Table 1 [3].

In this paper, we'll first give the detailed optimization of kicker with 3D simulation. Then the preliminary design of feedthrough is presented. Finally, we'll compare the simulation and testing results of the prototype kicker.

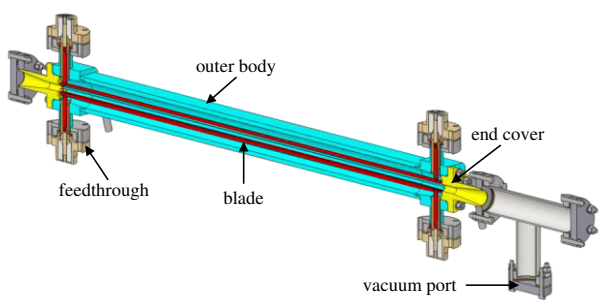

Figure 1: Section view of the stripline kicker.

Table 1: Specifications of the Stripline Kicker for HEPS-TF

Parameters	Value
Length of blades (mm)	750
Gap between the two blades (mm)	10
Good field region (mm)	±2.3 (x) ±1.0 (y)
Field uniformity	2%
Odd-mode impedance (Ω)	50±0.5
Even-mode impedance (Ω)	60±0.5
Operation pulse voltage (kV)	±20
Degree of vacuum (Torr)	1×10^{-9}

KICKER DESIGN OPTIMIZATION

The two-blade stripline kickers have been successfully operating at KEK [4] and DAΦNE [5]. New designs have been developed to achieve high field uniformity, maximum kicker strength, low beam impedance and short pulse width [6-8].

Our kicker design refers to the APS-U design [8-10] because of the similar machine parameters. Figure 2 shows the basic geometry of the kicker body. Robust "D" shape blades are adopted for easily achieving high field homogeneity, where *a*, *b* are the axes of the central ellipse, *blade* is the thickness, *gap* is the half distance, which define the blades geometry. The outer body half shell is composed of 2 connected half ellipses, where X_c, a_0, b_0 defines the central half ellipse, and X_c, a_{00}, b_0 defines the outer half ellipse. Adjusting the *vane* value can improve the mismatching of the even-mode impedance.

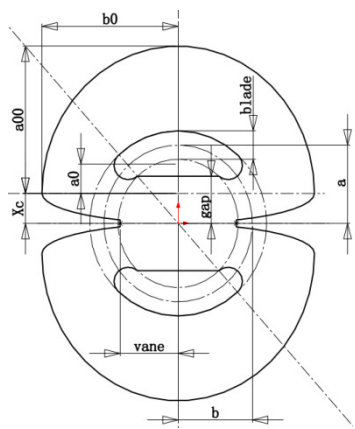

Figure 2: Basic geometry of the cross section.

The whole kicker consists of the main part of 650 mm and two taper parts of 50 mm, as shown in Figure 3. The odd-mode and even-mode impedance are optimized at the section of main part and end section of taper part

ISBN: 978-3-95450-206-6 doi:10.18429/JACoW-FLS2018-WEP2PT021

separately. The introduction of taper parts can improve the matching with feedthroughs and lower the beam impedance.

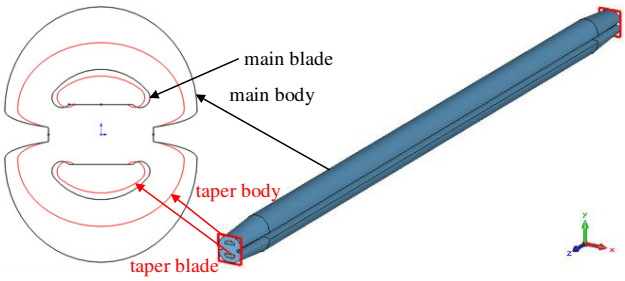

Figure 3: 3D kicker model.

First optimization is extending the vanes to decrease the coupling of the two blades with 3D CST [11]. As shown in Figure 4, the *vane* value changes from *vane* = *b* to *vane* < *b*. The even-mode impedance decreases from ~65 Ω to <60.5 Ω as the odd-mode impedance maintains ~50 Ω. The beam loss factor decreases from 1.042 V/pC to 0.893 V/pC in the Gauss beam (σ_z = 3 mm), as shown in Figure 5 that means the beam power loss is about 15% lower.

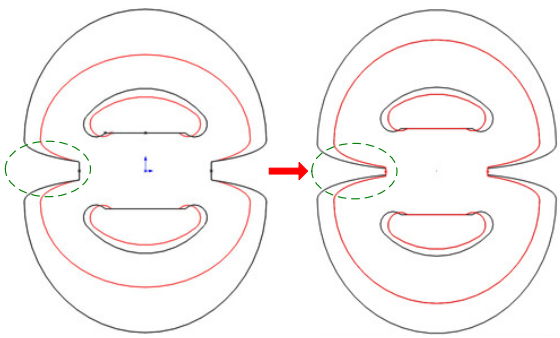

Figure 4: Optimization of the cross section.

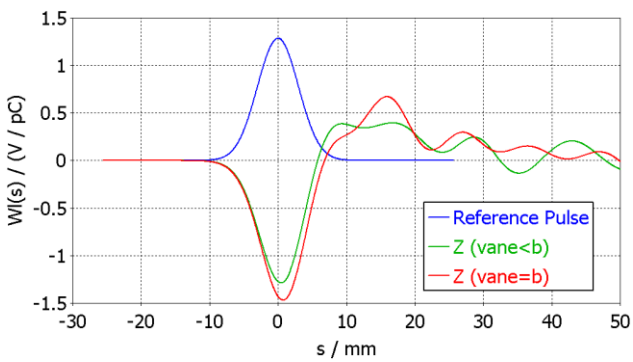

Figure 5: Comparison of the longitudinal wake potential (σ_z = 3 mm).

Further optimizations mainly focus on improving the taper parts. As shown in Figure 6, we improve the end section of taper parts firstly with increasing the vane width, then add two end covers (shown in Figure 1) at each end of taper parts. The beam power loss decreases 16% after both optimizations.

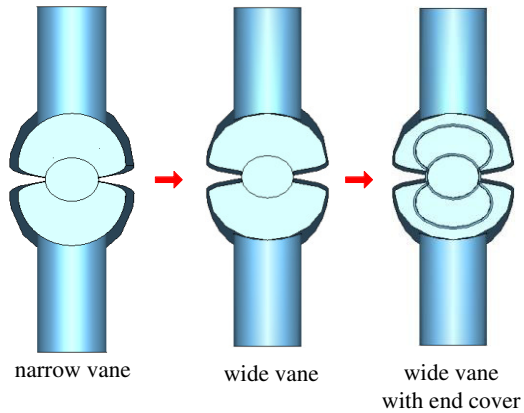

Figure 6: Taper parts improving.

FEEDTHROUGH DESIGN

The requirement of feedthrough is that it must withstand high voltage of above 20 kV, has ultrahigh vacuum degree of less than 1×10^{-9} Torr and enough frequency bandwidth of above 1 GHz.

The commercial FID RF feedthroughs have been assembled with the prototype kicker. The preliminary testing results in RF and high-voltage conditions show that they can meet the request of measurement. But it's very hard to connect to kicker blades because of inner conductor end structure, so it's necessary to develop special ones to satisfy our requirement.

The feedthrough model is shown in Figure 7. The machinable glass ceramic is chosen for the vacuum seal because of the low permittivity ~6, which is easier to achieve good 50 Ω matching. The optimized VSWR value has been below 1.3 up to 2 GHz, as shown in Figure 8.

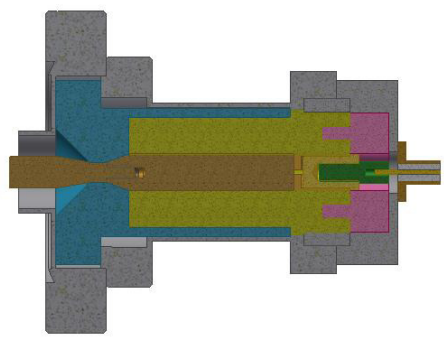

Figure 7: Cross section view of the feedthrough model.

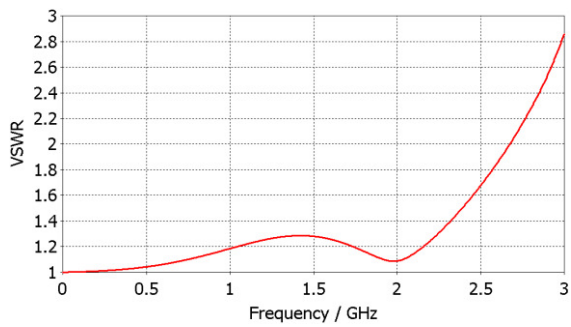

Figure 8: VSWR of the feedthrough.

ISBN: 978-3-95450-206-6 doi:10.18429/JACoW-FLS2018-WEP2PT021

RF MEASUREMENT

RF measurement has been done after assembling the 750 mm kicker and FID feedthroughs. The test setup is shown in Figure 9, and Keysight E5071C Network Analyser is used to measure the S parameters and Time-domain reflectometer (TDR) value.

The S parameters comparison is shown in Figure 10. Because we use the perfect coaxial feedthrough in simulation, testing values are worse than simulation ones, especially the insertion loss S21. But we think these values are acceptable.

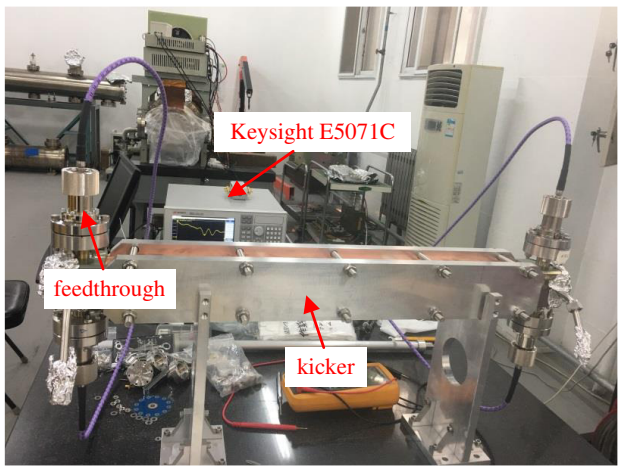

Figure 9: Kicker test setup.

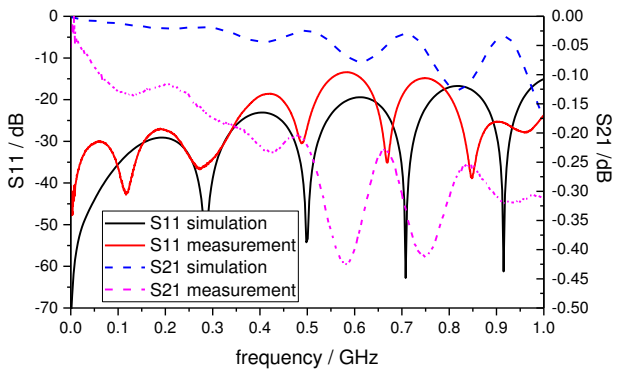

Figure 10: S parameters Comparison between simulation and testing results.

Our feedthrough model is adopted in the TDR simulation, and the TDR comparison is shown in Figure 11. We discover that the odd mode impedance (red line) drops in the middle of the blades and the minimum value is below 48 Ω. The long-blade deflection is thought to be the main reason, which can also lead to a decline of vertical field uniformity. We have considered several solutions, such as adding ceramic supports in the middle of the blades, more bigger and robust blades or lighter alumina blades.

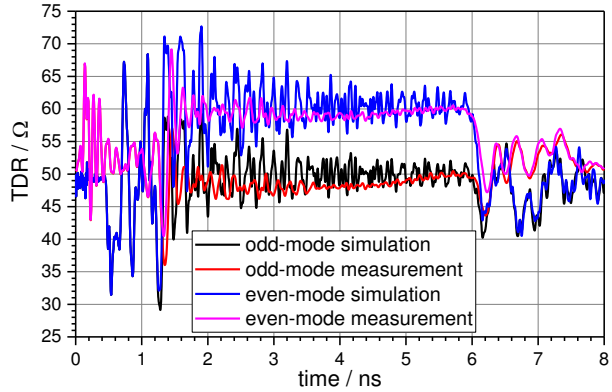

Figure 11: TDR Comparison between simulation and testing results.

CONCLUSION

The stripline kicker design optimization has been done. After extending the vanes, improving the end section of taper parts and adding the end cover at each end of the kicker, the total beam power loss can decrease about 31%.

The preliminary design of feedthrough has been finished and the machinable glass ceramic is adopted. In 0~2 GHz, the VSWR value can be below 1.3.

The kicker and FID feedthroughs have been assembled and tested. The test results of S parameters and TDR value agree well with the simulation ones.

REFERENCES

[1] G. Xu, J. H. Chen, Z. Duan, and J. Qiu, "On-axis beam accumulation enabled by phase adjustment of a double-frequency RF system for diffraction-limited storage rings", in *Proc. of IPAC'16*, Busan, Korea, 2016, pp. 2032-2035.

[2] J. H. Chen *et al.*, "Strip-line kickers and fast pulsers R&D at HEPS", in *Proc. of TWIIS2017*, HZB/BESSYII, Berlin, 2017.

[3] H. Shi *et al.*, "Progress on the fast pulsed kicker for the HEPS", in *Proc. of LER 2016*, Soleil, France, 2016.

[4] T. Naito *et al.*, "Multibunch beam extraction using the strip-line kicker at the KEK accelerator test facility", *Phys. Rev. ST Accel. Beams*, vol. 14, p. 051002, May 2011.

[5] D. Alesini *et al.*, "Design, test, and operation of new tapered stripline injection kickers for the e^+ e^- collider DA ΦNE", *Phys. Rev. ST Accel. Beams*, vol. 13, p. 111002, Nov. 2010.

[6] C. Belver-Aguilar, A. Faus-Golfe, F. Toral and M. J. Barnes, "Stripline design for the extraction kicker of Compact Linear Collider damping rings", *Phys. Rev. ST Accel. Beams*, vol. 17, p. 071003, July 2014.

[7] C. Pappas *et al.*, "Prototyping for ALS-U fast kickers", in *Proc. of IPAC'16*, Busan, Korea, 2016, pp. 3637-3639.

[8] C. Yao *et al.*, "Preliminary test results of a prototype fast kicker for APS MBA upgrade", in *Proc. of NAPAC 2016*, Chicago, IL, USA, 2016, pp. 950-952.

[9] C. Yao *et al.*, "Development of fast kickers for the APS MBA upgrade", in *Proc. of IPAC'15*, Richmond, VA, USA, 2015, pp. 3286-3288.

[10] X. Sun *et al.*, "Simulation studies of a prototype stripline kicker for the APS-MBA upgrade", in *Proc. of NAPAC 2016*, Chicago, IL, USA, 2016, pp. 928-930.

[11] Computer Simulation Technology (CST). https://www.cst.com

ISBN: 978-3-95450-206-6 doi:10.18429/JACoW-FLS2018-WEP2PT022

PHASE SHIFTER APPLICATION IN DOUBLE UNDULATOR CONFIGURATION OF HEPS

X. Y. Li, Y Jiao, S.K Tian
Key Laboratory of Particle Acceleration Physics and Technology, Institute of High Energy Physics, 100049 Beijing, China

Abstract

For over 6 meters long straight-section of HEPS, collinear double-cryogenic permanent magnet undulator(CPMU) is designed for high energy photon users to achieve higher brightness. Angular and spatial profiles of radiation produced by the double undulator configuration have been derived analytically. The efficiency of phase shifter on improving the brightness of double-CPMU is therefore evaluated with the beam energy spread and emittance are taken into account. Optimized beta-functions of electron beam are obtained.

INTRODUCTION

In the first phase of HEPS construction, a total of 14 ID-based beamlines are required for constructed, of which 7 are based on in-vacuum undulators [1]. In order to satisfy the requirement of high-energy users, the phase error of these Ids should be reduced to below 2-3 ° especially for the application of harmonics higher than 9th. Therefore, the maximum length of in-vacuum undulator has to be less than 3 meters due to the limitations of the current manufacturing process. This leads to the necessity of installing two undulators in series on one 6 meters long straight section. In this case, if is it necessary to install an additional phase shifter between the two undulators and its effects on the radiation performance when considering the real beam parameters has become a significant problem should be investigated.

An intuitive view of this issue is that it does necessary for the phase matching between the two undulators. coherence effect will increase the on-axis radiation intensity to 4 times higher that of single undulator for maximum which equivalent to an undulator with the total length doubled or reduce it to zero for minimum in the case of phase mismatch. The effects of emittance and energy spread has been ignored yet which cause this view divorced from reality. When taking the emittance and energy spread into account, a view is that the beam energy spread will seriously undermine the coherence condition between the two undulator radiations with increasing of energy spread, especially for high-energy hard X-rays. A characteristic periods number is defined by $N_{c,n} = \frac{1}{5n}\left(\frac{\sigma_\gamma}{\gamma}\right)^{-1}$ and equivalent periods number is defined by $N_{ep}=2N+\varphi/2\pi$. Where φ is the phase slip between the two undulators. Coherence effects could clearly observed only when $N_{c,n}>>N_{ep}$ [2] or the intensity distribution presents a geometrical superposition of intensity from two independent source points at the center of both undulators in the opposite case. The phase shifter has little effect in this case. However, it will see the conclusion is just opposite according to the work of this article later. Phase shifter is remain indispensable even if considering the effects of beam parameters.

To specify the performance of a synchrotron radiation (SR) source, photon flux density in the 4D phase space i.e. brilliance is the most common figure of merit. In general case, brilliance should be first calculated by the method of Wigner function [3] and then convoluted with the electron beam distribution in phase space to include the effects of emittance and energy spread. A widely used model to calculate the radiation brilliance from a single undulator is Gaussian approximation in the case of Gaussian electron beam distribution [4] which could help to simplify this calculation process. The only difference should be considered is that energy deviation of electrons will change the phase slip between the two undulators. Moreover, in most practical cases, it is sufficient to use on-axis brilliance to evaluated the SR performance. Therefore, we only calculate the on-axis brilliance in this paper.

RADIATION MODEL OF DOUBLE UNDULATOR CONFIGURATION

To start with the calculation of the spectra of the combination of two undulators with the phase shifter between them analytically, we illustrate the whole structure in Fig. 1 [5]:

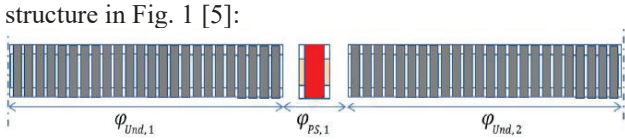

Figure 1: structure of the double undulator configuration.

Where $\varphi_{und,1}$ and $\varphi_{und,2}$ represent to the phase slip in each undulator. φ_{ps} is the phase slip between the two undulator. We ignore the front-ends of the two undulators for it only cause an additional phase slip which contain in φ_{ps}. The radiation field then is expressed by the sum of the two complex field emitted from both undulators as

$$E_{Double}(\omega,\theta,t) = \left[1 + e^{i(\varphi_{Und,1}+\varphi_{PS})}\right] E_{Single}(\omega,\theta,t),$$

Where E_{single} denote the field emitted from a single undulator. And the on-axis radiation intensity is written as

ISBN: 978-3-95450-206-6 doi:10.18429/JACoW-FLS2018-WEP2PT022

$$I_{Double}(\delta)=\left|e^{i\left[(1+\delta)n\varphi+\frac{2Nn\pi}{1+\delta}\right]}+1\right|^2 I_{Single}(\delta)$$

$$\propto 2\{1+\cos[(1+\delta)n\varphi-2Nn\pi\delta]\}Sinc^2(Nn\pi\delta).$$

Where $\delta=\Delta\omega/\omega_n$ is regarded as the detune factor. It is important to note that $\Delta\omega$ is the offset of the nth harmonic energy due to the electron energy deviation. It is differ from an arbitrary energy offset compare with the reference harmonic energy. N is the undulator periods number and φ represent the phase slippage between the two undulator without electron energy deviation.

On-Axis Angluar Flux Density

If we assumed the distribution of the energy spread is Gaussian with the RMS σ_ε, it caused the δ obeys the Gaussian distribution with the RMS $2\sigma_\varepsilon$. The on-axis angluar flux density is then a convolution shown as below.

$$I_{total}=\frac{1}{2\sqrt{2\pi}\sigma_\varepsilon}\int_{-\infty}^{\infty}e^{-\frac{\delta^2}{8\sigma_\varepsilon}}I_{Double}(\delta)d\delta$$

$$=\frac{1}{\sqrt{2\pi}\sigma_\varepsilon}(I_1+I_2)$$

$$I_1=\int_{-\infty}^{\infty}e^{-\frac{\delta^2}{8\sigma_\varepsilon}}Sinc^2(Nn\pi\delta)d\delta$$

$$I_2=\int_{-\infty}^{\infty}e^{-\frac{\delta^2}{8\sigma_\varepsilon}}\cos[(1+\delta)n\varphi-2Nn\pi\delta]Sinc^2(Nn\pi\delta)d\delta$$

It is indicated that I_{total} can be divided into two parts. The first part is the intrinsic angluar flux density emitted from each undulator and the second part is the contribution of coherence relate to the phase slippage φ. Integrate these two parts respectively.

There is an approximation in second integration is that

$$Sinc^2(Nn\pi\delta)\approx e^{-\frac{(Nn\pi\delta)^2}{2}}.$$

Figure 2 shows the effect of energy spread on on-axis angular flux density for different harmonics in the case of $\varphi=2\pi$. Where I_0 is the on-axis angular flux density of single undulator without energy spread. The total flux density is thus normalized by I_0. It is obviously that the flux density of high harmonics behaves more sensitive to the energy spread.

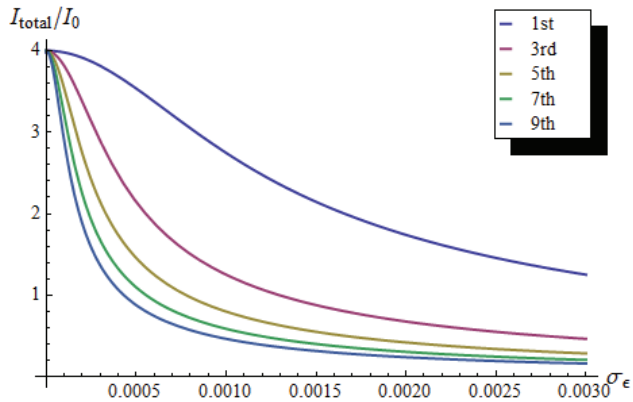

Figure 2: on-axis angular flux density of different harmonics vary with energy spread. We choose N=100 for the only undulator parameter during the calculation.

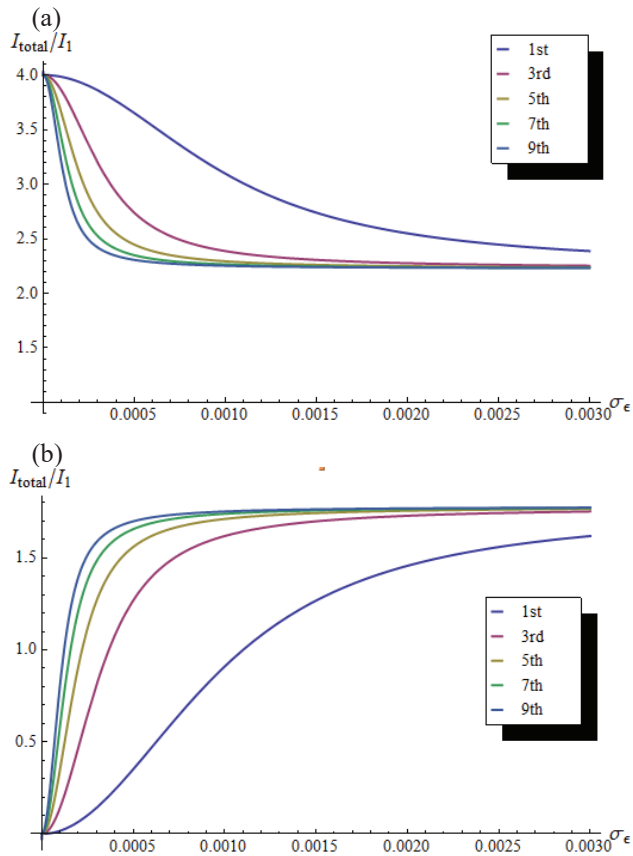

Figure 3: (a) gain of on-axis angular flux density of different harmonics vary with energy spread on the condition of phase matched. (b) gain of on-axis angular flux density of different harmonics vary with energy spread on the condition of phase mismatched.(N=100 in both case).

We introduce a gain factor defined by I_{total}/I_1 in order to tell if the phase shifter is necessary more intuitively. If the radiation from the two undulators was completely incoherence, the gain factor would be equal to 2. That means the total flux density is the sum of that from two undulators simply i.e. the phase shifter has little effects on the gain. It is clearly shown in Fig. 3 that even at the range of large energy spread the gain factor is not tend to

ISBN: 978-3-95450-206-6 doi:10.18429/JACoW-FLS2018-WEP2PT022

2 for both cases of phase matched and mismatched. It has at least 0.5-0.6 times of I_1 for difference between the two case which indicated the significance of phase matching by the phase shifter even taking the beam energy spread into account.

Angular Distribution of Photon Flux Density

We next investigate the angular flux distribution of double undulator configuration. We only interesting about the photon energy equals to the resonance energy without any deviation. In this case, the detune factor δ can be rewrite as a function of electron energy γ and observe angle θ given by

$$\delta(\theta,\gamma)=\frac{\omega_n(\gamma_0,0)-\omega_n(\gamma,\theta)}{\omega_n(\gamma,\theta)}$$

$$\omega_n(\gamma,\theta)=\frac{2\gamma^2}{\left(1+k^2/2+\gamma^2\theta^2\right)}\frac{2\pi c}{\lambda_u},$$

where λ_u is the period length of undulator and γ_0 represent to the energy without any offset. If we assume the offset of the electron energy $\Delta\gamma \ll \gamma_0$ it could be expressed the detune factor $\delta(\Delta\gamma,\theta)$ by

$$\delta(\Delta\gamma,\theta)=\frac{\gamma_0^2\theta^2}{1+k^2/2}-2\frac{\Delta\gamma}{\gamma_0} \qquad [6]$$

Substituted this expression into I_{double} derived above, angular flux distribution of nth harmonic is able to obtain analytically and shown as

$$I_{total}=\frac{2}{\sqrt{2\pi}\sigma_\varepsilon}\int_{-\infty}^{\infty}e^{-\frac{\varepsilon^2}{2\sigma_\varepsilon^2}}d\varepsilon \left\{1+\cos\left[\left(1+\delta(\varepsilon,\theta)\right)n\varphi-2Nn\pi\delta(\varepsilon,\theta)\right]\right\}Sinc^2\left(Nn\pi\delta(\varepsilon,\theta)\right) = 2\left(I_1+I_2\right),$$

where ε=Δγ/γ0 is the energy deviation. Integrate I1 and I2 respectively as before. The approximation of sinc function is still available in the integration.

Figure 4 shows the photon flux density distribution of observe angle at different harmonic energies. Figure 5 shows the comparison of the analytic results with the SPECTRA result. Both the results of the first and the third harmonic agree well.

It is also to see that energy spread extend the angular distribution range of radiation central cone according to Fig. 6. The RMS angular divergence can be derived from the angular flux distribution analytical as

$$\sigma_{r'}^2=\frac{\int_{-\infty}^{\infty}\theta^2 I_{total}(\theta,\sigma)d\theta}{\int_{-\infty}^{\infty}I_{total}(\theta,\sigma)d\theta}=\frac{DI_{total}}{TI_{total}}$$

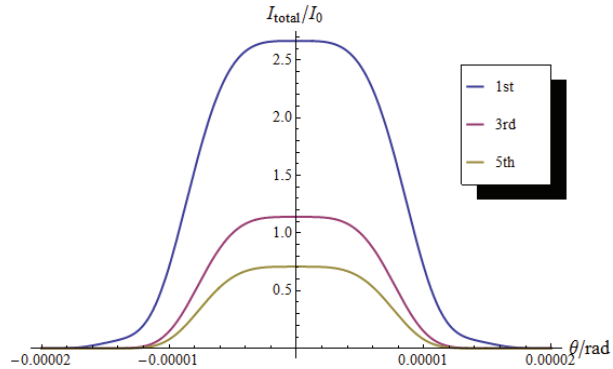

Figure 4: photon flux density distribution of observe angle at different on-axis harmonic energies. Parameters we chosen in this calculation are electron energy e equals to 6Gev, energy spread σε=0.1%, N=100, φ=2π, k=2.1.

(a)

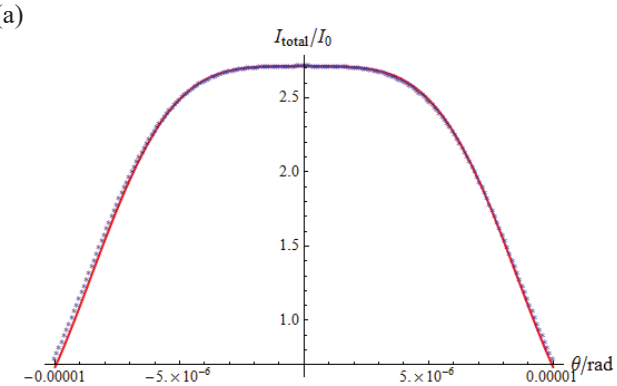

(b)

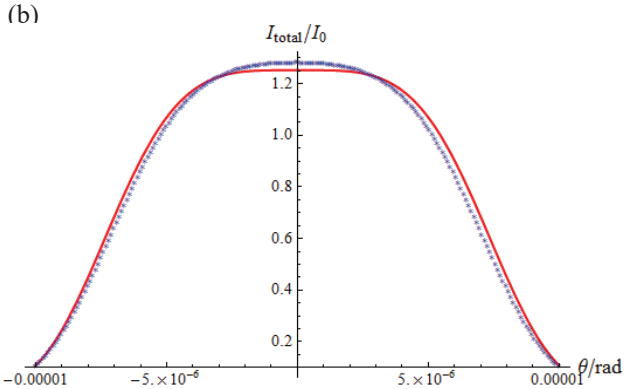

Figure 5: comparison of analytical results of angular flux density distribution with the SPECTRA result. where 5(a)for the first harmonic and 5(b)for the third harmonic. The dash line represent to the numerical results calculated by SPECTRA and the red line represent to the analytic result.

Substitutes the expression of I_{total} into the form above, the RMS angular divergence is obtained. Note that in the case of phase mismatched, the angular distribution of angular flux density is like a ring, only in the case of phase matched it makes the expressions above meaningful. The result of RMS angular divergence is shown in the Fig. 7.

ISBN: 978-3-95450-206-6 doi:10.18429/JACoW-FLS2018-WEP2PT022

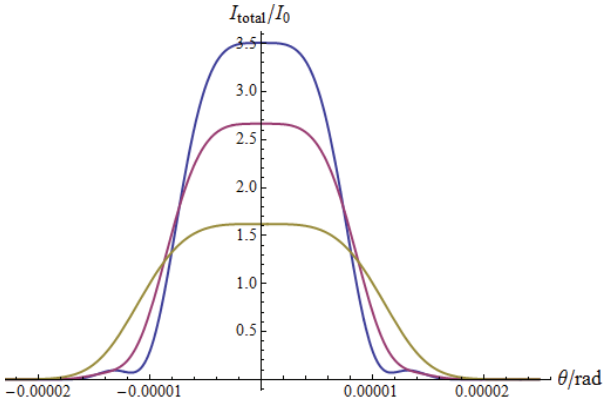

Figure 6: angular flux distributions with different energy spreads of first harmonic. Where Blue line, red line and yellow line represent to σε=0.05%, σε=0.1%, σε=0.2% respectively. Other parameters used in the calculation are the same with before.

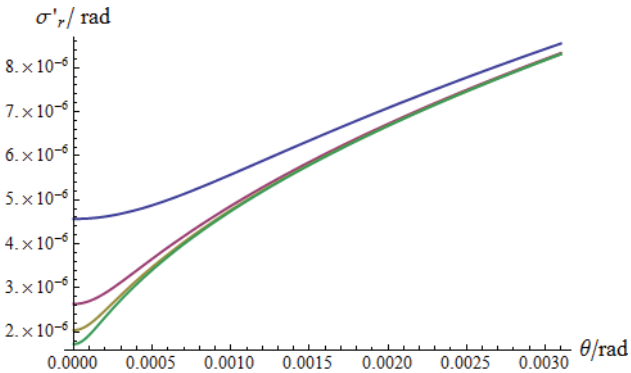

Figure 7: RMS angular divergences of different harmonics vary with energy spread. The condition of calculation is same as before.

Brilliance and Optimized Beta-Functions

Phase shifter works on the condition of phase matched in most cases for improving the brilliance. We also calculate the brilliance on this condition. For the angular distribution of photon density is near Gaussian, it is appropriate to use the well-know expression of brilliance in the Gaussian approximation as [4]

$$B = \frac{F}{4\pi^2 \Sigma_x \Sigma'_x \Sigma_y \Sigma'_y}$$

$$= \frac{F}{4\pi^2 \left[\sigma_x^2 + \sigma_r^2(\sigma_\varepsilon)\right]\left[\sigma'^2_x + \sigma'^2_r(\sigma_\varepsilon)\right]\left[\sigma_y^2 + \sigma_r^2(\sigma_\varepsilon)\right]\left[\sigma'^2_y + \sigma'^2_r(\sigma_\varepsilon)\right]}$$

where

$$F = 2\pi\sigma'^2_r I_{total}.$$

In order to calculate the brilliance, it is necessary to obtain the expression of photo source size which should obtain by the Fourier transform at the source points in general. We make a simplification treatment in this paper as shown below [7]:

$$\sigma_r(\sigma_\varepsilon) = Qs(\sigma_\varepsilon)\sigma_r(0)$$

$$\sigma_r(0) = \frac{\lambda_n}{4\sigma'_r(0)}$$

$$Qs(x) = 4\left[\frac{1}{2I_1(x/4) + 2I_2(x/4)}\right]^{2/3}$$

Assuming the electron and the photon beam waists are both located to the middle of the straight section. The optimized beta-function is then obtain by

$$\beta_0 = \frac{\sigma_r(\sigma_\varepsilon)}{\sigma'_r(\sigma_\varepsilon)}.$$

Figure 8 shows the brilliance tune-curve of CPMU18 which has the undulator parameters same as before. The beam parameters are chosen according to the latest HEPS lattice scheme which εx=34.2pm, βx=1.9m, εy=4pm, βy=2.2m, σε=0.106% and current I=0.2A. We compare the brilliance of double undulator configuration with the single undulator which the length is doubled. It is clearly to see the beam parameters effects on double undulator configuration is more significant than the latter. In Fig. 9 brilliance of CPMU18 calculated under two different lattice schemes of HEPS are compared. The brilliance of double undulator configuration is more sensitive to the energy spread than to the emittance especially for the high harmonics. It is indicated in Fig. 10 that the optimized beta-function the no more a constant but a function of the energy spread and harmonic number when take the energy spread into account.

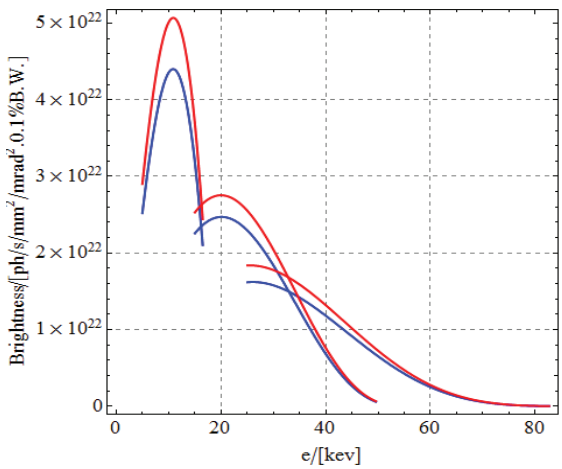

Figure 8: brilliance tune-curve of CPMU18. Where εx=34.2pm, βx=1.9m, εy=4pm, βy=2.2m and current I=0.2A. the remain parameters are the same as before. The red line represent to the brilliance of single undulator with the length doubled. The blue line is the brilliance of double undulator configuration.

ISBN: 978-3-95450-206-6 doi:10.18429/JACoW-FLS2018-WEP2PT022

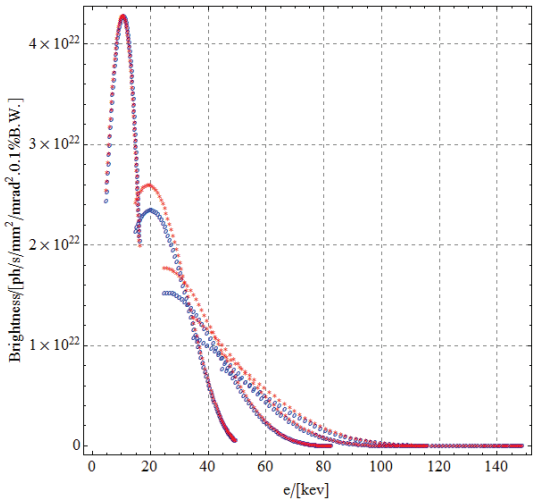

Figure 9: brilliance comparison of CPMU18 between the two different parameter schemes. The only two differences of parameters in these two schemes are emittance and energy spread. The blue points refer to the scheme with emittance εx=34.2pm and energy spread σε=0.106% while the red points refer to the scheme with emittance εx=40pm and energy spread σε=0.081%. Any other parameters are the same as that in Figure 9.

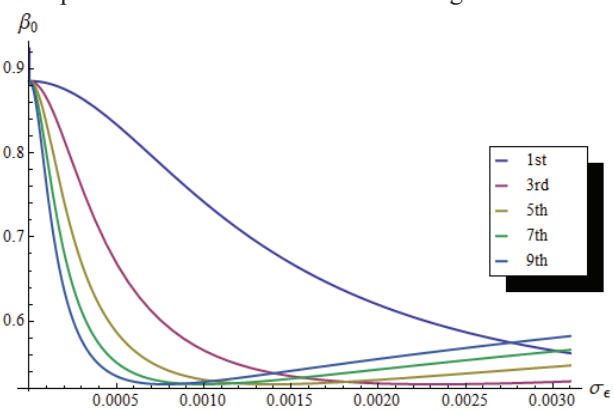

Figure 10: optimized beta-function vary with the energy spread at different harmonic number.

SUMMARY

An analytic expression of the on-axis brilliance and angular flux density distribution are derived. The analysis above indicates that the double undulator configuration with a phase shifter in the middle appears more sensitive to the energy spread than a single undulator which makes us to pay more concern about the energy spread during the lattice design of the storage ring. However, energy spread can not undermine the coherence thoroughly yet i.e. phase shifter is necessary in any cases. The optimized beta-function is then no longer a constant but a function of energy spread and harmonic number.

REFERENCE

[1] Toru Hara, Takashi Tanaka, and Hideo Kitamura, "Cryogenic permanent magnet undulators", *Phys. Rev. ST Accel. Beams*, vol. 7, p. 050702, 2004.

[2] Jui-Che Huang, HideoKitamura, Chin-KangYang, Mau-SenChiu, Cheng-Hsiang Chang, Ching-ShiangHwang, "Applicability of a double-undulator configuration", *Nucl. Instr. and Meth. A*, 808, p. 93-103, 2016.

[3] K.-J. Kim, in *Proc SPIE 1986*, vol. 582, p. 2.

[4] Kim K. J., "Brightness, coherence and propagation characteristics of synchrotron radiation". *Nucl. Ins. Meth. Phys. Res.Elsevier Science Publishers*, 1986, vol. A, p.246.

[5] Yuhui Li, Joachim Pflueger, "Phase matching strategy for the undulator system in the European X-ray Free Electron Laser", *Phys. Rev. ST Accel. Beams*, vol.20, p.020702, 2017.

[6] Elleaume P., "Undulators, wigglers and their applications", edited by H. Onuki and P. Elleaume. London : Taylor & Francis, 2003, pp. 598.

[7] Takashi Tanaka, Hideo Kitamura, "Universal function for the brilliance of undulator radiation considering the energy spread effect", *Journal of Synchrotron Radiation,* vol.16, p. 380-386, 2009.

ISBN: 978-3-95450-206-6 doi:10.18429/JACoW-FLS2018-WEP2PT023

PREPARATION AND CHARACTERIZATION OF NON-EVAPORABLE Ti–Zr–V GETTER FILMS FOR HEPS*

Ping He, Yong-Sheng Ma#, Yuchen Yang, Di-Zhou Guo, Baiqi Liu
Institute of High Energy Physics, CAS, Beijing, China

Abstract

For the low activation temperature and high pumping speed, surface pumping capacity, the TiZrV coatings were chosen to high energy photo source (HEPS). Films of TiZrV alloy have been deposited on 1.5 meter long, cylindrical vacuum chambers of 22mm diameter copper substrates in krypton ambient using DC magnetron sputtering system.

Film composition, the activation temperature and pumping properties have been investigated in order to optimize the deposition parameters for vacuum applications. The films were also studied using the X-ray photo-emission electron spectroscopy (XPS) after annealing them at different temperatures ranging from 180℃ to 300℃ for half hour in ultra-high vacuum environment.

Pumping speed and surface pumping capacity testing facilities were also being constructed to investigate the characterization of TiZrV.

INTRODUCTION

The present work is being undertaken in the frame of Beijing Advanced Light Source project at Institute of High Energy Physics (IHEP). To further develop the technologies necessary for diffraction-limited storage rings based light source, it involves five areas: vacuum system/non-evaporative getter (NEG) coating of small chambers, injection/pulsed magnets, RF systems/bunch lengthening, magnets/radiation production with advanced radiation devices, and beam physics design optimization. By focusing the current beam to develop high brightness x-ray synchrotron, it requires beam lines in centimetre or even millimetre range in diameter in order to gain good control of beam position and shape. When the vacuum conductance is much reduced in such narrow chambers, they are difficult to reach ultrahigh vacuum (UHV) that is necessary for accelerators. Getter films deposited on the inner surface of the chamber would transform the vacuum chamber from an outgassing source into a pump.

The extensive use of NEG based pumping systems for large UHV systems, such as particle accelerators and Tokamak reactors, was pioneered by the European Organization for Nuclear Research (CERN) at the time of the design phase of the Large Electron Positron (LEP) collider [1 - 3]. The NEG strip covered about 23 of the 27 km of the LEP machine, providing vacuum in the range of 10e-10 Pa. Since then, SAES-Getters have made the NEG strip commercially available. NEG pumps contribute to the achievement of UHV in storage rings for particle physics research and synchrotron radiation production, and are widely accepted by the accelerator community. In recent years [4 - 6], different getter materials have been investigated, Innovative vacuum pumps, based on the combination of sputter-ion pumps (SIPs) with NEG technology have been invented [7].

In this context, our work will focus on the progress of the deposition of NEG coatings in very narrow chambers, as well as engineering and physics challenges they face today.

PREPARATION OF THE GETTER FILMS

A schematic diagram of the experimental setup for NEG deposition is shown in Fig. 1. The sample is a 1.5 m long, 22 mm in inner diameter copper cylindrical tube. The cathode was made by twisting three wires of high-purity (99.95%) titanium, vanadium and zirconium, each of 1 mm diameter. TiZrV type was chosen because of its lowest activation temperature among ternary getters.

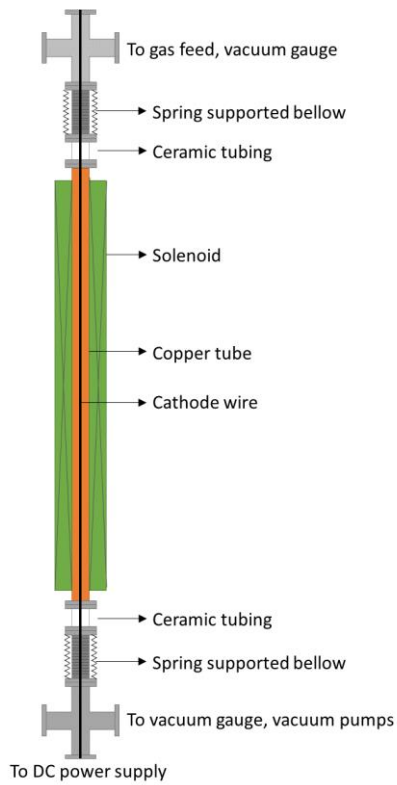

Figure 1: Schematic diagram of the experimental system for NEG deposition.

The tube sample is electrically isolated mounted to the chamber in the direction of gravity. The cathode wire runs through the tube sample and is positioned approximately

* Work supported by IHEP
#mays@ihep.ac.cn

ISBN: 978-3-95450-206-6 doi:10.18429/JACoW-FLS2018-WEP2PT023

along the axis of the tube. The bottom end of the cathode wire was connected to a high voltage feedthrough, and the top end was mounted to a viewpoint. Gas inlet was mount on the top of the system, and the vacuum pumps are mounted in the bottom. A solenoid was mounted outside and coaxial to the sample tube, providing a magnetic field parallel to the electric field.

The system was evacuated with a 350 l/s turbo molecular pump backed by an oil-free mechanical pump and baked for 2 days at 200℃ to a base pressure in the 1.0e-9 mbar range. High purity krypton was injected using a mass flow controller. The flow rate could be adjusted up to 10 sccm to obtain the desired operational pressure, which was typically in 1.5×10^{-2} mbar. The solenoid is powered by a DC power supply, providing a desired magnetic field about 200 ~1000G. The discharge was powered by a DC power supply, capable of delivering up to 1000V and 1A. During deposition, the power was set to be approximately 80 W. The deposition time was 12 h. As shown in Fig. 2, the NEG coating was uniformly deposited on the inner surface of the entire copper tube.

Figure 2: A photo of the NEG coating deposited on the inner surface of a 1.5 m long, 20 mm inner diameter copper tube. The tube was sliced open manually.

CHARACTERIZATION OF THE GETTER FILMS

The average composition of the TiZrV films, measured by Rutherford backscattering (RBS) analysis, is Ti 21at.%, Zr 29 at.%, and V 50 at.% with the assumption that the sum of the atomic percentage of Ti, Zr and V is 100%. XRD analysis showed that the size of nanocrystalline is lower than 5nm.

The Activation Process

The activation process of TiZrV films was characterized by the XPS in an ultra-high-vacuum (UHV) chamber. The thermal activation process was performed by heating at 80℃ for 8h to degas, and annealing at intervals throughout 180, 250 and 300 °C for 30 min and then were cooled down to room temperature. Then the XPS spectra were recorded. Figure 3 shows the Ti2p, V2p, Zr3d XPS spectra of TiZrV film. The binding energy (BE) of the Ti 2p spectrum peak of as-deposited (air-exposed) film is 458.3 eV (doublet separation of Ti 2p, Δ=5.7 eV), whose value corresponds to that of titanium oxide TiO_2, as shown in Fig. 3A. A mixture of metallic state Ti^0 at BE=454.1 eV and low valence Ti^{n+} ($n<4$) states is observed after activation at temperature of 180 °C or higher. The variations for V 2p spectrum peaks on the activation temperature are similar to those of Ti 2p, as shown in Fig. 3B. For the air-exposed TiZrV film, BE of the $V2p_{3/2}$ is 515.5 eV, whose value corresponds to oxidized V (V^{3+}). The vanadium oxide of the surface layer is markedly reduced to the metallic state V^0 after activation at temperature of 180 °C or higher. The series of Zr 3d spectra of TiZrV film are shown in Fig. 3C. For the air-exposed TiZrV film, the binding energy of the Zr $3d_{5/2}$ is 182.5 eV, whose value corresponds to closely oxidized Zr (Zr^{4+}). The Zr $3d_{5/2}$ peak also shifts to lower binding energy of lowly oxidized state Zr^{n+} ($n<4$) or metallic Zr state (Zr^0) after the activation from 180 °C to 300 °C. These mean that the highly oxidized Zr (Zr^{4+}) gradually changes to sub-oxidized Zr (Zr^{n+}, $n<4$) and metallic Zr^0 with the increase of activation temperature. [8]

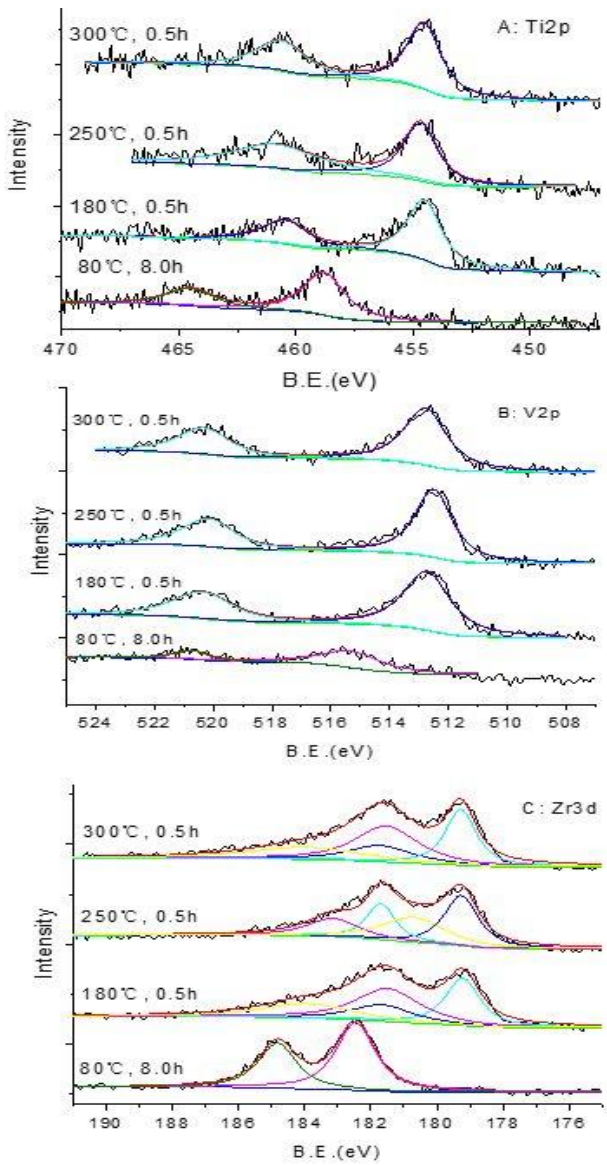

Figure 3: The series of Ti 2p, V 2p and Zr3d XPS spectra of TiZrV film at various heating temperatures.

ISBN: 978-3-95450-206-6 doi:10.18429/JACoW-FLS2018-WEP2PT023

Pumping Properties

The pumping speed per unit area is defined as:

$$S = \alpha \cdot C_{gas}\ [l \cdot s^{-1} \cdot \mathrm{cm}^{-2}] \quad (1)$$

where α is the sticking probability ($0 \leqslant \alpha \leqslant 1$), which could be calculated by Monte Carlo simulation through simulation, and C_{gas} is the conductance, expressed in $[l \cdot s^{-1} \cdot \mathrm{cm}^{-2}]$. In the molecular flow regime, C_{gas} does not depend on the pressure. It may be expressed as:

$$C_{gas} = 3.64\sqrt{\frac{T}{M}}\ [l \cdot s^{-1} \cdot \mathrm{cm}^{-2}] \quad (2)$$

The total gas absorbed by NEG film is define as:

$$Q_0 = \int_0^t C_{or} \cdot (P3 - P2)dt\ [\mathrm{mbar} \cdot l \cdot s^{-1}] \quad (3)$$

The schematic of pumping properties test facility of NEG pipe is show in Fig. 4. After 48h, 250℃ degassing of vacuum chamber, and 24h, 180℃ or higher activation process. The sticking factor of CO, H_2 were tested. From the test we would get the P_1/P_2 ratio corresponding to CO or H_2, and capacity of TiZrV NEG film calculated by equation (3). The conductance of orifice for CO is 3.89 l/s.

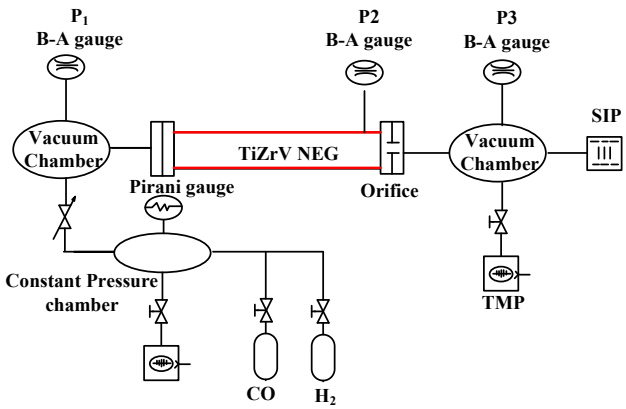

Figure 4: The schematic of pumping properties test facility of NEG pipe.

When CO inlet, P_1 is about 1.0×10^{-8}mbar, P_2 is about 1.0×10^{-5}mbar, P_3 is about 3.0×10^{-5}mbar. The pumping test result is show in Table 1. Maybe because the P_1 is measured by total pressure, so the P_2/P_1 ratio is very low and correspond sticking factor is lower than 0.01 which is about 1/80 of literature [9].

Table 1: Result of Pumping Test of NEG Film at Different Temperature

No. run	Test gas	capacity	Vacuum Ratio
		mbar.l/cm^2	P_2/P_1
NO30-4-300	CO	8.32E-05	717.9
NO30-5-180		7.36E-05	1454
NO30-6-180		6.67E-05	1200
NO30-7-250		7.78E-05	1333.3
NO30-9-250	H2	2.75E-03	220

CONLUTION

Facility of TiZrV NEG film coating system and pumping test system were built. 1.5 meter long and 22mm diameter cylindrical copper substrates vacuum chambers were coated. XPS analysis show that Ti2p, Zr3d, V2p spectra shift to low binding energy when activation temperature increase to 180℃. But may due to the measured error, the pressure ratio between two sides of NEG pipe is low. Consequently, the sticking factor α to CO and H_2 is low.

ACKNOWLEDGEMENT

The authors thank the Accelerator Centre of Institute of High Energy Physics for financial support. Also thanks to the experimental conditions and experimental guidance provided by the vacuum group of IHEP.

REFERENCES

[1] C. Benvenuti and J.C. Decroux, Proc. VII IVC, III ICSS, 1, 85, Vienna, 1977.
[2] C. Benvenuti, *Nucl. Instr. Meth.* 205, 391, 1983.
[3] T. A. Giorgi, *Jap. J. Appl. Phys. Suppl.* 2, 53, 1974.
[4] B. Malyshev, R. Valizadeh, A. N. Hannah, *Vacuum,* 100, 2014.
[5] J. Setinaa, S. Avdiajb, B. Erjaveca, *Vacuum,* 92, 2013.
[6] Y. Xu, J. Cui, H. Cui, H. Zhou, Z. Yang, J. Du, *J. Alloys Compd.* 661, 15, 2016.
[7] T. Porcelli, F. Siviero, G. A. Bongiorno, P. Michelato, C. Pagani, *Vacuum*, 123, 2016.
[8] C.C. Li, J.L. Huang, R.J. Lin. *Thin Solid Films*, 517, 2009, p.3672–3676.
[9] C. Benvenuti, P. Chiggiato, P. Costa Pinto. *Vacuum*, 60, 2001, p.57-65.

ISBN: 978-3-95450-206-6 doi:10.18429/JACoW-FLS2018-WEP2PT024

INFLUENCES OF HARMONIC CAVITIES ON THE SINGLE-BUNCH INSTABILITIES IN ELECTRON STORAGE RINGS

H. S. Xu*, N. Wang
Key Laboratory of Particle Acceleration Physics and Technology,
Institute of High Energy Physics, Chinese Academy of Sciences, Beijing, China

Abstract

Single-bunch instabilities usually determine the bunch performance at high charges as well as the highest single-bunch currents in storage rings. It has been demonstrated that the passive harmonic cavities, which have been widely used in electron storage rings of the third-generation synchrotron light sources, can generally make the beam more stable. However, the influences of the harmonic cavities on the single-bunch instabilities are still not fully understood. We hereby present our study of both longitudinal and transverse single-bunch instabilities when using different settings of the harmonic cavities.

INTRODUCTION

Harmonic cavities have been used to lengthen the bunches in the storage rings of many existing ring-based synchrotron light sources [1,2]. The increase of the Touschek lifetime due to the implementation of the harmonic cavities has been carefully studied and demonstrated in the operations of many machines [3–5]. Some studies show that the harmonic cavities help cure the longitudinal coupled-bunch instabilities [6–8]. Moreover, there are also some studies indicating that the harmonic cavities help stabilize the transverse coupled-bunch instabilities [9].

The newly proposed ultra-low emittance rings are usually more sensitive to the collective beam instabilities, while the total impedance of the rings tends to be higher since the the much narrower vacuum chambers will be used. Therefore, people pointed out that it would be essential for the ultra-low emittance rings to implement the harmonic cavities to lengthen the bunches.

However, almost all of the existing harmonic cavities work in the 'passive' mode, meaning that no external RF power source will be used, the voltage in the harmonic cavities is induced only by the charged particle beam. In the operation mode with passive harmonic cavities, the voltage and phase of the RF field in the harmonic cavities would be determined mainly by charged particle beams. Therefore, it's non-trivial to optimize the settings of the passive harmonic cavities for different operation modes due to the lack of knobs. We are also considering to propose the active harmonic cavities in the HEPS storage ring for keeping the flexibility to optimize the settings of the harmonic cavities in different operation modes. Nevertheless, we need to understand better the influences of the harmonic cavities on the singe-bunch instabilities first.

* haisheng.xu@ihep.ac.cn

In the longitudinal direction, microwave instability is usually dominant. Studies of the microwave instability in both cases without and with ideal lengthening harmonic cavities have been reported for different machines. It would be interesting to carry out more studies between these two conditions. In the transverse direction, both the Transverse Mode-Coupling Instability (TMCI) and the head-tail instability could be the limiting factors. There hasn't been a universal explanation of the influences of the harmonic cavities on both the above mentioned transverse single-bunch instabilities. We hereby would like to carry out simulation studies of the above mentioned single-bunch instabilities. Our work will help understand the influences of the settings of the harmonic cavities. Hereby, we use the lattice and the impedance model loosely based on HEPS, the key parameters of which are listed in Table 1.

Table 1: Key Lattice Parameters Used in the Studies, which are Loosely Based on the HEPS

Parameters	Symbols	Values and Units
Circumference	C	1360.4 m
Beam Energy	E_0	6 GeV
Total Current	I_0	200 mA
Vertical Tune	ν_y	106.16
Momentum Compaction Factor	α_c	1.28e-5
Natural Energy Spread	δ_p/p	1.14e-3
Average Radiation Energy Loss per Turn	U0	2.81 MeV
Harmonic Number of the Primary RF	h_1	756
Frequency of the Primary RF	f_0	166.60 MHz

The impedance model, consisting of most of the typical components, is shown in Figure 1. The simulations are mainly carried out by the `elegant` [10] and Pelegant [11] codes. Therefore, the convension used in Figure 1 is the same as the definition in `elegant`.

HIGHER HARMONIC CAVITY

As mentioned in Table 1, we propose to use 166.60 MHz as the frequency of the primary RF cavities. The third harmonic cavity (≈ 500 MHz) is chosen to provide bunch lengthening in our studies. If we consider using the active harmonic cavity, meaning that both the voltage and phase of the harmonic cavity can be adjusted freely, we can reach the

ISBN: 978-3-95450-206-6 doi:10.18429/JACoW-FLS2018-WEP2PT024

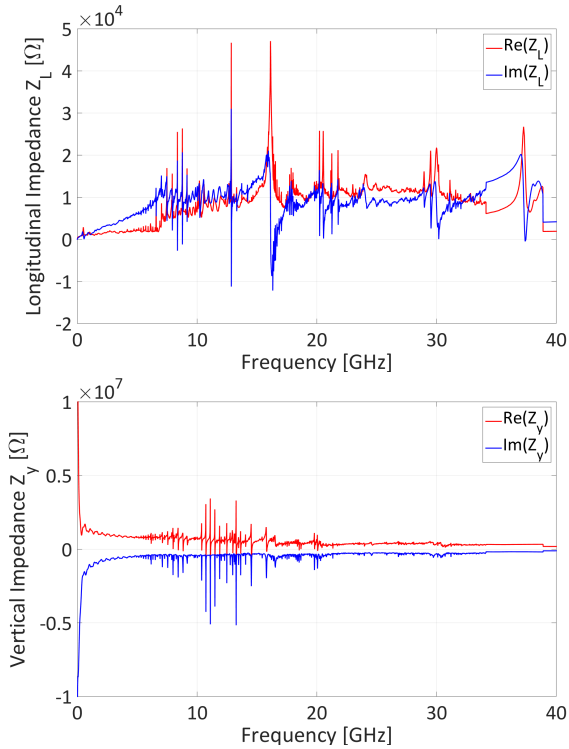

Figure 1: Impedance model used in the studies. The upper and lower subfigures correspond to the longitudinal and vertical impedance spectrum, respectively.

following ideal-flat potential condition [12]:

$$\sin\phi_s = \frac{V_{HC}}{V_{RF}}\sin\phi_{HC} + \frac{U_0}{eV_{RF}} \tag{1}$$

$$\cos\phi_s = \frac{V_{HC}}{V_{RF}} h\cos\phi_{HC} \tag{2}$$

$$\sin\phi_s = \frac{V_{HC}}{V_{RF}} h^2\sin\phi_{HC} \tag{3}$$

where, V_{RF} and V_{HC} are the peak voltage of the primary RF cavities and the peak voltage of the harmonic cavities, respectively; ϕ_s and ϕ_{HC} are respectively the synchronous phases of the primary RF cavities and the harmonic cavities; U_0 represents the average radiation energy loss per turn; $h = h_{HC}/h_1$ is the harmonic index.

However, besides the cases without harmonic cavity and with harmonic cavity under the ideal-flat potential condition, there are more settings in between, corresponding to different bunch lengthening conditions, different bunch distributions, etc. By adjusting the voltage of the harmonic cavities, we could get two typical conditions. When the voltage of the harmonic cavities is smaller than the value under the ideal-flat potential condition, the bunch lengthening is not as significant. This case is one of the typical settings of the harmonic cavities, marked as the 'HC set1' in the following text. Keep increasing the voltage of the harmonic cavity to higher than the case of the ideal-flat potential condition, there will be one unstable fix point in the middle of the RF bucket, in between of the two stable fix points. The bunch distribution will have 'double-hump' shape, as marked by the 'HC set4'.

Besides the above mentioned two typical settings, it's also interesting to study the dynamics near the ideal-flat potential condition. By adjusting the phase of the harmonic cavity to ±0.5°, we manage to get the two typical settings which correspond to the two different distorted distributions towards the head (HC set2) and the tail (HC set3) of the bunch, respectively.

The Hamiltonian tori of the above mentioned conditions are shown in Figure 2, while the corresponding bunch distributions are shown in Figure 3.

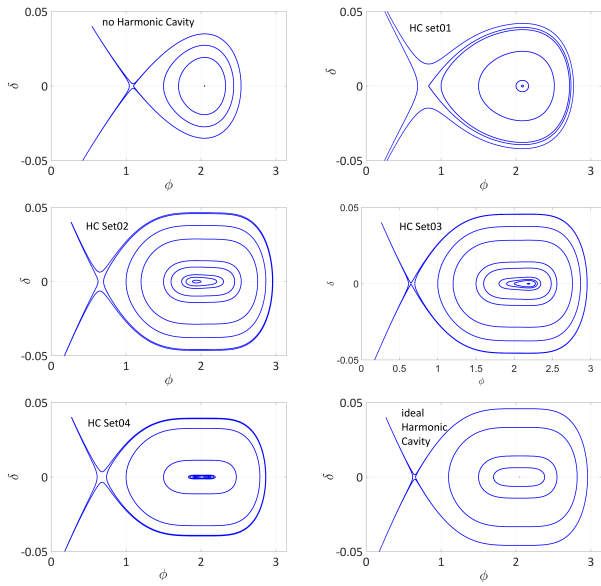

Figure 2: Harmiltonian tori at different settings of the harmonic cavity.

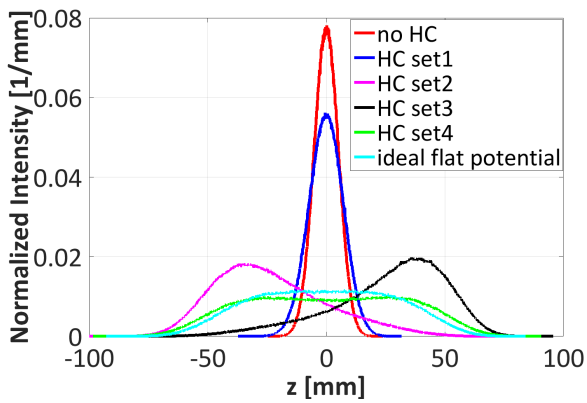

Figure 3: Equilibrium bunch distributions at different settings of the harmonic cavities without considering the beam coupled impedance.

ISBN: 978-3-95450-206-6 doi:10.18429/JACoW-FLS2018-WEP2PT024

MICROWAVE INSTABILITY

Microwave instability is a kind of very important longitudinal single-bunch instability which can induce the bunch turbulent in the longitudinal phase space and the increase of the energy spread of a bunch. It has been demonstrated that the bunch lengthening effect because of the implementation of the harmonic cavities manages to increase the microwave instability threshold. Implementing the above mentioned different settings of the harmonic cavities, we get the variation of the bunch length and the energy spread in different cases, as shown in Figure 4. The situation without harmonic cavities is also simulated to be used for comparison.

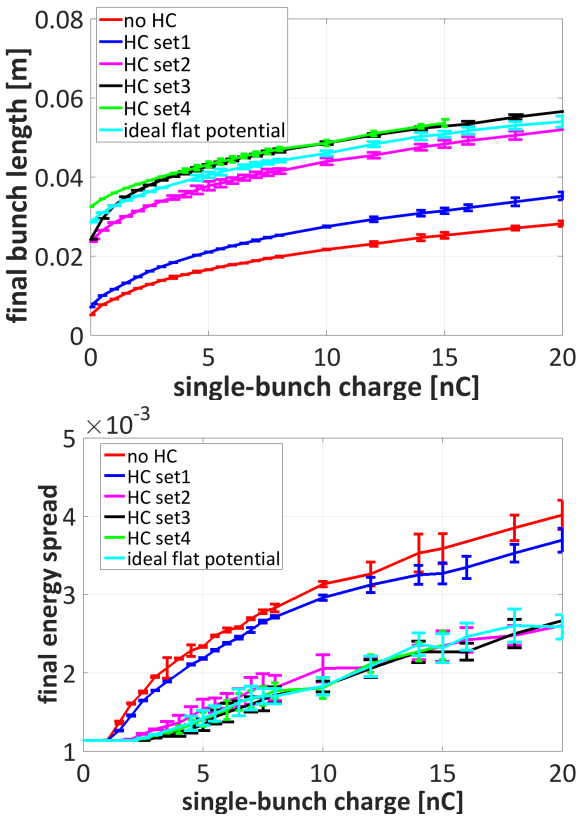

Figure 4: Bunch length and energy spread with the increasing single-bunch charge. The different curves are obtained using different settings of the higher harmonic cavity.

As we can see from the upper plot in Figure 4, the bunch length in the case without harmonic cavity is about 6 mm at zero current. The bunch length in the 'HC set1' is very closed to the case without harmonic cavities since the voltage in the harmonic cavities is much smaller than the ideal-flat potential condition. For the cases 'HC set2', 'HC set3', and 'HC set4', the bunch lengths are closer to the ideal-flat potential condition. We notice that the bunch is always longer when the bunch has a 'double-hump' in the 'HC set4' than the values in the ideal-flat potential condition. The 'HC set3' is more interesting since it has shorter bunch length than the ideal flat potential case at zero current. However, the bunch lengthening is faster than the ideal-flat potential condition case when increasing the single-bunch charges. This fact is mainly because the bunch distorts towards the tail of the bunch without considering the impedance effects. However, if we consider the beam impedance interactions, we can find that some particles losing energy and therefore moving towards the head of the bunch. when we keep increasing the single-bunch charge under the 'HC set3' condition, we can observe the bunch getting flatter first when we consider the potential-well distortion effect. The final bunch distributions (the bunch distributions at the 50000th turn) at different single-bunch charges under the conditions without harmonic cavity, HC set3, and with ideal-flat potential condition, are shown in the Figure 5.

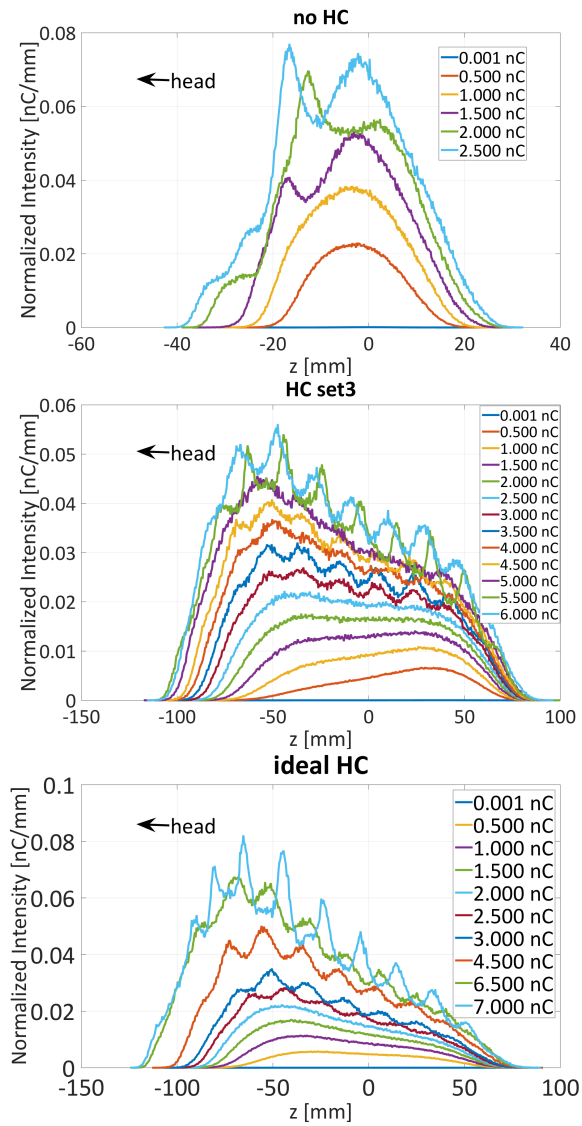

Figure 5: Bunch final distributions under different settings of the harmonic cavities at different sigle-bunch charges.

This fact makes the bunch becoming longer than the ideal flat bunch when the bunch charge is getting higher. Seeing the energy spread, we can see that the cases 'HC set2', 'HC set3', 'HC set4', as well as the ideal-flat potential case, have

ISBN: 978-3-95450-206-6 doi:10.18429/JACoW-FLS2018-WEP2PT024

similar threshold and the growth of the energy above the threshold current is also quite the same. It seems from the results that the microwave instability threshold is not very sensitive to the settings of the harmonic cavities if the bunch lengths are similar. This fact means that we can benefit from the harmonic cavity if the bunch lengthening effect can be obtained. For the purpose of increasing the microwave instability, the ideal-flat potential condition is not necessary.

TRANSVERSE SINGLE-BUNCH INSTABILITIES

We also carried out the studies of the transverse single-bunch instabilities under the above mentioned settings of the harmonic cavities. This problem itself is non-trivial since the influences of the harmonic cavities on the transverse single-bunch instabilities is still not very clear. Therefore, our studies would help get better understanding of this problem.

We first carried out particle tracking including the vertical short-range wake field at zero chromaticity. by observing the bunch centroid oscillation, we can distinguish whether the bunch is stable or not. The two curves in Figure 6 show the typical cases below and above the TMCI threshold current, corresponding to the stable beam motion and unstable motion, respectively. By fitting the envelope of the bunch centroid oscillation data, we manage to calculate the growth rates in different cases. The results show that the TMCI threshold current is a bit higher than the cases without harmonic cavity or HC set1. But the difference is quite small. More interesting phenomenon is that the threshold current in the non-ideal lengthening cases (HC set2, HC set3, and HC set4) are all a little bit higher than the ideal-flat potential case. This fact means that the so-called ideal-flat potential condition doesn't necessary to be better from the TMCI point of view.

When we implement finite chromaticity, e.g. $\xi_y = +1$, the similar simulations and analyses can be done, as shown in the lower plot in Figure 7. The increase of threshold currents due to the implementation of harmonic cavities can be clearly observed. By comparing the threshold currents between zero and +1 chromaticities under different harmonic cavities setttings respectively, one can find that the remarkable increase of the threshold current at +1 chromaticity. If comparing the threshold current among different harmonic cavities settings, we can find again that the ideal flat potential condition doesn't correspond to the optimum threshold current. Our preliminary study shows the fact clearly. We need carry out more systematic theoretical and tracking studies to understand this dynamics better.

CONCLUSION AND DISCUSSION

In this paper, we carried out some preliminary studies of the influences of the harmonic cavities on the longitudinal and transverse single-bunch instabilities. Six typical settings of the harmonic cavities (including the case without harmonic cavity) are used.

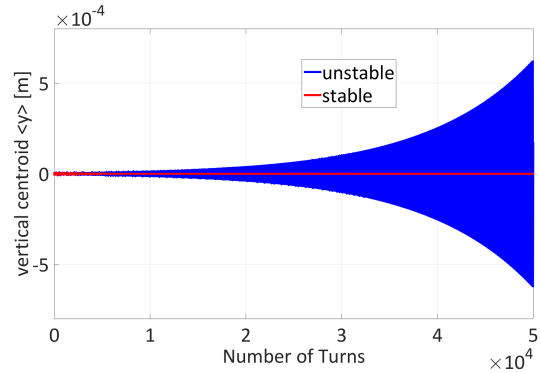

Figure 6: Beam centroid positions vs. number of turns at different single-bunch charges.

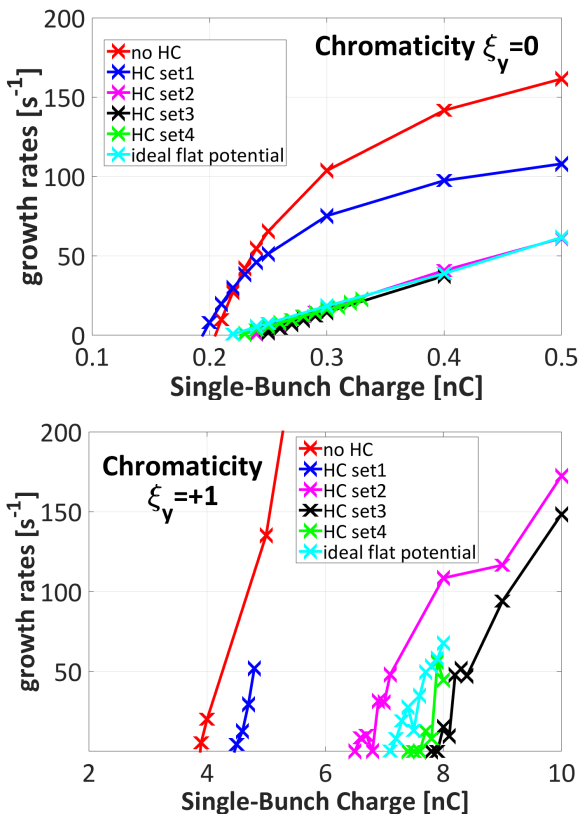

Figure 7: Growth rates at different chromaticities and different settings of the harmonic cavities.

In the longitudinal direction, the studies of the influences of the harmonic cavities settings on the microwave instability show that the longer bunch loosely corresponds to higher threshold current. when the bunch lengths in different cases are closed to the value under the ideal-flat potential condition, the microwave instability threshold current are quite similar. Therefore, there is no need to fulfill the ideal-flat potential condition for the purpose of increasing the microwave instability threshold.

The dependence of the transverse single-bunch instabilities on the settings of the harmonic cavities are a bit more complicated. The way of the harmonic cavities settings

ISBN: 978-3-95450-206-6 doi:10.18429/JACoW-FLS2018-WEP2PT024

influence the transverse single-bunch instability threshold currents depend also on the chromaticities. Anyway, we can loosely say that the longer bunch tends to be more stable. We still need to carry out systematic studies to understand the influences of the harmonic cavities settings on the transverse single-bunch instabilities.

ACKNOWLEDGMENT

The authors would like to thank the colleagues in the Accelerator Physics Group of IHEP for the fruitful discussions. The author Haisheng Xu would like to thank the '100 Talents Program of Chinese Academy of Sciences' for supporting most of the work presented in this paper.

REFERENCES

[1] M. Migliorati, *et al.*, "Bunch length control in DAΦNE by a higher harmonic cavity", *Nuclear Instruments and Methods in Physics Research* A 354 (1995) 215-223.

[2] J. M. Byrd and M. Georgsson, "Lifetime increase using passive harmonic cavities in synchrotron light sources", *Phys. Rev. ST Accel. and Beams*, Vol. 4, 030701 (2001)

[3] J. Jacob, *et al.*, "Effects of a Harmonic Cavity at the ESRF", in the Proceedings of the 1999 Particle Accelerator Conference, New York, 1999.

[4] J. M. Byrd, *et al.*, "Harmonic Cavities and Longitudinal Beam Stability in Electron Storage Rings" in the Proceedings of the 2001 Particle Accelerator Conference, Chicago, 2001.

[5] M. Pedrozzi, *et al.*, "SLS Operational Performance with Third Harmonic Superconducting System", in the Proceedings of the 11th Workshop on RF SuperConductivity, Lübeck/Travemünder, Germany.

[6] E. Weihreter, *et al.*, "Instability Studies and Double RF-System Operation at BESSY", *IEEE Transactions on Nuclear Science*, Vol. NS-32. No. 5. October 1985.

[7] R. A. Bosch and C. S. Hsue, "Suppression of Longitudinal Coupled-Bunch Instabilities by a Passive Higher Harmonic Cavity", IEEE, 1993.

[8] H. Damerau and L. Ventura, "Longitudinal Coupled-Bunch Instability Studies in the PS", in the Proceedings of the Injector MD Days 2017. Geneva, Switzerland, 23-24 March 2017.

[9] F. J. Cullinan, *et al.*, "Transverse Coupled-Bunch Instability Thresholds in the Presence of a Harmonic-Cavity-Flattened RF Potential", *Phys. Rev. Accel.* Beams 19, 124401 (2016).

[10] M. Borland, "elegant: A Flexible SDDS-Compliant Code for Accelerator Simulation", Advanced Photon Source LS-287, Septumber 2000.

[11] Y. Wang and M. Borland, "Pelegant: AParallel Accelerator Simulation Code for Electron Generation and Tracking", in the Proceedings of the 12th Advanced Accelerator Concepts Workshop, AIP Conf. Proc. 877, 241 (2006).

[12] K.Y. Ng, "Physics of Intensity Dependent Beam Instabilities", *World Scientific Publishing* Co. Pte. Ltd. 2006.

ISBN: 978-3-95450-206-6 doi:10.18429/JACoW-FLS2018-WEP2PT030

UNDULATOR DEVELOPMENT ACTIVITIES AT DAVV-INDORE

Mona Gehlot, Roma Khullar, Geetanjali Sharma[1] , Jeevakhan Hussain[2] , G. Mishra
IDDL, School of Physics, DAVV, Indore-452001, India
[1] Research Instruments GmbH, Gladbach, Germany
[2] National Institute of Technical Teachers' Training and Research, BhopaL, India

Abstract

Insertion Device Design Laboratory, DAVV has development activities on in-house design, fabrication and measurement of prototype undulators for synchrotron radiation and free electron laser application. The first prototype U50 was built with six periods, 50mm each period. It was PPM type. The next prototype U20 hybrid device based on NdFeB-Cobalt steel was built with aim to produce 0.24T to 0.05T in 10-20mm gap. The undulator is a 20mm period and there are 25 periods. The next one is U50-II PPM structure with 20 periods. In this paper we review the designs of all these undulators and briefly outline the user facilities of Hall probe bench, Pulsed wire bench and stretched wire magnetic measurement systems at IDDL.

U 50 UNDULATOR

A planar undulator of Halbach Configuration made from Pure Permanent magnet type of NdFeB magnets named as U50 is design and developed in IDD lab DAVV [1]. One period is of 5 cm and there are six periods in a jaw and the total length of the undulator is 30cm.The undulator is a variable gap type. The minimum gap is 22 mm which can be varied up to 50mm. The magnet size is 12.5 mm × 12.5 mm×50mm.

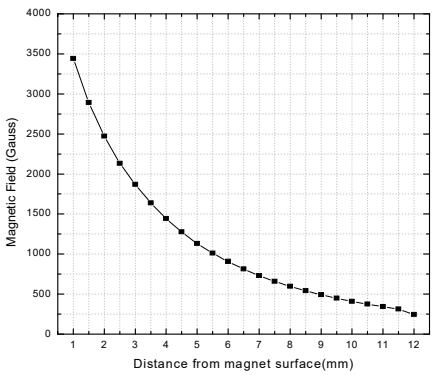

Figure 1: Magnetic field versus undulator gap for U50 undulator.

Figure.1 shows the graph for peak magnetic field with the variation in the distance from the surface of the undulator. At 1mm distance the field is around 3500Gauss.

The planar undulator was modify to a harmonic undulator by placing the shims on the required positions. We used CRGO shims for third harmonic undulator of $1.5\,mm \times 9.0\,mm \times 28\,mm$ in thickness, height and length respectively. The shims fitted in the Perspex sheet will be place on the upper and lower jaw of the undulator. By using the same method we will also modify the wiggler for $5^{th}, 7^{th}, 9^{th}$ harmonic undulator [2].

U 20 UNDULATOR

It has completed the design of a hybrid undulator [3] and installed in the measurement bench for performance studies. U20 is a NdFeB based hybrid undulator with two NdFeB magnets and two poles per period. The undulator has twenty five periods and twenty *mm* each period length. The poles are made from Cobalt steel. The gap is variable from 10mm to 80mm.Fig.2 shows the radia model of U 20 undulator and Fig 3. Shows the schematic of arrangement of undulator in a jaw. The gap is manually driven by Ball screw arrangement. The maximum field is 3000Gauss at 10mm and $\Delta B/B = 0.025$. Figure 4 shows the photograph of the hybrid undulator with its support structure.

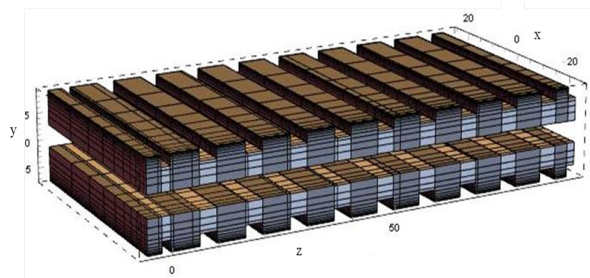

Figure 2: Radia model of U-20 undulator.

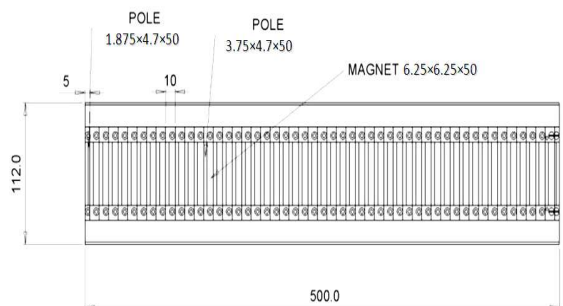

Figure 3: 0.5m Hybrid undulator design.

ISBN: 978-3-95450-206-6 doi:10.18429/JACoW-FLS2018-WEP2PT030

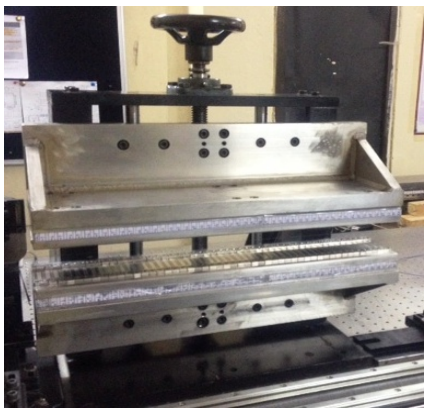

Figure 4: Hybrid Undulator.

Once the undulator is fabricated and installed in the structure, its magnetic filed profile is measured by Hall probe and RMS value for field and undulator peramete is is compared with the Radia result with the variation in the gap which is shown in the Fig.5. Figure 6 shows the inetrgarls with variation in the gap of the undulator.

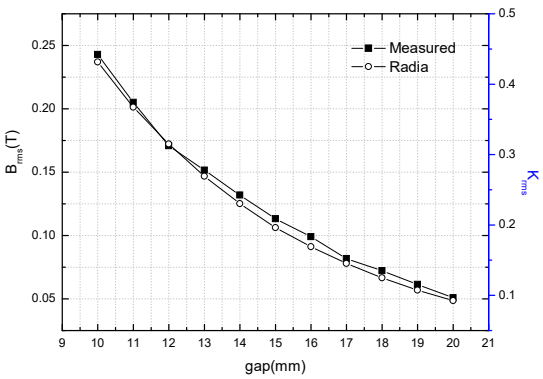

Figure 5: RMS magnetic field and undulator parameter versus undulator gap.

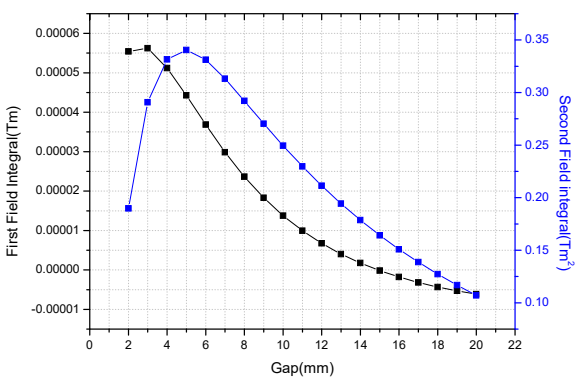

Figure 6: Field integrals for different gap.

The field in-homogeneities along the undulator length is an important design issue of consideration to a low phase error device. In Fig.7, the field in-homogeneities has been analyzed for the operating gap of the device. The maximum deviation in the magnetic flux density is less than 80 Gauss at 10 mm gap.

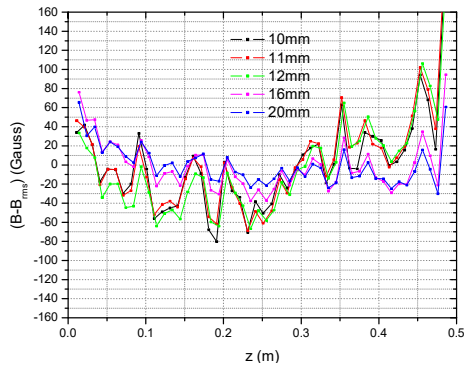

Figure 7: Field non uniformity of U20 along the undulator length.

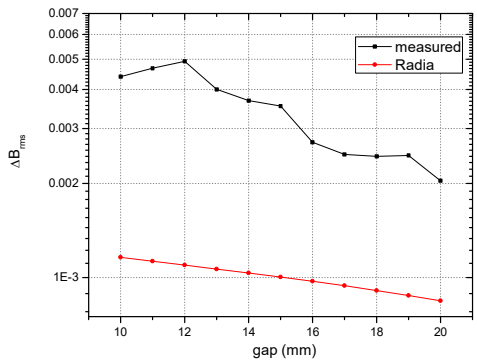

Figure 8: Deviation of magnetic flux density of U20 versus gap.

In Fig.8 , we plot ΔB_{rms} as defined in Eq.(1) with gaps for both Hall Probe and Radia data. The Radia shows the variation in 8 to 11 Gauss where the Hall probe results gives the variation of 20 to 43 Gauss in the operating gaps.

$$\Delta B_{rms} = \sqrt{\frac{1}{N}\sum_{i=1}^{N}\left(|B_i| - B_{rms}\right)^2} \qquad (1)$$

A comparison of the phase error plots from Hall probe data and Radia and is given in Fig. 9. At 10 mm gap, the plot reads 4.240, 3.120 .

ISBN: 978-3-95450-206-6 doi:10.18429/JACoW-FLS2018-WEP2PT030

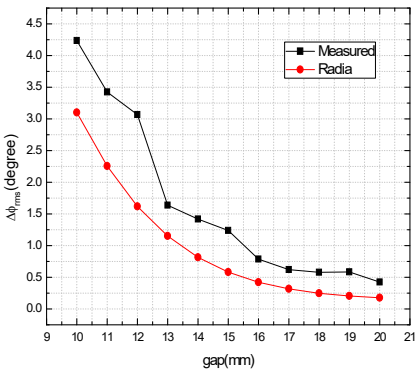

Fig 9. Phase error vesus gap.

U 50-II UNDULATOR

A new pure permanent magnet undulator is under development. It has 20 periods of 50mm period length so that the length of undulator is 1000mm long. The magnets blocks are hold on single SS 316 jaw by T- clamps. Figure 10 Shows the schematic of the undulator design and Fig. 11. Shows the schematic of the side view for the U 50-II undulator.

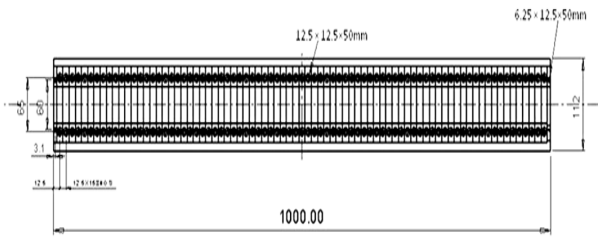

Figure 10: 1m PPM undulator design.

The dimension of the jaw is 1000×112×33mm. The jaws are prepared and are under testing by stretched wire method and the support structure is under development stage.

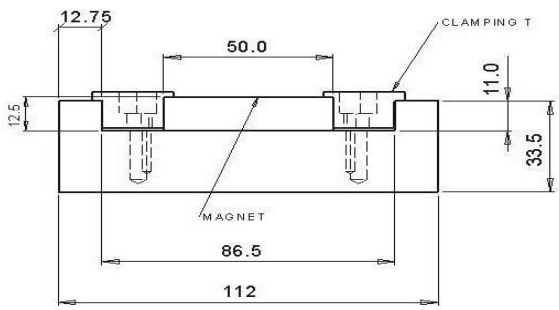

Figure 11: 1m PPM undulator design from side view.

The two jaws are hanged on a support structure providing variable gap from 3 to 30mm. The two jaws are fitted on a array and that array can move independently by four linear slides. The two arrays have vertical movement for varying gap and a rotary movement to upper jaw for maintaining parallelism between the two jaws. The vertical movement is such that we can manually change the either side of the array by four hand wheels so we can adjust the gap from four corners enabling the array to be longitudinal gap tapering for the magnetic field profile. The top array is attached with encoder of resolution 0.01degrees that provides lateral movement to the upper jaw. By this lateral movement we can adjust the alignment of both the jaws. All the readings are display on DRO (digital read out) of resolution 0.001mm. Figure 12 and Fig. 13 shows the front and side view schematic of the support structure. The support structure is heavy and made of Stainless steel for maintain the force of 2000N at 3mm gap between the two magnetic jaws. The total weight of the structure with arrays and undulator jaw is 400Kg.

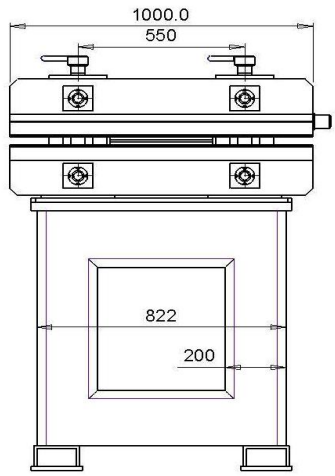

Figure 12: 1m PPM undulator with support structure.

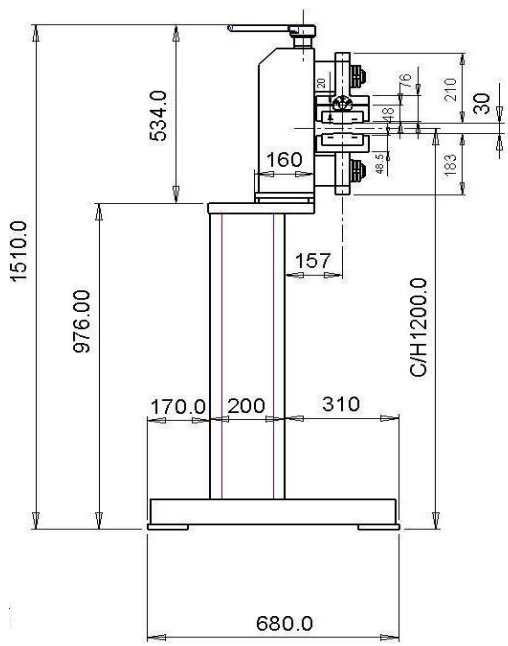

Figure 13: 1m PPM undulator with support structure (side view).

ISBN: 978-3-95450-206-6 doi:10.18429/JACoW-FLS2018-WEP2PT030

In Fig. 14 the peak magnetic field is shown from rhe calculations of Radia. Figure 15 is the result of field integrals by Radia. Then the jaws are assembled in the support structure and for the gap of 35mm the magnetic field profile is compared with the radia results which is shown in the Fig. 9.

The Hall probe measurement are under process we will measured the field from 10mm to 35mm in our Hall probe measurement system.

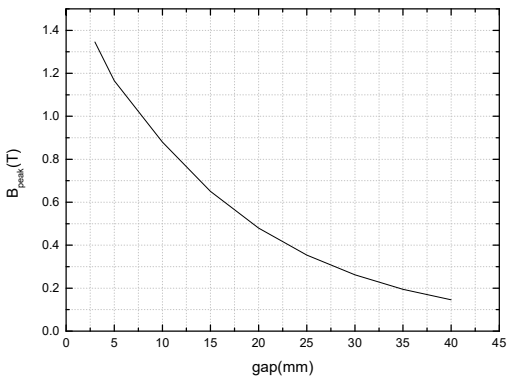

Figure 14: Peak magnetic field at different gaps.

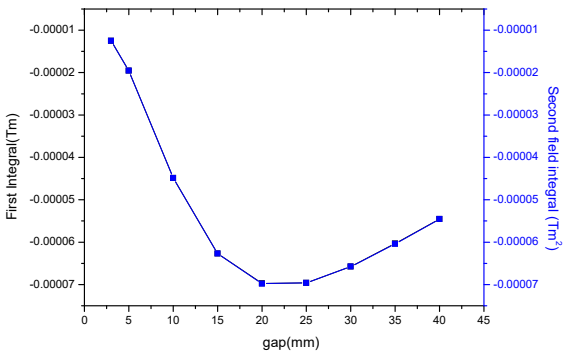

Figure 15: Field integrals for different gap.

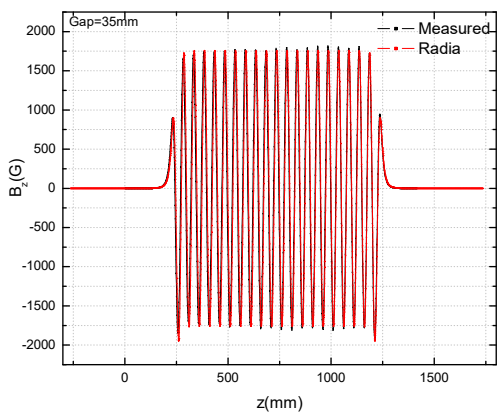

Figure 16: Magnetic field profile for the gap of 35mm.

U-14 UNDULATOR (PROPOSED)

Commercial NbTi wires with a cross section of 1 mm x 0.5 mm including its insulation will be used for fabrication of 14 mm period superconducting undulator [4-5]. The undulators will be composed of racetrack coils connected in series and wound on two ferromagnetic poles made up of carbon steel. The SCU will consist of 26 poles and 25 coils. Figure.17 shows the longitudinal view of the pole-coil of the superconducting undulator. The regular pole is 2 mm in length (beam direction), 40 mm in width (undulating direction) and 8 mm in height (vertical direction). The regular coil length with five turns is 5 mm (5 turns x 1 mm) and the coil height with 16 layers is 8 mm (16 layers x 0.5 mm). The undulator begins with a pole and runs with pole-coil–pole arrangement and ends with a pole in an asymmetric field configuration. The end field configuration in the scheme is 1:3/4:1/4. The total length of the magnetic structure (22 regular poles = 44 mm, 21 coils= 105 mm, end design= 2 x 13.56 mm (2 x (1.6 mm+5 mm+1.96 mm+5mm)) reaches a total length of 176.12 mm.

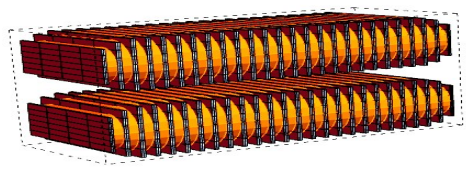

Figure 17: Longitudinal view of the SCU with end termination.

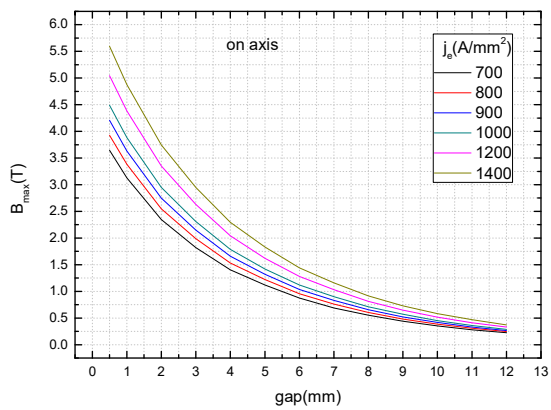

Figure 18: Magnetic flux density versus gap at different current density.

ISBN: 978-3-95450-206-6 doi:10.18429/JACoW-FLS2018-WEP2PT030

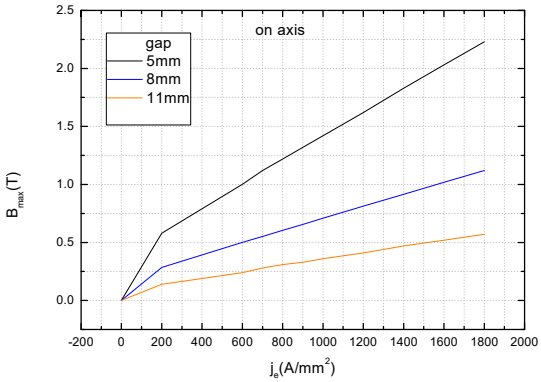

Figure 19: Magnetic flux density versus current density at different gaps.

An empirical fit formula with a, b, c coefficients similar to a hybrid undulator structure. The results fit an analytical formula for on axis field measurement

$$B_{axis}(\mathrm{T}) = a(J_e)\exp[-\mathrm{b}(J_e)\mathrm{g}+c(J_e)\mathrm{g}^2]$$

$$a(J_e) = 2.018 + 0.0031J_e$$

$$b(J_e) = 0.24731 + 0.10436\exp(-0.0012J_e)$$

$$c(J_e) = 0.00142 + 0.00682\exp(-0.0012J_e)$$

In the formula g is in mm and current densities are in A/mm2. The magnetic flux density at the surface of the coil is empirically fit as,

$$B_{coil}(\mathrm{T}) = A_1(J_e) + A_2(J_e)\exp[-B(J_e)\mathrm{g}]$$

$$A_1(J_e) = 1.02017 + 0.00155J_e$$

$$A_2(J_e) = 0.93484 + 0.00155J_e$$

$$B(J_e) = 0.4807 + 0.12691\exp(-0.0015J_e)$$

In Fig. 18. variation of magnetic field with different gap for different current density is shown and Fig. 19 shows the graph for the magnetic field density with the variation in the current density for different gap. In Fig. 20 the field integrals are calculated for different current density for different gap of the undulator.

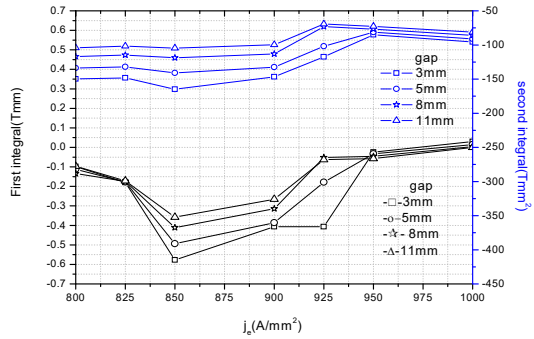

Figure 20: Field integrals versus current density for different gap.

ACKNOWLEDGEMENT

This work is supported by SERB-DST grant EMR/2014/00120 and financial support from UGC [F.15-1/2014-15/PDFWM-2014-15-GE-MAD-26801(SA-II)], Delhi.

REFERENCES

[1] G. Sharma *et. al*., "Analysis of Pulsed wire measurements on bi-harmonic undulator", *Measurement*, vol. 82, pp. 334–344, 2016.

[2] G. Sharma *et. al*., Pulsed wire measurements on bi-harmonic undulator, Advances in Synchrotron Radiation, *World Scientific Journals*, Vol. 3, No. 1 (2014) 1450001.

[3] G. Mishra *et. al*., Characterization of hybrid undulator, *IEEE Transactions on Magnetics*, pp. (99): 1-1, (2016).

[4] G. Mishra *et. al*., Magnetic design and modelling of a 14 *mm* period prototype superconducting undulator, *Journal of synchrotron radiation,* vol. 24, pp. 422–428, 2017.

[5] M. Gehlot *et. al*., Magnetic design of a 14 mm period prototype superconducting undulator, *Nuclear Instruments and Methods in Physics Research A*, vol. 846, pp.13–17, 2017.

ISBN: 978-3-95450-206-6 doi:10.18429/JACoW-FLS2018-WEP2PT032

FEASIBILITY STUDY OF HIGH ENERGY X-RAY SOURCE AT PLS-II

Jang-Hui Han†, Jaeyu Lee, Sangbong Lee, Sojeong Lee, Tae-Yeon Lee
Pohang Accelerator Laboratory, Pohang, Korea

Abstract

PLS-II operates for user service with the 34 beamlines since 2012. For engineering applications, especially for thick metal samples, a high energy X-ray beamline is under consideration to cover a photon energy up to 100 keV or beyond. By comparing the radiation spectra from various insertion devices types, superconducting wiggler was found to be a most promising candidate. A feasibility study to install the high field wiggler in the PLS-II ring is presented in this paper. Electron beam dynamics studies for a minimum impact on the electron beam parameters and engineering consideration to add more magnets are carried out.

INTRODUCTION

Pohang Light Source II (PLS-II) operates for user service with synchrotron radiation ranging from IR to hard X-ray [1]. The electron beam energy is 3 GeV. The nominal beam current is 400 mA with top-up operation. The 282 m circumference ring has 12 cells. Each cell has two, 6.88 m long and 3.69 m short, straight sections. The ring have 24 straight sections in total. Twenty out of them are used for insertion devices, and the other straights are used for electron beam injection and RF cavities installation.

The main radiation source of PLS-II is the in-vacuum undulators with a period of 20 mm. The twenty in-vacuum undulators have a maximum magnetic field of 0.97 T when the magnet gap is 5 mm. One in-vacuum revolver undulator with four different periods, three APPLE-II type elliptically polarizing undulators and one out-vacuum undulator are in use. Two multipole wigglers with periods of 100 mm and 140 mm have maximum fields of 1.80 T and 2.02 T, respectively. The wigglers provide radiations up to 40 keV with a flux enough for users.

There is a request from users to provide higher energy X-rays for engineering applications. For instance, a high energy X-ray of 100 keV can be used to investigate a thick metal sample with a thickness of a few millimeters. A new insertion device for this purpose can be installed at the 2C slot which is empty at present. In this paper, we find the best insertion device type to generate a high energy X-ray with the electron beam parameters of PSL-II. We then study the feasibility to install the insertion device into the PLS-II ring with minimum impacts to the performance of the existing radiation sources.

INSERTION DEVICE

Given the electron beam energy, a higher magnetic field generates an X-ray with higher photon energies. The critical energy (ε_c) in keV varies with the magnetic field in T as $\varepsilon_c = 0.67E^2B$, where E is the beam energy in GeV. To provide a sufficient flux at 100 keV, we need a critical energy of about 25 keV, which means a magnetic field of 4.2 T is required at the 3 GeV electron beam energy.

The flux densities from insertion devices under consideration, SCU16 (superconducting undulator with a 16 mm period) and SCW48 (superconducting wiggler with a 48 mm period), in addition to the existing ones, MPW10, MPW14 and IVU20, in PLS-II have been calculated by using the Spectra code [2] as shown in Fig. 1. A superconducting wiggler with a 4.2 T field and a 16 period can produce a flux density of more than one order of magnitude than the existing permanent magnet wigglers at the 100 keV photon energy. The parameters of the insertion devices used for the spectra calculation are summarized in Table 1.

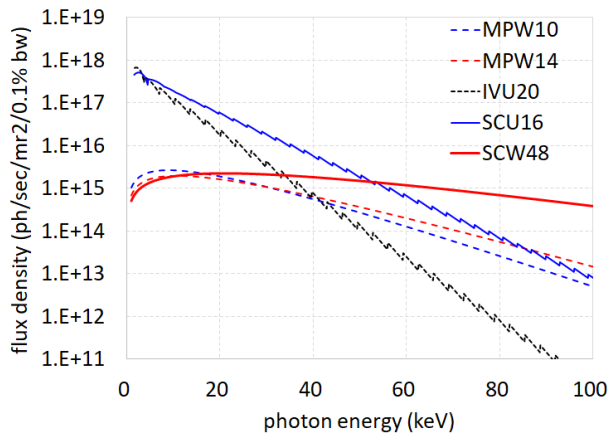

Figure 1: Spectra from insertion devices at PLS-II. At the 100 keV photon energy, a superconducting wiggler (SCW48) can provide a flux with more than an order of magnitude compared with the wigglers (MPW10 or MPW14) installed in the PLS-II ring.

Superconducting wigglers with a 4.2 T magnetic field are used at other synchrotron radiation sources [3]. Because of the available length of the 2C straight section, we consider a short SCW with a magnet length of about 0.8 m. In the 3.69 m long straight, a cryogenic tank to implement the SCW and additional quadrupole magnets for electron beam dynamics adjustment will be installed.

IMPACT TO THE ELECTRON BEAM PARAMETERS

An insertion device with a high magnetic field can generate high flux at high photon energies. However, an insertion device with such a high magnetic field may deteriorate the electron beam emittance if that is placed at a position with

† janghui_han@postech.ac.kr

ISBN: 978-3-95450-206-6 doi:10.18429/JACoW-FLS2018-WEP2PT032

Table 1: Parameters of Selected Insertion Devices at PLS-II

	MPW10	MPW14	IVU20	SCU16	SCW48
Period (mm)	100	140	20	16	48
B_{max} (T)	1.80	2.16	0.97	1.50	4.20
Critical energy (keV)	10.8	12.9	–	–	25.1
K	16.8	28.2	1.81	2.24	18.8
Number of periods	18	12	90	75	16
Magnet length (m)	1.8	1.68	1.8	1.2	0.768
Flux density at 35 keV	7.5×10^{14}	7.2×10^{14}	2.1×10^{15}	9.5×10^{15}	2.15×10^{15}
Flux density at 100 keV	4.8×10^{12}	1.3×10^{13}	3.6×10^{10}	8.1×10^{12}	1.22×10^{15}
Total power (kW)	13.3	20.1	3.9	6.1	30.9

the horizontal dispersion is not zero. Figure 2 shows the Twiss parameters of one cell of the present PLS-II lattice. The Twiss parameters were calculated by using the OPA code [4]. The blue rectangles on the top in the figure indicate the dipoles, the red ones the quadrupoles and the pale green ones the sextupoles. Currently, one short straight section is available for the installation of the superconducting wiggler. The short straight section is located at the center in Fig. 2. The horizontal dispersion at the short straight is 0.144 m and the insertion device at the non-zero dispersive section may lead to an emittance increase.

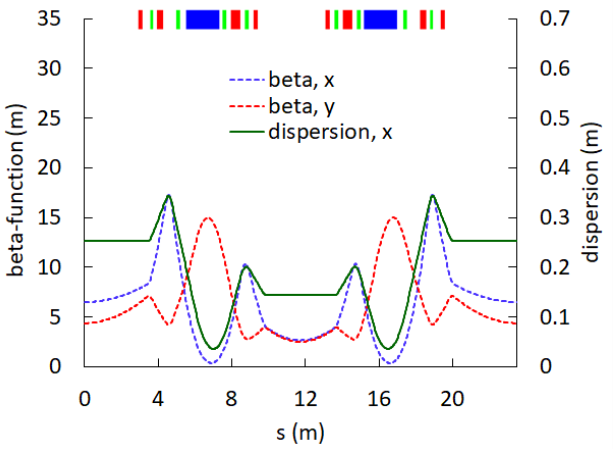

Figure 2: Twiss parameters of the present cell lattice.

The emittance change as a function of the dispersion for the beta-function of 2.7 m is plotted in Fig. 3. When the horizontal beta function is kept as present, the emittance does not increase if the dispersion is 0.058 m or smaller. Note that the emittance dependence on the dispersion changes with the beta function, which is not indicated here. With a higher beta function, the requirement for the dispersion is relaxed.

To minimize the emittance growth caused by the high magnetic field of the superconducting wiggler, we modified the local cell lattice as Fig. 4. Six quadrupoles were added in one cell and the strength of all quadrupoles in the cell were optimized to reduce the dispersion at the straight and to match the Twiss parameters to the neighbor cells. Maintaining the appropriate beta function and tune, we reduced the dispersion at the short straight section to 0.079 m.

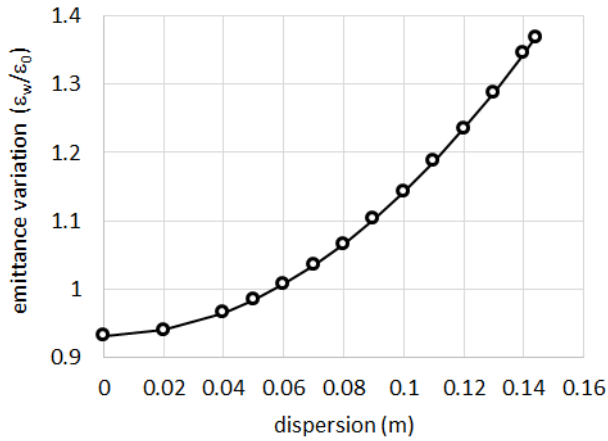

Figure 3: Emittance variation depending on the dispersion.

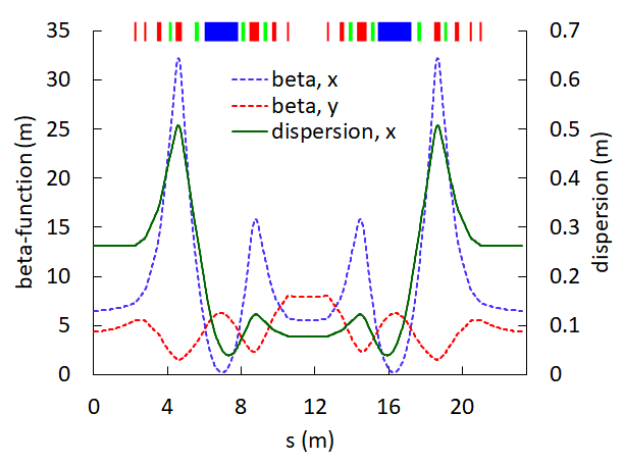

Figure 4: Twiss parameters of the modified cell lattice. The dispersion is reduced to 0.079 m and the horizontal beta function is increased to 6.3 m to suppress the emittance rise.

The new horizontal beta function in the modified PLS-II lattice is presented in Fig. 5. Only the second cell is modified and the other cells are unchanged. The horizontal emittance is changed from 5.8 to 6.3 nm. After the installation of the

ISBN: 978-3-95450-206-6 doi:10.18429/JACoW-FLS2018-WEP2PT032

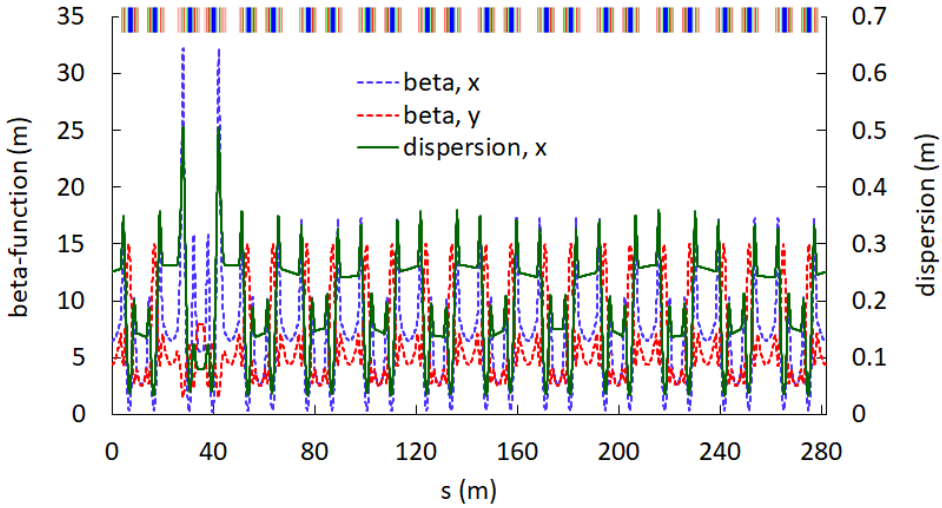

Figure 5: Twiss parameters of the ring lattice including the modified cell. The Twiss parameters are unchanged except for the second cell where a new wiggler is to be installed.

superconducting wiggler, the horizontal emittance is reduced to 6.2 nm and it is an acceptable change.

Figure 6 shows the dynamic aperture of the modified PLS-II ring. It was calculated using the OPA code for 1000 turns. The injection devices were not included in the OPA lattice.

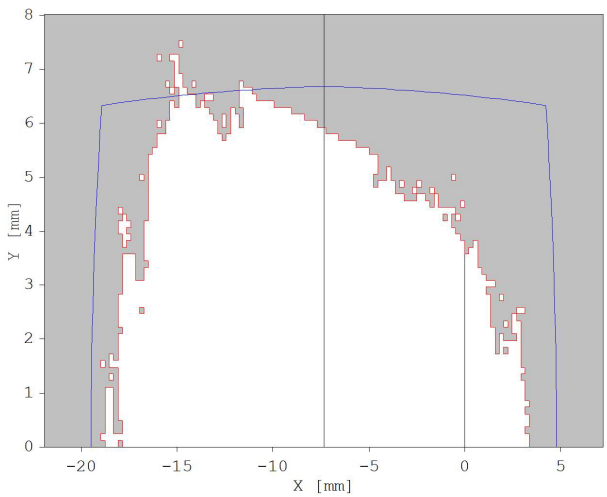

Figure 6: Dynamic aperture of the modified ring. The injection position is −15 mm.

After the cell modification, the dynamic aperture decreased dramatically because of the asymmetry. We optimized the sextupoles to increase the dynamic aperture using OPA. Also the energy offset was set to −3%.

The current injection point is x = −15 mm and y = 0 mm and it will be changed to x = −12 mm and y = 0 mm after the PLS-II injection system upgrade project which is ongoing. The transverse size of the injection bunch is about 1 mm. Therefore, the dynamic aperture of the the modified PLS-II ring is acceptable.

ENGINEERING ISSUES

To implement six additional quadrupoles and a cryotank with the superconducting wiggler, the availability was reviewed. In Fig. 7, the mechanical layout of Cell 2 of the PSL-II ring is presented. An electron beam passes from the left to the right.

The right side in the figure is the 2A slot where the EPU with a 72 mm period and a 2.58 m magnet length is installed. Between the EPU and the first quadrupole in the cell, there is a drift with a length of about 1.5 m. Two corrector magnets and an ion pump are installed in the drift. Two additional quadrupoles can be installed in the drift without a major mechanical modification.

The left side is the 3A slot where the in-vacuum revolver undulator is installed. In the drift between the las quadrupole and the revolver undulator, two additional quadrupoles can be installed without a major mechanical modification as for the 2A slot.

The center straight is the 2C slot where the superconducting wiggler is to be installed with two additional quadrupoles, one upstream and another downstream of the wiggler. A dummy chamber with a length of 2.385 m is installed now. When a wiggler tank length of 1.8 m is assumed, there is space for the quadrupoles and two additional corrector magnets.

CONCLUSION

Following the user's request, we studied the feasibility to install a high energy X-ray source in the PLS-II ring. We first reviewed the spectra from the present insertion devices and possible candidates as a high energy source. We concluded a superconducting wiggler with a magnetic field of 4.2 T can provide an X-ray up to 100 keV with a sufficient flux. Due to the non-zero dispersion in the straight section where a new superconducting wiggler is to be installed, the beam

ISBN: 978-3-95450-206-6 doi:10.18429/JACoW-FLS2018-WEP2PT032

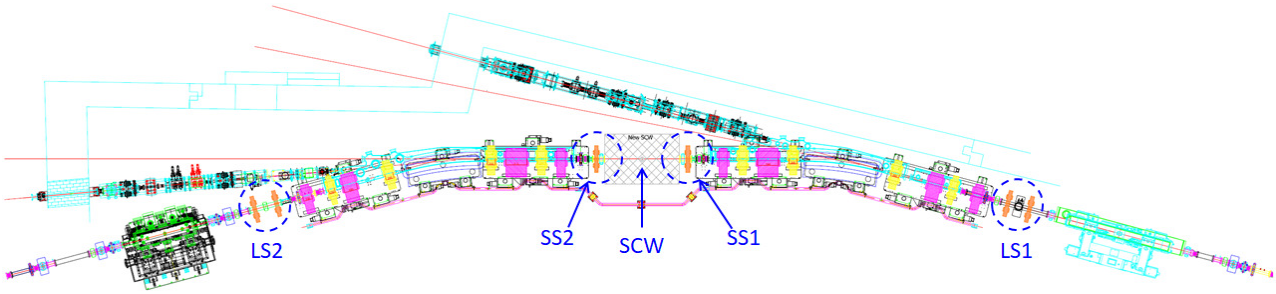

Figure 7: Mechanical layout of Cell 2 with additional six quadrupoles and a superconducting wiggler. The positions for the new quadrupole installation are indicated with blue circles. A new superconducting wiggler is to be installed in the rectangle box in the center.

dynamics was studied to minimize the impact to the performance of the existing insertion devices. We conclude that a new superconducting wiggler can be installed in Cell2 of the PSL-II ring without major issues in the beam dynamics and engineering point of view.

REFERENCES

[1] S., H. Nam, H.-S. Kang, I. S. Ko and M. Cho, "Upgrade of Pohang Light Source (PLS-II) and Challenge to PAL XFEL", *Synchrotron Radiation News* 26:4, 24 (2013).

[2] T. Tanaka and H. Kitamura, "SPECTRA: a synchrotron radiation calculation code", *J. Synchrotron Rad.* 8, 1221 (2001).

[3] N. Mezentsev, " Superconducting Multipole Wigglers for Generation of Synchrotron Radiation", in *Proc. 24th Russian Particle Accelerator Conf. (RuPAC'2014)*, Obninsk, Russia, Oct. 2014, paper THZ01, 296 (2014).

[4] A. Streun, OPA version 3.39, `https://ados.web.psi.ch/opa`

ISBN: 978-3-95450-206-6 doi:10.18429/JACoW-FLS2018-WEP2PT033

CONCEPTUAL DESIGN OF SUPERCONDUCTING TRANSVERSE GRADIENT UNDULATOR FOR PAL-XFEL BEAMLINE

S. Lee*, J.-H. Han, Pohang Accelerator Laboratory, Pohang, Korea

Abstract

Recently, the transverse gradient undulator (TGU) applications are suggested from laser plasma wake-field accelerator (LPWA) to ultimate storage ring (USR). Especially for X-ray FELs, TGU can be used to generate a large bandwidth radiation up to 10%. In this proceeding, a review of PAL-XFEL beam parameters and TGU requirements was done to apply a variable large bandwidth operation to the PAL-XFEL beamlines. Also, the conceptual design of TGU, based on superconducting undulator (SCU) was proposed, and B-field calculation results were introduced for large bandwidth operation modes of PAL-XFEL.

INTRODUCTION

The original TGU concept was introduced to overcome the large electron beam energy spread of an earlier stage of FEL development in the 1980s. The main parameter of TGU is the amount of K-value gradient in the transverse direction, defined by a parameter α. The α is defined as [1]

$$\alpha = \frac{\Delta K/K_0}{\Delta x} = \alpha_k/K_0. \quad (1)$$

Lately, the various types of TGU, canting pole geometry permanent undulator, and SCU were suggested and built for LPWA or USR to compensate the energy spread for compact FEL source development [2,3]. Other TGU applications are also suggested for X-ray FEL by using a small energy spread electron beam [4]. This application uses a TGU and an RF deflecting cavity to generate the large bandwidth X-ray radiation. A deflected electron beam sees different K-values of TGU and the bandwidth of X-ray FEL can be adjusted by changing the gradient amount of TGU, up to 10% order. By using this scheme, FEL beamlines can provide a variable X-ray FEL bandwidth to meet the requirements of users.

LARGE BANDWIDTH MODE OF PAL-XFEL

PAL-XFEL Beam Parameters

PAL-XFEL, an X-ray FEL user facility, has hard and soft x-ray beamlines based on Self Amplified Spontaneous Emission (SASE). The hard X-ray beamline uses a 10 GeV, 200 pC and 3.0 kA electron beam to provide 0.1 nm hard X-ray FEL by using twenty undulator units. For the soft X-ray beamline, seven undulator units are used to provide 1 nm soft X-ray FEL by using a 3.0 GeV, and 2.5 kA electron beam. Hard X-ray Undulator (HXU) and Soft X-ray Undulator (SXU) of PAL-XFEL are hybrid type undulators and Table 1 shows an undulator system parameters of each undulator systems.

Table 1: Undulator System Parameters of PAL-XFEL Beamlines

Parameters	HXU	SXU
Period	26.0 mm	35.0 mm
K	1.973	3.321
B_{eff}	0.812 T	1.016 T
gap_{min}	8.3 mm	9.0 mm
Length	5.0 m	5.0 m

The large bandwidth operation mode of PAL-XFEL requirements was calculated based on the suggested concept in Ref. [4] by using the PAL-XFEL beam and undulator parameters. The assumptions were used in this proceeding that a deflecting cavity is installed in front of the undulator beamlines and the TGU beamline, which can provide up to 10% bandwidth X-ray radiation, is installed. The deflected length of the electron beam was assumed as 1 mm for both the hard and soft X-ray beamlines for simple calculation. Table 2 shows a required K-value and gradient parameters to generate a 10% bandwidth radiation wavelength, λ_R, for the PAL-XFEL beamlines. For the calculation, the periods of the hard and soft X-ray TGUs were assumed as 26 mm and 35 mm, respectively.

Table 2: Undulator Parameters Required for 10% Large Bandwidth Operation of PAL-XFEL

Beamline	λ_R (nm)	K_0	$\alpha_K(m^{-1})$	$\alpha(m^{-1})$
Hard	0.1	1.973	99.6	50.5
Hard	0.06	1.239	95.2	76.8
Soft	3	3.321	130.8	39.4
Soft	1	1.531	109.9	71.8

Requirements for PAL-XFEL TGU

One of the important requirements of PAL-XFEL large bandwidth operation mode calculation was the variable bandwidth of X-ray FEL. To change the bandwidth of FEL, the TGU of PAL-XFEL can change the K-value and gradient by the user experiment requirements. Usually, the fixed gradient TGUs by using a canting pole geometry was proposed and built for the LPWA applications. These canting pole geometry TGUs can provide a fixed large gradient with a high K-value for short undulator periods. However, these canting pole geometry undulators are not proper for the PAL-XFEL large bandwidth operation mode.

* sojung8681@postech.ac.kr

ISBN: 978-3-95450-206-6 doi:10.18429/JACoW-FLS2018-WEP2PT033

On the other hand, a normal planar undulator or an APPLE-X type EPU can provide a variable gradient for a specific K-value. The normal planar undulator can change the K-value and the gradient by changing the offset between the center of the vacuum chamber and the undulator magnet structure. The APPLE-X type EPU, suggested by Swiss-FEL, can change the K-value and gradient by changing the magnet structure phase or breaking the symmetry between the four magnet arrays. However, the available K-value and gradient of these two types of undulators are decided by the mechanical magnet array movement range. Also, in case of the APPLE-X type EPU, it is hard to provide enough K_0 value when $\lambda_U = 26$ mm, the PAL-XFEL hard X-ray beamline case.

CONCEPTUAL DESIGN OF TGU

As introduced in the previous section, the normal planar undulator or APPLE-X type EPU can be a candidate of TGU for a large bandwidth operation of PAL-XFEL. However, in case of normal planar undulator, it needs to keep the offset between the electron beam and the magnet structure center to maintain the K-value and gradient. To do that, the electron beam position in the vertical direction needs to be kept constant, and the vertical positions of the multiple undulator segments need to be also kept along the long beamline of about 100 m for the hard X-ray beamline case. For the high gradient region, the tolerance of the offset between an electron beam and the undulator magnetic center needs to be tight for keeping the K-value and gradient of the normal planar undulator. On the other hand, the APPLE-X type EPU undulator can change the K-value and gradient by moving the four magnet arrays. For the linear polarization mode, the K-value difference between the right and left magnet arrays induces the gradient of K-value at the center of the vacuum chamber. To achieve a maximum gradient of APPLE-X type undulator, one magnet array needs to be set as a minimum gap and the other as a maximum gap. Also, the APPLE-X type undulator is a pure permanent magnet (PM) undulator, and the maximum field is also decided by the types of the magnet material.

Design Parmeters

The conceptual design of a TGU for a large bandwidth operation of PAL-XFEL was done under the several considerations. The first consideration of the design was minimizing the mechanical part. Another consideration was adopting the concept of an APPLE-X type undulator to generate the gradient. By using these two conditions, the design of a TGU for the PAL-XFEL beamline was done as shown in Fig. 1 based on a superconducting undulator (SCU). This design has two planar SCU magnet arrays, and the steel pole is placed between these two magnet arrays to concentrate the B-field at the center. The gradient of K-value is induced and changed by the current difference between the right and left coils. This SCU concept was used to replace the mechanical part of planar or APPLE-X type undulators. Also, the

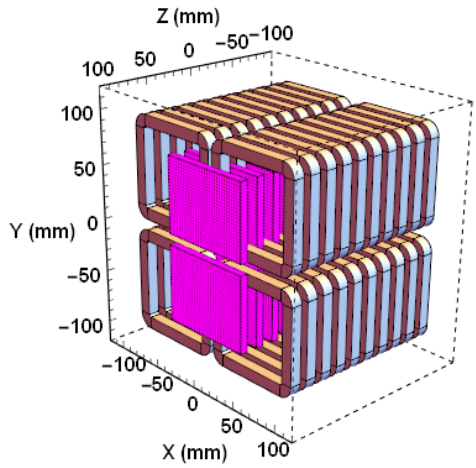

Figure 1: Dual superconducting TGU model for PAL-XFEL soft x-ray beamline.

magnetic gap was set to be larger than the 6.7 mm vacuum chamber height of PAL-XFEL by considering an SCU insulator thickness of about 2 mm. Figure 2 and Table 3 show the design parameters and value of the TGUs for the hard and soft x-ray beamlines. The maximum current density of the design was estimated by using the scaling law of SCU [5].

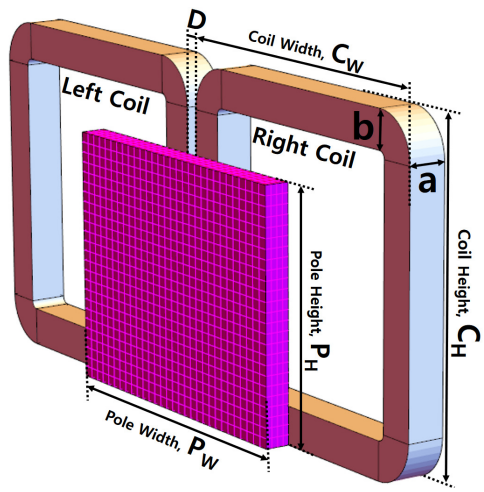

Figure 2: Parameters of superconducting undulator model design.

Magnetic Field of Superconucting TGU

The field distribution of a superconducting TGU was calculated by using the RADIA [6] magnetic field calculation code. Figures 3 and 4 are calculation results of B-field distribution. In Fig. 3, the blue dotted line shows the B_y field when the left coil array current density, J_L, is 900 A/mm^2 and the right one, J_R, is 0 A/mm^2. The black dotted line shows B-field distribution when $J_L = 0$ A/mm^2 and $J_R = 900$ A/mm^2. The solid red line shows one when $J_L = J_R = 900$ A/mm^2 and the center position of vacuum chamber has maximum K-value and zero gradients.

ISBN: 978-3-95450-206-6 doi:10.18429/JACoW-FLS2018-WEP2PT033

Table 3: Design and Simulation Parameter Values of Dual Superconducting Undulator for PAL-XFEL Beamlines

Parameters	Hard X-ray	Soft X-ray
a	7.5 mm	10.5 mm
b	7.5 mm	10.5 mm
C_W	30 mm	95 mm
C_H	31 mm	95 mm
D	2 mm	4 mm
P_H	58 mm	90 mm
P_W	16 mm	70 mm
J, Current Density	1200 A/mm^2	900 A/mm^2
Magnetic Gap	9.5 mm	10 mm

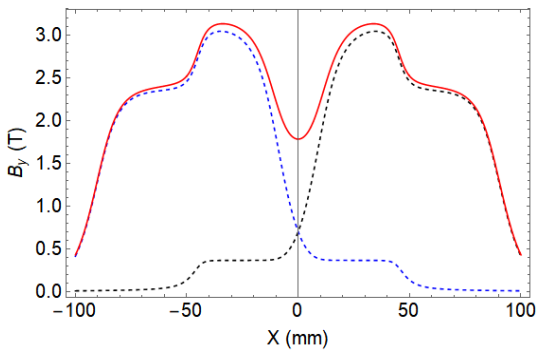

Figure 3: B-field distribution of dual superconducting TGU with $J_L = J_R = 900\,\mathrm{A/mm^2}$ for PAL-XFEL soft x-ray beamline.

On the other hand, Fig.4 shows a B-field distribution for $J_L = 900\,\mathrm{A/mm^2}$ and $J_R = -900\,\mathrm{A/mm^2}$. The gradient is the maximum value, and K-value is 0 for this case. By using the various combination of current density of two planar superconducting undulator coil, the gradient and K-value can be adjusted.

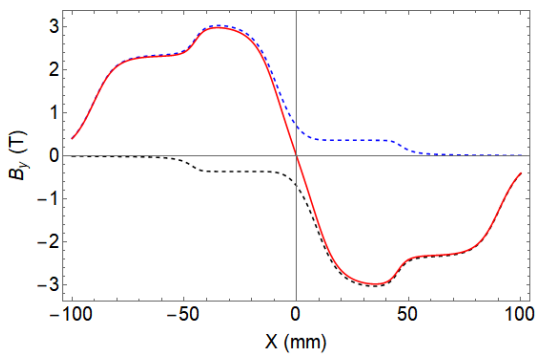

Figure 4: B-field distribution of dual superconducting TGU with $J_L = 900\,\mathrm{A/mm^2}$ and $J_R = -900\,\mathrm{A/mm^2}$ for PAL-XFEL soft x-ray beamline.

On the other hand, when there is an offset in the x-direction, the superconducting TGU can provide a maximum gradient with a non-zero K-value. Also, as shown in Fig.3 or by adjusting the combination of two coil current density, the offset point can provide zero gradients with non-zero K-values. The offset point can be changed by the requirements of gradient and K-value. However, to maintain the radiation point of an FEL, changing the offset point is not proper for a large bandwidth FEL application. Thus, by considering the requirements of applications, the operation point of the superconducting TGU needs to be fixed.

TRANSVERSE GRADIENT AND K-VALUES

The calculated transverse gradient and K-value of the superconducting TGU and operation points are shown in Fig. 5 and 6. For the hard x-ray beamline, 1200 A/mm^2 was used

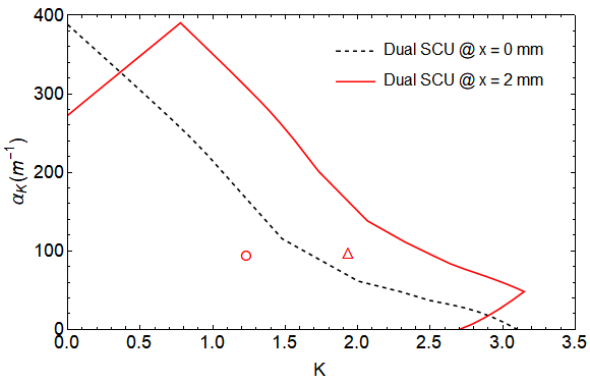

Figure 5: Gradient and K-value for PAL-XFEL hard x-ray beamline TGU.

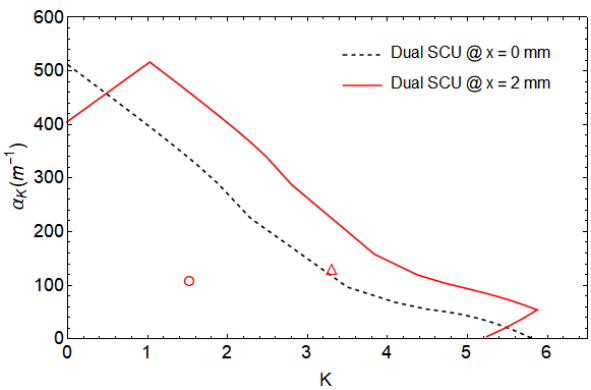

Figure 6: Gradient and K-value for PAL-XFEL soft x-ray beamline TGU.

as the coil maximum current density in this calculation. At the center position of the TGU, a 10% bandwidth operation for $\lambda_R = 0.06$ nm is possible. However, $\lambda_R = 0.1$ nm operation is hard to do at the center position due to the insufficient gradient. Instead, these two large bandwidth mode operations are possible by using the $x = 2$ mm offset point. Also, using the $x = 2$ mm point, a reduction of maximum current density can be expected to operate a large bandwidth mode at the hard x-ray beamline. Decreasing the maximum current density is beneficial for operating superconducting undulators.

ISBN: 978-3-95450-206-6 doi:10.18429/JACoW-FLS2018-WEP2PT033

For the soft x-ray beamline case, 900 A/mm^2 was used as a coil maximum current density for the calculation. At the center position of TGU, a 10% bandwidth operation for $\lambda_R = 1$ nm is possible. To meet the $\lambda_R = 1$ nm and $\lambda_R = 3$ nm operation requirements, a $x = 2$ mm offset point of the TGU is needed. Also, using the $x = 2$ mm point, a reduction of the maximum current density can be expected as for the hard x-ray beamline case.

CONCLUSION

In this proceeding, large bandwidth operation conditions of PAL-XFEL were calculated, and the conceptual design of a superconducting based TGU was carried out. The conceptual design consists of two normal planar SCUs. This superconducting TGU can change the K-value or gradient by changing the current density ratio between the two coils. By using a $x = 2$ mm offset point, the superconducting TGU can meet the requirements of the large bandwidth operation of PAL-XFEL. Also, using such an offset point, a reduction in the maximum current density, can be helpful for an SCU operation. Thus, this TGU type based on SCU can be an undulator option for an operation mode with a large bandwidth up to 10% at PAL-XFEL.

ACKNOWLEDGEMENT

This research was supported by Basic Science Research Program through the National Research Foundation of Korea (NRF) funded by the Ministry of Science and ICT (2017R1C1B1012852).

REFERENCES

[1] A. Bernhard *et al.*, “Radiation Emitted by Transverse-gradient Undulators”, *Phys. Rev. ST Accel. Beams*, vol. 19, p. 090704, Sep. 2016.

[2] Z. Huang *et al.*, “Compact X-ray Free-Electron Laser from a Laser-Plasma Accelerator Using a Transverse-Gradient Undulator”, *Phys. Rev. ST Accel. Beams*, vol. 109, p. 204801, Dec. 2012.

[3] G. Fuchert *et al.*, “A Novel Undultor Concept For Electron Beams with A Large Energy Spread”, *Nucl. Instr. and Meth. A*, vol. 672, p. 33, Dec. 2012.

[4] E. Prat *et al.*, “Generation of Ultra-Large-Bandwidth X-ray Free-Electron Laser Pulses with a Transverse-graduebt undulator", *J. Synchrotron Rad.*, vol. 23, p. 874, April. 2016.

[5] S. H. Kim, "A scaling law for the magnetic fields of superconducting undulators" *Nucl. Instr. and Meth. A*, vol.546, p. 604, March 2005.

[6] O. Chubar *et al.*, "A Three-Dimensional Magnetostatics Computer Code For Insertion Devices" *J. Synchrotron Rad.*, vol.5, p. 481, Oct. 1998.

ISBN: 978-3-95450-206-6 doi:10.18429/JACoW-FLS2018-WEP2PT034

BEYOND UNIFORM ELLIPSOIDAL LASER SHAPING FOR BEAM BRIGHTNESS IMPROVEMENTS AT PITZ

H. Qian#, J. Good, C. Koschitzki, M. Krasilnikov, F. Stephan, DESY, Zeuthen, Germany

Abstract

In the last decades, photoinjector brightness has improved significantly, driven by the needs of free electron lasers and many other applications. One of the key elements is photocathode laser shaping for reducing emittance growth from nonlinear space charge forces. At the photoinjector test facility at DESY in Zeuthen (PITZ), a uniform flattop laser was used to achieve record low emittance for a bunch charge from 20 pC to 2 nC. Due to the ideal 3D space charge force linearization in ellipsoidal electron bunches, uniform ellipsoidal photocathode laser shaping were proposed to improve beam emittance up to 33% for 1 nC beam at PITZ. In this paper, we will show even further transverse emittance improvements in simulations for both flattop and ellipsoidal laser pulses with parabolic radial distribution, versus uniform distributions. The laser shaping effects on longitudinal phase space are also discussed.

INTRODUCTION

Photoinjector development has seen great achievements in the past decades, enabling the success of X-ray free electron lasers (XFEL) and many other applications with high brightness electron sources. Besides high gradient gun and low thermal emittance cathode development, another key in improving photoinjector beam peak brightness is photocathode laser shaping for reducing emittance growth from nonlinear space charge forces. A temporal flattop laser pulse with uniform spatial distribution has been deployed at different photoinjectors to improve transverse beam emittance [1-3]. At the photoinjector test facility at DESY in Zeuthen (PITZ), a uniform flattop photocathode laser was used to achieve record low emittance for a bunch charge from 20 pC to 2 nC, fulfilling the nominal emittance specification of European XFEL injector.

Further improvement of state of the art photoinjector beam brightness is still wished by XFEL applications [4]. Besides going towards low bunch charge (<100 pC) for ultralow emittance (<0.1 μm.rad), there is also a wish for improving high bunch charge (>0.5 nC) beam brightness for high flux FELs. For high bunch charge in a high gradient pulsed gun, or even low bunch charge in a low gradient CW gun, the beam is more vulnerable to the space charge effects, and uniform ellipsoidal photocathode laser shaping is proposed to further reduce the nonlinear space charge effect beyond uniform flattop laser shaping [5-7]. The argument is that an ellipsoidal bunch with a uniform density has 3D linearized space charge forces. Simulations based on the PITZ photoinjector have shown ~33% emittance reduction between uniform ellipsoidal laser pulses and uniform flattop laser pulses for 1 nC bunch charge with ~50 A peak current [5]. Simulations based on LCLS-II CW injector have also shown ~33% emittance reduction with uniform ellipsoidal laser pulses for 100 pC bunch charge with 20 A peak current [6].

Compared to flattop laser shaping, uniform ellipsoidal laser shaping is more complicated due to the required 3D spatiotemporal control of the laser distribution. Generation of ellipsoidal photocathode laser pulses was first conceptually tested at ANL based on chromatic aberration of a dispersive lens, and is now under investigation at PITZ utilizing the Fourier masking technique [8, 9]. Besides 3D laser shaping, ellipsoidal electron beam was also demonstrated in blowout photoemission with longitudinal or transverse laser shaping only, but the optimum bunch charge is limited (~ pC) [10, 11].

In this paper, we will first revisit the photoinjector simulation with uniform flattop and unifom ellipsoidal laser based on the PITZ injector. Then flattop and ellipsoidal laser pulses with parabolic spatial shaping instead of 3D uniform distribution is proposed to further improve photoinjector beam brightness, and their effects on both transverse and longitudinal phase spaces are discussed with simulation results.

PITZ PHOTOINJECTOR SIMULATION

The PITZ gun is an L-band normal conducting gun for driving SC linac based FELs in pulsed mode. It features both high gradient (60 MV/m) and long RF pulse length (650 μs). A Cs_2Te cathode is used to generate photoelectron bunch trains at 10 Hz. To characterize the gun and optimize beam emittance, the PITZ facility was established at DESY for FLASH and European XFEL, see Fig. 1. The maximum beam momentum after the booster is ~25 MeV/c, and the space charge effect is still not fully negligible for high bunch charge cases, so transverse projected emittance is measured with slit scan technique at ~0.9 m downstream the booster exit.

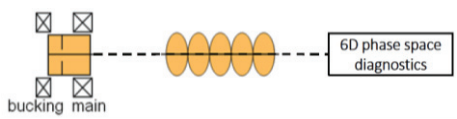

Figure 1: PITZ photoinjector layout.

In this paper, a MOGA tool developed at LBNL is used to drive ASTRA simulations for photoinjector optimization [12]. 10000 macro particles are used in MOGA simulations, and interesting solutions are refined with 200000 macro particles in ASTRA for detailed analysis. The PITZ injector layout is used as an example for investigating laser shaping effects on transverse emittance. The gun is set to 60 MV/m at maximum energy gain phase. The booster is set to maximum energy gain phase. The flattop laser is set to 22 ps FWHM with 2 ps edges, and the ellipsoidal laser is set

#houjun.qian@desy.de

ISBN: 978-3-95450-206-6 doi:10.18429/JACoW-FLS2018-WEP2PT034

to 19.3 ps FWHM to match the rms bunch length with flattop laser case. The cathode thermal emittance is set to 0.85 μm.rad/mm. The laser radius, booster amplitude and solenoid focusing are varied to optimize transverse emittance at slit scan location.

UNIFORM FLATTOP VS UNIFORM ELLIPSOIDAL LASER PULSE

The PITZ injector emittance was experimentally optimized with both Gaussian and uniform flattop laser pulses, and simulations show uniform ellipsoidal laser pulses could reduce the projected emittance by ~33% at 1 nC bunch charge [5]. Sliced bunch parameters are shown in Fig. 2 and Fig. 3. Figure 2 shows transverse slice emittance growth from the cathode to the measurement location. For the uniform ellipsoidal laser case there is still slice emittance growth at central slices close to the thermal emittance level, and the final slice emittances of the central slices are even higher than the projected emittance. Figure 3 shows the longitudinal phase space comparison after linear and quadratic energy chirp removal by post processing. Direct longitudinal phase space comparison without post processing shows similar longitudinal emittance between the two laser shapes, which is misleading. The similar longitudinal emittances are due to similar RMS bunch length and similar uncorrelated energy spread which is dominated by the RF curvature. After linear and quadratic energy chirp removal, the reduction of higher order (H.O.) energy spread reveals the advantage of ellipsoidal laser shaping on longitudinal phase space linearization.

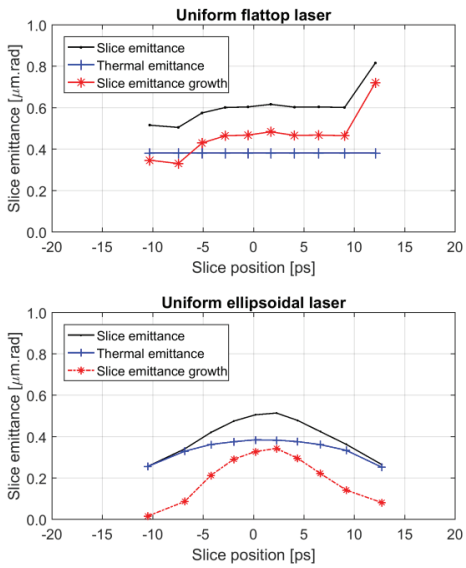

Figure 2: Slice emittance comparison between uniform flattop laser and uniform ellipsoidal laser (each slice contains equal charge).

With uniform ellipsoidal laser shaping, 3D space charge force linearization is expected, but emittance growth in the central slices is still not understood. One suspect is that the slice emittance growth happens during photoemission when part of the ellipsoidal beam is emitted and the transverse space charge force is not linear. To investigate this, the slice emittance near the cathode is shown in Fig. 4. Simulations show central slices keep the thermal emittance at 5 cm from cathode, so the final central slice emittance growth does not happen in the emission process.

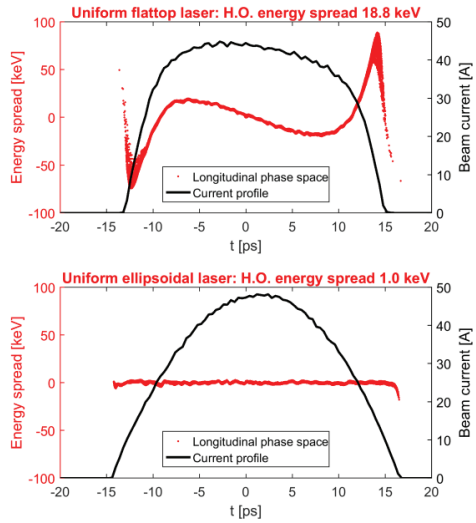

Figure 3: Longitudinal phase space comparison between uniform flattop laser and uniform ellipsoidal laser. 1st and 2nd order energy chirps are removed numerically, leaving only higher order (H.O.) energy spread.

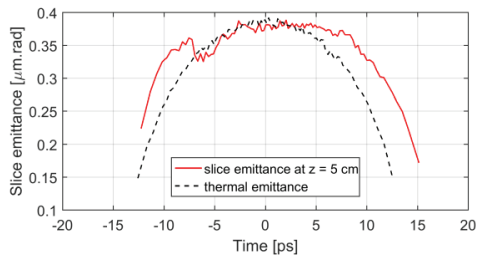

Figure 4: Slice emittance near cathode region for uniform ellipsoidal laser case.

PARABOLIC SPATIAL LASER SHAPING

Besides uniform flattop and uniform ellipsoidal laser pulses, a laser pulse with a special parabolic radial distribution was also proposed to linearize transverse space charge forces to the 3rd order [13].

$$I(r) = I_0\left(1 - \frac{r^2}{3R^2}\right). \quad (1)$$

r is the distance from beam center, R is the radius of the beam, I_0 is the peak beam intensity. Such a spatial distribution can be approximated by truncating Gaussian distribution at 0.9 sigma, see Fig. 5. The truncated Gaussian laser spatial shaping has been found at DESY and LCLS injectors in the 'pancake' photoemission regime,

ISBN: 978-3-95450-206-6 doi:10.18429/JACoW-FLS2018-WEP2PT034

improving transverse emittance compared to uniform transverse distribution [14 - 16].

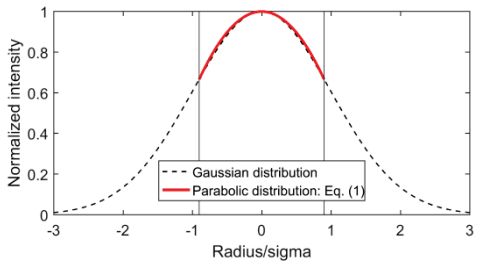

Figure 5: Parabolic Laser spatial intensity approximation by truncating Gaussian distribution at 0.9 sigma.

Laser spatial shaping with truncated Gaussian distribution was applied (in simulation) to the PITZ injector in the 'cigar' photoemission regime for both flattop laser pulses and ellipsoidal laser pulses. For flattop laser, the Gaussian truncation can be varied from 0.5 sigma to 1.5 sigma in the optmizer. The modulated ellipsoidal laser pulse shape is cut from a hard-edge flattop laser with truncated Gaussian transverse distribution, as shown in Fig. 6. Both the flattop case and ellipsoidal case have the same full temporal width as used in the previous simulations.

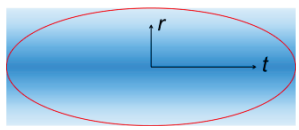

Figure 6: Illustration of modulated ellipsoidal laser pulse cut from a flattop laser pulse with transverse modulation.

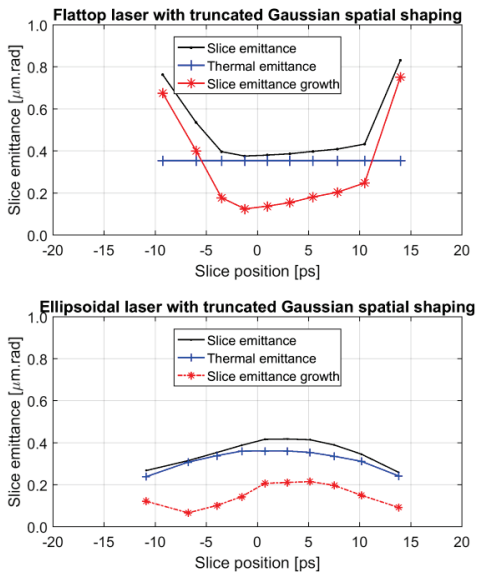

Figure 7: Slice emittance of flattop and ellipsoidal cases after truncated Gaussian spatial shaping is applied.

The optimized solutions for both distributions at 1 nC are shown in Fig. 7, and the comparisons between a uniform transverse distribution and a truncated Gaussian distribution are shown in Table 1. The optimum Gaussian truncations found from numerical simulations are 1 sigma cut for flattop laser and 0.9 sigma for ellipsoidal laser at a bunch charge of 1 nC, which are almost the same as theoretical predictions. Parabolic radial shaping improves the slice emittance by ~30% for the flattop laser case and by ~14% for the ellipsoidal laser case. Now the emittances of the central slices are almost the same as the thermal emittance for both lasers.

Table 1: Simulation comparison between lasers with uniform transverse distribution and truncated Gaussian distribution at 1 nC ($\langle\varepsilon_{slice}\rangle$ is the average emittance of the central 8 slices).

	Flat-U	Flat-G	Ellip-U	Ellip-G	Unit
$\varepsilon_{100\%}$	0.65	0.46	0.42	0.38	μm
$\varepsilon_{95\%}$	0.45	0.35	0.32	0.31	μm
$\langle\varepsilon_{slice}\rangle$	0.59	0.41	0.44	0.38	μm
$\delta E_{H.O.}$	18.8	15.5	1.0	1.6	keV

After parabolic radial shaping, the transverse emittance of the flattop laser case approaches that of ellipsoidal laser pulse, but the higher order energy spread is still one order of magnitude worse. Smaller higher order energy spread, i.e. a more linearized longitudinal phase space, will help longitudinal beam dynamics optimization in the main linac for XFEL applications. Radial parabolic distributions not only improve transverse emittance of both flattop and ellipsoidal laser pulse shapes, but also increase the laser shaping efficiencies.

CONCLUSION

In this paper, the PITZ photoinjector is used as a case study to further investigate laser spatial shaping for high bunch charge cases (~1 nC). With radial parabolic distribution approximated by Gaussian truncation at ~ 1 sigma, the slice emittance further improves by ~30% for the flattop laser case, and by ~14% for the ellipsoidal laser case, which makes the slice emittance almost the same as thermal emittance in the central slices. Such a radial laser shaping not only improves transverse emittance, but should also increase laser shaping efficiencies. With parabolic spatial shaping, the advantage of ellipsoidal laser on transverse emittance is reduced compared to the flattop laser, but the longitudinal phase space linearization is still one order of magnitude better.

REFERENCES

[1] M. Krasilnikov *et al.*, PRST AB 15, 100701 (2012).

[2] T. Schietinger *et al.*, PRST AB 19, 100702 (2016).

[3] R. Akre *et al.*, PRST AB 11, 030703 (2008).

[4] Report of the Basic Energy Sciences Workshop on the Future of Electron Sources (2016), https://science.energy.gov/~/media/bes/pdf/reports/2017/Future_Electron_Source_Worskhop_Report.pdf

[5] M. Khojoyan et al., in *Proc. FEL'13*, pp. 298.

[6] H. Qian *et al.*, in *Proc. FEL'17*, WEP008.

ISBN: 978-3-95450-206-6 doi:10.18429/JACoW-FLS2018-WEP2PT034

[7] C. Limborg-Deprey *et al*., NIM A 557, 106 (2006).

[8] Yuelin Li *et al*., PRST AB 12, 020702 (2009).

[9] J. Good *et al*., in *Proc. FEL'17*, WEP006.

[10] P. Musumeci *et al*., PRL 100, 244801 (2008).

[11] R. Li *et al*., PRST AB 15, 090702 (2012).

[12] C. F. Papadopoulos *et al*., in *Proc. FEL'14*, pp. 864.

[13] Triveni Rao, David H. Dowell, arXiv:1403.7539 (2014).

[14] F. Zhou *et al*., PRST AB 15, 090701 (2012).

[15] Tim Florian Plath, "A New Photo-Injector Laser for the Generation of Ultra-Short Electron Bunches at FLASH", master thesis, University at Hamburg, Germany, 2013.

[16] Marc Hänel, "Experimental Investigations on the Influence of the Photocathode Laser Pulse Parameters on the Electron Bunch Quality in an RF - Photoelectron Source", PHD thesis, University at Hamburg, Germany, 2010.

ISBN: 978-3-95450-206-6 doi:10.18429/JACoW-FLS2018-WEP2PT038

CONCEPTUAL DESIGN FOR SLS 2.0

M. Dehler, A. Streun, A. Citterio, T. Garvey, M. Hahn, L. Schulz, M. Negrazus, V. Vranković
PSI, Villigen PSI, Switzerland

Abstract

After 17 years of user operation, we plan to do an upgrade of the Swiss Light Source (SLS) in the period 2023-2024. The entire storage ring will be replaced by a new layout allowing operation at emittances lowered by factors of 40-50. This is made possible by small aperture magnets allowing for a multi bend achromat design and - a special feature for SLS 2.0 - with reverse bends combined with longitudinal gradient bends (LGB) leading to zero dispersion at the maximum magnetic field, thus minimizing the quantum excitation of the beam due to synchrotron radiation. The compact magnet layout makes use of offset quadrupoles, combined function magnets and longitudinal gradient bends. All vacuum chambers along the electron beam path will be coated with a non-evaporable getter (NEG) film to ensure low photo-desorption and a quick vacuum conditioning. Numerical simulations of instability thresholds have been performed. We expect values on the order of 2 mA for the single bunch current.

INTRODUCTION

Table 1: Main Parameters Of SLS 2.0 Compared To SLS

	SLS 2.0	SLS
Circumference [m]	290.4	288.0
Energy [GeV]	2.4	2.4
Current [mA]	400	400
Main RF frequency [MHz]	499.6	499.6
Nominal RF voltage [kV]	1420	2080
Harmonic number	484	480
Filling pattern gap	10%	19%
Damping times $\tau_{x,y,E}$ [ms]	4.9/8.4/6.5	8.6/8.6/4.3

The SLS started user operation in 2001 and has been operated in top-up mode since then. Today it is fully equipped with a set of 18 beam lines delivering about 5000 hours of user time per year with an excellent availability.

While it was state of the art at the time, a new generation of light sources are coming into operation or development, which make use of features such as advanced optics using low aperture magnets resulting in a dramatically reduced emittance. Given that the improved machine layout still needs to fit the existing facility with minimum changes, scaling existing designs, as e.g. for MAX-IV, would not have led to the required improvement in emittance of at least 30. A novel type of lattice was developed, which makes use of longitudinal gradient bends and reverse bends. At the price of stronger than anticipated modifications in the shielding walls and shifts in the source points of several beam lines, the old design with a three fold symmetry and three different types of straights will be replaced by a strictly regular layout with twelve fold symmetry.

The low vacuum chamber aperture of 20 mm diameter used in the design poses challenges from two sides. Vacuum conductance along the chamber (worse by more than a factor five in comparison to SLS) becomes negligible, so that distributed pumping becomes essential. Also resistive effects leading e.g. to microwave instabilities need to be investigated closely. A comparison of the main parameters of the upgrade with the original SLS is shown in Table 1.

OPTICS

The zero-current horizontal emittance in a storage ring is determined by the equilibrium between radiation damping and quantum excitation. The latter depends on the rate of photon emission, which is given by the strength of the magnetic field, and on the local dispersion function, because after emission of a photon, an electron starts an oscillation around the closed orbit corresponding to its reduced energy. The damping of horizontal oscillations thus excited is given by the total radiated power, which depends on the magnetic field strength, and by the horizontal 'share' of the overall damping, which is affected by transverse gradients in combined-function bending magnets.

The quantum excitation can be minimized by the use of longitudinal-gradient bends (LGBs, bending magnets for which the field varies along the beam path), while suppressing the dispersion at the LGB center, where the field is strongest. In a conventional periodic cell, this would lead to an over-focusing of the transverse beta function β_x, since also the bending magnets have a defocusing effects on the dispersion. This can be solved by the use of small reverse bends (RBs), realized in the SLS 2.0 lattice by generating the reverse kicks by a transverse offset of the horizontal-focusing quadrupoles nearby.

A welcome effect of this strategy is the enhanced radiation damping. The field variation in the LGB increases the radiated power compared to classical homogeneous bending magnets. In addition, the reverse bends increase the total absolute bending angle to values larger than 360^o. Altogether, a lattice cell combining LGBs and RBs can provide up to a five times lower equilibrium emittance compared to a conventional cell [1].

Figure 1 shows the fundamental building block of the lattice, a cell consisting of a center LGB with adjacent vertically focusing bends (VB) and two reverse bends. Five full and two half LGB-RB cells form one of the twelve identical 7-bend achromat arcs (7BAs) as shown in Fig. 2. Some cells will use LG-superbends of up to 6 Tesla peak-field [2] instead of the normal LGBs in order to provide x-rays in the 50 to 100-keV range. Table 2 compares the main parameters of

ISBN: 978-3-95450-206-6 doi:10.18429/JACoW-FLS2018-WEP2PT038

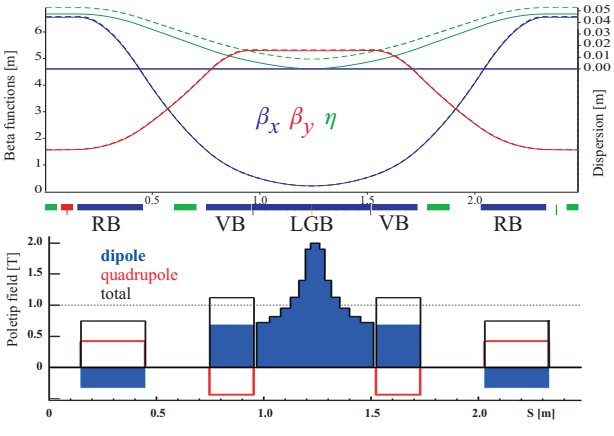

Figure 1: Optical functions and field components for the SLS 2.0 lattice cell containing a center LGB with adjacent vertically focusing bends (VB), and two RBs. If the RB were a pure quadrupole, the optical functions would follow the dashed lines in the upper plot and the emittance would be 4.5 time larger. The field components in the lower plot refer to the poletip field at 13 mm bore radius.

the upgraded lattice with the present SLS. An interesting property is the negative momentum compaction factor α as in proton synchrotrons below transition. Here the positive dependence between time-of-flight and momentum is over-compensated by the RBs.

All twelve straight sections are 5.5 m long. Eight full straights and three half straights are available for undulator installation, the others being required for injection elements and RF cavities. The higher lattice symmetry compared to SLS leads to modifications of the lattice footprint, mainly affecting the regions of the present longitudinal straights, while moderately affecting the others.

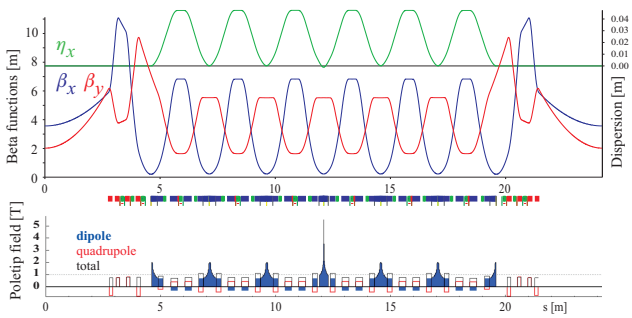

Figure 2: Optical functions and field components for one 7BA-arc where the center LGB has been interchanged by a super-LGB of 5.5 T peak field. Bending magnets are in dark blue, quadrupoles red and sextupoles green.

The lattice has a relative momentum acceptance of about 5% providing a Touschek-dominated beam lifetime of about 9 hours (similar to SLS now) and a horizontal dynamic aperture of about ± 6 mm at the point of injection. This allows off-axis injection, accumulation and top-up using the existing injector.

Table 2: Main parameters for the SLS 2.0 upgrade lattice including three superbends in comparison to the existing SLS lattice. The arrows ($\rightarrow$) indicates the increase due to intra-beam scattering at a nominal current of 400 mA in 400 of 484 bunches for 10 pm of vertical emittance and assume a third harmonic RF-system for bunch lengthening.

	SLS 2.0	SLS
Hor. damping partition J_x	1.71	1.00
Momentum compaction α [$\cdot 10^{-3}$]	-1.33	6.04
Total abs. bending angle	561.6^o	374.7^o
Lattice tunes $\nu_{x/y}$	39.2/15.3	20.4/8.7
Natural chromaticities $\xi_{x/y}$	$-95/-35$	$-67/-21$
Radiated power [kW]	221.6	219.5
Emittance [pm]	$98 \rightarrow 126$	5630
Energy spread [$\cdot 10^{-3}$]	$1.03 \rightarrow 1.07$	0.86

The injection makes use of a novel 'anti-septum' scheme based on an orbit bump formed by three dipole kickers. A current sheet is placed inside the middle kicker, which compensates the main field at the location where the injected beam passes [3]. The pulse of a kicker is weaker and shorter than in a septum magnet allowing the anti-septum to be as thin as 1 mm, reducing the distance between stored and injected beam and, therefore, the aperture requirements.

MAGNETS

Small apertures are a basic feature of low-emittance multi bend achromat lattices, because they enable an increase of magnet gradients and thus a reduction of magnet length and miniaturization of lattice cells. Many small magnets, in turn, result in small peak dispersion, such that sufficient momentum acceptance is still provided with small apertures. Due to miniaturization, the SLS 2.0 lattices contains 900 magnets in a 290.4 m circumference (of which 66 m are straights sections), which results in small inter-magnet distances and highs fields and gradients.

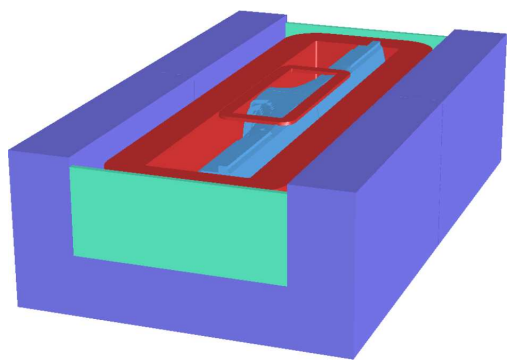

Figure 3: Resistive coil design for a central LGB with two vertical focusing combined function bends.

ISBN: 978-3-95450-206-6 doi:10.18429/JACoW-FLS2018-WEP2PT038

The core component is a compound magnet containing the central LGB with about 2-T peak field, and two vertically focusing combined-function bending magnets (VB) in a common yoke. The RBs are essentially radially shifted quadrupoles. Resistive coil and permanent-magnet designs are being evaluated in parallel for the RB and the LGB compound magnet, the final decision depending on costs and ongoing technological progress in the field. Modified versions of these magnets are used in the dispersion suppressor cells at the ends of the arcs, i.e., half-LGBs and RBs and VBs with modified gradients. Designs using resistive coils (Fig. 3) as well as permanent magnet materials (Fig. 4) are under investigation. Given the advantages, the permanent magnet version is strongly preferred and we are preparing to build a LGB/VB prototype using these materials.

Any of the 60 LGBs may be exchanged by a LG-superbend; it is planned to start with three of these. The design is based on two pairs of coils, Nb_3Sn racetrack-coils to create a narrow central field peak of 6 Tesla, and NbTi Helmholtz coils to provide the required field integral [2].

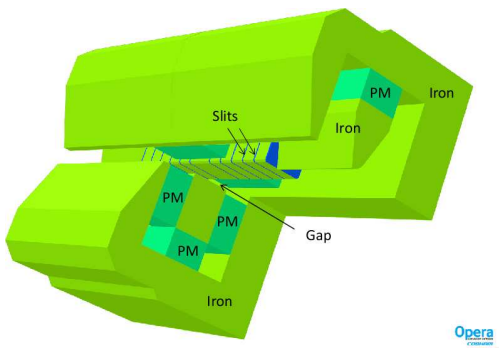

Figure 4: Three quarter model of central LGB with two vertical focusing combined function bends using permanent magnet material.

Quadruplets of quadrupoles on both ends of the arcs are used for matching to the straight sections and provide margin to compensate any focusing from the insertion device.

A total of 288 sextupoles and 144 octupoles are employed for correction of chromaticity and optimization of acceptance. Orbit control is performed using 120 horizontal and vertical dipoles realized with additional coils as integral part of some sextupoles and 24 small dipoles in the straight sections will be used to steer the photon beams from the undulators. Small quadrupoles for fine tuning and gradient corrections, and skew quadrupoles for coupling control, are realized with additional coils in some of the octupoles.

VACUUM

The vacuum chamber is based on a round beam pipe of 20-mm diameter. Sections with ante-chambers in the LGB regions, where radiation is emitted at high power, alternate with sections made from simple round pipes in the RB regions. Due to the high power density, the synchrotron radiation coming from the LGBs requires discrete crotch absorbers, otherwise distributed absorbers are used. The high

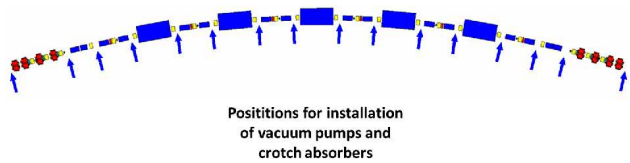

Figure 5: Magnet section with locations for vacuum pumps and crotch absorbers.

gas load originating at the crotch absorbers is evacuated in situ with local pumps (Fig. 5 shows the placement of pumps and absorbers). Vacuum conductance along the small diameter chamber is very low, therefore the vacuum chamber will be coated with non-evaporable getter (NEG) material for distributed pumping and to reduce radiation-induced gas desorption from the chamber walls. The NEG layer has a thickness of 1 μm in the ante-chambers but only 500 nm in the beam pipe in order to minimize the resistive wall effects.

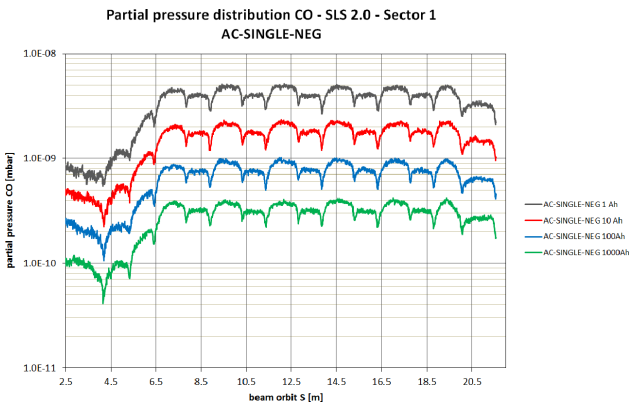

Figure 6: Pressure distributions for vacuum chamber with ante-chamber and NEG coating.

With Molflow+ [4] and Synrad+, the evolution of the pressure distribution inside the vacuum chamber with the ante-chamber was simulated for increasing beam doses (Fig. 6). A dose of 100 Ah should be sufficient to get below the required pressure of 10^{-9} mbar.

STABILITY

At the SLS, we have seen coupled bunch modes (CBM) in the longitudinal plane driven by higher order modes in the main RF cavities. In standard operation, suitable HOM tuning combined with Landau damping provided by a super conducting third harmonic cavity [5] is sufficient to control them. During filling of the ring, there are regions of instability, which require the longitudinal bunch by bunch feedback to be active. The upgrade will essentially use the same RF systems and the situation should be similar. An upgraded multi bunch feedback system with enhanced resolution and processing should even give give a higher robustness. Transversally, we expect CBMs driven by resistive wakes and ions, these will be controlled by transverse feedbacks and the fill pattern gap.

ISBN: 978-3-95450-206-6 doi:10.18429/JACoW-FLS2018-WEP2PT038

Ion trapping can cause several adverse effects of beam performance as e.g. coherent instabilities, beam blow up, tune shift and increased coupling. The effect is reduced for the small beam sizes, we expect in SLS 2.0 and, if a gap of empty buckets is introduced in the regular bunch pattern. A detailed study was performed [6]. It shows that already a gap of 10 empty buckets will clean most of the ions inside the machine.

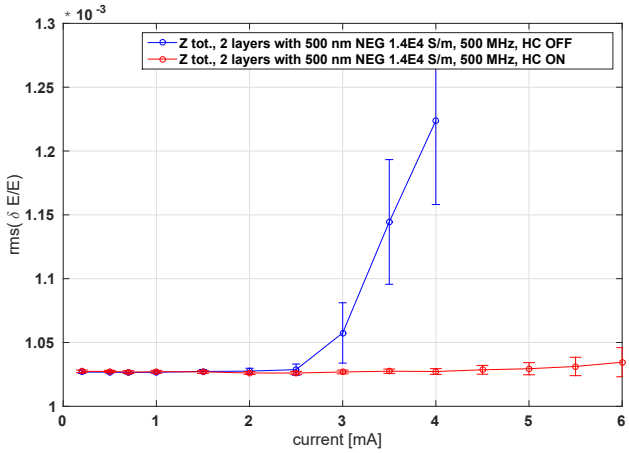

Figure 7: Single bunch energy spread versus bunch current as simulated with *mbtrack* (red: harmonic cavity on, blue, harmonic cavity off). The corresponding thresholds for the microwave instability are 1.5, resp. 3.5 mA.

The onset of turbulent bunch lengthening has been estimated using *mbtrack* [7]. The simulations (Fig. 7) include impedance contributions from vacuum chamber, beam-position monitors, tapers and cavities, the onset of the instability shows up as an increase of the single bunch energy spread with current. The resulting threshold current of 1.5 mA without, and 3.5 mA with an ideal third-harmonic RF system for bunch lengthening, is well above the desired beam current of about 1 mA per bunch (400 mA total current). CSR limits are of a similar order.

NEXT STEPS

The year 2017 saw the end of the conceptional phase of the upgrade with a review of the conceptional design report. Currently, we enter the technical design phase, which should be concluded in summer 2019. The beamlines, which partially require to be adapted to the new machine layout also go through conceptional and technical design phases until mid 2021. In 2023/2024, SLS will enter a 18 month long 'dark time' (without any user operation), during which the shielding will be modified, the storage ring and the undulators will be replaced and accelerator and beamlines will be commissioned.

The authors acknowledge the contribution of all team members of the SLS 2.0 project team.

REFERENCES

[1] A. Streun (Ed.), "SLS-2 Conceptual Design Report", PSI-Bericht 17-03, Paul Scherrer Institut, Villigen, Switzerland, Dec. 2017.

[2] C. Calzolaio et al., "Design of a Superconducting Longitudinal Gradient Bend Magnet for the SLS Upgrade", IEEE Trans. Applied Supercon., vol. 27, no. 4, 2017.

[3] C. Gough, M. Aiba, "Top-up injection with anti-septum", Proc. IPAC 2017, Copenhagen, Denmark, pp. 774-776, 2017

[4] M. Ady, R. Kersevan and M. Grabski, " Monte Carlo simulations of synchrotron radiation and vacuum performance of the MAX IV light source", Proc. IPAC-2014, Dresden, Germany (2014).

[5] M. Svandrlik et al., "The super-3HC project: An idle superconducting harmonic cavity for bunch length manipulation", Proc. EPAC-2000, Vienna, Austria (2000).

[6] A. Wrulich, "Ion trapping in SLS-2", Technical report SLS2-WA80_001. PSI, 2017

[7] G. Skripka et al., "Simultaneous computation of intrabunch and interbunch collective beam motions in storage rings", Nucl. Instr. and Meth. A 806, 221-230, 2016.

ISBN: 978-3-95450-206-6 doi:10.18429/JACoW-FLS2018-WEP2PT050

STATUS OF CAEP THz FREE ELECTRON LASER OSCILLATOR *

D. Wu, M. Li†, X. F. Yang, X. Luo, X. M. Shen, D. X. Xiao, J. X. Wang, P Li, X. K. Li, K. Zhou, C. L. Lao, P. Zhang, Y. Xu, S. F. Lin, Q. Pan, L. J. Shan, T. H. he, H. B. Wang
Institute of Applied Electronics, China Academy of Engineering Physics (CAEP/IAE), Mianyang, 621900, P.R.China

Abstract

China Academy of Engineering Physics tera-hertz free electron laser (CAEP THz FEL, CTFEL) is the first THz FEL oscillator in China, which was jointly built by CAEP, Peking university and Tsinghua university. The stimulated saturation of the CTFEL was reached in August, 2017. This THz FEL facility consists of a GaAs photocathode high-voltage DC gun, a superconducting RF linac, a planar undulator and a quasi-concentric optical resonator. The terahertz laser's frequency is continuous adjustable from 2 THz to 3 THz. The average power is more than 10 W and the micro-pulse power is more than 0.1 MW.

INTRODUCTION

Free electron laser (FEL) can be the most powerful tool as tera-hertz power source. It has many advantages, such as monochrome, high-power, linear-polarization, continuously-tunable frequency. A lot of FEL facilities, such as ELBE in Germany [1], FELIX in Holland [2], UCSB in the USA [3] and NovoFEL in Russia [4], have played important roles in the THz sciences. In the near future, of the 20 FEL facilities planned to be built in the whole world, there will be at least 8 ones operating in the THz range [5].

CAEP THz FEL (CTFEL) facility is the first high average THz source based on FEL in China [6, 7], which is driven by a DC gun with a GaAs photocathode [8, 9] and two 4-cell 1.3 GHz super-conducting radio frequency (SRF) accelerator [10]. The repetition of CTFEL is 54.167 MHz, one in twenty-fourth of 1.3 GHz. The effective accelerator field gradient is about 10 MV/m. The terahertz wave frequency is continuous adjustable from 2 THz to 3 THz. The average power is more than 10 W and the micro-pulse power is more than 0.1 MW. This paper gives an introduction of this facility and its THz laser characters.

FACILITY COMPONENTS

Overview

Figure 1 shows the layout of the CTFEL facility. High average power high-brightness electron beam emits from the high-voltage DC gun equipped with a GaAs photocathode. The beam is then accelerated by a 2×4-cell RF superconducting accelerator and gain a kinetic energy from 6 MeV to 8 MeV. Passing through an achromatic section, the beam then goes into the undulator magnet field and generate the spontaneous radiation. The radiation resonates in the THz optical cavity and reaches saturations.

Table 1 gives more information of the electron beam. The accelerator is designed to operate in both CW and macro-pulse mode. It is now working in macro-pulse mode in the first step. The typical output in this "step one" is in 1 ms and 1Hz macro-pulse mode. The duty cycle will update to >10% in 2018 as the "step two". And the CW operation will be reached in the "step three".

Table 1: Electron Beam Parameters

Parameters	Designed value	Unit
Bunch charge	10~100	pC
Micro-pulse repetition	54.167	MHz
Macro-pulse repetition	1~20	Hz
Duty cycle	10^{-5} ~1	
Kinetic energy	6~8	MeV
Normalized emittance	<10	μm
Micropulse length	4~8	ps
Energy spread	<0.75	%

High-voltage DC Electron Source

Figure 2 shows the system of the high-voltage DC electron source, which consists of a photocathode preparation chamber, a load-lock system, a drive laser, a high-voltage DC gun and some beam elements such as three solenoids and an RF buncher. The electron source can provide 320 keV high brightness beams both in CW mode and in macro-pulse mode. The average current has reached 1 mA 5 mA. The micro-pulse length is compressed to 8 ps by the RF buncher.

RF Superconducting Accelerator

Owing to the advantages of superconducting RF technology in CW mode operation, a 2×4-cell superconducting linac module has been adopted to accelerate 320 keV, 1~5 mA electron beams from the DC-gun up to an energy of 6~8 MeV. The 2×4-cell module is composed of two SRF cavities, two power couplers, two tuners and a cryostat, as shown in Fig. 3. With the goal of 5 mA, 54.17 MHz CW beams, the components have been designed accounting for higher-order modes (HOMs), beam loading and cryogenic issues. The phase stability of the low-level RF control system is 0.1°, and the amplitude stability is better than 0.05%. After the acceleration, the normalized emittance of the beam is less than 8 mm·mrad, and the relative energy spread is less than 0.2%.

* Work supported by China National Key Scientific Instrument and Equipment Development Project (2011YQ130018), National Natural Science Foundation of China with grant (11475159, 11505173, 11575264 and 11605190)
† liming@caep.cn

ISBN: 978-3-95450-206-6 doi:10.18429/JACoW-FLS2018-WEP2PT050

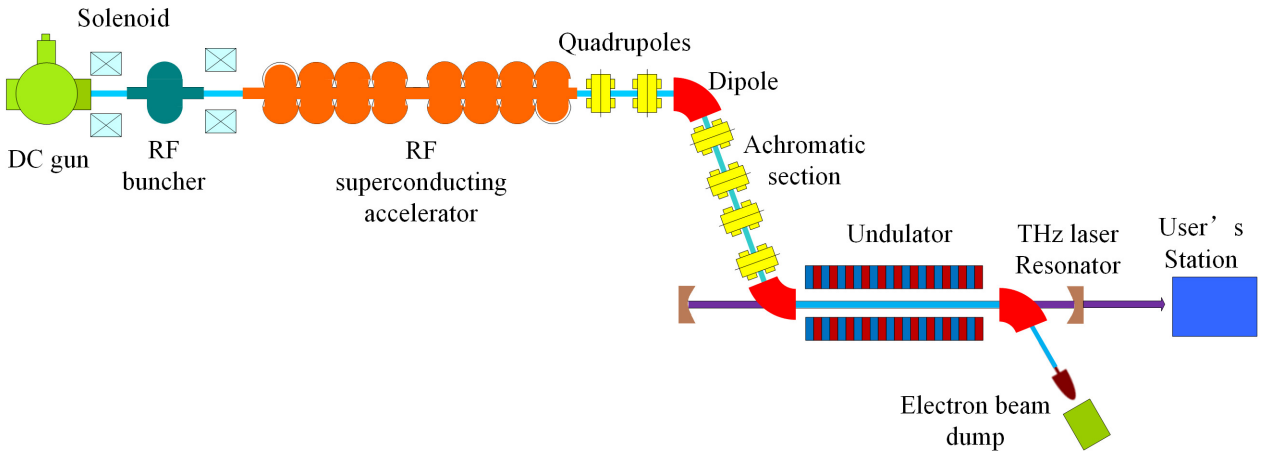

Figure 1: The layout of the CTFEL facility.

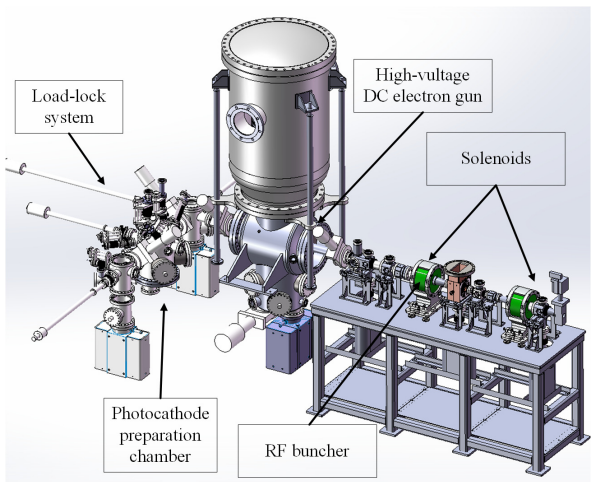

Figure 2: The high-voltage DC electron source.

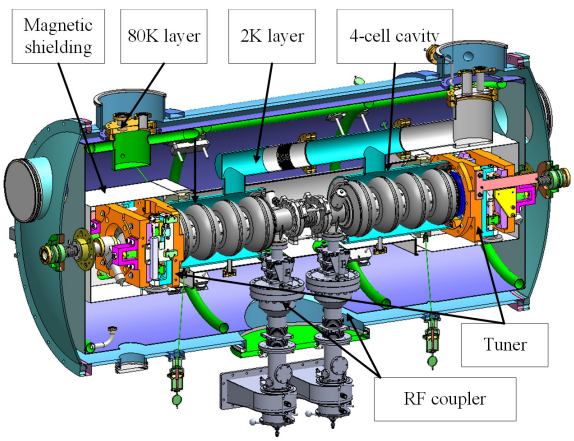

Figure 3: The RF superconducting accelerator.

Undulator and THz Resonator

The THz wave is generated and resonates in the undulator and THz optical cavity system, as shown in Fig. 4. The electron beam and the THz wave fly through a THz waveguide together. The wave guide is under the undulator magnetic field. The undulator has a period of λ_u=38 mm. And the field B_0 is tunable from 0.2 T to 0.55 T.

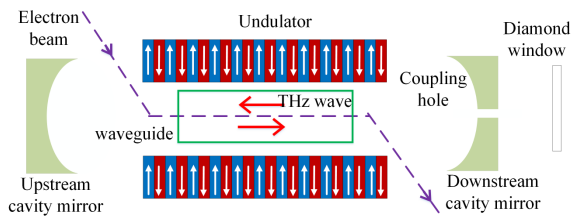

Figure 4: The undulator and the THz optical cavity.

The THz wave is reflected back and forth between the two cavity mirrors. The two mirrors form a quasi-concentric optical resonator. The terahertz laser power is then extracted by a hole of a few millimeters in the downstream mirror, and then goes through a diamond window to transmit to the user's lab.

THz LASER PARAMETERS

Table 2 shows the main parameters in the "step one" of the THz laser downstream the coupling hole.

Table 2: THz Laser Parameters

Parameters	Value	Unit
Tunable frequency range	1.87~3.3	THz
Spectral FWHM	~2	%
Macro-pulse average power	>9	W
Macro-pulse repetition	1~20	Hz
Macro-pulse length	0.3~2	ms
Micro-pulse RMS length	<1	ps
Micro-pulse interval	18.5	ns
Micro-pulse power	>0.1	MW
Minimum transverse radius	<0.5	mm
Polarization	Horizontal	

ISBN: 978-3-95450-206-6 doi:10.18429/JACoW-FLS2018-WEP2PT050

Figure 5 shows some measurement results of the THz laser at the user's lab. Figure5(a) is the average power measured by a TK absolute energy meter. The THz average power is given by [11]:

$$P_{avg} = \frac{V}{0.49T\tau r_{ji}}, \quad (1)$$

where is the output voltage of the energy meter, which is about 540 mV in Fig. 5 (a). T ≈0.55, which is the transmission of the TPX window. The pre-calibrated r_{ji}=0.233 mV·μJ^{-1}. On the bottom of the formula, 0.49 means that the absorption of the energy meter's metal film is about 49%. And 950 μs, which is the macro-pulse length measured by a GeGa detector, as shown in Fig. 5 (b). All the results indicate the macro-pulse average power is about 9 W. Therefore, the THz transmission does not lose too much power.

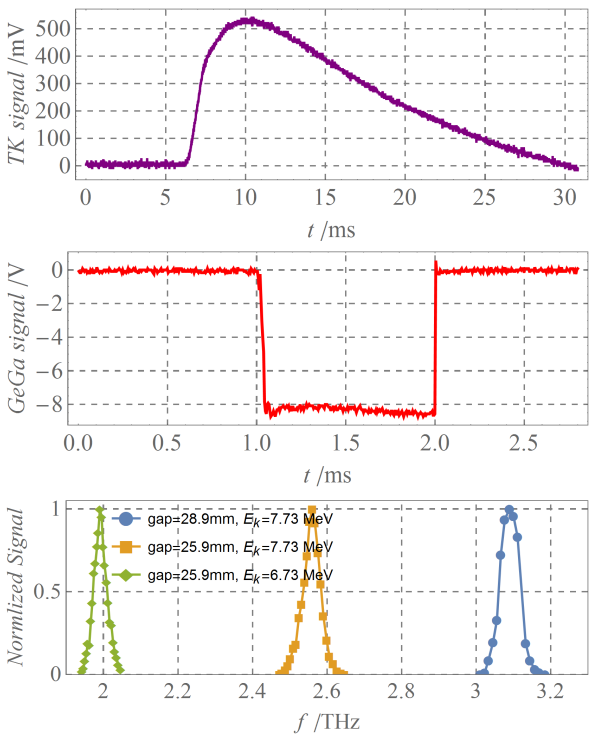

Figure 5: The THz power and frequency measurement.

The spectrum at three single spots is shown in Fig. 5 (c), which is measured by a grating spectrometer. The frequency is adjusted by both the undulator gap and the electron energy. The spectral FWHM is a little wider than theoretical simulation because the micro-pulse length is a little shorter, typically as short as about 400 fs (RMS), making the peak power more than 0.1 MW.

SUMMARY

This paper has briefly introduced the CTFEL facility, which is the first THz free electron laser oscillator in China. This facility mainly consists of a high-brightness high-voltage DC electron source, a CW RF superconducting accelerator and an undulator-optical-cavity system. The CTFEL facility provide monochrome, high-power, linear-polarization, and frequency-continuously-tunable THz laser. The terahertz frequency is continuous adjustable from 2 THz to 3 THz. The average power is more than 9 W and the micro-pulse power is more than 0.5 MW. This facility will greatly promote the develop-ment of the THz science and its applications on material science, chemistry science, biomedical science and many other cutting-edge areas in general.

REFERENCES

[1] F. Gabriel *et al.*, "The rossendorf radiation source ELBE and its FEL projects," *Nuclear Instruments and Methods in Physics Research Section B: Beam Interactions with Materials and Atoms*, vol. 161, pp. 1143–1147, 2000.

[2] D. Oepts, A. van der Meer, and P. van Amersfoort, "The free-electron-laser user facility FELIX," *Infrared Physics & Technology*, vol. 36, no. 1, pp. 297–308, 1995.

[3] G. Ramian, "The new UCSB free-electron lasers," *Nuclear Instruments and Methods in Physics Research Section A: Accelerators, Spectrometers, Detectors and Associated Equipment*, vol. 318, no. 1-3, pp. 225–229, 1992.

[4] G. Kulipanov *et al.*, "Research highlights from the Novosibirsk 400 w average power THz FEL," *Terahertz Sci. Technol*, vol. 1, no. 2, pp. 107–125, 2008.

[5] K. Cohn, J. Blau, W. Colson, J. Ng, and M. Price, "Free electron laser in 2015," in *Procedings of FEL2015*, Daejeon, Korea, 2015, pp. 625–629.

[6] Y.-H. Dou, X.-J. Shu, and Y.-Z. Wang, "3D-simulations of transverse optical modes of the free electron laser resonator with hole output coupling," *Communications in Computational Physics*, vol. 1, no. 5, pp. 920–929, 2006.

[7] P. Li, Y. Jiao, W. Bai, H. B. Wang, X. H. Cui, and X. K. Li, "Start-to-end simulation of CAEP FEL-THz beamline," *High Power Laser and Particle Beams*, vol. 26, pp. 213–217, 2014.

[8] H. Wang, K. Li, M. Li, D. Wu, D. Xiao, and X. Yang, "A GaAs photoemission dc gun for caep high-average-power THz FEL," *Proceeding of FEL 2014,Basel, Switzerland*, pp. 318–321, 2014.

[9] D. Wu *et al.*, "Studies on factors affecting the life-time of high average current GaAsphotocathode," in *Proceedings of SAP2014, LanZhou, China*, 2014, pp. 12–15.

[10] X. Luo *et al.*, "Design and fabrication of the 2×4-cell superconducting linac module for the free-electron laser," *Nuclear Instruments and Methods in Physics Research Section A: Accelerators, Spectrometers, Detectors and Associated Equipment*, vol. 871, pp. 30–34, 2017.

[11] *THz absolute power & energy installation and operation meter system instructions*, Thomas Keating Instruments. www.terahertz.co.uk

ISBN: 978-3-95450-206-6 doi:10.18429/JACoW-FLS2018-THA1WA03

GPT-CSR: A NEW SIMULATION CODE FOR CSR EFFECTS

S.B. van der Geer†, M.J. de Loos, Pulsar Physics, Eindhoven, The Netherlands
I.D. Setija, P.W. Smorenburg, ASML, Veldhoven, The Netherlands
P.H. Williams, STFC Daresbury Laboratory and Cockcroft Institute, Warrington, United Kingdom

Abstract

For future applications of high-brightness electron beams, including the design of next generation FEL's, correct simulation of Coherent Synchrotron Radiation (CSR) is essential as it potentially degrades beam quality to unacceptable levels. However, the long interaction lengths compared to the bunch length, numerical cancellation, and difficult 3D retardation conditions make accurate simulation of CSR effects notoriously difficult. To ease the computational burden, CSR codes often make severe simplifications such as an ultra relativistic bunch travelling on a prescribed reference trajectory. Here we report on a new CSR model, implemented in the General Particle Tracer (GPT) code [1], that avoids most of the usual assumptions: It directly evaluates the Liénard–Wiechert potentials based on the stored history of the beam. It makes no assumptions about reference trajectories, while also taking into account the transverse size of the beam. First results demonstrating microbunching gain in a chicane are presented.

INTRODUCTION

Here we add a new alternative to the list of simulation codes for CSR effects. Our version is implemented in the GPT code, and we intentionally steered away from the approaches used by other codes such as Elegant [2,3]. The goal we had in mind was not to create the 'best' CSR code per-se; we wanted to make a model that could answer the question what the consequences are of the assumptions made by the already exiting codes. In order to do so, we created a code that is based on direct evaluation of the retarded Liénard–Wiechert potentials.

The main approximation used in this GPT element is that the bunch is modeled as a parametric curve, sliced in the direction of average propagation. This is typically a very good approximation because the dynamics of the underlying process are governed by the rest-frame properties of the bunch. In this frame, the bunch is elongated by the Lorentz factor compared to the length in the laboratory frame, resulting in a very narrow ribbon of charge. In this GPT model, the ribbon itself is allowed to meander through 3D space, capturing the largest amount of 3D effects possible within the parametric 1D framework. The chosen approach makes use of the fact that if all individual beam segments that have radiated in the past are stored, this information is sufficient to calculate the electromagnetic fields everywhere in 3D space, at any later point in time.

The result of the chosen approach is that changes in bunch shape between the point where radiation is emitted and the interaction point are properly taken into account. Another advantage is that the usual ultra relativistic assumptions are not needed. A conceptual simplification compared to some other codes is that the radiation is emitted based on the derivative of the momentum, regardless of the reason: A very strong electrostatic deflection field will give rise to the same emitted radiation as a bend-magnet or a heavily misaligned quadrupole as long as the trajectories are the same. Furthermore, because the element is based on electromagnetic fields and not 'effects', radiation fields and the fields of other beamline components can all be correctly added. This allows for beamline components very close to the exit of a bend magnet, where a strong CSR wake can be travelling almost parallel to the bunch over long distances, to be properly simulated without degrading the accuracy of the CSR calculations. Finally, both the transverse and longitudinal fields are calculated, taking into account not only energy changes but also transverse effects that might vary along the bunch causing projected emittance growth.

The implementation of this element consists of two main parts: A history manager that maintains the history of the bunch, and a field calculator that integrates the radiation fields based on this stored history. They will be described in the following sections. We end by showing first simulation results, followed by a conclusion.

HISTORY MANAGER

The history manager of our new CSR code stores at discrete time intervals a 1D parameterization of the entire bunch, including basic information about transverse size. The first step is to switch to a new coordinate system, where **u** is the average direction of propagation, **v** lies in the bend-plane, and **w**=**u** x **v**. In this frame, an estimate of the current profile is obtained by slicing in **u**, and this in turn defines the non-equidistant charge quantiles of the beam. The recipe is shown schematically in Figure 1.

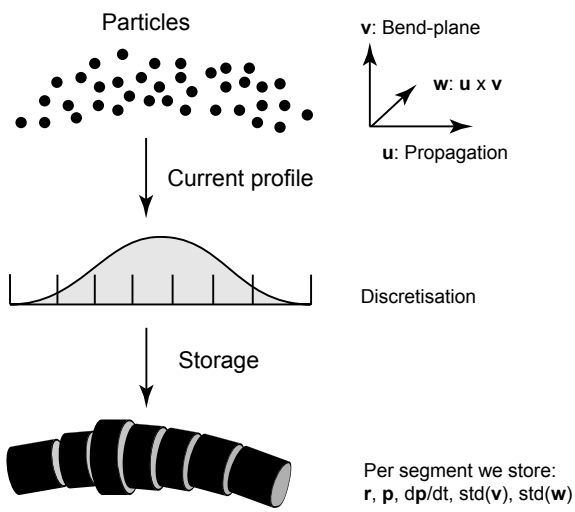

Figure 1: Schematic of the CSR history manager.

† info@pulsar.nl

ISBN: 978-3-95450-206-6 doi:10.18429/JACoW-FLS2018-THA1WA03

For each segment the total charge, average position, average momentum, average acceleration and transverse beam sizes are stored. As we will see, this information is all that is needed to calculate the CSR field at any position, at any later point in time.

When running simulations with large Lorentz factors and relatively smooth fields, it is possible that the average momentum changes direction over angles (much) larger than $1/\gamma$ during one timestep. This potentially results in cases where emitted radiation is partially missed due to relativistic beaming, also known as the headlight effect. In that case the history manager forces the Runge-Kutta integrator of GPT to reduce timesteps.

FIELD CALCULATION

At each Runge-Kutta substep in the GPT simulations, the electromagnetic radiation emitted in the past is reconstructed at the current bunch position, as schematically shown in Figure 2. The first step in this process is making a 1D parameterization of the bunch based on non-equidistant charge quantiles of the beam, fully analogous to the history manager. Subsequently, the centers $\mathbf{r}_i$ of each slice i are calculated, thereby avoiding the need for a reference path or trajectory and allowing significant differences in trajectories between the head and the tail of the bunch.

The crucial step in the CSR field calculation is calculating the actual electromagnetic **E** and **B** fields at the current timestep at each of these $\mathbf{r}_i$, by summing the Liénard-Wiechert potentials [4] for all segments $\mathbf{r}_s$ that fulfil the retardation condition $|\mathbf{r}-\mathbf{r}_s|=c\,\Delta t$:

$$\mathbf{E}(\mathbf{r},t)=\sum_{segments}\frac{q_s}{4\pi\varepsilon_0}\left(\ldots+\frac{\mathbf{n}\times\left((\mathbf{n}-\boldsymbol{\beta})\times\dot{\boldsymbol{\beta}}\right)}{c(1-\mathbf{n}\cdot\boldsymbol{\beta})^3\sqrt{|\mathbf{r}-\mathbf{r}_s|^2+R^2}}\right)_{tr}$$

$$\mathbf{B}(\mathbf{r},t)=\sum_{segments}\frac{\mathbf{n}(t_r)}{c}\times\mathbf{E}(\mathbf{r},t)$$

where

$$\mathbf{n}(t)=\frac{\mathbf{r}-\mathbf{r}_s(t)}{|\mathbf{r}-\mathbf{r}_s(t)|}$$

with $\beta=v/c$, and where q_s is the charge of the segment and where Δt is the time difference between the current timestep and the timestamp of the stored profile. When only a fraction of a stored segment fulfils the retardation condition, only the corresponding fraction of the charge in that segment is used in the equations. The … in the given equation denotes the Coulomb term, that will be discussed later.

In order to include transverse effects, we model each emitting slice by four (or sixteen) independent points, located at plus or minus 1 standard deviation off-axis. This gives us 4 (or 16) times more emission points $\mathbf{r}_s$ than segments, and because the bunch travels on a curved trajectory the retardation conditions for these points have to be individually evaluated. We observed that with only four point we are able to capture relevant 3D effects at a relatively low price and increasing this number to 16 did not show any significant differences for our initial test-cases.

The evaluated fields are singular when evaluated at $\mathbf{r}=\mathbf{r}_s$, but under normal circumstances this should not happen since a) the receiver's position **r** is on-axis and the emitting positions $\mathbf{r}_s$ are off-axis, and b) the bunch has moved forward since the last stored profile. Nevertheless, we add a tiny R in the denominator, analogous to the concept of Plummer spheres commonly used in the the astrophysical community, as safeguard.

The main challenge writing this CSR model was to prevent interference problems between consecutive interpolations steps. This problem was solved by choosing low-order interpolations to prevent undesired oscillations and using quantiles instead of equidistant arrays to prevent artificial spikes in the Fourier transformed solution. What remains is the challenge that the integrand, tracing 'vertically' back in time, always has two large peaks of opposite sign that almost cancel when integrated. That however is the nature of CSR interactions when working directly with the LW-potentials.

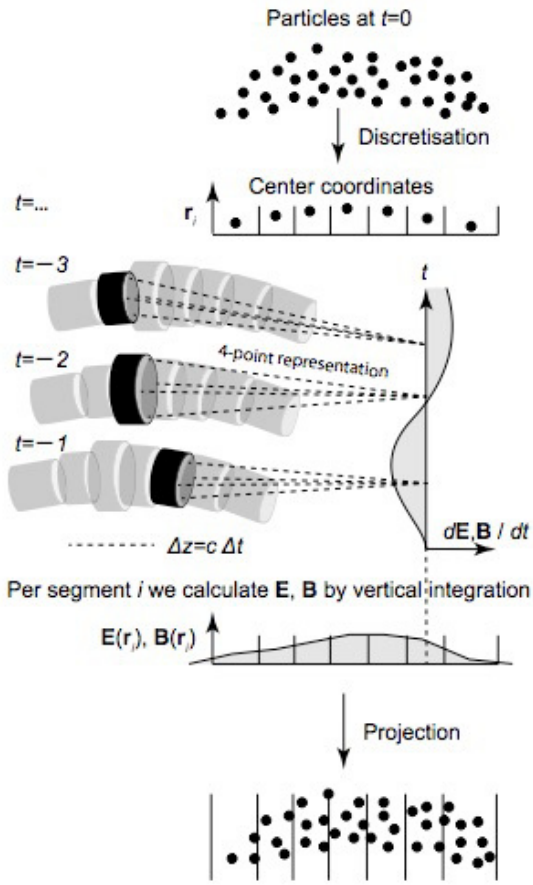

Figure 2: Schematic of field integration.

LIMITATIONS

Every simulation code has sweets spots in parameter space where it works best, gray areas preferably to be avoided, and no-go zones. In this section we describe the limitations of our code, and offer potential remedies and outlooks where applicable.

Slicing the bunch in the average direction of propagation is problematic in the case of roll-over compression.

ISBN: 978-3-95450-206-6 doi:10.18429/JACoW-FLS2018-THA1WA03

However, because the slicing problem only happens during very short timescales we are at this point not able to judge how severe the integrated error actually is.

The current implementation includes 3D effects for the emission process by having off-axis emission points. An analogous scheme is however not implemented for the receiving part, resulting in CSR fields that are independent on the transverse coordinate.

Adding the Coulomb term of the LW potentials to the interaction results in a r^{-2} singularity that sometimes causes numerical instabilities for bunches with very small transverse dimensions.

The current version does not allow for shielding effects. It is foreseen that this will be added using mirror bunches, at the expense of required computing power.

Due to relativistic beaming, the implemented method is not a good match for multi GeV beams and large deflection angles. It will work, but it will be slow.

TEST-CASE

As test case for the new CSR model in GPT we used the settings as proposed at the DESY 2002 workshop about Coherent Synchrotron Radiation [5]. The chosen scenario consists of a 1 nC, 1 µm emittance, 500 MeV beam sent through a four-magnet chicane, while being compressed longitudinally from 200 to 20 µm. These parameters are still relevant for designs today, although the charge is arguably a bit high.

The main result, the longitudinal phase space at the exit plane, is shown in Figure 3. It was obtained with 8M macro-particles and took 3.5 hours wall-clock time using 64-cores on a Linux cluster. It shows the well-known CSR-signature, where particles at the front are slightly accelerated. The average energy loss is 0.34%, being reasonably close to Elegants value of 0.42%. The main message of this paper is not a detailed comparison between GPT and other simulation codes: It is merely a demonstration that the method is available and is ready for testing.

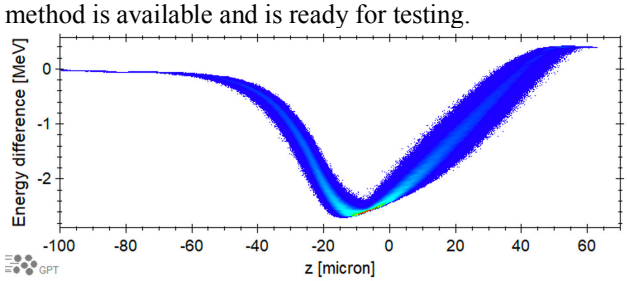

Figure 3: Raw GPT simulation result at the target plane at z=15 m. Head of the bunch is at the right.

To test the capabilities of the model in terms of numerical instabilities, we varied the initial density profile. Shown in figure 4 are the results of 1%, 2% and 5% initial density variation at fixed k_z=25/sigma. Because CSR is sensitive to the derivative of the current profile the expected result is a fluctuation in final energy [6]. Figure 4 clearly shows this effect, where we would like to emphasize that our from-first-principles approach yields this result without numerically taking the derivative of the current profile and thereby avoiding all related numerical issues.

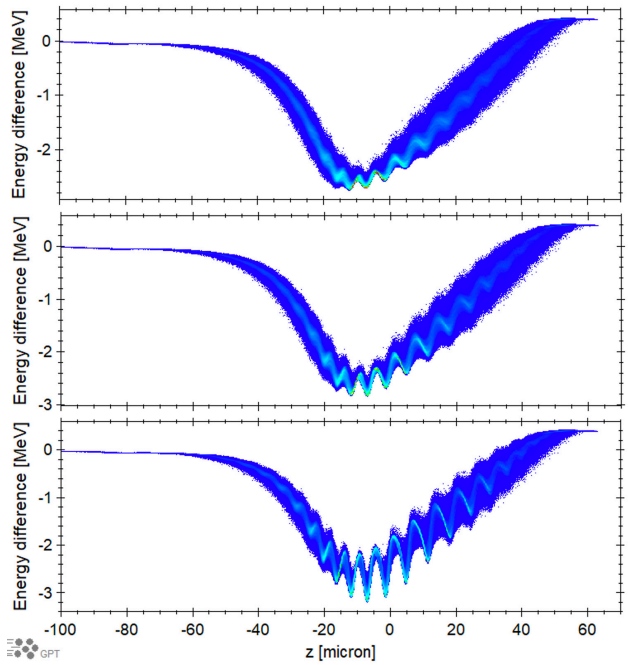

Figure 4: GPT simulation results based on the DESY 2002 workshop settings, with initial density fluctuations of 1% (top), 2% (middle) and 5% (bottom).

CONCLUSION

We created a new CSR model in the GPT code, based on evaluating retarded Liénard-Wiechert potentials from-first-principles. The model does not assume a reference trajectory, allows the head and tail of the bunch to be on different tracks, takes into account the transverse size of the bunch for the emission process, makes no ultrarelativisitc approximations, and correctly takes into account changes in the current profile between emission and interaction with emitted radiation. The code runs on MPI Clusters and shows consistent results for the testcase of the DESY 2002 workshop about CSR. Adding a small density fluctuation to the initial particle distribution shows that the code has sufficient numerical precision for microbunching simulations.

REFERENCES

[1] General Particle Tracer (GPT) code, Pulsar Physics, http://www.pulsar.nl/gpt

[2] M. Borland. *Elegant: A flexible SDDS-compliant code for accelerator simulation*. Proceedings of ICAP'00, Darmstadt, Germany, 2000.

[3] E. L. Saldin, E. A. Schneidmiller, and M. V. Yurkov. *On the coherent radiation of an electron bunch moving in an arc of a circle*. Nucl. Instrum. Meth. A, 398(2):373 – 394, 1997.

[4] J. D. Jackson. Classical Electrodynamics. Wiley, 1962

[5] http://www.desy.de/csr/

[6] E. L. Saldin, E. A. Schneidmiller, and M. V. Yurkov. *Longitudinal space charge-driven microbunching instability in the TESLA Test Facility linac*.NIM-A, 528(1):355, 2004.

ISBN: 978-3-95450-206-6 doi:10.18429/JACoW-FLS2018-THP1WB02

IMPEDANCE EVALUATION OF PF IN-VACUUM UNDULATOR (IVU) WITH THEORIES AND SIMULATIONS AND EXPERIMENTAL CONFIRMATION OF THEM BY THE TUNE MEASUREMENT

O. Tanaka†, N. Nakamura, T. Obina, and K. Tsuchiya, High Energy Accelerator Research Organization (KEK), Tsukuba, Japan

Abstract

Four In-Vacuum Undulators (IVU) were recently installed to Photon Factory (PF) at KEK. The estimate of their impedance and kick factors is a very important issue, because they could considerably increase the total impedance of PF. Moreover, the coupling impedance of the IVUs could lead to the beam energy loss, changes in the bunch shape, betatron tune shifts and, finally, to the various beam instabilities. Using the simulation tool (CST Particle Studio), longitudinal and transverse impedances of the IVUs were evaluated and compared to analytical formulas and measurement results. The study provides guidelines for mitigation of unwanted impedance, for an accurate estimate of its effects on the beam quality and beam instabilities and for the impedance budget of a newly designed next-generation machine which has many IVUs and small-aperture beam pipes.

INTRODUCTION

Accelerator components can interact with bunched particles through their inducing wake fields and impedance. Impedances lead to unwanted effects such as beam energy loss, changes in the bunch shape, betatron tune shifts, and to the various beam instabilities. Knowledge of impedances of the accelerator components is of a great importance because it allows to improve the performance the accelerator essentially. Therefore, they should be carefully estimated and evaluated in the very beginning of the design process of any high intensity machine.

At KEK Photon Factory (PF) light source, we have four newly installed In-Vacuum Undulators (IVUs). The IVU's vacuum chamber has a complex geometry. It consists of two taper transitions between the undulator and the beam chamber, one copper plate on the undulator magnets for RF shielding of the magnets from a beam, and two step transitions between the octagon and the taper region. Each part makes its own impact on the total frequency dependent impedance of the entire IVU. Design issues of IVU including taper regions, undulator plates and step transitions are well-studied (see, for example, [1 – 4]). Such Insertion Devices (IDs) are known to make small impacts on the total impedance of a machine [5]. However, the PF IVUs were installed much after the construction of the ring itself was completed, and there was a need of the proper IVU's impedance evaluations.

To quantify IVUs induced impedance we engaged both a powerful simulation tool (Wakefield Solver of CST Particle Studio [6]), and theoretical assessments (for cross-checking the results of simulation), and, finally, an experimental reconciliation of the impedance values obtained from our studies. Such a comprehensive analysis shown in this article will be a standard procedure for the design of new accelerators. It allows to predict the thresholds of instabilities and to assess the influence of collective effects [7 – 8].

A few decades ago only 2D modeling of devices with axial symmetry was available. And to evaluate the impedances of real sections of the accelerator, scientists had to rely entirely on the results of the measurements [9]. Nowadays 3D impedance simulation tools (CST Particle Studio, GdfidL, MAFIA, etc.) have comparably good reliability and improved performance. Therefore, they provide an ability to simulate IDs and accelerator components with their full geometries. For example, at PETRAIII the wakefields of the whole IVU vacuum vessel were evaluated, although it required a considerable computing powers [2]. In the process of simulation of wakefields and impedances, the attention of scientists has been gradually shifted to the consideration of chamber shapes different from the circular geometry (rectangular, elliptical). Thus, we began to distinguish between dipolar (or driving) and quadrupolar (or detuning) contributions to the transverse impedance, whereas only impedance of the dipole mode has been studied previously. This new treatment gives an advantage to obtain different impedance effects on the beam dynamics. Namely, the dipolar wake provides an information about instabilities growth rate. And quadrupolar wake impacts on incoherent effects such as emittance growth and damping. This approach is a courtesy of CERN impedance group [10 – 11].

In this study we show how we identify the major impedance contributors and evaluate their impedance using theoretical formulas, CST Studio simulations and measurements. The KEK future light source will include one IVU for each lattice cell, therefore many IVUs are planned to be installed. Evaluation and improvement of their impedance is one more target of the present study. Now, let us discuss the details of these impedance evaluations, and its experimental confirmation.

IMPEDANCE EVALUATION FOR PF IVU BY SIMULATIONS AND THEORY

The PF IVU consists of three parts (see Fig. 1 a) – c)). Each of these parts impacts on the total impedance of the IVU. They are:

- Taper between the flange and the undulator (200 μm thick) for the geometrical impedance.

† olga@post.kek.jp

ISBN: 978-3-95450-206-6 doi:10.18429/JACoW-FLS2018-THP1WB02

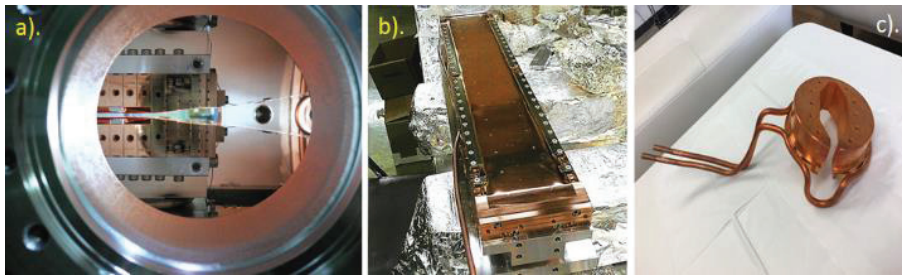

Figure 1: Three major impedance contributors of PF IVU: a). Taper between the flange and the undulator (200 μm thick) for the geometrical impedance; b). Copper plate (60 μm copper and 25 μm nickel coating) on top of the undulator for the resistive-wall impedance; c). Step transition from the octagon to the rectangular chambers.

- Copper plate (60 μm copper and 25 μm nickel coating) on top of the undulator for the resistive-wall impedance.
- Step transition from the octagon to the rectangular chambers.

In the following they will be treated separately.

Geometrical Impedance of Taper

To calculate the pure geometrical impedance of the taper, we first assume the perfectly conductive material instead of the copper resistivity. The CST model of the taper is shown in Fig. 2. It is known that a very fine mesh (Δz) is needed for accurate calculations of the taper impedance. The empirical formula [12]:

$$100 \le \frac{a\phi}{\Delta z} \cdot \frac{\sigma_z}{\Delta z}. \qquad (1)$$

Here a is a chamber radius, ϕ is a taper angle, and σ_z is the bunch length ($\sigma_z = 10mm$ in the PF case). For the PF IVU the mesh size is found to be $\Delta z \le 150\mu m$.

The IVU impedance is greatly affected by the size of its gap ($2b$ in Fig. 2). When the ID is closed, even a difference of 0.5 mm in the gap yields a drastic increase of impedance. For a better and more economical design in future, we also studied the dependence of kick factors on the taper width. Conclusion before the results are: the present 100 mm is reasonable and close to optimal width. For the future IVU designs, the length of the taper (or its angle) is one of the key parameters of impedance evaluation. Its consideration was excluded from the present study because the IVUs were already designed and installed.

The taper structure is known to produce nearly pure inductive impedance even with a vessel included:

$$Z_l = -i\omega L, \qquad W_{l0}(z) = Lc\frac{d}{dz}\delta(z/c), \qquad (2)$$

where Z_l is a longitudinal impedance of the taper, ω is a frequency, and L is the inductance. The theoretical formula for longitudinal impedance reads [13] (see Figs. 3 – 5):

$$\frac{Z_l}{n} = -i\frac{Z_0\omega_0}{4\pi c}\int_{-\infty}^{\infty}(g')^2 F\left(\frac{g}{w}\right)dz, \qquad (3)$$

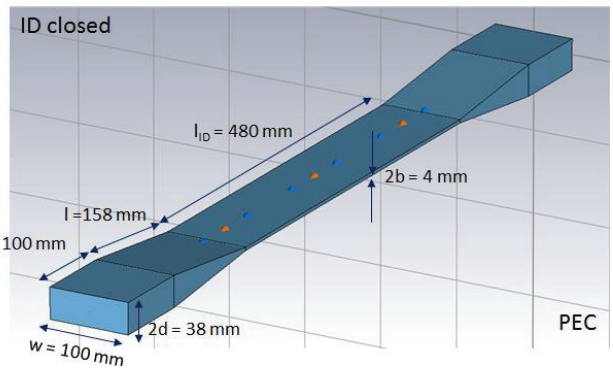

Figure 2: CST model of the IVU taper.

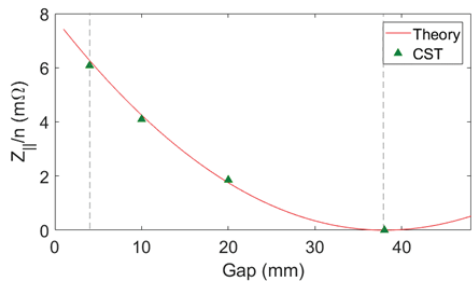

Figure 3: Normalized longitudinal impedance of the taper (gap dependence, width fixed to 100 mm) by theory (red line), and by simulations (green triangle).

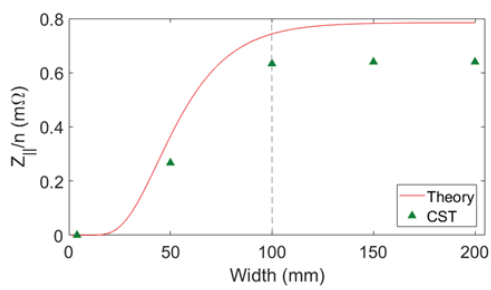

Figure 4: Normalized longitudinal impedance of the taper (width dependence, gap fixed to 50 mm) by theory (red line), and by simulations (green triangle).

ISBN: 978-3-95450-206-6 doi:10.18429/JACoW-FLS2018-THP1WB02

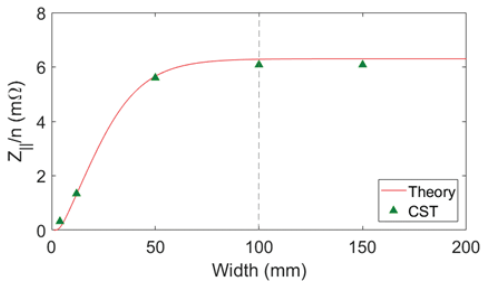

Figure 5: Normalized longitudinal impedance of the taper (width dependence, gap fixed to 4 mm) by theory (red line), and by simulations (green triangle).

$$F(x)=\sum_{m=0}^{\infty}\frac{1}{2m+1}\operatorname{sech}^2\left((2m+1)\frac{\pi x}{2}\right)\tanh\left((2m+1)\frac{\pi x}{2}\right). \quad (4)$$

Here Z_l/n is the normalized longitudinal impedance, $Z_0=377\Omega$ is the impedance of the free space, and ω_0 is the angular revolution frequency. At PF $\omega_0=2\pi\cdot 1.6MHz$. The parameter g describes the vertical profile of the taper along the z axis, and w is the width of the taper ($b\le w\le l$).

We need a careful treatment of the transverse impedance, since it includes both the dipolar and the quadrupolar components [10]:

$$W_{y,tot}(y_1,y_2,z)=W_{y,dip}(z)y_1+W_{y,quad}(z)y_2, \quad (5)$$

where $W_{y,tot}(y_1,y_2,z)$ is a total wake received by the beam. In CST simulations they can be calculated by displacing the beam and the wake integration path separately [11]. According to Krinsky [14], theoretical formula for dipolar impedance is as follows:

$$Z_{yD}(k)=-i\frac{Z_0}{2\pi b}\int_{-\infty}^{\infty}\frac{\xi^2}{\sinh^2\xi}\sum_{n=0}^{\infty}\delta_n\frac{H(k_n,k)+H(k_n,-k)}{2ik_nb}d\xi \quad (6)$$

and

$$P(p,k)=\int_{-\infty}^{\infty}\int_{-\infty}^{z_1}S'(z_1)S'(z_2)e^{i(p+k)(z_1-z_2)}dz_1dz_2, \quad (7)$$

where the width $w\to\infty$, the parameter k is a perturbation wave number, $k_nb=\sqrt{(kb)^2-\xi^2-(\pi n)^2}$. The function of the longitudinal position $S(z)=(a(z)-a_0)/a_0$ means a fractional deviation of the taper radius from the average one (a_0). For analytical estimation of the quadrupolar impedance, a formula derived by Stupakov [13] is used ($b\le w\le l$):

$$Z_{yQ}=-i\frac{\pi Z_0}{4}\int_{-\infty}^{\infty}\frac{(g')^2}{g^2}G\left(\frac{g}{w}\right)dz, \quad (8)$$

with

$$G(x)=x^2\sum_{m=0}^{\infty}(2m+1)\times\operatorname{sech}^2\left((2m+1)\frac{\pi x}{2}\right)\tanh\left((2m+1)\frac{\pi x}{2}\right). \quad (9)$$

Both the dipolar and the quadrupolar impedances produce vertical kick factors. In the case of Gaussian beam their relation could be expressed by the following:

$$k_y=\frac{\operatorname{Im}Z_yc}{2\sqrt{\pi}\sigma_z}. \quad (10)$$

Figures 6 - 9 show the comparison of the analytical Eqs. (6) – (7) and (8) – (9) with the CST simulation results for the dipolar and quadrupolar vertical kick factors of the taper.

To sum up, the calculation of kick factors is most important since it provides additional coherent vertical tune shift. During machine measurements a tune shift could be detected. It includes both of dipolar and quadrupolar impacts.

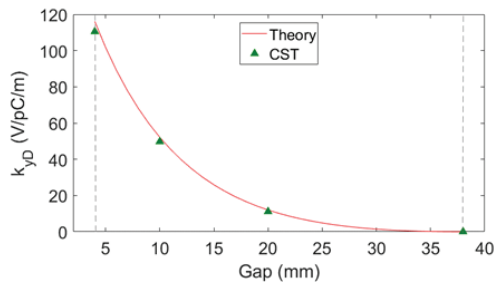

Figure 6: Dipolar vertical kick factor of the taper (gap dependence, width fixed to 100 mm) by theory (red line), and by simulations (green triangle).

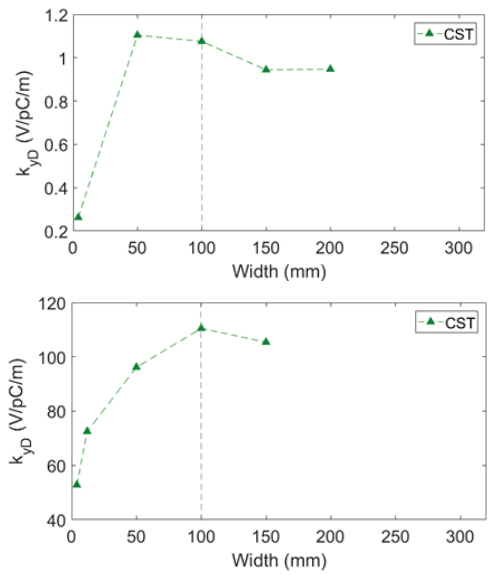

Figure 7: Dipolar vertical kick factor of the taper (width dependence) by simulations. The gap fixed to 50 mm (top), the gap fixed to 4 mm (bottom).

ISBN: 978-3-95450-206-6 doi:10.18429/JACoW-FLS2018-THP1WB02

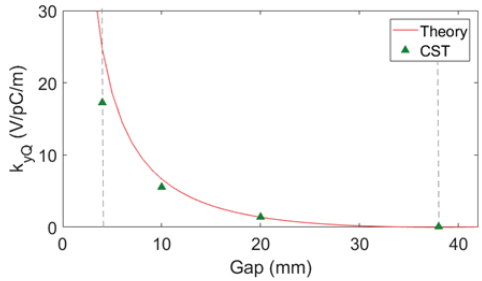

Figure 8: Quadrupolar vertical kick factor of the taper (gap dependence, width fixed to 100 mm) by theory (red line), and by simulations (green triangle).

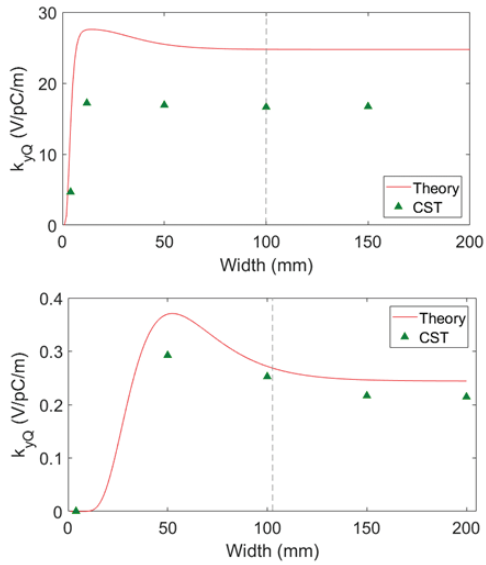

Figure 9: Quadrupolar vertical kick factor of the taper (width dependence, gap fixed to 4 mm (top), to 50 mm (bottom)) by theory (red line), and by simulations (green triangle).

Resistive-Wall Impedance of Undulator

By using the copper resistivity in CST, we can calculate the resistive-wall impedance of the undulator with the copper plate (the electric conductivity of copper is $\sigma_c = 5.9\times10^7 S/m$). The CST model of the undulator RF shielding with the Cu plate is shown in Fig. 10.

The vertical kick factor of the undulator plates was estimated using the following relation [15]:

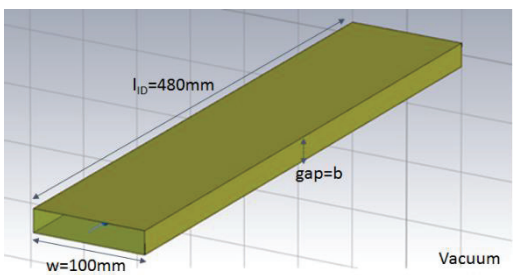

Figure 10: CST model of the undulator RF shielded by the copper sheet.

$$k_{yR.W.} = \frac{cL}{8b^3}\sqrt{\frac{2Z_0 c}{\sigma_z \sigma_c}}\Gamma\left(\frac{5}{4}\right), \tag{11}$$

where L is a length of the undulator ($L = 480mm$ for the PF IVU), and $\Gamma(5/4) = 0.9064$. The comparison between Eq. (10) and the CST simulation is given in Fig. 11. It demonstrates an excellent agreement between theory and simulations.

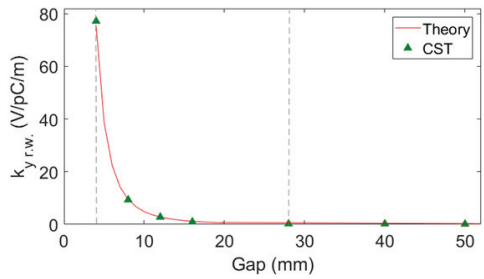

Figure 11: Resistive-wall vertical kick factor of the undulator (gap, dependence, width fixed to 100 mm, length fixed to 480 mm) by theory (red line), and by simulations (green triangle).

Geometrical Impedance of Step Transition

Low-frequency impedance of the step transition at the beginning of the taper was estimated using CST. Corresponding dipolar and quadrupolar kick factors have very small contributions to the total vertical kick factor and saturate at width $w = 150mm$. The impact of the step transition is three orders less than other components; therefore, we ignore it in the following treatment.

Total Transverse Impedance of the IVU

The total vertical kick factor due to 1 IVU including dipolar and quadrupolar kicks of the taper and resistive-wall kick of the undulator copper plates is summarized in Fig. 12. Table 1 provides more detailed information regarding the kick values.

An excellent agreement is seen between the theoretical predictions and the CST Studio simulations for PF IVU. Therefore, the new impedance evaluations of PF IVU are accurate enough in the framework of the theory and the simulation codes. We can use these calculation results and computation resources and techniques for future impedance measurements, for the design of new IVUs, and even for the impedance budget of the components of any new accelerator.

Before moving to the next section (tune shift measurement) some preparation work should be done. Namely, we need to evaluate an additional betatron tune shift ($\Delta\nu$) by 4 IVU at PF. We apply the well-known relation [16]:

$$\frac{\Delta\nu}{I_b} = -\frac{4\langle\beta k_y\rangle}{4\pi f_0 (E/e)}, \tag{12}$$

ISBN: 978-3-95450-206-6 doi:10.18429/JACoW-FLS2018-THP1WB02

where I_b is the bunch current, $f_0 = 1.6MHz$ is a revolution frequency of PF ring, and E is the beam energy ($E = 2.5GeV$ at PF). With the kick data shown in Table 1, and average betatron function in the center of the taper $\beta_{y,taper} = 0.6406\ m$, and in the center of the undulator $\beta_{y,R.W.} = 0.4657\ m$, one can obtain the tune shift value per unit of current $\Delta\nu / I_b = -9.33\times10^{-6}\,mA^{-1}$ as the simulation result, and $\Delta\nu / I_b = -9.967\times10^{-6}\,mA^{-1}$ as the analytical result.

Table 1: Vertical Kick Factors of PF IVU

Vertical kick factor per 1 IVU		CST PS	Theory
Taper vertical kick factor, V/pC/m	Dipolar	110.47	116.13
	Quadrupolar	16.64	24.61
Undulator vertical kick factor, V/pC/m	Dipolar	50.80	75.57
	Quadrupolar	26.40	
Total vertical kick factor, V/pC/m		204.31	216.31

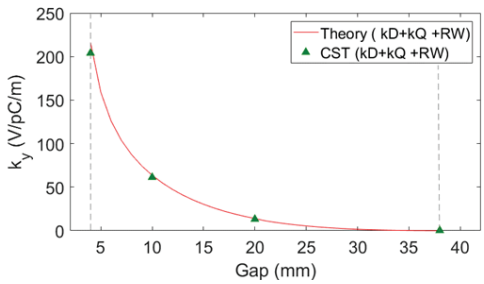

Figure 12: Total vertical kick factor of the IVU (gap dependence, width fixed to 100 mm) by theory (red line), and by simulations (green triangle).

MEASUREMENTS OF KICK FACTORS

We carried out tune shift measurements at PF based on the RF-KO (RF Knock Out) method [16]. In this method the responses of the strip line kicker oscillations were measured by sweeping the bunch current (equal to changing the betatron frequency) using a spectrum analyser equipped with a tracking generator. The switch to the single bunch operation mode and switch-off of the feedback system are crucial conditions for this measurement. In the multi-bunch mode, the current dependence of the tune shift is rather small. The feedback system introduces false signals and greatly influences the measurement result. Therefore, it is important to keep the bunch current below the instability threshold.

The additional tune shift corresponds to a difference of the vertical tune shifts for ID open (gap=38mm) and ID closed (gap=4mm) cases. We closed all four IVUs simultaneously to increase the effect. In fact, we tried to close the ID gaps one by one, and we do indicate reasonable tune shifts. One of the results of the tune shift measurement is shown in Fig. 13. The data were measured manually about 20 times at each current value with a step of 0.5~1 mA. We obtain the average tune shift of four measurements to be $\Delta\nu / I_b = (-11.7615 \pm 1.4955)\times10^{-6}\,mA^{-1}$ (including the data fitting error).

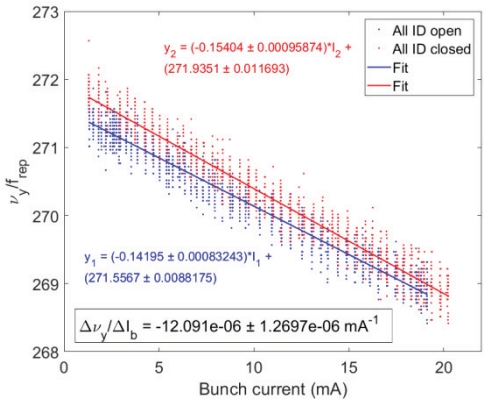

Figure 13: Tune shift measurement result.

An alternative method to measure the vertical kick factor of the IVU, called "the orbit bump" method, was introduced it in [17] and further developed in works [18 – 19]. It creates an orbit bump at the location including IVU. One needs to measure the orbit deviations at many BPM positions to reduce statistical errors. In addition, there is a need to repeat the above procedure for different orbit bumps and bunch charges to eliminate systematic errors caused by intensity dependent behavior of BPM electronics. Finally, using the analytical formula and the Twiss parameters of the ring, we can identify the kick factor of IVU. The orbit bump (y_0) creates orbit deviations proportional to the kick factor of IVU along the ring [1]:

$$\Delta y(s) = \frac{\Delta q}{E/e} k_y y_0 \frac{\sqrt{\beta(s)\beta(s_0)}}{2\sin(\pi\nu)} \cos\left[\left|\mu(s) - \mu(s_0)\right| - \pi\nu\right], \tag{13}$$

Here Δq is a bunch charge variation, $\beta(s)$ is a betatron function, s_0 is an impedance location, and $\mu(s)$ is a betatron phase advance. The corresponding measurement is scheduled in this spring.

CONCLUSION

In summary, we have identified the major impedance contributors of PF IVU and successfully evaluated their impedance using theoretical formulas, CST Studio simulations and measurements. The three evaluations show very good agreements. The present methods and procedures will greatly help the design of future IVU for further reduction of impedance.

ACKNOWLEDGEMENT

We would like to thank the members of PF storage ring and operational staff for their help in achieving the necessary stable injection rate to demonstrate the tune shift caused by four IVU. Additional thanks to the monitor group for many useful advises in experimental setup.

ISBN: 978-3-95450-206-6 doi:10.18429/JACoW-FLS2018-THP1WB02

REFERENCES

[1] V. Smaluk *et al.*, "Coupling impedance of an in-vacuum undulator: Measurement, simulation, and analytical estimation.", *Phys. Rev. ST Accel. Beams*, vol. 17, p. 074402, Jul. 2014.

[2] E. Gjonaj *et al.*, "Computation of wakefields for an in-vacuum undulator at PETRA III", in *Proc., 4th Int. Particle Accelerator Conf. (IPAC 2013),* Shanghai, China, May, 2013, paper TUPWA008, pp. 1736-1738.

[3] F. Cullinan *et al.*, "Evaluation of In-Vacuum Wiggler Wakefield Impedances for SOLEIL and MAX IV", presented at the 22nd European Synchrotron Light Source Workshop (ESLS XXII), Grenoble, France, Nov. 2014. http://www.esrf.eu/files/live/sites/www/files/events/conferences/2014/XXII%20ESLS/CULLINAN_wigglerimpedance.pdf

[4] T.F. Günzel, "Coherent and incoherent tune shifts deduced from impedance modelling in the ESRF-ring", in *Proc., 9th .8.124403 European Particle Accelerator Conf. (EPAC 2004),* Lucerne, Switzerland, July, 2004, paper WEPLT083, pp. 2044-2046.

[5] T. Tanaka, "In-vacuum undulators", in *Proc., 27th Int. Free Electron Laser Conf. (FEL2005)*, Palo Alto, USA, Aug. 2005, paper TUOC001, pp. 370-377.

[6] CST-Computer Simulation Technology, CST PARTICLE STUDIO, http://www.cst.com/Content/Products/PS/Overview.aspx.

[7] E. Belli *et al.*, arXiv:1609.03495.

[8] K. Bane, "Review of collective effects in low emittance rings", presented at the 2nd Topical Workshop on Instabilities, Impedance and Collective Effects (TWIICE2), Abingdon, UK, Feb. 2016.https://indico.cern.ch/event/459623/contributions/1131155/attachments/1224365/1791598/Bane_collective_ler.pdf

[9] T. Hara *et al.*, "SPring-8 in-vacuum undulator beam test at the ESRF", *Journal of Synchrotron Radiation*, vol. 5, part. 3, pp. 406-408, May. 1998.

[10] B. Salvant, "Transverse single-bunch instabilities in the CERN SPS and LHC", presented at the Beam Physics for FAIR Workshop, Bastenhaus, Germany, Jul. 2010. https://indico.gsi.de/event/1031/

[11] C. Zannini, "Electromagnetic simulation of CERN accelerator components and experimental applications", Ph.D. thesis, Phys. Dept., Ecole Polytechnique F´ed´erale de Lausanne, Lausanne, Switzerland, 2013.

[12] O. Frasciello, "Wake fields and impedances of LHC collimators", presented at the 100th National Congress of Italian Physical Society (SIF 2014), Piza, Italy, Sep. 2014.

[13] G.V. Stupakov, Phys. Rev. ST Accel. Beams 10, 094401 (2007).

[14] S. Krinsky, Phys. Rev. ST Accel. Beams 8, 124403 (2005).

[15] A. Piwinski., "Impedance in lossy elliptical vacuum chambers", DESY, Hamburg, Germany, Report No. DESY-94-068, Apr. 1994.

[16] S. Sakanaka, T. Mitsuhashi, and T. Obina, Phys. Rev. ST Accel. Beams 8, 042801 (2005).

[17] V. Kiselev and V. Smaluk, "Measurement of local impedance by an orbit bump method," Nucl. Instrum. Methods A 525, 433 (2004).

[18] L Emery, G. Decker, and J. Galayda, in *Proc., 19th Particle Accelerator Conference (PAC2001)*, Chicago, USA, Aug. 2001, paper TPPH070, pp. 1823-1825.

[19] E. Karantzoulis, V. Smaluk, and L. Tosi, Phys. Rev. ST Accel. Beams 6, 030703 (2003).

ISBN: 978-3-95450-206-6 doi:10.18429/JACoW-FLS2018-THP2WB02

AN OVERVIEW OF THE PROGRESS ON SSMB

Chuanxiang Tang*, Xiujie Deng†, Wenhui Huang, Tenghui Rui,
Alex Chao[1], Tsinghua University, Beijing, China
[1] also at SLAC, Menlo Park, USA
Jörg Feikes, Ji Li, Markus Ries, HZB, Berlin, Germany
Arne Hoehl, PTB, Berlin, Germany
Daniel Ratner, SLAC, Menlo Park, USA
Eduardo Granados, CERN, Geneva, Switzerland
Chao Feng, Bocheng Jiang, Xiaofan Wang, SINAP, Shanghai, China

Abstract

Steady State Microbunching (SSMB) is an electron storage ring based scheme proposed by Ratner and Chao to generate high average power coherent radiation and is one of the promising candidates to address the need of kW level EUV source for lithography. After the idea of SSMB was put forward, it has attracted much attention. Recently, with the promote of Chao, in collaboration with colleagues from other institutes, a SSMB task force has been established in Tsinghua University. The experimental proof of the SSMB principle and a feasible lattice design for EUV SSMB are the two main tasks at this moment. SSMB related physics for the formation and maintenance of microbunches will be explored in the first optical proof-of-principle experiment at the MLS storage ring in Berlin. For EUV SSMB lattice design, longitudinal strong focusing and reversible seeding are the two schemes on which the team focuses. The progresses made as well as some challenges from physical aspects for EUV SSMB will be presented in this paper.

INTRODUCTION

Storage ring based synchrotron radiation facilities and linac based free electron lasers are the main workhorses of nowadays accelerator light sources and deliver light with characteristics of high repetition rate and high peak power respectively. However, there are some applications demanding high average power. One example is the kW level 13.5 nm EUV source needed by semiconductor industry for lithography. To generate high average power radiation, high repetition rate or high peak power alone is not enough, we need to combine both. This hope of combination leads to the idea of SSMB [1], i.e. microbunching in a steady state, microbunching for high peak power and steady state for high repetition rate.

It can be seen from the introduction above that SSMB is a general concept and there are several different specific scenarios proposed since the first publication. Interested readers may read [1-5] for more details about these scenarios. As a new accelerator physics idea, SSMB has attracted a lot of attention. Recently, with the promote of Chao, in collaboration with colleagues from other institutes, a SSMB task force has been established in Tsinghua University with a final goal of kW level EUV source. The two main tasks at this moment are the experimental proof of the SSMB principle and a feasible lattice design for EUV SSMB. The PoP experiment is planned based on the Metrology Light Source (MLS) [6], the radiation source of the German national metrology institute (PTB). The possibility of conducting the experiment on MLS is being carefully evaluated. For the eventual EUV SSMB lattice design, longitudinal strong focusing and reversible seeding are the two schemes being pursued by the team. The progresses made as well as challenges encountered in the study will be given below.

STRONG FOCUSING SSMB

The natural idea of SSMB is a scaling from microwave to optical, i.e. using laser modulator to form optical buckets to microbunch the electron beam just like using RF to bunch electron beam in traditional storage rings.

One of the SSMB lattice scheme is the longitudinal strong focusing scheme. In the strong focusing scheme, a low alpha lattice is needed to let the beam microbunch in the optical buckets in a steady state. However, it is difficult to realize nm level microbunches needed for coherent EUV radiation by applying low alpha lattice alone due to challenges to be introduced momentarily. Longitudinal strong focusing will be applied to compress the bunch length further for coherent EUV generation. Two modulators sandwiching one radiator will play the role of longitudinal strong focusing not unlike the function of final focusing cell in a collider on the transverse dimension. Figure 1 shows the schematic configuration and the longitudinal phase space evolution of one strong focusing SSMB super-period.

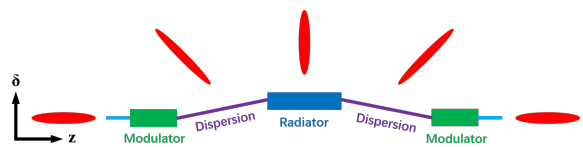

Figure 1: One super-period of longitudinal strong focusing.

In the reversible seeding scheme [3], on the other hand, there is no need of a low alpha lattice. The reversible seeding scheme is also investigated by the collaboration. We will start with the introduction of strong focusing SSMB.

* tang.xuh@tsinghua.edu.cn
† dxj15@mails.tsinghua.edu.cn

ISBN: 978-3-95450-206-6 doi:10.18429/JACoW-FLS2018-THP2WB02

Longitudinal Quantum Radiation Excitation

The reason we need low alpha lattice for the strong focusing scenario is based on the famous "zero current" bunch length formula $\sigma_s \propto \sqrt{\alpha_p}$, in which α_p is the momentum compaction function of the ring. It seems the bunch length can be as short as we want as long as α_p can be tuned as small as possible. But this formula breaks down when α_p approaches zero since the quantum excitation should then be considered more carefully. A zero α_p does not necessarily guarantee a very short electron bunch. An effect called longitudinal quantum radiation excitation [7] and a quantity called partial momentum compaction or partial alpha become more important in this situation. The definition of partial alpha is

$$\tilde{\alpha}(s_j) = \frac{1}{C_0}\int_{s_j}^{observation\ point} \frac{\eta(s)}{\rho(s)} ds \qquad (1)$$

in which s_j is the point of photon emission and C_0 is the circumference of the ring. Even if α_p of the whole ring is zero, the fluctuation of partial alpha would still be unavoidable. A stochastic fluctuation of where the photo emission takes place then produces a fluctuation of path length of one revolution, thus resulting in a bunch length limit [7]

$$\sigma_{lqe} = T_{rev}\delta_{EN}\sqrt{I_\alpha} \qquad (2)$$

where I_α is the variance of partial alpha, T_{rev} and δ_{EN} mean the revolution period and the conventional natural energy spread respectively. The physical picture of this effect is shown in Fig. 2.

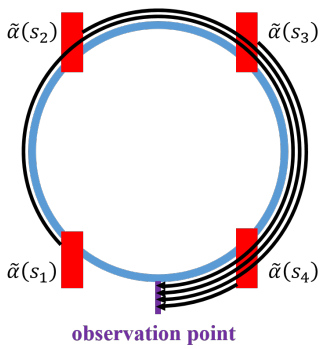

Figure 2: Partial alpha and longitudinal quantum radiation excitation.

Quantitative calculations and particle tracking show that the bunch length limit caused by this effect on MLS is about 36 µm when operated at 629 MeV low alpha mode [8], which means this effect should be carefully treated when doing EUV SSMB lattice design. It can be seen from the above analysis this effect is caused by dispersions at the dipoles cooperated with the stochastic quantum radiation. In order to lower this bunch length limit, possible solutions are:

- Minimizing dispersions at all dipoles;
- Lowering beam energy;
- Dividing the ring into N_{iso} isochronous sections, the standard deviation of partial alpha will be reduced by a factor of N_{iso}^2;
- Adopting the reversible seeding scheme for the EUV radiation.

Transverse Longitudinal Coupling

To generate 13.5 nm EUV coherent radiation, we need microbunch of about 2 nm which is much shorter than that can be reached in most existing storage rings. Many effects which can be ignored in traditional storage rings may play a vital role when we push the bunch length to such a small value. One example is the longitudinal quantum radiation excitation introduced above. Another effect is the transverse longitudinal coupling. The coupling effect can further be divided into the 1^{st} order [9] and the 2^{nd} order [10]. In this paper, we focus on the 1^{st} order horizontal longitudinal coupling and the 2^{nd} order coupling effect will be treated in a separate paper being prepared.

The 1^{st} order horizontal longitudinal coupling effect is easy to understand. Particles with different betatron amplitudes and phases pass bending magnets on different trajectories, resulting in longitudinal displacement differences and a bunch length limit [9]

$$\sigma_{hlc} = \sqrt{\varepsilon H},\ with\ H = \gamma\eta^2 + 2\alpha\eta\eta' + \beta\eta'^2 \qquad (3)$$

It can be seen from Eq. 3 this bunch length limit oscillates around the ring according to the square root of the product of horizontal emittance and chromatic H function. The biggest value of this limit on MLS is about 450 µm when operated at 629 MeV low alpha mode, which means the influence of this effect can be much larger than that caused by longitudinal quantum radiation excitation at some places. We need to place the radiator at a dispersion free section to make this limit equal zero. However, this effect can be helpful in some sense since very short bunch occurs only at specific locations and this will help mitigate the damages caused by collective effects like coherent synchrotron radiation and intra beam scattering.

Nonlinear Momentum Compaction

To store the microbunches steadily in optical buckets, a very small momentum compaction of the ring is needed in the strong focusing scenario. Momentum compaction of a ring is actually a function of the energy deviation

$$\alpha(\delta) = \alpha_0 + \alpha_1\delta + \alpha_2\delta^2 + \ldots \qquad (4)$$

When we push the momentum compaction to a value close to zero, the higher orders of the momentum compaction function will play a bigger role and transform the traditional RF bucket to α-bucket. This longitudinal nonlinear dynamics has been well studied by many authors and it is known the higher order terms should be lowered at the same time when we push α_0 to a small value to maintain high enough bucket height and long enough quantum life time [11]. Careful lattice design should be conducted to accomplish this.

ISBN: 978-3-95450-206-6 doi:10.18429/JACoW-FLS2018-THP2WB02

This requirement may potentially have some conflicts with the need of longitudinal chromaticity which relates to the higher order momentum compaction terms for longitudinal head-tail instability suppression and further study is needed to evaluate the influence.

Preliminary Lattice Design

It is obvious from the analysis above dedicated lattice design is needed for EUV SSMB. Some attempts have been tried by the collaboration and the layout of the preliminary lattice design is shown in Fig. 3. More details will be implemented with the research going on.

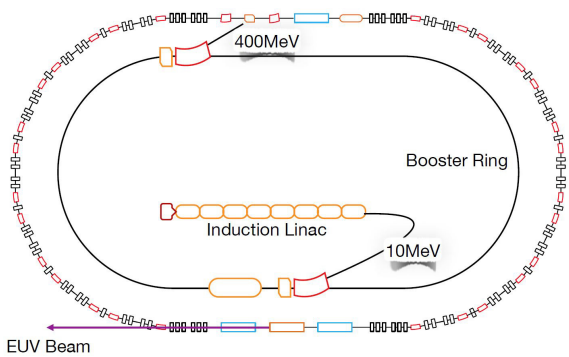

Figure 3: Layout of a SSMB optimized storage ring.

The circumference of the ring is 94.2 m and the main structures are the non-achromatic isochronous cells shown in Fig. 4. The lattice functions are calculated and plotted by Elegant [12]. This cell minimizes the effect of longitudinal quantum radiation excitation by canceling the momentum compaction in a single dipole which means the dispersion function crosses zero within the dipoles. The reason of abandoning the achromatic condition in usual lattice design is otherwise chromaticity correction would be too difficult. The low dispersion and small beta function of this design combined lead us to a low emittance ring.

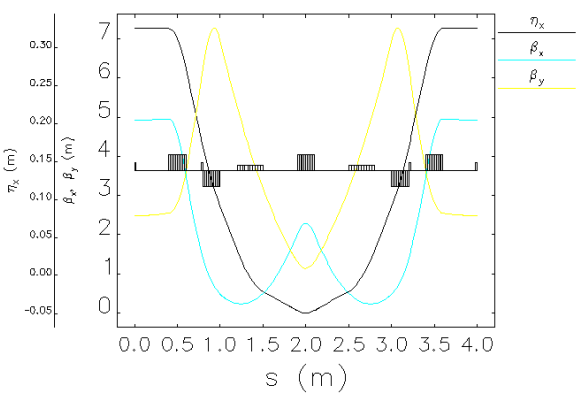

Figure 4: Non-achromatic isochronous cell.

As analyzed previously, the radiator should be placed at a dispersion free straight section to avoid the 1^{st} order horizontal longitudinal coupling. A separate dispersion suppression cell matching the non-achromatic isochronous cell is needed for insertion device, which is shown in Fig. 5.

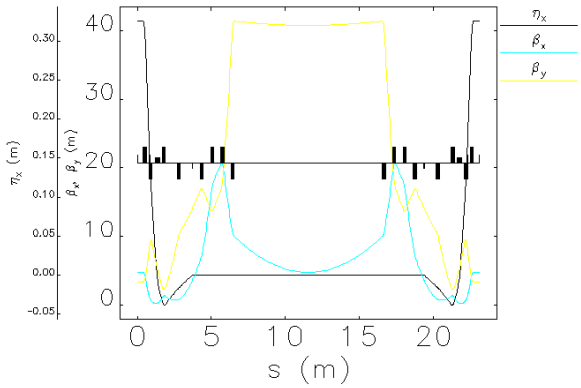

Figure 5: Dispersion suppression cell.

This dedicated lattice design has largely suppressed the bunch length limit caused by the longitudinal quantum radiation excitation, more quantitatively it is about 80 times smaller than that on MLS if operated at the same energy. As mentioned earlier, to reach EUV radiation, a strong focusing cell is needed in addition, as illustrated in Fig.1. The realization of this cell is under study. More details about the lattice design can be found in [13].

Collective Effects

For collective effects, some preliminary theoretical analysis has been conducted in previous research [5]. More in-depth study is continuing. It can be anticipated coherent synchrotron radiation and intra beam scattering will be the two dominant ones since now we have short bunch and low emittance at the same time. As a result of these considerations, the number of electrons per microbunch is limited to about 4000 in the present design.

REVERSIBLE SEEDING SSMB

As introduced earlier, the reversible seeding as a promising scheme is also investigated by the collaboration. It is conceptually the easiest approach and has few additional requirements on the lattice outside of the insertion section. The beam only microbunches within the radiator after modulation and dispersion and then restores to the normal state due to the opposite dispersion and reverse modulation process following the radiator. This reversible seeding scheme does not require low alpha lattice. But its seeding module would however need careful design to realize perfect cancellation.

The application range of this approach is determined by the wavelength of the seeding laser available and the harmonic number can be reached. In order to get significant bunching factor at 13.5 nm, which means the 20^{th} harmonic if we use 270 nm laser as seed, clever seeding skill should be used. The team adopts a recently proposed scheme [14] which makes full use of the characteristic that the vertical emittance is much smaller than the horizontal one in usual electron storage rings. A large bunching factor of

ISBN: 978-3-95450-206-6 doi:10.18429/JACoW-FLS2018-THP2WB02

high harmonic number can be realized with a small energy modulation since the energy modulation strength of a particle is correlated to its vertical slope y' in the modulation process. For further information about the progresses on the reversible seeding SSMB, readers are encouraged to read [15].

PROOF-OF-PRINCIPLE EXPERIMENT

Careful work is needed to realize SSMB due to challenges introduced. The first step would be a single pass proof-of-principle experiment to verify some basic ideas of SSMB. The PoP experiment is now planned to be conducted on MLS, the first storage ring optimized for generating coherent THz radiation [6]. Figure 6 shows the layout and some basic parameters of MLS. By applying a sextupole and octupole correction scheme, MLS is capable of reliable tuning of the low alpha optics, which is important for the PoP experiment.

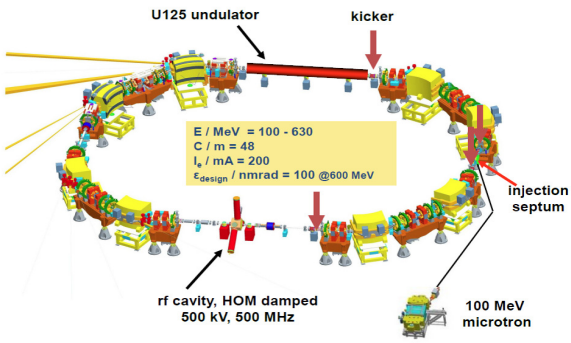

Figure 6: Layout of MLS.

The steps of the experiment would be:

- First let the electron beam reach natural equilibrium state;
- Then use the laser modulator to energy modulate the beam;
- The whole ring will play the role of a dispersive section converting energy modulation to density modulation;
- The microbunches formed one turn after modulation will radiate coherently at the modulation wavelength.

The goals of the experiment are:

- Verify microbunches can form and survive after traversing the whole ring;
- Realize amplification of the laser power by the coherent radiation one turn later, proving the SSMB amplifier scenario;
- Study parameters and effects influencing the decay (smearing) rate of microstructures which would also be important for true SSMB;
- Since the test is to be performed using IR laser, its success would be readily applicable to an IR SSMB with applications of its own without having to push towards EUV;
- Explore other potential related issues.

The final optimized choice of parameters is still under study. One example set of parameters is shown in Table 1. It can be seen there is significant bunching at the modulation wavelength one turn later after modulation and it can be expected coherent radiation with the same wavelength will be generated by the microbunches traversing the undulator. However, the peak current needed for amplification is beyond the present reach of MLS and methods to lower this requirement are being investigated.

Table 1: Example Choice of Parameters

Parameter	Value
Beam Energy	250 MeV
Momentum Compaction	2×10^{-5}
Modulation Laser Wavelength	800 nm
Modulation Laser Peak Power	500 kW
Undulator Parameter	2.05
800 nm Bunching Factor One Turn Later	0.25
Peak Current Needed For Amplification	48 A

CONCLUSION

A SSMB task force has been established in Tsinghua University collaborated with colleagues from other institutes and the SSMB research is being steadily pushed forward. As for the final goal of EUV SSMB, two schemes namely the longitudinal strong focusing and the reversible seeding are being studied in parallel by the team and good progresses have been made. More further work is needed to realize a feasible lattice design. The other main task namely a PoP experiment with the aim to better understand the physics related to SSMB is also being planned and prepared.

We have enlisted the challenges envisioned for the EUV SSMB, most of which comes from the short EUV wavelength. Challenging as it is, however, EUV SSMB offers an exciting area of research and the reward would be tremendous if realized.

REFERENCES

[1] Ratner, Daniel F., and Alexander W. Chao. "Steady-state microbunching in a storage ring for generating coherent radiation." *Physical review letters* 105.15 (2010): 154801.

[2] Jiao, Yi, Daniel F. Ratner, and Alexander W. Chao. "Terahertz coherent radiation from steady-state microbunching in storage rings with X-band radio-frequency system." *Physical Review Special Topics-Accelerators and Beams* 14.11 (2011): 110702.

[3] Ratner, Daniel, and Alex Chao. Reversible Seeding in Storage Rings. No. SLAC-PUB-14718. 2011.

[4] Chao, Alex, Daniel Ratner, and Yi Jiao. Steady State Microbunching for High Brilliance and High Repetition Rate Storage Ring-Based Light Sources. No. SLAC-PUB-15228. SLAC National Accelerator Lab., Menlo Park, CA (United States), 2012.

ISBN: 978-3-95450-206-6 doi:10.18429/JACoW-FLS2018-THP2WB02

[5] Chao, Alex, et al. "High power radiation sources using the steady-state microbunching mechanism." (2016): TUXB01, IPAC'16, Busan, Korea.

[6] Feikes, J., et al. "Metrology Light Source: The first electron storage ring optimized for generating coherent THz radiation." *Physical Review Special Topics-Accelerators and Beams* 14.3 (2011): 030705.

[7] Shoji, Yoshihiko, et al. "Longitudinal radiation excitation in an electron storage ring." *Physical Review E* 54.5 (1996): R4556.

[8] M. Ries, "Nonlinear Momentum Compaction and Coherent Synchrotron Radiation at the Metrology Light Source", PhD thesis, Humboldt-Universität zu Berlin, 2014 (cit. on pp. 42, 43).

[9] Shoji, Yoshihiko. "Bunch lengthening by a betatron motion in quasi-isochronous storage rings." *Physical Review Special Topics-Accelerators and Beams* 7.9 (2004): 090703.

[10] Shoji, Yoshihiko. "Dependence of average path length betatron motion in a storage ring." *Physical Review Special Topics-Accelerators and Beams* 8.9 (2005): 094001.

[11] Robin, David, et al. "Quasi-isochronous storage rings." *Physical Review E* 48.3 (1993): 2149.

[12] Borland, Michael. Elegant: A flexible SDDS-compliant code for accelerator simulation. No. LS-287. Argonne National Lab., IL (US), 2000.

[13] Tenghui Rui, Xiujie Deng, Alex Chao, Wenhui Huang, Chuanxiang Tang, "Strong Focusing Lattice Design for SSMB," presented at the 60^{th} ICFA Advanced Beam Dynamics Workshop on Future Light Sources. (FLS2018), Shanghai, China, March 2018, paper WEP2PT014, this conference.

[14] Feng, Chao, and Zhentang Zhao. "A Storage Ring Based Free-Electron Laser for Generating Ultrashort Coherent EUV and X-ray Radiation." *Scientific Reports* 7.1 (2017): 4724.

[15] Chao Feng, Bocheng Jiang, Changliang Li, Xiaofan Wang, Zhentang Zhao and Alex Chao, "A Possible Lattice Design for the Reversible SSMB in Storage Rings," presented at the 60^{th} ICFA Advanced Beam Dynamics Workshop on Future Light Sources. (FLS2018), Shanghai, China, March 2018, paper WEP2PT017, this conference.

ISBN: 978-3-95450-206-6 doi:10.18429/JACoW-FLS2018-THP2WB03

TRANSPARENT LATTICE CHARACTERIZATION WITH GATED TURN-BY-TURN DATA OF DIAGNOSTIC BUNCH-TRAIN

Y. Li, W. Cheng*, K. Ha and R. Rainer,
Brookhaven National Laboratory, Upton, New York 11973 USA

Abstract

Methods of characterization of a storage ring's lattice have traditionally been intrusive to routine operations. More importantly, the lattice seen by particles can drift with the beam current due to collective effects. To circumvent this, we have developed a novel approach for dynamically characterizing a storage ring's lattice that is transparent to operations. Our approach adopts a dedicated filling pattern which has a short, separate Diagnostic Bunch-Train (DBT). Through the use of a bunch-by-bunch feedback system, the DBT can be selectively excited on-demand. Gated functionality of a beam position monitor system is capable of collecting turn-by-turn data of the DBT, from which the lattice can then be characterized after excitation. As the DBT comprises only about one percent of the total operational bunches, the effects of its excitation are negligible to users. This approach allows us to localize the distributed quadrupolar wake fields generated in the storage ring vacuum chamber during beam accumulation. While effectively transparent to operations, our approach enables us to dynamically control the beta-beat and phase-beat, and unobtrusively optimize performance of National Synchrotron Light Source-II accelerator during routine operations.

INTRODUCTION

For high brightness synchrotron light sources, it is essential to mitigate lattice distortion to optimize performance during routine operations. At National Synchrotron Light Source-II (NSLS-II) [1], the deviation of the linear lattice has been observed but not quantitatively characterized during operations. Although there are several methods to characterize and correct the linear lattice during dedicated machine studies periods, they often interfere with stable beam conditions due to the magnitude of beam manipulation for lattice characterization. Common tools used for lattice characterization and/or correction include, but are not limited to: Linear Optics from Closed Orbit (LOCO) [2,3], TbT data of a short bunch-train excited by a short pulse excitation [4–9], or a long bunch-train excited by the bunch-by-bunch feedback system [10].

With modern advancements in BPM technology, storage ring lattices can be characterized with accurately aligned BPM turn-by-turn (TbT) data. To accomplish this, the beam is excited with a pulsed magnet, also known as a "pinger" magnet. At most light source facilities, however, the pulse width of a pinger wave usually lasts several micro-seconds, while the separation between two adjacent buckets is a few nanoseconds. Most of existing BPM systems are unable to resolve the bunch-by-bunch signals. The TbT data that reveals the centroid motion of the long bunch-train is therefore highly decoherent after excitation [11–13]. To obtain clean TbT data with such a long pulse width, one would need to utilize a shorter bunch-train. Or one could utilize a well designed pulsed magnet with a wide flat top waveform [14].

Another method of exciting long bunch-trains with a bunch-by-bunch feedback system (BBFB) has been developed at Diamond light source [10]. The excitation amplitudes are small (significantly less than the beam size) but at high frequencies. Their method involves collecting the TbT data with dedicated signal processing, after excitation. To characterize the lattice during operations, however, requires excitation of the whole operational bunch train. To achieve comparable resolution as the pinger excitation technique, their method also requires continuous excitation of the whole operational bunch train. Hereby, our method introduces a more transparent technique for lattice characterization that utilizes a short diagnostic bunch-train (DBT) developed at NSLS-II [15]. The DBT is isolated from the main user bunch-train and transversely excited with the BBFB system [16]. The TbT data of the DBT is collected using the gated functionality of BPMs. As the DBT (10 bunches) comprises only about one percent of the total bunches, and the excitation amplitude is less than 1 millimeter, the effects on the global beam motion are negligible to users. Additionally, an "on-demand" triggering mode is utilized to minimize the disturbance on the circulating beam. With minimal beam disturbance, this approach is effectively transparent to the beamlines and can be applied at any time during operations without interfering with experiments, even ones requiring high sensitivity.

SELECTIVE BUNCH EXCITATION AND GATED TBT DATA ACQUISITION

This section discusses the necessary requirements for lattice characterization by designing a technique which utilizes a dedicated filling pattern configuration, gated bunch-train excitation and data acquisition.

Diagnostic Bunch-Train (DBT)

During routine operation, various collective instabilities are suppressed by the transverse BBFB system. High precision lattice characterization, however, requires beam excitation which the BBFB would normally prevent. To bypass this, a short DBT is filled and is separated from the main, long operational bunch-train (see Fig. 1). The BBFB can be configured to only stabilize the operational bunch train, and not the DBT. The separation between the DBT and the

* W. Cheng and Y. Li contributed equally to this work

ISBN: 978-3-95450-206-6 doi:10.18429/JACoW-FLS2018-THP2WB03

main bunch-train(s) needs to be larger than 75 empty buckets (~ 150 ns) due to the ±10 MHz bandwidth of the band pass filter. During normal operations, the BPM system needs to deliver both 10 Hz data for slow orbit monitoring and 10 kHz data for fast orbit feedback at all times. The 10Hz and 10 kHz data need to be ungated to include all the bunch signals and the radio frequency (RF) attenuation on the BPMs set to correspond to the beam current. To obtain clean TbT signals with good signal-to-noise ratio the charge of the DBT needs to be maintained at a level of ~ 1% of the total charge of the operational bunches.

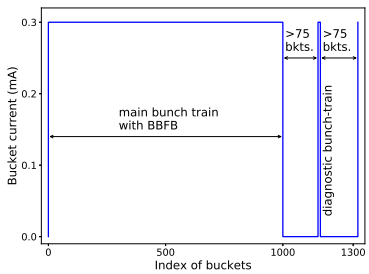

Figure 1: Bucket filling pattern with an extra DBT for transparent lattice characterization.

Selective Bunch Excitation

The selective bunch excitation on the DBT is accomplished with the BBFB system. The digitizer of NSLS-II BBFB system has an integrated function that can excite any selected bunches [17]. It typically takes less than 2 ms for the betatron amplitude to reach about 1 mm (see Fig. 2). The excitation trigger is configured for an external, on-demand mode. The same trigger needs to be synchronized with the BPM gated data acquisition.

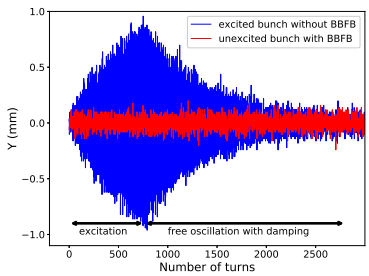

Figure 2: ADC signals (counts) from BPM buttons of an excited bunch (in blue) without BBFB suppression and an unexcited bunch (in red) with BBFB suppression. Excitation is performed through resonance driving for about 700 turns (≤ 2 ms). Free betatron oscillation then decays through radiation damping.

There are several bunches in the DBT which need to be excited in phase. Therefore, the whole DBT is excited at the first harmonic of the betatron oscillation frequency. Measuring the TbT data of the different bunches in the DBT with the dedicated BBFB pick-up reveals centroid data that is consistent with our expected results (see Fig. 3).

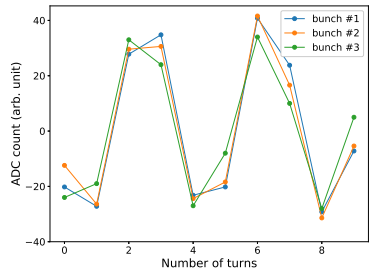

Figure 3: In-phase excitation of the DBT through resonance driving. Here the vertical ADC counts of 3 out of 10 bunches are shown. The signals are measured by the dedicated BPM used as the BBFB's pick-up, and its digitizer can distinguish different bunches in the train.

Gated TbT Data Acquisition

The gated BPM data acquisition is accomplished through in-house BPM technology developed at NSLS-II. If the diagnostics bunches are separated by more than 150 ns, the digitizer is then capable of resolving them. The gated functionality of the BPMs has been implemented inside the field-programmable gate array. The schematic diagram of the gated signal processing is shown in Fig. 4. Two signal-processing channels with separated gates are provided. The delay and width of each gate can be adjusted independently so that signals from different bunch-trains can be selected and processed separately and simultaneously. One of the channels (Gate 2) can then be dedicated to lattice characterization. Expanding the number of channels could allow processing of multiple DBTs for possible future use.

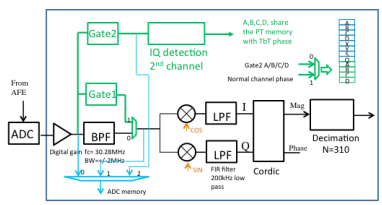

Figure 4: The schematic diagram of the gated signal processing. Two signal-processing channels with separated gates are provided. One of them (Gate 2) is dedicated to processing the DBT.

Under the filling pattern configuration seen previously in Fig. 1, TbT data is sampled at 117MHz with 310 samples per turn. The top of Fig. 5 illustrates the ADC raw data from one of the BPM buttons, labeled as "A". The signals from four buttons ("A-B-C-D") need to be overlapped and their cable delays must be well matched. The gate is then introduced (shown as the red boxes) and the signal processing only includes ADC data sampled from bunches inside the gap as illustrated at the bottom of Fig. 5. Fine timing alignment (8 ns steps) ensures all the BPMs around the ring process the signal from the same bunch(es).

For a short bunch-train, the gated TbT data has better resolution than the ungated TbT data [18], which can im-

ISBN: 978-3-95450-206-6 doi:10.18429/JACoW-FLS2018-THP2WB03

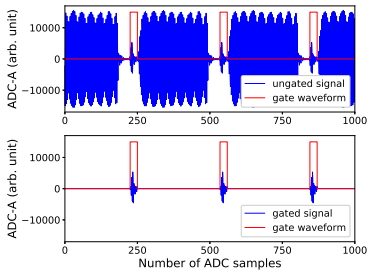

Figure 5: ADC signal of BPM button "A" with and without gated functionality. Ungated BPM signals are the sum of contributions from all buckets (top). After applying a gated waveform as illustrated by the red lines, the DBT signals can be filtered out and processed by the newly added channel (Gate 2) as seen in Fig. 4.

prove the lattice characterization precision. The improved resolution is noticeable in our measurements (see Fig. 6).

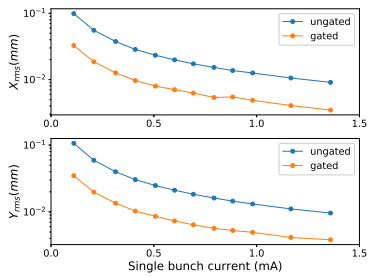

Figure 6: Comparison of the BPM resolutions for gated and ungated data. Gated BPM data resolution is measured ~ 3 times better than the ungated data in both the horizontal and vertical planes.

Measured TbT data include BPM gain and roll errors, which require calibration before use. For each BPM, four pre-calibrated coefficients fitted from a measured orbit response matrix with LOCO [2] are implemented.

Disturbance of User Beam

Beam disturbance during routine operations is something that all dedicated user facilities strive to minimize. As lattice characterization has traditionally required beam perturbation at levels that would affect users, particularly ones that require high sensitivity, it is important to note the impact that our technique has on the beam stability. To obtain the sufficient resolution for lattice characterization, the DBT amplitude is excited to a maximum of ~ 1 mm in our case. The disturbance averaged over all bunches as seen by the ungated BPM signal, however, is only 1% or 10 μm (see Fig. 7). The 10 μm centroid oscillation can be damped within a few ms. It should also be noted that the negligible disturbance created by excitation of the DBT can be triggered on-demand, making this measurement transparent to users, even ones with highly sensitive equipment.

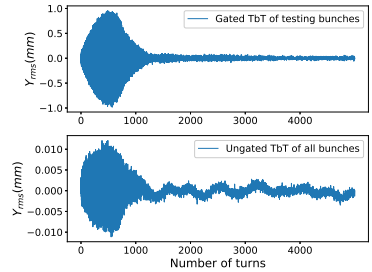

Figure 7: Comparison of the gated BPM TbT data of the DBT (top) and the ungated TbT data averaged over all filled buckets (bottom). Although the DBT amplitude reaches 1 mm for a few ms, the disturbance on the global beam stability is negligible. The ungated data of the combined bunch trains sees noise from either the power supplies or the RF cavities. Note that the two subplots' vertical scales are different.

LATTICE CHARACTERIZATION METHODS

This section briefly introduces the method used to characterize the linear lattice from TbT data at NSLS-II. There are other methods available as well, such as Principal component analysis (PCA) or model independent analysis (MIA) was proposed by Irwin and Wang [5, 6, 19], Independent Component Analysis (ICA) [7], which can be used for the same purpose, but are not covered here.

The approach of orthogonal decomposition [4] of beam TbT motion has been is used. In the absence of damping and decoherence, and after eliminating the contribution from the closed orbit, the TbT betatron oscillation as seen by a BPM is

$$x_i = A\sqrt{\beta_x(s)}\cos[2\pi\nu_x \cdot i + \psi_x(s)] \tag{1}$$

Here, s is the location of the BPM, $i \in [0, N-1]$ is the index of consecutive turns, and x_i is the reading of the BPM at the i^{th} turn. A is a constant determined by the initial condition, $\beta_x(s)$ and $\psi_x(s)$ are the betatron envelope function and phase at the location of s, and ν_x is the betatron tune per turn. Decomposing two orthogonal modes of the harmonic $\omega_x = 2\pi\nu_x$ yields

$$C = \sum_{i=0}^{N-1} x_i \cos(2\pi\nu_x \cdot i),\ S = \sum_{i=0}^{N-1} x_i \sin(2\pi\nu_x \cdot i) \tag{2}$$

The amplitude $A\sqrt{\beta_x}$ and phase ψ_x can be obtained after some algebraic manipulation

$$A\sqrt{\beta_x} = \frac{2\sqrt{C^2+S^2}}{N},\ \psi_x = -\tan^{-1}\left(\frac{S}{C}\right) \tag{3}$$

where the quadrant of the phase ψ_x can be determined by the signs of C and S. After determining the constant A by scaling the measured $A^2\beta_x$ with the design $\beta_{x,0}$, a measured β_x can be obtained. In Eq. (3), the phase measurement is independent of the BPM gain calibration, which ensures an accurate characterization of the ring lattice.

ISBN: 978-3-95450-206-6 doi:10.18429/JACoW-FLS2018-THP2WB03

Once the lattice functions (β, ψ) have been characterized, we can compare them with the design model. The distortion can be corrected iteratively with the linear response matrix between β, ψ and the focusing strength of the quadrupoles [7].

$$\begin{pmatrix} w_\beta \Delta\beta \\ w_\psi \Delta\psi \end{pmatrix} = \begin{pmatrix} w_\beta \mathbf{M}_\beta \\ w_\psi \mathbf{M}_\psi \end{pmatrix} \begin{pmatrix} \Delta K_1 \\ \Delta K_2 \\ \vdots \\ \Delta K_q \end{pmatrix}. \quad (4)$$

Here $\Delta\beta = \beta_{meas.} - \beta_{model}$ are the β-beats as seen at the locations of BPMs, $\Delta\psi = \psi_{meas.} - \psi_{model}$ are the phase-beats and $w_{\beta,\psi}$ are the weights to balance the β-beat and phase-beat correction. $\mathbf{M}_{\beta,\psi} = \frac{\partial(\beta,\psi)}{\partial K}$ are the response matrices of the beta and the phase depending on quadrupole strength. $K_i = \frac{1}{B\rho}(\frac{\partial B_y}{\partial x})_i, i = 1, 2, \cdots$ is the i^{th} quadrupole's strength normalized with the beam rigidity $B\rho$.

APPLICATIONS

In the past at NSLS-II, the lattice was optimized with ungated TbT data of a short bunch-train at a low current ($N_{bunch} \leq 50$, $I_b \leq 2$ mA) excited by the pingers. During beam accumulation, tune drifting has been observed, corresponding to the beam current (Fig. 8). While injecting to higher operations currents, the injection efficiency occasionally drops off as well. Although the tune-drift can be monitored and corrected, it is typically not possible to localize the distribution of quadrupolar wake fields. To correct the tune under these circumstances requires blind selection of arbitrary quadrupoles to bring the tune back to the nominal value. Blind tune correction such as this often results in extra β-beat and phase-beat.

To measure the lattice drifting with the beam currents, a low charge DBT was injected into the ring. Gated BPM TbT data was then used to measure the lattice function and the correction algorithm from Eq. (4) was applied iteratively to reach a set of optimal magnet settings. For a such low beam current, the effect of the wake fields are negligible. The lattice is solely determined by the external magnetic fields and we refer to the measured lattice under these conditions as the reference lattice. A long bunch-train with 1,000 bunches, which is used for operations, was then filled. Instead of filling a Camshaft bunch as has become our standard operating procedure, however, we filled a 10-bunch train in place of the Camshaft bunch. The total charge inside the diagnostic train was maintained at a level of about 1% of the total charge during beam accumulation. At different beam currents, the DBT was selectively excited and its gated TbT data was collected by all 180 BPMs around the ring for lattice characterization. When the stored beam was above ~ 50 mA, the beam became unstable. It was then necessary to have the BBFB system act on the main operational bunch train to suppress its instabilities.

From the gated BPM TbT data at different currents, we found the lattice was distorted gradually by the wake fields. Tune-shift, β and ψ-beat relative to the stored beam currents are illustrated in Fig. 8 and 9. The tune dependence on the beam current has contributions from both dipolar and quadrupolar wake fields. Dipolar fields shift tunes in both planes negative, while quadrupolar fields shift tunes in both planes in opposite directions. From Fig. 8 we see that the horizontal and the vertical tunes drift in opposite directions, and the vertical tune shifts faster than the horizontal one. Based on this, it seems most likely that the lattice distortion is mainly due to the quadrupolar wakes of the long-range wake fields of the non-circular vacuum chambers with finite resistivity [20].

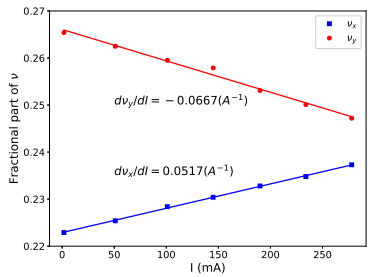

Figure 8: Tune-shifts with stored beam current.

The phase information of betatron oscillation can be measured more precisely than the envelope function β, therefore our lattice corrections rely heavily on the phase measurement in Eq. (4).

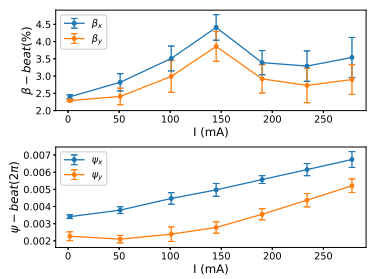

Figure 9: β-beat (top) and phase-beat (bottom) in relation to stored beam currents.

Based on the measured β and ψ-beats we can use Eq. (4) to locate the quadrupolar wake fields by putting numerous virtual quadrupoles around the ring. In Fig. 10, the variation of the vertical phase advance as a function of beam current is shown around the location of a 7 m long damping wiggler, which has a flat chamber.

Tune-drifts that correspond to beam current have been observed previously in several other high-energy storage rings and therefore are well understood [20–22]. The distributed wake fields were localized at other machines during dedicated beam study time [23, 24]. With the advent of our method, it is now possible to measure not only the incoherent tune-drifts, but also the distributed β-beat and phase-beat around the storage ring during user operation. A systematic correction strategy can therefore be implemented to mitigate distortion of the linear lattice.

ISBN: 978-3-95450-206-6 doi:10.18429/JACoW-FLS2018-THP2WB03

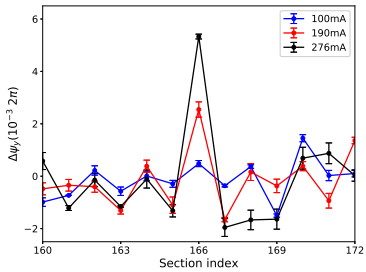

Figure 10: Variation of the vertical phase advance as a function of beam current around the location of a 7 m long damping wiggler (section 166), which has a flat chamber.

The dynamic aperture of modern storage rings' is highly sensitive to the phase advance among the sextupoles. At NSLS-II, 10-15% decrease in injection efficiency was frequently observed at the current nominal operating current (275-300 mA). To understand that, a simulation code, ELEGANT [25], was used to simulate the distorted lattice dynamic aperture. The simulation involved adding the corresponding quadrupole strength adjustments on top of the external quadrupole settings directly. The dynamic aperture was found to decrease gradually with increasing beam current if no linear lattice correction was implemented (see Fig. 11). Injection efficiency can sometimes be restored more or less by blindly moving the horizontal and vertical tunes back to their nominal values. The lattice distortion, however, cannot be restored in this fashion. If the lattice continues to become more distorted by repeatedly adjusting the tunes blindly, it could result in a reduction of the local energy acceptance (LMA) as well as the Touschek lifetime.

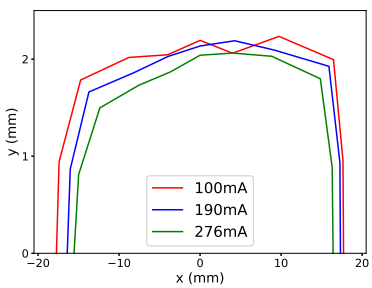

Figure 11: Dynamic aperture reduction at different stored beam currents without linear lattice correction at NSLS-II. In addition to the quadrupole nominal settings, localized quadrupolar wake fields are introduced in the lattice. The systematic and random multipole errors, closed orbit distortion and linear coupling are included in the simulations. Each dynamic aperture is obtained, accounting for random multipole error distributions in specific magnets, and averaged over 50 random seeds.

After accumulating ~ 275 mA in NSLS-II storage ring, the lattice distortion was mitigated with 300 independently powered quadrupoles. The β-beat and phase-beat after correction was worse than at 2 mA, but was significantly improved compared to the uncorrected lattice. Lattice distortion cannot be completely eliminated, owing to the quadrupolar wake fields generated at locations of noncircular vacuum chambers, such as dipoles chambers. While the quadrupoles used for lattice compensation are not located at the exact points of measurement, the lattice distortion can only be mitigated to a certain extent. Presently, NSLS-II operates at a stored beam current of 300 mA. Even at such a current the lattice distortion due to the quadrupolar wake fields is tolerable after a blind tune correction. The goal at NSLS-II is to eventually operate at Top-Off current of 500 mA. At this elevated current, lattice distortion can be expected to be greater and may not be as tolerable to blind tune corrections. It would therefore be prudent to implement a real-time lattice monitoring and correction program by scaling the wake fields with the beam current linearly.

SUMMARY

As a premiere 3^{rd} generation synchrotron light source, it is therefore paramount that performance of the accelerator is optimal. A key component of optimizing performance is minimizing linear lattice distortion. Traditional methods of lattice characterization have been intrusive during routine operations. We offer an improved, transparent approach. Our method applies selective gated transverse excitation and data acquisition of a small DBT. It overcomes several difficulties faced by traditional methods; common ones being interruption or disturbance of beamline experiments, or characterizing and correcting distortion from dynamic sources such as wake fields generated in vacuum chambers. Although the BPM system electronics at NSLS-II can be configured to resolve the signals of two well-separated bunch-trains, it will be necessary to develop a high resolution bunch-by-bunch BPM electronics system [26] to further improve diagnostics capabilities and therefore optimize machine performance.

ACKNOWLEDGMENTS

We would like to thank our NSLS-II colleagues for supporting this study. This work was supported by Department of Energy Contract No. DE-SC0012704.

REFERENCES

[1] BNL, https://www.bnl.gov/nsls2/project/PDR/

[2] J. Safranek, "Experimental determination of storage ring optics using orbit response measurements", *Nucl.Instrum.Meth.*, A 388, 1997, p.27-36.

[3] X. Huang, J. Safranek and G. Portmann, "LOCO with constraints and improved fitting technique", *ICFA Beam Dyn. Newslett.*, Vol. 44, 2007, p. 60-69.

[4] P. Castro-Garcia, "Luminosity and beta function measurement at the electron-positron collider ring LEP", CERN school, 1996, http://www-spires.fnal.gov/spires/find/books/www?cl=CERN-SL-96-070-BI

[5] J. Irwin, C.X. Wang, Y.T. Yan, K.L.F. Bane, Y. Cai, F.J. Decker, M.G. Minty, G.V. Stupakov and F. Zimmermann, "Model-independent beam dynamics analysis", *Phys.*

ISBN: 978-3-95450-206-6 doi:10.18429/JACoW-FLS2018-THP2WB03

Rev. Lett., Vol. 82, 1999, p. 1684-1687. doi:10.1103/PhysRevLett.82.1684

[6] C.X. Wang, "Model independent analysis of beam centroid dynamics in accelerators", at school at Stanford U., Phys. Dept., 1999.

[7] X. Huang, S. Lee, E. Prebys, and R. Tomlin, "Application of independent component analysis to Fermilab Booster", *Phys. Rev. ST Accel. Beams*, Vol. 8, 2005, p. 064001. doi:10.1103/PhysRevSTAB.8.064001

[8] R. Tomás, M. Aiba, A. Franchi and U. Iriso, "Review of linear optics measurement and correction for charged particle accelerators", *Phys. Rev. Accel. Beams*, Vol. 20, 5, 2017, p. 054801, doi:10.1103/PhysRevAccelBeams.20.054801

[9] A. Franchi, "Error analysis of linear optics measurements via turn-by-turn beam position data in circular accelerators", arXiv:1603.00281, 2016

[10] G. Rehm, M.G. Abbott, A.F.D. Morgan, J. Rowland and I. Uzun, "Measurement of Lattice Parameters Without Visible Disturbance to User Beam at Diamond Light Source", BIW, 2010.

[11] R.E. Meller, A.W. Chao, J.M. Peterson,S.G. Peggs and M. Furman, "Decoherence of Kicked Beams", SSC-N-360, 1987.

[12] S.Y. Lee, "Decoherence of the Kicked Beams II", SSC-N-749, 1991.

[13] I. Karpov, V. Kornilov and O. Boine-Frankenheim, "Early transverse decoherence of bunches with space charge", *Phys. Rev. Accel. Beams*, Vol. 19, 12, 2016, p. 124201. doi:10.1103/PhysRevAccelBeams.19.124201

[14] P. Lebasque, R. Ben El Fekih, M. Bol, J.P. Lavieville, A. Loulergue and D. Muller, "Improvement on Pulsed Magnetic Systems at SOLEIL", Particle accelerator. Proceedings, 11th European Conference, EPAC 2008, Genoa, Italy, June 23-27, 2008, WEPC081.

[15] W. Cheng, Y. Li and K. Ha, "Techniques for transparent lattice measurement and correction", *J. Phys. Conf. Ser.*, Vol. 874, 1, 2017, p. 012082, doi:10.1088/1742-6596/874/1/012082

[16] W. Cheng, B. Bacha, D. Teytelman, Y. Hu, H. Xu and O. Singh, "Commissioning of Bunch-by-bunch Feedback System for NSLS2 Storage Ring", Proceeding of IBIC2014, Monterey, CA, USA, 2014, p. 707.

[17] Dimtel Inc., http://www.dimtel.com

[18] B. Podobedov, W. Cheng, K. Ha, Y. Hidaka, J. Mead, O. Singh and K. Vetter, "Single Micron Single-Bunch Turn-by-Turn BPM Resolution Achieved at NSLS-II", Proceedings of 7th International Particle Accelerator Conference (IPAC 2016, Busan, Korea, May 8-13, 2016, WEOBB01, doi:10.18429/JACoW-IPAC2016-WEOBB01

[19] C.X. Wang, V. Sajaev and C.Y. Yao, "Phase advance and beta function measurements using model-independent analysis", *Phys. Rev. ST Accel. Beams*, Vol. 6, 2003, p. 104001, doi:10.1103/PhysRevSTAB.6.104001

[20] A. Chao, S. Heifets and B. Zotter, "Tune shifts of bunch trains due to resistive vacuum chambers without circular symmetry", *Phys. Rev. ST Accel. Beams*, Vol. 5, 2002, p. 111001, doi:10.1103/PhysRevSTAB.5.111001

[21] P. Brunelle, R. Nagaoka and R. Sreedharan, "Measurement and analysis of the impact of transverse incoherent wakefields in a light source storage ring", *Phys. Rev. Accel. Beams*, Vol. 19, 4, 2016, p. 044401, doi:10.1103/PhysRevAccelBeams.19.044401

[22] A. Blednykh, G. Bassi, Y. Hidaka, V. Smaluk and G. Stupakov, "Low-frequency quadrupole impedance of undulators and wigglers", *Phys. Rev. Accel. Beams*, Vol. 19, 10, 2016, p. 104401, doi:10.1103/PhysRevAccelBeams.19.104401

[23] D. Brandt, P. Castro, K. Cornelis, A. Hofmann, G. Morpurgo, G.L. Sabbi, J. Wenninger and B. Zotter, "Measurement of impedance distributions and instability thresholds in LEP", Proceedings of 16th Particle Accelerator Conference and International Conference on High-Energy Accelerators, HEACC 1995: Dallas, USA, May 1-5, 1995, p. 570-572.

[24] V. Sajaev, "Transverse impedance distribution measurements using the response matrix fit method at APS", *ICFA Beam Dyn. Newslett.*, Vol. 44, 2007, p. 101-109.

[25] M. Borland, "elegant: A Flexible SDDS-Compliant Code for Accelerator Simulation", *Advanced Photon Source LS-287*, 2000.

[26] J. Shanks, D. Rubin and D. Sagan, "Low-emittance tuning at the Cornell Electron Storage Ring Test Accelerator", *Phys. Rev. ST Accel. Beams*, Vol. 17, 4, 2014, p. 044003, doi:10.1103/PhysRevSTAB.17.044003

ISBN: 978-3-95450-206-6 doi:10.18429/JACoW-FLS2018-THP2WB04

LASER SEEDING OF ELECTRON BUNCHES FOR FUTURE RING-BASED LIGHT SOURCES*

S. Khan†, B. Büsing, N. M. Lockmann, C. Mai, A. Meyer auf der Heide,
B. Riemann, B. Sawadski, M. Schmutzler, P. Ungelenk
Zentrum für Synchrotronstrahlung (DELTA), TU Dortmund, 44227 Dortmund, Germany

Abstract

In contrast to free-electron lasers (FELs), ring-based light sources are limited in intensity by incoherent emission and in pulse duration by their bunch length. However, FEL seeding schemes can be adopted to generate intense and ultrashort radiation pulses in storage rings by creating laser-induced microbunches within a short slice of the electron bunch. Microbunching gives rise to coherent emission at harmonics of the seed wavelength. In addition, terahertz (THz) radiation is coherently emitted. At the 1.5-GeV electron storage ring DELTA, coherent harmonic generation (CHG) with single and double 40-fs pulses is routinely performed at seed wavelengths of 800 and 400 nm. Seeding with intensity-modulated pulses to generate tunable narrowband THz radiation is also performed. As a preparation for echo-enabled harmonic generation (EEHG), simultaneous seeding with 800/400-nm pulses in two undulators has been demonstrated. In addition to short-pulse generation, steady-state microbunching at ring-based light sources will be discussed.

INTRODUCTION

Synchrotron light sources based on electron storage rings are and will continue to be the workhorses to investigate the structure of matter on the atomic scale with photons in the vacuum-ultraviolet (VUV) to X-ray range [1]. Over half a century, remarkable progress has been made regarding intensity in terms of photon flux and brilliance as well as stability of the photon beams. With the MAX IV facility in Lund/Sweden, another step was taken in reducing the horizontal beam emittance by introducing a 7-bend achromat lattice [2], and other facilities have upgrade plans in the same direction.

In contrast to conventional synchrotron light sources, free-electron lasers (FELs) achieve extremely high average and peak brillance by using electron beams from linear accelerators (linacs) and by microbunching which gives rise to coherent emission of radiation [3]. While the beam in a storage ring is subject to a long-term equilibrium between radiation excitation and damping, the electron bunches in a linac exist only for a few microseconds and retain the small emittance and bunch length with which they are produced. A bunch length being orders of magnitude smaller than in a storage ring implies a high peak current which makes high-gain FEL amplification possible. In addition, the short pulse length of emitted radiation allows to study the dynamics of matter with a temporal resolution in the femtosecond regime.

The spectral power of radiation emitted by n_e electrons at frequency ω is given by [4]

$$\begin{aligned} P(\omega) &= n_e^2 \cdot \left| \frac{1}{n_e} \sum_{j=1}^{n_e} e^{-i\omega t_j} \right|^2 \cdot P_e(\omega) \qquad (1) \\ &= n_e^2 \cdot b^2(\omega) \cdot P_e(\omega) \\ &= n_e \cdot P_e(\omega) + \left| \sum_{j}^{n_e} \sum_{k \neq k}^{n_e} e^{i\omega(t_j - t_k)} \right| \cdot P_e(\omega) \\ &= n_e \cdot P_e(\omega) + n_e(n_e - 1) \cdot g^2(\omega) \cdot P_e(\omega), \end{aligned}$$

where $P_e(\omega)$ is the spectral power emitted by one electron, $b^2(\omega)$ is the bunching factor and $g^2(\omega)$ is the so-called form factor. Thus, $P(\omega)$ is proportional to n_e for randomly distributed electrons as in storage rings but has a component proportional to n_e^2 if the longitudinal distribution has a significant Fourier contribution at frequency ω. As sketched in Fig. 1, this is achieved by structures of the order of the wavelength $\lambda = c/\omega$, either (i) by a sufficiently short bunch, (ii) by a short dip in the longitudinal distribution (iii) by an instability with fluctuations of the electron density, or most efficiently (iv) by periodic microbunching.

A storage ring with microbunched electrons would combine the high repetition rate and stability of SR sources with the high radiation power of an FEL. These benefits have already been demonstrated, e.g., in the coherent emission of terahertz (THz) radiation at storage rings in low-alpha operation where the bunch length can be reduced to the order of 1 ps [5]. However, this example also shows a limiting peculiarity of storage rings, namely the so-called longitudinal microwave instability (or turbulent bunch lengthening) which causes the bunch length to increase above a given threshold of the bunch charge.

For short-wavelength radiation, the periodic microbunching of a short fraction (a "slice") of a long electron bunch gives rise to coherent emission of an equally short radiation pulse which can be employed for time-resolved studies in pump-probe experiments where, e.g., a laser pulse excites the sample and a short-wavelength pulse probes its state as a function of the delay between the two pulses [6]. Here, the time resolution depends on the lengths of both pulses and on the stability of the delay.

Starting from a random electron distribution in longitudinal phase space, microbunching requires a manipulation of

* Work supported by BMBF (05K16PEA, 05K16PEB), MERCUR (Pr-2014-0047), DFG (INST 212/236-1 FUGG) and the Land NRW.
† shaukat.khan@tu-dortmund.de

ISBN: 978-3-95450-206-6 doi:10.18429/JACoW-FLS2018-THP2WB04

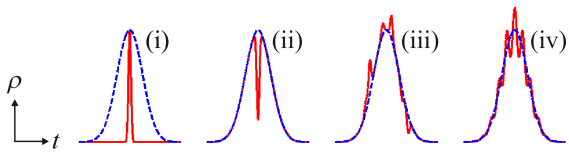

Figure 1: Longitudinal charge distributions (red) giving rise to coherent radiation at wavelengths shorter than the length of a standard bunch (blue). Left to right: a short bunch, a short dip, random fluctuations, periodic microbunching [6].

the longitudinal electron position via

$$\Delta z = r_{51} \cdot \Delta x + r_{52} \cdot \Delta x' + r_{56} \cdot \Delta E/E, \qquad (2)$$

where $(\Delta x, \Delta x')$ is the deviation in horizontal phase space, $\Delta E/E$ is the relative energy offset, and r_{5i} are the respective transfer matrix elements. Usually, the third term is employed by modulating the electron energy with a femtosecond laser pulse copropagating with the electrons in an undulator tuned to the laser wavelength (the "modulator"), which is followed by a sequence of dipole magnets (the "chicane") converting periodic energy modulation into microbunching. The other two terms of the equation tend to smear out the longitudinal structure and must be suppressed. Bunching by different velocities of the electrons is negligible with electron energies in the GeV range. Bunching by wake fields and by FEL amplification from random noise is also unlikely in storage rings due to the low charge density (compared to linac beams). The techniques to produce a microbunched slice within a storage ring bunch by laser-induced energy modulation are similar to those used for seeded FELs.

SHORT-PULSE GENERATION

Figure 2 shows different applications of laser-induced energy modulation in storage rings [6]. For an electron energy in the GeV regime, a laser pulse energy of several mJ is required which restricts the laser repetition rate to a few kHz. The undulator, from which the short pulses are emitted, is called "radiator".

In the femtoslicing scheme, off-energy electrons are transversely displaced by dispersion and their incoherently emitted synchrotron light passes an aperture while the radiation from the long bunch is blocked [7–11]. Here, no microbunching is employed and the radiation power is typically 10^{-4} of that from the whole bunch. The advantage of this scheme is that the radiator setting is independent of the seed wavelength and, despite the low photon flux, femtoslicing has been successful in producing scientific results.

Coherent harmonic generation (CHG) [12] is analogous to high-gain harmonic generation (HGHG) in seeded FELs [13], but without FEL gain. Periodic microbunching leads to coherent emission in a radiator set to a harmonic of the seed wavelength $\lambda_s = c/\omega_s$. Since the bunching factor decreases with $b^2(h \cdot \omega_s) \sim \exp(-h^2)$ with harmonic number h, only low harmonics (typically $h \leq 5$) fulfill the condition that the power ratio of coherently emitted radiation from n_{short} electrons in the slice and radiation from $n_{\text{long}} \approx 10^3 \cdot n_{\text{short}}$ electrons in the remaining bunch

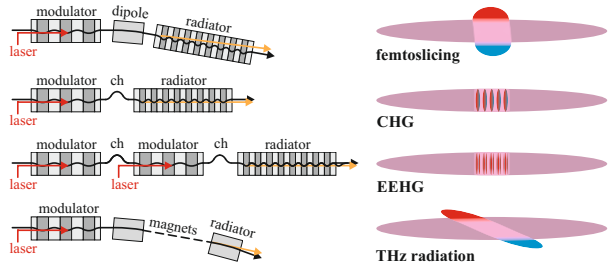

Figure 2: Short-pulse schemes making use of laser-induced energy modulation [6]. See text for details.

$$\frac{P_{\text{short}}}{P_{\text{long}}} = \frac{n_{\text{short}}^2\, b_h^2}{n_{\text{long}}} = f^2\, n_{\text{long}}\, b_h^2 \quad \text{with} \quad f \equiv \frac{n_{\text{short}}}{n_{\text{long}}} \qquad (3)$$

is significantly larger than unity. In the 1980s, CHG was demonstrated with relatively long laser pulses (12 ps) [14]. As a short-pulse scheme with femtosecond laser pulses, CHG was performed at UVSOR in Okazaki/Japan [15], Elettra near Trieste/Italy [16], and more recently at DELTA in Dortmund/Germany [17].

Echo-enabled harmonic generation (EEHG) has been proposed as a scheme for FEL seeding but may also be employed for microbunching in storage rings [18]. Here, a twofold laser-induced energy modulation creates a more complex density modulation allowing to reach higher harmonics with $b^2(h \cdot \omega_s) \sim h^{-1/3}$, where the combination of two energy modulation amplitudes and two chicane settings has to be tuned for each harmonic individually. EEHG has been demonstrated at NLCTA/SLAC in Menlo Park/USA [19], reaching the 75th harmonic of a 2.4-µm seed without FEL gain [20], and at the SDUV-FEL/SINAP in Shanghai/China with first lasing showing exponential growth at the 3rd harmonic of 1.05-µm seed pulses [21]. As a short-pulse scheme for storage rings, EEHG was considered at SOLEIL in Saint-Aubin/France [22] and HLS in Hefei/China [23], but DELTA in Dortmund/Germany is presently the only storage ring with a funded EEHG program [24, 25].

Along the storage ring lattice, the off-energy electrons move ahead or lag behind, leaving a short dip in the longitudinal charge distribution which gives rise to the coherent emission of a short pulse of broadband THz radiation [26]. From turn to turn, the power of this radiation decreases and its spectrum shifts to the sub-THz regime as the dip increases in length and becomes more shallow [27]. Seeding with an intensity-modulated laser pulse produced by chirped-pulse beating leads to several equidistant dips and the coherent emission of narrowband far-infrared radiation. This has been demonstrated at UVSOR for radiation up to 700 GHz [28] and at DELTA in a frequency range from 1 to 5.5 THz [29].

The coherent emission of high harmonics in the EEHG scheme is based on the generation of a phase space distribution with small energy spread. Another method to this end was proposed in [30] using the fact that longitudinal dips

ISBN: 978-3-95450-206-6 doi:10.18429/JACoW-FLS2018-THP2WB04

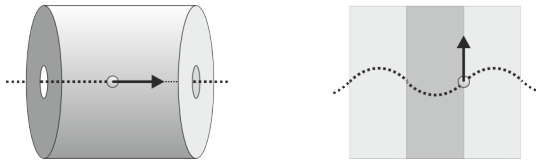

Figure 3: Sketch of an electron in an RF resonator (left) and copropagating with a laser pulse in an undulator (right). The dashed lines represent the electron path, the arrows indicate the force caused by the electric field of the RF wave or laser pulse, respectively (adapted from [31]).

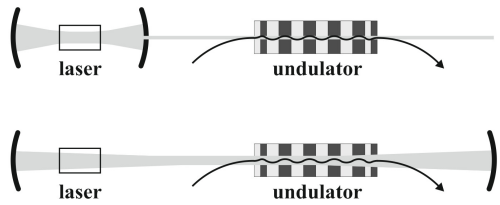

Figure 4: A light wave from a laser interacts with electrons in an undulator which may be outside (top) or inside (bottom) the optical cavity of the laser (adapted from [32]).

produced by an intensity-modulated laser pulse turns into energy stripes after a quarter of a synchrotron period. This effect has not yet been demonstrated because it requires two laser pulses with a delay of a few 10 μs which is not feasible with standard kHz-class laser systems.

STEADY-STATE MICROBUNCHING

The short-pulse schemes described above are based on standard laser technology, e.g., titanium:sapphire lasers with chirped-pulse amplification at a kHz repetition rate which is three orders of magnitude below the typical revolution frequency of storage rings. The objective of steady-state microbunching (SSMB) is the coherent emission of radiation at every turn which may either be achieved by sustained microbunching or by creating a longitudinal density modulation at each turn anew.

Low-alpha operation of storage rings [5] can be viewed as a type of sustained microbunching. The bunches are not narrowly spaced but the few-ps bunch length does support coherent far-infrared emission at every turn. Increasing the radiofrequency (RF) of a storage ring would reduce the spacing between the bunches as well as the bunch length. Lifetime and impedance issues may be mitigated by a reduced bunch charge while keeping the total beam current constant. Practical limitations arise from the reduced size of the RF resonators and the availability of continuous wave (cw) amplifiers. Here, a factor of 10 may be envisioned compared to the typical sub-GHz frequencies.

For higher frequencies, the RF resonator may be replaced by an undulator in which the electrons interact with a freely propagating electromagnetic wave (Fig. 3). This is the principle of laser-induced energy modulation discussed above. In contrast to the RF resonator, the electric field $\vec{\mathcal{E}}$ is not parallel but perpendicular to the electron velocity $\vec{v}$ which makes the interaction less efficient. The energy transfer is given by

$$\mathrm{d}E = -e\,\vec{\mathcal{E}}\cdot\vec{v}\,\mathrm{d}t = -e\left|\vec{\mathcal{E}}\right| x'\,c\,\mathrm{d}t, \qquad (4)$$

where x' is the transverse angle of the electrons in the undulator. Its value in radian can be viewed as an efficiency factor compared to the resonator case. In principle, this scheme is capable of producing buckets in which the electrons are trapped similar to conventional RF buckets. Two cases may be considered as being not totally unrealistic: a cw far-infrared FEL with a wavelength of a few 100 µm and a CO_2 laser with 10 µm. A short-pulse scheme with a far-infrared FEL producing microbuckets in addition to conventional RF buckets has been proposed and a numerical example was given in [31]. As reported in [32], the electric field of a 10-kW cw CO_2 laser with a beam focused onto an area of 1 mm^2 amounts to $2.7 \cdot 10^6$ V/m. With a maximum angle of $x'_{\max} = K/\gamma = 10^{-2}$ rad (e.g., given by undulator parameter $K = 20$ and Lorentz factor $\gamma = 2000$), the energy transfer over a 4 m long undulator would be 50 keV, which is sufficient to compensate the electron energy lost per turn. Tighter focusing and/or placing the undulator inside a laser cavity (Fig. 4) would intensify the electric field significantly.

A sustained-microbunching scheme as described above would require a highly isochronous storage ring. While a sufficiently small momentum compaction factor (around 10^{-5}) can be realized, a path length variation of only a few µm would be still difficult to achieve. One reason is the betatron motion [33], another is the stochastic nature of synchrotron radiation [34]. These and other limitations may be overcome by novel lattice designs or by a combination of laser and RF techniques, where only a fraction of the electrons is trapped in microbuckets while others form a "coasting beam" within the larger RF buckets.

An energy and density modulation produced at each turn is an option for SSMB at visible wavelengths and beyond [35]. With progress in laser technology and by employing a laser cavity instead of a single-pass scheme, a sufficiently high repetition rate may be achieved. However, microbuncing at the full revolution frequency may not even be desirable from the user perspective. Apart from technical issues, the repetition rate of laser-induced energy modulation is limited by the tolerable energy spread. In the present kHz short-pulse schemes, about 10^{-3} of the electrons participate in the interaction with the laser pulses. With typically 10 laser pulses per longitudinal damping time, about 10^{-2} of the electrons are outside the natural energy distribution of the bunch. At a much higher repetition rate, it is necessary to reverse the modulation process turn by turn, i.e., first inverting the density modulation and then applying another laser-electron interaction with the opposite phase.

A storage ring driven by a far-infrared FEL, as described above, may be a useful machine to provide intense THz radiation simultaneously for multiple users whereas SSMB in the visible or near-infrared regime is of little interest for practical

ISBN: 978-3-95450-206-6 doi:10.18429/JACoW-FLS2018-THP2WB04

Table 1: Parameters of the DELTA Short-Pulse Facility

storage ring circumference	115.2 m
electron beam energy	1.5 GeV
beam current (single/multibunch)	20/130 mA
horizontal emittance	15 nm rad
relative energy spread (rms)	0.0007
bunch length (FWHM)	100 ps
laser wavelength	800 nm
min. laser pulse duration (FWHM)	40 fs
seed pulse energy at 800/400 nm	8.0/2.8 mJ
seed repetition rate	1 kHz
modulator/radiator period length	250 mm
number of modulator/radiator periods	7
undulator periods used as chicane	3
max. modulator/radiator K parameter	10.5
max. chicane r_{56} parameter	140 µm

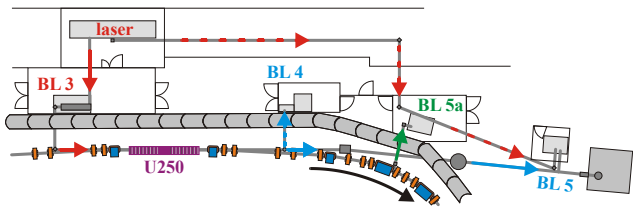

Figure 5: The short-pulse facility at DELTA comprising a laser system, a laser beamline (BL 3) guiding seed pulses to the undulator U250, a diagnostics beamline (BL 4), a soft X-ray beamline (BL 5), and a THz beamline (BL 5a).

applications. SSMB in the VUV or X-ray regime involves the task of converting the energy modulation provided by near-visible laser pulses into a density modulation that gives rise to the coherent emission of radiation at much shorter wavelengths, e.g., by employing an EEHG-like scheme that is performed and then reversed turn by turn.

THE SHORT-PULSE FACILITY AT DELTA

At the 1.5-GeV storage ring DELTA operated by the TU Dortmund University, CHG is routinely performed since 2011 [17] with up to 600 hours of beam time per year. The short-pulse facility (see Fig. 5 and Table 1) comprises a titanium:sapphire femtosecond laser system, a laser beamline, the undulator U250 in an optical-klystron configuration (modulator, chicane, radiator), a diagnostics beamline, a dedicated THz beamline, and a soft X-ray beamline operated by the Forschungszentrum Jülich/Germany. A telescope with lenses is employed to focus 800-nm pulses into the modulator while curved mirrors are used for seeding with frequency-doubled 400-nm pulses. The temporal overlap between laser pulses and spontaneous undulator radiation is established using a photodiode and a streak camera. The spatial overlap is found and optimized by visual inspection on a screen, followed by automated scanning of the last two laser mirrors while recording the THz signal.

CHG radiation with a minimum wavelength of 200 nm is characterized in air at the diagnostics beamline. Here, two Czerny-Turner-type spectrometers are employed, one measuring the radiation intensity with an avalanche photodiode while rotating a grating, the other recording single-shot spectra with a gated image-intensified CCD camera. For shorter wavelengths, the intensity and spectral distribution is determined using the plane-grating monochromator and photoelectron spectrometer of the soft X-ray beamline.

The spatial coherence of CHG radiation was studied by performing double-slit experiments with different slit separation. The temporal coherence length was determined using a Michelson interferometer and a double-slit setup with movable glass wedges to delay light from one slit with respect to the other. The temporal coherence length of the CHG pulses was found to be about three times longer than that of spontaneous undulator radiation [36]. Similar results were obtained by analyzing speckle patterns from CHG pulses passing through a diffuse organic film [37].

Laser seeding was also performed while modulating the RF phase of the storage ring cavity by twice the synchrotron frequency which is usually done to improve the beam lifetime [38]. By synchronizing the phase modulation with the laser pulses, microbunching is created at an electron density and energy spread which deviates significantly from equilibrium. The intensity of CHG pulses and coherently emitted THz radiation was found to increase by up to 30% depending on the modulation amplitude and phase as well as synchrotron frequency (tuned by changing the RF power).

The spectrotemporal properties of CHG radiation were studied under variation of the r_{56} value of the chicane between modulator and radiator and by introducing a laser chirp, i.e., a correlation between wavelength and position along the laser pulse [39]. The chicane setting controls the longitudinal distribution of microbunches while the chirp determines their spacing. Two groups of microbunches with equal spacing, as an example, give rise to interference fringes in the CHG spectrum.

First pump-probe experiments were performed probing the Cu(111) surface state by CHG pulses at 133 nm (the third harmonic of 400-nm seed pulses) showing a spectral shift of the photoelectrons due to Coulomb repulsion from the electron cloud induced by the laser pump pulse – see [40].

For the planned EEHG upgrade of the DELTA short-pulse facility, the hardware is funded and partly in house. Figure 6 shows the present CHG setup and a possible EEHG configuration. Replacing the 3- and 7-degree bending magnets by 10-degree magnets, a 20 m long straight section is created to accommodate three undulators and two chicanes. Two new electromagnetic undulators with a period length of 200 mm will be used as modulators while the present undulator U250 will be the radiator. In the present configuration, EEHG-like seeding was tested by performing a twofold laser-electron interaction of 400-nm pulses from second-harmonic generation (SHG) in one part of the undulator U250 and with the residual 800-nm pulses in the other part. The interaction of both pulses with the same electrons was verified by

ISBN: 978-3-95450-206-6 doi:10.18429/JACoW-FLS2018-THP2WB04

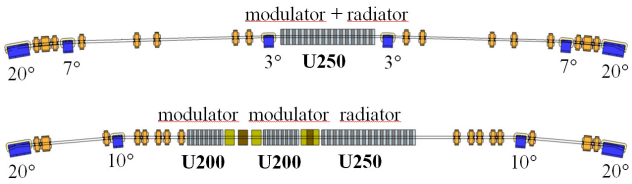

Figure 6: Present CHG configuration (top) and possible setup for EEHG (bottom) at the DELTA storage ring.

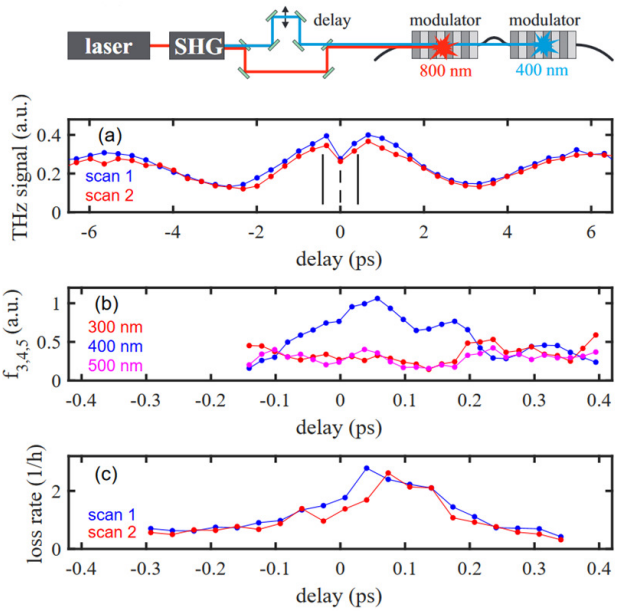

Figure 7: Seeding with 800- and 400-nm pulses in two modulators. Three quantities are shown as functions of delay between the two pulses: (a) THz radiation intensity, (b) Fourier coefficients of the THz signal for a delay variation in sub-wavelength steps, (c) beam loss rate [41].

different effects. The THz signal depends on the delay between the pulses and shows a dip indicating a reduction of the number of coherently emitting electrons at zero delay (Fig. 7a). Within the dip, the THz signal is sensitive to the relative phase of the two pulses as evidenced by a Fourier analysis (Fig. 7b). A twofold energy modulation results in a larger energy offset leading to an increased loss rate when the storage ring is operated with low RF power (Fig. 7c).

CONCLUSIONS

Seeding of electron bunches with laser pulses results in a periodic energy modulation which is converted to microbunching by the r_{56} matrix element of a chicane and gives rise to the coherent emission of radiation at a wavelength corresponding to the microbunch spacing or harmonics thereof. The emitted power is proportional to the number of contributing electrons squared which can either be used to generate radiation of very high intensity or to control the length, shape, and spectral properties of the coherently emitted pulses. Examples are the coherent emission of far-infrared pulses and the CHG scheme to generate ultrashort pulses in the VUV regime. For scientific applications, it is important to access shorter wavelengths by circumventing the limiting effect of the energy spread on the length of the microbunches. One possibility is EEHG involving a twofold laser-electron interaction, another is to compress the microbunches by introducing a correlation between the electron energy and a transverse coordinate ("cooled CHG", e.g., [42–45]).

At the DELTA short-pulse facility, CHG as well as the coherent emission of THz radiation is routinely performed since 2011. The implementation of EEHG is planned requiring a modification of 1/4 of the storage ring.

Using mJ laser pulses, the repetition rate of CHG or EEHG is presently limited to the kHz range. The ultimate dream is the coherent emission of short-pulse radiation at a much higher rate, possibly at every turn, combining the radiation power of FELs with the repetition rate of storage rings. Driving a storage-ring beam in a steady-state fashion by a laser rather than an RF wave can be envisioned at long wavelengths using powerful infrared FELs or lasers but is limited by the achievable isochronicity of the ring. Steady-state microbunching at shorter wavelengths can, in principle, be accomplished by laser seeding at every turn which, however, will require further progress in laser technology.

ACKNOWLEDGMENTS

The continuous support from our colleagues at DELTA and other institutes, e.g., DESY Hamburg, HZB Berlin, and KIT Karlsruhe is gratefully acknowledged. The hardware for EEHG at the DELTA short-pulse facility was partly funded by the Helmholtz ARD initiative through FZ Jülich.

REFERENCES

[1] J. Schneider, "Photon Science at Accelerator-Based Light Sources", in Review of Accelerator Science and Technology, A. W. Chao and W. Chou, Eds. Singapore: World Scientific, 2010, pp. 13-37.

[2] M. Eriksson et al., "Commissioning of the MAX IV Light Source", *Proc. IPAC'16*, Busan/Korea, 2016, pp. 11-15.

[3] P. Schmüser, M. Dohlus, J. Rossbach, "Ultraviolet and Soft X-Ray Free-Electron Lasers", Berlin, Heidelberg: Springer, 2008.

[4] H. Wiedemann, "Particle Accelerator Physics". Berlin, Heidelberg, New York: Springer, 2007.

[5] M. Abo-Bakr, J. Feikes, K. Holldack, G. Wüstefeld, H.-W. Hübers, "Steady-State Far-Infrared Coherent Synchrotron Radiation Detected at BESSY II", Phys. Rev. Lett. 88, p. 254801, 2002.

[6] S. Khan, "Ultrashort Pulses from Synchrotron Radiation Sources", in Synchrotron Light Sources and Free-Electron Lasers, E. Jaeschke, S. Khan, J. Schneider, J. Hastings, Eds. Basel: Springer International Publishing, 2016.

[7] A. A. Zholents and M. S. Zolotorev, "Femtosecond X-Ray Pulses of Synchrotron Radiation", Phys. Rev. Lett. 76, pp. 912-915, 1996.

ISBN: 978-3-95450-206-6 doi:10.18429/JACoW-FLS2018-THP2WB04

[8] R. W. Schoenlein et al., "Generation of femtosecond pulses of synchrotron radiation", Science 287, pp. 2237-2240, 2000.

[9] S. Khan, K. Holldack, T. Kachel, R. Mitzner, T. Quast, "Femtosecond Undulator Radiation from Sliced Electron Bunches", Phys. Rev. Lett. 97, p. 074801, 2006.

[10] P. Beaud et al., "Spatiotemporal Stability of a Femtosecond Hard–X-Ray Undulator Source Studied by Control of Coherent Optical Phonons", Phys. Rev. Lett. 99, p. 174801, 2007.

[11] M. Labat et al., "Commissioning of a Multi-Beamline Femtoslicing Facility at SOLEIL", J. Synchrotron Rad. 25, p. 385., 2018.

[12] R. Coisson and F. D. Martini, "Free-electron relativistic scatterer for UV-generation", in *Physics of Quantum Electronics IX*, edited by S. F. Jacobs et al., Addison-Wesley, 1982.

[13] L. H. Yu, "Generation of Intense UV Radiation by subharmonically Seeded Single-Pass Free-Electron Lasers", Phys. Rev. A 44, pp. 5178-5139, 1991.

[14] B. Girard et al., "Optical Frequency Multiplication by an Optical Klystron", Phys. Rev. Lett. 53, pp. 2405-2409, 1984.

[15] M. Labat et al., "Coherent harmonic generation on UVSOR-II storage ring", Eur. Phys. J. D 44, pp. 187-200, 2007.

[16] G. De Ninno et al., "Generation of Ultrashort Coherent Vacuum Ultraviolet Pulses Using Electron Storage Rings: A New Bright Light Source for Experiments", Phys. Rev. Lett. 101, p. 053902, 2008.

[17] S. Khan et al., "Generation of Ultrashort and Coherent Synchrotron Radiation Pulses at DELTA", Sync. Radiat. News 26(3), pp. 25-29, 2013.

[18] G. Stupakov, "Using the Beam-Echo Effect for Generation of Short-Wavelength Radiation", Phys. Rev. Lett. 102, p. 074801, 2009.

[19] D. Xiang et al., "Demonstration of the Echo-Enabled Harmonic Generation Technique for Short-Wavelength Seeded Free Electron Lasers", Phys. Rev. Lett. 105, p. 114801, 2010.

[20] E. Hemsing et al., "Echo-enabled harmonics up to the 75th order from precisely tailored electron beams", Nat. Photonics 10, pp. 512-515, 2016.

[21] Z. T. Zhao et al., "First lasing of an echo-enabled harmonic generation free-electron laser", Nat. Photonics 6, pp. 360-363, 2012.

[22] C. Evain et al., "Study of High Harmonic Generation at Synchrotron SOLEIL using the Echo Enabling Technique", in *Proc. IPAC'10*, Kyoto, Japan, 2010, pp. 2308-2310.

[23] H. Li, W. Gao, Q. Jia, L. Wang, "Echo-Enabled Harmonic Generation Based on Hefei Storage Ring", in *Proc. IPAC'13*, Shanghai, China, 2013, pp. 1208-1210.

[24] R. Molo et al., "Conceptual Layout of a New Short-Pulse Radiation Source at DELTA Based on Echo-Enabled Harmonic Generation", in *Proc. FEL'11*, Shanghai, China, 2011, pp. 219-222.

[25] S. Hilbrich et al., "Plans for an EEHG-based Short-Pulse Facility at the DELTA Storage Ring", *Proc. Free Electron Laser Conf. FEL'15*, Daejeon/Korea, 2015, pp. 363-367.

[26] K. Holldack, S. Khan, R. Mitzner, T. Quast, "Femtosecond Terahertz Radiation from Femtoslicing at BESSY", Phys. Rev. Lett. 96, p. 054801, 2006.

[27] C. Mai et al., "Observation of Coherent Pulses in the Sub-THz Range at DELTA" in *Proc. IPAC'15*, Richmond, USA, 2015, pp. 823-826.

[28] S. Bielawski et al., "Tunable narrowband terahertz emission from mastered laser–electron beam interaction", Nat. Physics 4, pp. 390-393, 2008.

[29] P. Ungelenk et al., "Continuously tunable narrowband pulses in the THz gap from laser-modulated electron bunches in a storage ring", Phys. Rev. Accel. Beams 20, p. 020706, 2017.

[30] S. Khan, "A New Method to Generate Ultrashort and Coherent Pulses of Short-Wavelength Synchrotron Radiation", in *Proc. IPAC'15*, Richmond, USA, 2015, pp. 1448-1451.

[31] V. N. Litvinenko et al., "Project for Generation of Femtosecond X-Ray Beams from the Duke Storage Ring", in *Proc. PAC'01*, Chicago, USA, 2001, pp. 2614-2616.

[32] S. Khan, "Ultrashort High-Brightness Pulses fron Storage Rings", Nucl. Intr. Meth. A 865, pp. 95-98, 2017.

[33] Y. Shoji, "Bunch Lengthening by a Betratron Motion in Quasi-Isochronous Storage Rings", Phys. Rev. ST - Accel. Beams 7, p. 090703, 2004.

[34] Y. Shoji, H. Tanaka, M. Takao, K. Soutome, "Longitudinal Radiation Excitation in an Electron Storage Ring", Phys. Rev. E 54, pp. R4556-R4559, 1996.

[35] D. F. Ratner and A. W. Chao, "Steady-State Microbunching in a Storage Ring for Generating Coherent Radiation" Phys. Rev. Lett. 105, pp. 154801, 2010.

[36] M. Huck et al., "Ultrashort and Coherent Radiation for Pump-Probe Experiments at the DELTA Storage Ring" in *Proc. IPAC'14*, Dresden, Germany, 2014, pp. 1848-1851.

[37] C. Gutt et al., "Femtosecond speckle and coherence experiments at the CHG short-pulse facility DELTA", in *Proc. SNI'14*, Bonn, Germany, 2014.

[38] M. A. Jebramcik et al., "Coherent Harmonic Generation in the Presence of Synchronized RF Phase Modulation at DELTA", in *Proc. IPAC'16*, Busan, Korea, 2016, pp. 2847-2850.

[39] S. Khan et al., "Spectral Studies of Ultrashort and Coherent Radiation Pulses at the DELTA Storage Ring", in *Proc. IPAC'16*, Busan, Korea, 2011, pp. 2851-2854.

[40] S. Khan et al., "Pilot Experiments and New Developments at the DELTA Short-Pulse Facility", in *Proc. IPAC'17*, Copenhagen, Denmark, 2017, pp. 2578-2581.

[41] S. Khan et al., "Seeding of Electron Bunches in Storage Rings", in *Proc. FEL'17*, Santa Fe, USA, 2017, MOP027.

[42] H. Deng, C. Feng, "Using Off-Resonance Laser Modulation for Beam-Energy-Spread Cooling in Generation of Short-Wavelength Radiation", Phys. Rev. Lett. 111, p. 084801, 2013.

[43] C. Feng, T. Zhang, H. Deng, Zh. Zhao, "Three-dimensional manipulation of electron beam phase space of seeding soft x-ray free-electron lasers", Phys. Rev. ST - Accel. Beams 17, p. 070701, 2014.

[44] S. Khan "Enhancing Coherent Harmonic Generation Using Tilted Laser Wavefronts", in *Proc. FEL'14*, Basel, Switzer-land, 2014, pp. 248-251.

[45] C. Feng and Z. Zhao "A Storage Ring Based Free-Electron Laser for Generating Ultrashort Coherent EUV and X-Ray Radiation", Scient. Reports 7, pp. 4724, 2017.

ISBN: 978-3-95450-206-6 doi:10.18429/JACoW-FLS2018-THA1WC01

COMPACT ARC COMPRESSOR FOR FEL-DRIVEN COMPTON LIGHT SOURCE AND ERL-DRIVEN UV FEL*

S. Di Mitri, †, Elettra – Sincrotrone Trieste S.C.p.A., 34149 Basovizza, Trieste, Italy
I. Akkermans, I. Setjia, ASML Netherlands B.V. Technology, 5501 Veldhoven, The Netherlands
D. Douglas, Thomas Jefferson National Accelerator Facility, Newport News, VA 23606, USA
C. Pellegrini[1], SLAC National Accelerator Laboratory, Menlo Park, CA 94025, USA
G. Penn, M. Placidi (retired), Lawrence Berkely National Laboratory, Berkeley, CA 94720, USA
[1]also at University of California, Los Angeles, CA 90095, USA

Abstract

Many research and applications areas require photon sources capable of producing extreme ultra-violet (EUV) to gamma-ray beams with reasonably high fluxes and compact footprints. We explore the feasibility of a compact energy-recovery linac-driven EUV free electron laser (FEL), and of a multi-MeV gamma-rays source based on inverse Compton scattering from a high intensity UV FEL emitted by the electron beam itself. In the latter scenario, the same electron beam is used to produce gamma-rays in the 10-20 MeV range and UV radiation in the 10-15 eV range, in a ~4x22 m^2 footprint system.

MOTIVATIONS

This work recalls design strategies for the minimization of Coherent Synchrotron Radiation (CSR) instability [1] in high brightness electron beams time-compressed in compact multi-bend lattices, i.e., compressive arcs. Two examples are given: a compact Energy Recovery Linac (ERL)-driven Free-Electron Laser (FEL) for production of ~100 W average FEL power in EUV [2], and a compact FEL-driven Inverse Compton Scattering (ICS) light source devoted to geo-archaeology [3]. The ERL-FEL design targets a cost-effective method of producing integrated circuits and high-volume microchips through nano-lithography. The FEL-ICS design aims at the generation of ~10 MeV range photons in a compact footprint, for applications in computed tomography of cultural heritage and medical diagnostics.

COMPACT ERL–FEL

Overview

Figure 1 sketches a compact non-recirculating ERL-FEL, whose footprint is approximately 20x50 m^2. Table 1 lists the main parameters of the facility. The linear bunch length compression factor to be exploited in the arc is:

$$C = \frac{1}{|1+h_i R_{56}|} \approx \frac{1}{|1+\frac{\sigma_{\delta,i}}{\sigma_{z,i}} R_{56}|} \quad (1)$$

where h_i is the linear energy correlation with particle's longitudinal coordinate internal to the bunch, normalized to the beam mean energy (linear energy chirp), $\sigma_{\delta,i}$ and $\sigma_{z,i}$ are the rms relative energy spread and bunch length, respectively, all variables intended at the arc entrance; R_{56} is the linear transport matrix term proportional to the first order momentum compaction of the arc. The approximation in the r.h.s. of Eq.1 is valid as long as the total beam energy spread is dominated by the linear correlation term. Since the maximum FEL peak power is achieved for $\sigma_{\delta,i} <$ 0.1%, and given the initial 2 ps bunch length, a relatively large R_{56} is required in order to obtain a large compression factor, targeting the final peak current of 1 kA at the bunch charge of 100 pC. A large value for R_{56} implies a large energy dispersion function at the dipole magnets, and, in turn, a large CSR-induced projected emittance growth due to radiation emission and absorption in a dispersive region. Optics strategies to counteract such CSR effect are described in the following.

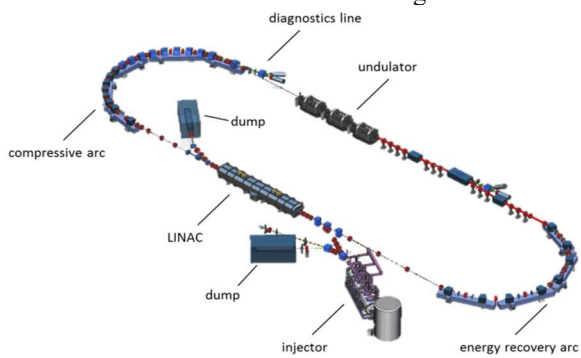

Figure 1: Conceptual scheme of an ERL-FEL; beam moves clock-wise. The scheme is not to scale, and a portion of the straight lines is omitted in order to make the arc lattice more evident. Copyright of APS.

Table 1: ERL-FEL Parameters

Parameter	Value	Unit
Bunch Charge	100	pC
Initial Bunch Duration	2.0	ps
Initial Proj. Norm. Emittance	0.5, 0.5	µm
Final Energy	1	GeV
Final Peak Current	1	kA
Final Relative Energy Spread	0.1	%
FEL Wavelength	13.5	nm
FEL Peak Power	1	GW
Arc Compression Factor	56	
Arc R_{56}	0.5	m
Proj. Norm. Emittance Growth	< 0.2	µm

* Work supported by Elettra Sincrotrone Trieste and ASML Netherlands B.V. Technology
† simone.dimitri@elettra.eu

ISBN: 978-3-95450-206-6 doi:10.18429/JACoW-FLS2018-THA1WC01

Arc Compressor

The impact of CSR kicks on the single particle's transverse momentum can be analytically calculated in the 1-D steady state approximation of CSR emission, for a longitudinal Gaussian charge distribution [4]. Assuming a localized kick and treating the magnet in thin lens approximation, the associated modification of the particle's transverse angular divergence in the dipole magnets and of its transverse position w.r.t. the reference dispersive trajectory can be analytically calculated assuming, e.g., a linear transport matrix formalism [2,5]. It is worth noticing that, since the bunch length is varying along the arc, the CSR kick at each dipole's location will depend on the bunch length at the entrance of the dipole, and therefore different kicks are expected along the arc even for identical optical functions at the magnets.

An analytical optimization of the Twiss parameters and of the betatron phase advance at the dipoles for the minimization of the cumulated CSR kick, and of the CSR-induced emittance growth, was given for a periodic arc compressor based on identical double-bend achromatic cells [6]. This solution, however, implies an arc length of at least 60 m at 1 GeV. Further reduction of the arc footprint is achieved as follows:

- the achromaticity condition at the end of each arc cell is relaxed, with the exception of the very last cell;
- the analytical prescription for the optimum value of Twiss parameters at each dipole (for minimum CSR kick) is relaxed, and strictly taken into account only in the very last cell, where largest CSR kicks are cumulated because of the shortest bunch duration;
- the two prescriptions above allow reducing the number of quadrupole magnets along the arc, leading to a more compact lattice. Eventually, a FODO-cell lattice is chosen, for a total arc length of 20 m;
- an optimization of the Twiss parameters and of the betatron phase advance for the cancellation of the cumulative CSR kick is carried out in the very last cell of the arc, where additional quadrupoles are inserted to this purpose.

The plot at the left side of Figure 2 shows the analytical prediction of the perturbation to the singe particle transverse coordinates at each dipole magnet, on the basis of the optics design illustrated in Fig.3. Figure 2-right plot shows an analytical prediction of emittance growth, based on the previous kicks calculation, as a function of the values of the Twiss parameters at the arc entrance. Such a scan allows a fine-tuning of the arc optics (which is no longer periodic, see Fig.3) once the quadrupole strengths are kept constant. The phase space diagram shows that most of the CSR kicks are relatively weak and lie in the upper-right side of the distribution. The last three kicks, instead, are larger in module and have opposite sign (both in x and x') respect to the others. Such a kicks configuration suggests the possibility of balancing the perturbations, thus providing a small global effect on the final beam emittance.

Particle tracking run with the `elegant` code [7], implementing 1-D CSR impedance and including transient CSR effects at the dipoles edges and in the drift sections, predicts a final projected normalized horizontal emittance of 0.73 μm rad, vs. the analytical prediction of 0.62 μm rad. No vertical emittance growth is predicted.

Second and third order transport matrix terms and CSR-induced nonlinear energy chirp contribute to distort the longitudinal beam phase space during the compression process. Nevertheless, an almost linear compression is obtained at the bunch head, where the current spike to 1 kA appears [2], by exploiting the leading linear energy chirp imparted by the CSR field [8]. An alternative and more complete linearization of the compression process would be possible with the insertion of sextupole magnets in the arc lattice [9], but at the expense of a longer beam line.

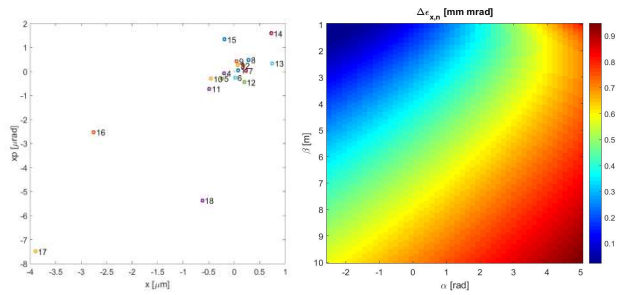

Figure 2: Left: particle transverse displacement in the horizontal phase space due to CSR energy-kicks in the FODO-compressive arc dipoles. The numbers correspond to CSR kicks at the eighteen consecutive dipoles. Right: normalized projected horizontal emittance growth as a function of Twiss parameters at the end of the beamline, calculated with the CSR kick model. Copyright of APS (2017).

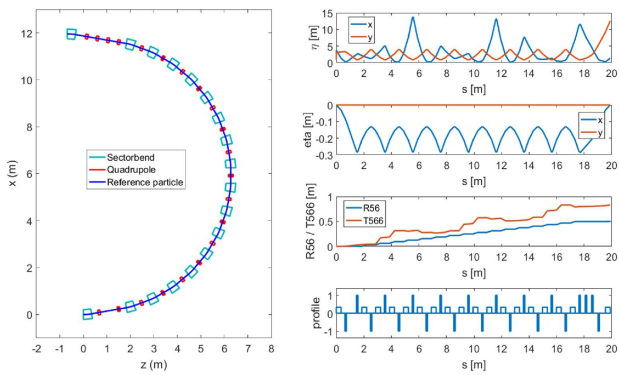

Figure 3: Left: top view of the compressive arc. Right: Optics functions along the arc compressor. From top to bottom: betatron functions, dispersion functions, first and second order transport matrix coefficients, magnetic elements. Copyright of APS (2017).

ISBN: 978-3-95450-206-6 doi:10.18429/JACoW-FLS2018-THA1WC01

COMPACT FEL–ICS

Overview

A sketch of the FEL-ICS light source is shown in Fig.4 and the main parameters are listed in Tab.2. Unlike a standard ICS light source driven by the interaction of an electron beam with an external laser, in the FEL-ICS approach the electron beam interacts with its own UV radiation produced in an undulator. This scheme provides a stronger scaling of the scattered photon energy with the electron beam energy (fourth power instead of the standard square law) [3]. The stronger scaling law involves a lower electron beam energy for a target photon energy, thus a shorter linac for a given accelerating gradient. In addition, coherent UV photon pulses and gamma rays are simultaneously provided for experimentation. The arc provides longitudinal compression to the incoming electron bunches in order to drive the FEL into the high gain regime with a relatively high peak current at the undulator, reducing its gain length while avoiding additional magnetic insertions (e.g., chicanes). As in the case of the ERL-FEL a moderate compression factor has to be obtained while keeping the beam energy spread, and therefore the linear energy chirp, quite low, as requested by efficient lasing in the undulator. For this reason, a relatively large R_{56} is desired (Tab.2). The arc extension determines the FEL-ICS transversal footprint and contributes to the overall length via the loop extension for a given value of the interaction angle at the IP.

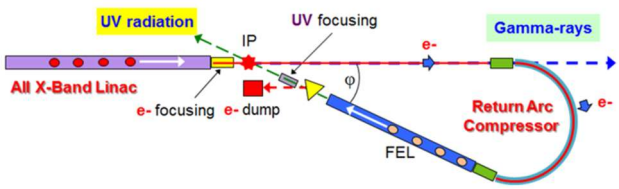

Figure 4: FEL-ICS scheme involving an electron beam return compressive arc. Two photon energies, UV and gamma-rays, are simultaneously available to experiments. Quadrupole triplets provide overlap control at the interaction point (IP) and beam properties matching for arc and undulator. The return arc provides longitudinal bunch compression for improved FEL performance. The system footprint is about 22x4 m^2.

Table 2: FEL-ICS Parameters

Parameter	Value	Unit
Bunch Charge	350	pC
Initial Bunch Duration	2.8	ps
Initial Proj. Norm. Emittance	0.5, 0.5	μm
Final Energy	0.3	GeV
Final Peak Current	0.5	kA
Final Relative Energy Spread	< 0.2	%
FEL Wavelength	150	nm
FEL Peak Power	0.7	GW
Arc Compression Factor	15	
Arc R_{56}	0.2	m
Proj. Norm. Emittance Growth	< 0.3	μm

Arc Compressor

Scaling of the ERL-FEL FODO-cell arc compressor (see previous Section) to the beam energy of 0.3 GeV implies a reduction of the arc length by approximately a factor 3. Since the CSR energy kick is inversely proportional to the beam energy, additional focusing along the arc is needed with the aim at controlling the emittance growth along the line at such reduced beam rigidity, as well as a higher bunch charge. Unlike the ERL-FEL arc compressor, sextupole magnets are added here for linearization of the compression process, while geometric and chromatic aberrations are partially compensated by a suitable arrangement of the sextupoles' location and strength, optimized through `elegant` tracking runs. The magnet list is collected in Tab.3. Figure 5 shows the linear optics functions (top plot), bunch length and transverse emittances along the arc as predicted by the `elegant` code.

Table 3: FEL-ICS Magnets

Type (Quantity)	Field / Gradient	Length
Dipole (7)	1.2 T	0.4 m
Quadrupole (21)	< 60 T/m	0.1 m
Sextupole (4)	< 200 T/m^2	0.1 m

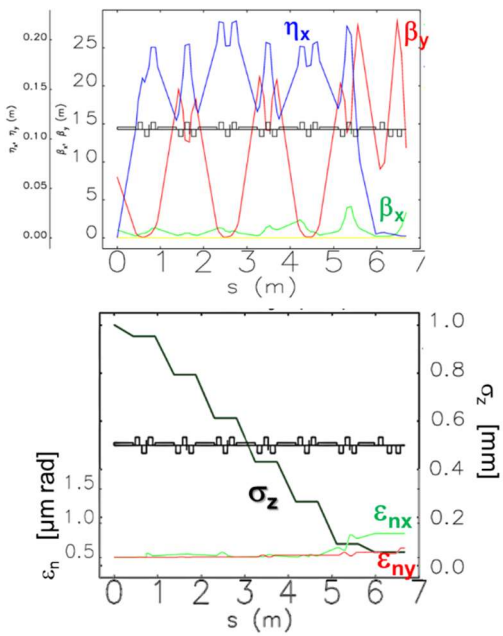

Figure 5: Top, linear optics functions along the FEL-ICS arc compressor. Bottom, rms bunch length and transverse normalized emittances along the arc.

Microbunching Instability

Because of the relatively low beam energy and large bending angle, CSR tends to modulate the beam distribution at wavelengths in the micron range, i.e., CSR drives broadband microbunching instability whose gain appears to be peaked at ~1 μm; energy and density modulations excite reciprocally through the particles' dispersive mo-

ISBN: 978-3-95450-206-6 doi:10.18429/JACoW-FLS2018-THA1WC01

tion. Elegant tracking run, although still affected by numerical sampling noise, reveals a not negligible modulation of the peak current profile at the arc exit, as shown in Figure 6. This effect is not yet consistently treated in the UV FEL simulation, although a preliminary estimation of the FEL performance in the presence of enlarged slice energy spread does not reveal any show stopper.

Recently, optics prescriptions to build up multi-bend *isochronous* transfer lines with unitary microbunching gain were proposed [10], and experimentally verified [11]. Similar treatment might be extended to non-isochronous arcs. It is likely, however, that a compromise shall be reached between the conflicting action of low microbunching gain and large momentum compaction.

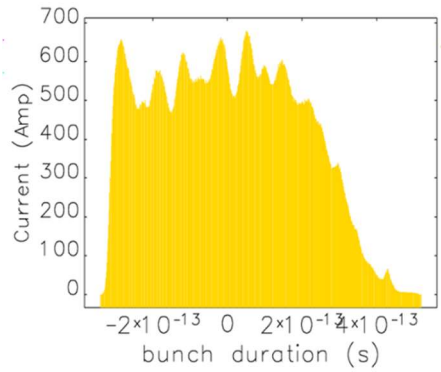

Figure 6: Current profile at arc exit in the presence of CSR-driven microbunching instability.

CONCLUSION

Optics design strategies for two compact arc compressors are illustrated, with application to an ERL-UV FEL devoted to nano-lithography, and to a FEL-based ICS light source devoted to tomography of cultural heritage and medical diagnostics. An approximated analytical calculation of CSR effect on the projected normalized emittance (in the bending plane) in the presence of an arbitrary number of dipoles is illustrated, whose accuracy of prediction w.r.t. 1-D tracking codes appears to be at level of 0.1 μm rad. The analytical guideline might be considered as a first step in arc compressors design, further processed by, e.g., MOGA-like algorithms. This study reveals the appearance of relatively strong microbunching instability in a return arc at beam energies lower than few hundreds of MeV. Minimization of microbunching gain and simultaneous preservation of transverse emittance can be achieved in isochronous lines. Obtaining similar result in arcs with large momentum compaction remains an open path of research.

ACKNOWLEDGEMENT

M. Cornacchia, P. Smorenburg, C.-Y. Tsai, B. Van der Geer, P. Williams and A. Brynes are acknowledged for insights on modelling of CSR and MBI instability.

REFERENCES

[1] Ya.S. Derbenev, J. Rossbach, E.L. Saldin and V.D. Shiltsev, "*Microbunch radiative tail-head interaction*", in *Proc. TESLA-FEL'95*, DESY, Hamburg, Germany (1995).

[2] J. A. G. Akkermans, S. Di Mitri, D. Douglas, and I. D. Setija, "Compact compressive arc and beam switchyard for energy recovery linac-driven ultraviolet free electron lasers", *Phys. Rev. Accel. Beams,* vol. 20, p. 080705, 2017.

[3] M. Placidi, S. Di Mitri, C. Pellegrini, G. Penn, "Compact FEL-Driven Inverse Compton Scattering Gamma-Ray Source", *Nucl. Instr. Meth. A*, vol. 855 (2017).

[4] E. L. Saldin, E. A. Schneidmiller, and M. V. Yurkov, "On the coherent radiation of an electron bunch moving in an arc of a circle", *Nucl. Instr. Meth. A* , vol. 398, p. 373 (1997).

[5] S. Di Mitri, M. Cornacchia, and S. Spampinati, "Cancellation of Coherent Synchrotron Radiation Kicks with Optics Balance", *Phys. Rev. Lett.*, vol. 110, p. 014801 (2013).

[6] S. Di Mitri and M. Cornacchia, "Transverse emittance-preserving arc compressor for high-brightness electron beam-based light sources and colliders", *Europ. Phys. Letters*, vol. 109, p. 62002.

[7] M. Borland, "elegant: A Flexible SDDS-Compliant Code for Accelerator Simulation", *Advanced Photon Source*, LS-287 (2000).

[8] S. Di Mitri , N. Adhlakha, P. Di Pietro, S. Nicastro, A. Perucchi, E. Roussel, S. Spampinati, M. Veronese, E. Allaria, L. Badano, G. De Ninno, B. Diviacco, G. Gaio, D. Gauthier, L. Giannessi, G. Penco, P. Rebernik, C. Spezzani, M. Trovo', "*Coherent THz Emission Enhanced by Coherent Synchrotron Radiation Instability*", to be published.

[9] S. Di Mitri, "Feasibility study of a periodic arc compressor in the presence of coherent synchrotron radiation", *Nucl. Instr. Meth. A*, vol. 806 (2015).

[10] C.-Y. Tsai, S. Di Mitri, D. Douglas, R. Li, and C. Tennant, "Conditions for coherent-synchrotron-radiation-induced microbunching suppression in multibend beam transport or recirculation arcs", *Phys. Rev. Accel. Beams*, vol. 20, 024401 (2017).

[11] S. Di Mitri and S. Spampinati, "Microbunching instability study in a linac-driven free electron laser spreader beam line", *Phys. Rev. Accel. Beams*, vol. 20, 120701 (2017).

ISBN: 978-3-95450-206-6 doi:10.18429/JACoW-FLS2018-THP1WD02

LCLS-II BEAM CONTAINMENT SYSTEM FOR RADIATION SAFETY*

C. Clarke†, J. Bauer, M. Boyes, Y. Feng, A.S. Fisher, R. Kadyrov, J. Liu, E. Rodriguez, M. Rowen, M. Santana-Leitner, F. Tao, J. Welch, S. Xiao, SLAC National Accelerator Lab, Menlo Park, USA
T. Allison, Trentronix, LLC, Hampton, USA
J. Musson, Jefferson Lab, Newport News, USA

Abstract

LCLS-II is a new xFEL facility under construction at SLAC National Accelerator Laboratory with a superconducting electron linac designed to operate up to 1.2 MW of beam power. This generates more serious beam hazards than the typical sub-kW linac operation of the existing xFEL facility, Linac Coherent Light Source (LCLS). SLAC uses a set of safety controls termed the Beam Containment System (BCS) to limit beam power and losses to prevent excessive radiation in occupied areas. The high beam power hazards of LCLS-II necessitate the development of new BCS devices and a larger scale deployment than previously done at LCLS. We present the new radiation hazards introduced by LCLS-II and the design development for the BCS.

INTRODUCTION TO LCLS-II

With the LCLS-II upgrade, the complexity and seriousness of potential beam generated hazards at the SLAC FEL facility expands greatly.

LCLS-II adds a second x-ray laser to the already established LCLS x-ray laser, which started operation in 2009 (Fig. 1). LCLS was the first hard x-ray laser and is used by hundreds of scientists each year to deliver 0.3 –13 keV x-rays at 120 Hz for imaging at the atomic level and visualisation of femtosecond-scale processes. LCLS-II will operate in parallel with LCLS, introducing new FEL capabilities to operate at up to 1 MHz with x-rays from 250 eV to 25 keV, utilizing Superconducting Radio Frequency (SRF) cavities at 1.3 GHz.

Each accelerator occupies one third of SLAC's existing linear accelerator tunnel. The electron beams traverse nearly 3750 meters of accelerator housing, cover an energy range of up to about 15 GeV for the LCLS (copper cavities) linac beams and above 4.0 GeV for LCLS-II SRF beams, and beam power of up to 250 kW for SRF beams. The SRF beams can simultaneously be sent to two different undulator lines and one additional dump line. The copper linac feeds the hard x-ray undulator only. Laser-like, high power x-ray beams are generated in the undulator lines by the electron beams and traverse another 300 meters to experiment "hutches". There are very many more complex configurations possible and expected in SLAC's future.

The new SRF linac runs CW, and the cryomodule cavities and the RF gun itself can generate beam hazards through field emission that can be captured and accelerated to high energies. Essentially there are six potential sources for beam related hazards after the LCLS-II upgrade that may be hard to distinguish from each other: Superconducting linac photo-current beam, field emission current generated by the RF Gun for the SRF linac, field emission current generated by superconducting cavities, secondary beam from SRF linac (FEL x-ray beam), copper linac photo-current beam, and secondary beam from copper linac (FEL x-ray beam).

HISTORY AND DEVELOPMENT OF BCS

A Beam Containment System (BCS), as defined at SLAC, is a set of mechanical, electronic, and electrical devices that limit beam power and beam losses to prevent excessive radiation in occupied areas.

SLAC's original BCS was for the 2-mile long (up to 50 GeV) SLAC accelerator, which could generate nearly 1 MW average beam power and operated up to 8 beamlines. A significant event occurred where 30 W positron beam struck shielding resulting in 360 R/h dose rates outside the 1.8 m concrete shielding [1]. This illustrates the importance of containing the beam before it can hit shielding.

At SLAC, beam is contained with stoppers and protection collimators. A series of tests using 18 GeV electron beam at average powers ranging from 165 kW to 880 kW demonstrated the highly destructive capability of such beams; the rapid burn-through of materials used in the construction of stoppers and collimators (typically seconds if not faster) clearly demonstrated the need for "an extensive electronic system to prevent damage to mechanical devices and to detect onset of destruction" in addition to power monitors, errant beam monitors and burn-through monitors.

The conclusion to these studies was to define the requirements for BCS. The SLAC BCS control system consists of robust, overlapping and type-redundant fault detection devices and beam shut-off systems that provide three functions:

1. To monitor and limit the beam power in a beam line to the allowed value within the capability of the dumps and shielding
2. To limit the losses along a beam line that is operating to its allowed power
3. To protect beam containment devices from damage by sensing when a beam hits it with enough power to damage it

In response to excessive beam power, losses or the risk of damage to beam containment devices, the BCS shuts off the beam using redundant and diverse technologies.

* Work supported by the U.S. Department of Energy under contract number DE-AC02-76SF00515 and DE-AC05-06OR23177.
† cclarke@slac.stanford.edu

ISBN: 978-3-95450-206-6 doi:10.18429/JACoW-FLS2018-THP1WD02

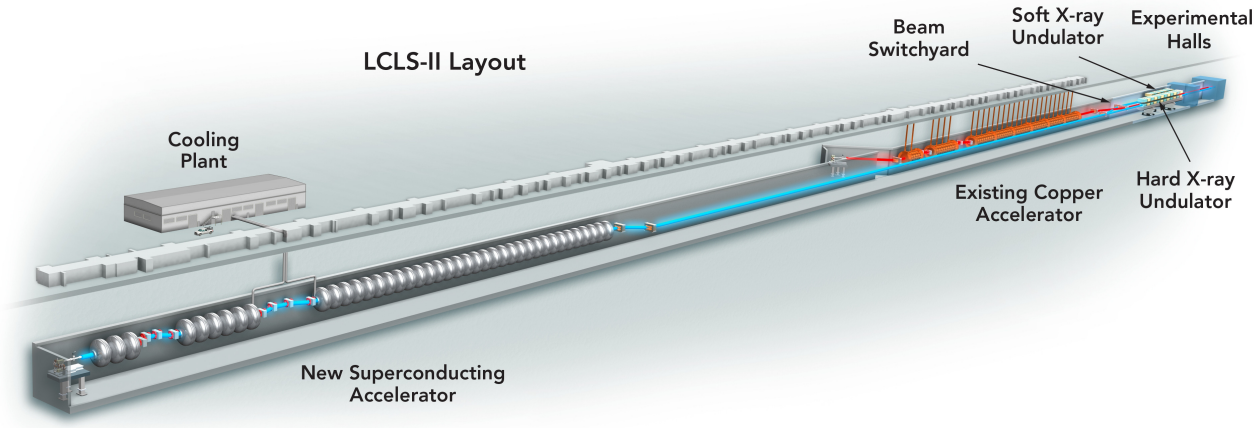

Figure 1: The SRF linac of the future LCLS-II X-ray laser (blue, left) occupies the first third of the existing SLAC accelerator housing. The existing LCLS copper linac (red, right) occupies the final third. Two undulators can be used to deliver x-rays to the experimental hutches. (SLAC National Accelerator Laboratory)

Because of the seriousness of the potential hazards, the systems must be tamper-proof, redundant and fail-safe, backed up by strict operational rules (that is, configuration control with regards to trip threshold values and device bypasses). Self-monitoring sensors are required where feasible to guarantee the continuity of the signal transmission path and to confirm the functionality of the processor.

These BCS design guidelines have withstood the test of multiple accelerator facilities hosted at SLAC. They have been formulated into a controlled document [2] that has been updated as new technologies are available and are applied equally to electron/positron beams as to secondary beams such as x-rays.

Although the linear accelerator shielding is designed for MW class beams, the LCLS FEL additions were shielded for beam power only up to 5 kW. With the LCLS-II upgrade they will contain two operating beamlines with power of up to 120 kW. In addition, the SLAC site has changed from a single-purpose laboratory to a site with multiple user facilities resulting in the presence of outside users bringing with it stricter regulatory limits. These factors increase the reliance on the BCS for LCLS-II.

BCS TECHNOLOGIES

In this section, we discuss the new technologies that are in development for LCLS-II BCS to detect potentially unsafe conditions and shut the beam off. Technologies that have been in use since the inception of BCS at SLAC (water flow interlocks, magnet current interlocks, etc.) are not discussed here but remain a part of BCS. The BCS is backed up by subsystems of monitors that can detect a burn-through of safety components, and by beam shut off ion chambers which detect radiation in occupied ares and operate through the Personnel Protection System (PPS).

BCS Controls Architecture

To begin, we will present the architecture within which the BCS sensors sit. BCS has historically been a series of (where possible) commercially available mechanical relays. More recently Siemens S7 safety programmable logic controller (PLC) solutions were developed for use in safety systems at SLAC. They have built-in redundancy, self-checking, extensive diagnostic monitors, and offer greater reliability over legacy hardware. The PLC and I/O modules would sit on a dedicated BCS network based on Profinet.

Some devices in BCS are required to shut the beam off much faster than 1 second, and these devices should remain hard-wired to the shut-off path. In such cases PLC solutions can provide a more supervisory role: reporting status, changing set-points, and managing device bypasses. The PLC system information can be available locally to accelerator operators.

Average Current Monitor

The BCS has Average Current Monitors (ACM) at the start of each beamline to limit beam current (and indirectly, beam power) to the approved values. The approved values depends on the power rating of the various dumps and the shielding through which the beams pass. It is expected to be increased in stages as the machine, diagnostics, and safety devices are commissioned. The proposed layout of ACMs is shown in Fig. 2.

Cavities have been proposed for the ACM sensor for LCLS-II. Compared to toroids, cavities have a low baseline drift, much better sensitivity, can detect dark current, and it is possible to continuously inject a pilot tone for constant sensor/system verification. The drawbacks for cavities are that they have to be temperature controlled and calibrated with beam against another calibrated beam device such as a Faraday Cup or toroid. Toroids can be calibrated using a

ISBN: 978-3-95450-206-6 doi:10.18429/JACoW-FLS2018-THP1WD02

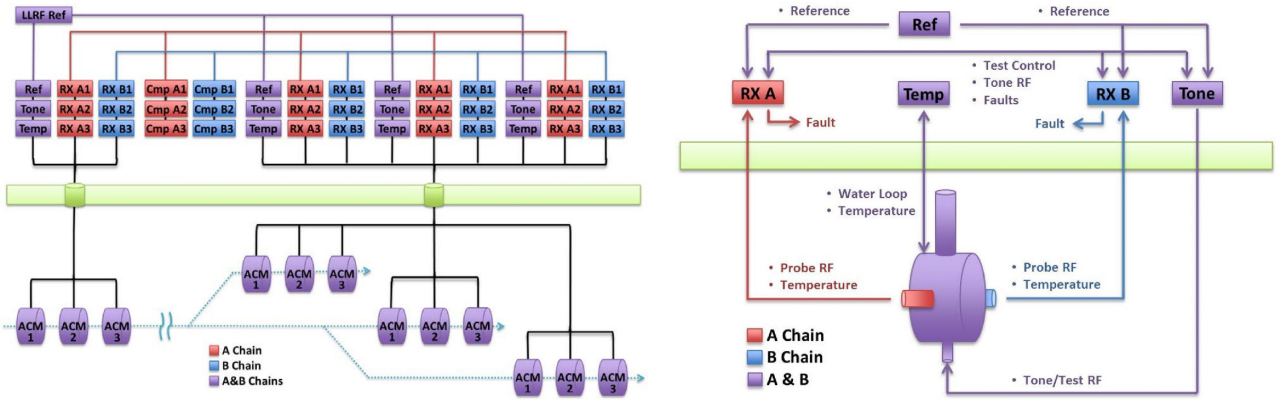

Figure 2: ACMs are located as triplets at start of linac and each beamline. It is recommended that two devices (each with pilot tones and redundant electronics chains) are employed with a third ACM cavity installed as a backup.

current source but only when beam is off and likely require frequent calibration due to baseline drifts. Specialized toroid electronics would also need to be developed to meet the accuracy, signal to noise ratio and dynamic range requirements. Therefore we are developing a cavity-based ACM device.

Each ACM cavity would have two probe ports that go to redundant (A and B) electronics chains. The A and B Receivers consist of the following main printed circuit boards (PCB): down converter board (a Fermilab LLRF down converter design), IF Digitizer and Signal Conditioner board, and FPGA Digital Signal Processing and Control board. The detected 1.3 GHz beam current signal will be compared to a limit for the absolute mode and the system will fault if the limit is breached. These Receivers will incorporate well established LCLS-II LLRF PCB and chassis designs.

Self-test is an important feature for the ACM. In order to constantly verify the end-to-end system functionality, a pilot tone that is 100 kHz off frequency from the 1300 MHz carrier can be continuously injected into a third test port of the ACM cavities. The chain A and B processing electronics compare the pilot tone signal fed to the cavity and the detected pilot tone signal as measured from the cavity to ensure that the system is functional and the cavity tune is not drifting. If the detected pilot tone signal drifts too far from the original then the electronics can generate a fault signal; this ensures that the ACM operates only with proper cavity tune.

The pilot tone generator could also produce a test signal to verify that the ACM will fault the BCS on an over-current.

FPGA use in ACM processing FPGAs are planned to be used in the signal processing for the Average Current Monitors. FPGAs are used in this capacity also at Argonne Light Source [3] and are widely used in accelerator Machine Protection Systems as well as in safety systems in aviation and nuclear power stations.

The SLAC BCS architecture for FPGA use for the ACMs includes two redundant logic controllers implemented on identical hardware. The LLRF BMB7 design by LBNL with Kintex-7 and Spartan-6 Xilinx FPGAs will be utilized. In the BMB7 board design, the communication and soft-processing logic is unloaded to a separate chip allowing the main FPGA do routine signal processing and avoiding peak loads and peak power dissipation.

Our approach is to have two separate programmers for the Chain A and Chain B FPGAs. We will also develop a single test bench for both chains by a third party, independent of the programmers. Safety standards do not require diversity in firmware to achieve the desired level; however there are concerns with regards to programmable devices in safety systems within the DOE Accelerator Laboratory complex. Industry practices commonly emphasize strict verification of the firmware rather than diversity of the firmware, however in practice in an accelerator laboratory environment, strict QA can be harder to enforce than programming diversity.

In addition to this diverse firmware implementation, each logic controller will use advanced safety design practices from Xilinx, such as the Soft Error Mitigation controller to monitor for Single Event Upsets (a common and most probable way of failure for programmable device) and generate a BCS fault if detected.

We will follow the IEC Functional Safety Standard IEC 61508. This provides guidance on how to implement software in a safety environment which can also be applied to firmware development.

Cherenkov Fibers to Limit Beam Loss

Shielding is the preferred mitigation tool for the prevention of radiation in occupied areas. The shielding at SLAC is designed to meet 25 rem/hr dose rates or 3 rem/event in a maximum credible incident. Below this level, shielding does not suffice and active controls are required.

Key to mitigating these risks is to cover the entire facility, with the exception of rare areas with sufficient earth shielding, with radiation monitors. Locations where beam loss is expected could be monitored with small, discrete radiation detector units; however this 4 km facility requires a more global solution that ensures coverage with the fewest sensors possible.

ISBN: 978-3-95450-206-6 doi:10.18429/JACoW-FLS2018-THP1WD02

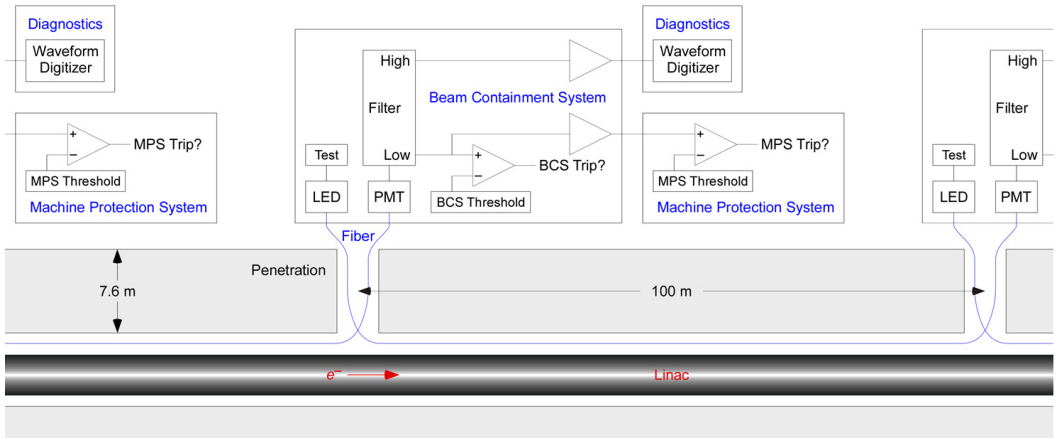

Figure 3: Fibers can cover hundreds of meters within the accelerator housing. A PMT at the downstream end detects Cherenkov light caused by radiation (beam loss). The signal is available for diagnostics as well as the generation of BCS and MPS faults.

Technologies were evaluated. These includes long ion chambers and ACM comparators. Long ion chambers (termed LIONs) have been used at SLAC since its inception [4]; however on this scale of deployment they would be expensive and unreliable due to the extensive gas system they require. In addition, the high repetition rate of LCLS-II means that the spacing between pulses is much shorter than the ion collection time in these devices. In an extended period of losses that are high but lower than the trip threshold, ions can build up between electrodes and screen the applied potential, reducing the collection of electrons and ions despite high losses [5]. ACM comparators would not meet sensitivity requirements to detect a few watts of beam loss using the same devices in the same locations as in the previous section.

We decided upon using Cherenkov emission in radiation-hard optical fibers [6] for our long beam loss monitors. A multi mode fiber with a 600 μm core was tested for radiation hardness up to 1.25 Grad for use in the LHC at CERN [7]. They found that radiation-induced fiber darkening resulted in high light attenuation below 380 nm and in the band 550 –680 nm, moderate attenuation in the band 400 –520 nm and "practically no attenuation above 700 nm". Based on these results, we decided to use an identical fiber material, a long pass optical filter at 680 nm and a red-sensitive silicon photomultiplier (SiPM) from Hamamatsu (H7422P-40). We integrate the SiPM signal and compare to a pre-set trip threshold to generate a BCS fault (Fig. 3).

As a conservative estimate, a fiber could be exposed to 25 MRad annual dose which, at 700 nm, results in below 3 dB attenuation. Operationally, we would set the trip threshold conservatively low to take into account expected changes to fiber transmission from radiation darkening and replace the fiber once it is 50%. At worst, this is replacement every year (for this conservative case). Replacing a fiber is straight forward and can be done in minutes with a "jetted" fiber technique using compressed air without requiring access to the accelerator housing.

The fibers and electronics can be checked routinely with a self-check mechanism to ensure they are operating correctly with an LED. The LED measures transmission through the fiber and can be used to generate a fault to test the trip mechanism.

Diamonds as Solid State Ion Chambers

Traditionally, ionization chambers have been used in SLAC BCS to protect beam containment devices from damage by sensing when a beam hits it with enough power to damage it. Modeling studies of ionization chambers indicate substantial uncertainty in their operation at high beam repetition rates and power. Scintillator or Cherenkov counters have been used at SLAC in non BCS applications. Cherenkov fibers will be a part of the LCLS-II BCS and can be used also for the protection of devices. However, diversity in beam loss technologies adds safety to the system therefore we are motivated towards solid state detectors for this device.

Diamond particle detectors, with their nanosecond time resolution, are a potential solution for fast beam loss detection. They have high radiation hardness, heat resistance, small size and don't require active cooling, making them relatively simple to install.

Diamond, because of its large resistivity, can be operated as a solid-state ionization chamber. A voltage is applied across a layer of diamond a few hundred microns thick. When a charged particle traverses the diamond, atoms in crystal lattice sites are ionized, promoting electrons into the conduction band and leaving holes in the valence band. On average, 36 electron-hole pairs are created in each μm of diamond traversed by a minimum ionizing particle. These charges drift across the diamond in response to the applied electric field producing a detectable electric signal.

We have been working with Cividec [8] to develop diamond detectors for use at SLAC. Experience Cividec has

ISBN: 978-3-95450-206-6 doi:10.18429/JACoW-FLS2018-THP1WD02

gained through diamond detector deployment at CERN is valuable such as the development of beryllium spring contacts to the diamond which are expected to survive 1 Grad, beyond the lifetime of the facility.

Self-checking of the diamond can be achieved by modulating the voltage applied across it at a known frequency and using a digital signal processor to monitor the amplitude at that frequency. UV flash lamps were also effective at producing a signal from the diamond; however in order to get enough signal, the flash lamp needed to be large and positioned directly against the sensor, making it a less convenient method than HV modulation.

Protection of Collimators with Photo-Diodes

The FEL x-ray beam can also damage safety components. The graphite-coated diamond disk, shown in Fig. 4, is on the upbeam side of the protection collimator and survives most LCLS-II operating conditions, but it can be damaged if extreme beam conditions are met.

In the event of a mis-steered beam striking the disk, the back-scattered X-rays can be detected by a 4-diode array positioned upstream of the diamond disk, generating a fault signal. The four X-ray diodes are divided into two groups connected to two independent circuits, providing the necessary redundancy for a BCS system. To detect the full energy range of the impinging X-rays, we have selected diode Model IRD-AXUV100Al from Opto Diode Corp.

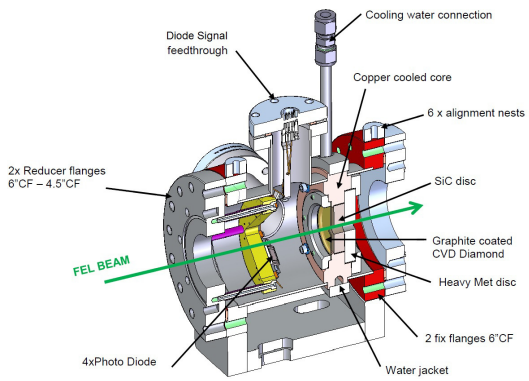

Figure 4: Components to the FEL Collimator. In-vacuum diodes detect scattered x-rays from a FEL beam mis-steer. (Engineer: Silvia Forcat-Oller)

Similar to the Cherenkov fibers, this lends itself to a simple self-check mechanism using an LED to periodically monitor the health of the X-ray diodes and the associated electronics.

Protection of Stoppers with Intensity Interlock

Unlike collimators, PPS stoppers need to be able to sustain FEL directly for an indefinite amount of time (PPS stoppers here act as insertable beam dumps to allow experimenters to access the x-ray hutch downstream). The solution to shut off the beam should FEL hit the stopper therefore cannot be applied. Instead, we plan to monitor the electron beam parameter (energy and bunch charge) and undulator gaps continuously, and shut-off the electron beams when FEL beams may potentially damage the CVD diamond layer on the PPS stoppers. This interlock is activated only when the PPS Stoppers could be in the beam path otherwise all FEL beams are permitted.

The trip threshold for this interlock is defined as the highest allowed temperature and is adjustable between 500°C to 2500°C. The trip threshold will be set conservatively at the beginning of operations. It may be raised when tests with the bootstrap processes demonstrate the safety at a higher threshold. The temperature is a function of electron bunch charge (as measured by a toroid) and FEL energy (which must be calculated from beam energy and undulator gap). The dangerous zone is the phase space of electron bunch charge and FEL energy within which the temperature will be higher than the limit. The calculations and comparison to the trip threshold can be done in a PLC.

This device is more complicated than most systems utilised in BCS and does not have a self-check mechanism however it is complemented with a burn-through monitor upstream of the PPS stoppers for a second layer of protection.

Fast Beam Shut-off

The BCS is required to shut off the beam using diverse technologies. The driving factor for the speed of the beam shut off is damage to safety components which can occur on a single shot (stress damage) with the onset of melting in milliseconds (in the case of the electron beam striking a collimator, stopper or beam dump). The BCS will include multiple beam shut off methods that work together on this timescale to ensure a safe and reliable system.

The fastest shut-off device proposed is an acousto-optic modulator (AOM) that is part of the delivered laser system for the LCLS-II injector laser. The AOM uses RF sound waves to deflect and extract the laser from the system. Without RF, the laser is undeflected into an internal laser dump and is not extracted. BCS can interrupt the RF to the AOM when there is a fault so that the laser power is internally dumped within microseconds. Overall our expected shut-off time using the AOM is expected to be less than 200 μs once signal time of flight, cabling and processing is taking into account, the dominant factor being the processing of the signals in the BCS relay and logic chassis.

CONCLUSION

LCLS-II sees a return to MW class electron beams for SLAC. The LCLS site, designed for a 5 kW beam, is repurposed leading to an increase of dependence on active safety systems. Existing SLAC standards for the beam containment system are followed. Due to new challenges in the scale of the deployment, dynamic range of the sensors required and faster response time required, technologies that have not been used in BCS at SLAC before are being developed. These include cavities, Cherenkov fibers, diamond detectors, photo-diodes and programmable devices such as PLCs and FPGAs.

ISBN: 978-3-95450-206-6 doi:10.18429/JACoW-FLS2018-THP1WD02

REFERENCES

[1] D. Walz *et al.*, "Tests and description of beam containment devices and instrumentation-problems.", *SLAC-PUB-1223*, 1973

[2] "Radiation Safety Systems Technical Basis Document.", *SLAC-I-720-0A05Z-002*, 2010.

[3] Anthony F. Pietryla and Glenn A. Decker, "Design of the beam shut-off current monitor upgrade for the advanced photon source.", in *AIP Conference Proceedings 546.1 (2000)*, pp. 527–534.

[4] T.N. Constant *et al.*, "LIONs at the Stanford Linear Accelerator Center.", *SLAC-PUB-7691*, 1998.

[5] A.S. Fisher, C. Field, and L. Nicolas, "Evaluating beam-loss detectors for LCLS-2", in *Proc. 5th International Beam Instrumentation Conference (IBIC 2016)*, Barcelona, Spain, Sept. 2016, paper WEPG23.

[6] S.H. Law *et al.*, "Optical fiber design and the trapping of Cerenkov radiation", in *Appl. Opt. 45.36 (Dec. 2006)*, pp. 9151–9159.

[7] K. Cankoçak *et al.*, "Radiation-hardness measurements of high OH- content quartz fibres irradiated with 24GeV protons up to 1.25Grad", in *Nuclear Instruments and Methods in Physics Research Section A: Accelerators, Spectrometers, Detectors and Associated Equipment 585.1 (2008),* pp. 20–27.

[8] Cividec, https://cividec.at/

ISBN: 978-3-95450-206-6 doi:10.18429/JACoW-FLS2018-THP2WD01

CONSTRUCTION AND OPTIMIZATION OF CRYOGENIC UNDULATORS AT SOLEIL

M. Valléau* , A. Ghaith, F. Briquez, F. Marteau, P. Berteaud, C. Kitegi, J. Idam, O. Marcouillé, A. Mary, M. Tilmont, J. DaSilva Castro, F. Lepage, K. Tavakoli, J.-M. Dubuisson, N. Béchu, C. Herbeaux, M. Louvet, P. Rommeluére, M. Sebdaoui, A. Lestrade, A. Somogyi, T. Weitkamp, P. Brunelle, L. Nadolski, A. Nadji, M.-E. Couprie,
Synchrotron SOLEIL, GIF-sur-YVETTE , France

Abstract

With permanent magnet undulators operating at cryogenic temperature, the magnetic field and coercivity are enhanced, enabling shorter periods with higher magnetic field. The first full scale (2 m long, 18 mm period) hybrid cryogenic undulator [1] using PrFeB [2] magnets operating at 77 K was installed at SOLEIL in 2011. Photon spectra measurements, in good agreement with the expectations from magnetic measurements, were used for precise alignment and taper optimization. The second and third 18 mm PrFeB cryogenic undulators, modified to a half-pole/magnet/half-pole structure, were optimized without any magnet or pole shimming after assembly, but mechanical sortings and some geometrical corrections had been done before assembly. A systematic error on individual magnets on the third U18 was also compensated. In-situ measurement benches, including a Hall probe and a stretched wire to optimize the undulator field at room and cryogenic temperature are presented. An upgrade of these in-situ benches will be detailed with the fabrication of a 15 mm period and 3 m long PrFeB cryogenic undulator at SOLEIL.

INTRODUCTION

In-Vacuum Undulators (IVU) generate high magnetic field by placing directly the magnets inside the vacuum chamber. Cryogenic Permanent Magnet Undulators (CPMUs) have been developed to reach intense brightness at higher energies as cooling down $RE_2Fe_{14}B$ enables to increase the remanent field and coercivity. The first prototype of 0.6 m length with a period of 14 mm, using high remanence $Nd_2Fe_{14}B$ grade cooled down to 140 K has been developed at SPring-8 [3]. After this first prototype, a 8 x 14.5 mm periods CPMU prototype has been built at Brookhaven National Laboratory (BNL) using $Nd_2Fe_{14}B$ grade reaching a magnetic gap of 5 mm [4–6]. Helmholtz-Zentrum Berlin (HZB) with the collaboration of UCLA, built two CMPU prototypes (20 x 9 mm period and magnetic gap of 2.5 mm), using $Pr_2Fe_{14}B$ magnets cooled down to 20-30 K [7]. At SOLEIL, three hybrid prototypes CPMU have been built and characterized: a 4 periods 18 mm length with $Nd_2Fe_{14}B$ magnets (BH50 Hitachi-Neomax) [8], a 4 x 18 mm period with $Pr_2Fe_{14}B$ (CR53 Hitachi-Neomax) [9], and a 4 x 15 mm period with $Pr_2Fe_{14}B$. The first full-scale cryogenic undulator had been developed at ESRF [10] with a period length of 18 mm using a relatively low remanence $Nd_2Fe_{14}B$ magnet grade (B_r=1.16 T) cooled down to around 150 K, reaching a gap of 6 mm. Then full scale undulators using $Nd_2Fe_{14}B$ based magnets where built for Diamond [11] or at SLS [12]. This article details the design, construction and operation with cryogenic undulators of SOLEIL. U18 n^{o}1 was the first full-scale Praseodymium based magnet undulator installed on a storage ring [2]. The second U18 is in use for COXINEL experiment [13, 14] since 2015 and the third one has been installed in the storage ring since Dec. 2017. A 15 mm period and 3 m long cryogenic undulator (U15) operating at 3 mm gap is also under construction.

MAGNETIC DESIGN

Detailed characterization of $Re_2Fe_{14}B$ permanent magnets have been carried out at SOLEIL [8]. Figures 1 and 2 show the dependence of the remanence and coercivity as a function of the temperature for $Nd_2Fe_{14}B$ and $Pr_2Fe_{14}B$ magnets. When Nd is used, the remanence temperature dependence exhibits a maximum at a temperature between 150 and 100 K, according to the employed grade. It results from the spin transition reorientation (SRT) [15] occurring from this type of magnet. Thus, it requires that Nb based cryogenic undulator to be cooled down to the liquid nitrogen temperature and heated back to the working temperature to 140 K, whereas $Pr_2Fe_{14}B$ based undulators can be directly cooled and operated at 77 K because of the absence of the SRT. Even larger field can be achieved with $Pr_2Fe_{14}B$ magnets by cooling even at lower temperatures than the one of the liquid nitrogen. The cryogenics becomes slightly more complex.

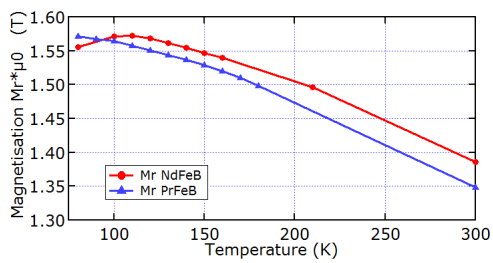

Figure 1: $Nd_2Fe_{14}B$ (red) and $Pr_2Fe_{14}B$ (blue) remanent field dependence with the temperature.

* mathieu.valleau@synchrotron-soleil.fr

ISBN: 978-3-95450-206-6 doi:10.18429/JACoW-FLS2018-THP2WD01

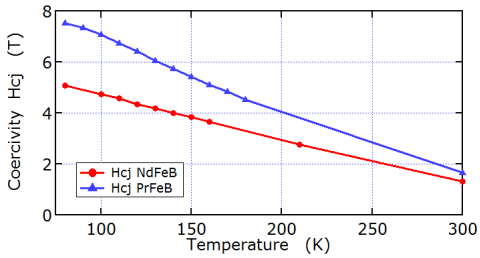

Figure 2: $Nd_2Fe_{14}B$ (red) and $Pr_2Fe_{14}B$ (blue) coercivity dependence with the temperature.

The SOLEIL U18 and U15 undulators characteristics are presented in Table 1. Both undulators have a hybrid structure consisting of $Pr_2Fe_{14}B$ magnets and Vanadium Permendur poles. U18 is 2 m long undulator, that can operate from 5.5 mm to 30 mm gap and provide a peak magnetic field of 1.155 T at cryogenic temperature. U15 is a 3 m long undulator that can operate from 3 mm to 30 mm gap and provide a peak magnetic field of 1.73 T at cryogenic temperature.

Table 1: Main Characteristics of U18 and U15 Undulators

Item	Unit	U18	U15
Technology		Hybrid	Hybrid
Magnet material		CR53	CR53
Remanence	T	1.32 to 1.35 @ 300 K	1.325 @ 300 K
		1.57 @ 77 K	1.55 @ 77 K
Coercivity	kA/m	1835 @ 300 K	1912 @ 300 K
Magnet size (x, z, s)	mm^3	$50 \times 30 \times 6.5$	$50 \times 30 \times 5.5$
Pole material		Vanadium Permendur	Vanadium Permendur
Pole size (x, z, s)	mm^3	$33 \times 22 \times 2.5$	
		$33 \times 22 \times 1.25$	$33 \times 22 \times 1$
Period	mm	18 @ 77 K	15 @ 77 K
Gap range	mm	5.5 to 30	3 to 30
Length	m	2	3
Peak field	T	1.155	1.735

MECHANICAL DESIGN

Figure 3 presents the mechanical design of the cryogenic undulators U18 and U15 inspired from SOLEIL's standard in-vacuum undulators. The carriage is consisting of a metallic base where the frame is welded. Two out-vacuum girders are fixed on the frame and can move vertically thanks to two series of sliders and ball screws. Magnet holders are fixed on two in-vacuum girders connected to the external ones by 36 rods for U15, whereas 24 are needed for U18. The in-vacuum girders are separated by an air gap varying from 3 mm for U15 and 5.5 mm for U18 to 30 mm thanks to two stepper motors. A third one is used to move vertically the undulator over a 10 mm range in order to align in the vertical direction the magnetic axis with the electron beam axis. The vacuum chamber is composed of several ion pumps, titanium sublimation pumps and different instrumentations to ensure an ultra-high vacuum in the vacuum chamber during the operation with electron beam. A 100 μm Cu-Ni foil is placed on the magnetic system and stretched at its extremities of the undulator by a spring-based tensioner system. Permanent magnets are equipped with temperature sensors (PT100) in order to measure the temperature during the cooling down and storage ring operation. Praseodymium based cryogenic undulators are cooled down directly to 77 K, in which the liquid nitrogen crosses the in-vacuum girders through a 12 mm diameter hole, where its inner surface is cooled directly by liquid nitrogen, guaranteeing a better temperature distribution and thus a smaller thermal gradient along the magnetic system.

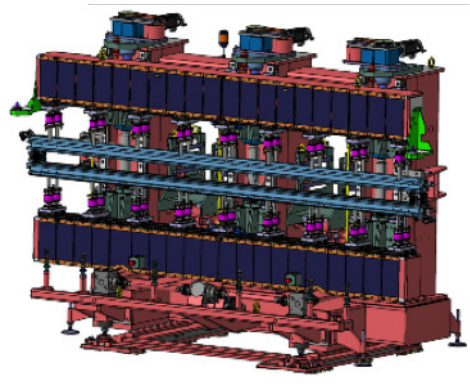

Figure 3: Mechanical design of the U15 cryogenic undulator.

ASSEMBLY OF THE UNDULATOR AT ROOM TEMPERATURE

The assembly and the magnetic corrections of the cryogenic undulators are performed at room temperature in the same conditions as a standard In-Vacuum Undulator (IVU). The figures of merit during the assembly and corrections are the field integrals, trajectories straightness and phase error. They have to be minimized to reduce the impact of the magnetic errors on the undulator performances in terms of photon spectrum and electron beam dynamics.

Modules Assembly and Measurements

As for previous IVUs of SOLEIL, a period of U18 n^{o}1 was constituted by two types of magnet holders. A first one with a single magnet and a second one with a magnet surrounded by two poles. To perform easier swapping after undulator assembly and to allow for a higher number of combinations during assembly, a single module has been designed, which enables to hold a magnet surrounded by two half poles. Figure 4 shows the evolution of modules holder since U18 $_{\text{n}}{}^o$1.

Before holders assembly, all the magnets and holders dimensions have been measured and couples have been calculated to reduce the dispersion of magnet altitudes after their mounting on the holders. Then, the poles are assembled on the holders and shimmed to be at the same altitude as the magnet. A specific torque was defined for all the screws so that all the modules are mechanically identical. Then all the modules are characterized using a rotating coil for field integral measurements and a Hall probe to measure the magnetic field profiles.

ISBN: 978-3-95450-206-6 doi:10.18429/JACoW-FLS2018-THP2WD01

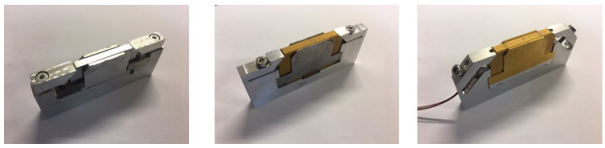

Figure 4: Modules design evolution from U18 n^{o}1 (left), U18 n^{o}2 (middle) and U18 n^{o}3 (right).

Undulator Assembly and Magnetic Corrections

Periods are assembled one by one, two modules on the bottom girder and two on the top one. Each module is adjusted in the longitudinal direction within 15 μm from its theoretical position. For U18 n^{o}2 and 3, all the modules on the girders were vertically pre-shimmed as a function of the magnet altitude and their longitudinal position on the girder. Besides, the longitudinal profile of these girders has been characterized using a Faro laser tracker, ensuring that all the elements of one girder are all at the same altitude. Then, the period is measured using the rotating coil with all the previous periods assembled. A genetic based algorithm software called IDBuilder [16] then deduces the next four convenient modules that fit our requirements.

For U18 n^{o}2 and 3, to obtain optimized trajectories straightness, tighter tolerances have been used during assembly to limit the on-axis field variations from one period to the next one. The on-axis field integrals in both planes should be less than 0.2 G.m, with low variations between two consecutive periods. Also a strong weight is applied so that modules peak field differences should be small.

After the whole assembly of the undulator, the taper of the undulator is adjusted to decrease the phase error and few iterations of rod adjustments are made to correct the low frequency variations of the vertical magnetic field. For all IVUs before U18 n^{o}2, in order to minimize the phase error and optimize the straightness of trajectories, a period of shimming was dedicated to adjust holders or magnets or poles. Thanks to these new mechanical adjustments of magnets and poles on girders and a better control of parameters during assembly, this shimming period was not necessary on U18 n^{o}2 and 3 to reach a very low 2.3 ^{o} and 2.5 ^{o} respectively with an optimized straightness in both planes.

To reduce the effect of the insertion device on the electron beam dynamics, on axis-field integrals have to be minimized so as multipolar terms. After the magic finger correction process on U18 n^{o}3, the on-axis field integrals are less than 0.15 G.m in both planes, integrated gradients are less than 30 G and the off-axis horizontal field integral is reduced from 1.5 G.m to 0.5 G.m and the off-axis vertical field integral from 0.75 G.m to 0.4 G.m.

MEASUREMENTS AND OPTIMIZATIONS AT CRYOGENIC TEMPERATURE

At SOLEIL, magnetic measurements benches have been developed to increase precision and be able to conduct measurements for insertion devices at low temperature. The local magnetic field created by the undulator is measured by a Hall probe (model Bel GH701) and field integrals by a stretched wire. These cryogenic magnetic measurement benches are installed inside the vacuum chamber and removed after the measurements and optimization of the undulator at cryogenic temperature. The Hall probe is mounted on a carriage driven by a stepper motor and slides along a thermalized rail. The position of the Hall probe is measured thanks to a Renishaw interferometer which also triggers the voltmeters. The angular and vertical deformations of the bench are corrected mechanically using shims with different thickness at specific locations. Residual deformations, measured thanks to a laser tracker are then used to correct directly the measured magnetic field.

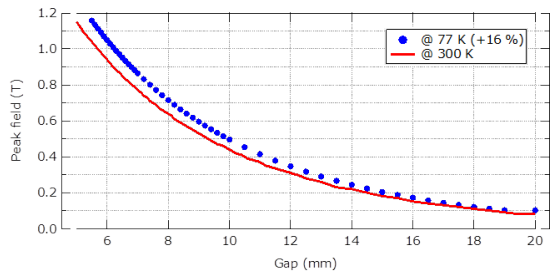

Figure 5: Peak field variation versus gap of U18 n^{o}3 at room (red) and cryogenic temperature (blue).

A temperature variation occurs during the Hall probe displacement along the undulator. The Hall probe resistance and offset dependence with temperature have been calibrated and taken into account to correct the magnetic field values. As shown in Figure 5, at minimal gap, the peak field value is increased by 16 % as expected from the RADIA model [17]. At room temperature, the RMS phase error of U18 n^{o}3 was reduced at 2.45 ^{o} but after cooling down, it increased to 9.5 ^{o}. The rods are contracted vertically by 1.3 mm and in-vacuum girders are contracted longitudinally by 12 mm. These contractions cause in-vacuum girders deformation and the phase error degradation. After few rod adjustments by 5 to 10 μm, the phase error dropped down to 2.6 ^{o} RMS. Figure 6 shows a few variations in the horizontal trajectory straightness and second integral value between room and cryogenic measurements of U18 n^{o}1.

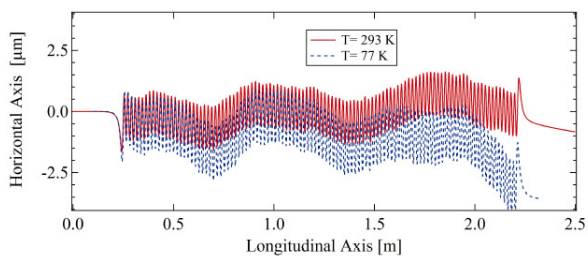

Figure 6: Horizontal trajectory of U18 n^{o}1 at room (red) and cryogenic temperature (blue).

ISBN: 978-3-95450-206-6 doi:10.18429/JACoW-FLS2018-THP2WD01

An evolution of the Hall probe cryogenic bench of U18 is under development for U15 undulator. The major improvement is a dynamic feedback of the Hall probe vertical and horizontal position while moving along the 4 m of the bench [18]. Thanks to Position Sensitive Detectors (PSD), horizontal and vertical positions of the carriage will always be adjusted on the magnetic axis of the undulator thanks to piezo stages, whatever the deformation of the rail guiding the Hall probe. Measurements shows that the thickness and diameter of the pinholes on the hall probe carriage have no effect and that PSD give consistent results thanks to the interferometer (less than 5 μm in both planes).

INSTALLATION ON SOLEIL STORAGE RING

Figure 7 presents the cryogenic undulators U18 n^{o}3 and U18 n^{o}1, installed in the long straight section SDL13 in SOLEIL storage ring. This straight section has been modified to allow for the installation of two canted cryogenic undulators [19] in order to extract two different long beamlines (U18 n^{o}3, dedicated to Anatomix beamline [20] and U18 n^{o}1, dedicated to Nanoscopium beamline) [21].

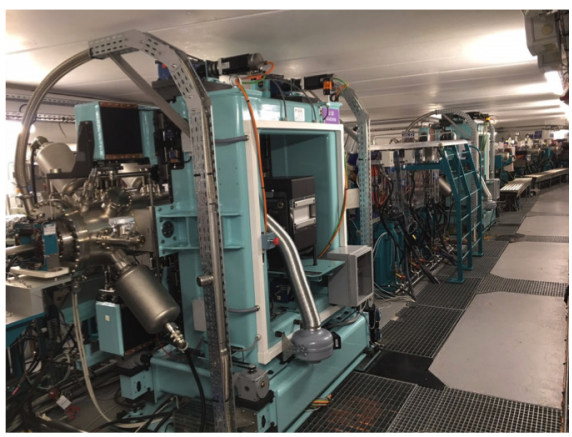

Figure 7: U18 n^{o}3 and U18 n^{o}1 installed in the long straight section 13 of the SOLEIL synchrotron.

Effects on the Electron Beam

After installation and alignment in the tunnel, the magnetic axis has to match with the electron beam path in the straight section. This optimization can be performed at closed gap by moving vertically the entire carriage and observing the vertical betatron tune variations (directly related to the peak magnetic field as shown in Figure 8), or the electron beam decay. Measurements of U18 n^{o}3, shows that this undulator has very low effect on the emittance, injection efficiency and chromaticities between an opened and closed gap.

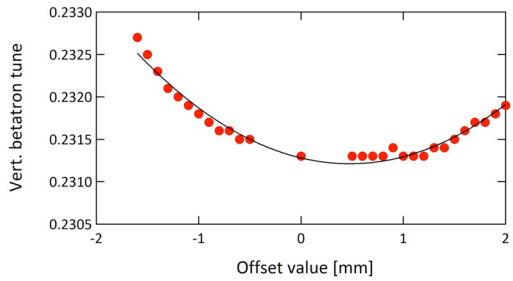

Figure 8: Vertical betatron tune shift variations of the electron beam of U18 n^{o}1 versus the offset of the undulator.

Photon Beam Measurements

The spectrum emitted by the cryogenic undulator U18 n^{o}1 has been measured on the Nanoscopium long beamline [1]. For the beamline commissionning and for regular verifications of the undulator alignment can be performed in a more precise manner in looking at the undulator harmonic shapes for different electron translations or bumps. The vertical offset of the undulator has been adjusted with the beamline so that the electron beam path perfectly matches with the magnetic axis of the undulator. The adjustment has been performed by monitoring the 11 th harmonic for different values of carriage offset, while keeping a magnetic gap of 5.5 mm. Then extracting the intensity and bandwidth of the harmonic, one can find the optimized offset where the intensity is maximal and bandwidth minimal. Same procedure can be applied for taper optimization, by changing the parallelism between top and bottom girders which varies the deflection parameter along the undulator axis. At high energies, few μm of taper can easily be seen. Figure 9 shows the harmonics 9 to 14 of U18 n^{o}1 after offset and taper optimization. It appears that spectra measured on the beamline 77 m away from the source in a 0.1 mm $\times$ 0.1 mm aperture are very close to the ones on an ideal undulator calculated using SRW [22].

Operation with Cryogenic Undulator

At SOLEIL, cryogenic undulators are cooled down with cryo-cooler from Research Instruments. During the 7 years of operation with U18 n^{o}1, only one failure of the cryo-cooler impacted the beam for a few hours. One warming up of the undulator is performed a year due to SOLEIL electrical shutdown. The warming up lasts approximately 24 hours by injecting warm nitrogen gas under 2.5 bar in the undulator. The cooling down of the undulator lasts approximately 6 hours to reach 77 K. The undulator vacuum pressure drops quite rapidly due to the cold mass which acts as a cryo-pump.

ISBN: 978-3-95450-206-6 doi:10.18429/JACoW-FLS2018-THP2WD01

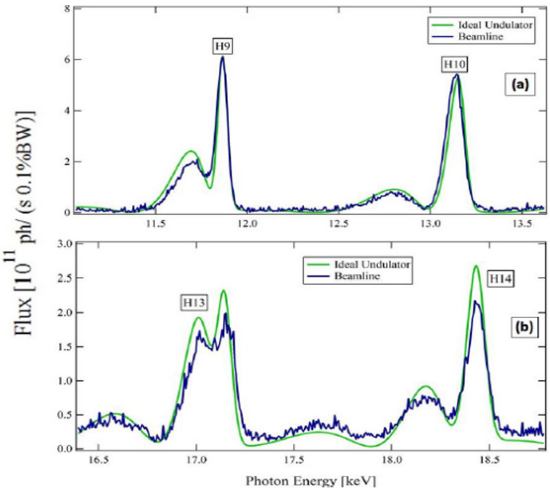

Figure 9: Comparison of the spectra of U18 n^{o}1 measured by Nanoscopium beamline (blue) and the one of an ideal undulator (green).

CONCLUSION

Three cryogenic undulators have successfully been built at SOLEIL, each with a phase error below 3 ^{o} RMS at cryogenic temperatures. New methods of optimizations based on a single module design enables to obtain an optimized undulator directly after assembly (case of the two last cryogenic undulators). These methods will be applied for the assembly of the 3 m long U15 undulator, which will use a SAFALI type bench for measurements at cryogenic temperatures.

ACKNOWLEDGEMENT

The authors thank the SOLEIL-Swedish collaboration for the construction of the U15 undulator. The construction of the ANATOMIX beamline is largely funded by the French National Research Agency (ANR) through the EQUIPEX investment program, project *NanoimagesX*, grant no. ANR-11-EQPX-0031.

REFERENCES

[1] C. Benabderrahmane, M. Valléau, M. E. Couprie *et al*, Development and Operation of a $Pr_2Fe_{14}B$ Based Cryogenic Permanent Magnet Undulator for a High Spatial Resolution X-ray Beamline, Physical Review Accelerators and Beams 20, 033201, (2017)

[2] C. Benabderrahmane, M. Valléau, M. E. Couprie et al, $Nd_2Fe_{14}B$ and $Pr_2Fe_{14}B$ magnets characterization and modeling for cryogenic permanent magnet undulator applications, *Nuclear Instruments and Methods*, A669, pp 1-6, (2012)

[3] T. Hara, T. Tanaka, H. Kitamura, T. Bizen, X. Marechal,T. Seike, T. Kohda, and Y. Matsuura, Cryogenic permanent magnet undulators, *Physical Review Special Topics-Accelerators and Beams*, vol. 7, no. 5, p. 050702, (2004)

[4] T. Tanabe, J. Ablett, L. Berman, D. A. Harder, S. Hulbert, M. Lehecka, G. Rakowsky, J. Skaritka, A. Deyhim, E. Johnson, et al., X-25 cryo-ready in-vacuum undulator at the NSLS, in Synchrotron Radiation Instrumentation; Part One(AIP Conference Proceedings Volume 14879), vol. 879, pp. 283-286, (2007)

[5] T. Tanabe, O. Chubar, D. A. Harder, M. Lehecka, J. Rank, G. Rakowsky, C. Spataro, R. Garrett, I. Gentle, K. Nugent, et al., Cryogenic field measurement of $Pr_2Fe_{14}B$ undulator and performance enhancement options at the NSLS-II, in *Proc AIP Conference*, vol. 1234, p. 29, (2010)

[6] C. Kitegi, P. Cappadoro, O. Chubar, T. Corwin, D. Harder, P. He, H. Fernendez, G. Rakowsky, C. Rhein, J. Rank, et al., Development of a $Pr_2Fe_{14}B$ cryogenic undulator at NSLS-II, Proceedings of International Particle Accelerator Conference, vol. 12, p. 762, (2012)

[7] J. Bahrdt, H. Backer, M. Dirsatt, W. Frentrup, A. Gaupp, D. Just, D. Pfluckhahn, M. Scheer, B. Schulz, et al., Cryogenic design of a PrFeB-based undulator, in *Proc. International Particle Accelerator Conference*, pp. 3111-3113, (2010)

[8] C. Benabderrahmane, P. Berteaud, M. Valléau, C. Kitegi, K. Tavakoli, N. Béchu, A. Mary, J. Filhol, and M. Couprie, $Nd_2Fe_{14}B$ and $Pr_2Fe_{14}B$ magnets characterization and modeling for cryogenic permanent magnet undulator applications, *Nuclear Instruments and Methodsin Physics Research SectionA: Accelerators, Spectrometers, Detectors and Associated Equipment*, vol. 669, pp. 1-6, (2012)

[9] M. Couprie, C. Benabderrahmane, P. Berteaud, F. Briquez, C. Bourassin-Bouchet, F. Bouvet, L. Cassinari, L. Chapuis, M. Diop, J. Daillant *et al*., The status of the LUNEX5 project, Proceedings of Free Electron Laser Conference, vol. 14, (2014)

[10] C. Kitegi, J. Chavanne, D. Cognie, P. Elleaume, F. Revol, C. Penel, B. Plan, and M. Rossat, Development of a cryogenic permanent magnet in-vacuum undulator at the ESRF, vol. 6, pp. 3559-3561, (2006)

[11] C. Ostenfeld and M. Pedersen, Cryogenic in-vacuum undulator at DANFYSIK, Proceedings of International Particle Accelerator Conference, vol. 10, pp. 3093-3095, (2010)

[12] T. Tanaka, T. Seike, A. Kagamihata, H. Kitamura, T. Schmidt, A. Anghel, M. Brugger, W. Bulgheroni, and B. Jakob, In-situ magnetic correction for cryogenic undulators, Proceedings of International Particle Accelerator Conference, vol. 10, pp. 3147-3149, (2010)

[13] M.-E. Couprie *et al*., An application of laser plasma acceleration: towards a free electron laser amplification, Plasma Physics And Controlled Fusion, vol 58, n^{o}3, (2016)

[14] A. Loulergue, M. Labat, C. Evain, C. Benabderrahmane, V. Malka, and M. Couprie, Beam manipulation for compact laser wakefield accelerator based free-electron lasers, *New Journal of Physics*, vol. 17, n^{o}2, 023028, (2015).

[15] D. Givord, H.S. Li., Magnetic properties of $Y_2Fe_{14}B$ and $Nd_2Fe_{14}B$ single crystals, Solid state communications, 51(11), pp 857-860, (1984)

[16] O. Chubar, O. Rudenko and al, Application of genetic algorithms to sorting, swapping and shimming of the SOLEIL undulator magnets, *AIP Conf. Proc.*, 879, 359, (2007)

[17] O. Chubar, P. Elleaume, and J. Chavanne., A three-dimensional magnetostatics computer code for insertion devices, *Journal of synchrotron radiation* 5.3, pp 481-484, (1998)

ISBN: 978-3-95450-206-6 doi:10.18429/JACoW-FLS2018-THP2WD01

[18] T. Tanaka, T. Seike, H. Kitamura, Measurement of SPring-8 XFEL undulator prototype with the SAFALI system, Proceedings of Free Electron Laser Conference, Gyeongju, Korea, pp 371-373, (2008)

[19] A. Somogyi, C. Kewish, F. Polack, and T. Moreno, The scanning nanoprobe beamline NANOSCOPIUM at synchrotron SOLEIL, in *Proc. 10th International Conference on X-ray Microscopy,* vol. 1365, pp. 57-60, (2011).

[20] A. Loulergue, C. Benabderrahmane, F. Bouvet, P. Brunelle, M.-E. Couprie, J.-C. Denad, T. Moreno, A. Nadji, L. Nadolski, F. Polack *et al*, Double low beta straight section for dual canted undulators at SOLEIL, *Proceedings of the IPAC conference*, WEPEA011, pp 2496-2499, (2010).

[21] T. Weitkamp, M. Scheel, J.-L. Giorgetta, V. Joyet, V. Le Roux, G. Cauchon, T. Moreno, F. Polack, A. Thompson, and J.-P. Samama, The tomography beamline ANATOMIX at Synchrotron SOLEIL, *J. Phys. Conf. Series* 849 (2017) 012037, doi:10.1088/1742-6596/849/1/012037

[22] O. Chubar, and P. Elleaume, Accurate and efficient computation of synchrotron radiation in the near field region, in *Proc. EPAC1998.*

ISBN: 978-3-95450-206-6 doi:10.18429/JACoW-FLS2018-FRA1PL01

SUMMARY OF WORKING GROUP A (WG-A): LINAC-BASED LIGHT SOURCES

Winfried Decking, DESY, Hamburg, Germany
Luca Giannessi, Elettra-Sincrotrone, Trieste, and ENEA C.R. Frascati, Italy
Heung-Sik Kang, Pohang Accelerator Laboratory, Pohang, Korea
Tor Raubenheimer†, SLAC, Menlo Park, CA, USA

INTRODUCTION

The WG-A program was broken into 6 sessions with 21 invited and contributed talks. A discussion was scheduled at the end of each pair of sessions and a set of questions had been developed to help focus the discussions in the working group. The sessions are listed below along with highlights from the discussions in each section.

MORE ON NEW FACILITIES

Presentations

1. **Dong Wang (SINAP) :** *The Shanghai Hard X-ray Free Electron Laser Project*
2. **Tor Raubenheimer (SLAC) :** *Progress on the LCLS-II and the High Energy Upgrade of LCLS-II*
3. **Chang-Ki Min (PAL):** *PAL-XFEL and its time-resolved experiment with sub-20-fs timing jitter*

There was no focused discussion on the new facilities although the tour on Friday took us through the Shanghai Synchrotron Radiation Facility (SSRF) and the Soft X-ray FEL (SXFEL) at SINAP.

MACHINE OPTIMIZATION

Presentations

1. **Daniel Ratner (SLAC):** *Report on an ICFA BD mini-workshop on "Machine learning for particle accelerators"*
2. **Lars Fröhlich (DESY):** *Automated Optimization of Machine Parameters at the European XFEL*
3. **Zeng Li (SINAP):** *The Feasibility of Neuron Network-Based Beam-Based Alignment*
4. **Haeryong Yang (PAL):** *FEL optimization through BBA with undulator spectrum analysis and undulator optics matching*

Focus Questions and Discussion:

1. What are the optimization strategies used in tuning a single pass, linac-based FEL for user operation?
2. Will artificial intelligence play a role in tuning and optimizing FEL sources?
3. What are the main differences between the optimization strategies in 3rd and 4th generation light sources?

Machine preparation is time consuming, automatic optimization reduces the preparation times and frees operators from repetitive annoying procedures. It reduces the possibility of errors and may help in retrieving conditions that are operator independent. Furthermore, the **tighter tolerances in 4th generation facilities may prevent them from relying simply on "design models"** because the real system is only partially known and diagnostics do not provide a complete picture. In this case, **automatic optimization becomes essential** to achieve the maximum performance in a reasonable time.

Artificial intelligence techniques are starting to be used to create more accurate "models." Some examples of applications include reconstruction of machine conditions by analysing large amount of stored data and running virtual machines to train optimizers. **In the next generation photon sources, automatic optimizations and machine learning with AI is also playing a role in the design phase** (see CompactLight design study, A. Latina in WG-C). **Interesting cases of non-trivial unexpected behaviors are being "discovered" by optimizers** with advanced algorithms, as the taper optimization (D. Ratner report WG-A). This is **very promising** for the future.

SCHEMES FOR PRODUCTION OF ULTRASHORT PULSES IN EUV AND X-RAY FELS

Presentations

1. **James Mac Arthur (SLAC) on behalf of A. Marinelli, J. Duris, & XLEAP team:** *X-ray Laser-Enhanced Attosecond Pulses*
2. **Xi Yang (BNL) (presented by Luca Giannessi):** *Generation of atto-second pulses in FELS: Ultrashort pulse generation and superradiance*
3. **Neil Thompson (STFC/DL/ASTeC):** *Free-Electron Laser R&D in the UK - steps towards a national XFEL facility*

Focus Questions and Discussion:

1. What are the main challenges and desiderata in the generation of ultrashort pulses in FELs?
2. What are the strategies for temporal synchronization of ultrashort (sub-fs) FEL pulses and of the light properties?

* This work supported in part by DOE Contract No. DE-AC02-76SF00515.
† torr@stanford.edu

ISBN: 978-3-95450-206-6 doi:10.18429/JACoW-FLS2018-FRA1PL01

In hard-Xray coherent diffraction imaging, **fs or sub-fs pulses are highly desirable** for single molecule imaging. Pulses below 10-15 fs are also needed in XUV-Soft xrays FELs in the study of non-linear processes and electron dynamics. **Techniques to achieve these conditions have been proposed and demonstrated.** However synchronization may indeed be an issue. **Seeded FELs provide fs synchronization** with external lasers. SASE is affected by the e-beam arrival time jitter, but **e-SASE can lock a single spike to an external laser.** Synchronization networks with resolution in the sub-fs range in new facilities is demonstrated in tests (F. Kaertner, plenary) and installed in new facilities. **Diagnostics are required to fully benefit of such short pulses.** High resolution diagnostics are being developed including optical streaking, TCAV's, …

LONGITUDINAL COHERENCE IN SOFT AND HARD X-RAY WAVELENGTH RANGES

Presentations

1. **Enrico Allaria (ELETTRA):** *EEHG experiment at FERMI*
2. **Kwang-Je Kim (ANL):** *An X-Ray FEL Oscillator for Novel Sciences*
3. **Evgeny Schneidmiller (DESY):** *Harmonic lasing in XFELs: theory and experiment*
4. **Shan Liu (DESY):** *Simulations and performance study of an optimized longitudinal phase space for the hard X-ray self-seeding at the European XFEL*

Focus Questions and Discussion:

1. Seeded FELs have many nice properties with respect to SASE sources, as improved stability and longitudinal coherence. What are the available options to extend the wavelength range of seeded FELs to shorter wavelengths, covering the soft and hard X-ray spectral range?
2. What are the main differences between self-seeding and external seeding from the point of view of the light properties?

The coherence of an XFELO looks promising and **outperforms all presently available alternatives.** A critical technology is the X-ray cavity which would benefit the XFELO as well as RAFEL configurations.

A recurring question is: **what is the lower wavelength limit for external seeding? I**t is believed that the main limitations from **microbunching instability and IBS** but the answer depends on R&D critical experiments that are going to give an indication about the best way to proceed. These include:

- EEHG test at SXFEL and FERMI
- Slippage enhanced-SASE configurations at CLARA and PSI
- Harmonic seeding studies at many facilities
- Further developments of Self seeding

It seems likely that the best solution may be some combination of these techniques that is optimized for the different wavelength regimes.

ELECTRON BEAM COLLECTIVE EFFECTS - MODELLING AND SIMULATION CODES

Presentations

1. **Martin Dohlus (DESY):** *Fast simulation code including collective effects*
2. **Kaiqing Zhang (SINAP):** *Eliminating the microbunching instability-induced sideband in a soft x-ray self-seeding FEL*
3. **Bas van der Geer (Pulsar Physics, Eindhoven):** *GPT-CSR: a new simulation code for CSR effects*
4. **Peter Williams (STFC/DL/ASTe):** *A Staged, Multi-User X-Ray Free Electron Laser & Nuclear Physics Facility based on a Multi-Pass Recirculating Superconducting CW Linac*

Focus Questions and Discussion:

1. What are the main challenges in the understanding and mitigating the microbunching instability in linac based accelerators?
2. How well do the present simulations codes reproduce the detailed FEL performance?
3. What be included in the ideal FEL simulation code suite?

There was no time for a formal discussion but the following comments were extracted from the questions and short discussion following the talks. Simulation codes do need to be **optimized** to deal with various aspects of **physics problems involved in the beamline: gun codes/linac codes/FEL codes/Photon codes. However the boundaries between systems are not completely separated**. Some problems require crossing these boundaries. Examples include:

- **EEHG and narrow bandwidth affected by microbunching instability**
- Phase space folding is missing in most FEL codes although detailed comparisons between codes have not seen large discrepancies.

One concern that was noted is that in dealing with the **interfaces between plasma acceleration and "linac" and "FEL"** codes, it is important to represent tails or details in phase space from the FEL/accelerator perspective.

MULTI-USER SIMULTANEOUS OPERATION

Presentations

1. **Aymeric Robert (SLAC) (on behalf of Diling Zhu):** *Results from the diamond grating multiplexing study at LCLS (January) to feed 3 experiments simultaneously*

ISBN: 978-3-95450-206-6 doi:10.18429/JACoW-FLS2018-FRA1PL01

2. **Giuseppe Penco (ELETTRA):** *Two-bunch operation with ns temporal separation at FERMI*
3. **Bart Faatz (DESY):** Optimizing of electron beam distribution at European XFEL and FLASH

Focus Questions and Discussion:

1. What are the ultimate challenges and limitation in simultaneously serving multiple beamlines in FEL facilities?
2. Can we start thinking to experiments with multiple FEL pulses from independent FEL lines?

Again, there was no time for a formal discussion but the following comments were extracted from the questions and short discussion following the talks. All the **upcoming facilities are planning** or operating simultaneous **multi-beam operation.** Different ways to generate and handle multiple bunches and beam splitting to different experiments were presented. In some cases, multi-pulse operation could even be dedicated to a single experiment, e.g. extending the capabilities of pump-probe investigations.

One thing stressed is the importance of moving toward a 2/1 oversubscription rate for a healthy "acceptance statistics." It is expected that this should change quickly (from the present 4:1) with the new facilities coming into operation and with simultaneous use of multiple FEL lines. It should be noted that the **efficiency of multiple FEL lines is not 100%** (2 FEL lines with 1 linac or beam splitting do not correspond to 200% equivalent beam time). The schedule becomes more rigid and last minute changes in the user's requests make it harder for beam sharing. Good question from Aymeric Robert: **What is the "Definition of success?" Experiments often require very different setups -> Do not lose flexibility.**

ACKNOWLEDGEMENTS

The working group conveners would like to thank all of the presenters and members of the discussion sessions as well as the Local Organizing Committee and the support staff for an excellent workshop.

ISBN: 978-3-95450-206-6 doi:10.18429/JACoW-FLS2018-FRA1PL02

WG-B: RING BASED LIGHT SOURCES - SUMMARY

Y. Li, BNL, Long Island, New York, USA
Q. Qin, IHEP, Beijing, China
R.P. Walker, DLS, Daresbury, UK

WORKING GROUP TOPICS

In the six Working Group B sessions there were 21 oral presentations which included:

i/ overviews of many of the current ring based light source projects that are underway or being studied around the world: APS-U, BESSY-VSR, ESRF-EBS, Elettra 2.0, HALS, HEPS, KEK-LS, PETRA IV, SOLEIL upgrade, SPS-II,

ii/ various reviews of 'hot topics' such as injection schemes (Z. Duan), short pulse schemes (A. Jankowiak), round beam challenges (P. Kuske, plenary talk) and collective effects (R. Nagaoka),

iii/ more specific talks on topics such as ion effects, impedances, transient beam loading and less conventional ring-based light source schemes.

WG-B was asked to consider the following questions:

- Are there new ideas for storage ring lattices that could go beyond currently-envisioned MBA lattices?
- Should we be making more use of permanent- or superconducting-magnet technologies?
- Should new facilities plan for a full-energy linac injector to allow pushing the ring as far as possible?
- How can we make short lifetimes workable, so we can continue pushing the emittance down?
- What theory and code developments do we need to ensure that next-generation rings work as planned?
- What experiments can be performed on existing rings to remove uncertainties for next-generation rings?
- Besides rings optimized for ultra-high-brightness, what other types of rings should we be designing?
- What's needed to make first-principles impedance models more accurate in predicting instabilities?
- What commissioning strategies are best for next-generation rings?
- How do storage ring design and beamline design interact; e.g., round vs flat beams, tailoring of beta functions vs lowest emittance?
- Can ultra-bright rings also provide short pulses?
- Is low emittance more demanding of insertion device quality, e.g., phase errors?
- Are there new beam stability challenges and what are the best ways to address these?

Although neither the presentations nor the discussions addressed these questions directly, in the following we will nevertheless attempt to make some relevant comments based on the content of the presentations at FLS2018.

RESPONSES TO QUESTIONS

Are there new ideas for storage ring lattices that could go beyond currently-envisioned MBA lattices?

The hybrid MBA lattice of ESRF-EBS has been adopted for APS-U and HEPS and is the current baseline lattice for PETRA IV and the SOLEIL upgrade. Anti-bends are incorporated in APS-U and in one option for HEPS (with anti-bends and superbends).

Z. Bai presented various MBA lattices with sextupoles distributed throughout the cell for HALS; these have additional symmetry planes and odd-π phase advance in both planes across the mid-plane. 6BA and 8BA lattices were presented with emittances of 26-36 pm at 2.4 GeV with DA of ±1.5-2 mm and large MA. A further MBA lattice type with two pairs of interleaved dispersion bumps with –I transformation between each was presented; a 7BA version of this produces 32 pm natural emittance with DA of ±3 mm and large MA. Adding longitudinal gradient bends, anti-bends, and 2T superbends produces a lattice with 23 pm emittance and similar DA/MA.

I. Agapov presented an alternative lattice for PETRA IV with "double –I optics": in the first part of the arc there is π phase advance between points of maximum dispersion and βx, and in the second part there is π phase advance between points of maximum βy. This was said to require further development, but looks promising.

In other cases the desire for the lowest possible emittance has been compromised for the advantage of gaining additional straight section space in the middle of the arc where insertion devices or other components can be located. What generically might be called "split-MBA" lattices are being considered for Elettra 2.0 (6BA), SPS-II (6BA) and KEK-LS (8BA).

Should we be making more use of permanent- or superconducting-magnet technologies?

We believe that permanent magnet technology in particular has many benefits for future light sources. In a first development of this kind, ESRF-EBS will use permanent magnet longitudinal gradient dipoles. In WG-D, A. Vorozhtsov presented a very interesting design of a high gradient (234 T/m) permanent magnet quadrupole with bore radius of 5.5 mm for possible application in a future upgrade of MAX-IV. The design presented has a tuning range of ±5% which might limit the flexibility of the lattice.

ISBN: 978-3-95450-206-6 doi:10.18429/JACoW-FLS2018-FRA1PL02

Should new facilities plan for a full-energy linac injector to allow pushing the ring as far as possible?

A 3 GeV linac injector is considered for SPS-II, however this is in view of a future short-pulse/FEL rather than for beam dynamics reasons. So far, no ring based light source is pushed to an extent where the booster/accumulator emittance or cycle time is a limiting factor and so would benefit from a full energy linac.

How can we make short lifetimes workable, so we can continue pushing the emittance down?

The small emittance required for future light sources naturally tends to reduce the lifetime through Touschek scattering and various ways of dealing with this have been developed. APS-U will use a 3rd harmonic cavity at 1.4 GHz while HEPS will employ low frequency RF and a 3rd harmonic at 500 MHz. Use of a 3rd harmonic cavity in PETRA IV is also being considered.

Short lifetime always places a greater demand on the injector, and this is particularly true for swap-out injection when the whole bunch charge needs to be injected. The required fill pattern uniformity will ultimately determine the cycle time of the injector. For example, in the high brightness mode in HEPS with 680 bunches with 5 hour lifetime, a continuous swap-out at 1 Hz results in nearly a 4% variation of bunch charge along the fill. Clearly a lower lifetime will either worsen the uniformity or require an increased injection rate.

Short lifetime also implies higher electron losses and so requires careful attention to radiation safety issues, particularly for swap-out schemes. This might result in greater emphasis on achieving high injection efficiency to minimise losses.

What theory and code developments do we need to ensure that next-generation rings work as planned?

There is generally a high degree of confidence in the single particle dynamics codes that are in general use and have been widely benchmarked against each other and against real machines. As apparent from the review talk on Collective Effects in Next-Generation Light Sources by R. Nagaoka however, more work is still needed in the area of impedances and collective effects to develop models, cross-check codes and benchmark against experiments.

What experiments can be performed on existing rings to remove uncertainties for next-generation rings?

Almost any experiments comparing non-linear single particle dynamics, impedance measurements or collective effects with simulations have a relevance for next generation rings since any discrepancies could potentially have far reaching consequences. A significant discrepancy between measured and simulated bunch lengthening in MAX-IV was mentioned.

Existing rings also serve as test-beds for new hardware R&D, such as BPM electronics and injection elements (APS), and also different operating modes. For example, tests of round beam operation have been made at APS and are planned at NSLS-II.

Besides rings optimized for ultra-high-brightness, what other types of rings should we be designing?

The vast majority of proposed new rings and ring upgrades are targeting lower emittance, driven by the science need for radiation with higher brightness and higher transverse coherence. There are exceptions however, one being the BESSY-VSR project (see presentation by A. Jankowiak) which is targeting instead short pulses.

S. Khan described Coherent Harmonic Generation experiments in DELTA and the planned ring modification in order to carry out EEHG experiments.

C. Tang presented the outline design of a ring designed for Steady-State Micro Bunching (SSMB). The goal of SSMB is to generate very high power EUV radiation with a small ring (less than 1 GeV), while the EUV power could be as high as 1 kW if successful, and appropriate for the purpose of lithography. The ring could be very cheap and small compared to a machine based on ERL or FEL.

What's needed to make first-principles impedance models more accurate in predicting instabilities?

In his review talk R. Nagaoka referred to a recent comparison between calculated and measured impedance in different machines [V. Smaluk, NIM A888 (2018) 22.] which in the majority of cases showed discrepancies of 100% or more. To pursue the possible origins of discrepancies, the following three possibilities were numerically studied with simple pillbox cavities (using ECHO): 1) Interference of wake fields, 2) Computation mesh size, 3) Impedance bandwidth. The results indicate that while the mesh size and impedance bandwidth influence by typically less than 10%, the interference causes more than 100% of variations. He also pointed out that such interference is likely to be enhanced for next generation rings as both the chamber dimensions and the spacing between objects is further reduced. Clearly this is an area that requires more work, more model and code development and comparison with measurements on existing machines.

What commissioning strategies are best for next-generation rings?

Commissioning strategies are clearly needed for next generation light sources. R. Lindberg pointed out that for APS-U simulations show zero chance of first turn without trajectory correction and low chance of multi-turn capture after first-turn trajectory correction if sextupoles are on. A great deal of effort has therefore gone in to developing a

ISBN: 978-3-95450-206-6 doi:10.18429/JACoW-FLS2018-FRA1PL02

commissioning simulation for APS-U with a high degree of realism including error generation, trajectory correction, first orbit correction leading to stored beam, final orbit correction and lattice correction. Simulations are tracking-based, including physical apertures, injection errors, static and variable and BPM shot-to-shot noise. The conclusion of this study is that fast commissioning is possible with >95% success rate. Y. Jiao also described a commissioning code for HEPS to achieve first turn and then stored beam.

How do storage ring design and beamline design interact; e.g., round vs flat beams, tailoring of beta functions vs lowest emittance?

As a general statement, it is clear that in next generation light sources in particular, ring and beamline design must go hand-in-hand in order to achieve the desired photon beam characteristics at the sample.

Optimum brightness from undulators is obtained in principle with beta functions of the order L/π, where L is the length of the device, however the sensitivity depends significantly on how close one is to, or far away from, the diffraction limit at the photon energy of interest. This is taken into account in the current design of the SOLEIL upgrade lattice with beta functions of 1m in both planes at the insertion device. On the other hand, the latest design of HEPS has alternating high/low beta sections. It is accepted that a lattice with identical cells may benefit nonlinear optimization by keeping more periodicity, but this does not satisfy the range of needs of users.

Round beams (strictly meaning equal beam sizes and divergences in both planes, however equal emittance is also often referred to as a round beam) were discussed by P. Kuske. Round beams are beneficial for the machine (decreased intra-beam and Touschek scattering) but not necessarily for beamlines. At high photon energies brightness and coherence are higher for flat beams than round beams. APS has round beams as the baseline, whereas for PETRA IV round beams were initially of interest but flat beams are now preferred. As P. Kuske pointed out, it might be easier and more stable to obtain 100% coupling than the 10-20% which is required to maintain vertical emittances similar to what is achieved today in many light sources (~10 pm) in rings of 50-100 pm horizontal emittance.

Can ultra-bright rings also provide short pulses?

As mentioned above, most new rings favour low frequency RF and/or bunch lengthening harmonic cavities to mitigate naturally short bunches and hence reduce IBS and increase Touschek lifetime. Nevertheless there is interest in short bunches in Elettra 2.0 and for the SOLEIL upgrade; in the latter case some consideration has been given to implementing the BESSY-VSR double harmonic RF scheme. A study of the same scheme in HEPS was also published some time ago [S-K. Tian et al., Chinese Physics C 39 (2015) 127001].

Is low emittance more demanding of insertion device quality, e.g., phase errors?

There were no relevant presentations or discussion on this point but our opinion is that current state-of-the art phase errors and trajectory correction will be sufficient. Tolerances on field integral (multipole) errors might however be more demanding depending on the sensitivity of the lattice.

Are there new beam stability challenges and what are the best ways to address these?

Orbit stability at the level of 10% of rms beam size is already achieved in existing rings with vertical emittance at the 10 pm level or less, so achieving this in next generation rings with similar vertical emittance and horizontal emittance which is still larger than this value should not be a major problem. Some improvement in bandwidth of correction may be needed to take into account that detectors on beamlines continue to increase in repetition rate. More widespread use of nano focused photon beams may also demand a more integrated approach with feedback from the beamline to the electron beam.

Another stability issue that was mentioned is that of the emittance. It was pointed out that in very low emittance lattices the emittance might be more sensitive to insertion device gap variation, and hence some emittance stabilisation might be needed to prevent fluctuations in intensity being seen by beamline users.

ISBN: 978-3-95450-206-6

List of Authors

Bold papercodes indicate primary authors; ~~crossed out~~ papercodes indicate 'no submission'

ISBN: 978-3-95450-206-6

ISBN: 978-3-95450-206-6

ISBN: 978-3-95450-206-6

— T —

— U —

— V —

— W —

— X —

ISBN: 978-3-95450-206-6

— Y —

— Z —

ISBN: 978-3-95450-206-6

Institutes List

ALBA-CELLS Synchrotron
Cerdanyola del Vallès, Spain
- Pérez, F.

Ankara University Institute of Accelerator Technologies
Golbasi, Turkey
- Aksoy, A.A.

ANL
Argonne, Illinois, USA
- Antipov, S.P.
- Berg, W.
- Borland, M.
- Byrd, J.M.
- Calvey, J.R.
- Dooling, J.C.
- Fuerst, J.D.
- Gluskin, E.
- Hasse, Q.B.
- Hui, D.
- Ivanyushenkov, Y.
- Kasa, M.
- Kesgin, I.
- Kim, K.-J.
- Lindberg, R.R.
- Power, J.G.
- Shiroyanagi, Y.
- Sun, Y.
- Xiao, A.
- Yang, B.X.
- Zholents, A.

AS - ANSTO
Clayton, Australia
- Dowd, R.T.

ASML Netherlands B.V.
Veldhoven, The Netherlands
- Akkermans, J.A.G.
- Setija, I.
- Smorenburg, P.W.

BNL
Upton, Long Island, New York, USA
- Cheng, W.X.
- Ha, K.
- Li, Y.
- Padrazo Jr, D.
- Rainer, R.S.
- Shaftan, T.V.
- Yang, X.

CAEP/IAE
Mianyang, Sichuan, People's Republic of China
- He, T.H.
- Lao, C.L.
- Li, M.
- Li, P.
- Lin, S.F.
- Luo, X.
- Pan, Q.
- Shan, L.J.
- Shen, X.
- Wang, H.
- Wang, J.
- Wu, D.
- Xiao, D.X.
- Xu, Y.
- Yang, X.
- Zhang, P.
- Zhou, K.

CERN
Geneva, Switzerland
- Charles, T.K.
- Latina, A.
- Schulte, D.
- Stapnes, S.
- Wuensch, W.

CFEL
Hamburg, Germany
- Shafak, K.

Cockcroft Institute
Warrington, Cheshire, United Kingdom
- Angal-Kalinin, D.
- Bailey, I.R.
- Brynes, A.D.
- Clarke, J.A.
- Cowie, L.S.
- Dunning, D.J.
- Goudket, P.
- Jackson, F.
- Jones, J.K.
- McIntosh, P.A.
- M^{c}Neil, B.W.J.
- Militsyn, B.L.
- Moss, A.J.
- Muratori, B.D.
- Owen, H.L.
- Smith, S.L.
- Surman, M.
- Thompson, N.
- Wheelhouse, A.E.
- Williams, P.H.

Cycle GmbH
Hamburg, Germany
- Shafak, K.

ISBN: 978-3-95450-206-6

Czech Republic Academy of Sciences, Institute of Physics
Prague, Czech Republic
- Korn, G.
- Molodozhentsev, A.Y.
- Pribyl, L.

DELTA
Dortmund, Germany
- Büsing, B.
- Khan, S.
- Lockmann, N.M.
- Mai, C.
- Meyer auf der Heide, A.
- Riemann, B.
- Sawadski, B.
- Schmutzler, M.
- Ungelenk, P.

DESY Zeuthen
Zeuthen, Germany
- Good, J.D.
- Koschitzki, C.
- Krasilnikov, M.
- Qian, H.J.
- Stephan, F.

DESY
Hamburg, Germany
- Agapov, I.V.
- Brinkmann, R.
- Chae, Y.-C.
- Decking, W.
- Dohlus, M.
- Faatz, B.
- Fröhlich, L.
- Gavaldà, X.N.
- Keil, J.
- Kocharyan, V.
- Kuhlmann, M.
- Liu, S.
- Rönsch-Schulenburg, J.
- Schneidmiller, E.
- Scholz, M.
- Schreiber, S.
- Tischer, M.
- Wanzenberg, R.
- Xin, M.
- Yurkov, M.V.

Deutsches Elektronen Synchrotron (DESY) and Center for Free Electron Science (CFEL)
Hamburg, Germany
- Kärtner, F.X.

Devi Ahilya University
Indore, India
- Gehlot, M.
- Khullar, R.
- Mishra, G.

DLS
Oxfordshire, United Kingdom
- Walker, R.P.

Elettra-Sincrotrone Trieste S.C.p.A.
Basovizza, Italy
- Allaria, E.
- D'Auria, G.
- Di Mitri, S.
- Geometrante, R.
- Giannessi, L.
- Karantzoulis, E.
- Penco, G.
- Spampinati, S.

ENEA C.R. Frascati
Frascati (Roma), Italy
- Giannessi, L.
- Nguyen, F.

ESRF
Grenoble, France
- Benabderrahmane, C.
- Chavanne, J.
- Jacob, J.
- Le Bec, G.
- Perron, T.P.
- Sanchez del Rio, M.

Euclid Beamlabs LLC
Bolingbrook, USA
- Antipov, S.P.
- Jing, C.-J.

Euclid TechLabs, LLC
Solon, Ohio, USA
- Antipov, S.P.
- Jing, C.-J.

FRIB
East Lansing, Michigan, USA
- York, R.C.

HIP
University of Helsinki, Finland
- Aicheler, M.

Hiroshima University, Graduate School of Science
Higashi-Hiroshima, Japan
- Hirano, K.

ISBN: 978-3-95450-206-6

HZB
Berlin, Germany
- Feikes, J.
- Jankowiak, A.
- Kuske, P.
- Li, J.
- Ries, M.

HZDR
Dresden, Germany
- Schramm, U.

IAP/RAS
Nizhny Novgorod, Russia
- Kuzikov, S.V.
- Savilov, A.V.

IFIC
Valencia, Spain
- Esperante Pereira, D.

IHEP
Beijing, People's Republic of China
- Chen, J.
- Cui, X.
- Deng, B.
- Duan, Z.
- Guo, D.Z.
- Guo, Y.Y.
- He, P.
- Huo, L.
- Ji, D.
- Jiao, Y.
- Li, J.Y.
- Li, Q.
- Li, X.Y.
- Liu, B.Q.
- Liu, B.
- Liu, P.
- Ma, Y.
- Peng, Y.M.
- Qin, Q.
- Shi, H.
- Shi, X.L.
- Tian, S.K.
- Wang, G.
- Wang, J.Q.
- Wang, L.
- Wang, N.
- Wei, Y.
- Xu, G.
- Xu, H.S.
- Yan, F.
- Yang, Y.C.
- Yu, C.H.
- Zhang, L.
- Zhao, Y.L.

INFN/LNF
Frascati (Roma), Italy
- Ferrario, M.

Institute of High Energy Physics (IHEP)
People's Republic of China
- Wang, X.J.

JLab
Newport News, Virginia, USA
- Allison, T.L.
- Benson, S.V.
- Douglas, D.
- Musson, J.
- Roblin, Y.
- Satogata, T.
- Spata, M. F.
- Tennant, C.

KEK
Ibaraki, Japan
- Harada, K.
- Higashi, N.
- Honda, T.
- Kobayashi, Y.
- Nakamura, N.
- Obina, T.
- Sakanaka, S.
- Takahashi, T.
- Tanaka, O.
- Tsuchiya, K.
- Yamamoto, N.

KIT
Karlsruhe, Germany
- Bernhard, A.
- Brosi, M.
- Bründermann, E.
- Caselle, M.
- Funkner, S.
- Kehrer, B.
- Müller, A.-S.
- Nasse, M.J.
- Niehues, G.
- Papash, A.I.
- Rota, L.
- Ruprecht, R.
- Schuh, M.
- Schönfeldt, P.
- Siegel, M.
- Steinmann, J.L.
- Weber, M.

KYMA
Trieste, Italy
- Geometrante, R.

ISBN: 978-3-95450-206-6

Kyoto University
Kyoto, Japan
- Kii, T.

LAL
Orsay, France
- Faus-Golfe, A.
- Vallerand, C.

Lancaster University
Lancaster, United Kingdom
- Bailey, I.R.

LBNL
Berkeley, California, USA
- Ambat, M.V.
- Barber, S.K.
- De Santis, S.
- Isono, F.
- Leemans, W.
- Luo, T.H.
- Pappas, G.C.
- Penn, G.
- Placidi, M.
- Schroeder, C.B.
- Steier, C.
- Swenson, C.A.
- van Tilborg, J.
- Waldron, W.L.

LOA
Palaiseau, France
- Corde, S.
- Gautier, J.
- Lambert, G.
- Mahieu, B.
- Malka, V.
- Phuoc, K.T.
- Thaury, C.

MAX IV Laboratory, Lund University
Lund, Sweden
- Andersson, Å.
- N'gotta, P.
- Tavares, P.F.
- Vorozhtsov, A.S.

MIT
Cambridge, Massachusetts, USA
- Granados, E.

National Technical University of Athens
Athens, Greece
- Gazis, E.N.

NITTTR
Bhopal, India
- Jeevakhan, H.
- Kumar, S.

PAL
Pohang, Kyungbuk, Republic of Korea
- Eom, I.
- Han, J.H.
- Hu, J.
- Jung, S.H.
- Kang, H.-S.
- Kim, S.H.
- Lee, H.-S.
- Lee, J.
- Lee, S.B.
- Lee, S.J.
- Lee, T.-Y.
- Min, C.-K.
- Park, S.S.
- Shin, S.
- Yang, H.

PhLAM/CERLA
Villeneuve d'Ascq, France
- Bielawski, S.
- Evain, C.
- Szwaj, C.

PSI
Villigen PSI, Switzerland
- Citterio, A.
- Dehler, M.M.
- Garvey, T.
- Hahn, M.
- Negrazus, M.
- Prat, E.
- Schmidt, T.
- Schulz, L.
- Streun, A.
- Vranković, V.

PTB
Berlin, Germany
- Hoehl, A.

Pulsar Physics
Eindhoven, The Netherlands
- de Loos, M.J.
- van der Geer, S.B.

QST
Tokai, Japan
- Hajima, R.

ISBN: 978-3-95450-206-6

RI Research Instruments GmbH
Bergisch Gladbach, Germany
- Sharma, G.

RIKEN SPring-8 Center
Sayo-cho, Sayo-gun, Hyogo, Japan
- Tanaka, H.

Sapienza University of Rome
Rome, Italy
- Mostacci, A.

Sigmaphi
Vannes, France
- Cosson, O.
- Forest, F.
- Jivkov, P.
- Lancelot, J.L.

SINAP
Shanghai, People's Republic of China
- Chen, H.J.
- Chen, J.
- Deng, H.X.
- Fang, W.
- Feng, C.
- Gao, B.
- Jiang, B.C.
- Leng, Y.B.
- Li, K.
- Wang, D.
- Wang, X.F.
- Yan, Y.B.
- Zeng, L.
- Zhang, K.Q.
- Zhou, W.M.

SLAC
Menlo Park, California, USA
- Bauer, J.
- Boyes, M.
- Chao, A.
- Clarke, C.I.
- England, R.J.
- Feng, Y.
- Fisher, A.S.
- Huang, X.
- Huang, Z.
- Kadyrov, R.A.
- Liu, J.C.
- Marinelli, A.
- Mayes, C.E.
- Pellegrini, C.
- Ratner, D.F.
- Raubenheimer, T.O.
- Robert, A.R.
- Rodriguez, E.
- Rowen, M.
- Santana-Leitner, M.
- Stupakov, G.
- Tao, F.
- Welch, J.J.
- Xiao, S.
- Zhou, F.

SLRI
Nakhon Ratchasima, Thailand
- Chanwattana, T.
- Juntong, N.
- Kittimanapun, K.
- Klysubun, P.
- Pulampong, T.
- Sudmuang, P.

SOLEIL
Gif-sur-Yvette, France
- André, T.
- Andriyash, I.A.
- Berteaud, P.
- Blache, F.
- Bouvet, F.
- Briquez, F.
- Brunelle, P.
- Béchu, N.
- Couprie, M.-E.
- Da Silva Castro, J.
- Dietrich, Y.
- Dubuisson, J.M.
- Duval, J.P.
- Ghaith, A.
- Herbeaux, C.
- Hubert, N.
- Idam, J.
- Kitegi, C.A.
- Labat, M.
- Leclercq, N.
- Lepage, F.
- Lestrade, A.
- Loulergue, A.
- Louvet, M.
- Marcouillé, O.
- Marteau, F.
- Mary, A.
- Nadji, A.
- Nadolski, L.S.
- Nagaoka, R.
- Oumbarek, D.
- Rommeluère, P.
- Roussel, E.
- Sebdaoui, M.
- Somogyi, A.
- Tavakoli, K.T.
- Tilmont, M.
- Tordeux, M.-A.
- Valléau, M.
- Vétéran, J.
- Weitkamp, T.

ISBN: 978-3-95450-206-6

SSRF
Shanghai, People's Republic of China
- Cao, S.S.
- Chen, F.Z.
- Lai, L.W.
- Leng, Y.B.
- Yan, Y.B.
- Zhou, W.M.

STFC/DL/ASTeC
Daresbury, Warrington, Cheshire, United Kingdom
- Angal-Kalinin, D.
- Brynes, A.D.
- Clarke, J.A.
- Cowie, L.S.
- Dunning, D.J.
- Goudket, P.
- Jackson, F.
- Jones, J.K.
- McIntosh, P.A.
- Militsyn, B.L.
- Moss, A.J.
- Muratori, B.D.
- Smith, S.L.
- Surman, M.
- Thompson, N.
- Wheelhouse, A.E.
- Williams, P.H.

The University of Melbourne
Melbourne, Victoria, Australia
- Charles, T.K.

TUB
Beijing, People's Republic of China
- Deng, X.J.
- Huang, W.-H.
- Lu, W.
- Rui, T.
- Tang, C.-X.

UCLA
Los Angeles, California, USA
- Rosenzweig, J.B.

UMAN
Manchester, United Kingdom
- Owen, H.L.

University of Hamburg
Hamburg, Germany
- Maier, A.R.

UNN
Nizhny Novgorod, Russia
- Savilov, A.V.

Uppsala University
Uppsala, Sweden
- Jacewicz, M.

USTC/NSRL
Hefei, Anhui, People's Republic of China
- Bai, Z.H.
- Liu, X.Y.
- Lu, P.
- Luo, Q.
- Sun, B.G.
- Tang, L.L.
- Wang, L.
- Wang, Q.
- Wei, J.H.
- Wu, F.F.
- Yang, Y.L.
- Zhou, T.Y.
- Zhou, Z.R.

USTRAT/SUPA
Glasgow, United Kingdom
- Cross, A.W.
- M^{c}Neil, B.W.J.

VDL ETG
Eindhoven, The Netherlands
- Priem, J.M.A.

XFEL. EU
Hamburg, Germany
- Geloni, G.
- Li, Y.
- Pflüger, J.
- Serkez, S.
- Tomin, S.I.